ELSEVIER

Contents lists available at SciVerse ScienceDirect

# Chemical Engineering and Processing: Process Intensification

journal homepage: www.elsevier.com/locate/cep



# Reactive distillation for synthesis of glycerol carbonate *via* glycerolysis of urea



Noppon Lertlukkanasuk<sup>a</sup>, Satit Phiyanalinmat<sup>b</sup>, Worapon Kiatkittipong<sup>c</sup>, Amornchai Arpornwichanop<sup>a</sup>, Farid Aiouache<sup>d</sup>, Suttichai Assabumrungrat<sup>a,\*</sup>

- <sup>a</sup> Department of Chemical Engineering, Faculty of Engineering, Chulalongkorn University, Bangkok 10330, Thailand
- <sup>b</sup> Department of Industrial Chemistry, Faculty of Science, Chiang Mai University, Chiang Mai 50200, Thailand
- c Department of Chemical Engineering, Faculty of Engineering and Industrial Technology, Silpakorn University, Nakhon Pathom 73000, Thailand
- d School of Chemistry and Chemical Engineering, Queen's University Belfast, Belfast BT9 5AG, Northern Ireland, United Kingdom

# ARTICLE INFO

# Article history: Received 23 January 2013 Received in revised form 30 April 2013 Accepted 1 May 2013 Available online 9 May 2013

Keywords: Glycerol Glycerol carbonate Reactive distillation Glycerolysis of urea

## ABSTRACT

This study developed a new process for synthesis of glycerol carbonate *via* glycerolysis of urea by reactive distillation. Missing thermodynamic parameters were estimated by various group contribution methods. The results of Gibbs free energy showed that Gani's method provided the lowest deviation. Equilibrium and kinetic model parameters of the glycerolysis obtained from batch experiments were employed for the simulation of the reactive distillation using Aspen Plus® software. High conversion of glycerol was achieved by reducing reactant loss in distillate through an increase in the number of stripping and reaction stages and a decrease in the number of rectifying stages. Moreover, glycerol and urea in distillate were recycled to the reactive section by increasing reflux ratio to a reasonable value. The suitable design and operating parameters were achieved at 3 stripping stages, 3 reactive stages, no rectifying stage, reboiler heat duty of 15 kW and reflux ratio of 2. This offered 93.6% conversion of glycerol, and 90.0% yield of glycerol carbonate with 100% purity in the final product. Compared with conventional *in vacuo* process, reactive distillation promoted glycerol conversion by 29.1% and saved in energy consumption by 37.1%.

© 2013 Elsevier B.V. All rights reserved.

# 1. Introduction

Nowadays, biodiesel is becoming an important renewable fuel for transportation sector. Biodiesel can be produced from many feedstocks but its production typically leads to the same by-product of glycerol. Glycerol is produced with the amount as one-tenth of biodiesel production. Most glycerol is removed from the biodiesel product during a purification process. At the present, the amount of glycerol produced for industrial utilization globally is around 160,000 tonnes per year and this amount is increasing at an annual rate of 2.8% [1]. On the other hand, the biodiesel production capacity in Europe is around 9.6 million tonnes per year and this capacity is increasing at an annual rate of 5.5% [2]. Therefore, a glut of glycerol is expected in a near future. On account of the rapid decrease in its price, new uses are being developed for glycerol to substitute petrochemical-based materials [3] and petroleum fuel [4,5].

Glycerol carbonate (4-hydroxymethyl-1,3-dioxolan-2-one) is an important derivative of glycerol as well as a new high value-added product. Glycerol carbonate is a colourless protic polar liquid,

non-toxic, low evaporation rate, low flammability, and high boiling point. Glycerol carbonate can be used for many applications *e.g.* a solvent for plastics and resins, additive in lithium battery, liquid membrane for carbon dioxide and nitrogen separations and a precursor for the production of polyesters, polyurethane, and polycarbonate [1].

Glycerol carbonate can be produced from glycerol by different routes. The reaction of glycerol with phosgene generates glycerol carbonate [6]. Phosgene, however, is very toxic. Glycerol carbonate can also be prepared by reaction of glycerol with cyclic carbonate such as propylene carbonate or ethylene carbonate [7]. Ethylene carbonate, however, is not a cost-effective reagent. Another route for producing glycerol carbonate is from the conversion of glycerol with carbon dioxide which suffers, however, from the drawback of high pressure operation and low conversion owing to its thermodynamic limitation [8-10]. In addition, glycerol carbonate can be prepared by the reaction between glycerol and dimethyl carbonate but requires high ratio of dimethyl carbonate to glycerol. In addition, it needs the chemical reaction equilibrium to be shifted and an expensive lipase catalyst [11]. An alternative route is the glycerolysis of urea. Glycerol and urea are both affordable reagents and easily available [12].

Normally, the glycerolysis of urea has to be operated under a vacuum condition or a sweeping gas to eliminate the by-product

Abbreviations: GC, glycerol carbonate; Gly, glycerol; p, product; r, reactant.

<sup>\*</sup> Corresponding author. Tel.: +66 22 186868; fax: +66 22 186877. E-mail address: Suttichai.A@chula.ac.th (S. Assabumrungrat).

ammonia, to shift the chemical equilibrium towards the products [13]. Moreover, to our knowledge, previous works on the glycerolysis of urea have been performed in batch operation making it difficult to be applied to industrial scale [14–16]. Another difficulty is the use of traditional soluble catalysts such as zinc sulfate causing additional costs towards catalyst recovery and product purification. Limited works have used heterogeneous catalysts. For example,  $\gamma$ -zirconium phosphate was employed at a pressure of 20 Pa, 140 °C and 1.5 h where the conversion achieved 80% and the selectivity achieved high values [12].

This research develops a new process to synthesize glycerol carbonate *via* glycerolysis of urea at atmospheric pressure and continuous operation by combination of reaction and separation units in a single reactive distillation column. The thermodynamic chemical equilibrium of the reaction is expected to be shifted by reducing the by-product ammonia in the reaction section. The effects of design and operating variables on the conversion of glycerol and both the yield and purity of glycerol carbonate will be discussed. The benefits of reactive distillation over conventional *in vacuo* system for glycerolysis of urea are elucidated in both reaction performance and energy efficient.

#### 2. Materials and methods

# 2.1. Estimation of missing parameters

Thermodynamic parameters of glycerol carbonate such as Gibbs free energy of formation cannot be obtained from the literature. Therefore, missing properties of glycerol carbonate were estimated by the group contribution methods such as Joback's method, Gani's method and Benson's method. The percent deviations of some known physical properties were compared between different methods to select the appropriate one for glycerol carbonate.

# 2.2. Batch reaction procedures

 ${\rm Co_3O_4/ZnO}$  was prepared by dry nanodispersion method [17]. 40 ml (0.55 mol) of glycerol (99.5%), 32.9 g (0.55 mol) of urea (99.5%) and 0.7566 g of  ${\rm Co_3O_4/ZnO}$  (urea/glycerol molar ratio = 1, catalyst load of 1.5% by weight with respect to glycerol) were mixed in the autoclave reactor. The impeller, sampling port and thermocouple were installed in a reactor. The mixture was stirred at 1163 rpm to reduce external mass transfer limitations and then was heated in an oil bath at selected reaction temperature under atmospheric pressure. The catalyst was separated from the liquid products by centrifugation. The reaction mixture was analysed by gas chromatography equipped with ZB-5HT capillary column and a flame ionization detector (FID).

# 2.3. Reactive distillation simulation

The simulations were carried out by using the RADFRAC module in the commercial Aspen Plus® software to predict the glycerol conversion, glycerol purity and yield in a reactive distillation column. On each stage of the column, vapor–liquid equilibrium was

assumed to be established using NRTL model while the reaction model is rate based using kinetic rate expression obtained from this study. Pressure drops were considered negligible along the column [18]. The Aspen Plus component database provided physical and chemical properties of all species except those of glycerol carbonate. The effects of design and operating variables including number of rectifying stage, stripping stage, reaction stage, reflux ratio and reboiler heat duty on the reactive distillation performance were studied. The results of reactive distillation simulation were compared with those from conventional method to synthesize glycerol carbonate under similar feed conditions. The conventional method, where ammonia is removed during the reaction *in vacuo*, was investigated to determine the conversion of glycerol, yield and purity of glycerol carbonate and their energy consumption for comparison.

# 3. Results and discussion

# 3.1. Equilibrium thermodynamic analysis

In order to prevent NH<sub>3</sub> escaping from liquid to vapor phase which lead to shift reaction equilibrium, the reaction was performed in a closed system and the volume of head space of the reactor is needed to be minimized. The equilibrium constant for synthesis of glycerol carbonate from the reaction between glycerol and urea based on equilibrium mole fraction of components in liquid phase at equilibrium conditions could be shown below:

$$K_{\text{eq}} = \frac{(x_{\text{GC}}) \cdot (x_{\text{NH}_3})^2}{(x_{\text{GIV}}) \cdot (x_{\text{Urea}})} \tag{1}$$

In addition, the theoretical value of equilibrium constant was obtained from the Gibbs free energy of components as shown in Eqs. (2) and (3):

$$\Delta G(T, P) = -RT \ln K_{eq} \tag{2}$$

$$\Delta G^{0} = \sum_{p} n_{p} \Delta G_{p}^{0} - \sum_{r} n_{r} \Delta G_{r}^{0}$$
(3)

The appropriate group contribution method was selected based on estimation of known thermodynamic properties of some chemicals with the relevant structures of glycerol carbonate such as propylene carbonate and ethylene carbonate by comparison between known properties from database and those estimated from different methods. The estimated standard Gibbs free energy and percent of deviations are shown in Table 1. The results show clearly that Gani's method [19] provides the lowest percent deviation among the three methods and was in fact in good agreement with cyclic carbonate compounds.

In this study,  $Co_3O_4/ZnO$  was used as catalyst for synthesizing glycerol carbonate [15]. Very high selectivity ca. 100% could be obtained in our system. It could be confirmed, herein, by using  $^{14}C$  NMR analysis that only signals of glycerol and glycerol carbonate were presented [12] (result not shown). Accordingly,

**Table 1**Standard Gibbs free energy from database and estimated values by group contribution methods.

Substances	$\Delta G^{\rm o}$ (kJ/mol) [Aspen Plus data]	Estimated 2	Estimated $\Delta G^{\rm o}$ (kJ/mol)			Deviation (%)			
		Joback	Gani	Benson	Joback	Gani	Benson		
Glycerol carbonate	-	-511.4	-539.3	-480.5	_	_	_		
Glycerol	-484.1	-477.8	-493.5	-480.1	1.30	-1.95	0.82		
Urea	-177.4	-52.1	-165.2	-201.1	70.62	6.89	-13.35		
Ethylene carbonate	-435.2	-360.2	-385.5	-325.7	17.23	11.42	25.17		
Propylene carbonate	-478.8	-361.2	-383.7	-256.7	24.56	19.87	46.39		

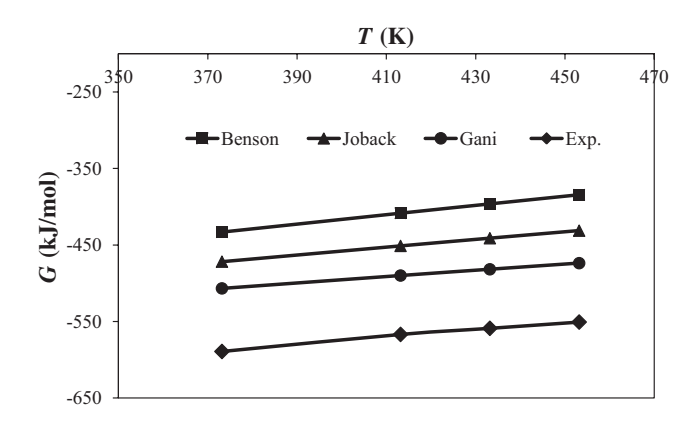


**Fig. 1.** Comparison of Gibbs free energy of glycerol carbonate from experimental results and estimated results by the group contribution methods.

determination of the reaction model parameters was performed based on the main reaction pathway as shown below:

$$Glycerol_{(1)} + Urea_{(1)} \leftrightarrow Glycerol\ carbonate_{(1)} + 2NH_{3(1)}$$
 (4)

The reaction model parameters were determined by fitting the model in Eq. (3) with the experimental data at different temperatures including 373, 413, 433 and 453 K. Fig. 1 illustrates the comparison of Gibbs free energy of glycerol carbonate at different temperatures from the experimental results and the estimated results by the group contribution methods. The results show that the Gibbs free energy of glycerol carbonate as a function of temperature had similar trend with the estimated results. Gani's method provided the best estimation among the three methods agreeing with the results in the estimation of missing parameters section. In addition, a fitting model by least square method using Matlab software for the equilibrium constant as a function of temperature is presented in Eq. (5):

$$\ln K_{\text{eq}} = -8041 + 291,370 \left(\frac{1}{T}\right) + 1316.80 \ln(T) + -1.4475(T)$$
(5)

# 3.2. Kinetic study

Polymath 5.1 software was used to fit the experimental data to the kinetic model and determine the kinetic rate constants. The rate expressions  $(r_i)$  could be written as:

$$-r_{\text{Gly}} = -r_{\text{Urea}} = r_{\text{GC}} = \frac{r_{\text{NH}_3}}{2} = k \left( x_{\text{Gly}} x_{\text{Urea}} - \frac{x_{\text{NH}_3}^2 x_{\text{GC}}}{K_{\text{eq}}} \right)$$
 (6)

The regressed temperature-dependent rate constants according to Arrhenius' equation are illustrated in Fig. 2. The rate expression could be determined as

$$k = \exp(1.194 - 3836/T) \tag{7}$$

where  $E_a = 31.89 \text{kJ} \text{ mol}^{-1}$ .

As shown in Fig. 3, the reaction model was in good agreement with experimental data.

# 3.3. Simulation of the glycerol carbonate synthesis process

# 3.3.1. Conventional method for synthesis of glycerol carbonate

The conventional method for synthesis of glycerol carbonate comprised a reactor operated with a sweep gas such as air to remove ammonia *in vacuo* and a distillation column as shown in Fig. 4. The developed kinetic model of the reaction was used to

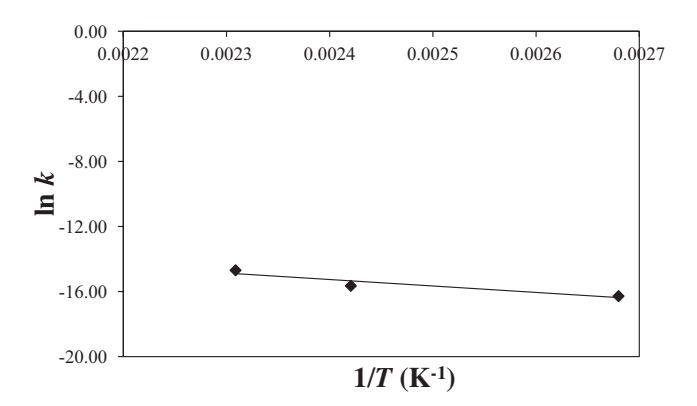
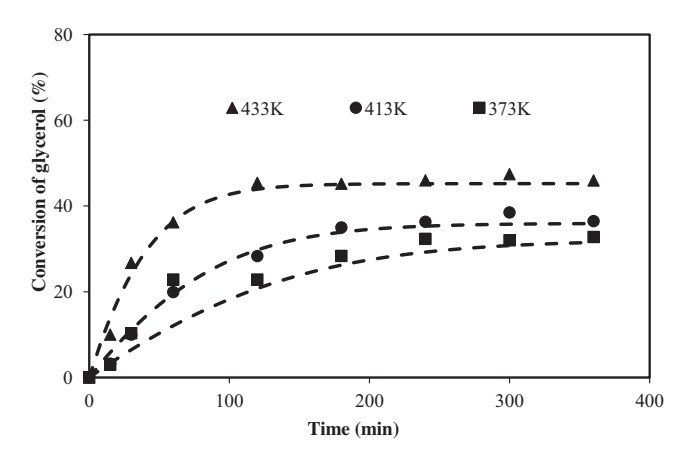


Fig. 2. Arrhenius's plots.



**Fig. 3.** Conversion of glycerol at different temperatures (symbols: experimental results and dashed line: reaction model).

predict the reaction using  $\text{Co}_3\text{O}_4/\text{ZnO}$  as a catalyst. The reaction conditions were selected based on the work of Rubio-Marcos et al. [15]. A specification of reactor, distillation column and operational parameters of conventional *in vacuo* process are summarized in Table 2. The configuration of distillation column was proposed as the minimum heat duty requirement to obtain 100% purity of glycerol carbonate in the bottom product.

The simulation results of the conventional process for synthesis of glycerol carbonate are shown in Table 3. The results show that 72.52% conversion of glycerol could be achieved from this

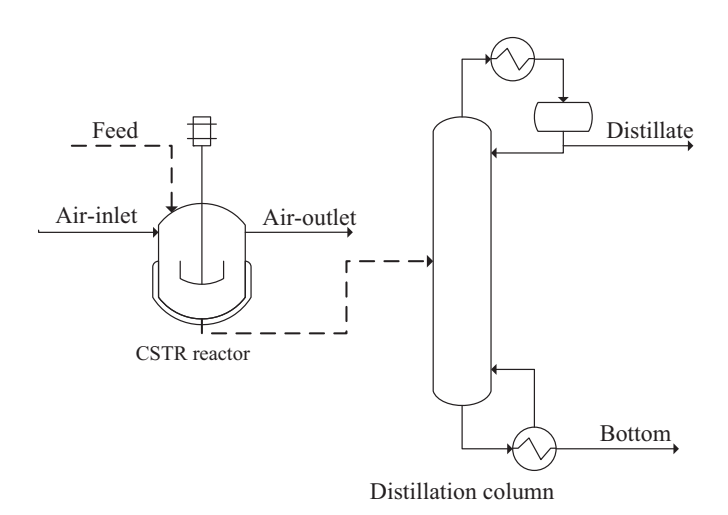


Fig. 4. Conventional process for synthesis of glycerol carbonate.

**Table 2**Specification of reactor, distillation column and operational parameters of conventional *in vacuo* process.

Feed conditions		Reactor conditions		Column specifications	
Glycerol feed flow rate (mol/h)	100	Pressure (bar)	1	Rectifying stages	3
Urea feed flow rate (mol/h)	100	Temperature (K)	418	Reaction stages	0
Temperature (K)	298	Residence time (h)	4	Stripping stages	2
Pressure (bar)	1	Net heat duty (kW)	4.68	Total stages (include condenser and reboiler)	7
				Reflux ratio	2
				Reboiler heat duty (kW)	18.01
				Pressure (bar)	1
				Bottom flow rate (mol/h)	74.91
				Distillate flow rate (mol/h)	42.12
				Feed location	Stage 4
				Type of condenser	Partial vapor-liquid

simulation which corresponds to the experimental results from Rubio-Marcos et al. [15] at the same conditions (69% conversion of glycerol). A distillation column was used to separate glycerol carbonate from the reaction mixture. Unreacted glycerol and urea were obtained in the distillate stream due to their lower boiling points. In addition, 100% high purity of glycerol carbonate could be obtained in the bottom stream.

# 3.3.2. Reactive distillation study

The aim of this section is to apply reactive distillation for synthesis of glycerol carbonate to achieve higher conversion and lower energy consumption than the conventional process.

The reaction performance including conversion of glycerol, yield and purity of glycerol carbonate were considered. The conversion of glycerol ( $X_{\rm Gly}$ ) and yield of glycerol carbonate ( $Y_{\rm GC}$ ) were defined as follows:

of glycerol carbonate owing to more urea and glycerol escaping through the distillate.

The effects of the number of reaction stages on the conversion of glycerol and purity of glycerol carbonate in the bottom stream are shown in Figs. 5 and 6. The results show that conversion of glycerol and purity of glycerol carbonate in bottom stream were enhanced with increasing the number of reaction stages and became constant at 3 reaction stages due to increasing the residence time.

The effect of heat duty of reboiler with different reflux ratios on the conversion of glycerol and purity of glycerol carbonate in bottom stream are illustrated in Figs. 7 and 8. At any reflux ratio, the conversion of glycerol and purity of glycerol carbonate increased as heat duty of reboiler was increased. This could occur because temperature in the reactive section increased driving more glycerol and urea from the stripping section to the reactive one. However, increasing more reboiler heat duty had negative effect on

$$X_{\text{Gly}} = \frac{\text{Difference in molar flow rates of glycerol between inlet and outlet streams} \times 100}{\text{Feed flow rate of glycerol}}$$
(8)

$$Y_{GC} = \frac{\text{Molar flow rate of glycerol carbonate in the bottom stream} \times 100}{\text{Difference in molar flow rates of glycerol between inlet and outlet streams}}$$
(9)

The effect of the number of stripping stages on the conversion of glycerol and purity of glycerol carbonate in the bottom stream was investigated as shown in Fig. 5. It shows that the conversion of glycerol and the purity of glycerol carbonate increased by increasing the number of stripping stages from 1 to 3 reaction stages. Even though the temperature of the reaction zone decreased slightly with increasing the number of stripping stages lead to the reduction of kinetic rates, however, higher glycerol carbonate purity can be obtained at the bottom of column and therefore the chemical equilibrium shifts towards the products.

The effect of the number of rectifying stages on the conversion of glycerol and purity of glycerol carbonate is shown in Fig. 6. The rectifying section was provided to remove a light component from the reactive section. It is clear that increasing the number of rectifying stages caused a slight decrease in conversion of glycerol and purity

conversion of glycerol as both reactants were displaced towards the rectifying section or distillate and vapor stream. The purity of glycerol carbonate and conversion of glycerol increased by increasing reflux ratio owing to higher concentration of glycerol and urea recycled in the reactive section. High purity (100%) of glycerol carbonate in bottom stream could be obtained with reflux ratio of 2 and no improvement of glycerol conversion with reflux ratio higher than 2.

According to the simulation results, the suitable design and operating variables for synthesis glycerol carbonate *via* glycerolysis of urea with reactive distillation for the used glycerol and urea feed flow rate of 100 mol/h are summarized in Table 4.

Mole fraction profiles of the components in the reactive distillation column with suitable conditions are shown in Fig. 9. It

**Table 3**Process streams of simulation results of glycerol carbonate synthesis *via* conventional *in vacuo* process.

	FEED	R-OUT	DIST	BOTT	AIR-IN	AIR-OUT
Temperature (K)	298	418	407	626	298	418
Pressure (bar)	1.00	1.00	1.00	1.00	1.00	1.00
Vapor fraction	0.00	0.00	0.00	0.00	1.00	1.00
Mole flow (mol/h)	200.00	119.32	47.34	71.98	100.00	253.20
Mole fraction						
Glycerol	0.50	0.23	0.57	0.00	0.00	0.00
Urea	0.50	0.16	0.40	0.00	0.00	0.03
Ammonia	0.00	0.00	0.01	0.00	0.00	0.57
Glycerol carbonate	0.00	0.61	0.02	1.00	0.00	0.00
Air	0.00	0.00	0.00	0.00	1.00	0.39

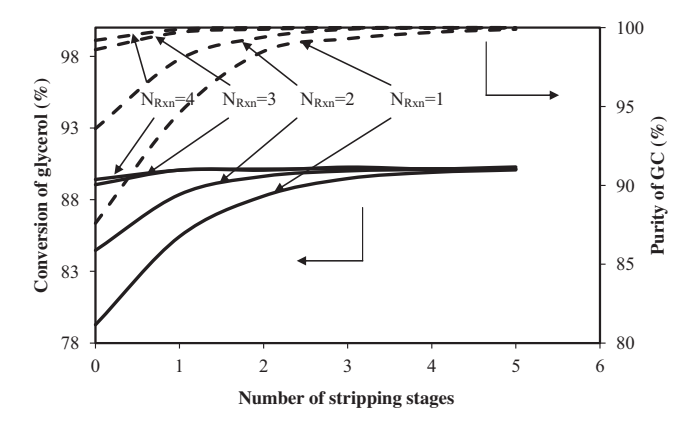


**Fig. 5.** Effect of number of stripping stages on conversion of glycerol and purity of glycerol carbonate in bottom stream (rectifying: 1 stage).

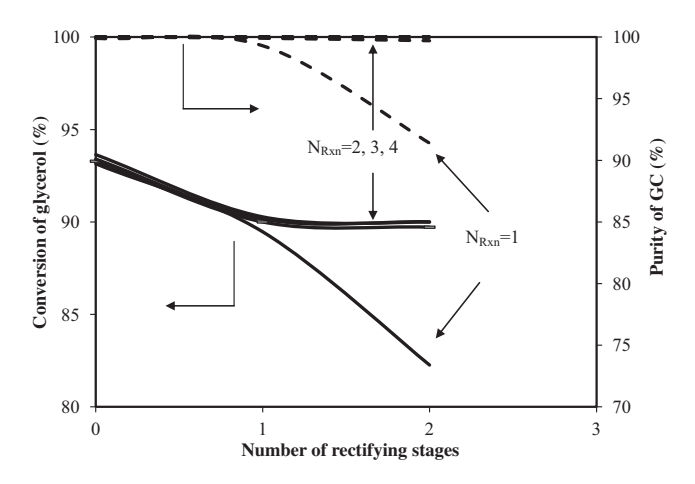


**Fig. 6.** Effect of number of rectifying stages on conversion of glycerol and purity of glycerol carbonate in bottom stream (stripping: 3 stages).

is worth to note that under the suitable condition, the value of glycerol carbonate yield of 90.0% can be obtained (represented by glycerol carbonate obtained in the bottom stream). This value is close to glycerol conversion (93.6%). This indicates that the glycerol carbonate which was lost in the distillate could be minimized. Temperature profile in the reactive distillation column at suitable conditions is illustrated in Fig. 10. Temperature of reboiler and condenser are 626 and 404 K, respectively. Temperature slightly decreased in the reaction section due to the mild endothermic reaction. The equilibrium model used in this study has been employed with success for preliminary design [18,20]. A more rigorous nonequilibrium model including the hydrodynamic, mass transfer and

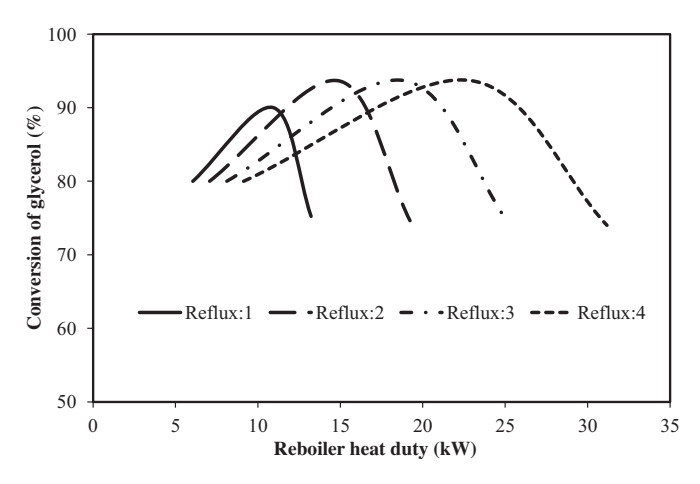


**Fig. 7.** Effect of heat duty of reboiler on the conversion of glycerol at various reflux ratio (stripping: 3 stages, reaction: 3 stages and without rectifying stage).

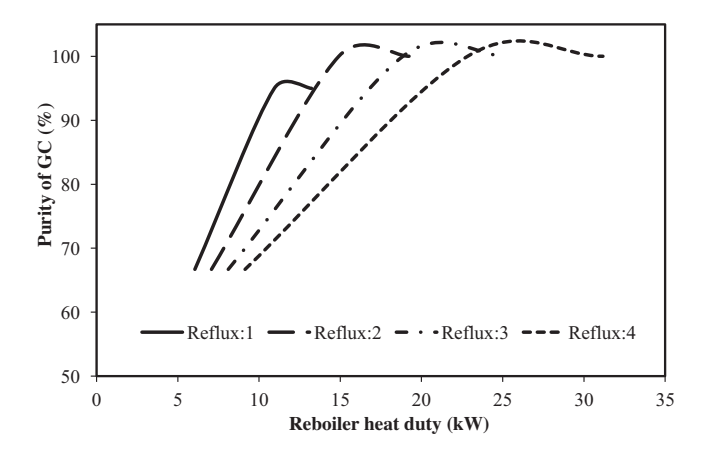


**Fig. 8.** Effect of heat duty of reboiler on purity of glycerol carbonate in bottom stream at various reflux ratio (stripping: 3 stages, reaction: 3 stages and without rectifying stage).

heat transfer effects, which requires detailed knowledge of column internals and flow dynamics, is being tested with experimental validation [20].

The comparison of glycerol carbonate synthesis by reactive distillation and conventional *in vacuo* process at similar feed conditions and outlet purity of glycerol carbonate are summarized in Table 5. The results show that higher conversion of glycerol (93.6%) could be achieved by using the reactive distillation compared with the 72.5% conversion for the conventional method. This could occur because the reactive distillation shifted effectively

**Table 4**Column configuration and operational parameters of reactive distillation.

Feed conditions		Column specifications	
Glycerol feed flow rate (mol/h)	100	Rectifying stages	0
Urea feed flow rate (mol/h)	100	Reaction stages	3
Temperature (K)	298	Stripping stages	3
Pressure (bar)	1	Total stages (include condenser and reboiler)	8
,		Reflux ratio	2
		Reboiler heat duty (kW)	15
		Pressure (bar)	1
		Bottom flow rate (mol/h)	90
		Distillate flow rate (mol/h)	12.2
		Feed location of glycerol	Stage 2
		Feed location of urea	Stage 5
		Type of condenser	Partial vapor–liquid
		Type of Reboiler	Kettle
		Liquid hold up in rxn. section (kg)	0.5

**Table 5**Comparison of glycerol carbonate synthesis by reactive distillation and conventional *in vacuo* process.

Method	% purity of glycerol carbonate	% conversion of glycerol	Overall energy consumption/mole GC (kW/mol GC)
Reactive distillation	100	93.6	0.215
Conventional <i>in vacuo</i> process	100	72.5	0.342

equilibrium reaction by combination reaction and separation unit that could remove ammonia in vapor phase to the top of column and introduce glycerol carbonate to the bottom of column by stripping section. Furthermore, the residues of glycerol and urea in the distillate could be recycled to the reactive section by controlling reflux ratio of the column. An overall energy consumption which includes the reboiler duty in reactive distillation or distillation and vacuum pump in conventional process, are shown in Table 5. The results show that the overall energy consumption per mole of glycerol carbonate produced in reactive distillation is lower than that of conventional reactor. The design of reactive distillation is therefore significantly cost-effective than the conventional process [21] while lower degrees of freedom from the combination of reaction and separation resulting in more difficult in controllability and narrower operability region [22].

In summary, it can be said that synthesis of glycerol carbonate by using reactive distillation could be carried out continuously under atmospheric operation leading to a reduction of plant operating costs and energy consumption, which can increase its potential industrial application.

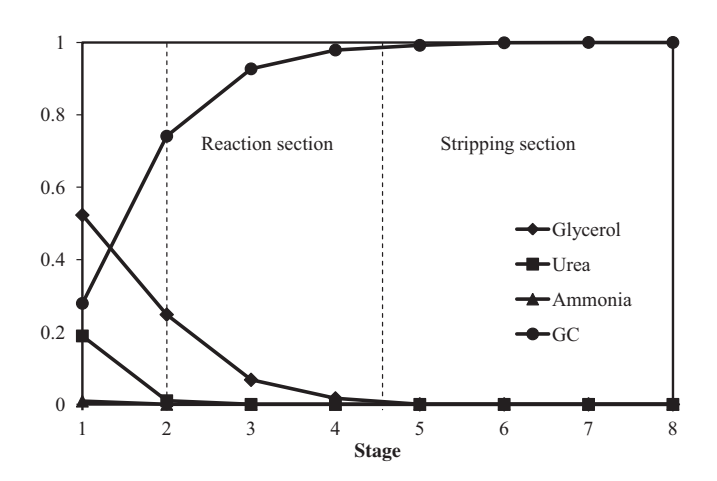


Fig. 9. Mole fraction profiles of the components in the reactive distillation column.

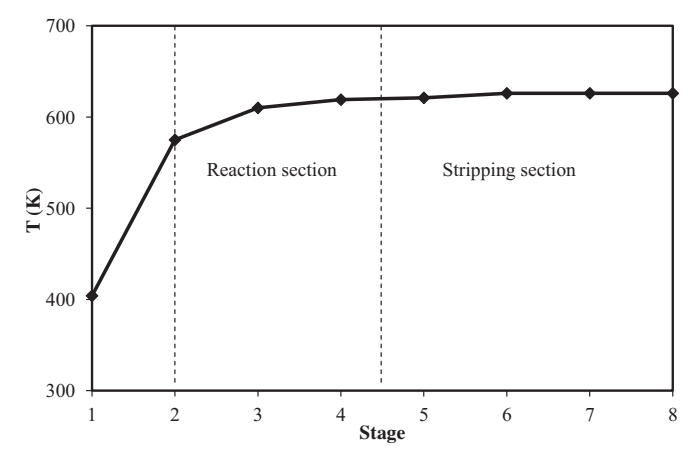


Fig. 10. Temperature profile in the reactive distillation column.

## 4. Conclusion

This work investigated the glycerolysis of urea by a promising process of reactive distillation. The reaction model parameters were determined experimentally from batch reactor tests and were employed for the simulation study of reactive distillation process. Missing parameters of glycerol carbonate were studied by group contribution methods including Benson's, Joback's and Gani's methods. It was found that Gani's method estimated the Gibbs free energy values closed to the available database and our experimental results. The suitable design and operating variables for synthesis glycerol carbonate by using reactive distillation were found as no rectifying stage, 3 reactive stage, 3 stripping stages, reflux ratio of 2 and reboiler heat duty of 15 kW for each glycerol and urea feed flow rate of 100 mol/h. From this configuration, 93.6% conversion of glycerol, 90.0% yield and 100% purity of glycerol carbonate were achieved. The synthesis of glycerol carbonate from the reaction between glycerol and urea by using reactive distillation was compared with a conventional in vacuo process. Based on the same feed conditions, reactive distillation provided higher conversion of glycerol and lower energy consumption than the conventional method.

# Acknowledgement

The authors gratefully acknowledge the support from the Thailand Research Fund.

pre-exponential factor of Arrhenius's plot (mol min<sup>-1</sup> g-

# Appendix A. Notations

Α

 $cat^{-1}$ )  $E_a$ activation energy (kJ mol<sup>-1</sup>) G Gibbs free energy (kJ mol $^{-1}$ )  $G^0$ standard Gibbs free energy (kJ mol-1)  $k^{+}$ reaction rate constant (mol min<sup>-1</sup> g-cat<sup>-1</sup>) equilibrium constant  $K_{eq}$ n number of mole (mol)  $N_{Rxn}$ number of reaction stage (stage) reaction rate of component i (mol min<sup>-1</sup> g-cat<sup>-1</sup>)  $r_i$ R gas constant (kJ  $mol^{-1} K^{-1}$ ) T temperature (K)  $x_i$ mole fraction of component i X conversion (%) yield (%)

# References

- [1] M. Pagliaro, M. Rossi, The Future of Glycerol: New Uses of a Versatile Raw Material, RSC Publishing, Cambridge, 2008, pp. 78–79.
- [2] European Biodiesel Board (EBB), EU Biodiesel Industry Production Forecasts. (Press release, October 18th, 2011), 2010–2011.
- [3] D.T. Johnson, K.A. Taconi, The glycerin glut: options for the value-added conversion of crude glycerol resulting from biodiesel production, Environmental Progress 26 (2007) 338–348.
- [4] N. Rahmat, A.Z. Abdullah, A.R. Mohamed, Recent progress on innovative and potential technologies for glycerol transformation into fuel additives: a critical review, Renewable & Sustainable Energy Reviews 14 (2010) 987–1000.

- [5] W. Kiatkittipong, S. Suwanmanee, N. Laosiripojana, P. Praserthdam, S. Assabumrungrat, Cleaner gasoline production by using glycerol as fuel extender, Fuel Processing Technology 91 (2010) 456–460.
- [6] J.J. McKetta (Executive Ed.), W.A. Cunningham (Associate Ed.), Encyclopedia of Chemical Processing and Design, vol. 20, Marcel Decker, New York, 1984, pp. 177.
- [7] Z. Mouloungui, J.W. Yoo, C.-A. Gachen, A. Gaset, to Organisation Nationale Interprofessionnelle Des Oleagineux-Onidol, Fr., Eur. Pat. EP0739888 (1996).
- [8] C. Vieville, J.W. Yoo, S. Pelet, Z. Mouloungui, Synthesis of glycerol carbonate by direct carbonation of glycerol in supercritical CO<sub>2</sub> in the presence of zeolites and ion exchange resins, Catalysis Letters 56 (1998) 245–247.
- [9] J. George, Y. Patel, S.M. Pillai, P. Munshi, Methanol assisted selective formation of 1,2-glycerol carbonate from glycerol and carbon dioxide using nBu<sub>2</sub>SnO as a catalyst, Journal of Molecular Catalysis A: Chemical 304 (2009) 1–7.
- [10] M. Aresta, A. Dibenedetto, F. Nocito, C. Pastore, A study on the carboxylation of glycerol to glycerol carbonate with carbon dioxide: the role of the catalyst, solvent and reaction conditions, Journal of Molecular Catalysis A: Chemical 257 (2006) 149–153.
- [11] S.C. Kim, Y.H. Kim, H. Lee, D.Y. Yoon, B.K. Song, Lipase-catalyzed synthesis of glycerol carbonate from renewable glycerol and dimethyl carbonate through transesterification, Journal of Molecular Catalysis B: Enzymatic 49 (2007) 75–78.
- [12] M. Aresta, A. Dibenedetto, F. Nocito, C. Ferragina, Valorization of bio-glycerol: new catalytic materials for the synthesis of glycerol carbonate via glycerolysis of urea, Journal of Catalysis 268 (2009) 106–114.
- [13] J. Li, T. Wang, Coupling reaction and azeotropic distillation for the synthesis of glycerol carbonate from glycerol and dimethyl carbonate, Chemical Engineering and Processing 49 (2010) 530–535.

- [14] A. Behr, J. Eilting, K. Irawadi, J. Leschinski, F. Lindner, Improved utilisation of renewable resources: new important derivatives of glycerol, Green Chemistry 10 (2008) 13–30.
- [15] F. Rubio-Marcos, V. Calvino-Casilda, M.A. Banares, J.F. Fernandez, Novel hierarchical Co<sub>3</sub>O<sub>4</sub>/ZnO mixtures by dry nanodispersion and their catalytic application in the carbonylation of glycerol, Journal of Catalysis 275 (2010) 288–293
- [16] M.J. Climent, A. Corma, P. De Frutos, S. Iborra, M. Noy, A. Velty, P. Concepcion, Chemicals from biomass: synthesis of glycerol carbonate by transesterification and carbonylation with urea with hydrotalcite catalysts. The role of acid-base pairs, Journal of Catalysis 269 (2010) 140–149.
- [17] J.F. Fernández, I. Lorite, F. Rubio-Marcos, J.J. Romero, M.A. García, A. Quesada, M.S. Martín-González, J.L. Costa-Krämer, Patent Numbers WO2010010220-A1; ES2332079-A1, 2010, to Consejo Superior de Investigaciones Científicas, CSIC.
- [18] W. Kiatkittipong, P. Intaracharoen, N. Laosiripojana, C. Chaisuk, P. Praserthdam, S. Assabumrungrat, Glycerol ethers synthesis from glycerol etherification with tert-butyl alcohol in reactive distillation, Computers and Chemical Engineering 35 (2011) 2034–2043.
- [19] L. Constantinou, R. Gani, New group contribution method for estimating properties of pure compounds, AIChE Journal 40 (1994) 1697–1710.
- [20] C. Buchaly, P. Kreis, A. Gorak, Hybrid separation processes—combination of reactive distillation with membrane separation, Chemical Engineering and Processing 46 (2007) 790–799.
- [21] D.B. Kaymak, W.L. Luyben, Quantitative comparison of reactive distillation with conventional multiunit reactor/column/recycle systems for different chemical equilibrium constants, Industrial and Engineering Chemistry Research 43 (2004) 2493–2507.
- [22] D.B. Kaymak, W.L. Luyben, Quantitative comparison of dynamic controllability between a reactive distillation column and a conventional multi-unit process, Computers and Chemical Engineering 32 (2008) 1456–1470.

# Electrochemical promotion of propane oxidation over Pd, Ir, and Ru catalyst-electrodes deposited on YSZ

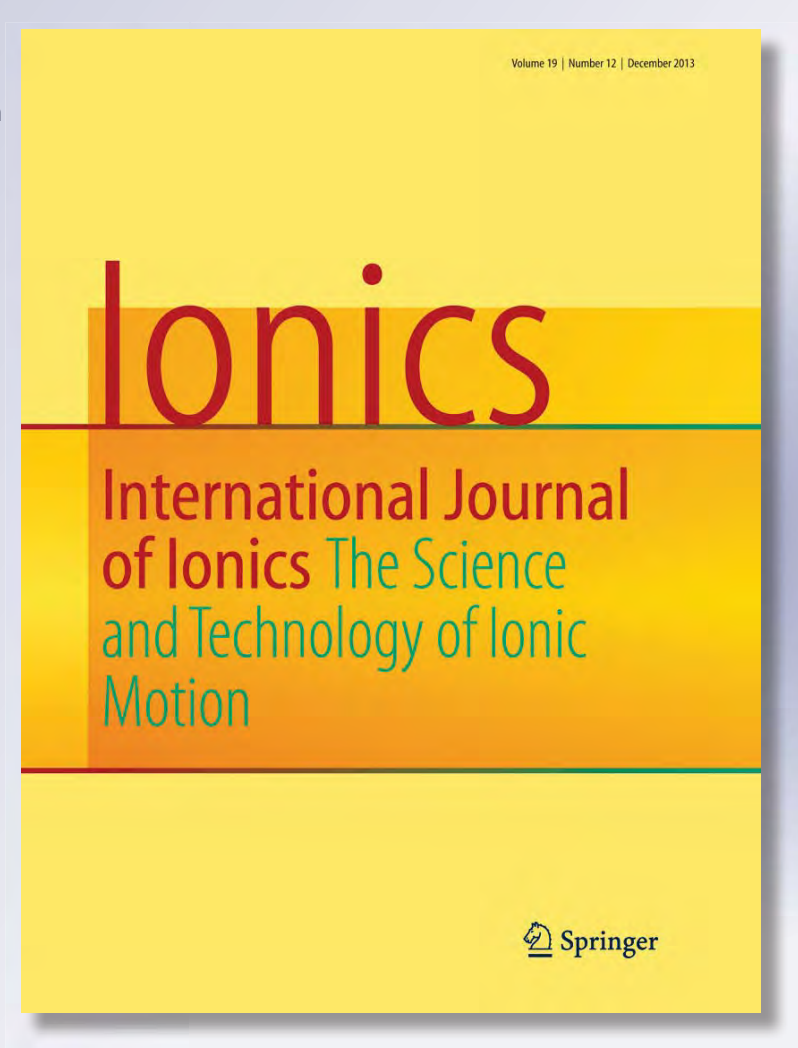
- S. Peng-ont, S. Souentie,
- S. Assabumrungrat, P. Praserthdam,
- S. Brosda & C. G. Vayenas

# **lonics**

International Journal of Ionics The Science and Technology of Ionic Motion

ISSN 0947-7047 Volume 19 Number 12

lonics (2013) 19:1705-1714 DOI 10.1007/s11581-013-0931-0





Your article is protected by copyright and all rights are held exclusively by Springer-Verlag Berlin Heidelberg. This e-offprint is for personal use only and shall not be selfarchived in electronic repositories. If you wish to self-archive your article, please use the accepted manuscript version for posting on your own website. You may further deposit the accepted manuscript version in any repository, provided it is only made publicly available 12 months after official publication or later and provided acknowledgement is given to the original source of publication and a link is inserted to the published article on Springer's website. The link must be accompanied by the following text: "The final publication is available at link.springer.com".



# **ORIGINAL PAPER**

# Electrochemical promotion of propane oxidation over Pd, Ir, and Ru catalyst-electrodes deposited on YSZ

S. Peng-ont · S. Souentie · S. Assabumrungrat · P. Praserthdam · S. Brosda · C. G. Vayenas

Received: 26 March 2013 / Revised: 31 May 2013 / Accepted: 1 June 2013 / Published online: 30 June 2013 © Springer-Verlag Berlin Heidelberg 2013

**Abstract** The effect of electrochemical promotion of catalysis was investigated for the oxidation of propane using Pd, Ir, and Ru catalyst-electrodes sputter-deposited on YSZ disks in the temperature range of 250–450 °C. Electrophobic type behavior was observed, i.e., the catalytic reaction rate was found to increase with catalyst potential. The observed rate changes under polarization were strongly non-Faradaic and exceeded under anodic potential application the electrocatalytic rate of O<sup>2-</sup> supply to the catalyst surface, *I*/2*F*, by up to a factor of 250 for Pd, 125 for Ir, and 15 for Ru catalyst-electrodes.

**Keywords** Propane oxidation · Electrochemical promotion · EPOC · NEMCA · Pd · Ir · Ru · Catalyst-electrode · Yttria-stabilized zirconia

# Introduction

The total oxidation of light hydrocarbon, e.g., methane, ethane, and propane, is an area of very significant importance in heterogeneous catalysis. Noble metal catalysts are known to be the most active catalysts for these systems. Among them, Pd is considered as the best catalyst for light hydrocarbon oxidation; however, the catalytically active chemical state of Pd, under different reaction conditions, is still a matter of discussion [1–5].

The combustion of propane in an electrochemical membrane reactor is a challenging alternative to the conventional

S. Peng-ont · S. Souentie · S. Brosda (△) · C. G. Vayenas LCEP, Department of Chemical Engineering, University of Patras, Patras 26504, Greece e-mail: brosda@chemeng.upatras.gr

S. Peng-ont · S. Assabumrungrat · P. Praserthdam
Center of Excellence in Catalysis and Catalytic Reaction
Engineering, Department of Chemical Engineering, Faculty of
Engineering, Chulalongkorn University, Bangkok, Thailand

catalytic combustion system, especially under conditions of electrochemical promotion where the rate and selectivity of the catalytic reaction can be reversibly modified by externally applying a potential or current between the catalyst-working electrode and a counter electrode. Electrochemical promotion of catalysis (EPOC, or non-Faradaic electrochemical modification of catalytic activity, NEMCA effect) has been investigated thoroughly for more than 120 catalytic systems [6–8], and it has been shown to be due to the electrochemically controlled migration (backspillover/spillover) of promoting or poisoning ionic species  $[O^{\delta-}]$  in case of yttria-stabilized zirconia (YSZ)] between the electrolyte support and the gasexposed catalyst surface. These backspillover species, which are accompanied by their compensating charge,  $\delta^+$ , in the metal, create an overall neutral "effective double layer" which modifies the catalyst work function and thus, its catalytic activity and selectivity [6-8].

When using YSZ as the solid electrolyte, the promoting ionic species  $(O^{\delta^-})$  are generated under positive polarization in an electrochemical step at the metal (M)–electrolyte–gas three-phase boundaries (tpb) at the working electrode:

$$O^{2-}(YSZ) \rightarrow \left[O^{\delta} - \delta^{+}\right](M) + 2e^{-} \tag{1}$$

at a rate I/2F, where I is the current and F the Faraday's constant.

The semi-reaction at the cathode (counter) electrode, where  $O^{2-}$  species are generated is:

$$O_2(g) + 4e^- \rightarrow 2O^{2-}(YSZ)$$
 (2)

Two parameters are commonly used to quantify the magnitude of EPOC effect [6–9]: the rate enhancement ratio,  $\rho$ , defined from:

$$\rho = r/r_0 \tag{3}$$



where  $r_{\rm o}$  is the open circuit, i.e. non-promoted catalytic rate and r the catalytic rate under polarization, and the apparent Faradaic efficiency,  $\Lambda$ , defined from:

$$\Lambda = (r - r_0)/(I/2F) \tag{4}$$

I/2F is equal to the rate of  $O^{2-}$  supply or removal to or from the catalyst-electrode. A reaction exhibits electrochemical promotion when  $\Lambda > 1$ , while electrocatalysis is limited to  $\Lambda \le 1$ .

The application of electrochemical promotion in propane oxidation has recently received increasing attention. Table 1 summarizes the catalytic systems based on O<sup>2-</sup> oxygen ion conductor supports which have been investigated [9–19]. The Pt catalyst-electrodes deposited on YSZ are among the most extensively studied systems, and rate enhancement ratios as a high as 1,450 [13] and 1,350 [16] have been found. As evidenced from Table 1 the mode of metal film preparation and the gas composition strongly affect the maximum measured  $\rho$  values. Permanent EPOC, the phenomenon which is described by the fact that the catalytic rate is not returning to its initial value after current interruption (the catalyst persists in a partially promoted state), is found only for Pt deposited on YSZ [11], where oscillatory behavior has been also observed [13].

At low to medium temperatures, the propane oxidation exhibits mainly electrophobic behavior, i.e., the rate increase under anodic polarization. At higher temperatures, usually higher than 450 °C, inverted-volcano behavior is found since both anodic and cathodic polarization lead to an increase in catalytic rate. Simple and rigorous rules describe the catalyst rate dependence on the applied potential,  $U_{\rm WR}$  on the basis of the unpromoted kinetics [20–23]. Table 1 summarizes the observed catalytic rate dependence on reactants partial pressure. In the case of electrophobic-type behavior, the rate is positive order for propane and negative or near zero order for oxygen.

Recently, Tsampas et al. [10] conducted isotopic-labeled experiments to distinguish the oxygen species coming from the solid electrolyte (promoting ionic oxygen) with those originating from the gas phase during electrochemically promoted propane oxidation. A two-compartment tubular Pt/YSZ electrochemical catalyst was utilized. The reaction compartment was exposed to propane and isotopic oxygen, while the other compartment was fed with air for replenishing the electrolyte with normal oxygen ( $^{16}O_2$ ). Catalytic activity measurements under positive polarizations have confirmed that the oxidation of propane with gaseous oxygen can be strongly electropromoted ( $C^{18}O_2$  production) with total Faradaic efficiencies up to  $\Lambda$ =45, while the  $C^{16}O_2$  production can be only attributed to the (sub)Faradaic electrochemical oxidation of propane ( $\Lambda$ ~1).

Table 1 Kinetic behavior of propane oxidation on metal supported on oxygen ionic conducting supports

Catalyst	Solid electrolyte	$P_{O_2}/P_{C_3H_8}$	T (°C)	$\rho_{\text{max}}$ (>1)	Kinetics in C <sub>3</sub> H <sub>8</sub>	Kinetics in O <sub>2</sub>	Rate vs $U_{\rm WR}$ behavior	Special features	Reference
Pt	YSZ <sup>a</sup>	5–12.5	344–365	2.5	?	_	(/)	Pt nanometric [9], Isotopic labeling [10], permanent EPOC γ=1.3 [11]	[9–12]
Pt	YSZ	0.5–10	350-500	1,400	+	+	(∪)	Comparison to Ag and Pd on YSZ, oscillatory behavior for Pt/YSZ [13]	[13–15]
Pt	YSZ	1-1.25	420-500	1,350	?	?	(∪)	Comparison to Rh on YSZ	[16, 17]
Pt	CGO <sup>b</sup>	11	267–336	<1.5	?	?	(/)	Pt nanoparticles dispersed in conductive LSCF matrix	[18]
Pd	YSZ	0.5–10	350–500	1.02	+	+	(∪)	Comparison to Ag, Pt, and Pd on YSZ	[15]
Pd	YSZ	0.9–55	350–480	2.6	+	-	(/)	Comparison to CH <sub>4</sub> oxidation on Pd sputtered YSZ electrodes	[19] and this work
Rh	YSZ	1.5–3	420–500	6	+	+	(∪)	Comparison to Pt on YSZ, stability limits of Rh <sub>2</sub> O <sub>3</sub>	[16, 17]
Ag	YSZ	0.5–10	350-500	4	+	0	(/)	Comparison to Pt and Pd on YSZ	[15]
Ir	YSZ	0.9–55	350–480	2.2	+	0/-	(/)	Comparison to Pd and Ru sputter-deposited on YSZ	This work
Ru	YSZ	0.9–55	350–480		?	?	(/)	Comparison to Pd and Ir sputter-deposited on YSZ (1) YSZ	This work

YSZ yttria-stabilized zirconia, CGO Ce<sub>0.9</sub>Gd<sub>0.1</sub>O<sub>1.95</sub>, LSCF La<sub>0.6</sub>Sr<sub>0.4</sub>Co<sub>0.2</sub>Fe<sub>0.8</sub>O<sub>3.-δ</sub>, ∕ electrophobic, ∪ inverted-volcano behavior



A recent innovative design combined an extremely low Pt loading ( $\sim$ 5 µg/cm²) with high dispersion ( $\sim$ 15 %) with non-direct polarization [18]. Pt nanoparticles, with an average size of 8 nm, were finely dispersed in the pores of a mixed ionic electronic conductor thin film interfaced on a dense pellet of gadolinium-doped ceria (CGO, Ce<sub>0.9</sub>Gd<sub>0.1</sub>O<sub>1.95</sub>). Small positive polarization strongly increased the catalytic performance at low temperatures (200–300 °C) with apparent Faradaic efficiency values up to 85.

The present work has focused on the electrochemical promotion of  $C_3H_8$  oxidation on Pd, Ir, and Ru catalyst-electrodes on YSZ. Via sputter deposition, uniformly thin films were deposited with low metal loading and reasonable high dispersion. The work was carried out mainly under excess of oxygen to replicate technology demands of emission and pollution control. Propane combustion is compared in terms of catalytic activity under open and closed circuit conditions. Furthermore, attention has been paid to the catalyst-electrode morphology and its possible modification during catalytic and electrocatalytic experiments.

# **Experimental**

Catalyst preparation and characterization

The solid electrolyte was a disk of 8 mol% yttria-stabilized zirconia (YSZ) of 18-mm diameter and 1-mm thickness provided by Ceraflex. Prior to Pd, Ir, or Ru deposition, no surface treatment was performed. Inert Au counter and reference electrodes were deposited on one side of the YSZ disk prior to the catalyst-electrode films. All metal electrodes were deposited by DC magnetron sputtering, which provides thin, well-adhered, and homogeneous films. High purity (99.95 %) metal targets were provided by MatecK GmbH. During deposition, the temperature of the substrate was kept at 50 °C, while the sputtering chamber was filled with pure argon (Ar). The geometric surface area of all catalyst-working electrodes was 1.9 cm². Table 2 summarizes the

deposition conditions, the final mass of the metal films, which was measured by weighting the samples, particle size, dispersion, and active surface area.

The crystalline phases of Pd, Ir, and Ru catalyst electrodes and YSZ support were examined by X-ray diffraction (XRD). A PANalytical diffractometer equipped with a X'Celerator detector with monochromatic Cu K $\alpha$ 1 radiation ( $\lambda$ =1.54 Å) was used. XRD patterns were recorded in the 2 $\theta$  range between 20° and 80°, with a scan step size of 0.017 s per step. For fresh and used samples, the crystallite size was calculated using the Debye-Scherrer equation. For the determination, the experimental width of the main Pd, Ir, or Ru reflections (metallic phase) is used in conjunction to Eq. (5):

$$d = \frac{0.9\lambda}{\beta_{1/2} \cos\theta} \tag{5}$$

where d is the particle diameter,  $\lambda$  is the X-ray wavelength,  $\beta_{1/2}$  is the line broadening at half the maximum intensity in radians, and  $\theta$  is the Bragg angle. Based on the obtained particle size and mass of the catalyst, the dispersion and active surface area,  $N_{\rm G}$ , has been calculated for fresh and used films.

The surface area of the used metal films was estimated using the galvanostatic transient technique [6]. First one measures the time,  $\tau$ , required for the rate increase to reach 63 % of its maximum steady-state value during anodic polarization. One then assumes a 1:1 surface Me/O ratio, and thus estimates the reactive oxygen uptake of the Pd, Ir, and Ru films and thus estimates the active catalyst surface area,  $N_{\rm G}$ , expressed in mol via [6]:

$$N_{\rm G} = I\tau/2F \tag{6}$$

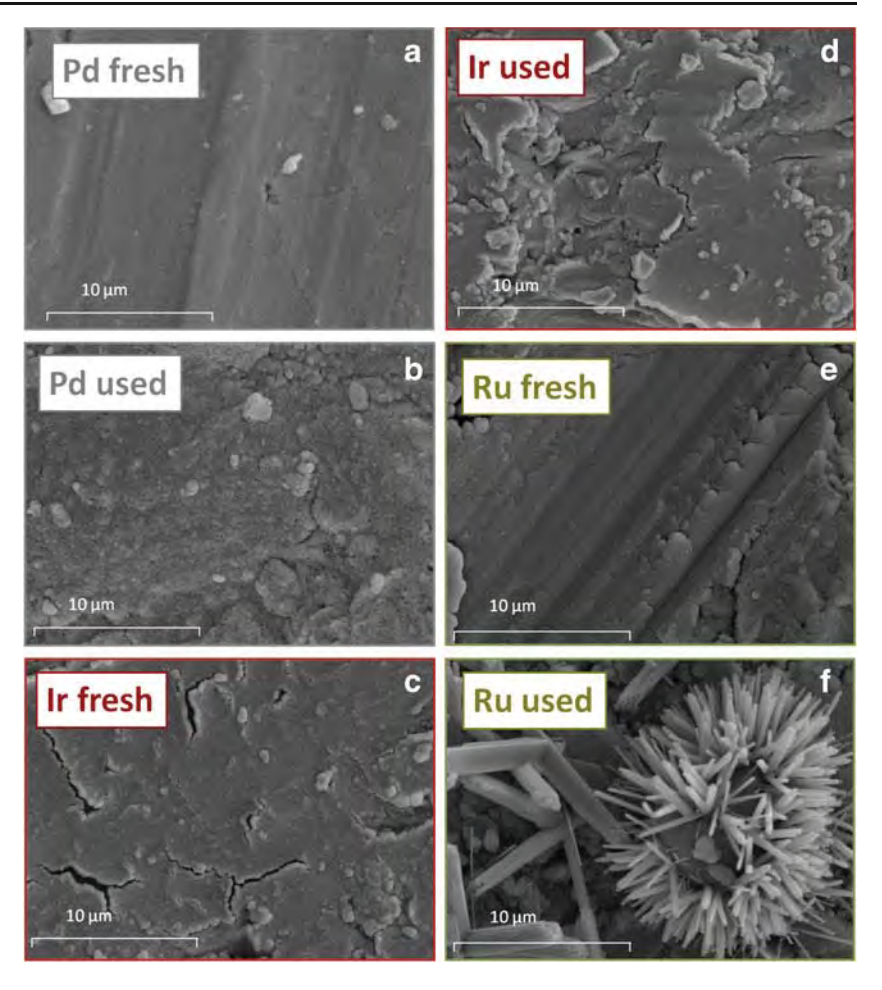
Using Eq. (6) in conjunction with galvanostatic transient experiments at constant temperature, the active catalyst surface area,  $N_{\rm G}$ , of the metal films was estimated to be in the order of  $10^{-7}$  mol Me. Table 2 summarizes the properties of the metal film catalyst-electrodes.

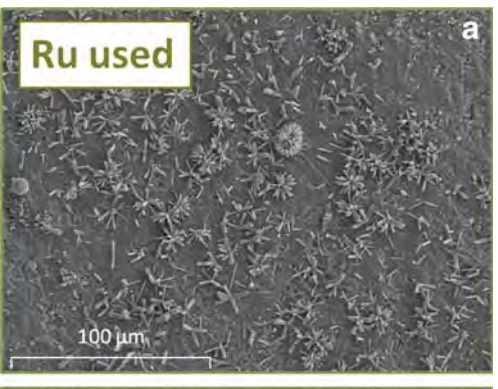
Table 2 Sputter-deposition conditions and resulting film characteristics for the catalyst-working (Pd, Ir, and Ru) and counter/reference (Au) electrodes

Metal	Discharge voltage/V	Power/W	Weight/mg	Particle size/nm	Film thickness/nm	Dispersion/%	$N_{G}/10^{-7}$ molMe (XRD)	N <sub>G</sub> /10 <sup>-7</sup> molMe (transient)
Pd fresh	376	209	0.8	17.5	350	5.7	4.3	_
Pd used				27.8		3.6	2.7	1.1
Ir fresh	479	232	0.9	24.2	210	4.1	1.9	_
Ir used				20.1		5.0	2.3	7.5
Ru fresh	336	162	0.8	7.0	340	14.2	11.3	_
Ru used				13.5		7.4	5.9	29
Au	455	250	1.1	_	300	_	_	_



Fig. 1 SEM micrographs of fresh and used a, c Pd, b, e Ir, and c, f Ru sputter-deposited catalyst-electrodes





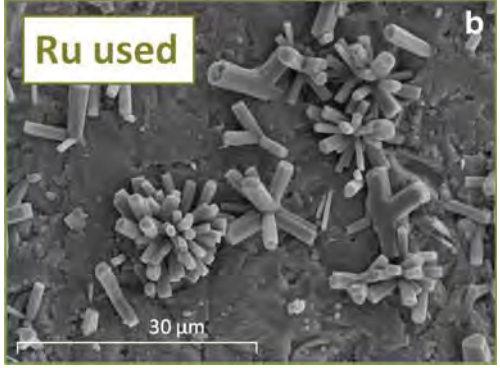


Fig. 2 SEM micrographs of used Ru sputter-deposited catalyst-electrodes



# Catalytic activity tests

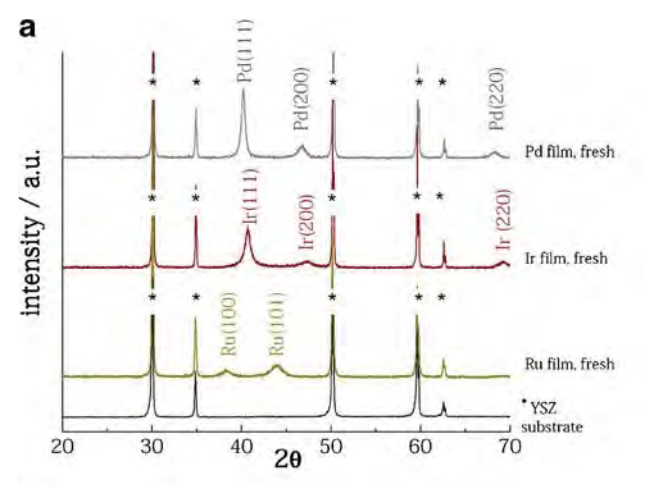
The experiments were carried out in a continuous flow atmospheric pressure quartz reactor in which all three electrodes are exposed to the same gas mixture (single pellet or single chamber reactor), as described in detail elsewhere [7]. Certified standards of 3.0 %  $C_3H_8$  in He (Linde), 20 %  $O_2$  in He (Linde), and He (L'Air liquid, 99.995 % purity) were used.

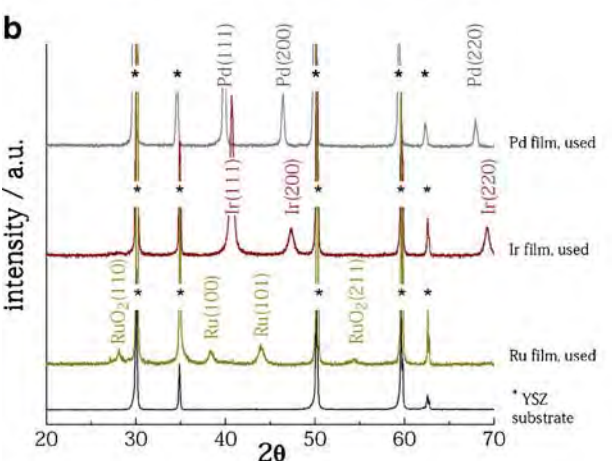
The behavior of the catalyst-electrodes was investigated using a gas mixture of 1.2 %  $C_3H_8$  and 10 %  $O_2$  in the temperature range between 250 and 450 °C and constant total gas flow rate of 170 cm<sup>3</sup> min<sup>-1</sup> (STP).

Gas analysis of reactants and products was performed via on-line gas chromatography (Shimadzu-A14 with a thermal conductivity detector, equipped with a Porapak column for separation of  $\rm C_3H_8$  and  $\rm CO_2$  and a molecular sieve for  $\rm O_2$  detection). Furthermore, an infrared analyzer, Rosemount Binos 100, was used for the continuous measurement of the  $\rm CO_2$  concentration. Constant currents or potentials were applied using a Solartron 1286 electrochemical interface.

The conversion of propane to CO<sub>2</sub> is defined from:

$$C_3H_8 conversion = \left( \left( y_{C_3H_8}^{in} - y_{C_3H_8}^{out} \right) / y_{C_3H_8}^{in} \right) \times 100$$
 (7)





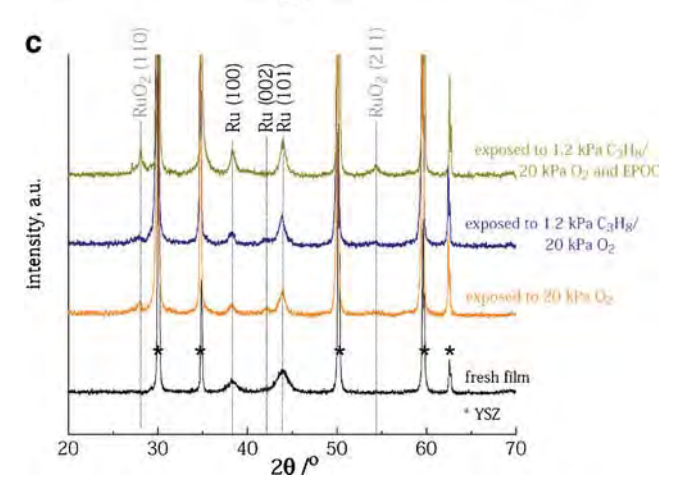


Fig. 3 XRD spectra of  $\bf a$  fresh and  $\bf b$  used sputter-deposited Pd, Ir, and Ru films on YSZ.  $\bf c$  XRD spectra of fresh and pretreated (used) sputter-deposited Ru films on YSZ

where  $y_{\text{C3H8}}$  is the molar fraction of  $\text{C}_3\text{H}_8$ . The concomitant  $\text{CO}_2$  formation rate,  $r_{\text{CO}2}$ , given in mol per second is:

$$r_{\text{CO}_2} = y_{\text{CO}_2} \cdot G \,\text{mol}\, \text{CO}_2 \, s^{-1} \tag{8a}$$

where  $y_{CO2}$  is the molar fraction of  $CO_2$  and G is the total molar flow rate.

Since the overall propane oxidation is represented by the following reaction

$$C_3H_8 + 5O_2 \rightarrow 3CO_2 + 4H_2O$$
 (9)

the rate of CO<sub>2</sub> formation throughout this study is expressed in molO per second:

$$r_{\text{CO}_2} = (10/3) \cdot y_{\text{CO}_2} \cdot G \text{ molO } s^{-1}$$
(8b)

The external surface structure, morphology characterization, and the estimation of film thickness of the different catalytic layers were carried out by scanning electron microscopy (SEM) using a JEOL JSM-6300 microscope.

# Results and discussion

Catalyst characterization

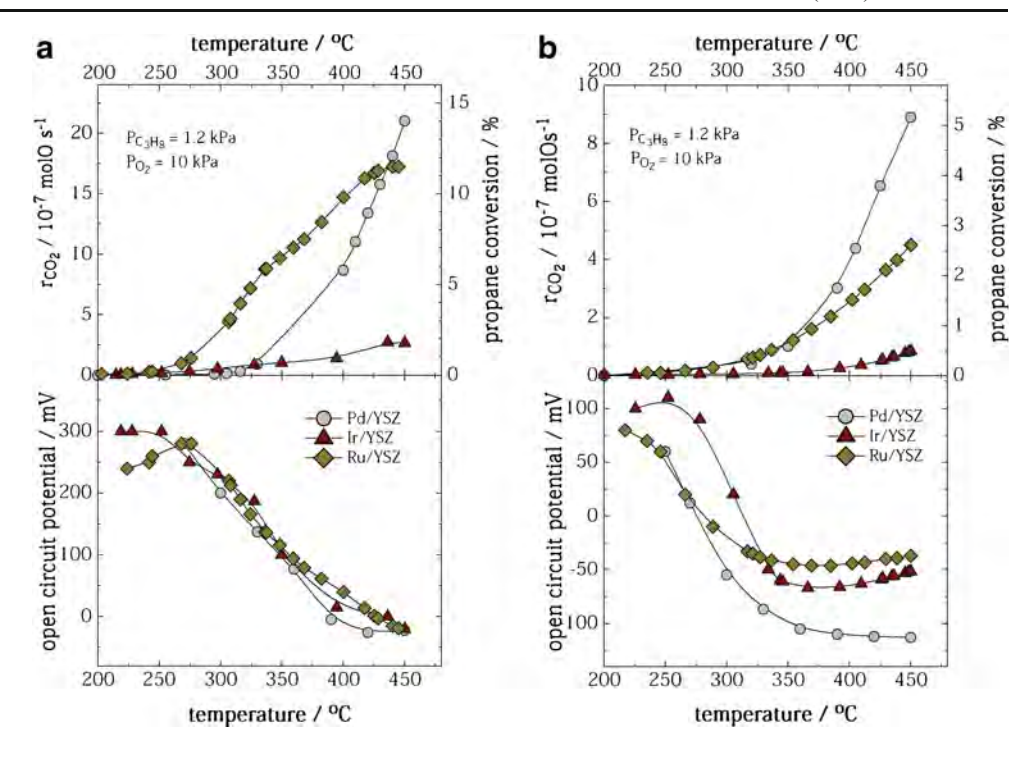
Figure 1 shows SEM micrographs of the surface morphology for Pd [20], Ir, and Ru catalyst electrodes deposited on YSZ before (a, c, and e) and after (b, d, and f) exposure to the reaction gas mixture and potential application. As shown in the figures, the fresh catalyst films consist of a smooth and homogeneous metal film. The sputter-deposited films are nearly dense after deposition but become quite porous after thermal treatment and catalytic reaction. The film thickness has been estimated from cross section SEM micrographs (not shown) and is found to be in the order of ~300 nm for sputter-deposited films (Table 2). After exposure to propane oxidation conditions (used catalysts), the Ru film exhibits a different morphology, while Pd and Ir have not changed significantly. In the case of Pd and Ir, enhanced film roughness and improved crystallinity are observed. More pronounced morphological differences are detected in the case of Ru films, where a remarkable and beautiful Ru oxide structure is formed. Additional SEM micrographs in Fig. 2a, b show these crystals in smaller magnification, which are found over the entire electrode surface.

The identification of the phase composition for all films was performed by XRD analysis, as shown in Fig. 3a–c. The crystal planes of the catalyst-electrode were confirmed according to the JCPDS crystallographic database. The reflection peaks of YSZ were observed for all metal sputtered films corresponding to the (111), (200), (220), and (311) planes (JCPDS-ICDD Card No. 01-082-1246).

Fresh films show reflections only of metallic Pd, Ir, or Ru phases corresponding to the (111), (200), and (220) planes of Pd<sup>0</sup> [20] and Ir<sup>0</sup>, and corresponding to the (100), (101), and (002) planes of Ru<sup>0</sup>. The presence of only metallic Pd, Ir, and Ru for the fresh sputter-deposited samples is expected since these films have been produced with the relevant high purity metal sputtering target without further treatment (Fig. 3a).



Fig. 4 Temperature effect on  $CO_2$  formation rate, propane conversion, and open-circuit potential utilizing fresh  $\bf a$  and used  $\bf b$  Pd/YSZ, Ir/YSZ, and Ru/YSZ catalyst-electrodes.  $P_{C3H8}$ =1.2 kPa,  $P_{O2}$ =10 kPa



After electrochemically promoted propane oxidation experiments (Fig. 3b), the metallic phases were identified for Pd [20] and Ir, accompanied by significant sharper reflections due to improved crystallinity. The oxide phases for Pd or Ir are not detectable via XRD. For the Ru film, reflections of the metal phase (Ru<sup>0</sup>, 100, 101, and 100) and metal oxide (RuO<sub>2</sub>, 110 and 211) were found. The particle size and dispersion of the Pd and Ir samples (Table 2) change only slightly after exposure to reaction conditions. The Ru film exhibits the most significant decrease in dispersion due to enhanced particle size, obtained only for the metal phase. The active surface area,  $N_{\rm G}$ , of the Pd and Ir films obtained from XRD data coincides very well with those obtained from galvanostatic transient experiments. For these samples,  $N_{\rm G}$ values of the order of  $10^{-7}$  mol metal have been found with both methods (XRD and galvanostatic transient technique). Only in the case of the Ru film  $N_G$  obtained from transients is overestimated by an order of magnitude  $(28 \times 10^{-7} \text{ molRu})$ due to the significant Ru oxide formation.

In order to investigate the formation of the very special crystalline structure of  $RuO_2$  (SEM Figs. 1f and Fig. 2a, b), two more Ru/YSZ samples have been treated as follows:

- Exposure to 20 kPa O<sub>2</sub> at 450 °C for 2 h
- Exposure to a reactive gas mixture of 10 kPa O<sub>2</sub> and 1.2 kPa propane at 450 °C for 2 h.

Both films have not been used for polarization experiments. SEM characterization (not presented here) showed that their surface after treatment does not exhibit the impressive RuO<sub>2</sub> crystals of Fig. 1f and Fig. 2a, b, but RuO<sub>2</sub> is formed as

in the case of the Ru sample discussed in the previous section. While fresh and used Ru samples exhibit an average particle size of 10–20 nm, obtained by SEM and XRD, the impressive crystalline structures of RuO $_2$  are found in the order of 1–2  $\mu m$ . Figure 3c presents these findings via XRD comparing with the fresh sputtered film. Most likely, the simultaneous prolonged polarization under higher oxidizing reaction conditions favors the reconstruction of the surface.

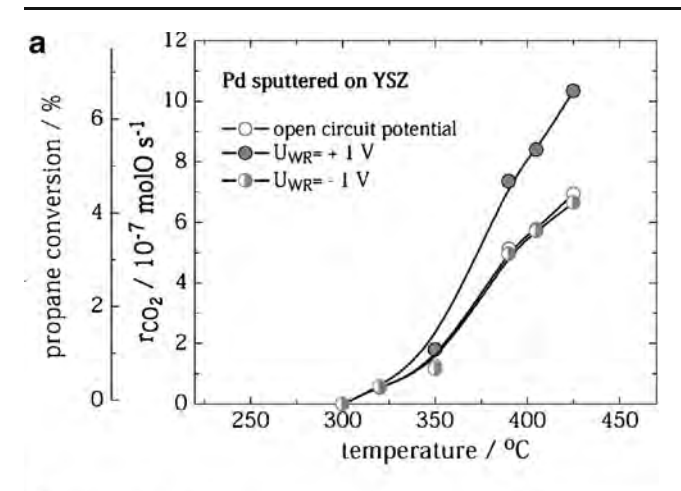
# Catalytic activity measurements

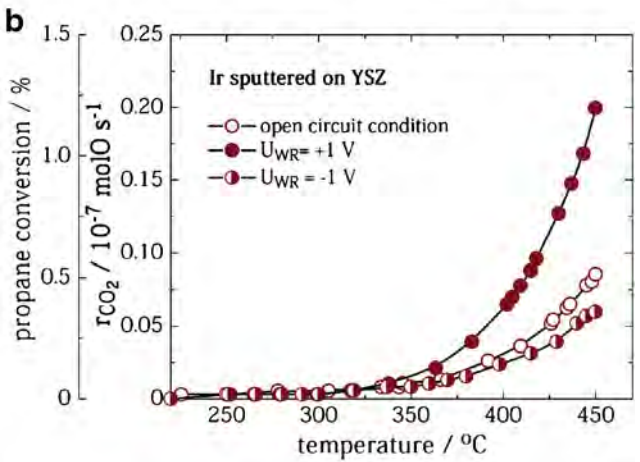
Figure 4a, b compares the steady-state effect of temperature on the catalytic  $\mathrm{CO}_2$  formation rate,  $\mathrm{C}_3\mathrm{H}_8$  conversion, and the open circuit potential (ocp) during the first (a) and second (b) light off experiment. As shown in Fig. 4a, the fresh Ru film exhibits higher catalytic activity than Pd and Ir. Only at higher temperatures (>400 °C) the catalytic activity of Pd exceeds slightly that of Ru. At 450 °C, the conversion of  $\mathrm{C}_3\mathrm{H}_8$  reaches 14, 11, and 2 % for Pd, Ru, and Ir catalyst-electrodes, respectively.

A significant catalyst deactivation is observed mainly for the Ru film which can be related to the formation of Ru oxides as observed by XRD and the sharp decrease in dispersion from 14.2 to 7.4 % (Table 2). Pd and Ir persist in their metallic phase, their dispersion is almost unchanged (Table 2), and the loss in catalytic activity is less pronounced.

 $RuO_2$  [24, 25] as well as  $IrO_2$  [26, 27] films have been recently used for ethylene [24–27] and toluene [25] oxidation in excess of oxygen. These electrodes have been prepared via wet impregnation in which successive steps of







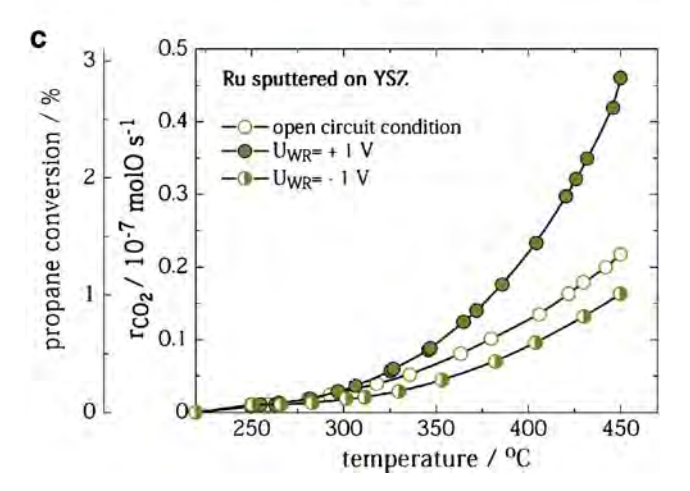


Fig. 5 Temperature programmed reaction (TPR):  $CO_2$  formation rate and propane conversion under open circuit and under both positive (+1 V) and negative (-1 V) potential application, **a** Pd/YSZ, **b** Ir/YSZ, and **c** Ru/YSZ. Conditions as in Fig. 3

deposition and thermal decomposition of a Ru precursor solution on YSZ are applied. The films are finally calcined at 500 and 550 °C, respectively. Only RuO<sub>2</sub> or IrO<sub>2</sub> as active phases were obtained in contrast to our study, in which Ru and Ir have been sputter-deposited and the non-treated films show only reflections of a metallic phase in conjunction to

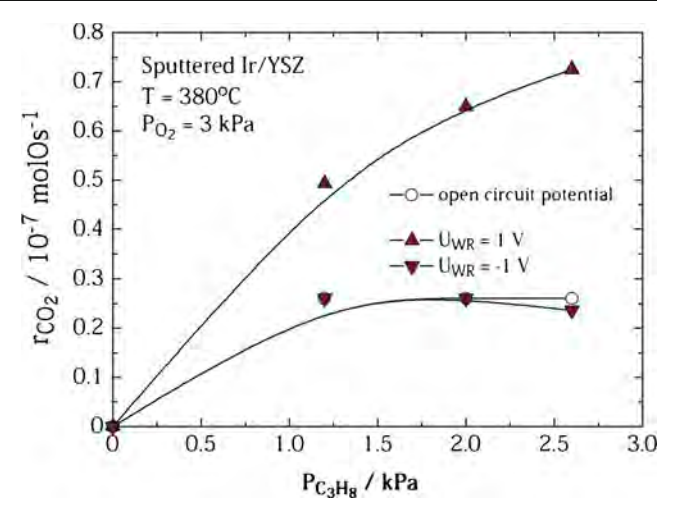


Fig. 6 Steady-state effect of  $P_{\rm C3H8}$  on the catalytic CO<sub>2</sub> formation at open and closed circuit conditions at constant  $P_{\rm O2}$ =3 kPa, T=380 °C

the highest catalytic activity in the first light off experiments (Fig. 4a). After the first exposure to reaction conditions, Ru is found to be partially oxidized (XRD in Fig. 3b).

The open circuit potential (OCV) decreases for all metal films in the first light-off experiment from  $\sim 300$  mV at 250 °C to  $\sim -50$  mV at 450 °C, while in the second light-off the OCV is overall much smaller with 100 mV at 250 °C, but decreases further with increasing temperature to -100 mV at 450 °C for the Pd sample.

Vernoux et al. [12] has carried out OCV measurements under oxidizing  $C_3H_8/O_2$  and  $C_3H_6/O_2$  mixture as a function of temperature. An electrochemical cell with two separate compartments was used, which allows to expose counter and reference electrodes to air (solid electrolyte potentiometry, SEP). The corresponding variations of  $U_{\rm WR}$  show a gradual increase with an increase in temperature under  $C_3H_8/O_2$  from

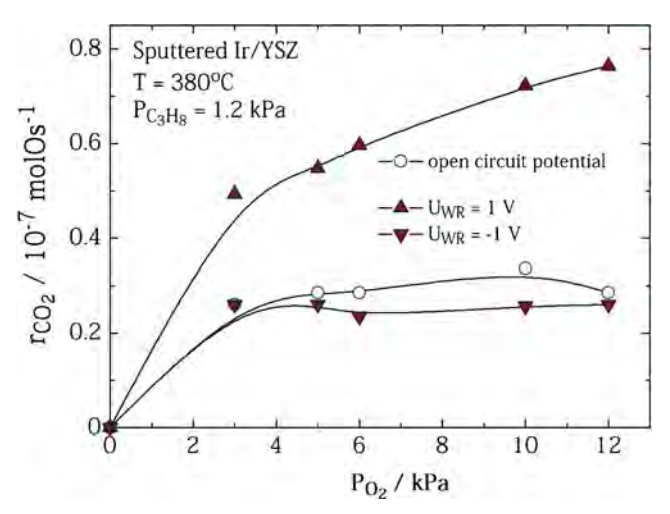
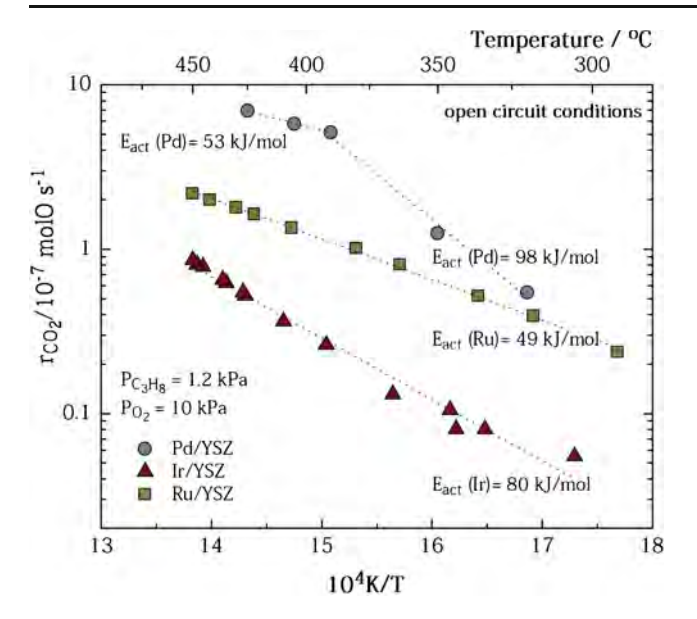


Fig. 7 Steady-state effect of  $P_{\rm O2}$  on the catalytic CO<sub>2</sub> formation at open and closed circuit conditions at constant  $P_{\rm C3H8}$ , T=380 °C





**Fig. 8** Arrhenius plots for the CO<sub>2</sub> formation rate obtained for Pd/YSZ, Ir/YSZ, and Ru/YSZ catalyst-electrodes under open circuit conditions. Conditions as in Fig. 3

290 °C (-173 mV) to 400 °C (-60 mV) and a much more pronounced increase in presence of  $C_3H_6/O_2$  from 290 °C (-546 mV) to 400 °C (-100 mV). This indicates that the oxygen activity on the catalyst surface can be directly related to  $U_{\rm WR}$  and thus to the hydrocarbon conversion. The SEP technique has not been applied in the present study since all three electrodes (working, counter, and reference) have been exposed to the reactive gas mixture, and comparison of open circuit potentials is therefore not straightforward. In the present case of Pd, Ir, and Ru electrodes the OCV was always

positive at low temperatures and decreased gradually with increasing temperature.

The continuous measurement of reaction rate r (by means of the effluent  $CO_2$  concentration), catalyst potential  $U_{WR}$ , and current I allowed for transient TPR (temperature programmed reaction) experiments to be performed. TPR experiments have been carried out with a constant heating rate of 2 K min<sup>-1</sup> in the temperature range from 200 to 450 °C at constant inlet partial pressures of oxygen and propane. First, the sample was investigated under open circuit conditions. After cooling the sample to 200 °C, a positive potential of  $U_{WR}=1$  V was applied, and the catalyst was heated under closed circuit conditions again to 450 °C. Finally, the same procedure was followed for negative potential application. The main findings are summarized in Fig. 5a for the Pd film, 5b for Ir, and 5c for Ru. The observed increase in catalytic rate is highest at 425 °C and led to only moderate rate enhancement ratios of <2.5 for all catalyst films of this study. For the three catalyst-electrodes, an electrophobic-type behavior is observed, i.e., the rate increases with positive potential and decreases with negative potential application. According to the rules of electrochemical and classical promotion [20-23], the observed electrophobic behavior suggests that the catalytic rate must be positive order in the fuel (propane, which is an electron donor) and zero or negative order in oxygen, which is an electron acceptor. This is indeed the case for Pd films as recently shown in [19], but also for propane oxidation on Ir films, where positive order in C<sub>3</sub>H<sub>8</sub> (Fig. 6) and zeroth order in O2 (Fig. 7) have been found. At the high oxygen partial pressures used in this study, the oxygen coverage is high, and

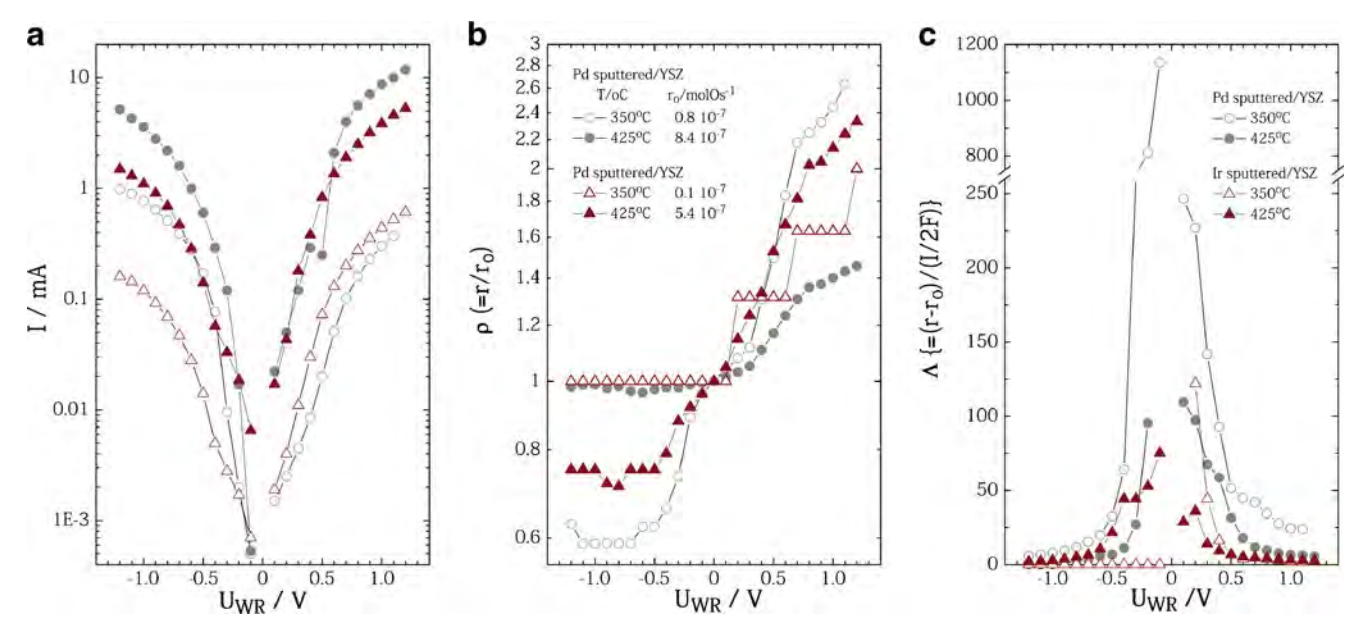


Fig. 9 Steady-state effect of applied potential,  $U_{WR}$ , on a measured current, **b** rate enhancement ratio,  $\rho$ , and **c** apparent Faradaic efficiency,  $\Lambda$ , using Pd and Ir catalyst-electrodes at 350 and 425 °C. Conditions as in Fig. 3



thus, the metal (Pd, Ir, and Ru) active sites for hydrocarbon activation are occupied almost entirely by oxygen.

Under anodic polarization, when the rate increases with applied potential, the effective double layer of  $[O^{\delta^-} - \delta^+]$  species is formed at the gas exposed surface, and the catalyst work function is increased (Eq. (1)). This results in a weakening of the Metal (M)-O bonds, since oxygen is an electron acceptor, and strengthening the M-propane bonds of which both prevent high oxygen coverage on the catalyst surface and lead finally to enhanced propane conversion.

Under negative polarization, the rate is slightly lower over the entire temperature range than the one obtained at open circuit conditions leading to rate enhancement values  $\rho$ <1 (Fig. 5a–c, Fig. 9b). The applied negative current leads to the reduction of oxygen coming from the gas phase:

$$O_2(g) + 4e^-(M) \rightarrow 2O^{2-}(YSZ)$$
 (2a)

and/or the removal of adsorbed oxygen species:

$$\left[O^{\delta-}-\delta^{+}\right](M) + 2e^{-}(M) \rightarrow O^{2-}(YSZ) \tag{1a}$$

at the working electrode. When oxygen anions are removed from the catalyst surface, then the average catalyst work function decreases and the chemisorptive bonds of oxygen become stronger. Since propane acts as an electron donor, the M-propane bonds become weaker and a catalytic rate decrease is finally observed.

Figure 8 shows an Arrhenius plot of the  $CO_2$  formation rate under open circuit conditions for all three catalyst electrodes of this study. Apparent activation energies,  $E_{\rm act}$ , of 98, 80, and 49 kJ/mol were obtained for Pd, Ir, and Ru catalyst-electrodes, respectively. In the case of Pd, at temperatures above 380 °C, the  $E_{\rm act}$  decreases to 53 kJ/mol. This change cannot be attributed to mass transfer limitation phenomena. If mass transfer is rate limiting,  $\Lambda$  should be limited to 1 in the case of slow  $O_2$  diffusion, or to 0 in the case of slow  $C_3H_8$  diffusion. The apparent activation energies increase slightly with negative and decreases with positive potential application, in agreement with EPOC theory [6, 24, 25, 28, 29].

Figure 9 shows the steady-state effect of the applied potential ( $U_{\rm WR}$ ) on the measured current (Fig. 9a), the rate enhancement ratio,  $\rho$  (Fig. 9b) and the apparent Faradaic efficiency,  $\Lambda$  (Fig. 9c) at 350 and 425 °C for Pd and Ir catalyst-electrodes. As shown in the Tafel plot (Fig. 9a), the potential-induced current is one order of magnitude larger for Pd catalyst-electrode than that of Ir. Rate enhancement ratios,  $\rho$ , of up to 2.6 were obtained for Pd and up to 2.3 for Ir at 425 °C. Both catalyst-electrodes show electrophobic behavior, the rate is increased with positive polarization, and decreased with negative one. Apparent Faradaic efficiency,

 $\Lambda$ , values (Fig. 9c) of up to 110 where recorded for Pd and up to 75 for Ir at 450 °C.

The exchange current density  $I_0$  is an important parameter for the quantitative description of electrochemical promotion because it allows to estimate the magnitude of the enhancement factor  $\Lambda$  using the open circuit (unpromoted) catalytic rate and exchange current,  $I_0$ , from Eq. (9) [6]:

$$\Lambda = 2Fr_0/I_0 \tag{10}$$

The exchange current  $I_0$  depends on the nature of the electrode (composition of the metal film supporting an equilibrium reaction), its structure, and morphology (i.e., length of tpb and surface roughness). It is generally strongly dependent on temperature and increases in the present study for Pd and Ir electrodes with temperature as expected and observed from Fig. 9a ( $I_0$  at 425 °C 1 (Pd) and 0.5 mA (Ir)). At 425 °C, the Faradaic efficiency  $\Lambda$ , which expresses the ratio of the promoted catalytic turnover number per electrochemically supplied  $O^{2-}$  species, is estimated to be 160 and 210 for Pd and Ir, respectively, which are in reasonable agreement with the experimental values.

# **Conclusions**

The electrochemical promotion of C<sub>3</sub>H<sub>8</sub> oxidation has been investigated over Pd, Ir, and Ru catalyst-electrodes which were sputter-deposited on YSZ disks in the temperature range between 250 and 450 °C. Under open circuit conditions, the catalytic activity of fresh catalysts was found to decrease in the order Ru>Pd>Ir; however, at steady state (used catalysts), the activity order was Pd>Ru>Ir. This change has been attributed to severe oxidation of the Ru catalyst-electrode surface, as confirmed also by SEM and XRD analyses. Electrophobic type behavior was observed for all studied catalyst-electrodes, i.e., the rate increases with positive potential application. This behavior has been attributed to the potential-induced weakening of the metal-O bond strength due to  $O^{\delta-}$  species migration (spillover) from the YSZ support to the catalyst surface under anodic polarization, which results in the formation of a more active O<sub>ads</sub> species and also lowers the oxygen coverage. Rate enhancement ratios,  $\rho$ , are moderate with values of up to 2.6 for Pd, 2.2 for Ir, and <2 for Ru.

Acknowledgments Saranya Peng-ont, Suttichai Assabumrungrat, and Piyasan Praserthdam would like to thank the financial supports from the Royal Golden Jubilee PhD program under the Thailand Research Fund and the Chulalongkorn University, and the TRF senior researcher scholar under the Thailand Research Fund. Susanne Brosda and Constantinos G. Vayenas gratefully thank the "Synergasia" and "Aristeia" programs of the Greek Secretary of Research and Technology (GSRT) for partial financial support.



# References

- Gélin P, Primet M (2007) Complete oxidation of methane at low temperature over noble metal based catalysts: a review. Appl Catal B 39:1
- Gélin P, Urfels L, Primet M, Tena E (2003) Complete oxidation of methane at low temperature over Pt and Pd catalysts for the abatement of lean-burn natural gas fuelled vehicles emissions: influence of water and sulphur containing compounds. Catal Today 83:45
- Ciuparu D, Pfefferle L (2001) Methane combustion activity of supported palladium catalysts after partial reduction. Appl Catal A 218:197
- Ciuparu D, Lyubovsky MRL, Altman E, Pfefferle LD, Datye A (2002) Catalytic combustion of methane over Palladium–based catalysts. Catal Rev 44:593
- 5. Glinrun T, Mekasuwandumrong O, Panpranot J, Chaisuk C, Praserthdam P (2010) Improvement of propane oxidation activity over Pt/Al $_2$ O $_3$  by the use of MIXED  $\gamma$  and  $\chi$ -Al $_2$ O $_3$  supports. Reac Kinet Mech Cat 100:441
- Vernoux P, Lizarraga L, Tsampas MN, Sapountzi FM, De Lucas-Consuegra A, Valverde JL, Souentie S, Vayenas CG, Tsiplakides D, Balomenou S, Baranova EA (2013) Ionically conducting ceramics as active catalyst supports. Chem Rev. doi:10.1021/cr4000336
- Vayenas CG, Bebelis SB, Pliangos C, Brosda S, Tsiplakidis D (2001) Electrochemical activation of catalysis: promotion, electrochemical promotion and metal-support interactions. Kluwer, New York
- Jiménez-Borja C, de Lucas-Consuegra A, Valverde JL, Dorado F, Caravaca A, Gonzáles J, (2012) On of the recent discoveries in catalysis: The phenomenon of electrochemical promotion. In: Taylor JC (ed) Advances in chemistry research, vol 14 ch 4. Nova Science Publishers, Hauppauge NY, USA
- Lizarraga L, Guth M, Billard A, Vernoux P (2010) Electrochemical catalysis for propane combustion using nanometric sputtered-deposited Pt films. Catal Tod 157:61
- Tsampas MN, Sapountzi FM, Boréave A, Vernoux P (2013) Isotopical labeling mechanistic studies of electrochemical promotion of propane combustion on Pt/YSZ. Electrochem Comm 26:13
- Souentie S, Lizarraga L, Papaioannou EI, Vayenas CG, Vernoux P (2010) Permanent electrochemical promotion of C3H8 oxidation over thin sputtered Pt films. Electrochem Comm 12:1133
- Vernoux P, Gaillard F, Bultel L, Siebert E, Primet M (2002) Electrochemical promotion of propane and propene oxidation on Pt/YSZ. J Catal 208:412
- Kokkofitis C, Stoukides M (2006) Rate and oxygen activity oscillations during propane oxidation on Pt/YSZ. J Catal 243:428

- Kokkofitis C, Karagiannakis G, Zisekas S, Stoukides M (2005) Catalytic study and electrochemical promotion of propane oxidation on Pt/YSZ. J Catal 234:476
- Kokkofitis C, Karagiannakis G, Stoukides M (2007) Electrochemical promotion in O<sup>2-</sup> cells during propane oxidation. Topics in Catal 44:361
- Kotsionopoulos N, Bebelis S (2005) Electrochemical promotion of the oxidation of propane on Pt/YSZ and Rh/YSZ catalyst-electrodes. J Appl Electrochem 35:1253
- Bebelis S, Kotsionopoulos N (2006) Non-faradaic electrochemical modification of the catalytic activity for propane combustion of Pt/ YSZ and Rh/YSZ catalyst-electrodes. Solid State Ionics 177:2205
- Kambolis A, Lizarraga L, Tsampas MN, Burel L, Rieu M, Viricelle JP, Vernoux P (2012) Electrochemical promotion of catalysis with highly dispersed Pt nanoparticles. Electrochem Comm 19:5
- Peng-Ont S, Praserthdam P, Matei F, Ciuparu D, Brosda S, Vayenas CG (2012) Electrochemical promotion of propane and methane oxidation on sputtered Pd catalyst-electrodes deposited on YSZ. Catal Lett 142:1336
- Vayenas CG, Brosda S, Pliangos C (2001) Rules and mathematical modeling of electrochemical and chemical promotion: 1. Reaction classification and promotional rules. J Catal 203:329
- Brosda S, Vayenas CG (2002) Rules and mathematical modeling of electrochemical and classical promotion: 2. Modeling. J Catal 208:38
- Vayenas CG, Brosda S, Pliangos C (2003) The double-layer approach to promotion, electrocatalysis, electrochemical promotion and metal-support interactions. J Catal 216:487
- Brosda S, Vayenas CG, Wei J (2006) Rules of chemical promotion. Appl Catal B 68:109
- Wodiunig S, Comninellis C (1999) Electrochemical promotion of RuO<sub>2</sub> catalysts for the gas phase combustion of C<sub>2</sub>H<sub>4</sub>. J Europ Ceram Soc 19:931
- Constantinou I, Bolzonella I, Pliangos C, Comninellis C, Vayenas CG (2005) Electrochemical promotion of RuO<sub>2</sub> catalysts for the combustion of toluene and ethylene. Catal Lett 100:125
- 26. Nicole J, Comninellis C (1998) Electrochemical promotion of  $\rm IrO_2$  catalyst activity for the gas phase combustion of ethylene. J Appl Electrochem 28:223
- Tsiplakides D, Nicole J, Vayenas CG, Comninellis C (1998) Work function and catalytic activity measurements of an IrO<sub>2</sub> film deposited on YSZ subjected to in situ electrochemical promotion. J Electrochem Soc 145:905
- Bebelis S, Vayenas CG (1989) Non-Faradaic electrochemical modification of catalytic activity: 1. The case of ethylene oxidation on Pt. J Catal 118:125
- Marwood M, Vayenas CG (1998) Electrochemical promotion of Pt catalyst dispersed on Au electrodes deposited on stabilized zirconia. J Catal 178:429





# Contents lists available at ScienceDirect

# Journal of Power Sources

journal homepage: www.elsevier.com/locate/jpowsour



# Evaluation of performance and operation viability of non-uniform potential solid oxide fuel cell fueled by reformed methane



- P. Piroonlerkgul <sup>a</sup>, W. Kiatkittipong <sup>b</sup>, S. Wongsakulphasatch <sup>b</sup>, F. Aiouache <sup>c</sup>, S. Assabumrungrat <sup>a</sup>, \*
- <sup>a</sup> Center of Excellence in Catalysis and Catalytic Reaction Engineering, Department of Chemical Engineering, Faculty of Engineering, Chulalongkorn
- University, Bangkok 10330, Thailand
  <sup>b</sup> Department of Chemical Engineering, Faculty of Engineering and Industrial Technology, Silpakorn University, Nakhon Pathom 73000, Thailand
- <sup>c</sup> Department of Engineering, Faculty of Science and Technology, Lancaster University, Lancaster LA1 4YR, United Kingdom

#### HIGHLIGHTS

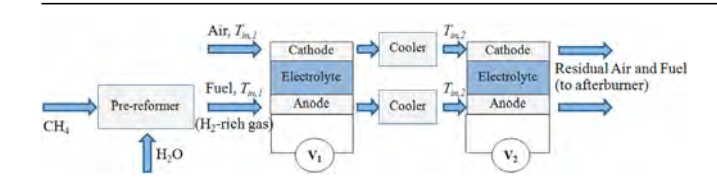
- The performance of SOFC with nonuniform potential operation was evaluated.
- Maximum stack temperature gradient and stack temperature were considered.
- Non-uniform potential SOFC stacks with a cooler show higher performance.

# ARTICLE INFO

Article history: Received 11 June 2013 Received in revised form 16 July 2013 Accepted 31 July 2013 Available online 15 August 2013

Keywords: Solid oxide fuel cell Non-uniform potential Methane Operation viability Two-stacks

## G R A P H I C A L A B S T R A C T



# ABSTRACT

The performance and the operation viability of solid oxide fuel cells (SOFC) fueled by reformed methane using the concept of non-uniform potential operation were evaluated by one-dimensional finite difference analysis. Two thermal constraints including maximum acceptable stack temperature gradient and maximum stack temperature were the criteria for considering the operation viability. The average power density was used as a performance indicator. In addition, two major process parameters: fuel and air inlet temperatures and the operating voltage were examined to determine the suitable values for different viabilities. The results revealed that non-uniform potential SOFC with two stack sections operating at different voltages could not offer a significantly higher average power density compared with the uniform potential SOFC owing to thermal constraint limitations. The installation of coolers between the stacks is important and it could offer 12.8% improvement in average power density.

© 2013 Elsevier B.V. All rights reserved.

# 1. Introduction

Due to the continuous increase in fossil fuel price, alternative developments of high-performance and environmental-friendly technologies for electricity generation are desirable. Fuel cell technologies have been of interest over the last decade owing to higher electrical efficiency compared with conventional combustion heat engines [1]. This is due to the direct conversion of

\* Corresponding author.

E-mail address: Suttichai.A@chula.ac.th (S. Assabumrungrat).

chemical energy to electrical energy via electrochemical reactions whilst a prior conversion of the chemical energy to thermal and mechanical energies takes place in the combustion heat engines along with greater irreversible losses. Among various types of fuel cells, the solid oxide fuel cell (SOFC) is a promising technology as it offers number of advantages: (1) high operating temperature which enhances the rate of electrochemical reactions and inhibits the overpotential losses, (2) improved electrical efficiency as the high-temperature exhaust gas (1073–1273 K) is utilized to produce additional electricity via gas turbine/engine cycle [1,2], and (3) fuel sources such as methane, ethanol, natural gas or oil derivatives can be used without pre-processing constraints.

The improvement of SOFC performance has been performed using three main methods: the development of a new component material to offer a low overpotential loss [3,4], the combination of SOFC stack with heat engines to generate additional electricity [5,6] and the optimization of operating conditions [7]. Among the optimization techniques, concept of using the so-called "non-uniform potential operation" is of interest [8-11]. In this concept, a SOFC stack is divided into several sections and operated at different operating voltages. Near the entrance of the fuel cell stack, where H<sub>2</sub> concentration in fuel gas and rate of electrochemical reaction are high, a high value of cell voltage is used to maximize the power density. Inversely, near the exit of the stack, low cell voltage is set to maintain SOFC power density at a high value although the electrochemical reaction rate is low due to low H<sub>2</sub> concentration of the fuel gas. Selimovic and Plasson [8] investigated the non-uniform potential operation in networked-SOFC stacks combined with a gas turbine cycle. They concluded that an increase in the electrical efficiency of 5% could be achieved by improving the thermal management. Also, Au et al. [9] found that 0.6% improvement in the electrical efficiency could be achieved for molten carbonate fuel cell (MCFC) when the concept of non-uniform potential operation was applied [9]. The implementation of this concept in polymer electrolyte membrane fuel cell (PEMFC) was also examined [10]. The results indicated that PEMFC implementing the concept of non-uniform potential operation offered 6.5% improvement in the power density compared with the conventional PEMFC. Vivanpatarakij et al. [11] investigated the implementation of this concept by considering power density as a performance indicator and achieved 9.2% enhancement in the power density by implementing a nonuniform potential operation. Although, non-uniform potential operation improved the performance of SOFC, further operating parameters such as the thermal behavior of solid part inside SOFC stack implementing this concept would promote even more the performance as a large amount of heat is generated due to the irreversibility of the electrochemical mechanism at higher level of the electrical generation. Recently, Guan et al. [12] developed an experimental method to measure temperatures inside stacks using thin K-type thermocouples and self-developed CAS-I sealing materials. The results have shown that temperature distribution of unit cells was nonuniform: the maximum temperature difference between inlet and outlet was about 200 K. The lack of knowledge in the selection of the operating conditions would cause high temperature gradients along the SOFC stack and some solid parts in the stack would be damaged.

In this study, the implementation of "non-uniform potential operation" concept in SOFC fueled by pre-reformed methane was examined using one-dimensional analysis (1-D analysis) for the investigation of stack performance and thermal behavior along the SOFC stack. The calculation using 1-D analysis could well represent the actual SOFC stack behavior as reported by Sorrentino et al. [13]. Methane is an attractive fuel gas as it is present at high concentrations in several fossil and renewable sources such as natural gas

[14,15] and biogas [16]. The utilization of methane as a fuel in SOFC has been widely studied [17–20]. Methane could be directly used as a fuel in an anode chamber of SOFC stack; the performance of methane-fueled SOFC stack was significantly lower than that of H<sub>2</sub>fueled SOFC stack as described in our recent work [21]. Moreover, direct utilization of methane in SOFC stack caused inhibition of the performance of SOFC stack due to carbon-deposited blocking inside anode pore [22]. Therefore, the pre-reformer is preferable to be installed in SOFC system in order to initially convert methane into hydrogen. An installation of pre-reformer not only inhibits carbon blockage in the anode chamber but also enhances the power density of the SOFC stack [23]. In this study, the average stack power density is considered as a performance indicator. Operating parameters and SOFC stack configuration are varied to examine operation patterns, inlet temperature and operating voltage that offer maximum power density under stringent thermal constraints i.e. maximum acceptable stack temperature gradient ( $T_{G,acp}$ ) and maximum acceptable stack temperature ( $T_{\text{max,acp}}$ ). Moreover, a new configuration of installing inter-cooler with non-uniform potential SOFC operation is proposed to achieve higher average power density.

# 2. Modeling

The operation of SOFC takes place at the following configuration. The reformed methane is fed into the SOFC stack at the entrance of anode chamber, while air, performing as the oxidizing agent, is fed at the entrance of cathode chamber of SOFC stack. Anode and cathode chambers are separated from each other by solid electrolyte. Inside the cathode, oxygen present in air is reduced to oxygen ions (Eq. (1)) which permeate via the solid electrolyte to the anode chamber where the reaction between oxygen ions and hydrogen takes place to generate steam (Eq. (2)). CO electro-oxidation was assumed to be negligible due to its lower reaction rate compared with H<sub>2</sub> electro-oxidation [24], and to be consumed in the anode chamber via water-gas-shift (WGS) reaction, where reaction rates are high at elevated operating temperatures [25–27]. The SOFC is composed of an anode chamber (Ni-yttria stabilized zirconia), an electrolyte (yttria stabilized zirconia), and a cathode chamber (Lanthanum strontium manganite—yttria stabilized zirconia).

$$\frac{1}{2}O_2 + 2e^- \rightarrow O^{2-} \tag{1}$$

$$H_2 + O^{2-} \rightarrow H_2O$$
 (2)

The open circuit voltage  $(E^j)$  was calculated using the Nernst equation (Eq. (3)).

$$E^{j} = E_{0}^{j} + \frac{RT_{e}^{j}}{2F} \ln \left( \frac{p_{H_{2}}^{j} \left( p_{O_{2}}^{j} \right)^{1/2}}{p_{H_{2}O}^{j}} \right)$$
 (3)

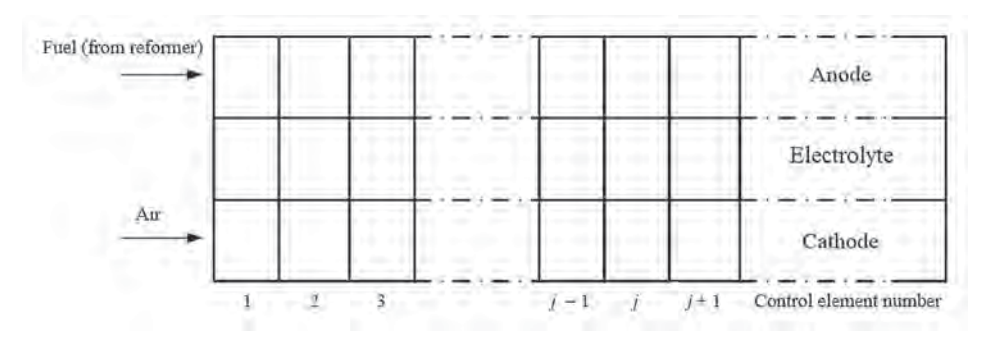


Fig. 1. A small element divided for the calculation in SOFC cell.

Irreversible loss generated inside the SOFC stack was calculated in term of overpotential. The difference between open circuit voltage and the summation of all irreversible loss was named operating voltage (Eq. (4)). In this study, three major types of overpotential were taken into account: activation overpotential, ohmic overpotential and concentration overpotential. The estimation of these overpotentials was given in our recent work [28].

$$V = E^{j} - \eta_{\text{act}}^{j} - \eta_{\text{ohm}}^{j} - \eta_{\text{con}}^{j}$$
 (4)

Inside the anode chamber, H2 was consumed via the electrochemical reaction. Additional hydrogen is obtained via methane steam reforming (Eq. (5)) and WGS (Eq. (6)). The rate of methane steam reforming reaction was computed using Eq. (7) [29], while WGS was assumed at chemical equilibrium due to its fast reaction rates at high operating temperatures [25-27]. Equations of mass and energy balances were solved for each small controlled volume (1mm distance) (Fig. 1) via one-dimensional (1-D) finite difference method in the flow direction of SOFC stack using computer coding in Visual Basic for MS Excel. The following assumptions were applied in order to simplify the calculation: (i) SOFC stack was operated in adiabatic mode; (ii) heat radiation between solid components inside the stack was neglected [13]; (iii) heat conduction in the solid electrolyte was neglected [13]; (iv) only electrochemical reaction via H<sub>2</sub> electro oxidation takes place; (v) pressure drop generation due to the flow of gas along the stack was neglected. The calculation of mass balance around the control volume was performed using Eqs. (8) and (9) for the anode and cathode chambers, respectively.

$$CH_4 + H_2O \leftrightarrow CO + 3H_2 \tag{5}$$

$$CO + H_2O \leftrightarrow H_2 + CO_2 \tag{6}$$

$$r_{\text{ref}}^{j} = 4274A^{j}e^{-\left(\frac{82000}{RT_{a}^{j}}\right)}p_{\text{CH}_{4}}^{j}\left(1 - \frac{p_{\text{CO}}^{j}(p_{\text{H}_{2}}^{j})^{3}}{p_{\text{CH}_{4}}^{j}p_{\text{H}_{2}O}^{j}K_{\text{ref}}^{j}}\right)$$
(7)

$$N_{a,k}^{j+1} = N_{a,k}^{j} + \sum_{n} \nu_{k,n} r_{n}^{j} + \frac{\nu_{k,\text{elec}} i^{j} A^{j}}{2F}$$
 (8)

$$N_{c,k}^{j+1} = N_{c,k}^{j} + \frac{v_{k,elec}i^{j}A^{j}}{2F}$$
 (9)

Operating voltage was assumed to be constant along the SOFC stack as its current collector usually has a high electrical conductivity. Heat generation in electrolyte due to the irreversibility of electrochemical mechanism and exothermic WGS are transferred into the bulk gas flow inside anode and cathode chambers through heat convection phenomena. Energy balance around solid tri-layer for each control volume was performed using Eq. (10). The energy balance of bulk fluid flow for anode and cathode chambers was calculated via Eqs. (11) and (12), respectively.

$$H_{\rm a}^{j+1} = H_{\rm a}^j + h_{\rm a} A^j \left( T_{\rm e}^j - T_{\rm a}^j \right)$$
 (11)

$$H_{\rm c}^{j+1} = H_{\rm c}^{j} + h_{\rm c} A^{j} \left( T_{\rm e}^{j} - T_{\rm c}^{j} \right)$$
 (12)

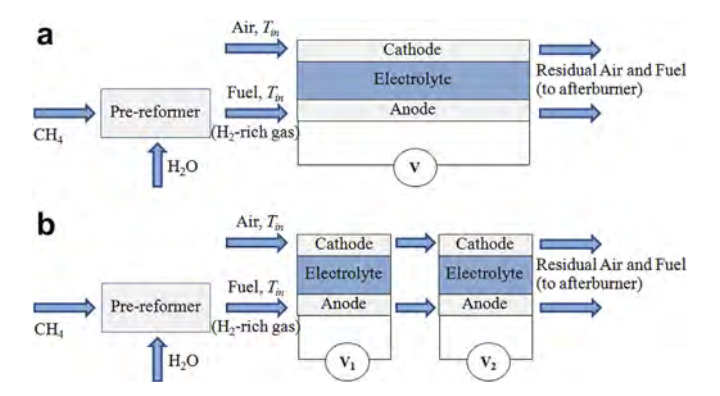


**Fig. 2.** Material flow schemes of a) uniform potential SOFC stack (1-section SOFC), and b) non-uniform potential SOFC with two sections (2-section SOFC).

To evaluate the viability of SOFC stack, two parameters were considered: the maximum stack temperature gradient ( $T_{\rm G}$ ) and the maximum stack temperature ( $T_{\rm max}$ ). The former parameter was defined as maximum spatial temperature change in electrolyte along the stack length and the maximum stack temperature was designated as maximum value of temperature along the SOFC stack. The maximum acceptable stack temperature gradient ( $T_{\rm G,acp}$ ) of 10 K cm<sup>-1</sup> [30] and maximum acceptable stack temperature ( $T_{\rm max,acp}$ ) of 1273 K were set as thermal constraints for the viable operation of SOFC stack in this study. The technical terms, i.e. average current density ( $i_{\rm avg}$ ), average power density ( $p_{\rm avg}$ ), total fuel utilization ( $U_{\rm f}$ ), electrical efficiency ( $\eta$ ) and %excess air ( $\varepsilon_{\rm air}$ ) were defined as expressed below;

$$i_{\text{avg}} = \frac{\sum_{j} i^{j} A^{j}}{\sum_{j} A^{j}} \tag{13}$$

$$p_{\text{avg}} = i_{\text{avg}}V \tag{14}$$

$$U_{\rm f} = \frac{\left(\frac{\sum_{j} i^{j} A^{j}}{2F}\right)}{4F_{\rm CH}} \tag{15}$$

$$\eta = \left[ \frac{P}{\left( \text{LHV}_{\text{fuel,in}} \right) \left( F_{\text{fuel,in}} \right)} \right] \times 100 \tag{16}$$

$$\varepsilon_{air} = \left[ \frac{0.21(F_{air,in})}{2F_{CH_4}} \right] \times 100 \tag{17}$$

Methane was assumed to be initially reformed using steam to methane molar feed ratio of 2.5 operated at SOFC feed temperature ( $T_{\rm in}$ ) prior to be fed to the anode chamber of SOFC stack as shown in Fig. 2. Chemical equilibrium was assumed for this reforming reaction in the pre-reformer. The term "methane flow rate,  $F_{\rm CH_4}$ " represents methane feed rate to the reformer and the term "% excess

$$-h_{a}A^{j}\left(T_{e}^{j}-T_{a}^{j}\right)-h_{c}A^{j}\left(T_{e}^{j}-T_{c}^{j}\right)+\left[\frac{(-\Delta H)_{elec}^{j}}{2F}-V\right]i^{j}A^{j}+\sum_{n}r_{n}^{j}(-\Delta H)_{n}^{j}=0$$
(10)

**Table 1**Summary of model parameters used in 1-D analysis [33–34].

Parameters	Value
SOFC cell	
l <sub>a</sub>	750 μm
$l_{c}$	50 μm
L	50 μm
Cell length	400 mm
Cell width	100 mm
Anode channel height	1 mm
Cathode channel height	1 mm
$h_a = h_c$	$0.2 \text{ kJ m}^{-2} \text{ s}^{-1} \text{ K}^{-1}$
Operating pressure	1 bar

air,  $\varepsilon_{\rm air}$ " was defined as percent of oxygen feed rate (to cathode chamber) to the stoichiometric flow rate of air for complete combustion of  $F_{\rm CH_4}$ . The values of  $\varepsilon_{\rm air}$  and  $F_{\rm CH_4}$  were kept constant at 240% and 1.08 mol h<sup>-1</sup>, respectively.

## 3. Results and discussion

The SOFC stack dimensions and input parameters were initially set as summarized in Table 1. Model verification for the calculation of SOFC stack's performance was performed as described in our previous work [31]. The verifying results confirmed that the utilized SOFC stack model could well predict the experimental results of Zhao and Virkar [32] for the mixture of 97% H<sub>2</sub> and 3% CO.

To improve the performance and operating viability of SOFC, the comparison between the performance of 1-section SOFC (Fig. 2a) and 2-section SOFC (Fig. 2b) was first investigated. Inlet temperature of reformed methane and air was set at 998 K, while the

operating voltage of SOFC stack was varied until its optimum value which offers the highest average power density was obtained. As shown in Fig. 3a and b, with the optimum operating voltage of 0.778 V, maximum power density was found at the stack length of 0.25 m while stack temperature and temperature gradient were always lower than their maximum acceptable values along the SOFC stack. Concentration of hydrogen in anode gas continuously decreased in the flow direction (Fig. 3b) due to the utilization of hydrogen in the electrochemical reaction. In the first half of SOFC stack, the power density increased in the flow direction until its maximum value was reached due to the decrease in overpotential (increase in stack temperature). However, near the gas exit of the stack, the power density decreased along the flow direction. This was due to both the decrease in hydrogen concentration (Fig. 3b) and rate of electrochemical reaction. Moreover, the open circuit voltage became very low near the gas exit (Fig. 3c) due to the high stack temperature. This would imply that the effect of the decrease in hydrogen concentration in anode bulk gas and open circuit voltage dominated the effect of the decrease in overpotential near the gas exit of SOFC stack. From the calculations, for the case of 1section SOFC, the optimum operating voltage of 0.778 V could provide average power density and fuel utilization of 0.29 W cm<sup>-2</sup> and 0.645, respectively.

From the results observed with the 1-section SOFC, the difference between the open circuit voltage and operating voltage is very high and becomes lower at the exit point of the stack (Fig. 3c). This envisions different behaviors inside the SOFC stack and suggests that division of SOFC stack into various sections with different operating voltage may improve the average power density of SOFC stack. The performance of 2-section SOFC was therefore considered using two scenarios: (a) 2-section SOFC with high voltage at the 1st

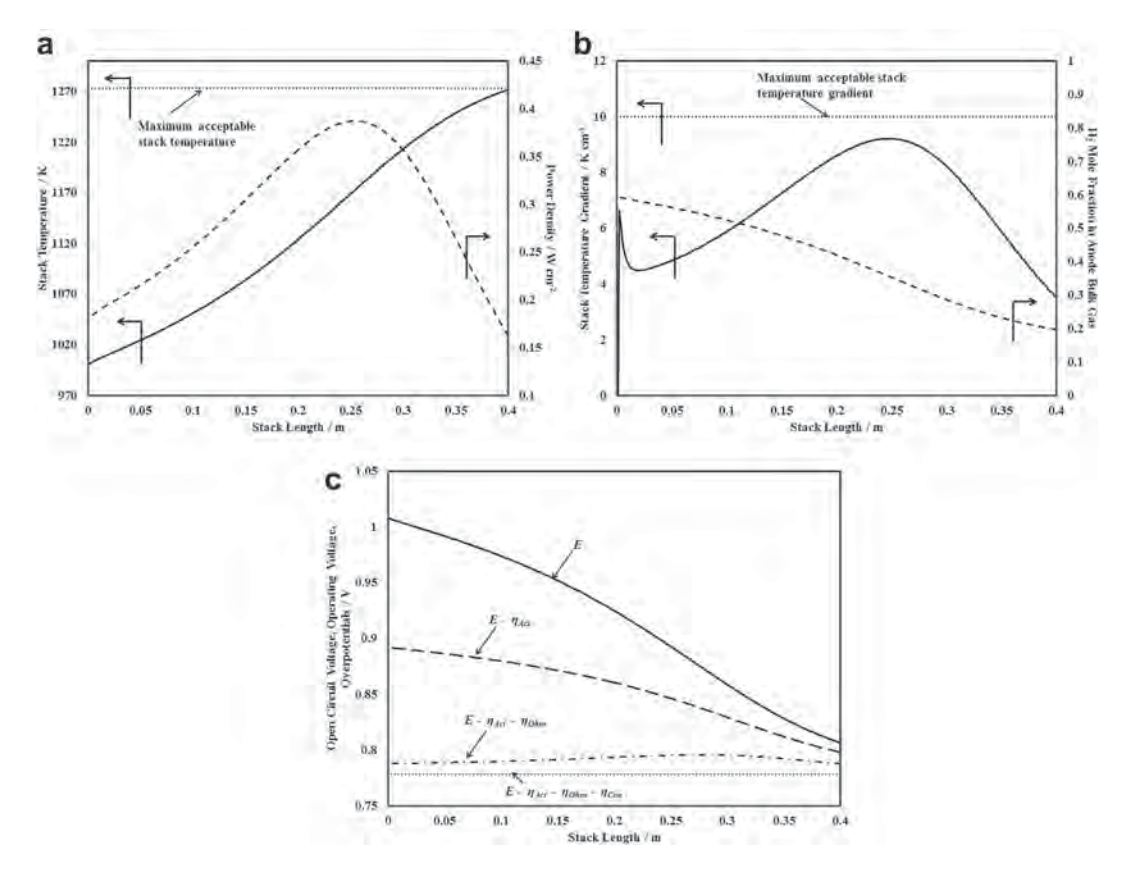
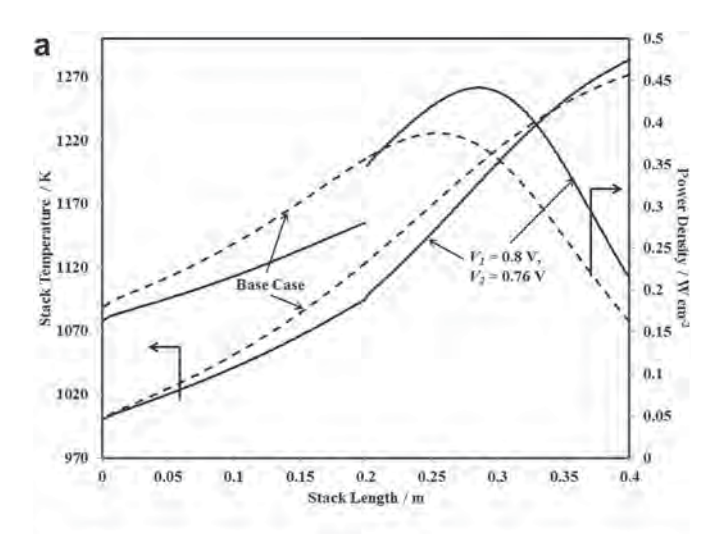
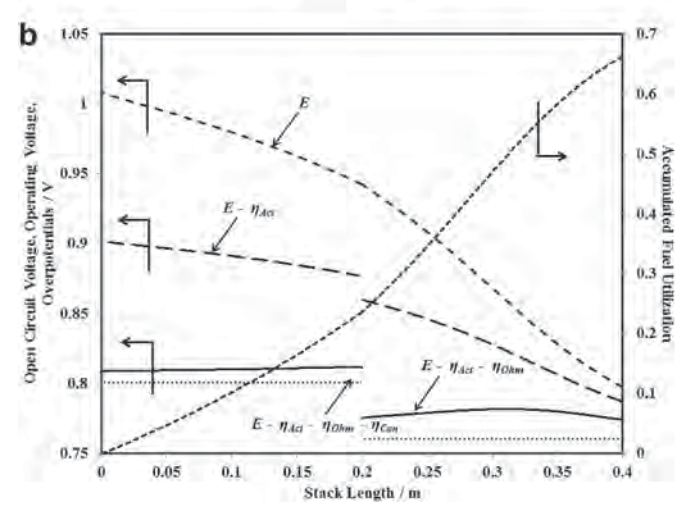


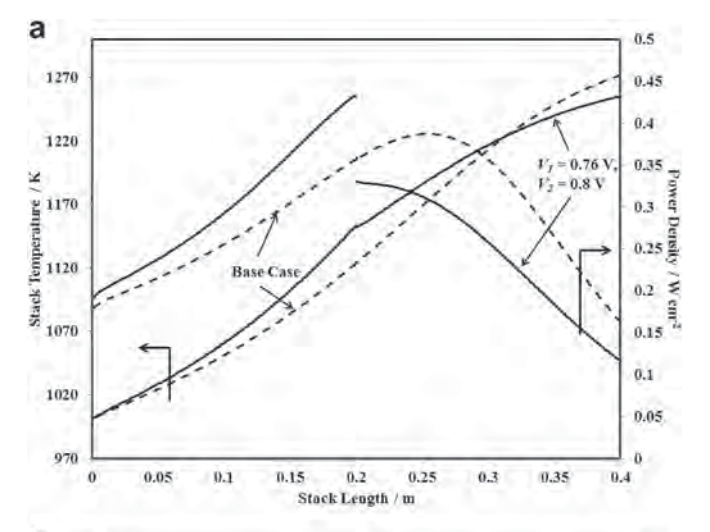
Fig. 3. The distributions of a) stack temperature and power density, b) stack temperature gradient and  $H_2$  concentration in anode bulk gas, and c) open circuit voltage/operating voltage/overpotential along the stack for 1-section SOFC at maximum average power density ( $T_{in} = 998$  K with optimal operating voltage of 0.778 V).

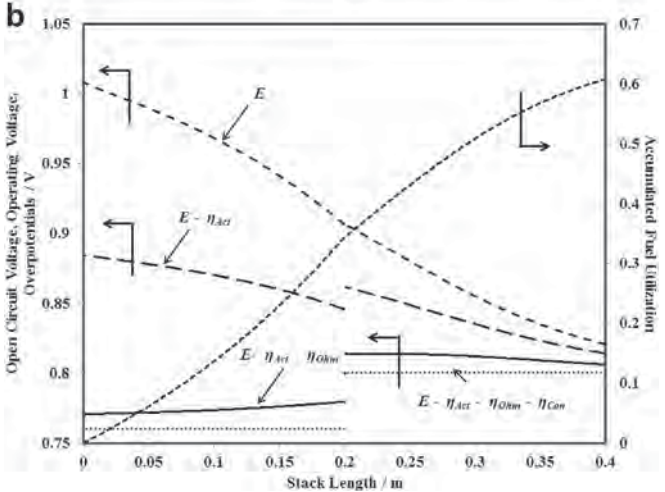
section (2S-1 V) and (b) 2-section SOFC with high voltage at the 2nd section (2S-2 V). For the section operating at high operating voltage, the operating voltage and the low-voltage section were set to 0.8 V and 0.76 V, respectively. To evaluate the stack performance for these scenarios, the 1-section SOFC operating at the optimum operating voltage was considered as a base case. The performance of the 2-section SOFC illustrated in terms of power density, operating voltage and fuel utilization is demonstrated in Figs. 4 and 5. For 2S-1 V scenario (Fig. 4), the power density at the 1st section is lower than the base case although the operating voltage was higher than that of the base case. This is because the increase in temperature and also fuel utilization were lower, and the power density was therefore inhibited. However, 2S-1 V offered a higher power density at the 2nd stack section compared with the base case. This could be explained by the fact that there were large amounts of remaining H<sub>2</sub> fed to the 2nd section of anode chamber due to low fuel utilization in the 1st section of stack, leading to high electrochemical reaction rate at the 2nd section of SOFC stack and hence a higher power density. Due to high fuel utilization at the 2nd section of stack, the increase in stack temperature of 2S-1 V was also higher when compared with that of the base case. For 2S-2 V scenario (Fig. 5), superior power density to the base case was



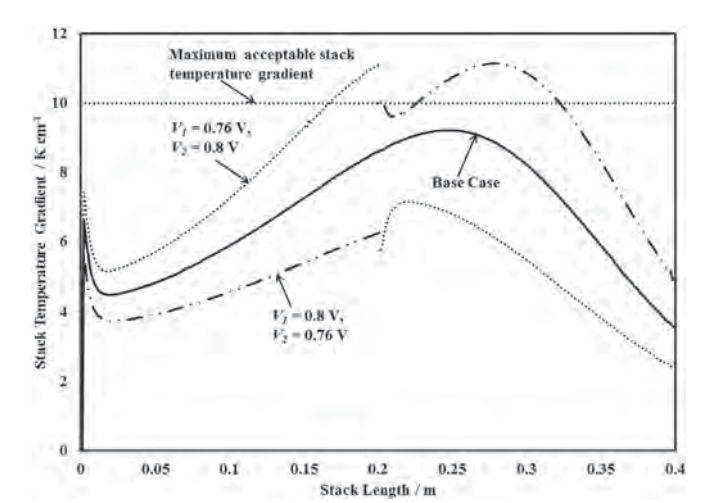


**Fig. 4.** The distribution of a) power density and stack temperature and b) open circuit voltage/operating voltage/overpotential and accumulated fuel utilization along the stack between the base case and 2-section SOFC with  $V_1=0.8~\rm V$  and  $V_2=0.76~\rm V$  ( $T_{\rm in}=998~\rm K$ ).

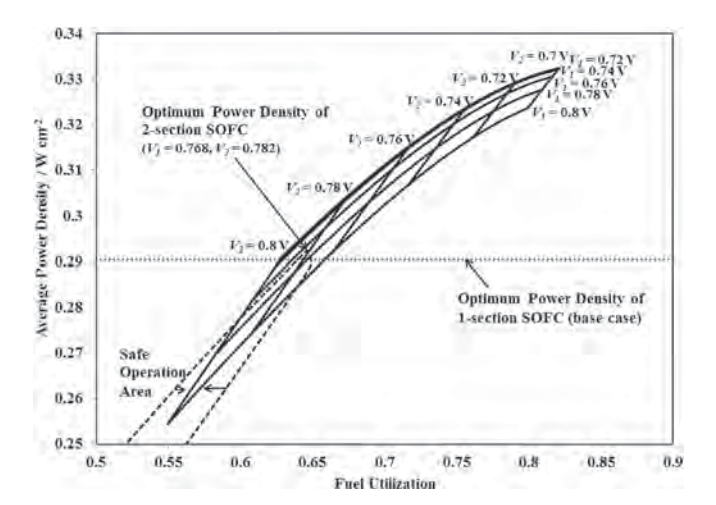




**Fig. 5.** The distribution of a) power density and stack temperature and b) open circuit voltage/operating voltage/overpotential and accumulated fuel utilization along the stack between the base case and 2-section SOFC with  $V_1=0.76~\rm V$  and  $V_2=0.8~\rm V$  ( $T_{\rm in}=998~\rm K$ ).



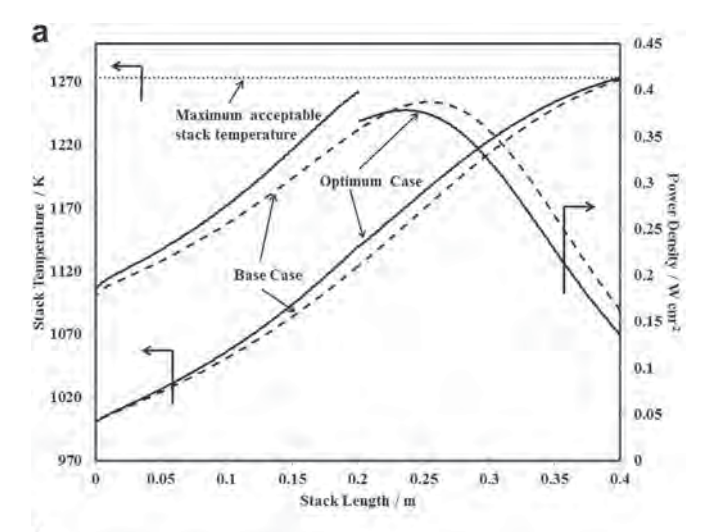
**Fig. 6.** Comparison of the distribution of stack temperature gradient along the stack between the base case, 2-section SOFC with  $V_1=0.76$  V and  $V_2=0.8$  V, and 2-section SOFC with  $V_1=0.8$  V and  $V_2=0.76$  V ( $T_{\rm in}=998$  K).



**Fig. 7.** Effect of operating voltage ( $V_1$  and  $V_2$ ) on the average power density and fuel utilization of 2-section SOFC ( $T_{\rm in}=998~{\rm K}$ ).

achieved at the 1st stack section due to higher fuel utilization. This also caused a sharp increase of temperature in the 1st stack section for 2S-2 V. However, the power density of 2S-2 V in the 2nd stack section became lower when compared with that of the base case. This might be due to lower H2 concentration and rate of electrochemical reaction. These results imply that the difference in the open circuit voltage and operating voltage majorly controlled the fuel utilization as shown in Fig. 5b, the voltage difference increased along with the fuel utilization rate. The accumulated fuel utilization presented in Figs. 4b and 5b for 2S-1 V and 2S-2 V, respectively, indicates the total fuel utilization from the gas entry of SOFC stack to the specified stack position. An increase in the voltage difference represents a high overpotential making the temperature gradient at the 1st stack section for 2S-2 V and at the 2nd stack section for 2S-1 V over the limit as shown in Fig. 6. It could be concluded that the decrease in operating voltage enhances the power density; however, thermal constraint of SOFC operation could also be infringed. By considering the reason above, the selection of suitable operating voltage for 2-section stack should be carefully considered.

The values of operating voltage for the 1st section  $(V_1)$  and 2nd section  $(V_2)$  of 2-section SOFC stack were varied to study their effects on average power density and fuel utilization as shown in Fig. 7. The results demonstrate that the decrease in  $V_1$  and  $V_2$  could improve the average power density and also promote fuel utilization of SOFC stack. However, it is not likely that operation of 2-section SOFC offered a greater average power



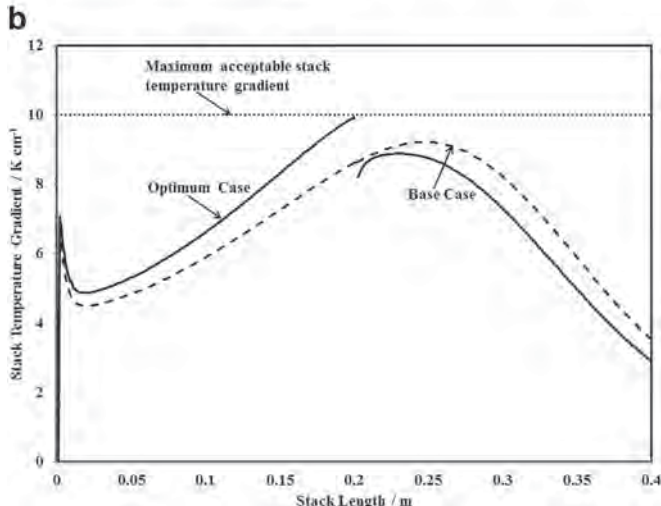


**Fig. 8.** The distribution of a) stack temperature and power density and b) stack temperature gradient along the stack between the base case and the optimum operation of 2-section SOFC ( $T_{\rm in}=998$  K).

density than the base case under the safe operation area (the area where the operating conditions offered  $T_{\rm G}$  and  $T_{\rm max}$  below their maximum acceptable values). In this work, the optimum values of  $V_1$  and  $V_2$  of 2-section SOFC were found to be at 0.768 and 0.782 V, respectively (Fig. 7). As summarized in Table 2, an insignificant improvement of 0.69% in average power density of 2-section SOFC over 1-section SOFC is observed. At the optimum

 Table 2

 Comparison of the performance of the optimum cases of 1-section SOFC, 2-section SOFC, 2-section SOFC-T and 3-section SOFC-T.

Operation mode	Optimum case of 1-section SOFC	Optimum case of 2-section SOFC	Optimum case of 2-section SOFC-T	Optimum case of 3-section SOFC-T
$F_{\text{CH}_4,\text{eq}} \text{ (mol s}^{-1}\text{)}$	0.0003	0.0003	0.0003	0.0003
$\varepsilon_{\rm air}$ (%)	240	240	240	240
$U_{\rm f}(-)$	0.6451	0.6462	0.7739	0.7425
Operating voltage (V)	0.778	$V_1 = 0.768$	$V_1 = 0.79$	$V_1 = 0.789$
		$V_2 = 0.782$	$V_2 = 0.731$	$V_2 = 0.755$
				$V_2 = 0.719$
Average Power density (W cm <sup>-2</sup> )	0.2903	0.2923	0.3274	0.3090
Average Current density (A cm <sup>-2</sup> )	0.3732	0.3738	0.4479	0.4297
η (%)	39.13	39.40	44.13	41.65
Electricity produced (W)	116.14	116.93	130.96	123.60
Maximum stack temperature (K)	1271.71	1273.11	1227.57	1169.14
Maximum stack temperature gradient (K cm <sup>-1</sup> )	9.21	9.93	9.94	9.97

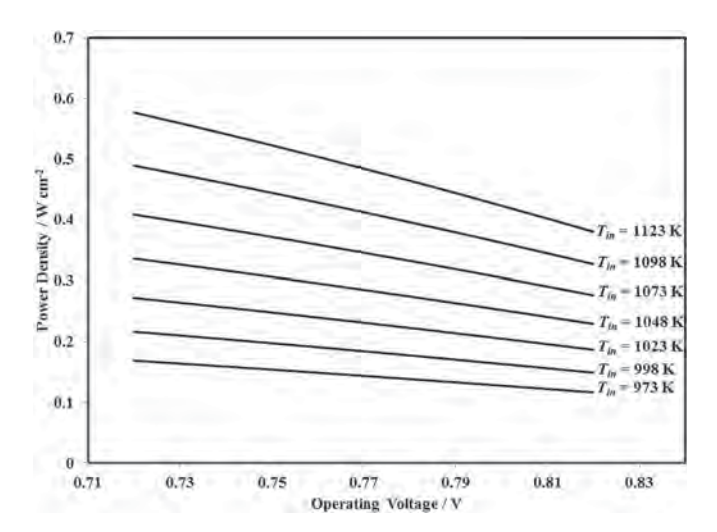


**Fig. 9.** Effect of operating voltage and operating temperature on power density of SOFC calculated based on the chemical equilibrium composition of steam methane reforming reaction with the steam to carbon ratio of 2.5.

operation, the profiles of power density, stack temperature, and stack temperature gradient along the SOFC stack of 2-section SOFC were almost similar to those of the base case as shown in Fig. 8a and b. This is due to the narrow thermal-safe operation area which limited the operation of 2-section SOFC (Fig. 7). It could be concluded that the operation of 2-section SOFC with the consideration of a solely operating voltage cannot significantly improve the SOFC performance.

As discussed previously, although the stack temperature played the major role in controlling the stack performance, thermal constraint is another important factor that could limit its performance. In Fig. 9, it is shown the effect of operating voltage and operating temperature on the power density of SOFC operation, which were calculated based on the chemical equilibrium composition of methane steam reforming reaction. The results show that the power density was improved when SOFC was operated at high temperature and low operating voltage. To further envision the effect of stack temperature on the SOFC performance, the effect of inlet temperature of fuel and air  $(T_{in})$  was studied for 1-section SOFC. The results, as demonstrated in Fig. 10, show that despite the fact that the operation of SOFC at high temperature and low voltage could offer a high power density, this operation was still impractical as  $T_G$  and  $T_{max}$  exceeded their limiting values. As shown in Fig. 10a and b, when Tin was higher than 998 K, the operation of 1-section SOFC was controlled by the constraint of  $T_{\text{max,acp}}$ , while the constraint of  $T_{G,acp}$  became an operation-controlling criteria as the inlet fuel temperature was lower than 998 K. Moreover, for high  $T_{\rm in}$ , 1-section SOFC could not be operated at low operating voltage due to the thermal constraints. To overcome the thermal constraints, values of the operating voltage larger than 0.81 V were required when  $T_{\rm in}$  is 1048 K, while a value of the operating voltage as low as 0.778 V could be operated for 1-section SOFC operating at  $T_{\rm in}$  of 998 K (Fig. 10a). Operation of SOFC at a higher  $T_{\rm in}$  (ranging from 1048 K to 998 K) caused lower average power density (Fig. 10a) and total fuel utilization (Fig. 10c).

To operate at favored conditions (high temperature and low operating voltage) with the thermal-secured operation, the new SOFC configuration, "non-uniform potential and 2-section SOFC

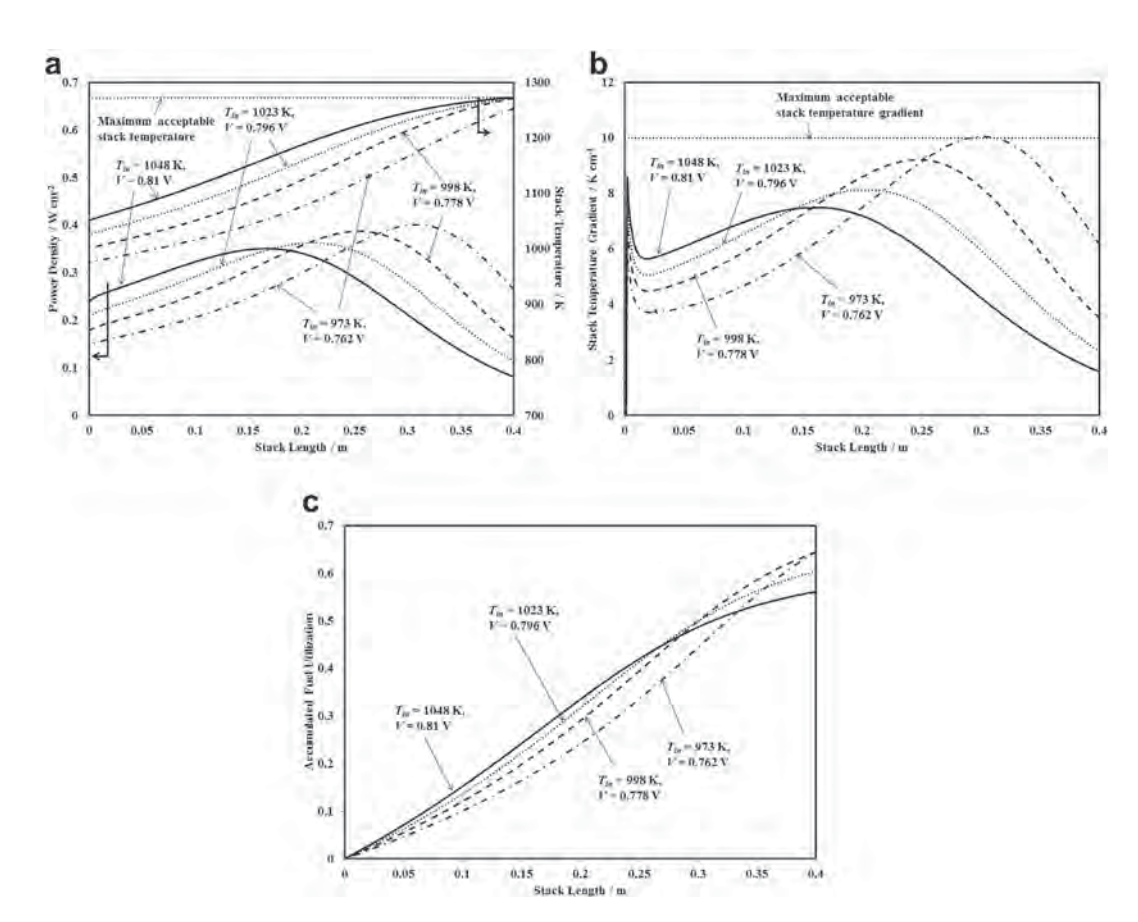


**Fig. 10.** The distribution of a) stack temperature and power density, b) stack temperature gradient, and c) accumulated fuel utilization along the SOFC stack for the optimum operation of 1-section SOFC at different  $T_{\rm in}$ .

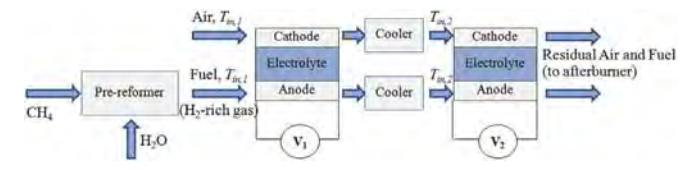


**Fig. 11.** Schematic diagram of non-uniform potential 2-section SOFC stack equipped with cooler, 2-section SOFC-T.

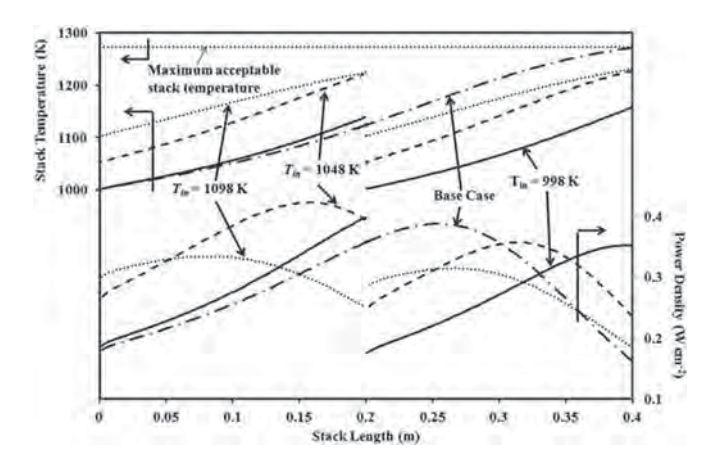


**Fig. 12.** The distribution of stack temperature and power density along the SOFC stack for the optimum case of 2-section SOFC-T operating at different  $T_{\rm in}$ .

stack equipped with a cooler, (2-section SOFC-T)" was proposed. The scheme of this configuration was similar to that of 2-section SOFC, except installation of an additional cooler between the first and the second sections of the stack as shown in Fig. 11. With this configuration, the outlet gas streams from the cathode and anode chambers of the 1st section of stack were fed to the cooler, where temperature of gas stream was reduced to  $T_{\rm in,2}$  prior to be fed to the 2nd section of stack. The effects of inlet temperatures ( $T_{\rm in,1}$ ) and ( $T_{\rm in,2}$ ) of fuel and air for the 1st and 2nd stack sections, respectively, as well as those of operating voltages ( $V_1$ ) and ( $V_2$ ) of the 1st and the 2nd stack sections, respectively, on performance of 2-section SOFC-T were studied. To simplify the calculations,  $T_{\rm in,1}$  was assumed equal to  $T_{\rm in,2}$  and both of them were similar to  $T_{\rm in}$ 

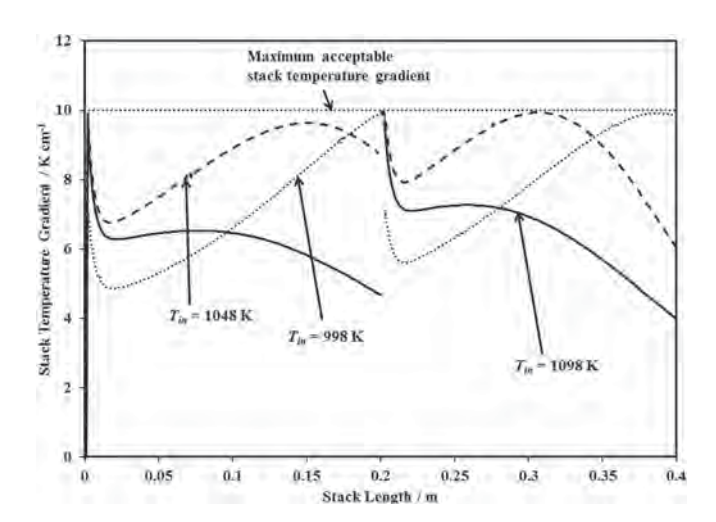


**Fig. 13.** The distribution of stack temperature gradient along the SOFC stack for the optimum operation of 2-section SOFC-T at different  $T_{\rm in}$ .

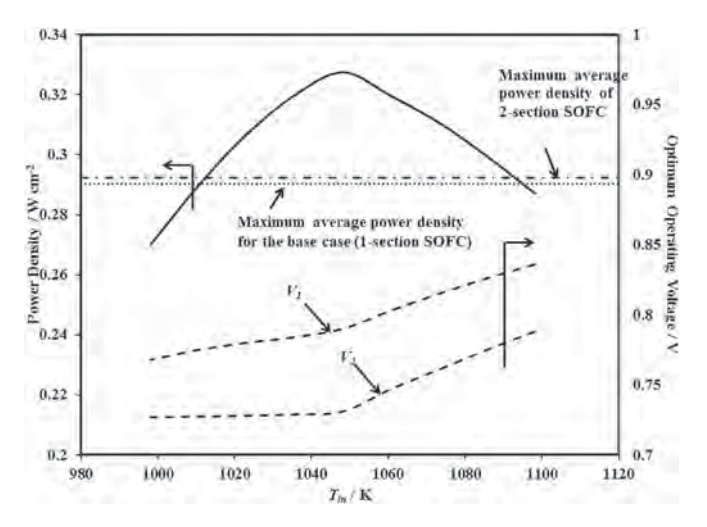


**Fig. 14.** Power density and optimum  $V_{1}$ , and  $V_{2}$  of 2-section SOFC-T at different  $T_{in}$ .

The operating voltages  $V_1$  and  $V_2$  were varied until their optimum values (the value that allowed the maximum average power density of 2-section SOFC-T) were achieved and all thermal constraints were pursued. The stack temperature and power density profiles for the optimum case of 2-section SOFC-T along the stack with the variation of  $T_{\rm in}$  are illustrated in Fig. 12. The results show that  $T_{\text{max}}$  of 2-section SOFC-T operated at  $T_{\text{in}}$  between 998 K and 1098 K were largely lower than those of the base case (1-section SOFC) and  $T_{\text{max,acp}}$ . Therefore, the thermal constraint for the operation of 2-section SOFC-T was the controlling of  $T_G$  of SOFC stack to be lower than  $T_{G,acp}$ . As shown in Fig. 13, unlike the 1section SOFC and 2-section SOFC, the limitation of the value of  $T_{\rm G}$  is challenged with the operation of 2-section SOFC-T, especially for the operation at  $T_{\rm in} = 1048$  K, where this situation is found at both gas entry and middle position of the two SOFC sections. The thermal constraint challenge at the gas entry was caused by the high H<sub>2</sub> concentration of anode fuel gas stream that accelerates the rate of electrochemical reaction at this stack position, while the challenge at the middle of the stack was caused by the enhancement in the electrochemical reaction rate due to the increase in stack temperature. However, the selection of the appropriate  $T_{in}$  is also an important issue for the control of the performance of 2-section SOFC-T. At  $T_{\rm in}=998$  K, the thermal constraint challenge for 2-section SOFC-T is found only at near the gas exit of both two sections. For the case that  $T_{\rm in}=1098$  K, the thermal constraint was challenged only at the gas entries of each section. This is because the rate of electrochemical reaction at the gas entry was very high due to its high operating temperature. Moreover, with high  $T_{in}$ , desirable low operating voltage could not be operated due to the thermal constraint at the gas entry. The summary of average power density and optimum operating voltage at different  $T_{\rm in}$  of 2-section SOFC-T are given in Fig. 14. The maximum power density of 0.327 W cm<sup>-2</sup> was achieved at  $T_{\rm in} = 1048$  K and optimum values of  $V_1$  and  $V_2$  of 0.79 and 0.731 V, respectively. The maximum average power density of 2-section SOFC-T is 12.77% higher than that of the base case (1-section SOFC). If  $T_{in}$  was lower than its optimum value, average power density of 2-section SOFC-T became lower due to lower electrochemical reaction rate. Increase in power density of 2-section SOFC-T was also inhibited when operating at high  $T_{\rm in}$  (Fig. 14). This is due to the fact that low desirable operating voltage cannot be operated at high  $T_{\rm in}$  owing to the thermal constraint. The 2section SOFC-T could offer a higher stack performance compared with the 1-section SOFC.

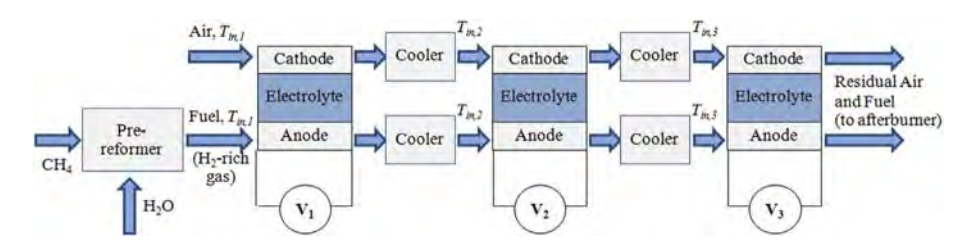
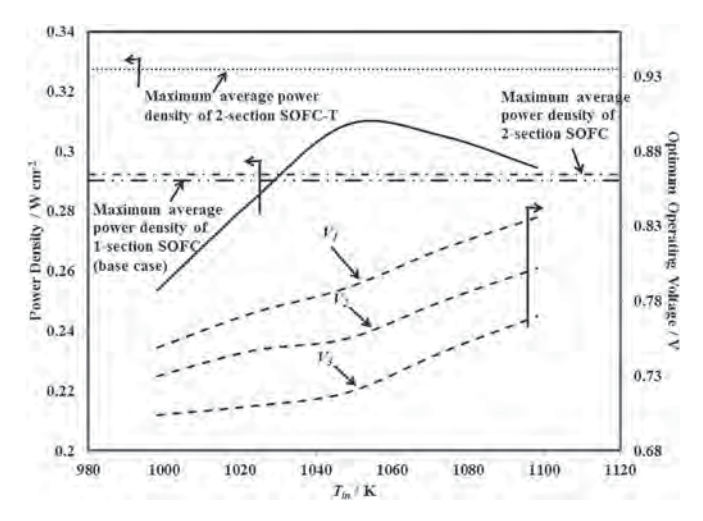


Fig. 15. Schematic diagram of non-uniform potential 3-section SOFC stack equipped with two coolers, 3-section SOFC-T.

To further evaluate the performance of non-uniform potential SOFC stack equipped with a cooler, the non-uniform potential SOFC stack with 3 sections equipped with 2 coolers, 3-section SOFC-T, was proposed as shown in Fig. 15. With this configuration, the length of each stack section was set to be similar to one another while inlet temperatures of fuel gas and air streams for each stack were assumed similar and equal section  $(T_{\rm in} = T_{\rm in.1} = T_{\rm in.2} = T_{\rm in.3})$ .  $T_{\rm in}$  of 3-section SOFC-T was varied and optimum values of  $V_1$ ,  $V_2$ , and  $V_3$  for each  $T_{\rm in}$  were examined. As shown in Fig. 16, similar to the case of 2-section SOFC-T, the maximum average power density of 3-section SOFC-T was achieved when  $T_{in} = 1048$  K. To achieve the maximum average power density for each  $T_{in}$ ,  $V_1$  was always set to be higher than  $V_2$  and  $V_2$  to be higher than  $V_3$ . It is observed that the increase in the number of sections could not improve the SOFC performance. As summarized in Table 2, maximum achieved average power density of 3-section SOFC-T was 0.309 W cm<sup>-2</sup>, which was lower than that of 2-section SOFC-T (0.327 W cm<sup>-2</sup>). As shown in Fig. 17a, since the length of each stack section of 3-section SOFC-T was too short, its power density could not reach its maximum value. With the defined SOFC stack dimension and electrochemical reaction rate, unlike 2-section SOFC-T, adequately high stack temperature could not be achieved at the gas exit of each section for 3-section SOFC-T as shown in Fig. 17b. This result reveals that, apart from the operating voltage, average power density as well strongly depended on the stack temperature.

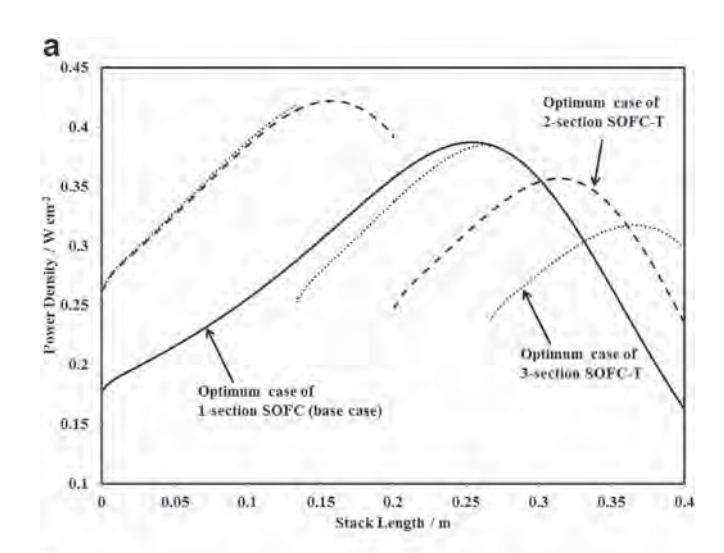
It is noted that this work presented the success of applying nonuniform potential SOFC with a novel inter-cooler to overcome the limitation of temperature gradient by trial methodology. However, using complete optimization methodology could offer more precise suitable operating parameters. In addition, the effects of other design parameters such as the length of each stack section, the gas inlet temperature for each stack section, and % excess air should also be considered.



**Fig. 16.** Power density and optimum  $V_1$ ,  $V_2$ , and  $V_3$  of 3-section SOFC-T at different  $T_{\rm in}$ .

# 4. Conclusion

In this study, one-dimensional finite difference method was applied to evaluate the performance of non-uniform potential SOFC stack. Power density was considered as a performance indicator of the operation of SOFC stack fueled by reformed methane. The evaluation was performed based on two thermal constraints: maximum acceptable stack temperature of 1273 K and maximum acceptable stack temperature gradient of 10 K cm<sup>-1</sup>. Initially, the first proposed non-uniform potential SOFC with two sections (2-section SOFC) was evaluated. With this configuration, SOFC stack was divided into two sections operating at different operating voltages. The values of



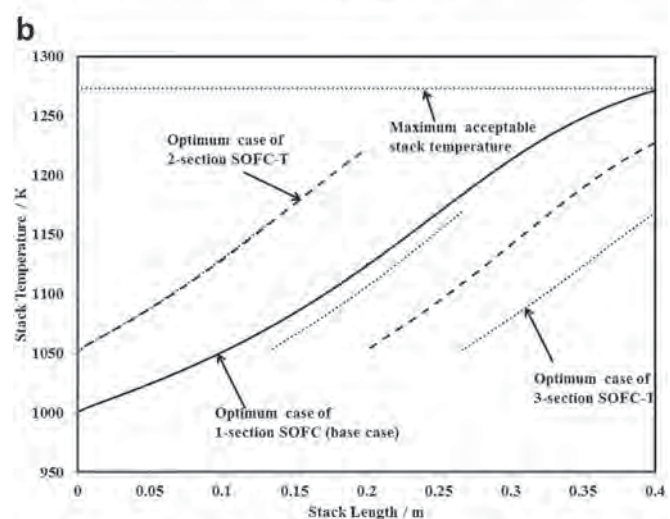


**Fig. 17.** The distribution of a) power density and b) stack temperature along stack length of the optimum cases of 1-section SOFC, 2-section SOFC-T and 3-section SOFC-T.

operating voltage of each section of 2-section SOFC were varied to determine maximum average power density under the two thermal constraints. The results indicated that 2-section SOFC can offer only 0.69% average power density higher than traditional 1-section SOFC with the optimum values of operating voltage of 0.768 V for the 1st section and of 0.782 V for the 2nd section. To achieve a high power density and simultaneously overcome the thermal constraints, a new configuration of non-uniform potential SOFC, non-uniform potential and 2-section SOFC stack equipped with a cooler (2-section SOFC-T) was proposed. In this configuration, the cooler was installed to reduce temperatures of the fuel gas and air outlet from the 1st section prior to be fed to the 2nd section. It was found that not only operating voltage that played an important role in the operation of 2section SOFC-T but also the inlet fuel and air temperatures are critical factors affecting the performance of 2-section SOFC-T. The value of the temperature should, therefore, be well selected to overcome the thermal constraints and minimize the overpotential. The maximum average power density of the 2-section SOFC-T was achieved when the inlet fuel temperature was set at 1048 K and the values of operating voltages of the 1st and 2nd sections were equal to 0.79 and 0.731 V, respectively. By operating at this condition, the 2-section SOFC-T offered 12.8% improvement in average power density compared with the 1-section SOFC. With the defined SOFC stack dimension and electrochemical reaction rate, an increase in the number of section from 2 sections to 3 sections (3-section SOFC-T) could not improve the average power density since the high stack temperature was not reached at the gas exit of each section for 3section SOFC-T and its overpotential was high. Further detailed study should be performed in order to optimize other process parameters of 2-section SOFC-T, such as the length of each stack section and the fuel gas inlet temperature for each stack section.

# Acknowledgments

The supports from Postdoctoral fellowship (Ratchadaphiseksomphot Endowment Fund) from Graduate School Chulalongkorn University and the TRF Senior Researcher Scholar from the Thailand Research Fund are gratefully acknowledged.

# References

- P. Kuchonthara, S. Bhattacharya, A. Tsutsumi, J. Power Sources 124 (2003) 65–75.
- [2] M.C. Williams, Fuel Cells 7 (2007) 78–85.
- S.P. Yoon, J. Han, S.W. Nam, T.H. Lim, S.A. Hong, J. Power Sources 136 (2004) 30-36.
- [4] S.D. Kim, S.H. Hyun, J. Moon, J.H. Kim, R.H. Song, J. Power Sources 139 (2005) 67–72. Y. Yi, A.D. Rao, J. Brouwer, G.S. Samuelsen, J. Power Sources 132 (2004) 77-85.
- [6] V. Liso, Y. Zhao, N. Brandon, M.P. Nielsen, S.K. Kaer, Int. J. Hydrogen Energy 36 (2011) 13715-13726.
- [7] H. Wen, J.C. Ordonez, J.V.C. Vargas, Appl. Therm. Eng. 50 (2013) 12-25.
- [8] A. Selimovic, J. Palsson, J. Power Sources 106 (2002) 76-82.
- [9] S.F. Au, N. Woudstra, K. Hemmes, J. Power Sources 122 (2003) 28-36.
- [10] S.M. Senn, D. Poulikakos, Electrochem. Commun. 7 (2005) 773–780.
- [11] S. Vivanpatarakij, S. Assabumrungrat, N. Laosiripojana, J. Power Sources 167 (2007) 139-144.
- [12] W.B. Guan, H.J. Zhai, L. Jin, C. Xu, W.G. Wang, Fuel Cells 12 (2012) 24-31.
- [13] M. Sorrentino, C. Pianese, Y.G. Guezennec, J. Power Sources 180 (2008) 380-392.
- [14] G. Karavalakis, T.D. Durbin, M. Villela, J.W. Miller, J. Nat. Gas Sci. Eng. 4 (2012)
- [15] G.P. McTaggart-Cowan, S.N. Rogak, S.R. Munshi, P.G. Hill, W.K. Bushe, Fuel 89 (2010) 752–759.
- [16] R.J. Spiegel, J.L. Preston, J. Power Sources 86 (2000) 283-288.
- Y. Patcharavorachot, A. Arpornwichanop, in: Proceedings of the 22nd European Symposium on Computer Aided Process Engineering, 17–20 June 2012. London.
- K. Nikooyeh, A.A. Jeje, J.M. Hill, J. Power Sources 171 (2007) 601-609.
- [19] E. Vakouftsi, G. Marnellos, C. Athanasiou, F.A. Coutelieris, Chem. Eng. Res. Des. 89 (2011) 224-229.
- [20] Y. Wang, F. Yoshiba, M. Kawase, T. Watanabe, Int. J. Hydrogen Energy 34 (2009) 3885-3893.

- [21] P. Piroonlerkgul, W. Wiyaratn, A. Soottitantawat, W. Kiatkittipong, A. Arpornwichanop, N. Laosiripojanad, S. Assabumrungrat, Chem. Eng. J. 155
- [22] S. Baron, N. Brandon, A. Atkinson, B. Steele, R. Rudkin, J. Power Sources 126 (2004) 58-66.
- [23] V.M. Janardhanan, V. Heuveline, O. Deutschmann, J. Power Sources 172 (2007) 296 - 307
- [24] M.A. Khaleel, Z. Lin, P. Singh, W. Surdoval, D. Collin, J. Power Sources 130 (2004) 136-148.
- [25] R. Blom, I.M. Dahl, A. Slagtem, B. Sortland, A. Spjelkavik, E. Tangstad, Catal. Today 21 (1994) 535-543.
- [26] M.C.J. Bradford, M.A. Vannice, Appl. Catal. A Gen. 142 (1996) 97–122.
- [27] H.M. Swaan, V.C.H. Kroll, G.A. Martin, C. Mirodatos, Catal. Today 21 (1994) 571 578.
- [28] P. Piroonlerkgul, S. Assabumrungrat, N. Laosiripojana, A.A. Adesina, Chem. Eng. Process. Process Intensif. 48 (2009) 672-682.
- [29] E. Achenbach, E. Riensche, J. Power Sources 52 (1994) 283–288.
- [30] L.T. Lim, D. Chadwick, L. Kershenbaum, Ind. Eng. Chem. Res. 44 (2005) 9609-9618
- [31] P. Piroonlerkgul, S. Assabumrungrat, N. Laosiripojana, A.A. Adesina, Chem. Eng. J. 140 (2008) 341-351.
- [32] F. Zhao, A.V. Virkar, J. Power Sources 141 (2005) 79-95.
- [33] P. Aguiar, D. Chadwick, L. Kershenbaum, Chem. Eng. Sci. 59 (2004) 87-97.
- [34] M. Ni, M.K.H. Leung, D.Y.C. Leung, Energy Convers. Manage. 48 (2007) 1525-1535.

#### Nomenclature

```
A: SOFC stack active area [m<sup>2</sup>]
E: electromotive force [V]
E_0: electromotive force at standard pressure [V]
F: Faraday constant (9.6495 \times 10^4) [C mol<sup>-1</sup>]
F_{air,in}: inlet air flow rate to SOFC [mol s<sup>-1</sup>]
F_{CH_4,eq}: methane equivalent flow rate [mol s<sup>-1</sup>]
F_{fuel,in}: inlet fuel flow rate to SOFC [mol s<sup>-1</sup>] 
h: heat transfer coefficient [W m<sup>-2</sup> K<sup>-1</sup>]
\Delta H_i: heat of reaction for reaction i [J mol<sup>-1</sup>]
H: energy rate [J s<sup>-1</sup>]
i: current density [A cm<sup>-2</sup>]
K_{ref}: equilibrium constant for steam reforming reaction [Pa<sup>2</sup>]
1: thickness [um]
LHV<sub>fuel,in</sub>: lower heating value of SOFC inlet fuel [J mol<sup>-1</sup>]
N_k: molar flow rate of component k [mol s<sup>-1</sup>]
p_k: partial pressure of component k [Pa]
p: power density [W cm<sup>-2</sup>
P: electricity produced [W]
r_n: reaction rate for reaction n \text{ [mol s}^{-1}\text{]}
R: gas constant (8.3145) [J mol<sup>-1</sup> K<sup>-1</sup>]
T: temperature [K]
T_G: maximum stack temperature gradient [K cm<sup>-1</sup>]
T_{G,acp}: maximum acceptable stack temperature gradient [K cm<sup>-1</sup>]
T_{in}: SOFC inlet temperature of fuel and air streams [K]
T_{max}: maximum stack temperature [K]
T_{max\,acp}: maximum acceptable stack temperature [K]
U_f: total fuel utilization [-]
V: operating voltage [V]
V_n: operating voltage of section n [V]
```

#### Greek letters $\varepsilon_{air}$ : % excess air [%] η: electrical efficiency [%] $\eta_{act}$ : activation loss [V] $\eta_{con}$ : concentration loss [V] $\eta_{ohm}$ : ohmic loss [V]

Subscripts

 $v_{k,i}$ : stoichiometric coefficient of component k in reaction i [-]

```
Superscript j: j<sup>th</sup> control volume (0, 1, 2,..., 400)
```

a: anode chamber avg: average c: cathode chamber e: electrolyte elec: electrochemical reaction k: component (CH<sub>4</sub>, CO, CO<sub>2</sub>, H<sub>2</sub>, H<sub>2</sub>O, O<sub>2</sub>, N<sub>2</sub>) n: reaction (ref, WGS, elec) ref: reforming reaction WGS: water gas shift reaction

This article was downloaded by: [Chulalongkorn University]

On: 25 August 2014, At: 17:38 Publisher: Taylor & Francis

Informa Ltd Registered in England and Wales Registered Number: 1072954 Registered office: Mortimer House,

37-41 Mortimer Street, London W1T 3JH, UK



# Separation Science and Technology

Publication details, including instructions for authors and subscription information: <a href="http://www.tandfonline.com/loi/lsst20">http://www.tandfonline.com/loi/lsst20</a>

# Effect of KI and KOH Impregnations over Activated Carbon on H<sub>2</sub>S Adsorption Performance at Low and High Temperatures

Russamee Sitthikhankaew  $^{a\ d}$  , David Chadwick  $^{b}$  , Suttichai Assabumrungrat  $^{c}$  & Navadol Laosiripojana  $^{a}$ 

- <sup>a</sup> The Joint Graduate School of Energy and Environment, CHE Center for Energy Technology and Environment, King Mongkut's University of Technology Thonburi, Bangkok, Thailand
- <sup>b</sup> Department of Chemical Engineering, Imperial College London, UK
- <sup>c</sup> Department of Chemical Engineering , Faculty of Engineering, Chulalongkorn University , Bangkok , Thailand
- <sup>d</sup> Department of General Science , Faculty of Science and Technology, Muban Chombueng Rajabhat University , Ratchaburi , Thailand

Accepted author version posted online: 26 Sep 2013. Published online: 17 Jan 2014.

To cite this article: Russamee Sitthikhankaew , David Chadwick , Suttichai Assabumrungrat & Navadol Laosiripojana (2014) Effect of KI and KOH Impregnations over Activated Carbon on  $H_2S$  Adsorption Performance at Low and High Temperatures, Separation Science and Technology, 49:3, 354-366, DOI: 10.1080/01496395.2013.841240

To link to this article: <a href="http://dx.doi.org/10.1080/01496395.2013.841240">http://dx.doi.org/10.1080/01496395.2013.841240</a>

# PLEASE SCROLL DOWN FOR ARTICLE

Taylor & Francis makes every effort to ensure the accuracy of all the information (the "Content") contained in the publications on our platform. However, Taylor & Francis, our agents, and our licensors make no representations or warranties whatsoever as to the accuracy, completeness, or suitability for any purpose of the Content. Any opinions and views expressed in this publication are the opinions and views of the authors, and are not the views of or endorsed by Taylor & Francis. The accuracy of the Content should not be relied upon and should be independently verified with primary sources of information. Taylor and Francis shall not be liable for any losses, actions, claims, proceedings, demands, costs, expenses, damages, and other liabilities whatsoever or howsoever caused arising directly or indirectly in connection with, in relation to or arising out of the use of the Content.

This article may be used for research, teaching, and private study purposes. Any substantial or systematic reproduction, redistribution, reselling, loan, sub-licensing, systematic supply, or distribution in any form to anyone is expressly forbidden. Terms & Conditions of access and use can be found at <a href="http://www.tandfonline.com/page/terms-and-conditions">http://www.tandfonline.com/page/terms-and-conditions</a>

ISSN: 0149-6395 print/1520-5754 online DOI: 10.1080/01496395.2013.841240



# Effect of KI and KOH Impregnations over Activated Carbon on H<sub>2</sub>S Adsorption Performance at Low and High Temperatures

# Russamee Sitthikhankaew, <sup>1,4</sup> David Chadwick, <sup>2</sup> Suttichai Assabumrungrat, <sup>3</sup> and Navadol Laosiripojana <sup>1</sup>

<sup>1</sup>The Joint Graduate School of Energy and Environment, CHE Center for Energy Technology and Environment, King Mongkut's University of Technology Thonburi, Bangkok, Thailand

<sup>2</sup>Department of Chemical Engineering, Imperial College London, UK

In the present work, commercial-grade activated carbon was modified by steam activation to improve its surface properties for high temperature desulfurization. The modified sample was also further upgraded by impregnating with KOH and KI to promote the chemisorption with of H<sub>2</sub>S. The H<sub>2</sub>S adsorption performance was tested under the temperature range of 30-550°C using the temperature program adsorption technique to understand the effect of adsorption temperature on the material adsorption characteristic. It was found that at ambient temperature, the impregnation of activated carbon with KOH can promote the H2S adsorption capacity of activated carbon, whereas the impregnation with KI does not provide a significant beneficial effect. At high adsorption temperature (upto 550°C), both KOH and KI impregnation considerably improve the H<sub>2</sub>S adsorption performance of activated carbon in terms of the adsorption capacity and breakthrough time. It was revealed from N<sub>2</sub> adsorption, SEM and EDS measurement that the chemical reactions between H<sub>2</sub>S and alkaline compounds (KOH and KI) are promoted at high temperature. Based on all experimental results, the equilibrium adsorption model using the linear isotherm was developed to predict the adsorption behavior of these sorbents in terms of equilibrium isotherm constant and mass transfer coefficient for later scaling-up process.

**Keywords** activated carbon; adsorption; alkaline impregnation; hydrogen sulphide

# **INTRODUCTION**

Gasification of coal and biomass is a process operated under limited oxygen content and steam environment at

Received 18 September 2012; accepted 2 September 2013. Address correspondence to Navadol Laosiripojana, The Joint Graduate School of Energy and Environment, CHE Center for Energy Technology and Environment, King Mongkut's University of Technology Thonburi, Bangkok, Thailand. E-mail: navadol\_l@jgsee.kmutt.ac.th

high temperature for producing synthesis gas that can be used for heat production, generation of mechanical and electrical power, and production of chemical compounds (e.g., NH<sub>3</sub>) and liquid fuel (e.g., Fischer-Tropsch-diesel) (1-8). The product gas from coal and biomass gasification generally contains the major components (i.e., CO, H<sub>2</sub>,  $CH_4$ ,  $H_2O$ ,  $CO_2$ , and  $N_2$ ) and inorganic impurities (e.g.,  $H_2S$  and COS) (5–10). The composition of the product gas from the gasification process depends on the type of fuel sources and reactor, and conditioning parameters of the process (5–8,11,12). Typically, the concentration of sulphur species obtained from the gasification of the woody compounds (e.g., black liquor) from pulp and paper manufacturing is in the range of 2000 to 3000 ppmv (13). It has been commonly known that H<sub>2</sub>S is a poisonous gas, which is not only toxic for humans but also highly corrosive for machines and engines (e.g., gas turbine) (4–16). Thus, most of the refinery and power plants must remove H<sub>2</sub>S from the synthesized gas produced from gasification before being passed onto gas turbines or other engines (4–10,12).

Conventional H<sub>2</sub>S removal process in Integrated Gasification Combined Cycles (IGCC) power plant is wet scrubbing process. This process decreases thermal efficiency of the power plant because the temperature of the gas is cooled down during the gas purification process so the purified gas must be preheated to high temperature before it is fed into a gas turbine (4,5,8–10). The high temperature desulfurization process can eliminate the cooling and heating step of gas before it turns to gas turbine and raises the thermal efficiency of the power plant (4,5). Thus researchers are trying to develop adsorbents for high temperature desulfurization process (4–6,8–12,18–20). Adsorbents that had been used for downstream hot gas desulfurization were

<sup>&</sup>lt;sup>3</sup>Department of Chemical Engineering, Faculty of Engineering, Chulalongkorn University, Bangkok, Thailand

<sup>&</sup>lt;sup>4</sup>Department of General Science, Faculty of Science and Technology, Muban Chombueng Rajabhat University, Ratchaburi, Thailand

transition metal oxides (e.g., ZnO, CuO, Mn<sub>2</sub>O<sub>3</sub>, Fe<sub>2</sub>O<sub>3</sub>, CeO<sub>2</sub>) and mixed transition metal oxides (e.g., zinc ferrite; ZnFe<sub>2</sub>O<sub>4</sub>, Zn-Ti-O, CuO-CeO<sub>2</sub>) (4,7,10,18,19,21,22). Typically, these metal oxides are converted to metal sulfides during the sulfidation step and are sequentially regenerated by the oxidation of metal sulfides to metal oxides. However, the sulfidation and regeneration cycles of these adsorbents lead to the degradation or pulverization into fine powder of the adsorbents (4,7,9,10,18,19,21,22). In addition, SO<sub>2</sub> is a by-product from the regeneration step and it has been known that it is a toxic and corrosive gas (18,23). Therefore, SO<sub>2</sub> must be removed from the flue gas of the power plant before being vented out to the atmosphere, so the adsorption process of SO<sub>2</sub> is needed in the desulfurization of synthesis gas produced from coal gasification (23,24).

The other disadvantage of transition metal oxide is an expensive adsorbent. For example, the price of zinc oxide desulfurization catalysts is US \$1,500-10,000/ton (25,26). The price of coconut shell activated carbon that is used for non-specific gas purification is made by a manufacturer in Thailand is US \$ 1,500/ton (27). Besides the low cost of activated carbon for downstream hot gas desulfurization, the other advantage of activated carbon is the elimination of regeneration of the adsorbent and SO<sub>2</sub> removal from flue gas (5,6,9). Thailand has abundant agricultural waste materials that could be raw material for the production of activated carbon (i.e., coconut shell, corncob, rice husk, bagasse, palm-oil shell, sawdust fly ash, macadamia nutshell, bamboo, and Jatropha curcas fruit shell) (28-37). At present, manufacturers in Thailand produce various types of activated carbon from the agricultural materials and use in non-specific liquid and gas purifications (37-39). Especially, commercial-grade activated carbon is an inexpensive adsorbent; therefore, our research aims to upgrade this commercial-grade activated carbon for specific H<sub>2</sub>S adsorption application (e.g., treatment of hot gas from the gasification process).

Previously, researchers have studied and reported the performance of potassium hydroxide (KOH) and potassium iodide (KI) impregnated activated carbons on H<sub>2</sub>S removal at ambient temperature under dry, moist air, or biogas condition (40–45). Nevertheless, the performances of KOH and KI impregnated activated carbons at high temperature using temperature program adsorption have not been intensively investigated. In the present work, the commercial-grade activated carbon was modified by

- i. wet impregnation of potassium compounds (i.e., KOH and KI) and
- ii. the combination of steam re-activation and wet impregnation method with an aim to promote both the surface area properties and the chemisorptions of the sorbent.

This is a novel method for upgrading the activated carbon for  $H_2S$  adsorption at ambient and importantly at high

operating temperature, which is greatly beneficial for high temperature desulphurization applications. The H<sub>2</sub>S adsorption performance of these activated carbons was studied at both low and high adsorption temperatures in order to understand the effect of adsorption temperature on the material adsorption characteristic, which would be useful for high temperature desulphurization applications. From the study, the influence of surface area, pore volume, and surface chemistry of each potassium-based impregnated activated carbon on H<sub>2</sub>S adsorption performance was discussed and the H<sub>2</sub>S adsorption mechanism on the KOH and KI impregnated activated carbons at low and high temperature were proposed. In addition, based on the experimental results, the computational simulation of H<sub>2</sub>S adsorption was developed in order to predict the adsorption behavior of developed sorbents for later scaling up step.

# **EXPERIMENTAL**

# **Activated Carbon Sample**

Samples in this experiment are commercial and modified activated carbons. The commercial-grade of granular activated carbon (namely in the present work as "AC") is supplied from Carbokarn Company Limited (Thailand). The surface properties of this commercial activated carbon are given in Table 1. The methods for modification of the AC were a wet impregnation method and the combination of steam re-activation and wet impregnation method. For the first method, 0.00125 mole of KOH was dissolved with deionized water. Then, 1g of the AC was soaked with KOH solution for 30 min before being heated at 100°C to evaporate water and dried at 110°C for 24 h. Activated carbon, which was impregnated with 0.00125 mole of KOH, is referred to as "AC\_KOH". The letter "E" that is added to the sample name means the exhaustion of activated carbon in the H<sub>2</sub>S adsorption process. For example, AC\_KOH-E is an exhausted KOH impregnated activated carbon.

The second method combines the steam re-activation and wet impregnation. First, the AC was filled in a quartz tube reactor. Then it was heated up from room temperature to 900°C under a constant  $N_2$  flow of  $100\,\mathrm{cm^3\,min^{-1}}$ . After that, it was kept isothermal for 1 h under the flow of vaporous steam. Finally, it was cooled down to room temperature under the  $N_2$  flow. Then, the wet impregnation was sequentially carried out by impregnating 1 g of the sample with 0.00125 mole of KOH or KI. The final product which was impregnated with KOH and KI is referred to as "SC\_KOH" and "SC\_KI", respectively.

# **Material Characterization**

Characterizations of all activated samples include the nitrogen adsorption, X-ray diffraction measurement, surface morphology and elemental measurement, and thermal

Sulli	Surface properties of unmoduled and Korr and Kr impregnated activated carbons									
Name of sample	Total surface area (m <sup>2</sup> /g)	Total pore volume (cm <sup>3</sup> /g)	Micropore volume (cm <sup>3</sup> /g)	Average pore size (nm)	Average micropore size (nm)					
AC	1343	0.47	0.45	1.72	0.67					
AC-E	1283	0.44	0.42	1.69	0.66					
AC_KOH	1037	0.36	0.35	1.75	0.67					
AC_KOH-E*	762	0.29	0.26	1.82	0.69					
SC_KOH	1336	0.50	0.46	1.77	0.70					
SC_KOH-E	976	0.36	0.34	1.76	0.70					
SC_KI	1068	0.40	0.38	1.77	0.71					
SC KI-E	846	0.36	0.30	1.95	0.73					

TABLE 1
Surface properties of unmodified and KOH and KI impregnated activated carbons

analysis. The nitrogen adsorption on fresh and exhausted AC, AC\_KOH, SC\_KOH, and SC\_KI was measured using a Belsorp mini II instrument at −196°C to predict the specific surface area of sorbents. Prior to the adsorption measurement, the samples were heated at 110°C for 5 hours under nitrogen flow. The nitrogen isotherm of activated carbons was used to determine the volume of adsorbate as a function of pressure, while total surface area  $(S_t)$ , micropore volume  $(V_{\rm mic})$ , and the average micropore size  $(D_{\rm mic})$  were calculated by t-plot method. The total pore volume  $(V_t)$ and average pore size  $(D_t)$  were calculated by the BET method. Next, the fresh activated carbons that were impregnated with potassium compounds were measured with the X-ray diffraction (XRD) technique to observe chemical compounds that could be formed in activated carbon. The X-ray diffraction meter that was used for analysis of activated carbon is PANalytical brand (Model: X' Pert PRO). The activated carbon samples were scanned from the diffraction angle 5–80°, at a constant scanning speed. Then, surface morphology and the elemental content of fresh and exhausted activated carbons was measured with the scanning electron microscope (SEM), energy dispersive X-ray spectroscopy (EDS), and X-ray fluorescence analyzer (Bruker AXS, S4 Explorer). SEM measurement was performed using JSM-5800 LV, JEOL attached with EDS, Oxford ISIS 300. Lastly, thermal analysis of fresh unmodified and modified activated carbons was measured with the thermal analyzer (TA Instruments, QA500), from which the temperature increased from 30°C to 550°C with the heating rate of 10°C/min under nitrogen flow of 60 mL/min. Then, the temperature was kept constant at 550°C for 120 min.

# **Adsorption Test**

The  $H_2S$  adsorption system consists of a fixed-bed reactor in the horizontal furnace, gas supply unit, and gas monitor system. The mixture of helium gas and  $H_2S$  was passed through the fixed-bed reactor. Mass flow controller was

used to regulate the gas flow rate. The fixed-bed reactor was filled with  $1.0\,\mathrm{g}$  of activated carbon, from which  $3000\,\mathrm{ppmv}$   $H_2S$  with a constant flow rate of  $100\,\mathrm{mL/min}$  was introduced to the system.  $H_2S$  analyzer (QRAE model PGM-50Q) was applied to continuously monitor the concentration of  $H_2S$  at the outlet of the reactor.

For the temperature program adsorption study, it consisted of 2 parts. The first part was processed at 30°C, from which H<sub>2</sub>S gas was fed into the reactor and the concentration of H<sub>2</sub>S was recorded until the concentration at the outlet reached 3000 ppmv. For the second part, the temperature was programmed to increase from 30°C to 550°C with the rate of 10°C/min. Then, the reactor temperature was held constant at 550°C until the outlet H<sub>2</sub>S concentration reached 3000 ppmv. Finally, the reactor was cooled down to room temperature. When the concentration of H<sub>2</sub>S at the outlet was 300 and 3000 ppmv, the breakthrough time and adsorption time were recorded, respectively. The adsorption capacity of activated carbon was calculated using the integrated area above the adsorption curve (the difference between the inlet concentration and the outlet concentration curves), the flow rate, and the mass of activated carbon.

# RESULTS AND DISCUSSION Characterization of Unmodified and Modified Activated Carbons

The nitrogen adsorption of fresh AC, AC\_KOH, SC\_KOH, and SC\_KI are shown in Table 1 and Fig. 1. It was found that unmodified and modified activated carbons mainly contain micropore volume rather than mesopore and macropore volume, which is suitable for gas adsorption. AC\_KOH has lower total surface area, total pore volume, and micropore volume than the unmodified activated carbon. However, the average micropore size of AC KOH is in the same range as AC.

It is noted that the total pore volume and micropore volume of SC\_KOH were higher than AC and AC\_KOH

<sup>\*</sup>Exhausted sample from the adsorption testing

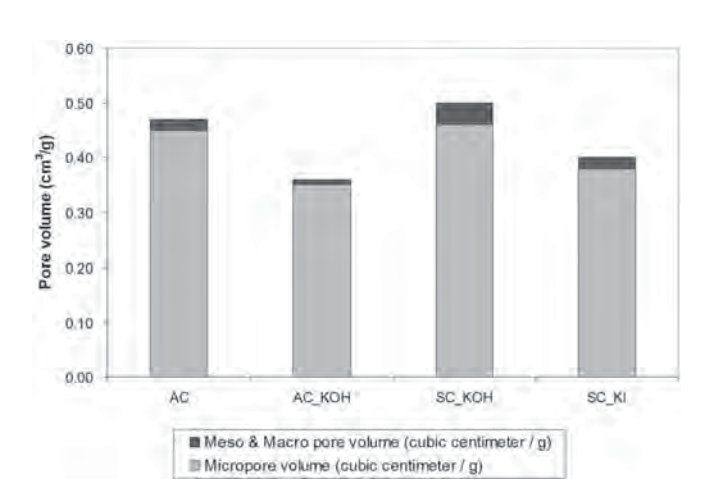


FIG. 1. Fraction of micropore and meso- and macro-pore volume of activated carbons.

since the re-activation of activated carbon with steam at 900°C increase porosity within a porous carbon by partly burning off the raw carbon under the oxidizing environment. The total surface area, total pore volume, and micropore volume of SC\_KI were lower than those of SC\_KOH because the molecular weight of KI was higher than KOH. Therefore, with the equivalent mole of KOH and KI, the weight of KI that impregnated on the pore and surface of activated carbon is higher than that of KOH. The content of element in fresh unmodified and modified activated carbons was analyzed by X-ray fluorescence (XRF) analyzer as shown in Table 2. AC sample contains K of 1.24%; whereas K contents in AC\_KOH, SC\_KOH, and SC\_KI are around 4.5%.

The formations of potassium compound in activated carbons were measured by XRD as shown in Figs. 2–3. These X-ray diffraction patterns were matched with the standard pattern (ICSD). In Fig. 2, the X-ray diffraction pattern of fresh AC\_KOH and SC\_KOH match with standard KOH No. 00-015-0890. It can be seen that the pattern and the intensities of peaks for AC\_KOH and SC\_KOH almost identical. In Fig. 3, the X-ray diffraction pattern of fresh SC\_KI correspond with standard KI No. 01-073-0382, from which the peaks location of 21.8°, 25.2°, 44.5°, and 51.8° correspond to KI.

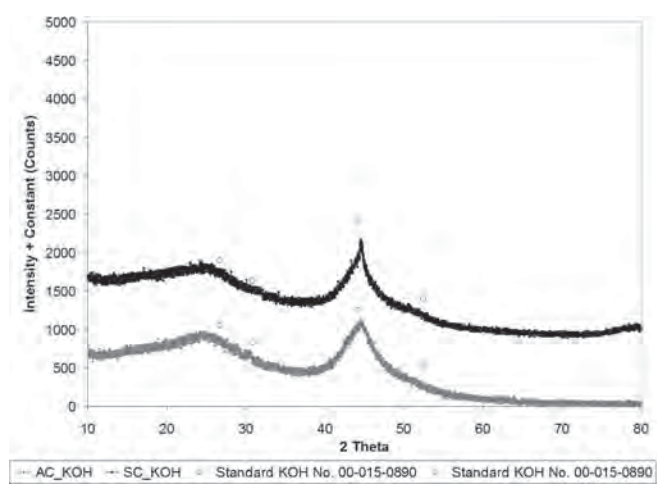


FIG. 2. X-ray diffraction patterns of fresh AC\_KOH and SC\_KOH.

# Adsorption of H<sub>2</sub>S at Room Temperature

Performances of AC, AC\_KOH, SC\_KOH, and SC\_KI for H<sub>2</sub>S adsorption at 30°C were tested as shown in Fig. 4. It can be seen that AC\_KOH and SC\_KOH provided higher H<sub>2</sub>S breakthrough time and adsorption time compared to the AC. In detail, the breakthrough time of AC, AC\_KOH, and SC\_KOH were 15, 39, and 26 minutes, while the adsorption time was 67, 330, and 178 minutes, respectively. It is also noted that, for AC\_KOH, the concentration of H<sub>2</sub>S came out at the outlet gas was almost 0 ppmv for 19.2 minutes.

As seen in Table 1, AC\_KOH contains lower surface area and pore volume than AC but its  $H_2S$  adsorption capacities was almost 4 times higher (6.5  $g_{\rm H2S}/100\,g_{\rm activated}$   $_{\rm carbon}$ ). In addition, the adsorption capacity of the AC\_KOH was higher than KOH impregnated activated carbon prepared by Tsai et al. (2.3  $g_{\rm H2S}/100\,g_{\rm activated}$  carbon) (40). This suggests that the  $H_2S$  adsorption on AC\_KOH is not only physical adsorption but also chemical adsorption. In addition, the chemical adsorption appeared to show the greater effect on  $H_2S$  adsorption than the physical adsorption.

For physical adsorption, the gaseous phase  $H_2S$  adsorbed into the pore of activated carbon (Eq. 1). The

TABLE 2 Elementals content of unmodified and KOH and KI impregnated activated carbons

		Content of element (%)									
Sample	K	Na	I	S	P	Si	Fe	Ca	Mg	Cl	
AC	1.24	0.13	0.00	0.08	0.05	0.08	1.72	0.04	0.04	0.06	
AC_KOH	4.45	0.12	0.00	0.07	0.04	0.08	0.43	0.04	0.03	0.05	
SC_KOH	4.49	0.12	0.00	0.06	0.04	0.12	0.11	0.05	0.04	0.05	
SC_KI	4.44	0.0	12.44	0.05	0.04	0.06	0.13	0.06	0.0	0.04	

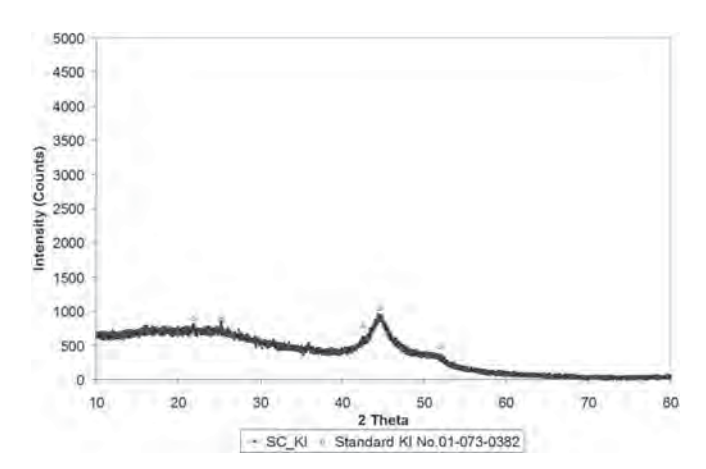


FIG. 3. X-ray diffraction patterns of fresh SC\_KI.

impregnation of KOH led to the dissociation of  $H_2S$  to generate hydrogen sulfide ions (HS<sup>-</sup>) and hydrogen ions (H<sup>+</sup>) (Eq. 2). It is noted that the pK<sub>a</sub> constants of hydrogen sulfide for dissociations via Eqs. (1) and (2) are 7.2 and 14, respectively. Then, the acid-base reaction and chemical reaction occur via Eqs. (3–5) to form water, potassium hydrosulfide (KHS), and potassium sulfide (K<sub>2</sub>S).

$$H_2S (ads) \rightarrow H_2S (ads - liq)$$
 (1)

$$H_2S \; (ads\text{-liq}) \rightarrow HS^- \; (ads) + H^+ \qquad \qquad (2)$$

$$H^+ + OH^- \to H_2O \tag{3}$$

$$HS^-$$
 (ads) +  $K^+$  (ads)  $\rightarrow$  KHS (ads) (4)

$$S^{2-}$$
 (ads) + 2K<sup>+</sup> (ads)  $\to$  K<sub>2</sub>S (ads) (5)

In the case of SC\_KOH, its  $H_2S$  adsorption capacity was slightly lower than that of AC\_KOH (4.5  $g_{H2S}/100\,g_{activated\ carbon}$ ). During production of SC\_KOH, AC was heated up under  $N_2$  flow until 900°C and could result in the water evaporation. The thermal analysis of AC, AC\_KOH, SC\_KOH, and SC\_KI in Fig. 5 indicates the weight losses of 7%, 15%, 2%, and 5% at the temperature range between 30–110°C, which confirms the low content of water for steam re-activation samples. The difference of humidity inside these KOH impregnated activated carbons could affect the dissociation of  $H_2S$  in Eqs. (1–2) and results in the low  $H_2S$  adsorption capacity.

For SC\_KI, the  $H_2S$  adsorption capacity of SC\_KI was  $2.4\,g_{H2S}/100\,g_{activated\ carbon}$ , which is lower than that of SC\_KOH and only slightly higher than that of AC. This implied that the chemical reaction between  $H_2S$  and KI rarely occurs at 30°C. It is known that KI is a weak alkaline salt, which leads to the low dissociation of  $H_2S$ , acid-base reaction, and chemical reaction and consequently results in the low  $H_2S$  adsorption capacity.

# Temperature Program Adsorption of H<sub>2</sub>S

The  $H_2S$  adsorption curves of AC, AC\_KOH, SC\_KOH, and SC\_KI at high temperature are shown in Fig. 6. During the heating up period, the outlet concentration of  $H_2S$  decreased to less than 200 ppmv for all

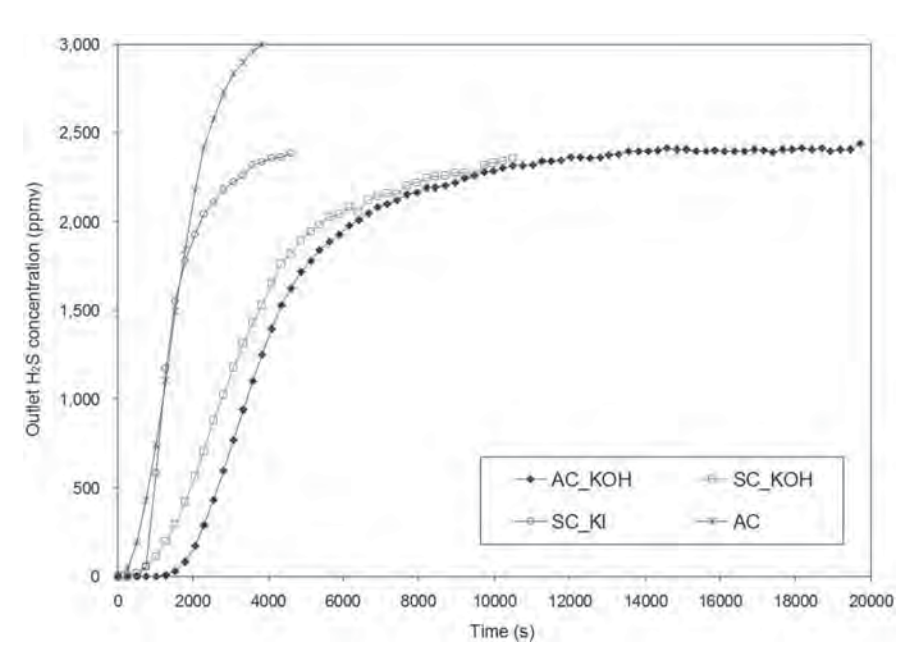


FIG. 4. Adsorption curves of H<sub>2</sub>S by the unmodified and KOH and KI impregnated activated carbons at 30°C.

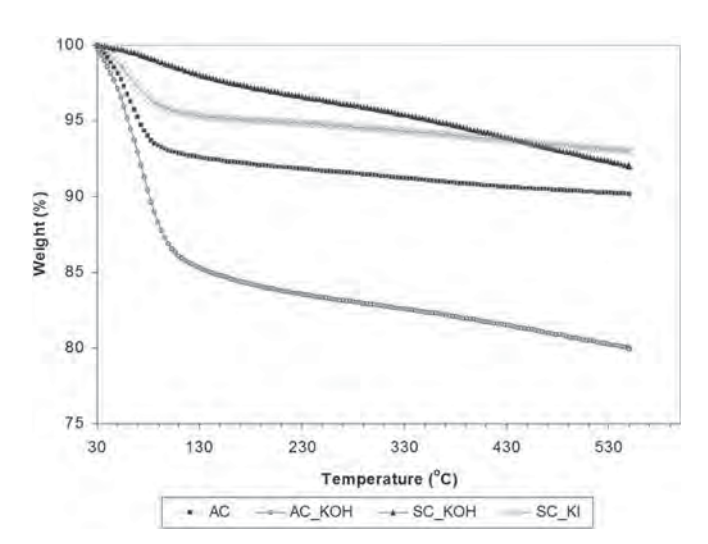


FIG. 5. Thermal analysis of the unmodified and KOH and KI impregnated activated carbons.

samples. At 550°C, the outlet concentration of H<sub>2</sub>S for SC\_KI was about 0 ppmv, while that for AC\_KOH, the SC\_KOH, and AC was 27, 29, and 187 ppmv, respectively. The outlet gas that contains H<sub>2</sub>S less than 100 ppmv is safe for gas turbine and prevents the corrosion of gas turbine (7). It was observed that, at high temperature operation, the breakthrough times of AC\_KOH, SC\_KOH, and SC\_KI were significantly longer than the AC (217, 312, 185 mins for AC\_KOH, SC\_KOH, and SC\_KI compared to 71 mins for AC). Furthermore, the H<sub>2</sub>S adsorption capacity was considerably improved. Among all samples, SC\_KOH provide the highest H<sub>2</sub>S adsorption capacity of 32.1 g<sub>H2S</sub>/100 g<sub>activated carbon</sub> while, the H<sub>2</sub>S adsorption

capacities of AC\_KOH, the SC\_KI, and AC were 21.1, 18.4, and 1.4 g<sub>H2S</sub>/100 g<sub>activated carbon</sub>, respectively. From the calculation, the sorption capacities of SC\_KOH, AC\_KOH, SC\_KI, and AC were 30.2, 19.9, 17.3, and  $1.33\,g_{sulfur}/100\,g_{sorbent}$  respectively. As seen in Table 3, the sorption capacity of the SC\_KOH was higher than other carbon-based and metal oxide-based sorbents previously reported in the literature (i.e., the activated coke and coal, ZnO supported on TiO2 namely, L-992 and Z-Sorb-III, Copper-based sorbent namely, IGTSS-145, Cu-V mixed oxide, Iron oxide based sorbent, Ce-Mn mixed oxide). In addition, AC\_KOH, SC\_KI also provide higher sorption capacities than sorbents listed in Table 3. It is noted that at high temperature, the reactions of H<sub>2</sub>S and KI occur as presented in Eqs. (6-7), from which H<sub>2</sub>S reacted with KI to form KHS and K2S.

$$H_2S(g) + KI(ads) \rightarrow KHS(ads) + HI(g)$$
 (6)

$$H_2S(g) + 2KI(ads) \rightarrow K_2S(ads) + 2HI(g)$$
 (7)

It is clear that the high temperature operation can promote the chemical reaction between H<sub>2</sub>S and alkaline compounds which was supported by N<sub>2</sub> adsorption, SEM, and EDS measurement of the fresh and exhaust materials. As shown in Table 1, the total pore volume and surface area of materials decreased after testing; furthermore, the decreasing proportion is in good agreement with the H<sub>2</sub>S adsorption capacities. From the EDS measurement, it can be seen that the fresh KOH impregnated activated carbon contains high content of C, K, and trace amount of O, P, Ca, Fe, and Si (Figs. 7–9). After H<sub>2</sub>S adsorption test, the content of K and iodine decreased,

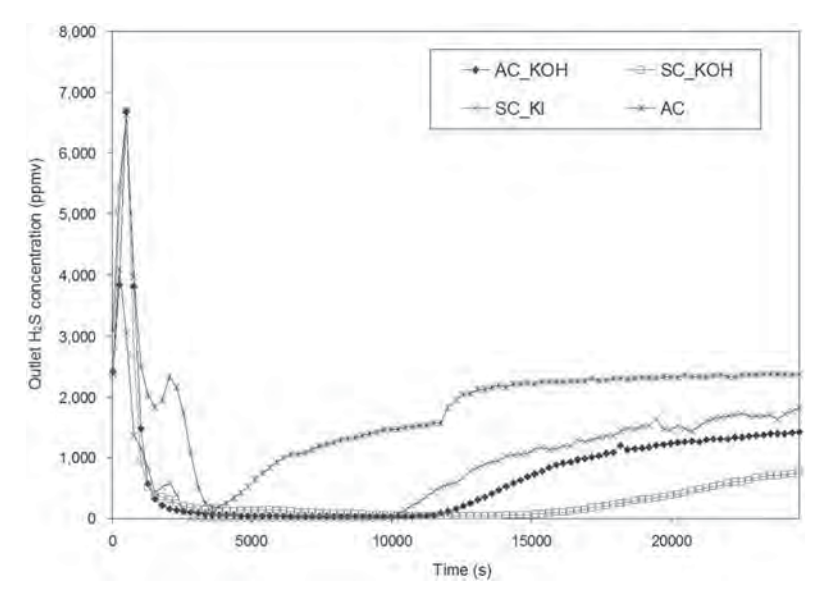


FIG. 6. Adsorption curves of H<sub>2</sub>S by the unmodified and KOH and KI impregnated activated carbons at high temperature.

TABLE 3
Summarization of sorption capacities of various sorbents at high temperature

Sorbents	Inlet H <sub>2</sub> S Concentration (%)	Sulfidation temperature (°C)	Sorption capacity $(g_{sulfur}/100 g_{sorbent})$	Reference
Activated coke	0.02	250	0.02	(9)
Activated coal	0.5	550	6.1	(5)
ZnO supported on TiO <sub>2</sub>	0.325	500-600	11	(10)
$ZnO/TiO_2$ (name, L-992)	1.0 - 1.4	600-700	16	(46)
ZnO/TiO <sub>2</sub> (name, Z-Sorb-III)	1	400-500	6.2	(47)
Copper-based sorbent (name, IGTSS-145)	2	450-600	9.3	(48)
Cu-V mixed oxide	1	300-700	17	(49)
Iron oxide based sorbent	0.2 - 0.3	500	20.2-27.5	(50)
Ce-Mn mixed oxide (molar ratio of $Ce/Mn = 3/1$ )	1	600	6.1	(51)

whereas high content of solid state S was found. These results indicated the occurring of the chemical reaction between KOH and/or KI with  $H_2S$  at high temperature. Furthermore, the occurrence of solid state S from EDS measurement corresponds with SEM micrographs of the fresh and exhaust materials especially the AC\_KOH sample (Figs. 10–11), from which the pore and surface of exhaust AC\_KOH were covered with solid particles that are formed during the  $H_2S$  chemisorption at high temperature.

## Computational Simulation of H<sub>2</sub>S Adsorption

Based on the experimental results, the computational simulation was developed in order to predict the adsorption behavior of developed sorbents for later scaling-up step. It is noted that the equilibrium adsorption model applied in this computational simulation was the linear isotherm. The adsorption curve was simulated by the numerical method as shown in Eqs. (8–20), from which the adsorption data (i.e., the adsorption curve, breakthrough time, adsorption time, and adsorption capacity) from the experiments

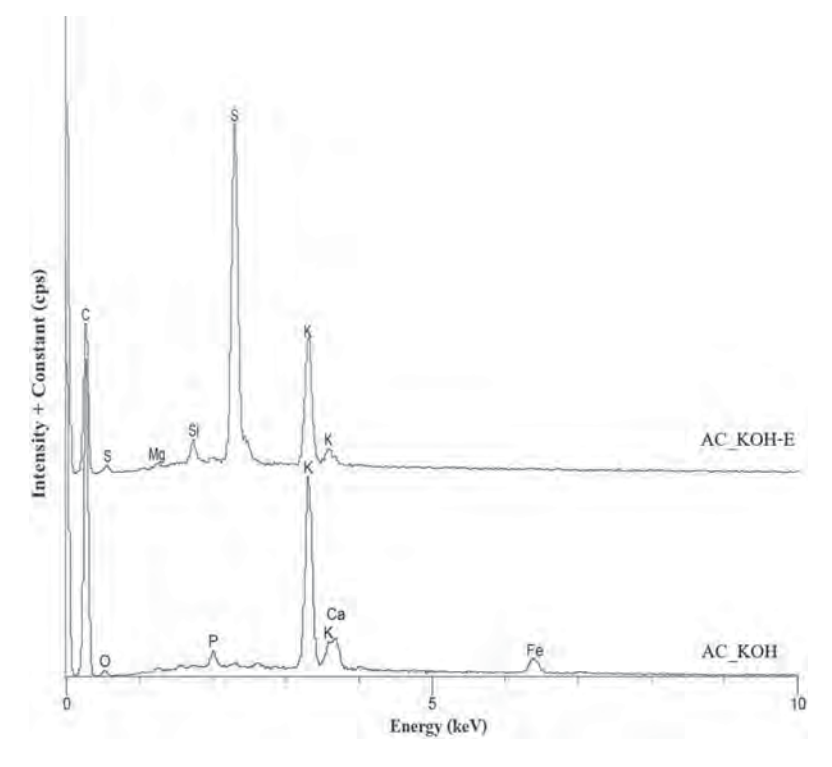


FIG. 7. EDS chromatogram of fresh and exhausted AC\_KOH.

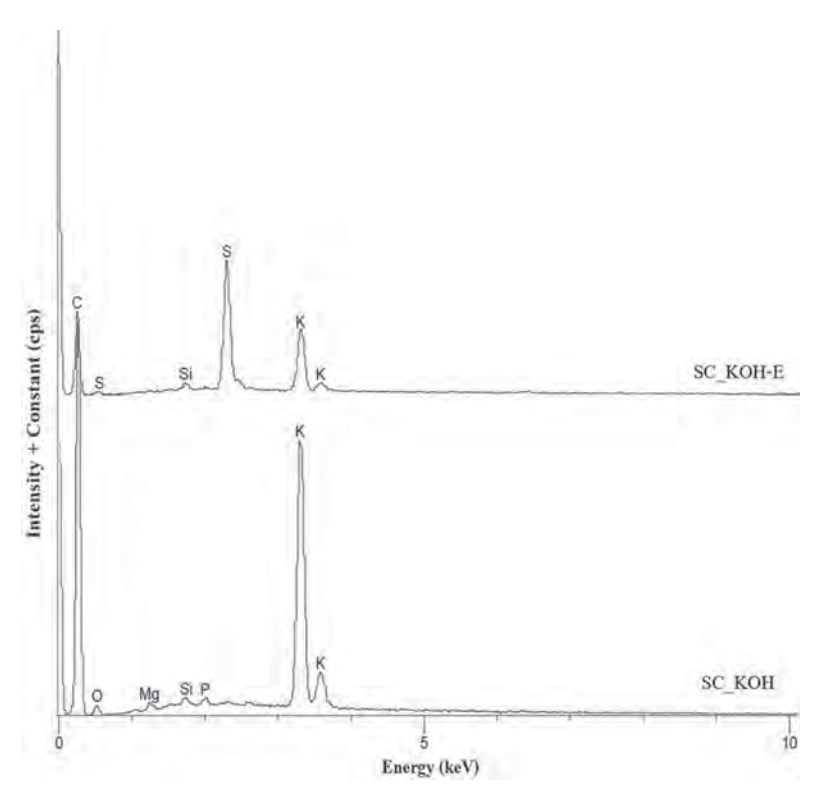


FIG. 8. EDS chromatogram of fresh and exhausted SC\_KOH.

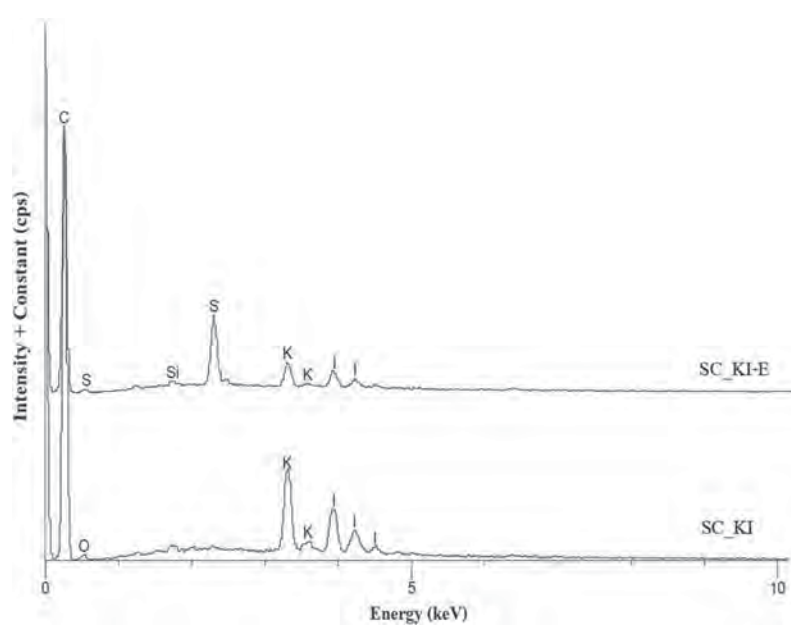


FIG. 9. EDS chromatogram of fresh and exhausted SC\_KI.

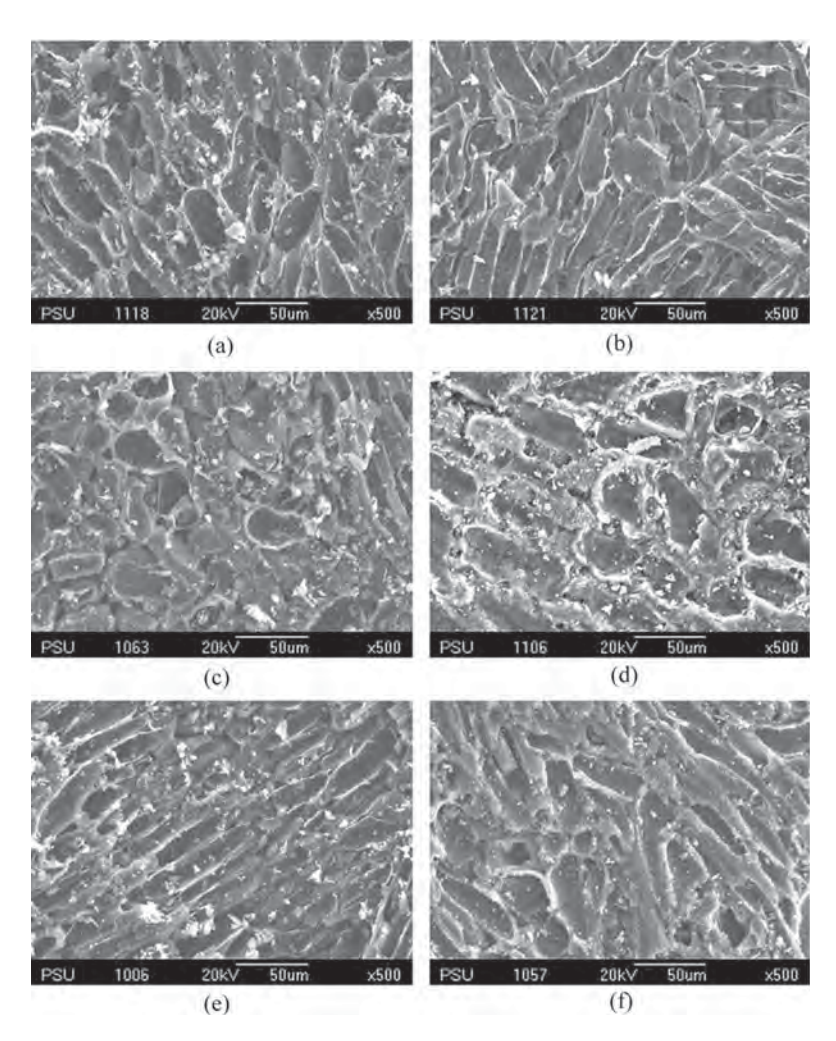


FIG. 10. SEM micrographs of fresh and exhaust unmodified and KOH impregnated activated carbon (a) AC; (b) AC-E; (c) AC\_KOH; (d) AC\_KOH-E; (e) SC\_KOH; (f) SC\_KOH-E.

and the computational simulation were compared. As a result, the optimized constants (i.e., equilibrium isotherm constant (K) and mass transfer coefficient (k)) can be obtained from the computational simulation.

Governing dynamic behavior of the adsorption column

$$-D_L \frac{\partial^2 c}{\partial z^2} + u \frac{\partial c}{\partial z} + \frac{\partial c}{\partial t} + \frac{(1 - \varepsilon_b)}{\varepsilon_b} \frac{\partial \overline{q}}{\partial t} = 0$$
 (8)

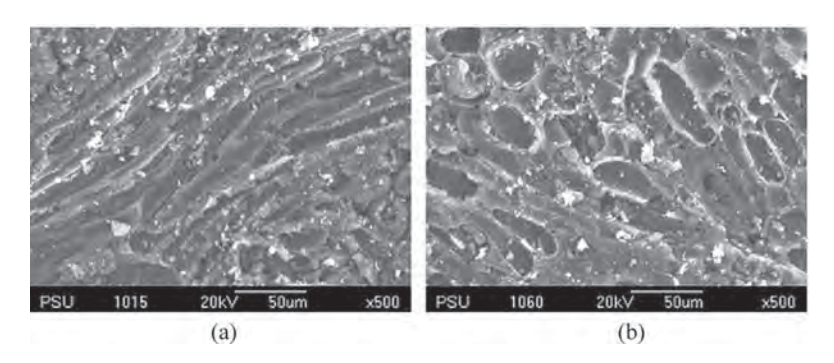


FIG. 11. SEM micrographs of fresh and exhaust KI impregnated activated carbon (SC\_KI) (a) SC\_KI and (b) SC\_KI-E.

"c" and "q" are a concentration of adsorbate on gaseous phase or solid, whereas " $q_{eq}$ " is the concentration of adsorbate on solid at equilibrium point. "t", "z", " $D_L$ ", "u", and " $\varepsilon_b$ " are time, distance, diffusivity, interstitial velocity, and porosity of the adsorption column, respectively.

Mass transfer equation : 
$$\frac{\partial \overline{q}}{\partial t} = k(q_{eq} - \overline{q})$$
 (9)

Linear isotherm : 
$$q_{eq} = Kc$$
 (10)

Hence,

$$\frac{\partial \overline{q}}{\partial t} = k(Kc - \overline{q}) \tag{11}$$

$$-D_L \frac{\partial^2 c}{\partial z^2} + u \frac{\partial c}{\partial z} + \frac{\partial c}{\partial t} + \frac{(1 - \varepsilon_b)}{\varepsilon_b} k(Kc - \overline{q}) = 0$$
 (12)

By considering that  $D_L \frac{\partial^2 c}{\partial z^2} = 0$ ,

$$u\frac{\partial c}{\partial z} + \frac{\partial c}{\partial t} + \frac{(1 - \varepsilon_b)}{\varepsilon_b} k(Kc - \overline{q}) = 0$$
 (13)

$$u\left(\frac{c_{i+1,j} - c_{i,j}}{\Delta z}\right) + \left(\frac{c_{i,j+1} - c_{i,j}}{\Delta t}\right) + \left(\frac{1 - \varepsilon_b}{\varepsilon_b}\right)$$
$$\left(k\left(Kc_{i,j} - \overline{q}_{i,j}\right)\right) = 0 \tag{14}$$

$$u\left(\frac{c_{i+1,j} - c_{i,j}}{\Delta z}\right) = -\left(\frac{c_{i,j+1} - c_{i,j}}{\Delta t}\right) - \left(\frac{1 - \varepsilon_b}{\varepsilon_b}\right)$$

$$\left(k\left(Kc_{i,j} - \overline{q}_{i,j}\right)\right)c_{i+1,j} = c_{i,j} + \frac{\Delta z}{u}$$

$$\left[-\left(\frac{c_{i,j+1} - c_{i,j}}{\Delta t}\right) - \left(\frac{1 - \varepsilon_b}{\varepsilon_b}\right)\left(k\left(Kc_{i,j} - \overline{q}_{i,j}\right)\right)\right]$$

$$c_{i+1,j} = f_1(c_{i,j}, c_{i,j+1}, \overline{q}_{i,j})$$

$$(15)$$

Concentration of the adsorbate on solid at any time (t) and distance (z) is referred to  $\bar{q}_{i,j}$ , and concentration of

substance on gaseous phase at any time and distance is referred to  $c_{i,i}$ .

$$\frac{\partial \overline{q}}{\partial t} = k(Kc - \overline{q}) \tag{11}$$

$$\frac{\overline{q}_{i,j+1} - \overline{q}_{i,j}}{\Lambda t} = k \left( K c_{i,j} - \overline{q}_{i,j} \right) \tag{16}$$

$$\overline{q}_{i,j+1} = \overline{q}_{i,j} + k\Delta t \left( K c_{i,j} - \overline{q}_{i,j} \right) 
\overline{q}_{i,j+1} = f_2(c_{i,j}, \overline{q}_{i,j})$$
(17)

At initial condition, c(z,t) is a concentration of the adsorbate on gaseous phase that is a function of distance and time, while q(z,t) is a concentration of the adsorbate on solid that is a function of distance and time.

At an initial time (t=0),

$$c(z,0) = 0; z > 0 (18)$$

$$q(z,0) = 0; z \ge 0 \tag{19}$$

Boundary condition:

At 
$$z = 0$$
,  $c(0, t) = c_f$  for  $t \ge 0$  (20)

Computational simulation of  $H_2S$  adsorption curve starts with the optimization of equilibrium isotherm constant (K) and mass transfer coefficient (k). Then, the  $H_2S$  adsorption curve can be predicted from these values, while the breakthrough time (BT Time) and adsorption capacity (AD Capacity) can also be calculated. The breakthrough time is time that the outlet concentration per inlet concentration ratio (C/ $C_0$ ) is 0.100.

Table 4 and Figs. 12–13 compares the breakthrough time, the adsorption capacity, and H<sub>2</sub>S adsorption curve obtained from the simulation with those from the experimental studies. The equilibrium isotherm constant and mass transfer coefficient of each material was also estimated. It

TABLE 4

H<sub>2</sub>S adsorption performance of unmodified and KOH and KI impregnated activated carbons at 30°C

Experiment				Computational simulation				
Sample BT time AD capacity $(min)$ $(g_{H2S}/100 g_{activated carbon})$		K	k	BT time (min)	AD capacity (g <sub>H2S</sub> /100 g <sub>activated carbon</sub> )			
AC	15	1.7	1.127	9.960	25	3.4		
AC_KOH	39	6.5	1.325	10.591	36	3.9		
SC_KOH	26	4.5	0.977	16.463	27	2.9		
SC_KI	15	2.4	0.610	17.855	13	1.8		

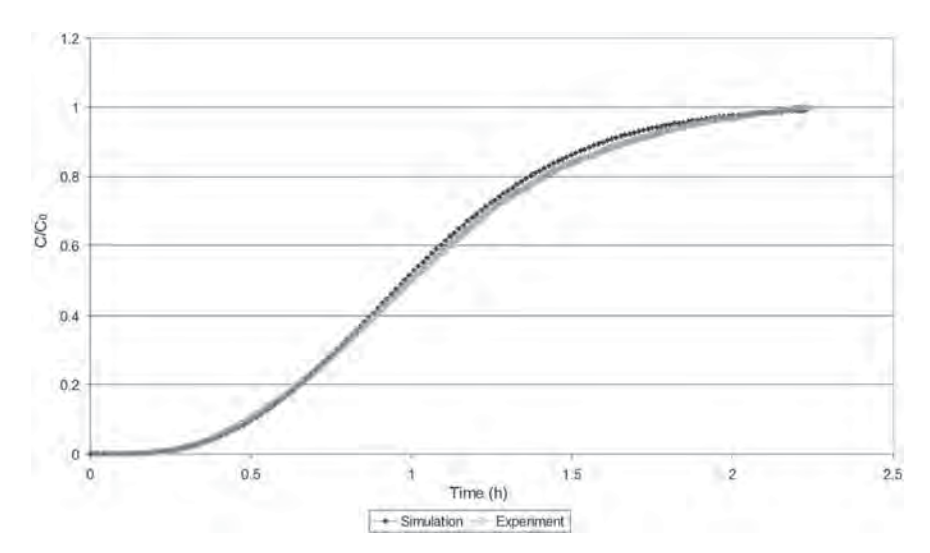


FIG. 12. Adsorption curves of  $H_2S$  from experimental testing and computational simulation (adsorbent is the commercial-grade activated carbon (AC)).

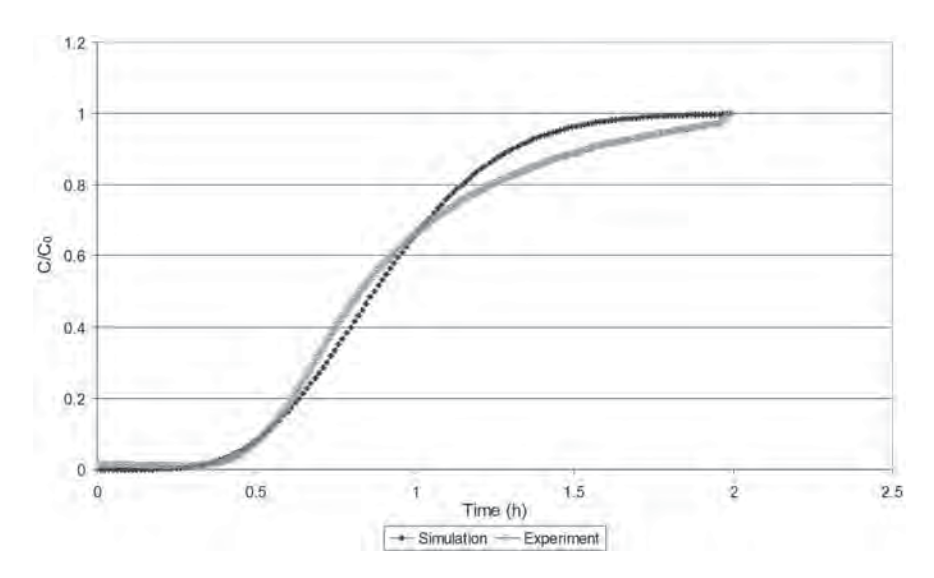


FIG. 13. Adsorption curves of  $H_2S$  from experimental testing and computational simulation (adsorbent is the KOH impregnated activated carbon (SC\_KOH)).

can be seen from Figs. 12–13 that the H<sub>2</sub>S adsorption curves of AC and SC\_KOH from the computational simulations are in good agreement with those from the experimental studies (with the difference percentage of 5.9%). Furthermore, the breakthrough times estimated from the computational simulation are also in the same range with those from the experimental studies. Therefore, it can be revealed that this developed computational simulation is applicable for prediction of the adsorption behavior (i.e., H<sub>2</sub>S adsorption curve, breakthrough time, and H<sub>2</sub>S adsorption capacity) of the unmodified and KOH and KI impregnated activated carbons under the conditions studied in the present work.

## **CONCLUSIONS**

The impregnation of activated carbon with KOH can promote the H<sub>2</sub>S adsorption capacity of activated carbon at ambient temperature, whereas the impregnation with KI does not provide significant beneficial effect. At higher adsorption temperature (up to 550°C), both KOH and KI impregnation considerably improve the H<sub>2</sub>S adsorption performance of activated carbon due to the promotion of chemical reactions between H<sub>2</sub>S and alkaline compounds (KOH and KI) at high temperature. Based on all experimental results, the equilibrium isotherm constant and mass transfer coefficient of these sorbents can be predicted.

#### **FUNDING**

This research was supported by the National Research University (NRU) grant of King Mongkut's University of Technology Thonburi and PTT Public Company Limited. Financial support from the Thailand Research Fund (RTA5480003) and the Royal Golden Jubilee Ph.D. Program (Grant No. PHD/0162/2550) are acknowledged.

#### **REFERENCES**

- Rapagnà, S.; Jand, N.; Kiennemann, A.; Foscolo, P.U. (2000) Steam-gasification of biomass in a fluidized-bed of olivine particles. *Biomass & Bioenergy*, 19: 187.
- Boerrigter, H.; Uil, H.D.; Calis, H. (2003) Green diesel from biomass via Fischer–Tropsch synthesis: New insights in gas cleaning and process design, paper presented at Pyrolysis and Gasification of Biomass and Waste, Expert Meeting, 30 September-1 October 2002, Strasbourg, France.
- Leibold, H.; Hornung, A.; Seifert, H. (2008) HTHP syngas cleaning concept of two stage biomass gasification for FT synthesis. *Powder Technology*, 180: 265.
- 4. Ko, T.H.; Chu, H.; Chaung, L.K. (2005) The sorption of hydrogen sulfide from hot syngas by metal oxides over supports. *Chemosphere*, 58 (4): 467.
- Cal, P.M.; Strickler, B.W.; Lizzio, A.A. (2000) High temperature hydrogen sulfide adsorption on activated carbon I. Effects of gas composition and metal addition. *Carbon*, 38 (13): 1757.
- Cal, P.M.; Strickler, B.W.; Lizzio, A.A. (2000) High temperature hydrogen sulfide adsorption on activated carbon II. Effects of gas temperature, gas pressure, and sorbent regeneration. *Carbon*, 38 (13): 1767.
- Meng, X.; Jong, W.D.; Pal, R.; Verkooijen, A.H.M. (2010) In bed and downstream hot gas desulphurization during solid fuel gasification: A review. Fuel Processing Technology, 91: 964.
- 8. Tsukada, M.; Abe, K.; Yonemochi, Y.; Ameyama, A.; Kamiya, H.; Kambara, S.; Moritomi, H.; Uehara, T. (2008) Dry gas cleaning in coal gasification systems for fuel cells using composite sorbents. *Powder Technology*, 180: 232.
- Itaya, Y.; Kawahara, K.; Lee, C. Wo; Kobayashi, J.; Kobayashi, N.; Hatano, S.; Mori, S. (2009) Dry gas cleaning process by adsorption of H<sub>2</sub>S into activated cokes in gasification of carbon resources. *Fuel*, 88 (9): 1665.
- Elseviers, W.F.; Verelst, H. (1999) Transition metal oxides for hot gas desulphurization. Fuel, 78: 601.
- Jong, W.D.; Andries, J.; Hein, K.R.G. (1999) Coal/biomass co-gasification in a pressurised fluidised bed reactor. *Renewable Energy*, 16: 1110.
- 12. Álvarez-Rodríguez, R.; Clemente-Jul, C. (2008) Hot gas desulphurisation with dolomite sorbent in coal gasification. *Fuel*, 87 (17–18): 3513.
- Torres, W.; Pansare, S.S.; Goodwin, J.G.J. (2007) Hot gas removal of tars, ammonia, and hydrogen sulfide from biomass gasification gas. Catalysis Reviews, 49: 407.
- Lin, C.H.; Mao, I.F.; Tsai, P.H.; Chuang, H.Y.; Chen, Y.J.; Chen, M.L. (2010) Sulfur-rich geothermal emissions elevate acid aerosol levels in metropolitan Taipei. *Environmental Research*, 110: 536.
- Heaney, C.D.; Wing, S.; Campbell, R.L.; Caldwell, D.; Hopkins, B.; Richardson, D.; Yeatts, K. (2010) Relation between malodor, ambient hydrogen sulfide, and health in acommunity bordering a landfill. *Environmental Research*, 111: 847.
- Lambert, T.W.; Goodwin, V.M.; Stefani, D.; Strosher, L. (2006) Hydrogen sulfide (H<sub>2</sub>S) and sour gas effects on the eye: A historical perspective. Science of the Total Environment, 367: 1.
- Wieckowska, J. (1995) Catalytic and adsorptive desulphurization of gases. Catalysis Today, 24: 405.

- Abbasian, J.; Slimane, R.B. (1998) A regenerable copper-based sorbent for H<sub>2</sub>S removal from coal gases. *Ind. Eng. Chem. Res.*, 37: 2775.
- Ikenaga, N.; Ohgaito, Y.; Matsushima, H.; Suzuki, T. (2004) Preparation of zinc ferrite in the presence of carbon material and its application to hot-gas cleaning. *Fuel*, 83 (6): 661.
- Yin, F.; Yu, J.; Gupta, S.; Wang, S.; Wang, D.; Yang, Li.; Tahmasebi,
   A. (2012) Sulfidation of a novel iron sorbent supported on lignite chars during hot coal gas desulfurization. *Physics Procedia*, 24 (Part A): 290.
- Lew, S.; Sarofim, A.F.; Flytzani-Stephanopoulos, M. (1992) Sulfidation of zinc titanate and zinc oxide solids. *Industrial & Engineering Chemistry Research*. 31: 1890.
- Li, Z.J.; Flytzani-Stephanopoulos, M. (1997) Cu–Cr–O and Cu–Ce–O regenerable oxide sorbents for hot gas desulphurization. *Industrial & Engineering Chemistry Research*, 36: 187.
- Tseng, H.H.; Wey, M.Y. (2004) Study of SO<sub>2</sub> adsorption and thermal regeneration over activated carbon-supported copper oxide catalysts. *Carbon*, 42 (11): 2269.
- Zhua, J.L.; Wanga, Y.H.; Zhanga, J.C.; Maa, R.Y. (2005) Experimental investigation of adsorption of NO and SO<sub>2</sub> on modified activated carbon sorbent from flue gases. *Energy Conversion and Management*, 46 (13–14): 2173.
- http://hlchem.en.alibaba.com/product/537119579-212920811/90\_ ZnO\_content\_Zinc\_Oxide\_Desulfurization\_Catalyst.html [access 2 August 2013]
- 26. http://m.alibaba.com/trade/search?SearchText=Zinc+Oxide+Desulfurization+adsorbent [access 2 August 2013]
- 27. http://carbokarn.igetweb.com/index.php [access 2 August 2013]
- Gratuito, M.K.B.; Panyathanmaporn, T.; Chumnanklang, R.-A.; Sirinuntawittaya, N.; Dutta, A. (2008) Production of activated carbon from coconut shell: Optimization using response surface methodology. *Bioresource Technology*, 99: 4887.
- Sirichote, O.; Innajitara, W.; Chuenchom, L.; Chunchit, D.; Naweekan, K. (2002) Adsorption of iron (III) ion on activated carbons obtained from bagasse, pericarp of rubber fruit and coconut shell. Songklanakarin J. Sci. Technol., 24: 235.
- Aworn, A.; Thiravetyan, P.; Nakbanpote, W. (2008) Preparation and characteristics of agricultural waste activated carbon by physical activation having micro- and mesopores. J. Anal. Appl. Pyrolysis, 82: 279.
- 81. Boonpoke, A.; Chiarakorn, S.; Laosiripojana, N.; Towprayoon, S.; Chidthaisong, A. (2011) Synthesis of activated carbon and MCM-41 from bagasse and rice husk and their carbon dioxide adsorption capacity. *Journal of Sustainable Energy & Environment*, 2: 77.
- Boonpoke, A.; Chiarakorn, S.; Laosiripojana, N.; Towprayoon, S.; Chidthaisong, A. (2012) Investigation of CO<sub>2</sub> adsorption by bagassebased activated carbon. Korean J. Chem. Eng., 29: 89.
- 33. Simaratanamongkol, A.; Thiravetyan, P. (2010) Decolorization of melanoidin by activated carbon obtained from bagasse bottom ash. *Journal of Food Engineering*, 96: 14–17.
- Panumati, S.; Chudecha, K.; Vankhaew, P.; Choolert, V.; Chuenchom, L.; Innajitara, W.; Sirichote, O. (2008) Adsorption of phenol from diluted aqueous solutions by activated carbons obtained from bagasse, oil palm shell and pericarp of rubber fruit. Songklanakarin J. Sci. Technol., 30: 185.
- Vitidsant, T.; Suravattanasakul, T.; Damronglerd, S. (1999) Production of activated carbon from palm-oil shell by pyrolysis and steam activation in a fixed bed reactor. *ScienceAsia.*, 25: 211.
- Hirunpraditkoon, S.; Tunthong, N.; Ruangchai, A.; Nuithitikul, K. (2011) Adsorption capacities of activated carbons prepared from bamboo by KOH activation. World Academy of Science, Engineering and Technology, 78: 712–715.
- Tongpoothorn, W.; Sriuttha, M.; Homchan, P.; Chanthai, S.; Ruangviriyachai, C. (2011) Preparation of activated carbon derived from Jatropha curcas fruit shell by simple thermo-chemical activation

- and characterization of their physico-chemical properties. *Chemical Engineering Research and Design*, 89: 335.
- 38. Boonamnuayvitaya, V.; Sae-ung, S.; Tanthapanichakoon, W. (2005) Preparation of activated carbons from coffee residue for the adsorption of formaldehyde. *Separation and Purification Technology*, 42: 159.
- Babel, S.; Kurniawan, T.A. (2004) Cr (VI) removal from synthetic wastewater using coconut shell charcoal and commercial activated carbon modified with oxidizing agents and/or chitosan. *Chemosphere*, 54: 951.
- Tsai, J.H.; Jeng, F.T.; Chiang, H.L. (2001) Removal of H<sub>2</sub>S from exhaust gas by use of alkaline activated carbon. *Adsorption*, 7: 357.
- Pipatmanomai, S.; Kaewluan, S.; Vitidsant, T. (2009) Economic assessment of biogas-to-electricity generation system with H<sub>2</sub>S removal by activated carbon in small pig farm. *Applied Energy*, 86: 669.
- Choi, D.Y.; Lee, J.W.; Jang, S.C.; Ahn, B.S.; Choi, D.K. (2008) Adsorption dynamics of hydrogen sulfide in impregnated activated carbon bed. *Adsorption*, 14: 533.
- Bagreev, A.; Bandosz, T.J. (2005) On the mechanism of hydrogen sulfide removal from moist air on catalytic carbonaceous adsorbents. *Ind. Eng. Chem. Res.*, 44: 530.
- Yan, R.; Liang, D.T.; Tsen, L.; Tay, J.H. (2002) Kinetics and mechanisms of H<sub>2</sub>S adsorption by alkaline activated carbon. *Environ. Sci. Technol.*, 36: 4460.

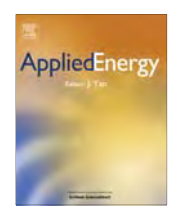
- 45. Yan, R.; Chin, T.; Ng, Y.L.; Duan, H.; Liang, D.T.; Tay, J.H. (2004) Influence of surface properties on the mechanism of H<sub>2</sub>S removal by alkaline activated carbons. *Environ. Sci. Technol.*, 38: 316.
- Bu, X.P.; Ying, Y.J.; Zhang, C.Q.; Peng, W.W. (2008) Research improvement in Zn-based sorbent for hot gas desulphurization. *Powder Technology*, 180: 253.
- Sánchez-Hervás, J.M.; Otero, J.; Ruiz, E. (2005) A study on sulphidation and regeneration of Z-Sorb III sorbent for H<sub>2</sub>S removal from simulated ELCOGAS IGCC syngas. *Chemical Engineering Science*, 60: 2977.
- 48. Slimane, R.B.; Abbasian, J.B. (2000) Copper-based sorbents for coal gas desulphurization at moderate temperatures. *Industrial & Engineering Chemistry Research*, 39: 1338.
- Yasyerli, S.; Dogu, G.; Ar, I. (2001) Activities of copper oxide and Cu-V and Cu-Mo mixed oxides for H<sub>2</sub>S removal in the presence and absence of hydrogen and predictions of a deactivation model. *Industrial & Engineering Chemistry Research*, 40: 5206.
- Fan, H.L.; Li, C.H. (2005) Testing of iron oxide sorbent for hightemperature coal gas desulfurization. Energy Sources, Part A: Recovery Utilization and Environmental Effects, 27: 245.
- Yasyerli, S. (2008) Cerium-manganese mixed oxides for high temperature H<sub>2</sub>S removal and activity comparisons with V-Mn, Zn-Mn, Fe-Mn sorbents. *Chemical Engineering and Processing*, 47: 577.



#### Contents lists available at ScienceDirect

# **Applied Energy**

journal homepage: www.elsevier.com/locate/apenergy



# Thermodynamic analysis of biomass gasification with CO<sub>2</sub> recycle for synthesis gas production



Paphonwit Chaiwatanodom<sup>a</sup>, Supawat Vivanpatarakij<sup>b,\*</sup>, Suttichai Assabumrungrat<sup>a</sup>

- <sup>a</sup> Center of Excellence in Catalysis and Catalytic Reaction Engineering, Department of Chemical Engineering, Faculty of Engineering, Chulalongkorn University, Phyathai Road, Wang Mai, Phatumwan, Bangkok 10330, Thailand
- <sup>b</sup> Energy Research Institute, Chulalongkorn University, Phyathai Road, Wang Mai, Phatumwan, Bangkok 10330, Thailand

#### HIGHLIGHTS

- Cold gas efficiency does not take system energy into account, another factor is proposed.
- Recycled CO<sub>2</sub> improves efficiency and CO<sub>2</sub> per syngas production at some operating conditions.
- Optimum CO<sub>2</sub>/C is around 0.1–0.2 for pressurized and low temperature gasification.

#### ARTICLE INFO

#### Article history: Received 15 July 2013 Received in revised form 8 September 2013 Accepted 18 September 2013

Keywords: Biomass gasification Syngas production CO<sub>2</sub> gasifying agent

#### ABSTRACT

Thermodynamic analysis of biomass gasification with recycled  $CO_2$  was investigated in this work to determine optimum operation mode and  $CO_2/C$  ratio. Gasification System Efficiency (GSE), which takes into account the energy demand in the system, and  $CO_2$  emission per syngas production ( $CO_2/Sg$ ) were calculated to evaluate the performance of the gasification system. Considering the production of syngas at a  $H_2/CO$  ratio of 1.5, it was revealed that indirect gasification using biomass as fuel is the most efficient and environmental-friendly operation mode. The recycled  $CO_2$  proves to increase syngas production. However, when considering the additional energy demand required for processing the  $CO_2$  recycle, it was demonstrated that there are only some ranges of operating conditions (high pressure and low temperature) which offer the benefit of the  $CO_2$  recycle. The optimum  $CO_2/C$  was reported to be around 0.1–0.2 for pressurized and low temperature gasification.

© 2013 Elsevier Ltd. All rights reserved.

## 1. Introduction

Continuous growth in world economy has caused numerous problems as much as it solved. Declining petroleum resources [1] and increasing global warming impact pose a formidable challenge to research community in finding effective solutions. Biomass is identified as an attractive feedstock [2–5] for green production, zero net carbon dioxide emission, and biomass gasification is reported to be among the most cost-effective processes with near-term applications [3,6]. Gasification process mainly produces carbon monoxide and hydrogen, called "syngas", from carbonaceous materials through thermal cracking reactions. Syngas with a variety of  $H_2/CO$  compositions can be used with many downstream processes [7–9] such as heat and electricity generation [10–12], synthetic natural gas (SNG) production [13–15],  $H_2$  production [16,17], and other valuable chemicals productions applicable to both energy and chemical industry [18–21].

E-mail address: supawat@chula.ac.th (S. Vivanpatarakij).

Many gasification processes utilize air [22,23], air-steam [24], steam [25-28], oxygen [29], and oxygen-steam [30,31] as gasifying agents to produce syngas at a desirable H<sub>2</sub>/CO ratio. Air is the cheapest gasifying agent as it is readily available at almost no cost but the syngas product has a very low heating value [32]. The use of oxygen, in lieu of air, increases heating value of syngas product at the cost of oxygen purifying facility [29]. Steam has been reported to increase the yield of H<sub>2</sub> production; however, its use requires more heat input compared to air and oxygen gasification. Recently, CO<sub>2</sub> has been proposed as a candidate for gasifying agent since its utilization has the potential to further reduce CO2 emission [8,33-38]. Moreover, the use of  $CO_2$  as the gasifying agent offers several other advantages [8,34] including (1) producing a more reactive char resulting in efficient gasification and reduction in residual char, (2) being a less corrosive gasification medium compared with steam, and (3) offering more flexibility in syngas production suitable for various downstream applications.

Many researchers have performed experimental studies on gasification in CO<sub>2</sub> atmosphere with various feedstocks (e.g. coal [39–41], wheat straw char [42], olive residue [43], biomass char

<sup>\*</sup> Corresponding author.

#### Nomenclature x<sub>C</sub>, x<sub>H</sub>, x<sub>O</sub> mass faction of carbon, hydrogen, and oxygen in bio-**Abbreviations** mass (-) emission $M_{\rm H}$ mass flow rate of atomic hydrogen in biomass (kg/h) sg syngas biomass molar flow rate of ith component in syngas product bm total $\Delta H_{\nu}^{0}$ Heat of reaction at standard condition 298 K (MJ/kmol) LHV lower heating value (MJ/kg) $H_{i,298}^{0}$ Heat of combustion of ith component in syngas product HHV higher heating value (MJ/kg) (MJ/kmol) gasification system efficiency (-) GSE Μ cold gas efficiency (-) Mass flow rate (kg/h) **CGE** latent heat of vaporization of water at standard condi-RBD Reverse Boudouard reaction $L_{298}$ tion 298 K (MJ/kg) SR steam reforming CO<sub>2</sub>/C mole of CO<sub>2</sub> as gasifying agent per mole of carbon in PO Partial Oxidation WGS water gas shift biomass (-) $O_2/C$ mole of O2 as gasifying agent per mole of carbon in bio-**RWGS** reverse water gas shift MF mass (-) methane formation $H_2O/C$ mole of steam as gasifying agent per mole of carbon in MR Methane reforming **DGOC** dry-gasification oxy combustion biomass (-) H<sub>2</sub>/CO molar ratio of H<sub>2</sub> to CO in product syngas (-) **IGCC** integrated gasification combined cycle **CCRG** catalytically controlled reaction gasification CO<sub>2</sub>/Sg molar flow rate of total CO<sub>2</sub> emission per syngas production (-)

[37], cardboard and paper [35], and oil palm shell char [44]). Overall, reaction rates increase with temperature and vary among different feedstocks. It has been reported that CO<sub>2</sub> gasification generally has lower reaction rates than steam gasification [40,45].

Apart from experimental studies, many authors have studied different gasification processes using  $CO_2$  based on thermodynamic analysis. Walker et al. [46] have recently proposed the use of recycled flue gas (61%  $CO_2$  and 32%  $H_2O$ ) in a fluidized bed gasifier as part of a dry-gasification oxy combustion (DGOC) system. Thermodynamic study of the process demonstrated the superiority of DGOC over IGCC in terms of process efficiency and water consumption. The study of catalytically-controlled reaction gasification (CCRG) system by Castaldi and Dooher [47] showed that the addition of  $CO_2$  enhanced  $H_2$  and power generation. Thermodynamic analysis of hydrocarbon feedstocks such as methane [48] and glycerol [49,50] using  $CO_2$  has been studied in the literature. The results show good  $CO_2$  utilization potential since it can increase syngas production.

In the case of carbonaceous feedstock, most of the thermodynamic studies focus on the use of oxygen and/or steam as gasifying agents [51–54]. Very recently, Renganathan et al. [34] have studied utilization of  $CO_2$  with carbonaceous feedstock. The use of  $CO_2$  is reported to increase the production of CO but reduce that of  $H_2$ . Additionally, cold gas efficiency (CGE), a ratio between LHV of product syngas and LHV of feedstock, has improved with increase in  $CO_2$  amount. However, the CGE does not take energy requirement into account and can be misleading for overall efficiency evaluation [54,55]. Moreover, the benefits of  $CO_2$  addition have not been clearly studied in previous literatures.

In the present work, the thermodynamic analysis of biomass gasification using  $CO_2$ , steam, oxygen, and combination of the agents is studied using Aspen Plus software. Since downstream processes require different  $H_2/CO$  ratios of syngas, this work sets the same final ratio of  $H_2/CO$  in syngas product for performance comparison. Various processes use syngas with the  $H_2/CO$  ratio between 1 and 2 for valuable chemicals production [19,56–58]. Thus, a fixed  $H_2/CO$  ratio of 1.5 in syngas product, normally used for dimethyl ether (DME) production [19], is used to compare performance of each operating condition. The performance is analyzed

both in terms of efficiency and CO<sub>2</sub> emissions. An efficiency factor based on energy requirement of the entire process is also proposed in order to better evaluate the advantages and disadvantages of CO<sub>2</sub> utilization. Further, configurations using direct- and indirect-heated gasification are studied. In the case of indirect-heated gasification, options using biomass or syngas as fuel are assessed. Finally, optimum conditions for CO<sub>2</sub> gasification are investigated.

## 2. Process description of gasification systems

Process flow diagram is illustrated in Fig. 1. Inlet conditions of feedstock and gasification agents are summarized in Table 1. Steam was produced from water (at 25 °C) and oxygen was supplied from air purification process. Three gasification modes are compared: direct-heated, indirect-heated with syngas as fuel, and indirect-heat with biomass as fuel. Direct-heated is defined as having no external heat source for the gasifier, through the addition of oxygen for internal combustion as displayed in the inner boundary of Fig. 1. Indirect-heated is defined as having external heat source for the gasifier, through the combustion of product syngas or biomass in the furnace, as displayed in the outer boundary of Fig. 1.

After feedstocks and gasifying agents pretreatment, biomass and the mixture of gasifying agents were then transferred to the gasifier. The main reactions for gasification under  $CO_2$ ,  $O_2$ , and  $H_2O$  atmosphere are illustrated as follows:

Reverse Boudouard reaction (RBD) : 
$$C + CO_2 \leftrightarrow 2CO$$
 
$$\Delta H_r^0 = 172 \; MJ/kmol \eqno(1)$$

Steam reforming (SR): 
$$C + H_2O \leftrightarrow CO + H_2$$
 
$$\Delta H_r^0 = 131 \text{ MJ/kmol} \eqno(2)$$

Partial Oxidation (PO): 
$$2C + O_2 \leftrightarrow 2CO$$
  
 $\Delta H_r^0 = -221 \text{ MJ/kmol}$  (3)

Water gas shift (WGS) : 
$$CO + H_2O \leftrightarrow CO_2 + H_2$$
 
$$\Delta H_r^0 = -41 \; MJ/kmol \eqno(4)$$

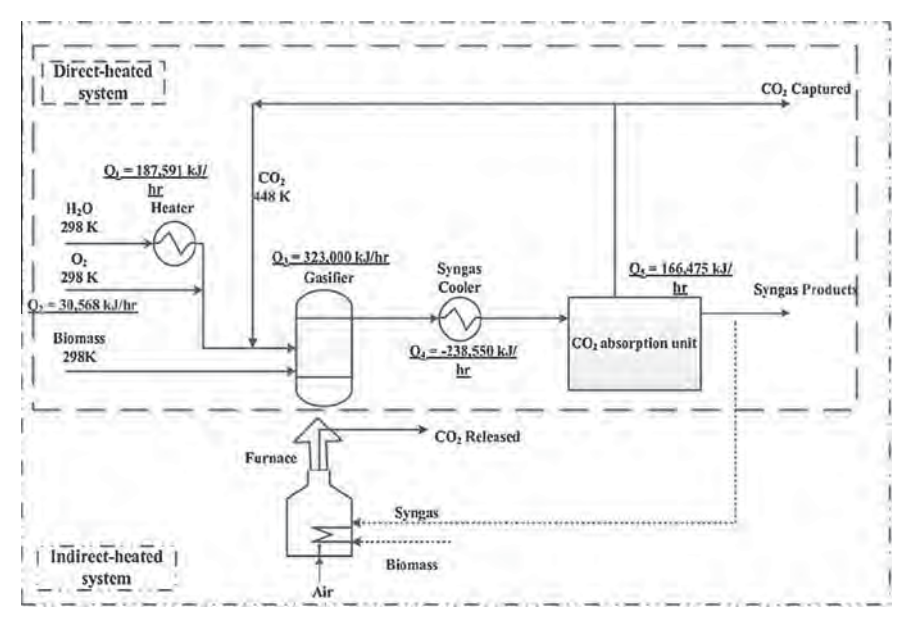


Fig. 1. Biomass gasification diagram using recycled CO<sub>2</sub> as gasifying agent.

**Table 1**Different operating conditions.

Feedstock	CH <sub>1.4</sub> O <sub>0.6</sub>
Inlet temperature of biomass and O2	25 °C
Inlet temperature of CO <sub>2</sub>	150 °C
Inlet temperature of steam	327 °C
Gasifier Temperature	800-1200 °C
Pressure	1-60 bar
CO <sub>2</sub> /C	0-1
O <sub>2</sub> /C	0–1

$$\label{eq:methane formation (MF): C+2H2} \begin{split} &\text{Methane formation (MF): C+2H}_2 \leftrightarrow \text{CH}_4 \\ &\Delta H_r^0 = -74 \text{ MJ/kmol} \end{split}$$

Methane reforming (MR) : 
$$CH_4 + H_2O \leftrightarrow CO + 3H_2$$
 
$$\Delta H_r^0 = 206 \text{ MJ/kmol} \eqno(6)$$

Gasifier effluent was later cooled down to 40 °C and fed to  $CO_2$  absorption unit. The absorption unit was set to remove 90% of  $CO_2$  in effluent [59]. Some of the  $CO_2$  absorbed was recycled (the amount was controlled by inlet  $CO_2/C$  ratio) to the gasifier and the remaining was calculated as the amount of  $CO_2$  captured. The gasifier effluent leaving the absorption unit is called syngas product.

## 3. System modeling

Thermodynamic modeling of biomass gasification can be done using either stoichiometric or non-stoichiometric approaches, also called Gibbs minimization approach. In case of stoichiometric approach, a set of reactions and the extent of each reaction occurring in the gasifier are specified. In contrast, in non-stoichiometric approach, only a set of expected components in product gas has to be specified. Many literatures have verified the results of Gibbs minimization approach with good accuracy compared with experimental values [52,60–63].

For this work, the simulation is carried out using Aspen Plus software and a gasifier is simulated as two separate reactors (RGibbs and RYield). As biomass is represented as an unconventional component in Aspen Plus, it has to be split into its constituent

**Table 2**Detail of Aspen Plus input data.

Input	Attributes
Stream class	MCINCPSD
Valid phases	Vapor-liquid
Thermodynamics properties	Peng-Robinson
NC Props	
Enthalpy	HCOALGEN (user specified option code 6)
Density	DCOALIGT

elements/molecules before feeding into RGibbs reactor. The RYield reactor is used to break down the biomass into its constituent elements/molecules. Then, these elements/molecules are fed to RGibbs reactor along with other gasifying agents. For nonconventional components, the heat of combustion calculation method has to be specified as summarized in Table 2. The high heating value (HHV) of biomass is calculated using the correlation proposed by Channiwala and Parikh [62] shown in Eq. (7). Gasifier heat input is the combination of heat duty in RYield and RGibbs reactors. This heat input represents heat required to maintain gasifier at specified temperature.

HHV 
$$(MJ/kg) = 0.3491x_C + 1178.3x_H - 0.1034x_0$$
 (7)

The simulation results of this work are in good agreement with those of Renganathan et al. [34], with the difference being less than 10% as shown in Table 3. A ratio of H<sub>2</sub>/CO in syngas product depends on various operating parameters such as temperature, pressure, and feed composition. In this study, a H<sub>2</sub>/CO ratio of syngas product, set at 1.5 in this study, is controlled by adjusting H<sub>2</sub>O/ C using the design specification feature in Aspen Plus. Sensitivity Analysis is carried out by varying the temperature or pressure of the gasifier and the flow rate of each gasifying agent, as specified in Table 1. Isothermal operation in gasifier is assumed in the simulation. Biomass feed rate is 100 kg/h in all cases. The feedstock is assumed to consist of only carbon, hydrogen, and oxygen with no moisture content. The representative biomass composition used is CH<sub>1.4</sub> O<sub>0.6</sub> (Ranges of H/C and O/C for biomass are 1.2-1.7 and 0.4-0.85 respectively [54]). Though simplified composition feedstock is used, these three elements make up around 90% of biomass and the results do not deviate much when other elements are

**Table 3** Model validation (biomass  $CH_{1.56}O_{0.78}$ ,  $CO_2/C = 0.5$ , P = 1 bar).

	<i>T</i> = 800 °C		<i>T</i> = 1000 °C	T = 1000 °C		<i>T</i> = 1200 °C	
	Renganathan [25]	This work	Renganathan [25]	This work	Renganathan [25]	This work	
yCO <sub>2</sub>	0.098	0.0901	0.081	0.0733	0.067	0.0628	7.91
yCO	0.6	0.5978	0.625	0.6241	0.650	0.6429	0.53
$yH_2$	0.307	0.3098	0.290	0.3025	0.290	0.2943	2.24
yCH <sub>4</sub>	0	0.0430	0.000	0.0587	0.000	0.0710	0.00
1-Xc	0	0.0000	0.000	0.0000	0.000	0.0000	0.00
CGE	1.21	1.2160	1.220	1.2217	1.22	1.2241	0.32

included [54]. The components assumed to be present at equilibrium are  $C_{(s)}$ ,  $CO_2$ ,  $H_2O$ ,  $O_2$ , CO,  $H_2$ , and  $CH_4$ . Long-chained hydrocarbons were also reported in a very small amount in other study [24].

Performance is evaluated in terms of both efficiency and CO<sub>2</sub> emission. When evaluating the efficiency of gasification system, cold gas efficiency or CGE (Eq. (8)) is normally used as a determining factor. It is defined as in Ravikran et al. [54]:

$$CGE = \frac{M_{syngas}LHV_{syngas}}{M_{biomass}LHV_{biomass}}$$
(8)

where

$$LHV_{biomass} = \frac{M_{biomass}HHV_{biomass} - 0.5M_{H}L_{298}}{M_{biomass}} \tag{9}$$

$$LHV_{syngas} = \frac{n_{CO}H_{CO,298}^{0} + n_{H_{2}}H_{H_{2},298}^{0} + n_{CH_{4}}H_{CH_{4},298}^{0}}{M_{syngas}}$$
(10)

However to take energy requirement into account, we have

However, to take energy requirement into account, we have proposed a gasification efficiency factor, GSE, as shown in Eq. (11). The energy associated with the equation includes thermal energy required or produced at above 150 °C and LHV of both products and reactants. Energy for O<sub>2</sub> production is assumed to be 305 kW h/ton O<sub>2</sub> produced [63] while the energy required for CO<sub>2</sub> capture is considered to be 3 MJ/kg CO<sub>2</sub> captured by amine absorption process [59]. It should be noted that heat transfer efficiency, heat loss, and ease of operation are not in the scope of analysis.

$$GSE = \frac{Energy \ output \ produced}{Energy \ input}$$
 (11)

$$GSE = \frac{M_{\text{syngas}}LHV_{\text{syngas}} + Q_4}{M_{\text{biomass}}LHV_{\text{biomass}} + Q_1 + Q_2 + Q_3 + Q_5}$$
(12)

where  $Q_1$  is energy required for steam production (kJ/h),  $Q_2$  is energy required for oxygen production (kJ/h),  $Q_3$  is energy required for gasifier (kJ/h),  $Q_4$  is energy produced from cooling syngas (kJ/h) and  $Q_5$  is energy required for  $CO_2$  absorption (kJ/h).

In case of excess heat, this value is calculated as energy output produced shown in Eq. (13)

$$GSE = \frac{M_{syngas}LHV_{syngas} + Q_4 + Q_3}{M_{biomass}LHV_{biomass} + Q_1 + Q_2 + Q_5}$$
 (13)

 $CO_2$  emission is measured by total  $CO_2$  emission per syngas production ( $CO_2/Sg$ ), including both captured  $CO_2$  and released  $CO_2$  (Eqs. (14)–(16)). Captured  $CO_2$  is also included in  $CO_2$  emission because it is still unclear whether  $CO_2$  storage is feasible on a large scale

$$CO_2/Sg = \frac{Captured\ CO_2 + Released\ CO_2}{Flow\ syngas\ product} \eqno(14)$$

$$\begin{aligned} \text{Captured CO}_2 \ (kmol/h) &= \text{mole flow} \ (\text{CO}_2)_{absorbed} \\ &- \text{mole flow} \ (\text{CO}_2)_{input} \end{aligned} \tag{15}$$

Captured 
$$CO_2$$
 (kmol/h) = mole flow  $(CO_2)_{absorbed}$   
- mole flow  $(CO_2)_{input}$  (16)

where  $(CO_2)_{absorbed}$  is  $CO_2$  which is absorbed in absorption unit,  $(CO_2)_{input}$  is  $CO_2$  which is recycled back to the process,  $(CO_2)_{syngas}$  is  $CO_2$  which is present in syngas product,  $(CO_2)_{fuel}$  is  $CO_2$  which is released by fuel combustion (for heating). Complete combustion is assumed. Heat released from combustion is calculated from LHV of each fuel.

#### 4. Results and discussion

The simulation results for biomass gasification using combinations of various gasification agents are reported as follows:

## 4.1. Effects of CO<sub>2</sub> addition on syngas production

The simulations were conducted to study the effects of  $CO_2$  addition under various operating conditions. It is desirable to evaluate how it affects the composition, flow rate, and  $H_2/CO$  ratio of syngas product. Fig. 2 shows %composition of  $H_2$ , CO,  $CH_4$  (after removal of  $H_2O$  and  $CO_2$ ) at various  $CO_2/C$  ratios. Regardless of temperature, pressure, steam/C, and  $O_2/C$ , the trend of % $H_2$  and % $CH_4$  decreases while %CO increases with  $CO_2$  addition, resulting in a decrease in  $H_2/CO$  of product syngas. This is because both RBD and WGS reactions favor CO production with the increase of  $CO_2$  concentration. The by-product,  $H_2O$ , also reacts with methane to form  $H_2$  and CO; hence, reducing the amount of  $CH_4$ . The RBD reaction also favors the higher concentration of  $CO_2$ , competing with MF reaction. Clearly,  $H_2/CO$  ratios change sharply over different ranges

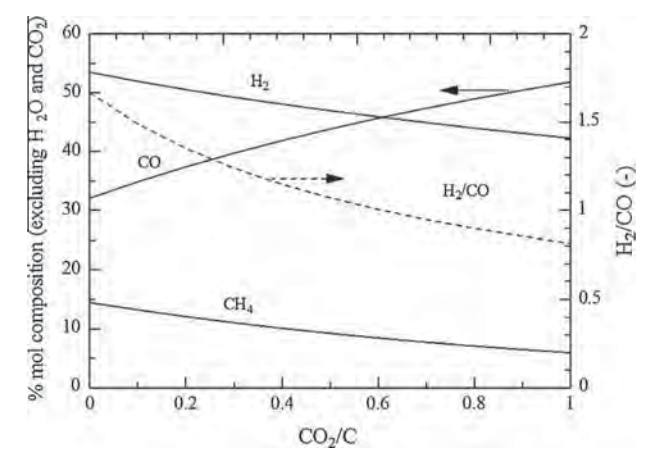


**Fig. 2.** Syngas product composition at different  $CO_2/C$  ratios ( $T = 800 \, ^{\circ}C$ ,  $P = 20 \, \text{bar}$ ,  $H_2O/C = 1.0$ , and  $O_2/C = 0$ ).

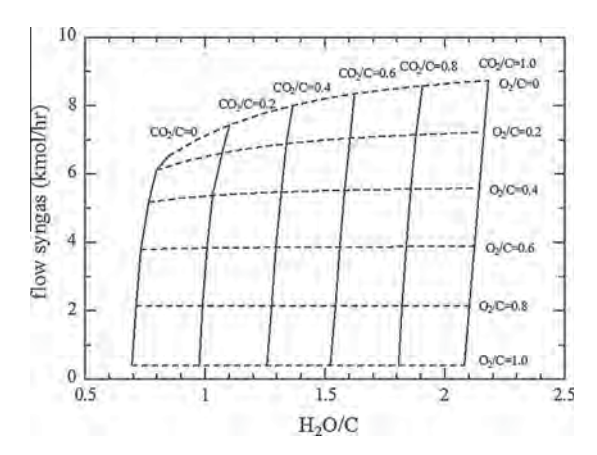


**Fig. 3.** Syngas product flow rate and  $H_2O/C$  required for  $H_2/CO = 1.5$  at various  $CO_2/C$  and  $O_2/C$  ratios (P = 10 bar, T = 800 °C).

of CO<sub>2</sub>/C. In order to keep the ratios constant, steam is added to increase H<sub>2</sub> production. Flow rate of syngas product (molar flow rate of  $H_2$  and CO) and steam/C ratio required for  $H_2/CO = 1.5$  are shown in Fig. 3 for different  $O_2/C$  and  $CO_2/C$  ratios (P = 10 bar, T = 800 °C). Steam requirement increases with CO2 since RBD reaction produces CO, to maintain H<sub>2</sub>/CO at 1.5 (more steam is required to increase H<sub>2</sub> production). The flow rate of syngas product increases with increasing  $CO_2$  at low  $O_2/C$  but, with higher  $O_2/C$ , some minor differences in syngas flow rate are exhibited. This is because the addition of O2 also produces CO2 through combustion and increasing the amount of CO<sub>2</sub> further has little impact on syngas production. At higher temperature or lower pressure, the addition of CO<sub>2</sub> also gives less impact on syngas flow rate. At any temperature and pressure, O2 addition reduces the flow rate of syngas product because more biomass is combusted. It can be seen that CO<sub>2</sub> addition has a positive effect on syngas production at various operating conditions; however, a more comprehensive study that includes the effects on energy requirements should be carried out.

#### 4.2. Efficiency factor

Since CGE does not take heat requirement into consideration, it cannot be evaluated whether the increase in syngas product by adding  $CO_2$  offsets the additional energy requirement (mostly in the gasifier). The proposed factor, GSE, takes energy requirement into account. Fig. 1 shows the distribution of energy requirement in gasification process at T = 800 °C, P = 1 bar,  $O_2/C = 0.87$ . Most of

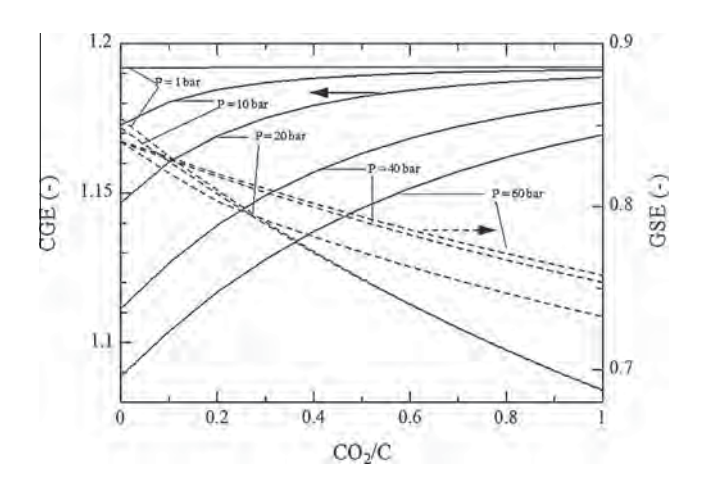


**Fig. 4.** CGE and GSE comparison at different CO<sub>2</sub>/C ratio and pressure (H<sub>2</sub>/CO = 1.5, T = 900 °C and O<sub>2</sub>/C = 0).

the unit operations consume energy with the exception of syngas cooling. Gasifier is the largest energy consumer in the process followed by steam heater and CO<sub>2</sub> absorption unit. Fig. 4 illustrates variations in CGE and GSE with the addition of CO<sub>2</sub> at various pressures ( $T = 900 \,^{\circ}$ C,  $O_2/C = 0$ ). It can be seen that while CGE increases monotonically with CO<sub>2</sub>, GSE decreases sharply. This is because even though syngas product may increase with CO2 addition, the energy requirement to produce syngas product rises at a greater rate. At lower pressure, CGE increases slightly while GSE declines steadily with the addition of CO<sub>2</sub>. This suggests that CO<sub>2</sub> does not increase much syngas production and its effect on energy requirement is very high in comparison. In the case of high pressure, even though CGE and GSE change differently when added CO<sub>2</sub>, the difference between the two is much smaller, indicating that CO2 addition has an impact on increasing syngas production and energy requirement is more equal. This finding suggests that CGE may not be a good indicator whether CO<sub>2</sub> addition is beneficial, hence GSE was used in later stages. It is important to note that even though CO<sub>2</sub> addition does not improve GSE in this case, there are some conditions in which adding CO<sub>2</sub> does improve GSE, as discussed in later sections.

#### 4.3. Gasifier operating mode

Among the three operating modes, it is desirable to find optimal operating modes of the gasifier at various conditions. The condition for comparison is an equal amount of the total biomass input through the system. Direct-heated gasification requires high purity oxygen for internal combustion. This option is beneficial in terms of heat transfer efficiency since heat is generated directly in the gasifier. However, it requires air separation unit and complicates the control of gasifying agent composition (internal combustion also creates CO<sub>2</sub> and H<sub>2</sub>O directly in the gasifier). In contrast, indirect gasification supplies heat from external combustion, hence heat transfer efficiency is not as good as direct gasification. However, air can be used instead of high purity oxygen and controlling gasifying agent amount is also easier by adjusting inlet condition. Either biomass or syngas product can be used as fuel in this case. Syngas could be beneficial in terms of ease of operation compared with biomass since gas burner is easier to operate than that of solid. Nevertheless, biomass is cheaper and does not require gasification processing.

The comparison, in terms of GSE and CO<sub>2</sub>/Sg, is illustrated in Fig. 5. It can be seen that among the three options, indirect-heated

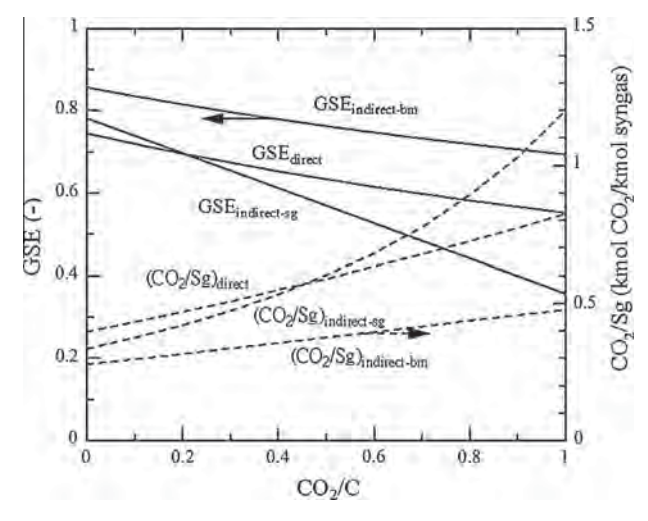


**Fig. 5.** GSE and total  $CO_2$  emission/syngas production at various  $CO_2/C$  and operating modes ( $H_2/CO = 1.5$ , T = 800 °C, P = 1 bar, and  $O_2/C = 0$ ).

with biomass as fuel source alternative is the most thermodynamically efficient and environmental friendly mode of operation. Indirect-heated with biomass as fuel appears to be the optimal operating mode for all temperatures, pressures, and CO<sub>2</sub>/C ratios, in the range of this study. Direct-gasification has lower thermal efficiency because 30–50% of biomass has to be combusted in order to supply heat to the gasifier. This results in excess CO<sub>2</sub> which consumes additional heat load in the gasifier. In the case of indirect-gasification using syngas, utilization of syngas as heat supply increases the heat requirement per syngas production since part of the syngas is required as heat for syngas production. Based on this findings, later sections will focus on indirect-heated gasification with biomass as fuel.

### 4.4. Effects of CO<sub>2</sub> addition on GSE and CO<sub>2</sub>/Sg

The effects of  $CO_2$  addition on gasification system efficiency (GSE) and  $CO_2$  emission per syngas production ( $CO_2/Sg$ ) have been studied at various temperatures and pressures. At low pressure, it can be seen from Fig. 6a and b that  $CO_2$  addition does not have a positive effect on both GSE and  $CO_2/Sg$ . Also, increasing  $O_2$  has negative impact on both factors. This can result from the fact that at low pressure, RBD reaction is already moving towards the product side. Hence, adding  $CO_2$  does not significantly increase the production rate; nevertheless, it strongly affects energy requirement to heat up excess  $CO_2$ . This can be seen from Fig. 6b that at higher temperature, the addition of  $CO_2$  has a higher impact over GSE.

Fig. 6c presents the results of  $CO_2$  addition at low temperature and high pressure. In this case, by slightly adding  $CO_2$  GSE moderately increases while  $CO_2$ /Sg decreases with  $CO_2$  addition. This is

because higher CO<sub>2</sub> partial pressure pushes RBD reaction to the right producing more CO against high pressure effects (carbon in biomass is not completely converted without CO<sub>2</sub>), thereby increasing efficiency. By consuming CO<sub>2</sub>, it also decreases CO<sub>2</sub>/Sg. However, adding O<sub>2</sub> still has negative effects on both GSE and CO<sub>2</sub>/Sg. It is important to note that without the addition of CO<sub>2</sub> or O<sub>2</sub>, H<sub>2</sub>/CO cannot be controlled at 1.5. Hence, introducing CO<sub>2</sub> or O<sub>2</sub> also increases the flexibility of operation. At high temperature and pressure, Fig. 6d, the result from temperature is more significant than CO<sub>2</sub> partial pressure since RBD and RWGS reaction is highly endothermic; hence, the addition of CO<sub>2</sub> has little impact on syngas production and negative effect on efficiency and CO<sub>2</sub> emission overall.

#### 4.5. Optimum $CO_2/C$ ratio at different pressures and temperatures

It is therefore desirable to find the optimum  $CO_2/C$  ratio at various operating conditions. Best GSE point is chosen for each  $CO_2/C$  ratio  $(O_2/C$  may vary) and plotted at different pressures and temperatures. From Fig. 7, it can be seen that at pressure 10 bar  $(T=800\,^{\circ}\text{C})$ ,  $CO_2$  addition begins to have a positive effect in terms of  $CO_2/Sg$ , even though GSE reduces with  $CO_2$ . At this stage,  $CO_2$  increases the syngas production rate; however, its negative impact on energy requirement is still higher. For higher pressure,  $CO_2$  benefits both GSE and  $CO_2$  emission per syngas production. By adding  $CO_2$  beyond an optimum point  $(CO_2/C=0.1$  at pressure 20 bar,  $CO_2/C=0.2$  at pressure 40 and 60 bar), GSE starts to decline again. It is important to note that even though low pressure gasification is normally used since energy production is the major end usage, high pressure gasification is beneficial for downstream chemical

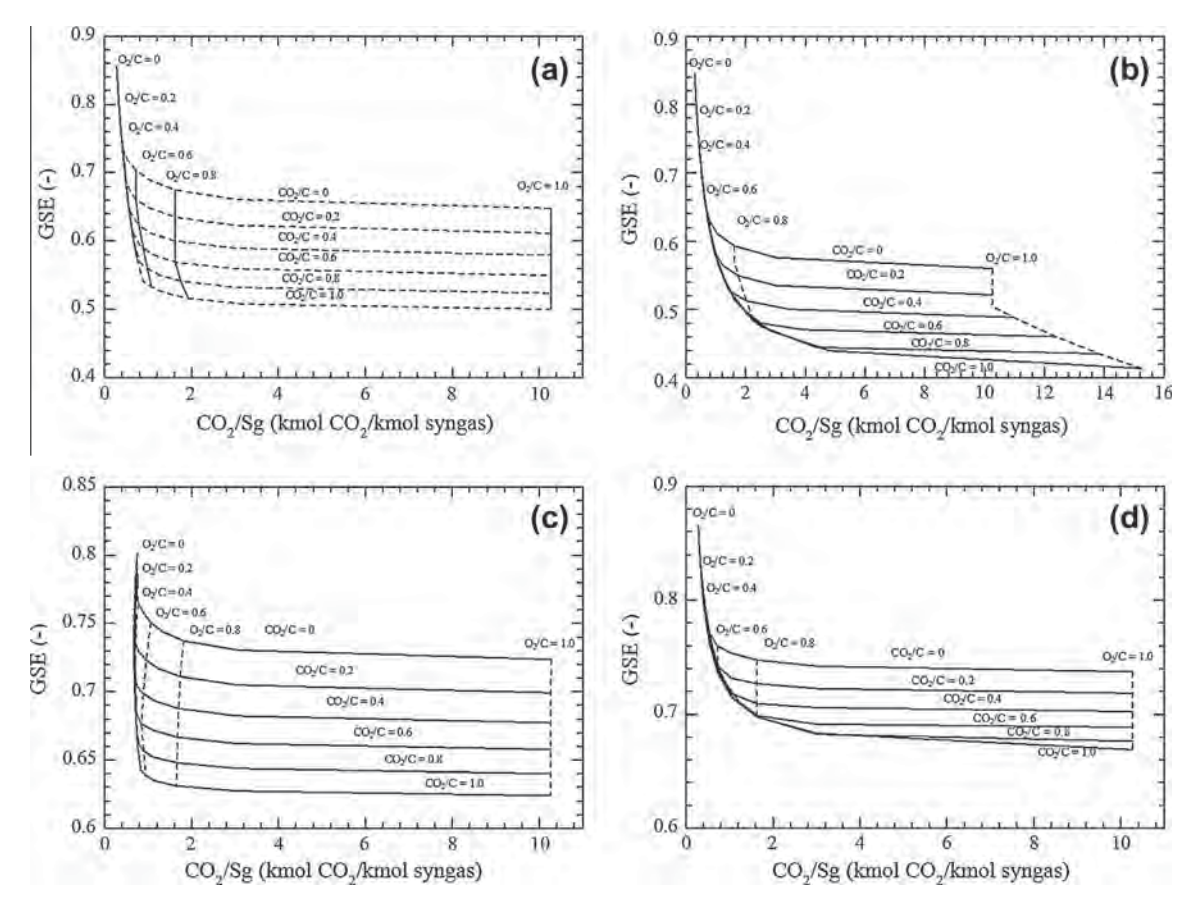
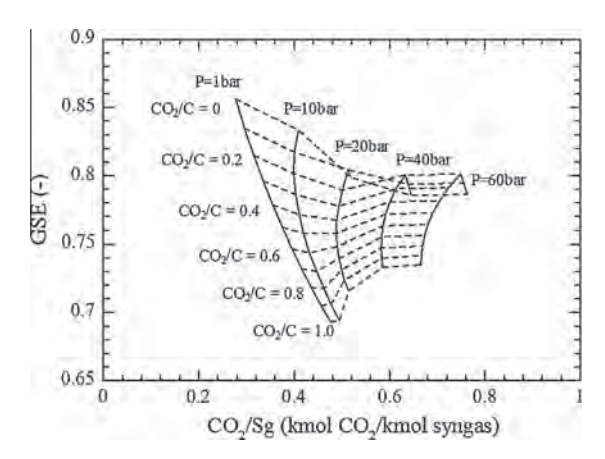
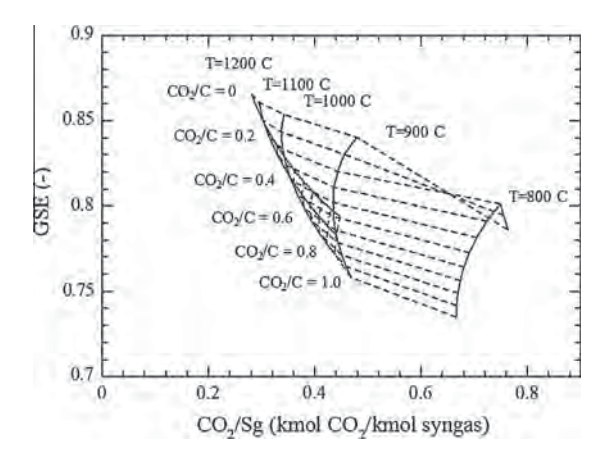


Fig. 6. GSE and total CO<sub>2</sub> emission/syngas production for H<sub>2</sub>/CO = 1.5 at various CO<sub>2</sub>/C and O<sub>2</sub>/C. (a) P = 1 bar, T = 800 °C, (b) P = 1 bar, T = 1200 °C, (c) P = 60 bar, T = 800 °C and, (d) P = 60 bar, T = 1200 °C.



**Fig. 7.** GSE and total CO<sub>2</sub> emission/syngas production for  $H_2/CO = 1.5$  at optimum condition for each  $CO_2/C$  (P = 1-60 bar, T = 800 °C).



**Fig. 8.** GSE and total CO<sub>2</sub> emission/syngas production for  $H_2/CO = 1.5$  at optimum condition for each CO<sub>2</sub>/C (P = 60 bar, T = 800 - 1200 °C).

productions. This is due to the fact that high pressure gasification minimizes the requirement of recompression for succeeding downstream conversion process (gas compression is more energy intensive than liquid pressurization). Moreover, high pressure gasifier may be much smaller per throughput [18,58].

Fig. 8 shows optimum  $CO_2/C$  ratio at various temperature (P = 60 bar). It can be seen that beyond 900 °C introducing  $CO_2$  does not have a positive effect on GSE. Nevertheless,  $CO_2$  addition is still beneficial in terms of  $CO_2$  emission per syngas production at temperature between 900 and 1000 °C. Beyond 1100 °C,  $CO_2$  utilization has a negative impact on both GSE and  $CO_2$  emissions as seen in Fig. 6d. It is noteworthy to add that choices of operating temperatures vary greatly between different types of gasifier. Entrained flow gasifier has the highest operating temperature followed by fluidized bed and fixed bed gasifier respectively [9].

## 5. Conclusion

The recycle of  $\mathrm{CO}_2$  to the biomass gasification shows the potential benefit on the syngas production; however, the study reveals that the additional energy requirement for  $\mathrm{CO}_2$  heating may overwhelm this benefit. GSE is a suitable indicator for the system-wide analysis since energy requirement in the system is also included. In terms of operating mode, indirect-gasification with biomass as fuel source appears to be the best operating mode when thermodynamics efficiency and  $\mathrm{CO}_2$  emission are considered. This is due to the fact that excess  $\mathrm{CO}_2$  from direct-combustion and utilization

of syngas as heat supply has negative impacts on thermodynamics efficiency. Analyzing the effects of  $CO_2$  addition on GSE and  $CO_2/Sg$ , it is shown that at low temperature and high pressure,  $CO_2$  has positive effects on both factors while at ambient pressure,  $CO_2$  addition has no benefit to both factors. The introduction of  $O_2$  minimizes the requirement of external heat-supply; nevertheless, it has negative impacts on both GSE and  $CO_2/Sg$ . Optimum  $CO_2/C$  at Temperature  $800\,^{\circ}C$  is around 0.1-0.2 for pressurized gasification. The addition of  $CO_2$  beyond this point may have moderate benefits in terms of  $CO_2$  emission. For higher temperature operation,  $CO_2$  addition may have a positive impact on  $CO_2/Sg$  while GSE monotonically decreases. It is important to note that  $CO_2$  or  $O_2$  addition also offers more flexibility in adjusting  $H_2/CO$  of end product especially at low temperature and high pressure.

#### Acknowledgment

The authors gratefully acknowledge the support from the Thailand Research Fund.

#### References

- Zainal ZA, Ali R, Lean CH, Seetharamu KN. Prediction of performance of a downdraft gasifier using equilibrium modeling for different biomass materials. Energy Convers Manage 2001;42:1499–515.
- [2] McKendry P. Energy production from biomass (part1): overview of biomass. Bioresour Technol 2002;83:37–46.
- [3] McKendry P. Energy production from biomass (part2): conversion technology. Bioresour Technol 2002;83:47–54.
- [4] Budzianowski W. Negative carbon intensity of renewable energy technologies involving biomass or carbon dioxide as inputs. Renew Sustain Energy Rev 2012;16:6507–21.
- [5] Chen WH, Chen AJ, Hung CI, Shen CH, Hsu HW. A comparison of gasification phenomena among raw biomass, torrefied biomass and coal in an entrainedflow reactor. Applied Energy 2013;112:421–30.
- [6] Anex RP, Aden A, Kazi FK, Fortman J, Swanson RM, Wright MM, et al. Technoeconomic comparison of biomass-to-transportation fuels via pyrolysis, gasification, and biochemical pathways. Fuel 2010;89:29–35.
- [7] Balat M, Kırtay E, Balat H. Main routes for the thermo-conversion of biomass into fuels and chemicals Part 2:Gasification systems. Energy Convers Manage 2009:50:3158–68.
- [8] Butterman HC, Castaldi MJ. CO<sub>2</sub> as a carbon neutral fuel source via enhanced biomass gasification. Environ Sci Technol 2009;43:9030–7.
- [9] Mondal P, Dang GS, Garg MO. Syngas production through gasification and cleanup for downstream applications—recent developments. Fuel Process Technol 2011:92:1395-410.
- [10] Rodrigues M, Faaij APC, Walter A. Techno-economic analysis of co-fired biomass integrated gasification/combined cycle systems with inclusion of economies of scale. Energy 2003;28:1229–58.
- [11] Piroonlerkgul P, Assabumrungrat S, Laosiripojana N, Adesina AA. Selection of appropriate fuel processor for biogas-fuelled SOFC system. Chem Eng J 2008;140:341–51.
- [12] Liu H, Shao Y, Li J. A biomass-fired micro-scale CHP system with organic Rankine cycle (ORC) thermodynamic modelling studies. Biomass Bioenergy 2011;35:3985–94.
- [13] Gassner M, Maréchal F. Thermo-economic process model for thermochemical production of Synthetic Natural Gas (SNG) from lignocellulosic biomass. Biomass Bioenergy 2009;33:1587-604.
- [14] Naqvi M, Yan J, Dahlquist E. Synthetic gas production from dry black liquor gasification process using direct causticization with CO<sub>2</sub> capture. Appl Energy 2012;97:49–55.
- [15] Grobl T, Walter H, Haider M. Biomass steam gasification for production of SNG – process design and sensitivity analysis. Appl Energy 2012;97:451–61.
- [16] Guoxin H, Hao H. Hydrogen rich fuel gas production by gasification of wet biomass using a CO<sub>2</sub> sorbent. Biomass Bioenergy 2009;33:899–906.
   [17] Long H, Qinhui W, Zhongyang L, Nai R, Guangyi D. H<sub>2</sub> rich gas production via
- [17] Long H, Qinhui W, Zhongyang L, Nai R, Guangyi D. H<sub>2</sub> rich gas production via pressurized fluidized bed gasification of sawdust with in situ CO<sub>2</sub> capture. Appl Energy 2013;109:36–43.
- [18] Hamelinck CN, Faaij APC, den Uil H, Boerrigter H. Production of FT transportation fuels from biomass; technical options, process analysis and optimisation, and development potential. Energy 2004;29:1743–71.
- [19] Tock L, Gassner M, Maréchal F. Thermochemical production of liquid fuels from biomass: thermo-economic modeling, process design and process integration analysis. Biomass Bioenergy 2010;34:1838–54.
- [20] Holmgren KM, Berntsson T, Andersson E, Rydberg T. System aspects of biomass gasification with methanol synthesis – process concepts and energy analysis. Energy 2012;45:817–28.
- [21] Valle CR, Perales VAL, Vidal-Barrero F, Gomez-Barea A. Techno-economic assessment of biomass-to-ethanol by indirect fluidized bed

- gasification:Impact of reforming technologies and comparison with entrained flow gasification. Appl Energy 2013;109:254–66. [22] Cao Y, Wang Y, Riley JT, Pan WP. A novel biomass air gasification process for
- producing tar-free higher heating value fuel gas. Fuel Process Technol 2006;87:343-53.
- [23] Kim YD, Yang C, Kim B, Kim K, Lee J, Moon J, et al. Air-blown gasification of woody biomass in a bubbling fluidized bed gasifier. Appl Energy 2013. Available online 24 April 2013; http://dx.doi.org/10.1016/ .apenergy.2013.03.072.
- [24] Hernández JJ, Aranda G, Barba J, Mendoza JM. Effect of steam content in the air-steam flow on biomass entrained flow gasification. Fuel Process Technol 2012;99:43-55.
- Skoulou V, Swiderski A, Yang W, Zabaniotou A. Process characteristics and products of olive kernel high temperature steam gasification (HTSG). Bioresour Technol 2009:100:2444-51
- [26] Nipattummakul N, Ahmed II, Kerdsuwan S, Gupta AK. Hydrogen and syngas production from sewage sludge via steam gasification. Int J Hydrogen Energy 2010:35:11738-45.
- [27] Ngo SI, Nguyen TDB, Lim YI, Song BH, Lee UD, Choi YT, et al. Performance evaluation for dual circulating fluidized-bed steam gasifier of biomass using quasi-equilibrium three-stage gasification model. Appl 2011:88:5208-20.
- [28] Umeki K, Yamamoto K, Namioka T, Yoshikawa K. High temperature steamonly gasification of woody biomass. Appl Energy 2010;87:791-8.
- [29] Valero A, Usón S. Oxy-co-gasification of coal and biomass in an integrated gasification combined cycle (IGCC) power plant. Energy 2006;31:1643-55.
- [30] Barisano D, Freda C, Nanna F, Fanelli E, Villone A. Biomass gasification and inbed contaminants removal: performance of iron enriched olivine and bauxite in a process of steam/O2 gasification. Bioresour Technol. 2012;118:187-94.
- Hannula I, Kurkela E. A parametric modeling study for pressurised steam/O2blown fluidised-bed gasification of wood with catalytic reforming. Biomass Bioenergy 2012;38:58-67.
- [32] Schuster G, Loffler G, Weigl K, Hofbauer H. Biomass steam gasification an extensive parametric modeling study. Bioresour Technol. 2001;77:71-9.
- [33] Garcia L, Salvador ML, Arauzo J, Bilbao R. CO2 as a gasifying agent for gas production from pine sawdust at low temperatures using a Ni/Al coprecipitated catalyst. Fuel Process Technol 2001;69:157–74.
- Renganathan T, Yadav MV, Pushpavanam S, Voolapalli RK, Cho YS. CO<sub>2</sub> utilization for gasification of carbonaceous feedstocks:A thermodynamic analysis. Chem Eng Sci 2012;83:159–70.

  [35] Ahmed I, Gupta AK. Characteristics of cardboard and paper gasification with
- CO<sub>2</sub>. Appl Energy 2009;86:2626-34.
- [36] Ahmed I, Gupta AK. Kinetics of woodchips char gasification with steam and carbon dioxide. Appl Energy 2011;88:1613-9.
- [37] Lin L, Strand M. Investigation of the intrinsic CO2 gasification kinetics of biomass char at medium to high temperatures. Appl Energy 2013;109:220-8.
- Thanapal SS, Annamalai K, Sweeten JM, Gordillo G. Fixed bed gasification of dairy biomass with enriched air mixture. Appl Energy 2012;97:525-31.
- [39] Ochoa J, Cassanello MC, Bonelli PR, Cukierman AL. CO2 gasification of Argentinean coal chars:a kinetic characterization. Fuel Process Technol 2001;74:161-76.
- [40] Irfan MF, Usman MR, Kusakabe K. Coal gasification in CO<sub>2</sub> atmosphere and its kinetics since 1948: a brief review. Energy 2011;36:12-40.
- Gonzalo-Tirado C, Jiménez S, Ballester J. Kinetics of CO2 gasification for coals of different ranks under oxy-combustion conditions. Combust Flame 2013;160:411-6.
- Mani T, Mahinpey N, Murugan P. Reaction kinetics and mass transfer studies of biomass char gasification with CO<sub>2</sub>. Chem Eng Sci 2011;66:36-41.

- [43] Ollero P, Serrera A, Arjona R, Alcantarilla S. The CO2 gasification kinetics of
- olive residue. Biomass Bioenergy 2003;24:151–61. Lahijani P, Zainal ZA, Mohamed AR. Catalytic effect of iron species on  ${\rm CO_2}$ gasification reactivity of oil palm shell char. Thermochim Acta 2012;546:24–31.
- [45] Roberts DG, Harris DJ. Char gasification in mixtures of CO2 and H2O: competition and inhibition. Fuel 2007;86:2672-8.
- [46] Walker ME, Abbasian J, Chmielewski DJ, Castaldi MJ. Dry gasification oxycombustion power cycle. Energy Fuels 2011;25:2258-66.
- Castaldi MJ, Dooher JP. Investigation into a catalytically controlled reaction gasifier (CCRG) for coal to hydrogen. Int J Hydrogen Energy 2007;32:4170-9.
- [48] Amin NAS, Yaw TC. Thermodynamic equilibrium analysis of combined carbon dioxide reforming with partial oxidation of methane to syngas. Int J Hydrogen Energy 2007;32:1789-98.
- [49] Wang X, Li M, Wang M, Wang H, Li S, Wang S, et al. Thermodynamic analysis of glycerol dry reforming for hydrogen and synthesis gas production. Fuel 2009;88:2148-53.
- [50] Kale GR, Kulkarni BD. Thermodynamic analysis of dry autothermal reforming of glycerol. Fuel Process Technol 2010;91:520-30.
- [51] Prins MJ, Ptasinski KJ, Janssen FJJG. Thermodynamics of gas-char reactions: first and second law analysis. Chem Eng Sci 2003;58:1003-11.
- [52] Melgar A, Perez JF, Laget H, Horillo A. Thermochemical equilibrium modeling of a gasifying process. Energy Convers Manage 2007;48:59-67.
- [53] Vivanpatarakij S, Assabumrungrat S. Thermodynamic analysis of combined unit of biomass gasifier and tar steam reformer for hydrogen production and tar removal. Int J Hydrogen Energy 2013;38:3930-6.
- Ravikran A, Renganathan T, Pushpavanam S, Voolapalli RK, Cho YS. Generalized analysis of gasifier performance using equilibrium modeling. Ind Eng Chem Res 2012;51:1601–11.
- [55] Giuffrida A, Romano M, Lozza G. Thermodynamic analysis of air-blown gasification for IGCC applications. Appl Energy 2011;88:3949-58.
- [56] Wang L, Fang D, Huang X, Zhang S, Qi Y, Liu Z. Influence of reaction conditions on methanol synthesis and WGS reaction in the Syngas-to-DME process. J Nat Gas Chem 2006:15:38-44.
- [57] Khoshbin R, Haghighi M. Direct syngas to DME as a clean fuel: The beneficial use of ultrasound for the preparation of CuO-ZnO-Al<sub>2</sub>O<sub>3</sub>/HZSM-5 nanocatalyst. Chem Eng Res Des 2013;91:1111-2.
- [58] Trippe F, Frohling M, Schultmann F, Stahl R, Henrich E, Dalai A. Comprehensive techno-economic assessment of dimethyl ether (DME) synthesis and Fischer-Tropsch synthesis as alternative process steps within biomass-to-liquid production. Fuel Process Technol 2013;106:577–86.
- [59] Peters L, Hussain A, Follmann M, Melin T, Hagg MB. CO<sub>2</sub> removal from natural gas by employing amine absorption and membrane technology - a technical and economical analysis. Chem Eng J 2011;172:952-60.
- [60] Rodrigues R, Secchi AR, Marcilio NR, Godinho M. Modeling of biomass gasification applied to a combined gasifier-combustor unit: equilibrium and Kinetics Approaches, In: 10th International sympotium on process systems engineering; 2009. p. 657-62.
- [61] Shabbar S, Janajreh I. Thermodynamic equilibrium analysis of coal gasification using Gibbs energy minimization method. Energy Convers Manage 2013:65:755-63.
- Channiwala SA Parikh PP A unified correlation for estimating HHV of solid liquid, and gaseous fuels. Fuel 2002:81:1051-63.
- Tijmensen MJA, Faaij APC, Hamelinck CN, van Hardeveld MRM. Exploration of the possibilities for production of Fischer-Tropsch liquids and power via biomass gasification. Biomass Bioenergy 2002;23:129-52.

## Suttichai Assabumrungrat

**Date:** Thu, 14 Nov 2013 10:34:14 +0700 **From:** Yan Zhao <Yan.Z@chula.ac.th>

Subject: [EJ] Editor Decision

To: "wisitsree wiyaratn" <wisitsree@gmail.com>

**Cc:** "EJ Editor" <editor@engj.org> , "Kiatkittipong Worraphon" <Wisitsree.Wiy@kmutt.ac.th> , "Suttichai Assabumrungrat" <suttichai.a@chula.ac.th> , "Navadol Laosiripojana" <navadol@jgsee.kmutt.ac.th>

Dear wisitsree wiyaratn,

Regarding your recent submission entitled, "Reactivity of Au/Lal-xSrxCrl-yNiyO3-δ toward Oxidative Coupling of Methane for C2 and C3 Hydrocarbons Production", we are pleased to inform you that your article has been accepted for publication in Engineering Journal.

We will write to you again as soon as your proof is ready for you to check, correct and return to us. Thank you for your interest in Engineering Journal. We look forward to publishing your article.

Yan Zhao Managing Editor

Engineering Journal (EJ)
Web: http://engj.org/

ISSN: 0125-8281



Contents lists available at ScienceDirect

## Fuel Processing Technology

journal homepage: www.elsevier.com/locate/fuproc



# Effects of humidity, O<sub>2</sub>, and CO<sub>2</sub> on H<sub>2</sub>S adsorption onto upgraded and KOH impregnated activated carbons



Russamee Sitthikhankaew a,e, David Chadwick b, Suttichai Assabumrungrat c, Navadol Laosiripojana a,d,\*

- a The Joint Graduate School of Energy and Environment, CHE Center for Energy Technology and Environment, King Mongkut's University of Technology Thonburi, Bangkok 10140, Thailand
- <sup>b</sup> Department of Chemical Engineering, Imperial College London, SW7 4RU, UK
- <sup>c</sup> Department of Chemical Engineering, Faculty of Engineering, Chulalongkorn University, Bangkok 10330, Thailand
- d PTT Group Frontier Research Center, PTT Public Company Limited, 555 Vibhavadi Rangsit Road, Chatuchak, Bangkok 10900, Thailand
- e Department of General Science, Faculty of Science and Technology, Muban Chombueng Rajabhat University, Ratchaburi 70150, Thailand

#### ARTICLE INFO

#### Article history: Received 13 September 2012 Received in revised form 11 April 2013 Accepted 9 March 2014 Available online 28 March 2014

Keywords: Activated carbon Adsorption Hydrogen sulfide Gas purification

#### ABSTRACT

In the present work, low grade activated carbon was upgraded by steam activation to improve its surface properties and further impregnated with potassium hydroxide (KOH) to promote the  $H_2S$  chemisorption for desulfurization applications. The  $H_2S$  adsorption performance of these prepared samples was tested at ambient temperature under various operating conditions i.e. in the presence of isolated and integrated relative humidity (70%),  $O_2$  (2%), and  $CO_2$  (40%). It was found that the KOH impregnated activated carbons provide significantly higher  $H_2S$  adsorption capacity and breakthrough time than the non-impregnated sample. Importantly, the presence of  $O_2$  in the gas stream greatly increases the breakthrough time of  $H_2S$  adsorption, while the presence of humidity significantly increases the  $H_2S$  adsorption capacity; these positive effects are related to the promotion of  $H_2S$  oxidation to elemental sulfur and  $H_2S$  dissociation. In contrast, the presence of  $CO_2$  strongly inhibited  $CO_2$  addsorption due to competitive adsorption and reaction between  $CO_2$  and  $CO_2$  and  $CO_3$  and humidity along with  $CO_3$  can efficiently minimize this negative effect; therefore, this highlights the importance of  $CO_3$  and humidity addition for biogas purification.

© 2014 Elsevier B.V. All rights reserved.

## 1. Introduction

Agricultural industries and livestock farms generally produce several organic wastes and wastewaters, which greatly affect air and water pollution [1-3]. Anaerobic digestion of organic waste and wastewater not only minimizes this pollution but also produces biogas, fertilized solid, and treated water for later useful utilizations [1-6]. Among the products of anaerobic digestion, biogas can be efficiently used for heat and electricity generation as well as for replacing gasoline in transportation applications [7,8]. Typically, biogas contains 40–75% methane (CH<sub>4</sub>), 25–40% carbon dioxide (CO<sub>2</sub>), 0.5–2.5% nitrogen (N<sub>2</sub>), 0.1–1% oxygen  $(O_2)$ , and 0.1–0.5% hydrogen sulfide  $(H_2S)$  [9]. The composition of biogas depends mainly on the content of organic residues, retention time, and bio-digester conditions; for instance, the average composition of biogas from animal farms in Thailand is 53-66% CH<sub>4</sub>, 27-47% CO<sub>2</sub>, 2-7% N<sub>2</sub>,  $0-2\% O_2$ ,  $0.2-0.3\% H_2S$ , and humidity [5,6,8]. It is known that  $H_2S$  is toxic at high concentrations, and corrosive to most engines. H<sub>2</sub>S can also negatively affect several systems of the human body [10]. Therefore, it must carefully be removed from biogas before the utilization of biogas in heat production, electrical generation, and transportation.

\* Corresponding author.

E-mail address: navadol@jgsee.kmutt.ac.th (N. Laosiripojana).

It is known that the adsorption process using activated carbon as an adsorbent has been widely applied for H<sub>2</sub>S removal from gas streams due to its safety and high effectiveness [11-24]. Currently, several local manufacturers in Thailand have been producing commercialgrade activated carbon from various agricultural materials (i.e. coconut shell and palm-oil shell) [25-28]. Nevertheless, these local grade activated carbons have been generally used in non-specific gas and liquid adsorption applications [29–31]. Our research aims to upgrade this low-price commercial-grade activated carbon for specific H<sub>2</sub>S adsorption application. It has been reported that the low-grade activated carbon can be upgraded by steam activation in order to increase its specific surface area. Furthermore, the impregnation of activated carbon with alkaline compounds i.e. potassium hydroxide (KOH) can greatly improve the chemical adsorption performance [32]. It should also be noted that several researchers have previously tested the H<sub>2</sub>S adsorption performance of activated carbon under dry condition, simulated biogas, and in the presence of moist air [11–20]. Nevertheless, the intensive study related to the effects of humidity, O<sub>2</sub>, and CO<sub>2</sub> present in the H<sub>2</sub>S-containing feed on the H<sub>2</sub>S adsorption performance of the unmodified, surface property upgraded, and KOH impregnated activated carbons has not been investigated.

In the present work, the H<sub>2</sub>S adsorption performance of unmodified, upgraded, and KOH impregnated activated carbons was studied

under several operating conditions (i.e. dry condition, with isolated and integrated  $2\% \text{ v/v O}_2$ ,  $40\% \text{ v/v CO}_2$ , and 70% relative humidity conditions). In addition, the surface properties and chemistry of the pre- and post-adsorption samples were analyzed by several techniques to understand the relation between the activated carbon surface characteristics and its  $H_2S$  adsorption capacity. Based on these experimental results, the reaction mechanism of  $H_2S$  adsorption onto activated carbons operated under these conditions was discussed.

#### 2. Material and methods

#### 2.1. Material preparations and characterizations

The granular-shape commercial grade activated carbon (namely in the present work as "A") was supplied by Carbokarn Company Limited (Thailand). Its surface properties are presented in Table 1. This activated carbon was upgraded by steam activation, from which the sample was heated up to 900 °C under a constant nitrogen flow of 100 cm<sup>3</sup>/min. Then, it was kept isothermally for 1 h under the flow of vaporous steam before being cooled down to room temperature under the nitrogen flow. It is noted that this upgraded activated carbon by steam activation at 900 °C is referred to as "S 900" and also termed "upgraded" in this article. In addition to the surface upgrading by steam activation, the activated carbon samples (both A and S 900) were further impregnated with KOH by soaking the samples in KOH solution for 30 min before heated at 100 °C to evaporate water. Eventually, the samples were dried at 110 °C for 24 h; it is noted that the weight percentage of KOH per weight of activated carbon was kept constant at 7% for all samples. The A and S 900 samples, which were impregnated with KOH, are referred to as "A\_KOH" and "S\_KOH" and also termed "KOH impregnated" in this article.

Nitrogen adsorption of all samples was measured using a Belsorp mini II instrument at - 196 °C to predict their specific surface area. Prior to the measurement, the samples were out-gassed by heating at 110 °C under  $\rm N_2$  flow and ambient pressure for 5 h before cooling down to room temperature. The nitrogen isotherm of activated carbons was used to determine the volume of adsorbate as a function of pressure, from which the total surface area and average pore size were calculated by t-plot method. Pore volumes of the activated carbons were calculated by t-plot and  $\alpha_{\rm s}$  methods and referred to as " $V_{\rm t-plot}$ " and " $V_{\rm Cs}$ ,", respectively.

The elemental contents of carbon, nitrogen, and hydrogen in fresh activated carbons were analyzed with an Elemental Analyzer (FLASH EA 1112). The standard that was used in this analysis was 2,5-bis(5-tert-butyl-benzoxazol-2-yl)thiophene (BBOT). In addition, the contents of oxygen in fresh activated carbons were analyzed with a microoxygen analyzer (TruSpec CHNSO, LECO). Furthermore, the contents of sulfur in the fresh and exhausted activated carbons were analyzed with a sulfur analyzer (TruSpec CHNSO, LECO), from which all samples were analyzed in triplicate.

The surface morphology and elemental contents of the fresh activated carbons were measured with a scanning electron microscope (SEM) and energy dispersive X-ray spectroscopy (EDS) using JSM-5800 LV, JEOL attached with EDS, Oxford ISIS 300. In addition, the contents of K

**Table 1**Surface properties of the unmodified, upgraded, and KOH impregnated activated carbons.

Sample	Total surface area (m²/g)	$V_{\text{t-plot}}^{\text{a}}$ (cm <sup>3</sup> /g)	$V_{\alpha_s}^{a}$ (cm <sup>3</sup> /g)	Average pore size (nm)
A	1343	0.45	0.44	0.67
S 900	1621	0.60	0.59	0.75
A_KOH	1037	0.35	0.34	0.67
S_KOH	1336	0.46	0.45	0.70

<sup>&</sup>lt;sup>a</sup>  $V_{\text{t-plot}}$  is the pore volume of activated carbon calculated by t-plot method.  $V_{\alpha_s}$  is the pore volume of activated carbon calculated by  $\alpha_s$  method.

and other elements in the fresh materials were analyzed with an X-ray fluorescence analyzer (Bruker AXS, S4 Explorer).

#### 2.2. H<sub>2</sub>S adsorption testing

The system for H<sub>2</sub>S adsorption testing consists of a gas supply unit, a fixed-bed reactor in the horizontal furnace, and a gas monitoring system. The mixtures of gaseous helium, H<sub>2</sub>S, O<sub>2</sub>, CO<sub>2</sub>, and moist N<sub>2</sub> gas were controlled by mass flow controllers and passed through the fixed-bed reactor, where 1.0 g of activated carbons was packed. H<sub>2</sub>S analyzer (QRAE model PGM-50Q) was applied to continuously monitor the outlet H<sub>2</sub>S concentration from the reactor. In all tests, the concentration of H<sub>2</sub>S in the inlet gas (C<sub>0</sub>) was kept constant at 3000 ppmv and the total flow rate of inlet gas was 100 mL/min. The inlet gas was fed into the reactor and the concentration of H2S was recorded until the concentration at the outlet reached 3000 ppmv again. When the concentrations of H<sub>2</sub>S at the outlet (C) were 300 and 3000 ppmv, the breakthrough time and adsorption time were identified, respectively. The adsorption capacity of activated carbon was calculated using the integrated area above the adsorption curve (the difference between the inlet concentration and the outlet concentration curves), and the mass of activated carbon.

In the present study, the  $H_2S$  adsorption performance was tested at 30 °C under six operating conditions. In detail, the 1st operating condition was carried out under dry and inert atmospheres, while the 2nd, 3rd and 4th operating conditions were in the presence of isolated 2% v/v of  $O_2$ , 40% v/v of  $CO_2$  and 70% humidity respectively. The 5th operating condition was in the presence of integrated 2% v/v of  $O_2$  with 70% humidity, while the 6th operating condition was under integrated 2% v/v of  $O_2$ , 40% v/v of  $CO_2$ , and 70% relative humidity as simulated biogas condition.

## 3. Results and discussion

3.1. Surface analyses of unmodified, upgraded, and KOH impregnated activated carbons

The N<sub>2</sub> adsorption isotherms of the unmodified, upgraded, and KOH impregnated activated carbons are shown in Fig. 1. It can be seen that all isotherms are Type I, which are typical of microporous materials [33]. In the early stage of adsorption, the volume of N<sub>2</sub> increases rapidly due to the adsorption into micropores; hence the slope of the adsorption curve is sharp. When the adsorption into micropores is complete, the adsorption occurs only on the external surface of activated carbon. Among all samples, S 900 adsorbed N<sub>2</sub> greater than A due to its high surface area, large pore volume, and microporous size. In addition, S\_KOH adsorbs less N<sub>2</sub> than S 900, while A\_KOH adsorbed less N<sub>2</sub> than A because the micropore of activated carbon is partially filled or blocked by the deposited KOH. From this N<sub>2</sub> adsorption experiment, the surface properties (i.e. total surface area, pore volume, and average pore size) of these activated carbons can be calculated as presented in Table 1. It was found that A has total surface area of 1343 m<sup>2</sup>/g, pore volume of 0.45 cm<sup>3</sup>/g, and average pore size of 0.67 nm, while S 900 has higher total surface area and pore volume of 1621 m<sup>2</sup>/g and 0.60 cm<sup>3</sup>/g. This improvement is due to the partial burn off of the activated carbon during the steam reactivation, which eventually increases the porosity of the sample. On the other hand, the total surface areas of S\_KOH and A\_KOH are lower than the non-impregnated samples; furthermore, the pore volume of the KOH-impregnated sample also decreases from 0.45 to 0.35 cm<sup>3</sup>/g. The decrease in pore volume is related to the partial occupation of KOH on the activated carbon surface due to impregnation.

Surface morphology and elemental analysis of activated carbons were then performed using a scanning electron microscope (SEM) and energy dispersive X-ray spectroscopy (EDS), as shown in Figs. 2 and 3. In Fig. 2, it can be observed that the activated carbons contain pores of different sizes which is a common characteristic of activated

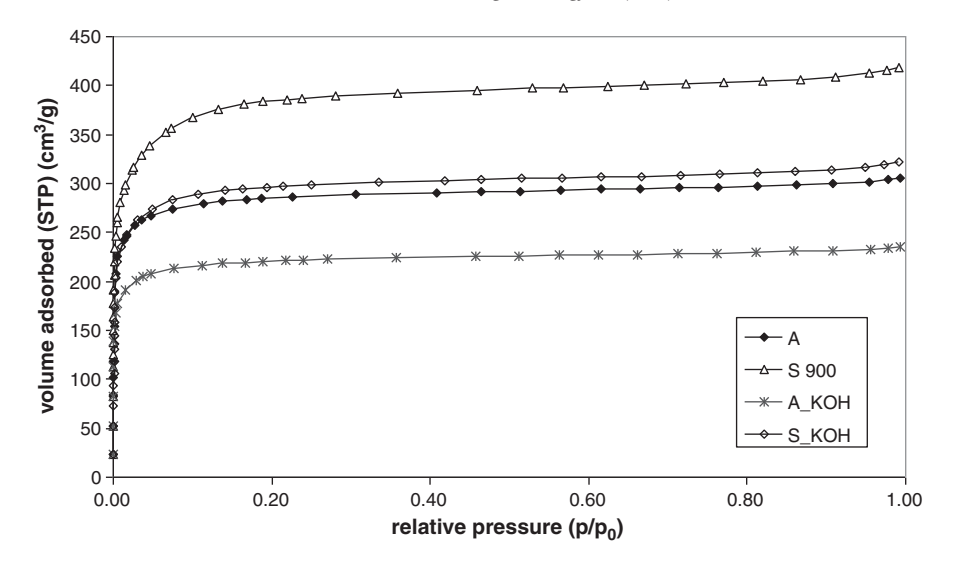


Fig. 1. Nitrogen adsorption isotherms for the unmodified, upgraded, and KOH impregnated activated carbons.

carbon [34]. The contents of C, N, H, O, and S in all the activated carbons were analyzed by an Elemental Analyzer as presented in Table 2. It was found that C content of S 900 is the highest, whereas O content is the lowest; this result is consistent with the EDS result in Fig. 3. In addition, the contents of K and the others in the fresh activated carbons were analyzed with the X-ray fluorescence analyzer (XRF) as shown in Table 3. It is noted that K was also observed from EDS and XRF in all samples since the activated carbon derived from coconut shell generally contains potassium. Among all samples, S\_KOH and A\_KOH have significantly higher K and O contents than S 900 and A samples due to the impregnation of KOH. In addition, EDS analysis of A\_KOH sample showed slight content of Ca and Fe in this sample. Sahu et al. reported that the

presence of Fe $_2$ O $_3$  and CaO could react with H $_2$ S at ambient temperature to form FeS $_2$ , FeS, and CaSO $_4\cdot$ 2H $_2$ O [35]. Thus, the presence of Ca and Fe in the A\_KOH sample could also promote the H $_2$ S adsorption performance of this material.

3.2.  $H_2S$  adsorption performance of unmodified, upgraded, and KOH impregnated activated carbons

The  $H_2S$  adsorption performances of all samples under dry condition at 30 °C were tested and the results are presented in Figs. 4–7. For A sample, after  $H_2S$  exposure, the concentration of  $H_2S$  reached almost 0 ppmv for 3–4 min and increased to 300 ppmv after 15 min; then the

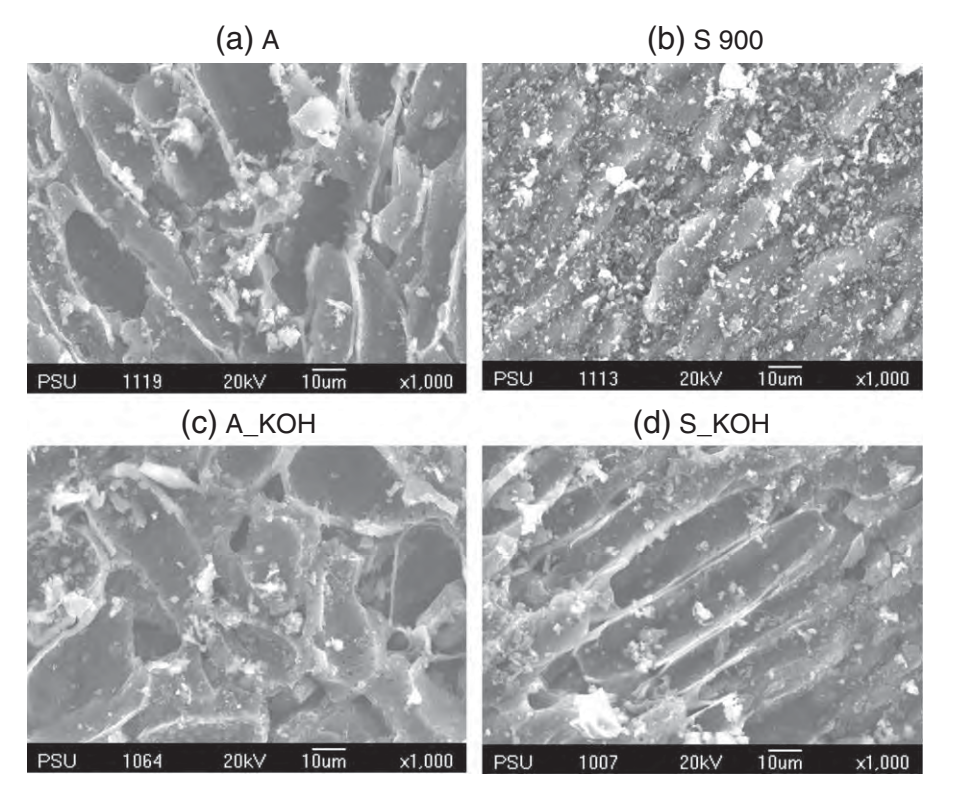


Fig. 2. SEM micrograph of the unmodified, upgraded, and KOH impregnated activated carbons.

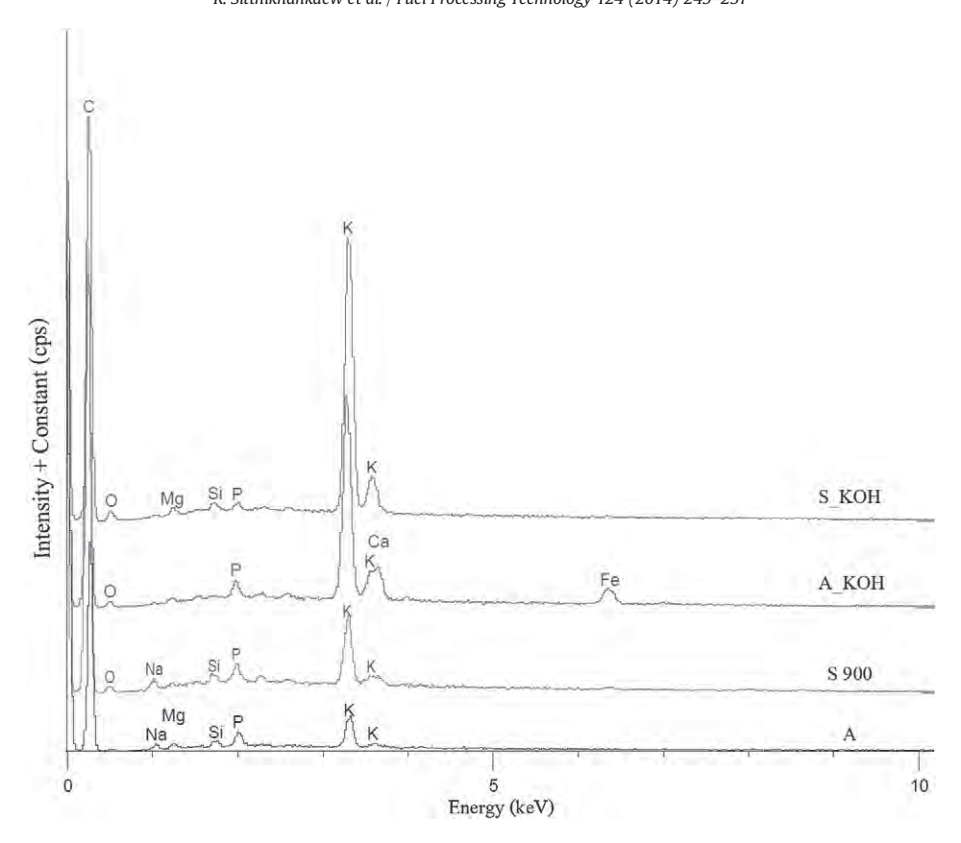


Fig. 3. EDS graph of fresh unmodified, upgraded, and KOH impregnated activated carbons.

concentration of H<sub>2</sub>S increased continuously to 3000 ppmv. The adsorption time of A was 67 min. From the calculation, the H<sub>2</sub>S adsorption capacity of A is 1.1 L/100  $g_{activated\ carbon}$ . For S 900, the  $H_2S$  adsorption capacity was greater than A (2.6  $L/100~g_{activated~carbon}$ ) due to its high specific surface area for H<sub>2</sub>S adsorption. As seen in Figs. 4-7 and Tables 4–5, it was observed that the modified activated carbons with KOH impregnation (both A\_KOH and S\_KOH) significantly enhance breakthrough time, adsorption time, and H2S adsorption capacity compared to the activated carbons without KOH impregnation. In particular, the H<sub>2</sub>S adsorption capacities of A\_KOH and S\_KOH were 4.3 and 3.0 L/100  $g_{\text{activated carbon}}$ , while the breakthrough and adsorption times were 39 min and 330 min for A\_KOH and 26 and 178 min for S\_KOH, respectively. This positive effect is mainly due to the chemical reaction of H<sub>2</sub>S with KOH that occurs along with physical adsorption. A conceptual reaction of H<sub>2</sub>S adsorption is proposed as follows: (i) H<sub>2</sub>S transferred from the bulk stream into the pore or surface of the activated carbon; and (ii) H<sub>2</sub>S adsorbed on activated carbon (Eq. (1)), from which H<sub>2</sub>S (g) and H<sub>2</sub>S (ads) correspond to H<sub>2</sub>S in gas and/or adsorbed phases.

$$H_2S(g) \rightarrow H_2S(ads)$$
 (1)

By impregnating of KOH, H<sub>2</sub>S could react with KOH at the carbon surface to produce potassium hydrogen sulfide (KHS) and potassium

sulfide ( $K_2S$ ) (Eqs. (2)–(3)), from which KOH(q) – C is the KOH impregnated on the activated carbon covered by the water film generated by water produced from the reaction; KHS(q) – C and  $K_2S(q)$  – C are sulfide compounds that formed on the surface of the activated carbon covered by the water film.

$$H_2S(g) + KOH(q) - C \rightarrow KHS(q) - C + H_2O$$
 (2)

$$H_2S(g) + 2KOH(q) - C \rightarrow K_2S(q) - C + 2H_2O$$
 (3)

It is noted from this study that A\_KOH shows slightly higher  $H_2S$  adsorption capacity than S\_KOH, which could possibly be due to the less residual water vapor content for S\_KOH. The effect of humidity on the  $H_2S$  adsorption performance will be presented and discussed in detail in the next section.

## 3.3. Effects of O<sub>2</sub>, CO<sub>2</sub> and humidity on H<sub>2</sub>S adsorption capacity

As the next step, the effects of  $O_2$ ,  $CO_2$ , and humidity on  $H_2S$  adsorption capacity were performed individually. Firstly, the  $H_2S$  adsorption characteristics in the presence of 2% v/v dry  $O_2$  at 30 °C were carried out as presented in Figs. 4–7 and Tables 4–5. It can be seen that the breakthrough time, adsorption time, and  $H_2S$  adsorption capacity of all

**Table 2**Elemental contents in unmodified, upgraded, and KOH impregnated activated carbons analyzed by the Elemental Analyzer.

Sample	Modification method	N (%)	C (%)	H (%)	O (%)	S (%)
A	-	0.3	75.4	1.3	4.9	0.60
S 900	Steam activation	0.3	81.8	0.2	3.5	0.68
A_KOH	KOH impregnation	0.4	65.2	2.9	13.4	0.38
S_KOH	Steam activation & KOH impregnation	0.1	78.0	1.8	14.0	0.33

**Table 3**Elemental contents in unmodified, upgraded, and KOH impregnated activated carbons analyzed by the X-ray fluorescence analyzer.

Sample	K (%)	Na (%)	P (%)	Si (%)	Fe (%)	Ca (%)	Mg (%)
AC	1.24	0.13	0.05	0.08	0.10	0.04	0.04
S 900	1.33	0.11	0.05	0.09	0.09	0.04	0.04
A_KOH	4.45	0.12	0.04	0.08	0.43	0.06	0.03
S_KOH	4.49	0.12	0.04	0.12	0.11	0.05	0.04

samples are considerably increased by the presence of  $O_2$ ; particularly for A\_KOH and S\_KOH, from which 100%  $H_2S$  removal is sustained for 110 and 118 min, respectively. This result clearly indicates the benefit of oxygen addition for  $H_2S$  adsorption of activated carbon, which could lead to the gas-phase oxidation reaction (Eq. (4)) along with physical adsorption and chemical adsorption.

$$^{1/2}O_{2} + H_{2}S \rightarrow S + H_{2}O$$
 (4)

Regarding the mechanism of oxidation reaction, the free active site of carbon ( $C_f$ ) first reacts with oxygen to form adsorbed oxygen (C(O)) via Eq. (5); then  $H_2S$  reacts with C(O) and turns to elemental sulfur (S) and water via Eq. (6). It should be noted that further reactions between elemental sulfur with oxygen and  $H_2S$  to form  $SO_2$  and polysulfides ( $HS_xSH$ ) could also take place via Eqs. (7) and (8) [13,21].

$$^{1}/_{2}O_{2} + C_{f} \rightarrow C(0)$$
 (5)

$$H_2S + C(0) \rightarrow S + C_f + H_2O$$
 (6)

$$O_2 + S \rightarrow SO_2 \tag{7}$$

$$H_2S + S \rightarrow HSSH$$
 (8)

Furthermore, for A\_KOH and S\_KOH samples, the reactions of KHS and  $K_2S$  (generated from the chemical reaction between  $H_2S$  and KOH in Eqs. (2)–(3)) with  $O_2$  to form sulfur element and generated KOH could also occur (Eqs. (9)–(11)) and eventually result in the high  $H_2S$  adsorption capacity of A\_KOH and S\_KOH compared to A and S 900.

$$^{1}/_{2}O_{2} + KHS \rightarrow KOH + S$$
 (9)

$$^{1}/_{2}O_{2} + K_{2}S + H_{2}O \rightarrow 2KOH + S$$
 (10)

$$2O_2 + 2KOH + H_2S \rightarrow K_2SO_4 + 2H_2O$$
 (11)

Then, the  $H_2S$  adsorption characteristic in the presence of 40% v/v dry  $CO_2$  at 30 °C was tested and the results are presented in Figs. 4–7 and Tables 4–5. It can be seen that with  $CO_2$  addition, all samples show lower breakthrough time, adsorption time, and  $H_2S$  adsorption capacity. In detail, adsorption times of the A, S 900, A\_KOH, and S\_KOH were 45, 58, 88, and 80% less than those of dry condition, whereas  $H_2S$  adsorption capacities of the A, S 900, A\_KOH, and S\_KOH were 35, 67, 82, and 69% less than those of dry condition. This negative effect could be due to the competition between  $CO_2$  and  $H_2S$  to adsorb on the surface of activated carbon. In addition, for A\_KOH and S\_KOH, KOH could react with  $CO_2$  to produce potassium hydrogen carbonate (KHCO<sub>3</sub>), potassium carbonate ( $K_2CO_3$ ), and KHS (Eqs. (12)–(14)). Hence, the content of KOH could decrease and affect the chemical reaction between  $H_2S$  and KOH.

$$CO_2 + KOH \rightarrow KHCO_3$$
 (12)

$$CO_2 + 2KOH \rightarrow K_2CO_3 + H_2O \tag{13}$$

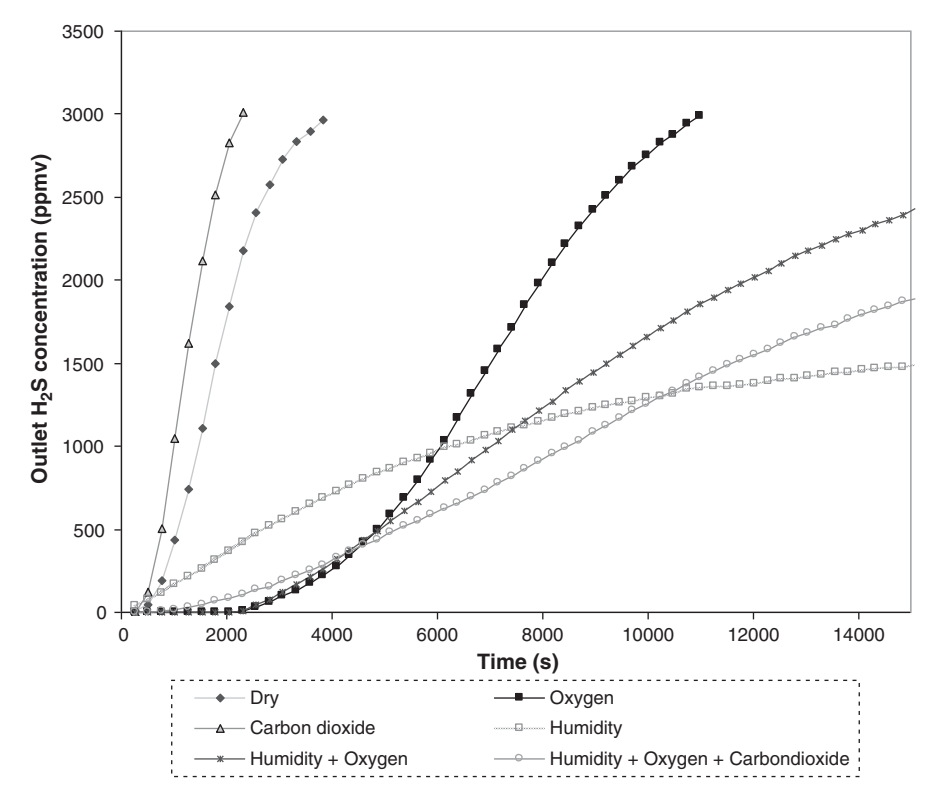


Fig. 4. Adsorption curves of H<sub>2</sub>S by A under various conditions at 30 °C.

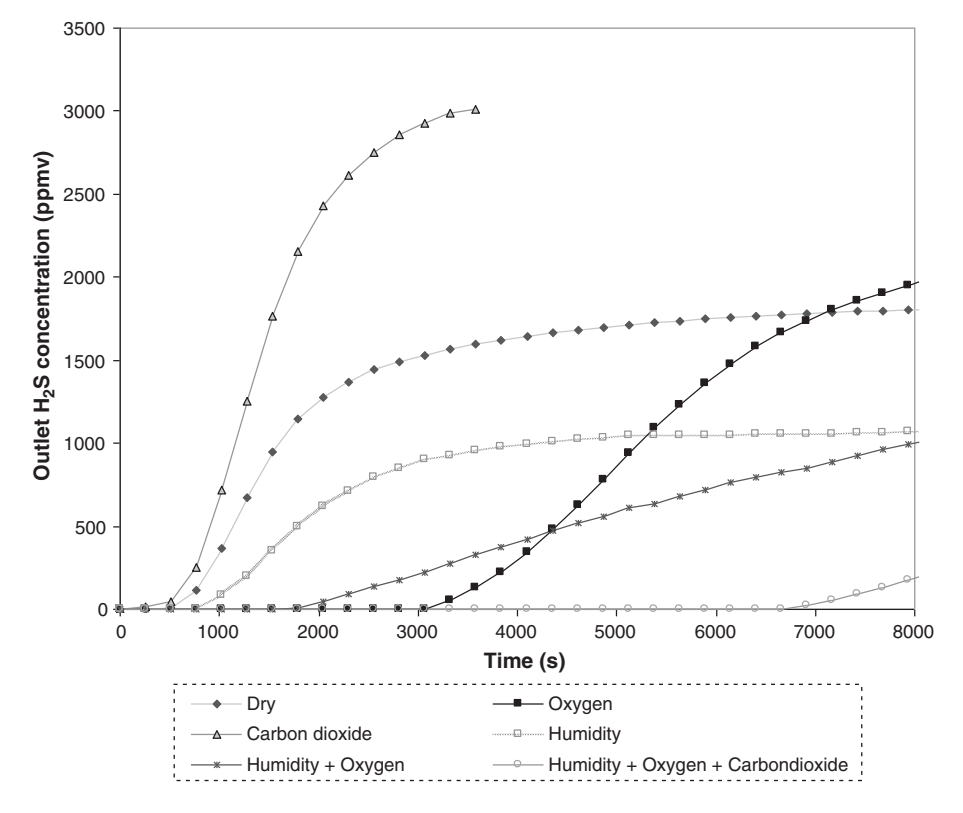


Fig. 5. Adsorption curves of H<sub>2</sub>S by S 900 under various conditions at 30 °C.

(14)

$$K_2CO_3 + H_2S \rightarrow KHCO_3 + KHS$$

Next, the  $H_2S$  adsorption characteristics of all samples were studied under 70% relative humidity at 30 °C. As shown in Figs. 4–7 and

Tables 4–5, it was found that all samples show significantly higher adsorption time and  $H_2S$  adsorption capacity than those of the dry conditions and in the presence of 2% v/v dry  $O_2$ . Nevertheless, the breakthrough time of all samples in the presence of 70% relative humidity is

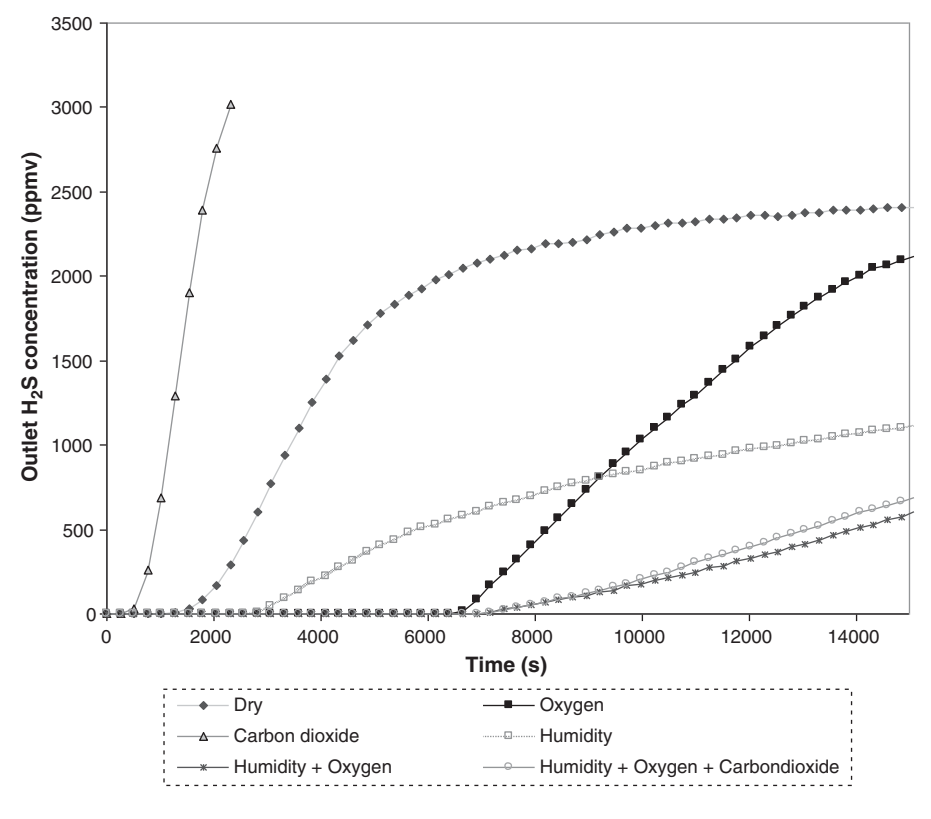


**Fig. 6.** Adsorption curves of  $H_2S$  by A\_KOH under various conditions at 30  $^{\circ}$ C.

(18)

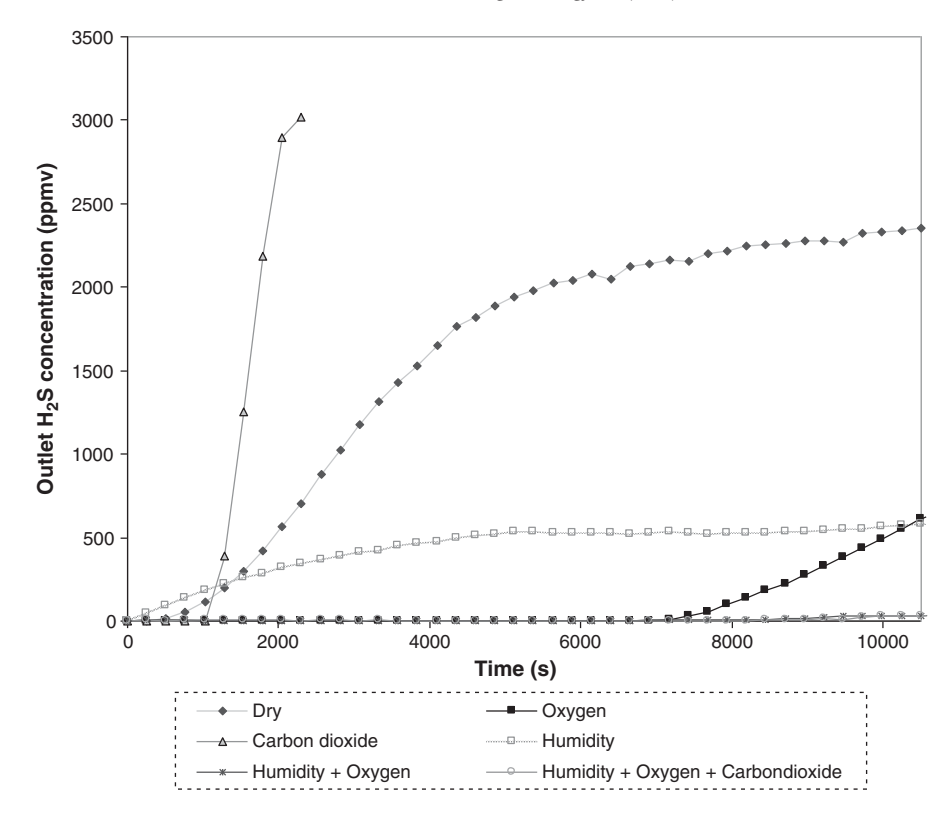


Fig. 7. Adsorption curves of H<sub>2</sub>S by S\_KOH under various conditions at 30 °C.

considerably lower than those in the presence of 2% v/v dry  $O_2$ . This result reveals that oxygen can promote the  $H_2S$  adsorption better than the humidity at low  $H_2S$  concentrations, whereas the humidity efficiently increases the  $H_2S$  adsorption at high  $H_2S$  concentrations. In the presence of 70% relative humidity, the adsorbed  $H_2S$  could dissolve in the water film (Eq. (15)) and dissociate to hydrogen sulfide ions (HS $^-$ ) and hydrogen ions (H $^+$ ) (Eq. (16)). Furthermore, for A\_KOH and S\_KOH, KOH can absorb water vapor easily and the basic property of KOH leads to the acid–base reaction (Eq. (17)). Therefore, A\_KOH and S\_KOH contribute to the dissociation of  $H_2S$  and  $H_2S$  in the gas stream can be adsorbed largely.

$$H_2S(ads) \rightarrow H_2S(ads - liq)$$
 (15)

$$H_2S(ads - liq) \rightarrow HS^-(ads) + H^+$$
 (16)

$$H^+ + OH^- \rightarrow H_2O \tag{17}$$

3.4. Effects of  $O_2$  + humidity and  $O_2$  + humidity +  $CO_2$  on  $H_2S$  adsorption capacity

The  $\rm H_2S$  adsorption characteristics of all samples were then studied under the combinative mixture of 70% relative humidity and 2% v/v  $\rm O_2$  at 30 °C. As presented in Figs. 4–7 and Tables 4–5, although the  $\rm H_2S$  adsorption capacity of the samples under this combination is lower than with 70% relative humidity, interestingly, the  $\rm H_2S$  adsorption capacity as well as the breakthrough time and adsorption time under this combination are obviously higher than the condition with 2% v/v  $\rm O_2$ , particularly for the A\_KOH and S\_KOH samples. This result suggests that the presence of mixed humidity and  $\rm O_2$  can efficiently promote the  $\rm H_2S$  adsorption at low  $\rm H_2S$  concentrations. In the presence of humidity and  $\rm O_2$ , the concept of  $\rm O_2$  dissociation can be applied. First, an  $\rm O_2$  molecule transfers from the bulk stream and adsorbs into the pore or surface of the activated carbon. Then, the adsorbed  $\rm O_2$  dissolves in a water film to form  $\rm O_2$  (ads-liq) and is dissociated to produce dissociative adsorbed oxygen (0\*) (Eqs. (18)–(20)) [22,23].

Table 4

H<sub>2</sub>S adsorption times by the commercial, upgraded, and KOH impregnated activated carbons under various conditions at 30 °C.

Sample	H <sub>2</sub> S adsorption	H <sub>2</sub> S adsorption time (min)								
	Fresh	2% O <sub>2</sub>	40% CO <sub>2</sub>	70% RH <sup>a</sup>	70% RH + 2% O <sub>2</sub>	70% RH + 2% O <sub>2</sub> + 40% CO <sub>2</sub>				
A	67	184	37	2787	471	1128				
S 900	136	1077	57	4118	1097	1972				
A_KOH	330	955	38	5118	4089	2415				
S_KOH	178	2842	35	5324	5955	4238				

 $O_2(g) \rightarrow O_2(ads)$ 

a RH is relative humidity.

**Table 5**H<sub>2</sub>S adsorption capacities by the commercial, upgraded, and KOH impregnated activated carbons under various conditions at 30 °C.

Sample	H <sub>2</sub> S adsorption capacity (L/100 g <sub>activated carbon</sub> )								
	Fresh	2% O <sub>2</sub>	40% CO <sub>2</sub>	70% RH <sup>a</sup>	$70\%  RH  +  2\%  O_2$	$70\% \text{ RH} + 2\% \text{ O}_2 + 40\% \text{ CO}_2$			
A	1.1	4.0	0.7	28.4	5.9	9.1			
S 900	2.6	6.3	0.9	77.6	9.2	18.2			
A_KOH	4.3	8.5	0.8	47.4	41.7	26.0			
S_KOH	3.0	21.9	0.9	90.9	65.6	55.8			

<sup>&</sup>lt;sup>a</sup> RH is relative humidity.

$$O_2(ads) \rightarrow O_2(ads - liq) \tag{19}$$

$$O_2(ads - liq) \rightarrow 20 * (ads)$$
 (20)

The dissociative adsorbed oxygen can react with  $HS^-$  ions to produce elemental sulfur and water (Eq. (21)). It is noted that a small portion of  $HS^-$  ion can also be oxidized to generate  $SO_2$  (Eq. (22)), which can be further oxidized to  $H_2SO_4$  (Eq. (23)).

$$O*(ads) + HS^{-}(ads) \rightarrow S(ads) + OH^{-}$$
(21)

$$30*(ads) + HS^{-}(ads) \rightarrow SO_{2}(ads) + OH^{-}$$
(22)

$$O*(ads) + SO2(ads) + H2O(ads) \rightarrow H2SO4(ads)$$
 (23)

For the S\_KOH sample, the high  $H_2S$  adsorption capacity can be achieved since physical adsorption, dissociation of  $H_2S$ , dissociation of  $O_2$ , oxidation reaction, and chemical adsorption take place. The chemical reaction between  $H_2S$  and KOH leads to the generation of KHS,  $K_2S$  and water, from which KHS and  $K_2S$  can further react with  $O_2$  to form the elemental sulfur and regenerate KOH.

Lastly, the  $H_2S$  adsorption characteristic under the combinative mixture of 70% relative humidity, 2% v/v  $O_2$ , and 40% v/v  $CO_2$  was studied at 30 °C. As presented in Figs. 4–7 and Tables 4–5, the results show that in the presence of  $CO_2$  the  $H_2S$  adsorption capacities of A\_KOH and S\_KOH decrease due to the reaction of KOH and  $CO_2$  to produce KHCO3 and  $K_2CO_3$ , which eventually reduce the chemical reaction between KOH and  $H_2S$ . Nevertheless, the  $H_2S$  adsorption capacity under this operating condition remains higher than that under the dry and with only 2% v/v  $O_2$  conditions; this clearly indicates the importance of humidity for  $H_2S$  removal particularly to purify biogas, which generally contains 40%  $CO_2$ .

It is noted that the contents of sulfur in all activated carbons before and after  $H_2S$  adsorption tests were measured by the sulfur analyzer, as presented in Table 6. The trend of sulfur contents under various operating conditions is in good agreement with the  $H_2S$  adsorption capacities reported earlier, from which the sulfur contents after  $H_2S$  adsorption test of KOH impregnated activated carbon samples (i.e. A\_KOH and S\_KOH) are higher than the samples without KOH impregnation (A and S 900), particularly for the tests in the presence of  $O_2$  that the chemical adsorption is involved.

#### 4. Conclusions

The surface properties (i.e. total surface area and pore volume) of low grade activated carbon can be efficiently improved by steam activation at 900 °C, while further impregnation with 7% KOH strongly promotes the  $\rm H_2S$  chemisorption and results in improved  $\rm H_2S$  adsorption performance in terms of overall adsorption capacity and breakthrough time. The presence of  $\rm O_2$  in the gas stream greatly increases the breakthrough time of  $\rm H_2S$  adsorption, while the presence of humidity significantly increases the  $\rm H_2S$  capacity. In contrast, the presence of  $\rm CO_2$  inhibited the  $\rm H_2S$  adsorption performance due to the competitive adsorption and reaction between  $\rm CO_2$  and  $\rm H_2S$  on the surface of the activated carbon; nevertheless, this negative effect can be minimized by adding  $\rm O_2$  and humidity in the gas stream.

## Acknowledgments

This research was supported by PTT Research and Technology Institute. Financial supports from The Thailand Research Fund and National Research University are acknowledged.

## References

- S. Prasertsana, B. Sajjakulnukitb, Biomass and biogas energy in Thailand: potential, opportunity and barriers, Renewable Energy 31 (2006) 599–610.
- [2] C. Cornejo, A.C. Wilkie, Greenhouse gas emissions and biogas potential from livestock in Ecuador, Energy for Sustainable Development 14 (2010) 256–566.
- [3] W. Wongsapai, P. Thienburanathum, P. Rerkkriengkrai, Biogas situation and development in Thai swine farm, www.icrepq.com/icrepq-/269\_wongsapai.pdf (access 20-08-2012).
- [4] T.K.V. Vua, M.T. Tranb, T.T.S. Dang, A survey of manure management on pig farms in Northern Vietnam, Livestock Science 112 (2007) 288–297.
- [5] S. Pipatmanomai, S. Kaewluan, T. Vitidsant, Economic assessment of biogas-toelectricity generation system with H<sub>2</sub>S removal by activated carbon in small pig farm, Applied Energy 86 (2009) 669–674.
- [6] N. Tippayawong, A. Promwungkwa, P. Rerkkriangkrai, Long-term operation of a small biogas/diesel dual-fuel engine for on-farm electricity generation, Biosystems Engineering 98 (2007) 26–32.
- [7] P.M. Duc, K. Wattanavichien, Study on biogas premixed charge diesel dual fuelled engine, Energy Conversion and Management 48 (2007) 2286–2308.
- [8] N. Tippayawong, P. Thanompongchart, Biogas quality upgrade by simultaneous removal of CO<sub>2</sub> and H<sub>2</sub>S in a packed column reactor, Energy 35 (2010) 4531–4535.
- [9] R. Arthur, M.F. Baidoo, Edward Antwi, Biogas as a potential renewable energy source: a Ghanaian case study, Renewable Energy 36 (2011) 510–1516.
- [10] J.B. Locey, Encyclopedia of Toxicology, 2005.
- [11] A. Bagreeva, S. Katikanenib, S. Parabb, T.J. Bandosz, Desulfurization of digester gas: prediction of activated carbon bed performance at low concentrations of hydrogen sulfide, Catalysis Today 99 (2005) 329–337.
- [12] W. Yuan, T.J. Bandosz, Removal of hydrogen sulfide from biogas on sludge-derived adsorbents, Fuel 86 (2007) 2736–2746.

**Table 6**Contents of sulfur in fresh and exhausted activated carbons (under various adsorption conditions).

Sample	Sulfur (wt.%)									
	Fresh	2% O <sub>2</sub>	40% CO <sub>2</sub>	70% RH <sup>a</sup>	70% RH + 2% O <sub>2</sub>	$70\% \text{ RH} + 2\% \text{ O}_2 + 40\% \text{ CO}_2$				
A	0.60 ± 0.21	5.03 ± 0.08	1.25 ± 0.03	26.10 ± 0.44	11.23 ± 0.06	11.87 ± 0.15				
S 900	$0.68 \pm 0.36$	$6.10 \pm 0.09$	$1.19 \pm 0.02$	$28.97 \pm 0.38$	$13.63 \pm 0.12$	$16.73 \pm 0.60$				
A_KOH S_KOH	$\begin{array}{c} 0.38\pm0.07 \\ 0.33\pm0.05 \end{array}$	$7.57 \pm 0.09$ $13.43 \pm 0.15$	$\begin{array}{c} 1.66 \pm 0.28 \\ 1.55 \pm 0.05 \end{array}$	$29.93 \pm 0.67$ $23.90 \pm 0.44$	$\begin{array}{c} 24.73 \pm 0.15 \\ 29.77 \pm 0.75 \end{array}$	$\begin{array}{c} 25.13 \pm 0.46 \\ 30.50 \pm 1.12 \end{array}$				

<sup>&</sup>lt;sup>a</sup> RH is relative humidity.

- [13] A. Bagreev, T.J. Bandosz, On the mechanism of hydrogen sulfide removal from moist air on catalytic carbonaceous adsorbents, Industrial and Engineering Chemistry Research 44 (2005) 530–538.
- [14] R. Yan, D.T. Liang, L. Tsen, J.H. Tay, Kinetics and mechanisms of H<sub>2</sub>S adsorption by alkaline activated carbon, Environmental Science and Technology 36 (2002) 4460–4466.
- [15] R. Yan, T. Chin, Y.L. Ng, H. Duan, D.T. Liang, J.H. Tay, Influence of surface properties on the mechanism of H<sub>2</sub>S removal by alkaline activated carbons, Environmental Science and Technology 38 (2004) 316–323.
- [16] Y. Elsayeda, M. Seredychb, A. Dallasa, T.J. Bandosz, Desulfurization of air at high and low H<sub>2</sub>S concentrations, Chemical Engineering Journal 155 (2005) 594–602.
- [17] T.J. Bandosz, A. Bagreev, F. Adib, A. Turk, Unmodified versus caustics-impregnated carbons for control of hydrogen sulfide emissions from sewage treatment plants, Environmental Science and Technology 34 (2000) 1069–1074.
- [18] M. Seredych, T.J. Bandosz, Sewage sludge as a single precursor for development of composite adsorbents/catalysts, Chemical Engineering Journal 128 (2007) 59–67.
- [19] A. Bagreev, F. Adib, T.J. Bandosz, pH of activated carbon surface as an indication of its suitability for H<sub>2</sub>S removal from moist air streams, Carbon 39 (2001) 1897–1905.
- [20] J.H. Tsai, F.T. Jeng, H.L. Chiang, Removal of H<sub>2</sub>S from exhaust gas by use of alkaline activated carbon, Adsorption 7 (2001) 357–366.
- [21] A. Bagreev, T.J. Bandosz, A role of sodium hydroxide in the process of hydrogen sulfide adsorption/oxidation on caustic-impregnated activated carbons, Industrial and Engineering Chemistry Research 41 (2002) 672–679.
- [22] A. Bagreev, T. Bandosz, Carbonaceous materials for gas phase desulfurization: role of surface heterogeneity, Preprints of Papers—American Chemical Society, Division of Fuel Chemistry 49 (2004) 817–821.
- [23] Y. Xiao, S. Wang, D. Wu, Q. Yuan, Catalytic oxidation of hydrogen sulfide over unmodified and impregnated activated carbon, Separation and Purification Technology 59 (2008) 326–332.
- [24] Y. Xiao, S. Wang, D. Wu, Q. Yuan, Experimental and simulation study of hydrogen sulfide adsorption on impregnated activated carbon under anaerobic conditions, Journal of Hazardous Materials 153 (2008) 1193–1200.
- [25] M.K.B. Gratuito, T. Panyathanmaporn, R.-A. Chumnanklang, N. Sirinuntawittaya, A. Dutta, Production of activated carbon from coconut shell: optimization using response surface methodology, Bioresource Technology 99 (2008) 4887–4895.

- [26] O. Sirichote, W. Innajitara, L. Chuenchom, D. Chunchit, K. Naweekan, Adsorption of iron (III) ion on activated carbons obtained from bagasse, pericarp of rubber fruit and coconut shell, Songklanakarin Journal of Science and Technology 24 (2002) 235–242
- [27] S. Panumati, K. Chudecha, P. Vankhaew, V. Choolert, L. Chuenchom, W. Innajitara, O. Sirichote, Adsorption of phenol from diluted aqueous solutions by activated carbons obtained from bagasse, oil palm shell and pericarp of rubber fruit, Songklanakarin Journal of Science and Technology 30 (2008) 185–189.
- [28] T. Vitidsant, T. Suravattanasakul, S. Damronglerd, Production of activated carbon from palm-oil shell by pyrolysis and steam activation in a fixed bed reactor, ScienceAsia 25 (1999) 211–222.
- [29] W. Tongpoothorn, M. Sriuttha, P. Homchan, S. Chanthai, C. Ruangviriyachai, Preparation of activated carbon derived from *Jatropha curcas* fruit shell by simple thermochemical activation and characterization of their physico-chemical properties, Chemical Engineering Research and Design 89 (2011) 335–340.
- [30] V. Boonamnuayvitaya, S. Sae-ung, W. Tanthapanichakoon, Preparation of activated carbons from coffee residue for the adsorption of formaldehyde, Separation and Purification Technology 42 (2005) 159–168.
- [31] S. Babel, T.A. Kurniawan, Cr (VI) removal from synthetic wastewater using coconut shell charcoal and commercial activated carbon modified with oxidizing agents and/ or chitosan. Chemosphere 54 (2004) 951–967.
- [32] R. Sitthikhankaew, S. Predapitakkun, R. Kiattikomol, S. Pumhiran, S. Assabumrungrat, N. Laosiripojana, Performance of commercial and modified activated carbons for hydrogen sulfide removal from simulated biogas, 2011 IEEE First Conference on Clean Energy and Technology (CET) Proceeding, 2011, pp. 135–139.
- [33] R.M.A. Roque-Malherbe, Adsorption and Diffusion in Nanoporous Materials, CRC Press, Taylor & Francis Group, New York, 2007.
- [34] C.R. Bansal, M. Goyal, Activated Carbon Adsorption, CRC Press, Taylor & Francis Group, New York, 2005.
- 35] R.C. Sahu, R. Patel, B.C. Ray, Removal of hydrogen sulfide using red mud at ambient conditions, Fuel Processing Technology 92 (2011) 1587–1592.

VOL. 37, 2014

Guest Editors: Eliseo Ranzi, Katharina Kohse- Höinghaus Copyright © 2014, AIDIC Servizi S.r.I., ISBN 978-88-95608-28-0; ISSN 2283-9216



DOI: 10.3303/CET1437035

# Removal of Tar from Biomass Gasification Process by Steam Reforming over Nickel Catalysts

Supawat Vivanpatarakij<sup>\*a</sup>, Daranee Rulerk<sup>b</sup>, Suttichai Assabumrungrat<sup>b</sup>

<sup>a</sup> Energy Research Institute, Chulalongkorn University, Phyathai, Wang Mai, Phatumwan, Bangkok 10330, Thailand. <sup>b</sup> Center of Excellence in Catalysis and Catalytic Reaction Engineering, Department of Chemical Engineering, Faculty of Engineering, Chulalongkorn University, Phyathai, Wang Mai, Phatumwan, Bangkok 10330, Thailand. • supawat.v@chula.ac.th

Tar steam reforming (TSR) is a very attractive technique for tar removal. It converts high molecular weight hydrocarbons of tar into smaller gas products including  $H_2$ ,  $CH_4$ , CO and  $CO_2$ . Preliminary research focuses on simulation of tar steam reforming. It was assumed to be at thermodynamic equilibrium and the calculations were performed using Aspen Plus Program. The simulation results help understand the effect of operating condition and identify suitable operating conditions (reaction temperature, S/C ratio) for the experimental tar steam reforming. Representative tar consisted of  $C_{10}H_8$ ,  $C_7H_8$ ,  $C_6H_6O$  and  $C_{16}H_{10}$  whose compositions varied with temperatures of biomass gasification (700-800  $^{\circ}C$ ). The experimental study of the tar steam reforming reaction was carried out at different temperatures (450-650  $^{\circ}C$ ), S/C ratios (1-5), type of supports (Al<sub>2</sub>O<sub>3</sub>, CaO and MgO) and %metal loading of a nickel catalyst (10, 15 and 20 %). The experimental results follow the trends observed from the simulations that the reaction at high temperature and S/C ratio produce more hydrogen content. 20 %Ni/Al<sub>2</sub>O<sub>3</sub> was reported as a suitable catalyst which offered stable and efficiency activity for tar steam reforming.

## 1. Introduction

Nowadays, depletion of fossil fuel sources and environmental problems such as global warming are the world's major issues. However, due to the growth of the world's population, the energy demand is still continuously increasing. Therefore, a number of current researches have been focusing on renewable energy in order to replace the conventional fossil fuel-based energy. In this study the focus is on biomass gasification which is expected to be a real commercial process. Biomass gasification has attracted huge interest by producing a gas rich in H<sub>2</sub> and CO (Saxena et al., 2008) which can be used as a gaseous fuel for electricity generation or fuel cell (Devi et al., 2003).

The major problem of biomass gasification is that the produced gas usually contains unacceptable levels of tar causing process-related problems. Tar from fuel gas condenses at low temperatures, thus blocking, fouling corrosion, erosion and abrasion of process equipment such as engines and turbines. Tar is a complex mixture of aromatics which composition of biomass gasification tars as reported (Milne et al., 1998) includes benzene, toluene represent one-ring aromatic hydrocarbons, naphthalene represent two-ring aromatic hydrocarbons, etc. There are 6 classes of tar based on the tar classification system developed (Bergman et al., 2002). Each class is also divided into different types of tar according to its different nature. Comprehensive significant compounds in tars, it has been grouped as a mixture of four compounds with each compound representing a specific class of compounds and the composition equal to group in actual tars is used. The species and their amounts that were chosen to represent tars are toluene representing all the one-ring compounds, naphthalene representing two-ring compounds, phenol representing phenolic and other heterocyclic compounds, pyrene representing three-rings and higher compounds (Singh et al., 2005).

Several methods for tar removal are possible (Stassen et al., 2002): tar removal by physical processes (Milne et al., 1998) (e.g. filters, scrubbers, wet electrostatic precipitators and cooling tower (Vivanpatarakij et al., 2013) and chemical processes (e.g. thermal cracking, catalytic cracking and catalytic reforming). Tar steam reforming is a very attractive technique for tar removal, converted into useful gas containing H<sub>2</sub>, CH<sub>4</sub>, CO and CO<sub>2</sub>. Several kinds of catalytic reforming have been studied, developed and used in removal of tar, such as mineral resource: dolomites, magnesites, zeolites, olivine, mayenite mineral, alkali metal

catalysts, Ni-based catalysts and novel metal catalysts (Han et al., 2008). However, it was reported that these catalysts have many of the problems, although they showed good activity in removal of tar. Without a pretreatment, natural mineral catalysts suffer from low activity and stability. Nickel-based catalysts have shown high activities for reforming of biomass gasification tar. When being used as the secondary catalysts, the supported nickel catalysts could attain nearly complete decomposition of both tar and ammonia decomposition (Han et al., 2008). However, Ni catalyst suffers from coke deposition, leading to deactivation of the catalysts (Dayton et al., 2002). Ni/CeO<sub>2</sub>(75 %)-ZrO<sub>2</sub>(25 %) showed the most pronounced catalytic performance in the steam reforming of benzene and showed strong resistance to coke deposition. Its activity is superior to a commercial Ni catalyst (Park et al., 2010). Steam reforming of toluene as a tar model compound using Ni/olivine catalyst was reported to have much higher activity and selectivity towards syngas than olivine alone (Swierczynski et al., 2007). Three Ni-based catalysts (ICI46-1, Z409 and RZ409) were proven to be effective in eliminating heavy tars (Zhang et al., 2004). Apart from Ni-based catalysts, there have been other catalysts developed for tar removal. The conversion rate of tar catalyzed by dolomite was difficult to reach or exceed 90-95 %, although dolomite could reduce the tar in syngas (Xiaodong et al., 2003).

In this work, tar removal and hydrogen production from steam reforming was investigated. This study focused on finding suitable condition for the highest amount of  $H_2$  yield and tar conversion by preliminary simulations using Aspen Plus program. It is also aimed at finding a suitable catalyst to be used in the steam reforming of tar for different mixtures of  $C_{10}H_8$ ,  $C_7H_8$ ,  $C_6H_6O$  and  $C_{16}H_{10}$  as model compounds of tar at different temperatures of biomass gasification. The effect of operating parameters on the hydrogen production is also investigated.

## 2. Experimental

Figure 1 show the tar compositions at different temperatures, used in this study (Brage et al., 1996). The steam reforming reactions of tar representative compounds are given in Eqs (1-4). The methane steam reforming (Eq (5).) and water gas-shift reaction (Eq (6).) were also considered.

$$C_7H_8 + 7H_2O \longleftrightarrow 7CO + 11H_2$$
  $\Delta H_{393K} = +881.74 \text{ kJ/mol}$  (1)

$$C_{10}H_8 + 10H_2O \longleftrightarrow 10CO + 14H_2 \qquad \Delta H_{393K} = +1,177.8 \text{ kJ/mol}$$
 (2)

$$C_{16}H_{10} + 16H_2O \longleftrightarrow 16CO + 21H_2 \qquad \Delta H_{393K} = +651.7 \text{ kJ/mol}$$
 (3)

$$C_6H_6O + 5H_2O \longleftrightarrow 6CO + 8H_2$$
  $\Delta H_{393K} = +1,834.7 \text{ kJ/mol}$  (4)

$$CH_4 + H_2O \longleftrightarrow CO + 3H_2 \qquad \Delta H_{393K} = +209.44 \text{ kJ/mol}$$
 (5)

$$CO + H_2O \leftrightarrow CO_2 + H_2 \qquad \Delta H_{393K} = -40.01 \text{ kJ/mol}$$
 (6)

The reactants used for the reaction study are  $C_{10}H_8$ ,  $C_7H_8$ ,  $C_6H_6O$  and  $C_{16}H_{10}$  (Analytical grade). The catalytic tests were performed in a flow system shown diagrammatically in Figure 2. The setup consists of three sections. The first section is for preparing a tar model compounds with a controlled composition and flow rate. The second section is the reactor system including the fixed bed reactor and temperature control device. The third section is the analysis system where the gases from the reactor are analyzed by gas chromatography (GC). The instruments used in this system are listed and explained as follows.

The experiments were carried out at atmospheric pressure in a fixed-bed quartz reactor (9 mm diameter and 500 mm length) placed in a furnace with a temperature controller. The catalyst bed (0.3 g) was diluted with silicon carbide (1.0 g) by quartz wool in the uniform temperature zone (GHSV = 1,900 h<sup>-1</sup>). The temperature was monitored by a thermocouple placed outside of the reactor. Two motorized syringe pumps were used to introduce the liquids: water and mixture tar model compounds including  $C_{10}H_8$ ,  $C_7H_8$ ,  $C_6H_6O$  and  $C_{16}H_{10}$  which are then evaporated and carried to the reactor by a nitrogen flow controlled by a mass flow controller. The different operating parameters were studied as summarized in Table 1.

Table 1: Experimental condition for catalytic reaction.

Composition Tar	_		Temperature		
N <sub>2</sub> balance C <sub>10</sub> H <sub>8</sub> , C <sub>7</sub> H <sub>8</sub> ,C <sub>6</sub> H <sub>6</sub> O, C <sub>16</sub> H <sub>10</sub>	(20 mL/min)	(0.06 mL/min	) 450-650 <sup>0</sup> C	1 – 5	Atmosphere

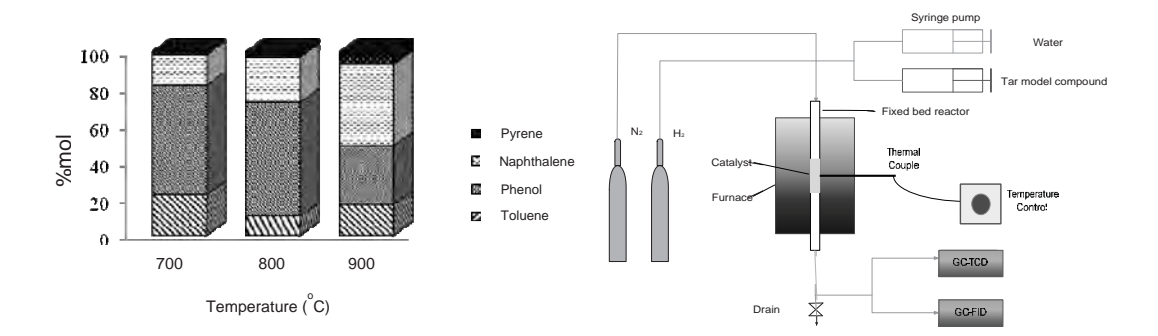


Figure 1: Major compounds chosen to represent tar model compound.

Figure 2: Schematic of the experimental system.

## 3. Results and Discussions

## 3.1 Catalytic performance on tar steam reforming

#### 3.1.1 Effect of support and %Ni loading

Figure 3.a shows the  $H_2$  yields. The support of  $Al_2O_3$  offers the highest % $H_2$  yield of 13 %. From the result, it was clear that  $Al_2O_3$  offers superior reactivity to the CaO and MgO supports. Figure 3.b, the results indicate that at 15 %Ni/Al $_2O_3$  offers the highest % $H_2$  yield compared to 10 %Ni/Al $_2O_3$  and 20 %Ni/Al $_2O_3$ . It should be noted that after 2 h reaction, for 10 %Ni/Al $_2O_3$  H $_2$  concentration decreased rapidly. Considering % $H_2$  yield (Figure 3.b), it was found that 20 %Ni/Al $_2O_3$  showed the largest value of % $H_2$  yield.

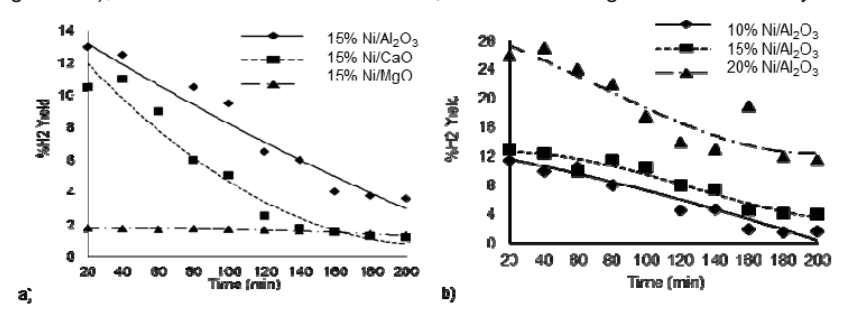


Figure 3: a) Effect of catalyst support on the  $H_2$  yield from tar steam reforming, b) effect of %Ni loading on %  $H_2$  yield of tar steam reforming (T = 450 °C, S/C ratio:5).

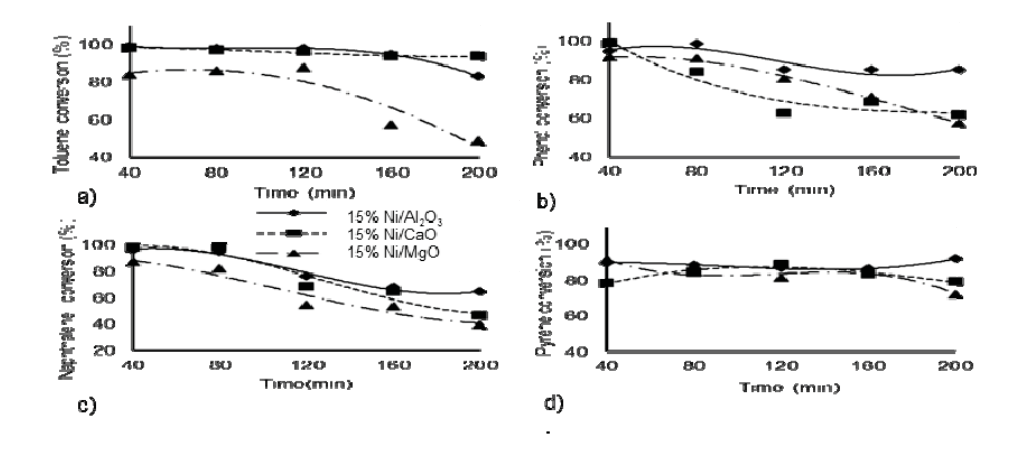


Figure 4: Tar conversion of supported catalysts on the tar steam reforming of a)  $C_7H_8$ , b)  $C_6H_6O$ , c)  $C_{10}H_8$ , and d)  $C_{16}H_{10}$ , ( $T=450\,^{\circ}C$ , S/C ratio = 5).

The tar conversions on various supported catalyst and %Ni loading are shown in Figure 4 and 5, respectively. It was found that 15 % Ni/MgO gives the lowest tar conversion. The 20  $\%Ni/Al_2O_3$  has almost the highest tar conversion of most tar components. Among different tar components, naphthalene conversion is the lowest probably because naphthalene has the most complex structure and therefore it is the most difficult to be decomposed.

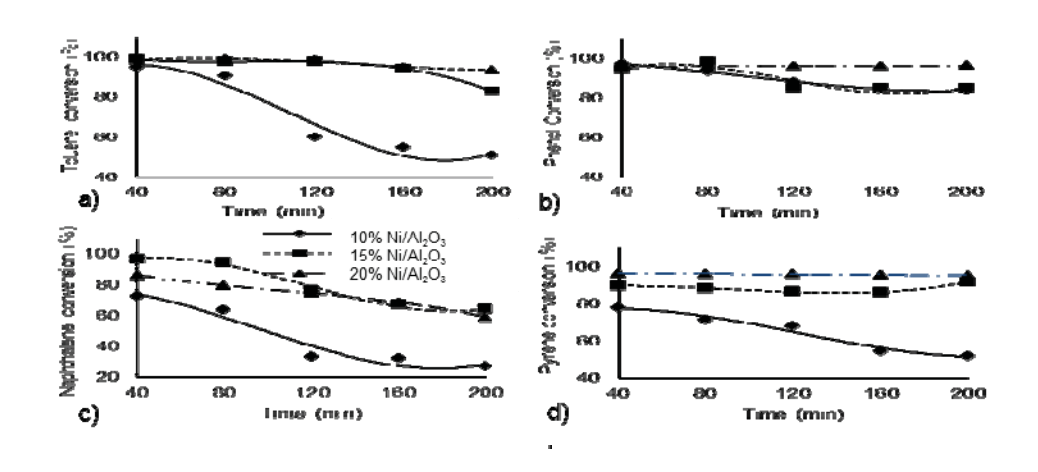


Figure 5: Tar conversions of Ni/Al $_2$ O $_3$  at different %Ni loadings of a)  $C_7H_8$ , b)  $C_6H_6O$ , c)  $C_{10}H_8$ , and d)  $C_{16}H_{10}$ , (T= 450  $^{\circ}C$ , S/C ratio = 5).

#### 3.1.2 Effect of reaction temperature and S/C ratio

Figure 6.a show the product compositions of the tar steam reforming of 20 %Ni/Al $_2$ O $_3$  at 450-650  $^{\circ}$ C and S/C ratio of 5. The results indicated that higher H $_2$  concentration (%mol) and H $_2$  product (mol/min) was achieved with increasing reaction temperature. At T = 650  $^{\circ}$ C, the value of the %H $_2$  yield is the largest (about 61 %). This is because the tar steam reforming is an endothermic reaction and, therefore, the reaction is favourable at high operating temperature due to both the thermodynamics and the improved kinetics at elevated temperature. The results on tar conversions are shown in Figure 7. All tar components could be better decomposed at higher temperatures. The conversions slightly decreased with increasing temperature except naphthalene which is the most difficult component with most difficult to be decomposed.

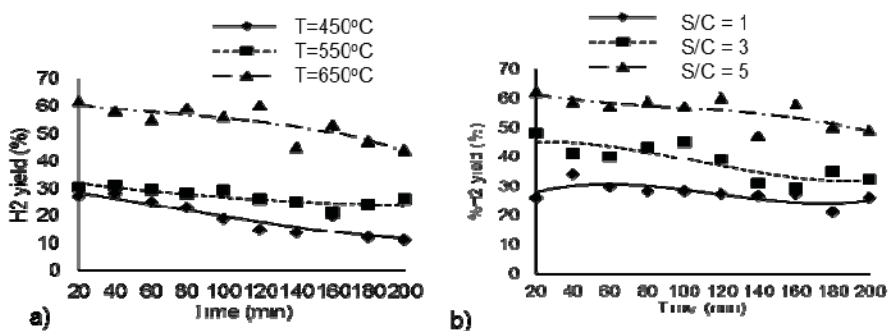


Figure 6: a) Effect of reaction temperature (S/C ratio = 5) and b) Effect of S/C ratio on  $\%H_2$  yield of tar steam reforming of 20  $\%Ni/Al_2O_3$  (T = 650  $^{\circ}C$ ).

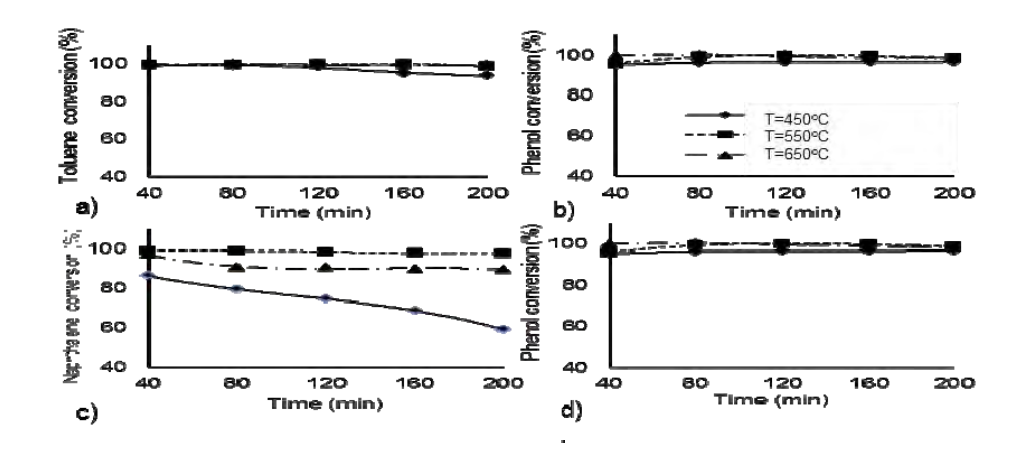


Figure 7: Tar conversions of 20 %Ni/Al<sub>2</sub>O<sub>3</sub> catalyst on the tar steam reforming at various reaction temperatures of a)  $C_7H_8$ , b)  $C_6H_6O$ , c)  $C_{10}H_8$ , and d)  $C_{16}H_{10}$ , (S/C ratio =5).

The effect S/C ratio 1-5 on tar steam reforming was performed using 20 %Ni/Al<sub>2</sub>O<sub>3</sub> at 650  $^{0}$ C. Increasing S/C ratio resulted in increasing H<sub>2</sub> product as well as %H<sub>2</sub> yield. The observed H<sub>2</sub> concentration and H<sub>2</sub> yield (Figure 6.b) varied in ranges of 74-85 and 25-62 %mol, respectively. The highest H<sub>2</sub> product was observed at the S/C ratio of 5. Additional steam in the feed could help to improve the conversions of all tar components (Figure 8). The increased S/C ratio did not only promote the steam reforming but also the water gas shift reaction, resulting in higher H<sub>2</sub> concentration and yield.

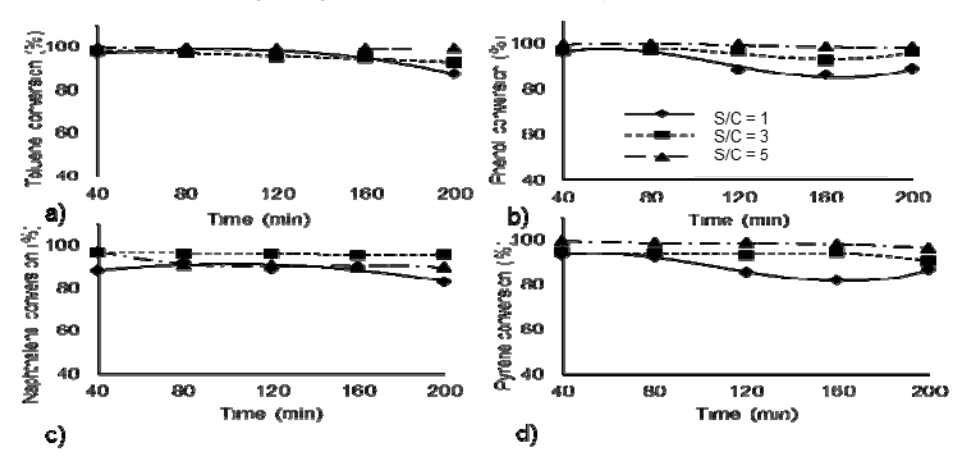


Figure 8: Tar conversions of 20 %Ni/Al<sub>2</sub>O<sub>3</sub> catalyst at various S/C ratios of a)  $C_7H_8$ , b)  $C_6H_6O$ , c)  $C_{10}H_8$ , and d)  $C_{16}H_{10}$  ( $T=650~^0C$ ).

## 4. Conclusions

The results of catalytic reactions in tar steam reforming reaction indicate that tar was favorably converted to synthesis gas ( $H_2$ ,  $CO_2$ ,  $CH_4$  and CO) at high temperatures and S/C molar ratio. The composition of tar derived from biomass gasification at 800  $^{\circ}$ C offers the highest  $H_2$  content. The support  $Al_2O_3$  allows the nickel loading into pore volume and surface area. When the %Ni loading was increased, the Ni distribution on surface area of alumina support becomes better. From experimental results, high temperature operation and S/C ratio are favorable to hydrogen production. Then, 20  $^{\circ}$ Ni/Al $_2O_3$  catalyst has good stability and suitability in tar steam reforming reaction at 650  $^{\circ}$ C and S/C ratio of 5.

## 5. Acknowledgement

This research has been supported by the Ratchadaphiseksomphot Endowment Fund of Chulalongkorn University (RES560530193-EN). The authors gratefully acknowledge the support from the Thailand Research Fund.

#### References

- Bergman P.C.A., van Paasen S.V.B., Neeft .J.P.A., Kiel J.H.A., 2002, Primary measures for tar reduction, reduce the problem at the source, 12<sup>th</sup> European conference on biomass for energy, industry and climate protection, 17-22 June, Amsterdam, The Netherlands, 597-599.
- Brage C., Yu Q., Sjostrom K., 1996, Characteristics of evolution of tar from wood pyrolysis in a fixed-bed reactor. Fuel 75(2), 213-219.
- Dayton D., 2002, A review of the literature on catalytic biomass tar destruction, National Renewable Energy Laboratory, Golden, Colorado, USA.
- Devi L., Ptasinski K.J., Janssen F.J.J., 2003, A review of the primary measures for tar in biomass gasification processes, Biomass Bioenergy 24, 125-140.
- Han J., Kim H., 2008, The reduction and control technology of tar during biomass/pyrolysis: an overview. Renewable and Sustainable Energy Reviews 12, 397-416.
- Milne T.A., Evans R.J., Abatzoglou N., 1998, Biomass gasifier "tars": their nature, formation, and conversion, National Renewable Energy Laboratory, Golden, Colorado, USA.
- Park H.J., Park S.H., Sohn J.M., Park J., Jeon J., Kim S.S., Park Y.K., 2010, Steam reforming of biomass gasification tar using benzene as a model compound over various Ni supported metal oxide catalysts, Bioresource Technology 101, 101-103.
- Saxena R.C., Seal D., Kumar S., Goyal H.B., 2008, Thermo-chemical routes for hydrogen rich gas from biomass: a review, Renewable and Sustainable Energy Reviews 12, 1909-1927.
- Singh D., Hern'andez-Pachecoa E., Huttonb P.N., Patelb N., Mann M., 2005, Carbon deposition in an SOFC fueled by tar-laden biomass gas: a thermodynamic analysis, Journal of Power Sources 142, 194-199.
- Stassen H.E.M., Prins W., Swaaij W.P.M., 2002, Thermal conversion of biomass into secondary products: the case of gasification and pyrolysis, 12<sup>th</sup> European Biomass Conference, 17-21 June, Amsterdam, The Netherlands, 38-44.
- Swierczynski D., Courson C., Kiennemann A., 2008, Study of steam reforming of toluene used as model compound of tar produced by biomass gasification, Chemical Engineering and Processing 47, 508–513.
- Vivanpatarakij S., Assabumrungrat S., 2013, Thermodynamic analysis of combined unit of biomass gasifier and tar steam reformer for hydrogen production and tar removal, International Journal of Hydrogen Energy 38, 3930-3936.
- Xiaodong Z., 2003, The mechanism of tar cracking by catalyst and the gasification of biomass, The Ph.D. dissertation of Zhejiang University (China).
- Zhang R., Brown R.C., Suby A., Cummer K., 2004, Catalytic destruction of tar in biomass derived producer gas, Energy Conversion and Management 45, 995-1014.

FLSEVIER

Contents lists available at ScienceDirect

# Chemical Engineering Journal

journal homepage: www.elsevier.com/locate/cej

Chemical Engineering Journal

## Multiphase parallel flow stabilization in curved microchannel



C. Kositanont <sup>a</sup>, S. Putivisutisak <sup>c</sup>, T. Tagawa <sup>b</sup>, H. Yamada <sup>b</sup>, S. Assabumrungrat <sup>a,\*</sup>

- <sup>a</sup> Center of Excellence in Catalysis and Catalytic Reaction Engineering, Department of Chemical Engineering, Faculty of Engineering, Chulalongkorn University, Bangkok 10330, Thailand
- <sup>b</sup> Department of Chemical Engineering, Nagoya University, Chikusa-ku, Nagoya-shi, Aichi 464-8603, Japan <sup>c</sup> Department of Mechanical Engineering, Faculty of Engineering, Chulalongkorn University, Bangkok 10330, Thailand

## HIGHLIGHTS

- The organic-aqueous parallel flow was studied in a curved microchannel with using computational fluid dynamics.
- The effects of guideline structure and surface modification on the flow were investigated.
- The surface modification method shows good flow improvement results.

## ARTICLE INFO

Article history: Received 8 January 2014 Received in revised form 5 May 2014 Accepted 6 May 2014 Available online 22 May 2014

Keywords:
Microchannel
Two-phase flow
Parallel flow
CFD
Guideline structure
Silanization

#### G R A P H I C A L A B S T R A C T



## ABSTRACT

The effect of liquid multiphase parallel flow stabilizing method (i.e. guideline structure addition and surface modification) was studied in a curved microchannel by using CFD simulation. A phase separator function can be combined within a microchannel by operating under stable parallel flow conditions. Based on our simulation conditions, the flow pattern could not be improved by using the guideline structure but the surface modification proves to be beneficial.

© 2014 Elsevier B.V. All rights reserved.

## 1. Introduction

Microreactor a process-intensifying equipment, has been applied to improve various separation and reaction systems [1–5]. An important advantage is mass and heat transport enhancement. In case of multiphase systems, the mass transfer path between phases can be decreased. The immiscible fluid systems such as organic-aqueous flows with mass transfer limitations have been studied in microreactors [6–12].

Due to large surface-to-volume ratio, surface effects become important. Therefore, multiphase flow with many interfaces in microstructures shows different flow patterns from typical size systems. Two common patterns of liquid multiphase flow, parallel and slug flows, have been studied. In this work, parallel flow is focused because it can provide phase separation at the outlets. Therefore, the requirement of a post-treatment unit can be reduced. This microdevice with phase separation is expected to be used in design of continuous flow integrated microsystems. In order to stabilize parallel flow pattern in a microdevice, guideline structure addition [13–15] and surface modification [16–18] have been proposed for liquid multiphase systems. In our previous

<sup>\*</sup> Corresponding author. Tel.: +66 2 2186868; fax: +66 2 2186877. E-mail address: suttichai.a@chula.ac.th (S. Assabumrungrat).

Nome	enclature			
Ca d <sub>H</sub> De F	Capillary number Hydraulic or equivalent diameter Dean number Surface tension force	t u v	Time Superficial velocity Velocity	
n n n n w tw p R Re	Surface normal Unit surface normal Unit vector normal to the wall Unit vector tangential to the wall Pressure Curve radius Reynolds number	Greek α κ μ ρ σ	letters Volume fraction Curvature Viscosity Contact angle at the wall Density Surface tension coefficient	

studies, the effects of guideline structure and surface modification were investigated in straight glass microchannels [19,20]. The results show that the parallel flow pattern could be improved by these two techniques.

Computational fluid dynamics (CFD) is a useful method to study fluid flow. Several works have applied this technique to study flows in microdevices especially slug flow [21–23] because it can provide detailed flow field information. Glatzel et al. [24] studied the performance of four CFD software programs, CFD-ACE+, CFX, Flow-3D and FLUENT by simulating four different microfluidic applications in 3D.

A straight microchannel has been studied in a number of works. In practice, a serpentine channel is widely used because of its compactness. It can provide high heat and mass transport and narrow residence time distributions [25,26]. In this work, the effect of parallel flow stabilizing method, i.e. guideline structure addition and surface modification, was studied in the curved microchannel by using ANSYS FLUENT, a well-known commercial CFD program.

## 2. Numerical simulation

Three-dimensional geometrical models were generated by GAMBIT and the simulations were performed with FLUENT 12.0 [27]. The interface was tracked by using the volume of fluid (VOF) method. The immiscible liquids were considered as isothermal incompressible Newtonian fluids. The conservation equations for momentum and mass can be written as:

$$\rho \left( \frac{\partial \vec{v}}{\partial t} + \vec{v} \cdot \nabla \vec{v} \right) = -\nabla p + \mu \nabla^2 \vec{v} + \vec{F} \tag{1}$$

$$(\nabla \cdot \vec{\mathbf{v}}) = \mathbf{0} \tag{2}$$

where  $\vec{v}$ , p and  $\vec{F}$  are the velocity, pressure and surface tension force, respectively.

The physical properties  $\rho$  and  $\mu$  are density and viscosity respectively which were calculated by averaging based on the individual fluid volume fraction in each control volume. The interface between the phases was identified by the continuity equation for the volume fraction  $(\alpha)$  which can be expressed as:

$$\frac{\partial \alpha}{\partial t} + \vec{v} \cdot \nabla \alpha = 0 \tag{3}$$

The surface tension effect was included using the continuum surface force (CSF) model proposed by Brackbill et al. [28] in the VOF calculation. The calculated surface tension force was added as an additional source term in the momentum conservation equation. The force for two phases is modelled as:

$$F_{\text{vol}} = \sigma \frac{\rho \kappa \nabla \alpha}{\frac{1}{2} (\rho_1 + \rho_2)} \tag{4}$$

where  $\sigma$  and  $\kappa$  are the surface tension coefficient and the curvature which was computed from the divergence of the unit surface normal:

$$\kappa = \nabla \cdot \hat{\mathbf{n}} \tag{5}$$

where,

$$\hat{n} = n/|n| \tag{6}$$

and the surface normal defined as the gradient of the volume fraction:

$$n = \nabla \alpha \tag{7}$$

The surface normal in the cell next to the wall is corrected by including the wall adhesion effect and can be written as:

$$\hat{n} = \hat{n}_{w} \cos \theta_{w} + \hat{t}_{w} \sin \theta_{w} \tag{8}$$

where  $\hat{n}_w$  and  $\hat{t}_w$  are the unit vectors normal and tangential to the wall, respectively and  $\theta_w$  is the contact angle at the wall.

Our simulation approach was validated by comparison with the previously published work [29]. Two phase liquid flows were simulated in the 156,000 cell T-shaped microchannel model. Water and kerosene with the surface tension of 0.045 N/m were fed as aqueous and organic phases, respectively. The contact angle of kerosene in water on PMMA calculated using Young's equation was 77.48°. The simulation results showed slug and parallel flow patterns at low and high flow rates, respectively, which agree well with the previous study. The measured water slug lengths were compared with the experimental and 78° contact angle simulated results in Fig. 4 of the literature. At a water flow rate of 10 mL/h, the simulated slug lengths were 1.77, 1.38 and 1.15 mm when kerosene was fed at 20, 40 and 60 mL/h, respectively. These results were between the published experimental and simulation results.

The microchannel 3D model was created based on a standard product of Institute of Microchemical Technology Co., Ltd. (IMT). The channel width, height and curvature radius are 100, 40 µm and 0.5 mm, respectively. In order to study the effect of curvature on the parallel flow pattern, microchannels with curve radius of 1 and 3 mm were also created. The microchannel model with microtexture called guideline structure was generated to study the structure effect on flow characteristics. The guideline wall and interval lengths were 100 µm as in the straight microchannels in our previous work [19]. Without guideline structure, the 0.5, 1 and 3 mm curvature radius microchannels were meshed to 50,000, 60,000 and 90,000 cells, respectively. For the guided microchannel case, the model has 51,776 cells. Fig. 1 shows the model outline and meshed model parts of microchannel with guideline structure. The meshed parts in Fig. 1(b)-(e) were enlarged from the rectangle areas in Fig. 1(a). In Fig. 1(e), the black lines are wall grids and white lines are interior grids. Water and toluene were fed

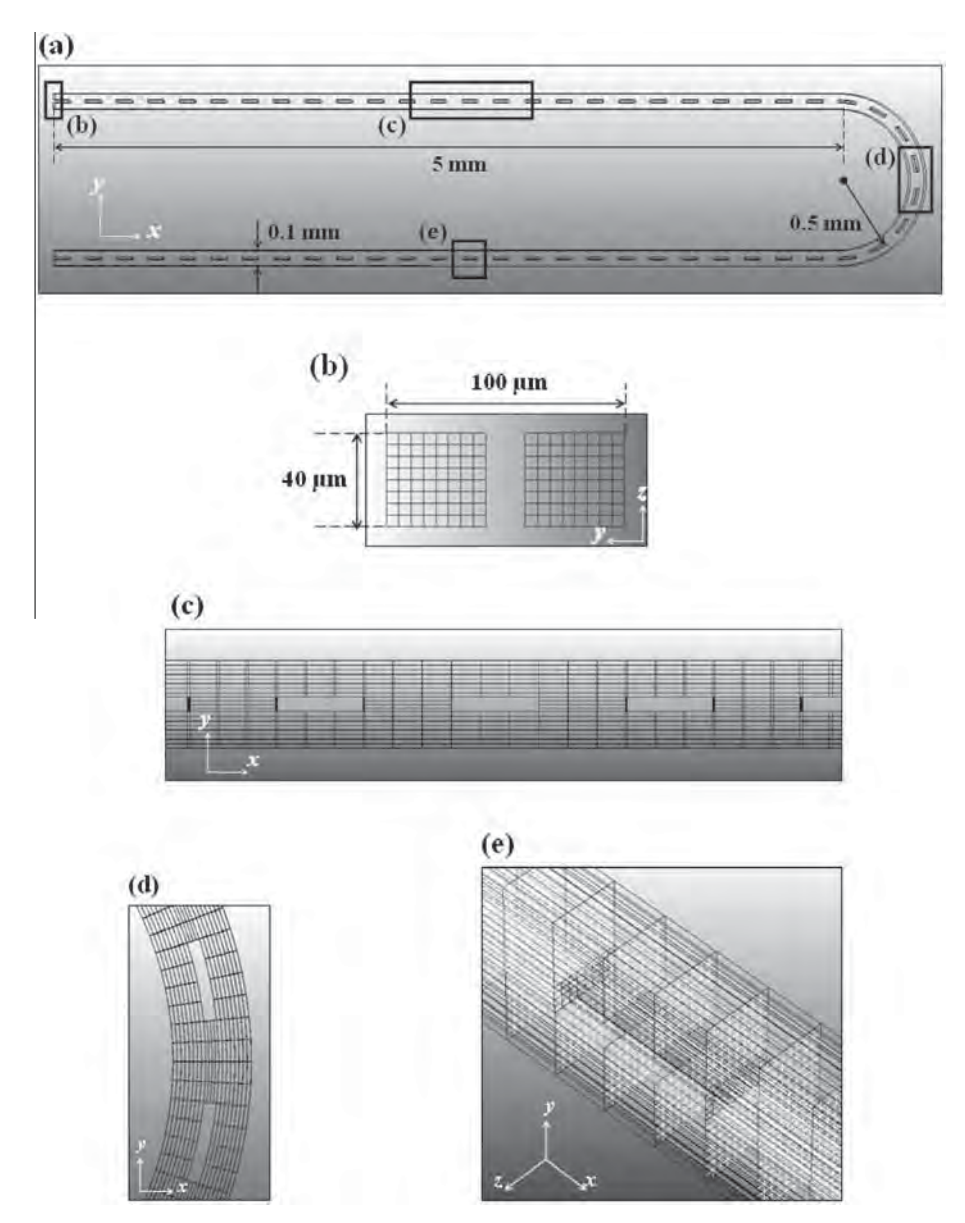


Fig. 1. Meshed microchannel with guideline structure (a) outline, (b) inlet, (c) wall, (d) curve and (e) wall with interior meshes.

in parallel with two possible inlet arrangements to generate the parallel flow. In the first arrangement, toluene inlet was at the outer side and water inlet was at the inner side of the curve and for the second case, toluene was fed at the inner side and water was fed at the outer side. The channel was initialized with water. Constant velocities normal to the boundary were specified for the inlet boundaries. The outlets were assumed a zero normal gradient for all flow variables except pressure. No-slip condition was applied on the microchannel and guideline walls. The contact angles were specified at the wall boundaries as the surface properties. The surface tension between water and toluene was set at  $0.0371 \text{ kg/s}^2$  [30]. The effect of surface modification was investigated by comparing the results of modified surface microchannels with unmodified microchannels. In the unmodified case, the bare glass surface contact angle was applied on the whole surface. For the modified surface case, the surface was divided into two parts corresponding with water and organic phases. The bare glass surface contact angle was applied only on the water part and the silanized glass surface contact angle was applied on the wall of organic part. From the experiment, the observed contact angles

were 37° and 143° for the bare and silanized glass surfaces, respectively [20].

For all simulation models, grid refinements were carried out to confirm that the solutions were grid resolution independent. All cases were simulated until the flow patterns did not change with time. The results were displayed as phase volume fraction contour and velocity vectors. Both top view and cross section view at positions specified in Fig. 2(positions a–e) were analyzed. All simulation results are colored by phase. For color graphics, blue color represent water and red is toluene. For grey scale graphics, dark and light grey are water and toluene, respectively. Other colors between two phases are interfaces.

The proportion of forces in the system can be quantified by dimensionless numbers. The Reynolds number (Re) expresses the ratio of inertia forces which are resistant to change or motion to viscous forces that tend to produce random eddies, vortices and other flow instabilities:

$$Re = \frac{\rho u d_H}{\mu} \tag{9}$$



Fig. 2. Cross section plane position.

**Table 1** Flow patterns after bend in unmodified microchannel.

Outer phase	Flow rate (mL/min)				
	0.025	0.0625	0.25	0.5	1
Toluene Water	Parallel Parallel	Parallel Parallel	Parallel Parallel	Parallel Annular	Parallel Phase switch

where, u is the linear or superficial velocity,  $d_H$  is the hydraulic or equivalent diameter of the channel.

Capillary number (Ca) expresses the ratio of viscous shear forces to elongate an interface to the interfacial tension forces which act to minimize interfacial area between the phases. This number has been used in many works [31,32] to analyze fluid flows in microscale because the viscous forces and the interfacial tension are the dominating forces in this small scale:

$$Ca = \frac{\mu u}{\sigma} \tag{10}$$

Dean number (De) expresses the ratio of the square root of the inertial and centrifugal force product to the viscous force. It is used to explain fluid flow in the curved channel where the centrifugal force induces the instability [33,34] and is a magnitude measure of the secondary flow that is a result of the centrifugal force:

$$De = Re\sqrt{\frac{d_H}{2R}} \tag{11}$$

where, R is the curvature radius.

## 3. Results and discussion

For a curved microchannel with a radius of 0.5 mm, five values of feed flow rate, 0.025, 0.0625, 0.25, 0.5, 1 mL/min of each phase were simulated in unmodified, modified surface and guided microchannels. Two cases of inlet position were considered for all microchannel models.

In the unmodified curved microchannel, the simulated stable flow patterns in the straight part before curve were parallel flows

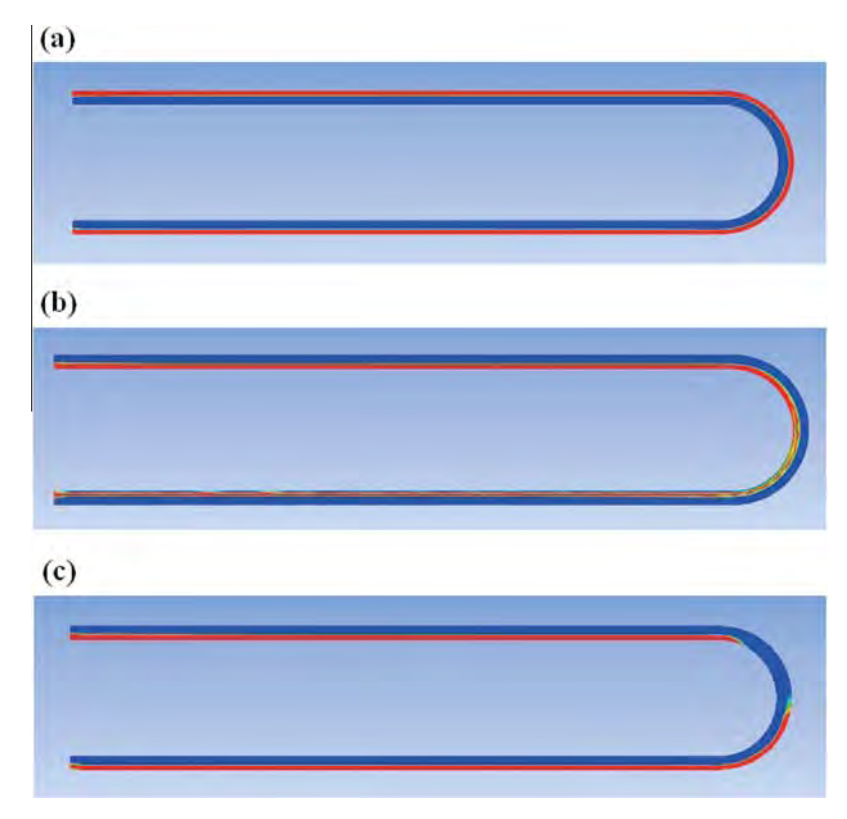


Fig. 3. Flow patterns in unmodified curved microchannel of phase feed flow rates at (a) 0.5 mL/min with outer toluene, (b) 0.5 mL/min with outer water and (c) 1 mL/min with outer water.

**Table 2**Volume fractions at positions a—e of some flows in unmodified curved microchannel.

D '''	Flow rate (mL/min), Outer phase						
Position	0.025, Toluene	0.025, Water	0.5, Toluene	0.5, Water	1, Water		
a			)				
b							
С							
d			)				
e			)		)		

**Table 3** Flow patterns after bend in microchannel with guideline structure.

Outer phase	Flow rate (mL/min)				
	0.025	0.0625	0.25	0.5	1
Toluene Water	Parallel Parallel	Parallel Parallel	Parallel Parallel	Parallel Annular	Parallel Annular

whose interfaces were shifted to the toluene phases at all feed flow rates. By investigating the contour at the microchannel cross section, the interface showed more curvature and the toluene phase took less area at higher feed flow rate. The flow patterns after passing the bend are shown in Table 1. When toluene was fed at the outer side of the curve, the flow patterns after turn were still parallel in all feed flow rates. However, the flow patterns were changed to annular and parallel with phase switch at the feed rates of 0.5 and 1 mL/min, respectively; in the case that water was fed at the outer lane. Fig. 3 shows the different flow patterns observed in the unmodified microchannel. The cross section volume fraction contours of some flow results at positions a-e are shown in Table 2. In the case that parallel flow pattern could be maintained, the interface shape was not changed significantly between each position. In the case that parallel flow changed to annular pattern, water gradually surrounded the toluene stream from position c. In the phase switch after bend case, the toluene stream moved from inner to outer lane after entering the curve part and was surrounded by water at position c. After that the side water films were disappeared and the parallel flow with flat interface was observed at position d. The flat interface was developed to the curved interface again as shown in position e. The centrifugal instability of a fluid flow inside a curved tube can be explained by the dimensionless Dean number. With constant channel diameter and curvature radius, the number is increased with the Reynolds number. Comparing between toluene and water, the Reynolds number of toluene is greater at the same velocity and channel diameter. Thus the centrifugal force, which acts towards the outer wall, in toluene is stronger than in water. This might cause the toluene stream dislocation when it was fed at the inner path of the curve at high flow rate.

From the results, the system with bend could not maintain the parallel flow when the flow rate was too high. In order to stabilize the parallel flow, the guideline structure and surface modification methods were applied in the curved microchannel.

With guideline structure, the simulated stable flow patterns in the straight part before curve were similar to that in the unmodified microchannel. At low feed flow rate, the flow patterns after turn were still parallel as in the unmodified microchannel. The parallel flows were changed to annular patterns at the feed flow rates of 0.5 and 1 mL/min in the case that toluene was in the inner lane. The flow patterns after passing the bend are summarized in Table 3. Comparing to the unmodified microchannel, the guideline structure could not stabilize the parallel flow pattern in this operation range. Fig. 4 shows the flow patterns in microchannel with guideline. The cross section volume fraction contours of some flow results at positions a-e are shown in Table 4. The interface shapes were similar to the unmodified case but there were smaller areas of toluene phase confined by the guideline wall at 0.025 and 0.05 mL/min with outer toluene. At higher flow rate, water surrounded the toluene phase as in the unmodified channel before the toluene stream was divided into two or more parts by the guideline wall. Thus the guideline structure could not improve the flow pattern and the phase separation in this system.

When the surface modification method was applied, all flow patterns both before and after turn in the simulation range were parallel as shown in Fig. 5. For all flow rates, the interfaces were posed at the middle of the microchannel width. Although the observed flow patterns were not different in the top view, the interfaces in the cross section view showed the distinct behaviors. The cross section volume fraction contours at the feed flow rates of 1 and 0.025 mL/h at positions a–e are shown in Table 5. As can be

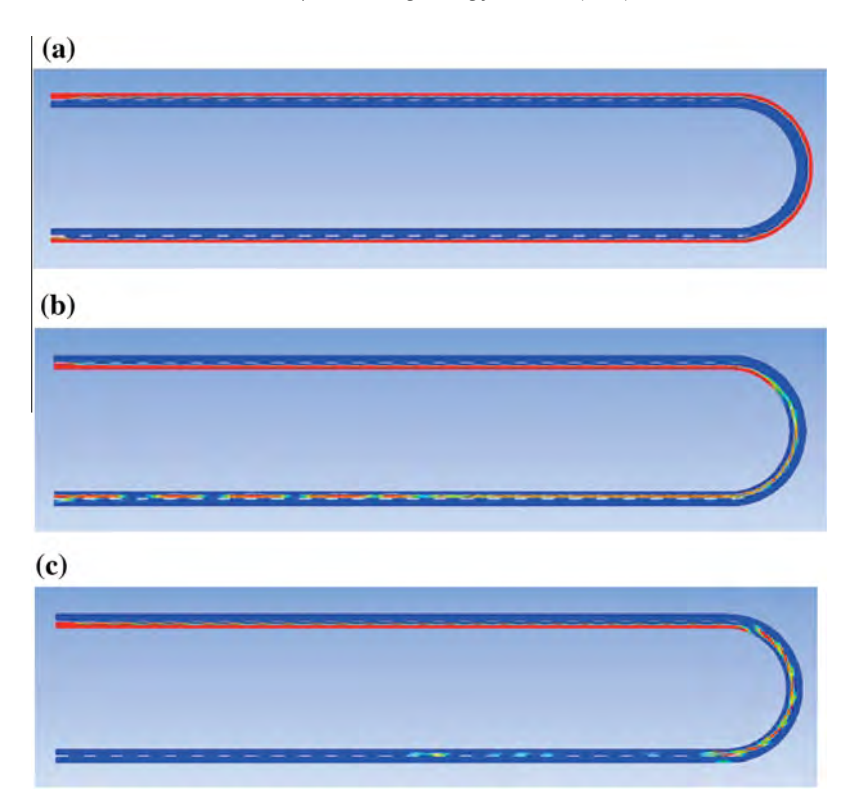


Fig. 4. Flow patterns in curved microchannel with guideline structure of phase feed flow rates at (a) 0.5 mL/min with outer toluene, (b) 0.5 mL/min with outer water and (c) 1 mL/min with outer water.

**Table 4**Volume fractions at positions a–e of some flows in curved microchannel with guideline structure.

D:4:		Flow ra	te (mL/min), Out	er phase	
Position	0.025, Toluene	0.025, Water	0.5, Toluene	0.5, Water	1, Water
a					
b					
С					9(
d				·• ()	)» (\$
e				• ()	0.0

seen, at the lower flow rate, curved interfaces were not changed along the channel for both inlet position cases. Although the interfaces were perturbed by the bend at the higher flow rate, at position e, it was returned to the same shape as in position a.

The velocity was largest near the middle of the channel and therefore, the centrifugal force was strongest at this area. When the velocity field was considered, only the results at 0.025 mL/min show non-uniform velocity vector directions in both

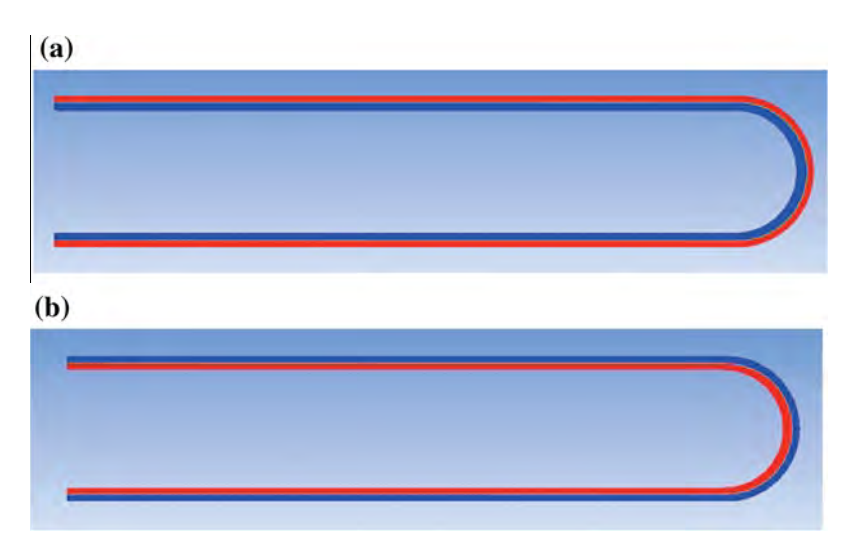


Fig. 5. Flow patterns in curved microchannel with surface modification of phase feed flow rates at (a) 0.025 mL/min with outer toluene and (b) 1 mL/min with outer water.

**Table 5**Volume fractions at positions a–e of some flows in curved microchannel with surface modification.

D 12		Flow rate (mL/mi	in), Outer phase	
Position	0.025, Toluene	0.025, Water	1, Toluene	1, Water
a				
b				)
С	(		(	
d				
e				

inlet arrangements. The velocity vectors and their side views at the feed flow rates of 0.025 and 1 mL/min in the unmodified microchannel at positions a, c and e are shown in Table 6. Considering based on the Capillary number, the ratio of viscous force over interfacial force is decreased when flow rate is minimized. The instability at lower flow rate is caused by the dominating interfacial force, which acts on the interface. The pattern of velocity vectors at position c were changed at both flow rates by influence of the curvature. At 0.025 mL/min, two vortices were observed similar to the single phase dean vortices. For 1 mL/min, the velocity direction and the maximum velocity magnitude were shifted to the outer side of

the curve. These velocity vector changes by the centrifugal force at the bend may help improve transport processes.

However, in the microchannel with modified surface, when the flow rate was further increased from 1 mL/min, the system could not maintain the parallel flow pattern. The effect of curvature radius was also investigated. The flow at 1 mL/min in unmodified microchannel was simulated with the curve radius of 1 and 3 mm. The contour of 1 mm radius channel shows parallel flow with phase position switch at the curve similar to that observed at the same feed flow rate in the 0.5 mm radius channel, while the result of 3 mm curve radius channel shows annular pattern

**Table 6**Velocity vectors at position a, c and e cross section in unmodified curved microchannel.

		Flow rate (mL/mi	in), Outer phase	
Position	0.025, Toluene	0.025, Water	1, Toluene	1, Water
a	<b>用热剂</b>			
	all Marine.	animandin.	All IIII.	aililliillii.
с	帳酬			
	all Million.	.militarin.	: The Times.	Mark Hilliam.
e				
	All Mills.	.mitting.	.iffilith.	.iiiiiiiiiiiiiiiiiiiiiiiiiiiiiiiiiiiii

after bend which is similar to the result at the flow rate of  $0.5 \, \text{mL/min}$  in the  $0.5 \, \text{mm}$  radius channel. From these results, the stable parallel flow pattern was expected at larger curve radius. It is suggested that the effect of geometry such as channel, curve and guideline dimensions should be studied comprehensively in the future works.

#### 4. Conclusion

The organic-aqueous flow behaviors in curved microchannel and parallel flow stabilization methods were studied in this work by applying CFD method. In unmodified channel, the inner toluene stream detached from their corresponding path at high feed flow rate. The results show that the intermittent guideline wall could not help stabilize the parallel flow in the simulated flow rate range. In contrast, the surface modification can clearly maintain the parallel flow pattern at high flow rate and help shift the interface wall contact point to the microchannel centre. Moreover, the perturbed interface by the curve could completely return to the observed shape before the bend. As a result, the separation at the outlets can be improved. In this work, because of the curvature interface shape, the complete phase separation by utilizing the parallel flow pattern may be difficult to be obtained. However, one phase in its outlet with a trace of the other phase can be expected. By considering the velocity vectors, there were non-uniform directions observed at low flow rate by the interfacial force. The vector directions and the maximum velocity magnitude positions were changed at the bend by the centrifugal force.

#### Acknowledgements

The supports from The Thailand Research Fund, Dusadeepipat scholarship from Chulalongkorn University and Nagoya University Program for Academic Exchange (NUPACE) are gratefully acknowledged.

#### References

- S. Goto, T. Tagawa, S. Assabumrungrat, P. Praserthdam, Simulation of membrane microreactor for fuel cell with methane feed, Catal. Today 82 (2003) 223–232.
- [2] J.L.H. Chau, A.Y.L. Leung, K.L. Yeung, Zeolite micromembranes, Lab Chip 3 (2003) 53–55.
- [3] W.N. Lau, K.L. Yeung, R. Martin-Aranda, Knoevenagel condensation reaction between benzaldehyde and ethyl acetoacetate in microreactor and membrane microreactor, Microporous Mesoporous Mater. 115 (2008) 156–163.
- [4] K.L. Yeung, S.M. Kwan, W.N. Lau, Zeolites in microsystems for chemical synthesis and energy generation, Top. Catal. 52 (2009) 101–110.
- [5] D. Arndt, J. Thöming, M. Bäumer, Improving the quality of nanoparticle production by using a new biphasic synthesis in a slug flow microreactor, Chem. Eng. J. 228 (2013) 1083–1091.
- [6] J.R. Burns, C. Ramshaw, The intensification of rapid reactions in multiphase systems using slug flow in capillaries, Lab Chip 1 (2001) 10–15.
- [7] G. Dumann, U. Quittmann, L. Gröschel, D.W. Agar, O. Wörz, K. Morgenschweis, The capillary-microreactor: a new reactor concept for the intensification of heat and mass transfer in liquid-liquid reactions, Catal. Today 79–80 (2003) 433–439.
- [8] J.H. Xu, J. Tan, S.W. Li, G.S. Luo, Enhancement of mass transfer performance of liquid-liquid system by droplet flow in microchannels, Chem. Eng. J. 141 (2008) 242–249.
- [9] S. Aljbour, H. Yamada, T. Tagawa, Rate enhanced and green ethoxylation of pchloronitrobenzene in a microchannel reactor, J. Chem. Eng. Jpn. 42 (suppl. 1) (2009) 90–95.
- [10] K. Wang, Y.C. Lu, Y. Xia, H.W. Shao, G.S. Luo, Kinetics research on fast exothermic reaction between cyclohexanecarboxylic acid and oleum in microreactor, Chem. Eng. J. 169 (2011) 290–298.
- [11] H.W. Shao, Y.C. Lu, K. Wang, G.S. Luo, Liquid-liquid flow and mass transfer characteristics in micro-sieve array device with dual-sized pores, Chem. Eng. J. 193–194 (2012) 96–101.
- [12] K. Burlage, C. Gerhardy, H. Praefke, M.A. Liauw, W.K. Schomburg, Slug length monitoring in liquid-liquid Taylor-flow integrated in a novel PVDF microchannel, Chem. Eng. J. 227 (2013) 111–115.
- [13] M. Tokeshi, T. Minagawa, K. Uchiyama, A. Hibara, K. Sato, H. Hisamoto, T. Kitamori, Continuous-flow chemical processing on a microchip by combining microunit operations and a multiphase flow network, Anal. Chem. 74 (2002) 1565–1571.
- [14] T. Maruyama, J. Uchida, T. Ohkawa, T. Futami, K. Katayama, K. Nishizawa, K. Sotowa, F. Kubota, N. Kamiya, M. Goto, Enzymatic degradation of p-chlorophenol in a two-phase flow microchannel system, Lab Chip 3 (2003) 308–312.
- [15] T. Tagawa, S. Aljbour, M. Matouq, H. Yamada, Micro-channel reactor with guideline structure for organic-aqueous binary system, Chem. Eng. Sci. 62 (2007) 5123-5126.

- [16] B. Zhao, J.S. Moore, D.J. Beebe, Surface-directed liquid flow inside microchannels, Science 291 (2001) 1023–1026.
- [17] A. Smirnova, K. Mawatari, A. Hibara, M.A. Proskurnin, T. Kitamori, Micromultiphase laminar flows for the extraction and detection of carbaryl derivative, Anal. Chim. Acta 558 (2006) 69–74.
- [18] S. Aljbour, H. Yamada, T. Tagawa, Sequential reaction-separation in a microchannel reactor for liquid-liquid phase transfer catalysis, Top. Catal. 53 (2010) 694-699.
- [19] C. Kositanont, S. Putivisutisak, P. Praserthdam, S. Assabumrungrat, H. Yamada, T. Tagawa, Flow pattern of liquid multiphase flow in microreactors with different guideline structures, J. Chem. Eng. Jpn. 44 (2011) 649–652.
- [20] C. Kositanont, T. Tagawa, H. Yamada, S. Putivisutisak, S. Assabumrungrat, Effect of surface modification on parallel flow in microchannel with guideline structure. Chem. Eng. J. 215–216 (2013) 404–410.
- structure, Chem. Eng. J. 215–216 (2013) 404–410.

  [21] N. Harries, J.R. Burns, D.A. Barrow, C. Ramshaw, A numerical model for segmented flow in a microreactor, Int. J. Heat Mass Transfer 46 (2003) 3313–3322
- [22] M.N. Kashid, I. Gerlach, S. Goetz, J. Franzke, J.F. Acker, F. Platte, D.W. Agar, S. Turek, Internal circulation within the liquid slugs of a liquid–liquid slug-flow capillary microreactor, Ind. Eng. Chem. Res. 44 (2005) 5003–5010.
- [23] D. Malsch, M. Kielpinski, R. Merthan, J. Albert, G. Mayer, J.M. Köhler, H. Süße, M. Stahl, T. Henkel, μPIV-analysis of Taylor flow in micro channels, Chem. Eng. J. 135S (2008) S166–S172.
- [24] T. Glatzel, C. Litterst, C. Cupelli, T. Lindemann, C. Moosmann, R. Niekrawietz, W. Streule, R. Zengerle, P. Koltay, Computational fluid dynamics (CFD)

- software tools for microfluidic applications a case study, Comput. Fluids  $37\,(2008)\,218-235.$
- [25] V. Kumar, S. Vashisth, Y. Hoarau, K.D.P. Nigam, Slug flow in curved microreactors; hydrodynamic study, Chem. Eng. Sci. 62 (2007) 7494–7504.
- [26] D.M. Fries, P. Rudolf von Rohr, Liquid mixing in gas-liquid two-phase flow by meandering microchannels, Chem. Eng. Sci. 64 (2009) 1326–1335.
- [27] ANSYS Inc., ANSYS FLUENT 12.0 Theory Guide, ANSYS Inc., USA, 2009.
- [28] J.U. Brackbill, D.B. Kothe, C. Zemach, A continuum method for modeling surface tension, J. Comput. Phys. 100 (1992) 335–354.
   [29] S.K. Reddy Cherlo, S. Kariveti, S. Pushpavanam, Experimental and numerical
- [29] S.K. Reddy Cherlo, S. Kariveti, S. Pushpavanam, Experimental and numerical investigations of two-phase (liquid-liquid) flow behavior in rectangular microchannels, Ind. Eng. Chem. Res. 49 (2010) 893–899.
- [30] A. Dessimoz, L. Cavin, A. Renken, L. Kiwi-Minsker, Liquid-liquid two-phase flow patterns and mass transfer characteristics in rectangular glass microreactors, Chem. Eng. Sci. 63 (2008) 4035–4044.
- [31] V. Reddy, J.D. Zahn, Interfacial stabilization of organic-aqueous two-phase microflows for a miniaturized DNA extraction module, J. Colloid. Interface Sci. 286 (2005) 158–165.
- [32] D. Liu, S. Wang, Hydrodynamics of Taylor flow in noncircular capillaries, Chem. Eng. Proc. 47 (2008) 2098–2106.
- [33] D.M. Fries, S. Waelchli, P. Rudolf von Rohr, Gas-liquid two-phase flow in meandering microchannels, Chem. Eng. J. 135S (2008) S37-S45.
   [34] S. Vashisth, K.D.P. Nigam, Prediction of flow profiles and interfacial
- [34] S. Vashisth, K.D.P. Nigam, Prediction of flow profiles and interfacial phenomena for two-phase flow in coiled tubes, Chem. Eng. Proc. 48 (2009) 452–463.

#### CHERD-1646; No. of Pages 15

### ARTICLE IN PRESS

CHEMICAL ENGINEERING RESEARCH AND DESIGN XXX (2014) XXX-XXX



Contents lists available at ScienceDirect

# Chemical Engineering Research and Design



journal homepage: www.elsevier.com/locate/cherd

# Techno-economic evaluation of different GO<sub>2</sub>-based processes for dimethyl carbonate production

Pichayapan Kongpanna<sup>a</sup>, Varong Pavarajarn<sup>b</sup>, Rafiqul Gani<sup>c</sup>, Suttichai Assabumrungrat<sup>a,\*</sup>

- <sup>a</sup> Center of Excellence in Catalysis and Catalytic Reaction Engineering, Department of Chemical Engineering, Faculty of Engineering, Chulalongkorn University, Bangkok 10330, Thailand
- <sup>b</sup> Center of Excellence in Particle Technology, Department of Chemical Engineering, Faculty of Engineering, Chulalongkorn University, Bangkok 10330, Thailand
- <sup>c</sup> CAPEC, Department of Chemical and Biochemical Engineering, Technical University of Denmark, Soltofts Plads 1, Building 229, DK-2800 Lyngby, Denmark

#### ABSTRACT

In this work, several chemical processes for production of dimethyl carbonate (DMC) based on  $CO_2$  utilization are evaluated. Four  $CO_2$ -based processes for production of DMC are considered: (1) direct synthesis from  $CO_2$  and methanol; (2) synthesis from urea; (3) synthesis from propylene carbonate; and (4) synthesis from ethylene carbonate. The processes avoid the use of toxic chemicals such as phosgene, CO and NO that are required in conventional DMC production processes. From preliminary thermodynamic analysis, the yields of DMC are found to have the following order (higher to lower): ethylene carbonate route > urea route > propylene carbonate route > direct synthesis from  $CO_2$ . Therefore, only the urea and ethylene carbonate routes are further investigated by comparing their performances with the commercial BAYER process on the basis of kg of DMC produced at a specific purity. The ethylene carbonate route is found to give the best performance in terms of energy consumption (11.4% improvement), net  $CO_2$  emission (13.4% improvement), in global warming potential (58.6% improvement) and in human toxicity-carcinogenic (99.9% improvement) compared to the BAYER process. Also, the ethylene carbonate option produces ethylene glycol as a valuable by-product. Based on the above and other performance criteria, the ethylene carbonate route is found to be a highly promising green process for DMC production.

© 2014 The Institution of Chemical Engineers. Published by Elsevier B.V. All rights reserved.

Keywords: Dimethyl carbonate;  $CO_2$ -based synthesis; Process evaluation; Energy consumption; Net  $CO_2$  emission; Sustainability analysis

#### 1. Introduction

Carbon dioxide accumulation in the atmosphere is a major cause of concern with respect to the increasing global temperature of the earth and severe climate changes. The  $CO_2$  is primarily released from long-term storage via combustion of fossil-fuel. It has been estimated that the worldwide energy-related  $CO_2$  emissions are increasing at a rate of about 2.1% per year (Xu et al., 2010). It is therefore necessary to decrease the emission of  $CO_2$  to the atmosphere on a global scale. The  $CO_2$  emissions from the petrochemical sector, for example,

oil refineries, LNG sweetening, ammonia, ethane and other petrochemical process and ethylene oxide to atmosphere are estimated around 1460 MtCO<sub>2</sub>/year, while, CO<sub>2</sub> utilization in chemical process such as urea, methanol, dimethyl ether, tertbutyl methyl ether (TBME) and organic carbonate is estimated around 178 MtCO<sub>2</sub>/year (Aresta et al., 2013). Although, no single solution will be sufficient in reducing this large net CO<sub>2</sub> emission, a potential strategy could be to more utilize CO<sub>2</sub> as a chemical feedstock for conversion to more valuable chemicals (Centi and Perathoner, 2009). However, the utilization of CO<sub>2</sub> for the production of fine chemicals is severely limited by the

E-mail addresses: Suttichai.A@chula.ac.th, Suttichaia@yahoo.com (S. Assabumrungrat).

http://dx.doi.org/10.1016/j.cherd.2014.07.013

0263-8762/© 2014 The Institution of Chemical Engineers. Published by Elsevier B.V. All rights reserved.

Please cite this article in press as: Kongpanna, P., et al., Techno-economic evaluation of different  $CO_2$ -based processes for dimethyl carbonate production. Chem. Eng. Res. Des. (2014), http://dx.doi.org/10.1016/j.cherd.2014.07.013

<sup>\*</sup> Corresponding author. Tel.: +66 2 2186868; fax: +66 2 2186877.

reaction equilibrium in most cases and they have been widely reported (Omae, 2012). The high stability of carbon dioxide leads to a very low driving force, which has to be compensated if higher value chemical products are to be produced what is necessary is to first create a full reaction tree of higher value chemicals that can be produced directly or indirectly with  $\rm CO_2$  as a reactant. This requires each synthesis route to be investigated for thermodynamic feasibility and availability of catalysts, when necessary. Having the reaction tree, different synthesis routes can be investigated to find the best set of value-added products by  $\rm CO_2$  utilization and thereby reduction of net  $\rm CO_2$  emission as a first step, the synthesis routes for a selected set of higher value products could be investigated based on known reaction data.

This work focuses on the evaluation of the production of dimethyl carbonate (DMC) by several reaction routes. DMC is an important carbonylating and methylating reagent used in various fields such as medicine, pesticides, composite materials, flavoring agent and electronic chemicals (Omae, 2012; Pacheco and Marshall, 1997). Although processes for the production of DMC are well-established, for example, BAYER (Kricsfalussy et al., 1996), UBE (Matsuzaki and Nakamura, 1997) and ENIChem (Tundo and Selva, 2002), the synthesis of DMC utilizing CO2 is an option worth investigating since it offers direct benefits to the environment while creating valuable products from the emitted and undesired CO2. In this paper, CO<sub>2</sub> based processes for production of DMC are selected for evaluation and compared according to a set of performance criteria that includes yield, energy consumption and CO2 emission. For a consistent comparison, the various criteria are evaluated for the same product specification (that is, a fixed purity) and per unit mass of the desired product.

#### 2. DMC production process alternatives

The production of DMC is classified here in terms of two main types, namely conventional processes and  $CO_2$ -based processes. Among the conventional processes, the productions of DMC from phosgene, through partial carbonylation of methanol (BAYER process) and from methyl nitrile (UBE process) are well-known. The processes utilizing  $CO_2$  include direct synthesis with methanol and integrated processes involving intermediate compounds such as urea, propylene carbonate and ethylene carbonate, which are derived from  $CO_2$ . The involved reactions and associated thermodynamic data are given in Table 1 for the above process routes.

#### 2.1. Conventional process

#### 2.1.1. Synthesis of DMC from phosgene

This process employs the traditional (pre-1980) method to produce DMC (Pacheco and Marshall, 1997). Here, phosgene reacts with methanol to form methyl chloroformate (CH $_3$ OCOCl), which further reacts with methanol to form DMC according to Eq. (1) in Table 1. However, phosgene is an extremely hazardous material (Matsuzaki and Nakamura, 1997) and is classified by the US Department of Transportation (DOT) as a class-A poison. Consequently, there is an incentive to phase out phosgene (Matsuzaki and Nakamura, 1997).

2.1.2. DMC from partial carbonylation (BAYER process)
This non-phosgene process produces DMC by reacting methanol, carbon monoxide and oxygen in liquid phase, as

Table 1 – List of reactions found in DMC production.	MC production.				
Process	Reaction		$\Delta G_{ m r25^{\circ}C}$ (kJ/mol)	$\Delta H_{ m r25^{\circ}C}$ (kJ/mol)	K25 °C
Phosgene route Partial carbonylation	$COCI + 2CH_3OH = (CHO)CO + 2HCI$ $CO + 1/2O_5 + 2CH_5OH = (CH_5O)_5CO + H_5O$	(1)	-305.543 -233.077	-321.670 -300 399	0.883
Methyl nitrile	$CO + 2CH_3ONO = (CH_3O)_2CO + 2NO$	(3)	-115.438	-107.945	0.954
CO <sub>2</sub> direct synthesis	$CO_2 + 2CH_3OH \Rightarrow (CH_3O)_2CO + H_2O$	(4)	29.583	-15.259	1.012
Urea route		(5)	21.009	-0.042	1.000
	$CH_3 OCONH_2 + CH_3 OH = CH_3 OCONH_2 + NH_3$ $CH_3 OCONH_2 + CH_3 OH = (CH_3 O)_2 CO + NH_3$	(A)	- 13.240 15.390	-10.510 13.11	0.993
Propylene carbonate route	$C_3H_6O + CO_2 = CH_3(C_2H_3O_2)CO$ $CH_3(C_2H_3O_2)CO + 2CH_3OH = (CH_3O)_2CO + C_3H_8O_2$	(8)	-0.054 35.115	-0.908 22.854	0.999
Ethylene carbonate route	$C_2H_4O + CO_2 = (CH_2O)_2CO$ $(CH_2O)_2CO + 2CH_3OH = (CH_3O)_2CO + (CH_2OH)_2$	(10) (11)	-0.025 -14.926	_0.083 27.500	0.999

Fig. 1 - Concept of CO<sub>2</sub>-based processes for production of dimethyl carbonate by CO<sub>2</sub> conversion.

given by Eq. (2) in Table 1. As the catalyst, Cu(I)Cl and KCl in various ratios are usually employed (Kricsfalussy et al., 1996; Tundo and Selva, 2002). The process however suffers from low production rate, difficulties in downstream separation because of the existence of binary azeotropes in the system methanol-water-DMC, and the need for corrosion resistant reactors. Nevertheless, the process has been licensed by BAYER for commercial production of DMC.

#### 2.1.3. DMC from methyl nitrite process

The oxidative reactions using the alkyl nitrites as an oxidant have been developed by UBE (Matsuzaki and Nakamura, 1997; Tundo and Selva, 2002). In the alkyl nitrite reactions, substrates such as CO and carbonyl-compounds are oxidized over palladium catalysts. The DMC, dialkyl oxalates and other useful chemicals are synthesized efficiently under moderate conditions by this type of alkyl nitrite reactions. In the case of DMC, methyl nitrile reacts with carbon monoxide to produce DMC and nitric oxide, as given by Eq. (3) in Table 1. This processing route has difficulties due to the production of nitric oxide, which is toxic and therefore, its release must be controlled and regulated. However, it is noteworthy that this methyl nitrile process has been employed for further production of dimethyl oxalate (Matsuzaki and Nakamura, 1997).

#### 2.2. CO<sub>2</sub> as chemical feedstock for DMC production

Production of DMC from CO2 is feasible through direct reaction with methanol or via the formation of intermediate compounds such as urea, propylene carbonate or ethylene carbonate. The latter is highlighted in Fig. 1. In this work, it is assumed that a pure  $CO_2$  feed stream, captured through a process is available, irrespective of the emission source. Some of the sources of CO2 emitted streams could be natural gas sweetening process, ammonia process, ethylene oxide process, H2 production process and fermentation process. The CO<sub>2</sub> from higher concentration sources has the advantage that they may be directly applicable in the considered reaction scheme, thereby avoiding additional purifying steps. On the other hand, high purity CO<sub>2</sub> streams would avoid catalyst deactivation, avoid side reaction from impurities and lead to low energy consumption in utilities and separation sections. It should be noted that the savings being considered here is not in the effort to capture and purify but in the potential effort to sequestrate. In this way, the capture effort is the same and must be done but the sequestration effort is reduced by diverting some of the CO<sub>2</sub> for utilization efforts.

2.2.1. DMC from direct synthesis from  $CO_2$  and methanol For the direct use of  $CO_2$  to produce DMC, it has been reported that  $CO_2$  could react with methanol at critical temperature and critical pressure of  $CO_2$  as highlighted by Eq. (4) in Table 1

(Wu et al., 2006; Gu et al., 2008; Fang and Fujimoto, 1996). Under mild conditions, a basic catalyst (ZrO<sub>2</sub>–MgO), a promoter (methyl iodide) and butylene oxide as a chemical trap to shift the chemical equilibrium are needed (Eta et al., 2011).

This direct reaction route results in high atom-efficiency and avoids the use of toxic chemicals such as phosgene. However, industrial utilization of  $CO_2$  in the direct DMC synthesis is still a significant challenge because  $CO_2$  lies in a deep potential energy well of about -400 kJ/mol that requires a huge amount of energy for activation (Eta et al., 2011).

#### 2.2.2. DMC synthesis from urea (urea-route)

DMC can also be synthesized from CO<sub>2</sub> via urea (Sun et al., 2005). This process, proposed as a new alternative, integrates the synthesis of urea and DMC, where CO<sub>2</sub> is used as a chemical feedstock. The process starts with the reaction between CO<sub>2</sub> and ammonia in the urea synthesizer, which is operated at 165–190 °C and 135–205 bar (Sheppard and Yakobsin, 2003). The product stream is pumped to the purification section to remove water, excess CO<sub>2</sub> and ammonia from urea. Then, methanol is added for the alcoholysis reaction to produce DMC by using ionic liquid Et<sub>3</sub>NHCl–ZnCl<sub>2</sub> or emimBr–ZnCl<sub>2</sub> (Wang et al., 2009). It has been reported that the process involves a two-step reaction with methyl carbamate as the reaction intermediate as given by Eqs. (5)–(7) in Table 1 (Wang et al., 2009).

2.2.3. DMC synthesis from propylene carbonate (PC-route) One of the most promising ways to effectively utilize CO2 in DMC production is through cycloaddition of CO<sub>2</sub> to epoxides to form cyclic carbonates (Watile et al., 2012), which gives 100% atom efficiency. Propylene carbonate (PC) is synthesized from propylene oxide (PO) and  $CO_2$  at 130 °C and 20 bar (see Eq. (8) in Table 1). Subsequently, DMC is obtained through the transesterification of propylene carbonate and methanol (see Eq. (9) in Table 1). Various types of catalysts can be used such as basic quaternary ammonium ion exchange resins with hydroxide counter ions. Also, Verkade super bases can be effective at low catalyst loadings for the rapid transesterification of propylene carbonate with methanol under mild conditions and with high product selectivity (Williams et al., 2009; Li et al., 2006). For this reaction, propylene glycol which is a valuable chemical is obtained as a by-product.

2.2.4. DMC synthesis from ethylene carbonate (EC-route) Similar to the synthesis of propylene carbonate, ethylene carbonate (EC) is also produced from cycloaddition of  $CO_2$  to ethylene oxide (EO) (see Eq. (10) in Table 1). The reaction condition is relatively mild, i.e., 30 °C and 25 bar in immobilized ionic liquid on amorphous silica (Kim et al., 2010). Subsequent transesterification of ethylene carbonate with methanol produces DMC and ethylene glycol (see Eq. (11) in Table 1). It

# ARTICLE IN PRESS

CHEMICAL ENGINEERING RESEARCH AND DESIGN XXX (2014) XXX-XXX

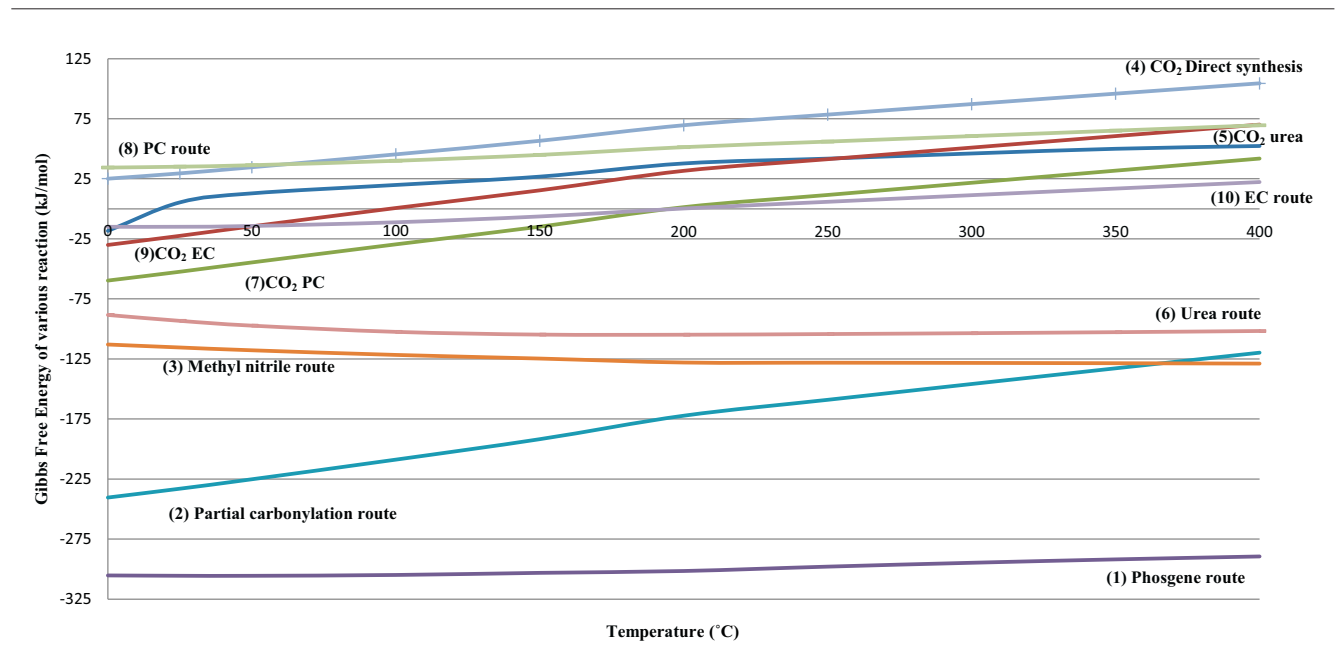


Fig. 2 – Gibbs free energy for different reactions involving DMC production: phosgene route (1), partial carbonylation route (2), methyl nitrile route (3), direct CO<sub>2</sub> synthesis route (4), urea route (6), propylene carbonate route (8) and ethylene carbonate route (10) and CO<sub>2</sub> coupling reaction to urea (5), propylene carbonate (7), and ethylene carbonate (9).

has been reported that the conversion of ethylene carbonate to DMC is 81.2% at  $250\,^{\circ}$ C and 90 bar. Various types of catalysts can be used, such as poly-4-vinyl pyridine as a novel base catalyst and DABCO-derived (1,4-diazobicyclo[2.2.2]octane) basic ionic liquids (Jagtap et al., 2008; Yang et al., 2010).

#### 3. Screening of process routes

The objective of this analysis is to preselect three of the most promising process alternatives as candidates for further analysis based on the thermodynamic feasibility of their synthesis routes together with environmental, safety and health concerns.

#### 3.1. Thermodynamic analysis

The reaction equilibrium for different reactions is calculated using Aspen Plus® software where all necessary model parameters are available. The feasibility of reactions is verified through the equilibrium reactor model in Aspen Plus®, which is based on Gibbs free energy minimization. The liquid activity calculation, the UNIQUAC model (Zhang et al., 2005; Holtbruegge et al., 2013) has been used and these values were cross-checked with the NRTL (Khoshtinat Nikoo and Amin, 2011) and PSRK (Müller et al., 2014; Smith et al., 2005) models. In Table 1 the calculated values of Gibbs free energy, the heat of reaction and the equilibrium constant at 25 °C are listed for all the reactions involved, while in Fig. 2, calculated values of the Gibbs free energy as a function of temperature and at standard pressure of 1 bar are highlighted. Based on these results, the CO<sub>2</sub> direct synthesis route is eliminated because of the positive Gibbs energy values, while the phosgene route and the methyl nitrile route are eliminated because of environmental, safety and health issues, even though the involved reactions have very favorable Gibbs free energy values. Their designs and performance are also well documented.

Considering the CO<sub>2</sub>-based processes, the urea-route, EC-route and PC-route are considered as at higher pressures they

are thermodynamically favorable. At the temperature of the reaction of urea synthesis (reaction (5)), the Gibbs energy is positive, as given in Table 1 and shown in Fig. 2. However, the Gibbs free energy for reaction (5) has been found to be negative at 160 bar and 200 °C, while the Gibbs free energy of  $\rm GO_2$  to urea synthesis is  $-70\,\rm kJ/mol$ , even though at 1 bar and 25 °C it is 21 kJ/mol (Zhang et al., 2005). The  $\rm GO_2$  coupling reactions to propylene carbonate (reaction (8)) and ethylene carbonate (reaction (10)) show slightly negative values of Gibbs free energy at lower temperatures, indicating that these two reactions are feasible for  $\rm GO_2$  utilization. This leaves for further analysis, the partial carbonylation route (BAYER process), the  $\rm GO_2$ -based urea-route, EC-route and PC-route.

#### 3.2. Sensitivity analysis

A sensitivity analysis is now performed for the three CO<sub>2</sub>-based DMC production routes to identify the reactor operating windows for these processes in terms of product (DMC) yield, temperature and pressure. The simulations are based on the equilibrium reactor model in Aspen Plus<sup>®</sup> and the calculated values are validated-compared with known experimental values. In these simulations, the feed compositions of urea–MeOH, EC–MeOH and PC–MeOH are kept constant at their stoichiometric ratios (1:2 for all reactions), while pressure (P) and temperature (T) are varied. The operating conditions for these synthesis routes are known to vary as follows:

- Urea route (Wang et al., 2009): 4–12 bar for pressure; 125–250 °C for temperature. A yield of 67.4% is reported for the reaction between urea and methanol using polyphosphoric acid as a catalyst at 8 bar and 150 °C (Wang et al., 2009).
- EC route (Watile et al., 2012; Kim et al., 2010; Feng et al., 2005): 1–15 bar for pressure; 25–250 °C for temperature. The yield is reported to be 75.3% for the reaction between ethylene carbonate and methanol using immobilized ionic liquids on MCM-41 (mesoporous molecular sieves) at 11.3 bar and 180 °C (Kim et al., 2010) while a value of 81.2% is reported

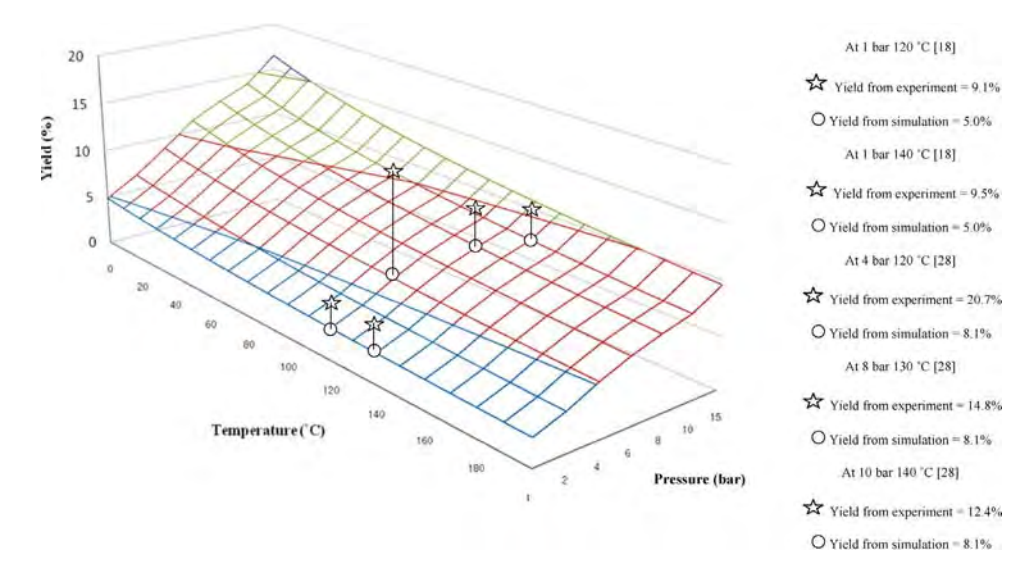


Fig. 3 - DMC yield from the propylene carbonate route (propylene carbonate:methanol = 1:2).

for the same reaction operated without any catalyst under supercritical conditions at 90 bar and 250 °C (Feng et al., 2005). This condition, however, has not considered in the current work.

PC route (Williams et al., 2009; Li et al., 2006; Wei et al., 2003): 1–15 bar for pressure; 0–200 °C for temperature. The low yields are confirmed by reported values for this route (Wei et al., 2003).

The calculated DMC yields are compared with known experimental values in Figs. 3–5, for the urea-route, the ECroute, and the PC-route, respectively.

From the calculated values as well as the known experimental values, it is clear that the yields of DMC from the urea-route and the EC-route are much higher than the PC-route. The highest yields of DMC are 78.7% for the urea-route and 78% for the EC-route, while for the PC-route, the yield is only 5–20%. Based on these results, the EC-route together with the urea-route is retained for further detailed analysis instead of the PC route.

Therefore, the urea-route and the EC-route are selected for further investigation and analysis together with the BAYER process. Also, these two CO<sub>2</sub>-based alternatives are interesting because others have also studied the production of DMC from the urea-route (Wang et al., 2009; Zhang et al., 2012) and from the EC-route (Kim et al., 2010; Jagtap et al., 2008; Yang et al., 2010; Feng et al., 2005; Lu et al., 2004) under different

conditions (kinetics and supercritical condition) and catalysts (chemical and ionic liquids).

#### 4. Performance evaluation

Because of the concerns on issues such as the depletion of natural resources, environmental-safety-health impacts, as well as sustainability of the chemical process, it is not enough to simply find the optimal chemical process converting given raw materials to specified products. It is necessary to also make the process sustainable. In this work, the well-known sustainability metrics (Azapagic, 2002; Carvalho et al., 2008) together with life-cycle assessment factors and some green chemistry indicators have been used. Three principal criteria, in addition to the process requirements have been selected for purposes of comparison. These are the energy consumption for unit product (at a specified purity), net CO2 emission, the atom efficiency and the life-cycle assessment factors (global warming potential, carbon footprint, measure of toxicity, etc.). Many industries and businesses these days have better awareness on the environment issues. Consequently, life cycle assessment has become a key factor for establishing more sustainable options in process design and synthesis. So, the final design in terms of a selected set of performance criteria, such as amount of raw material used per kg of product or the amount of energy used per kg of product, are compared for all feasible alternatives. The systematic methodology for

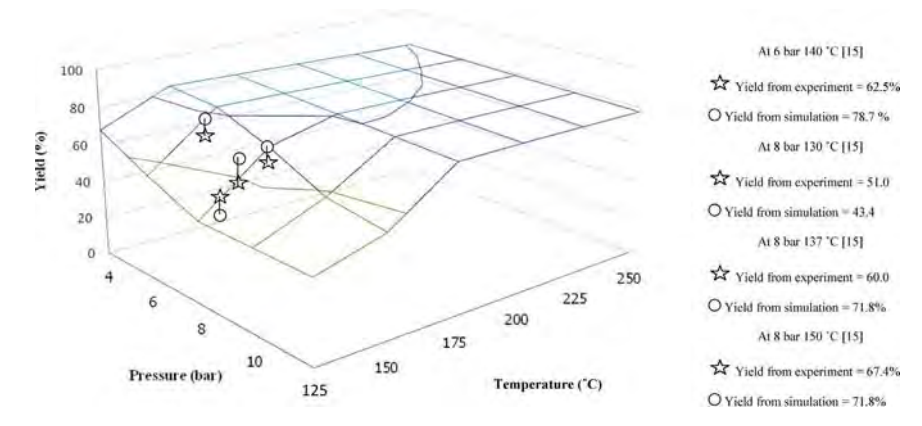


Fig. 4 - DMC yield from the urea route (urea:methanol = 1:2).

# ARTICLE IN PRESS

CHEMICAL ENGINEERING RESEARCH AND DESIGN XXX (2014) XXX-XXX

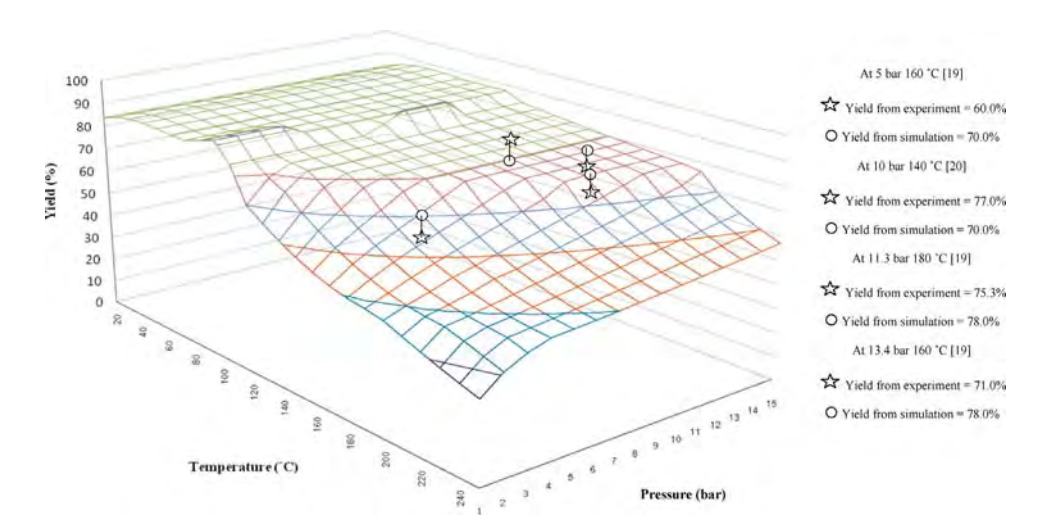


Fig. 5 - DMC yield from the ethylene carbonate route (ethylene carbonate:methanol = 1:2).

evaluating process alternatives for DMC production includes four key performance indicators based on the following criteria: energy consumption, net  $CO_2$  emission, atom efficiency and life cycle assessment.

#### 4.1. Methods and tools used

The work-flow (method) used to calculate the selected set of performance criteria is as follows:

Step-1: identify a process design for the selected process (it is assumed that a base case design is available for each process considered)

Step-2: perform the process simulation

Step-3: calculate the energy consumption, atom efficiency

Step-4: calculate the life-cycle assessment factors and the net CO<sub>2</sub> emission

Step-5: perform the overall analysis

#### 4.1.1. Process simulation

Steady state process simulation has been performed with Aspen Plus<sup>®</sup>. For the reactor, the Gibbs free energy based equilibrium model has been employed. For distillation columns, the RADFRAC model has been used. The details of the thermodynamic models used are given in the corresponding simulation results (see Section 4.2). The process simulation results include mass and energy balances for each process.

#### 4.1.2. Energy consumption

The energy consumptions in all equipment are calculated from the steady state simulation results and these are summed to obtain the net energy consumption (MJ/h) per unit mass of DMC product (kg/h). This is in accordance with the definitions of sustainability metrics (Azapagic, 2002; Carvalho et al., 2008). The reaction/separation ratio (R/S), defined here as the ratio between the energy consumption in reaction parts and that in separation parts of the process, is also considered as a performance indicator. Low R/S ratio is usually caused by reaction with low product yield, which consequently requires high energy in downstream separation processes.

#### 4.1.3. Atom efficiency

Atom efficiency is a criterion that considers efficiency of a reaction in terms of atoms of reacting substances that are

present in the desired product. The process that generates by-product or contains side-reaction is considered having low atom efficiency. For example, in urea synthesis according to Eq. (5) in Table 1, carbon atom in the feed stream is converted to urea, while only four atoms of hydrogen from the reactants are found in urea. Therefore, the atom efficiency of C atom is 78.7%, while that of H atom is only 24.7% because H atom was loss to form by-product water compound which reduce atom efficiency of urea synthesis reaction.

#### 4.1.4. Life cycle assessment

The issue of environmental impact is considered for the evaluation of the process alternatives. LCSoft (Piyarak, 2012; Kalakul et al., 2014), which is a computer aided tool for generation of LCA factors, has been used in this work. LCSoft performs the life cycle assessment, using US-EPA and IPCC emission factors to calculate the environmental impact for a given process. The performance evaluation of process alternatives are established in terms of carbon footprint (CF), which is the overall amount of carbon dioxide and other greenhouse gas emissions associated with 1kg of product. The carbon footprint is related to other indicators such as the global warming potential (GWP) in terms of kg of CO2 equivalent. From a health and safety points of view, indicators such as the human toxicity-carcinogenic (HTC) in terms of kg of benzene equivalent, human toxicity potential by exposure both dermal and inhalation (HTPE) in unit of time-weighted averages (1/TWA) are also considered (Kalakul et al., 2014).

#### 4.1.5. Net $CO_2$ emission

Since one of the main goals in this work is to identify DMC production processes that have low impact on environments,  $CO_2$  emissions from all associated processes for each synthesis route are calculated and compared. That is, the  $CO_2$  created (or used) from the reactions is considered together with those generated (emitted) because of the use of energy. Therefore, in this work, it is assumed that all energy utilized as heat energy in all unit operations is obtained from complete combustion of methane, which releases 1 mol of  $CO_2$  per 1 mol of methane combustion and provides a heating value of 889 MJ/kmol. Therefore, the total  $CO_2$  emission in each DMC processing route is represented in terms of  $CO_2$  emission per one unit mass of DMC product (kg of  $CO_2$ / kg of DMC).

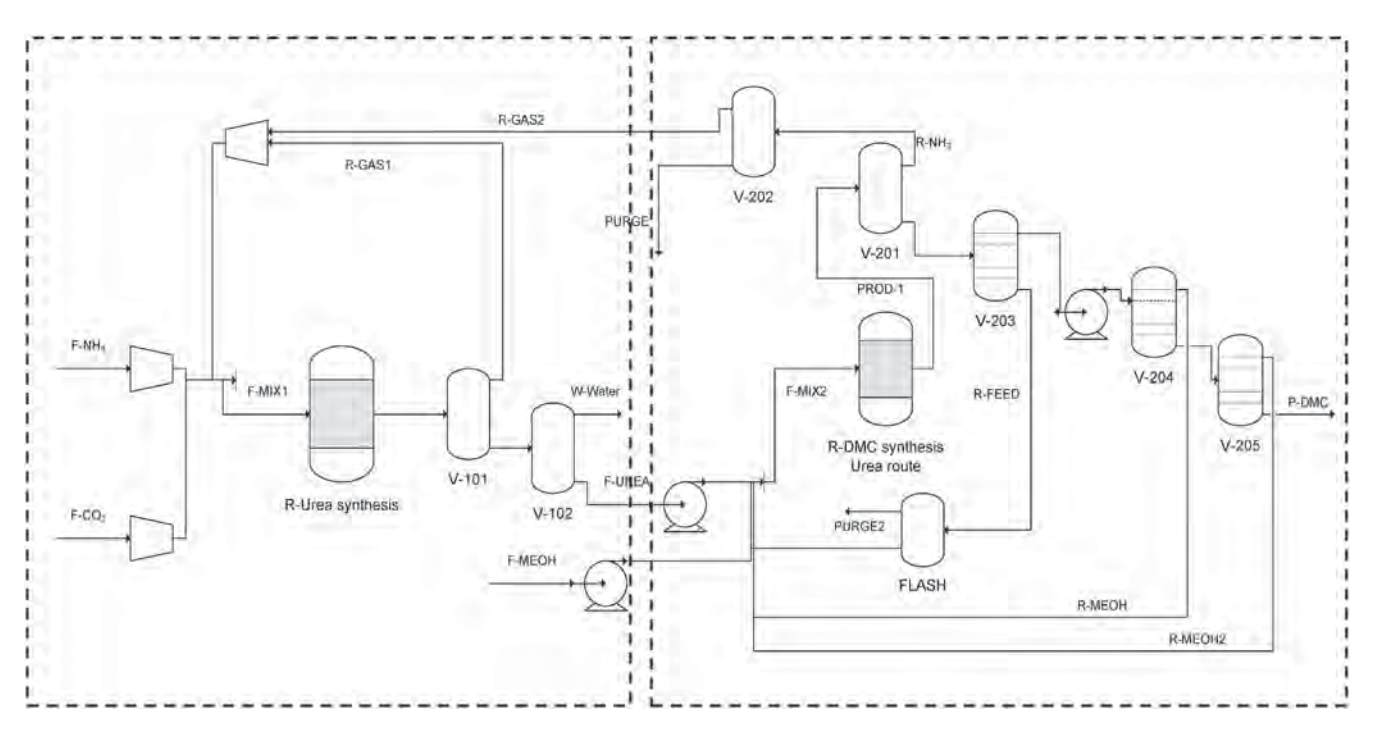


Fig. 6 - Process flow diagram for the urea route for dimethyl carbonate production.

#### 4.2. Process simulation and design analysis

Here, the two CO<sub>2</sub>-based processes, that is, the urea-route and the EC-route are evaluated in terms of the selected performance criteria and compared with the commercial BAYER process. The design of the BAYER process is taken from the available data (Kricsfalussy et al., 1996).

#### 4.2.1. Urea route

The process flowsheet for this process is highlighted in Fig. 6, where it is shown that the process is divided into two sections: (1) the urea synthesis section and (2) the DMC synthesis section. The extended electrolytic UNIQUAC equation has been used to describe the non-ideality of liquid phase of  $NH_3-CO_2-H_2O$ —urea system under high pressure and high temperature, and the perturbed-hard-sphere (PHS) equation of state has been used to predict the vapor fugacity coefficients have been used to represent the VLE of  $CO_2-NH_3$ —urea system (Zhang et al., 2005).

Section 1: Urea is synthesized from ammonia and carbon dioxide in the first reactor (R-Urea synthesis). Similar to the analysis of reaction (6) (see Table 1) and Fig. 4, the conditions of operation for the synthesis of urea from  $CO_2$  has been investigated for ratio of 4.25:1 for  $NH_3:CO_2$ . The calculated urea yields at equilibrium are shown in Fig. 7. It can be noted that it is possible to achieve a yield of 73.8% when operating at P=180 bar and  $T=160\,^{\circ}C$ . This conclusion agrees well with known experimental data (yield=70%) reported by Zhang et al. (2005). The reaction product stream flows into separator V-101 for recovery and recycle of the unreacted raw materials. The urea stream is sent to separator V-102 to purify urea by eliminating water.

Section 2: In this section, the urea and methanol react to produce dimethyl carbonate. An equilibrium reaction is assumed. The energy consumption and yield of DMC are the key performance parameters for evaluation of optimum process condition. The reaction temperature slightly affects the yield of DMC, and so it is fixed at  $140\,^{\circ}\text{C}$  (see Fig. 4).

The operating pressure is varied between 1 and 20 bar and the pressure corresponding to the minimum energy usage is selected which correlate well with known experimental data (Sun et al., 2005). The results from process simulation, which confirms the reported experimental data, are shown in Fig. 8, where the yield of DMC and the corresponding energy usage are plotted as a function of pressure.

A feed molar ratio of MeOH:urea = 8 in the reactor (R-DMC) has been reported (Sun et al., 2005). The effect of methanol/urea molar ratio on the DMC yield has been studied by increasing it from 8 to 14. If the molar ratio of methanol/urea is lower than 8, the urea and MC (methyl carbamate) concentration is higher, the side reactions (the reactions of MeOH with urea) significantly reduces the DMC formation rate. Higher methanol/urea molar ratio therefore is desirable in order to increase the DMC yield. However, when the molar ratio of methanol/urea is higher than 14, the DMC yield begins to fall (Sun et al., 2005). Hence, a methanol/urea molar ratio of 8 was selected for this work.

The product stream (PROD-1) contains DMC, ammonia, unreacted of urea, methanol and small amount of methyl carbamate is sent to the V-201 to flash  $NH_3$  gas and then the bottom stream is sent to V-203 to separate the unreacted urea. The effluent distillate stream from V-203 contains 12,435 kg/h of MeOH and 4366 kg/h of DMC and sent to a series of pressurized distillation column (V-204 and V-205). The azeotropic mixture of DMC and MeOH is pressure dependent, and therefore, distillation columns V-204 and V-205 are used in a pressure-swing configuration with the pressure of V-204 and V-205 fixed at 30 and 20, respectively. The first column (V-204) is operated at 30 bar and the distillate (MeOH) stream is recycled (R-MeOH; 12,279 kg/h of MeOH and 478 kg/h of DMC) to the reaction section and the bottom stream from V-204 (156 kg/h of MeOH and 3887 kg/h of DMC) is sent to the V-205 for purifying the DMC product. The V-205 column operates at 20 bar and gives a DMC product of 99.7 wt% purity as bottom stream (P-DMC; 3.51 kg/h of MeOH and 3773 kg/h of DMC),

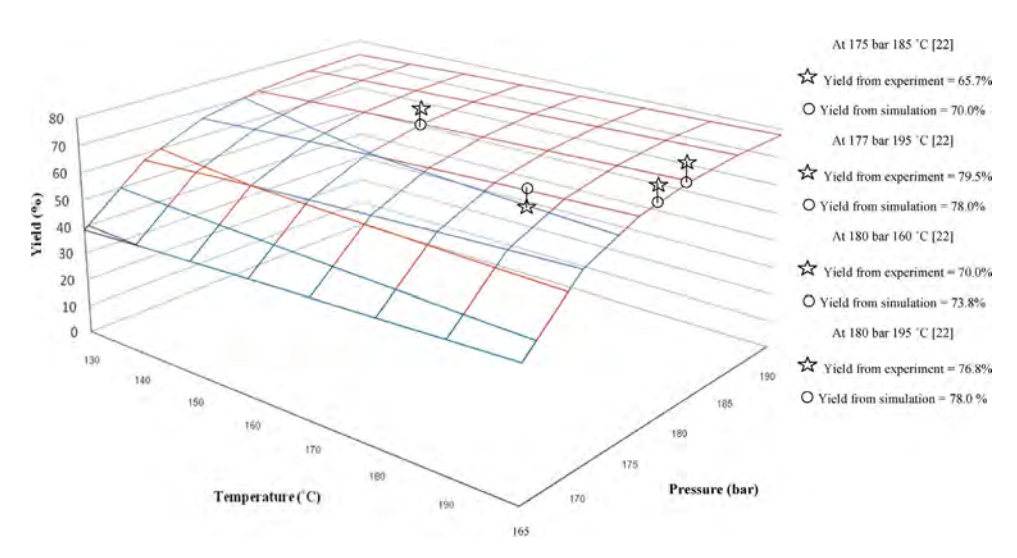


Fig. 7 - Sensitivity analysis of urea production from CO<sub>2</sub> and NH<sub>3</sub>.

while the distillate stream (R-MEOH2; 152 kg/h of MeOH and 114 kg/h of DMC) is recycled to the DMC synthesis section.

The important variables from the process simulation of the DMC production process through the urea-route are given in Table 2.

#### 4.2.2. Ethylene carbonate route

The base case design for DMC production based on the ECroute is illustrated in Fig. 9. The PSRK model (Müller et al., 2014; Smith et al., 2005) is used for the calculation of vapor-liquid equilibrium, since for a system consisting of methanol, ethylene carbonate and ethylene glycol, use of this model has been reported by others (Gmehling et al., 2012). This process is also divided into two sections: (1) the ethylene carbonate synthesis section and (2) the DMC synthesis section.

Section 1: Ethylene carbonate is synthesized from ethylene oxide and carbon dioxide in the first reactor (R-EC synthesis). Similar to the analysis of reaction (10) (see Table 1) and Fig. 4, the conditions of operation for the synthesis of EC from  $\rm CO_2$  has been investigated for ratio of 2.4 for  $\rm CO_2$ :EO. The calculated EC yields at equilibrium are shown in Fig. 10. It can be noted that it is possible to achieve a yield of 84.73% when

operating at P=125 bar and  $T=110\,^{\circ}$ C, which agrees well with experimental data (85.6%) reported by Lu et al. (2004). The reaction product stream flows into separator V-101 for recovery and recycle of the unreacted raw materials. The ethylene carbonate stream is sent to DMC synthesis section through a pump.

Section 2: In this section, the ethylene carbonate and methanol are reacted to produce dimethyl carbonate. An equilibrium reaction is assumed. The energy consumption and yield of DMC are the key performance parameters with respect to selection of the reactor operating condition. The reaction temperature slightly affects the yield of DMC from 140 °C to 170 °C, and so it is fixed at 160 °C (see Fig. 5). The operating pressure is varied between 1 and 20 bar (see Fig. 11) and the pressure corresponding to the minimum energy usage is selected, matching the reported data (Kim et al., 2010). In Fig. 11, the yield of DMC and the corresponding energy usage are plotted as a function of pressure.

A feed molar ratio of MeOH:EC = 2.3 is sent to R-DMC, where a yield of DMC that matches with the reported value (Kim et al., 2010) is obtained. The product stream (PROD-1) containing DMC, ethylene glycol (EG), unreacted of EC and MeOH is

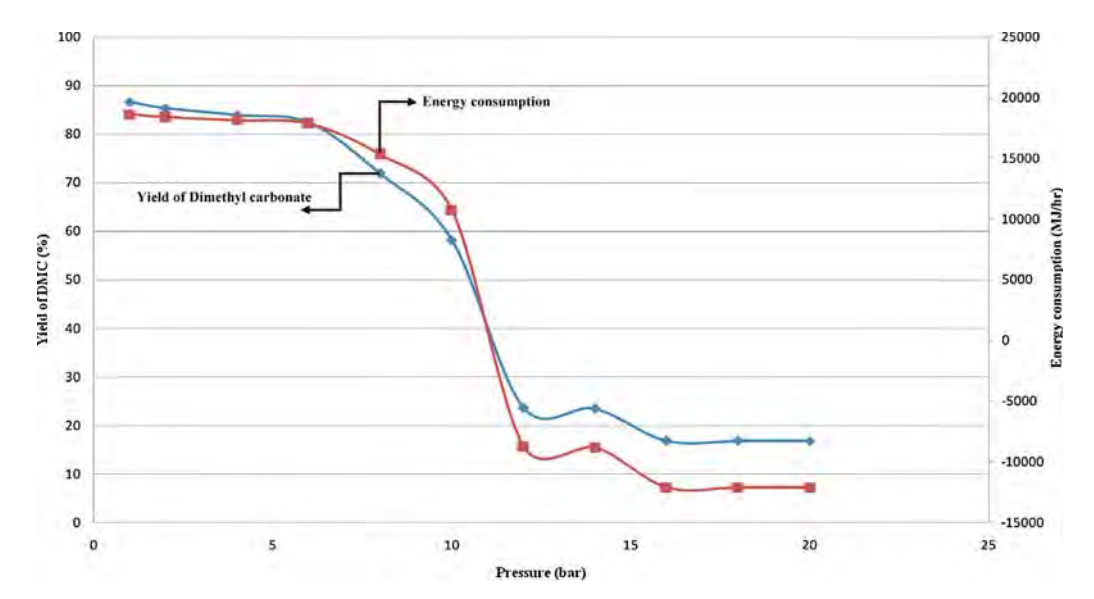


Fig. 8 - Effect of pressure on DMC yield and energy consumption in urea transesterification process.

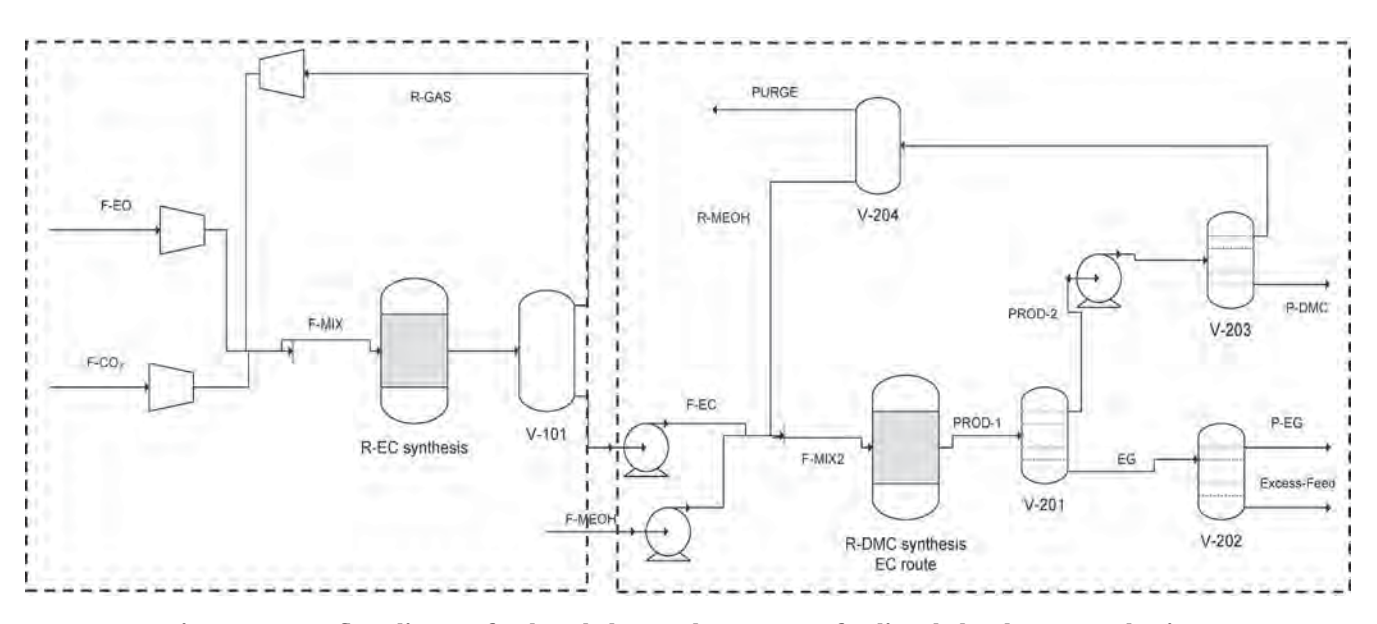


Fig. 9 - Process flow diagram for the ethylene carbonate route for dimethyl carbonate production.

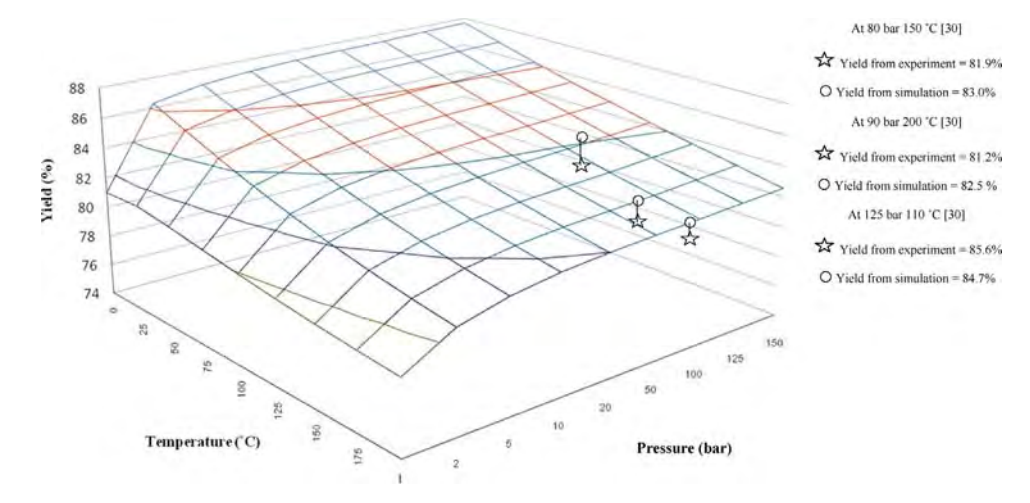


Fig. 10 - Sensitivity analysis of ethylene carbonate production from CO2 and ethylene oxide.

separated using the distillation column (V-201), operating at P=10 bar. The distillate stream of V-201 (PROD-2) containing 1807 kg/h of MeOH and 4215 kg/h of DMC is sent to pressurized distillation column (V-203) from where, MeOH is recycle and

the DMC product of specified purity is obtained. The stream R-MeOH, after the purge (V-204) contains 1795 kg/h of MeOH and 258 kg/h of DMC and the bottom stream of V-203 contains 3956 kg/h of DMC at 99.2 wt% purity as product. The ethylene

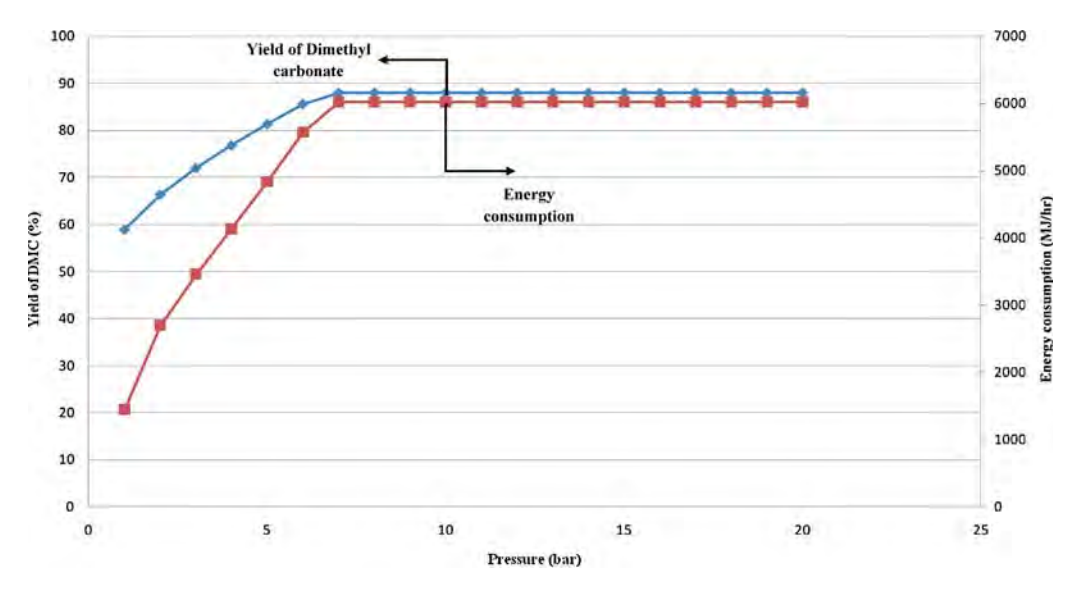


Fig. 11 - Effect of pressure on DMC yield and energy consumption in ethylene carbonate transesterification process.

10

# ARTICLE IN PRESS

CHEMICAL ENGINEERING RESEARCH AND DESIGN XXX (2014) XXX-XXX

Table 2 – Mass balance simulation results for the production of DMC thr	e simulation re	esults for the pro	duction of DMC		ough the urea transesterific	cation process and CO <sub>2</sub> conversion	nd CO <sub>2</sub> conversi	on.		
	F-MIX1	F-MIX2	F-urea	PROD-1	R-MIX	W-water	R-MEOH	R-MEOH2	R-Feed	P-DMC
Temperature (°C)	304.8	133.4	191.4	140	129	65	184.9	167.5	80.9	221.7
Pressure (bar)	180	<b>∞</b>	1	<b>∞</b>	∞	1	30	20	1	20
Vapor fraction	1	0.174	0	0.929	0.22	0	0	0	0	0
Mole flow (kmol/h)	420.95	581.66	63	581.66	6.03	74	388.63	6.03	40	42
Mass flow (kg/h)	9343.85	20,783.44	3783.5	20,783.44	266.98	1380.229	12,759.76	266.98	1811.72	3776.93
Volume flow $(M^3/h)$	1264.26	451.74	3.31	2322.35	5.82	1.52	22.91	0.39	1.76	5.37
Enthalpy (MJ/h)	-42,467.6	-136,649.4	-20,166.8	-121,168.6	-1757.2	-19,120.8	-86.0	-1757.2	-11,129.4	-23,806.9
Mass flow (kg/h)										
CO <sub>2</sub>	3520.78	0	0		0	0.062	0	0	0	0
$NH_3$	5790.39	1.43	0	1510.35	0	142.16	1.43	0	0	0
Urea	0.107	3783.49	3783.49	1122.28	0	90.09	0	0	1122.28	0
Water	3.07	0.002	0.002	0.002	0	1152.97	0	0	0.002	0
МЕОН	22.76	16,405.59	0	13,566.62	152.64	18.58	12,279.69	152.64	80.629	3.51
DMC	6.73	592.92	0	4582.37	114.33	6.37	478.63	114.33	8.55	3773.42
Methyl carbamate	0	0	0	1.80	0	0	0	0	1.80	0

glycol stream which is separated as bottom stream in distillation column (V-201) was sent to the distillation column (V-202) where the pressure is 10 bar. Here, 2793 kg/h of EG is obtained as distillate stream at 99.99% purity (see Fig. 9).

The important variables from mass and energy balance simulations of the DMC production process integrated with the EC plant are given in Table 3.

#### 4.2.3. BAYER process

The simulation of the BAYER process is based on the information provided in the patent (Kricsfalussy et al., 1996). The process flow diagram is shown in Fig. 12. The UNIQUAC model (Gmehling et al., 2012) is used for the vapor-liquid equilibrium calculations. The partial carbonylation reaction of CO and MeOH is carried out in a reactive-distillation unit (Bhatia et al., 2007; Simasatitkul et al., 2013). Here, a gas-phase exothermic reaction is taking place where the excess reactant is removed, the equilibrium conversion shifted and azeotrope formations are avoided. The reaction temperature is known to vary between 120 °C and 300 °C, but values between 120 °C and 180 °C are preferred (Kricsfalussy et al., 1996). The reaction is carried out at atmospheric pressure. However, to achieve a sufficiently high reaction rate, it is advantageous to carry out the reaction at a higher pressure, preferably between 10 and 50 bar, with the optimal between 12 and 22 bar. Water, which is formed from the reaction, is removed from the system, optionally after distilling off organics such as the DMC. In the zone of the reactive-distillation unit, molten salts, methanol and DMC are distilled off, together with small amounts of volatile by-products such as, formaldehyde and dimethyl acetal.

Methanol introduced into the reaction zone contains relatively large amounts of DMC which, for example, has a composition corresponding to the MeOH/DMC azeotrope. It is possible to obtain a higher yield of DMC by shifting the equilibrium through the addition of excess MeOH. The BAYER process has also been simulated through Aspen Plus® using the reported design (Kricsfalussy et al., 1996). The simulation results are given in Table 4 and agree well with those reported in the patent, in terms of DMC yield of 99.5% and the process stream compositions.

#### 4.3. Comparison of DMC production alternatives

#### 4.3.1. Energy consumption

The simulated energy consumption in the DMC production process, for the urea-route this is found to be 59.36 MJ/kg DMC. The simulated energy consumption in the EC-route is found to be 9.13 MJ/kg DMC. The energy consumption in the BAYER process is found to be 10.55 MJ/kg DMC. In terms of energy consumption, DMC synthesis from urea-route is found to have high energy consumption due to the large molar ratio of MeOH:urea that is employed to shift the reaction equilibrium in the R-DMC reactor and the energy consumption in the downstream separation of the azeotrope mixture of MeOH/DMC.

#### 4.3.2. Atom efficiency

Table 5 gives details of the atom efficiency calculations for the three process alternatives. Since the DMC production section is common to all three process alternatives, only this section is compared in terms of atom efficiency, energy requirement and net  $\text{CO}_2$  emission.

Considering atom efficiency (Table 5) of the two CO<sub>2</sub>-based processes, it is found that the atom efficiency of the EC-route

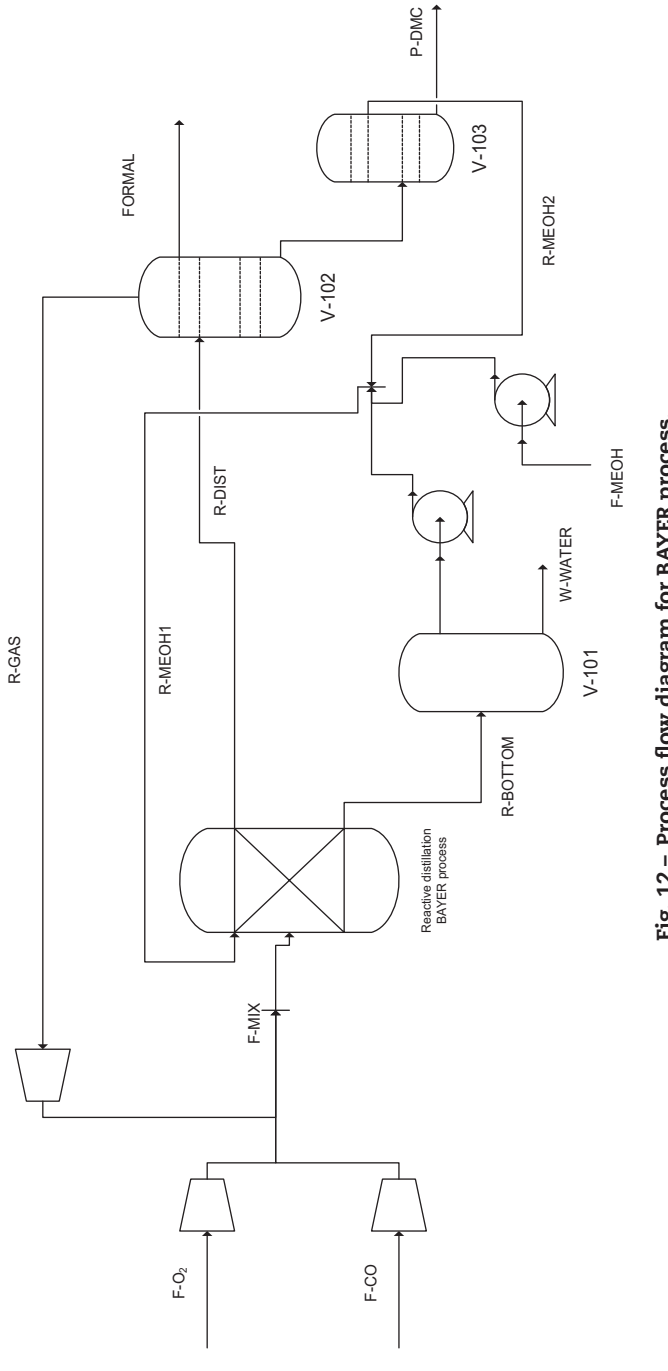


Fig. 12 - Process flow diagram for BAYER process.

Table 3 – Mass balance simulation results for the production of DMC th	ice simulation r	esults for the p	production of D	MC through the	ethylene carbona	ate transesterific	ation process an	nd CO <sub>2</sub> conversion	on.	
	F-MIX	F-EC	F-MIX2	PROD-1	PROD-2	EG	P-EG	P-DMC	Excess feed	R-MEOH
Temperature (°C)	588.7	248	154.9	160	141.2	306.1	294.3	220.3	353	165.9
Pressure (bar)	125.0	1	10	10	10	10	10	20	10	20
Vapor fraction	1	0	0.185	0	0	0	0	0	0	0
Mole flow (kmol/h)	260.98	65	215	168.2	103.2	65	44	44.3	21	58.9
Mass flow (kg/h)	11,708.70	5724.09	10,530.42	10,530.42	6022.86	4507.54	2731.01	3968.90	1776.53	2053.96
Volume flow $(M^3/h)$	149.60	5.19	151.90	11.80	7.60	5.15	3.29	5.62	1.89	3.35
Enthalpy (MJ/h)	-68,743.1	-34,601.6	-67,864.4	-69,789.1	-40,000.0	-28,451.2	-17,949.3	-25,020.3	-10,376.3	-13,974.56
Mass flow (kg/h)										
CO <sub>2</sub>	7921.76	0	0	0	0	0	0	0	0	0
Ethylene oxide	3348.04	0	0	0	0	0	0	0	0	0
Ethylene carbonate	438.90	5724.09	5724.09	1602.74	0	1602.74	0.003	0	1602.74	0
MEOH	0	0	4806.32	1807.17	1807.17	0	0	11.92	0	1795.25
DMC	0	0	0	4215.69	4215.68	0	0	3956.97	0	258.71
Ethylene glycol	0	0	0	2904.80	0	2904.80	2731.0	0	173.79	0

Table 4 – Mass balance simulation results for the production of DMC	e simulation result	ts for the produc	tion of DMC thre	ough the BAYER pr	ocess.				
	F-MIX	$I-CO_2$	PURGE	R-bottom	R-DIST	R-MEOH1	W-water	P-formal	P-DMC
Temperature (°C)	401.90	25	25	150	150	35.8	98.5	25	183.3
Pressure (bar)	20	1	10	20	20	20	₽	10	10
Vapor fraction	1	1	1	0	0.93	0	0	0	0
Mole flow (kmol/h)	187.35	10.60	11.66	45.29	169.56	95.90	44.38	3.15	43
Mass flow (kg/h)	7148.26	466.65	493.67	853.34	9502.11	3242.50	828.95	179.64	3873.39
Volume flow $(M^3/h)$	525.75	262.85	28.90	0.99	281.27	4.05	06:0	0.2	4.90
Enthalpy (MJ/h)	-43,095.0	-4142.1	-3932.96	-12,593.8	-66,985.8	-23,890.6	-12,510.16	-1129.6	-24,811.1
Mass flow (kg/h)									
00	1267.30	0	0.76	0	7.60	0	0	0.003	0
02	1193.89	0	50.88	0	509.05	0	0	0.25	0
CO <sub>2</sub>	4444.99	466.65	442.03	0	4444.99	0	0	24.61	0
Water	0	0	0	802.97	0	12.85	790.11	0	
МЕОН	35.94	0	0	7.92	71.34	2951.06	4.74	35.39	0
DMC	14.67	0	0	42.44	4202.21	278.58	34.09	43.92	3873.39
Formal	191.45	0	0		266.90	0.009		75.44	0

Please cite this article in press as: Kongpanna, P., et al., Techno-economic evaluation of different  $CO_2$ -based processes for dimethyl carbonate production. Chem. Eng. Res. Des. (2014), http://dx.doi.org/10.1016/j.cherd.2014.07.013

# **ARTICLE IN PRESS**

CHEMICAL ENGINEERING RESEARCH AND DESIGN XXX (2014) XXX-XXX

Table 5 – Ator	n efficie	ncy analys	is of various	s DMC pro	duction pr	ocesses.			
Process		Atom of su	ıbstance in f	feed	A	Atom of su	bstance in	product	Atom efficiency (%)
	C	Н	0	N	C	Н	0	N	(C,H,O,N)
BAYER	137	368	148.5	0	129	258	129	0	(94.1, 70.0, 86.8, 0)
Urea-DMC									
Urea	80	1020	160	340	63	252	63	126	(78.7, 24.7, 39.3, 37.0)
DMC and NH <sub>3</sub>	575	2300	575	126	125.7	517.2	125.7	88.6	(21.8, 22.4, 21.8, 70.3)
EC-DMC									
EC	332	304	436	0	195	260	195	0	(58.7, 85.5, 44.7, 0)
DMC and EG	345	860	345	0	219.7	527.4	219.7	0	(63.6, 61.3, 63.6, 0)

Performance evaluation	Ethylene carbonate route	Urea route	BAYER process
Production evaluation			
DMC production rate	3968.90	3776.93	3873.39
DMC purity (%)	99.2	99.7	100.0
By-product production rate	2731.0	0	0
By-product purity (%)	99.9	0	0
Energy evaluation			
Energy usage in DMC section (MJ/h)			
Energy usage in reaction unit	1916.0	15,510.0	12,366.0
Energy usage in separation units	34,308.0	208,509.0	25,734.0
Energy usage in utilities units	42.59	133.33	2787.0
Reaction: separation ratio	0.055	0.074	0.48
Energy usage in CO <sub>2</sub> utilization section (MJ/h)			
Energy usage in reaction unit	15,748.0	7794.0	0
Energy usage in separation units	56,588.0	35,212.0	0
Energy usage in utilities units	7911.0	5122.0	0
Energy efficiency			
Energy usage in DMC production section (MJ/h)	36,267.0	224,153.0	40,888.0
Energy usage per kg of product (energy usage in DMC production section MJ/kg of DMC)	9.13	59.36	10.55
Total kg of CO <sub>2</sub> emission in DMC production section (referred to CH <sub>4</sub> combustion to provide energy 889 MJ/kmol of CH <sub>4</sub> )	1794.0	11,094.0	2023.0
CO <sub>2</sub> emission per one unit of DMC (kg/kg)	0.452	2.938	0.522
Total energy consumption (MJ/h)	116,516.0	272,283.0	40,888.0

has higher values(C: 63.6, H: 61.3, O: 63.6, N: 0) than the urearoute (C: 21.8, H: 22.4, O: 21.8, N: 70.3) because ethylene glycol is considered as a valuable by-product from the petrochemical industry. Also, since the urea-route requires high feed molar ratio, its atom efficiency of the process is reduced. Moreover, in

the urea synthesis step, water is generated as by-product and need to be removed from the process. This is done through V-102, but leads to loss of urea in the W-WATER stream. For BAYER process, which uses partial carbonylation of CO, the formation of water is considered as waste and needs further

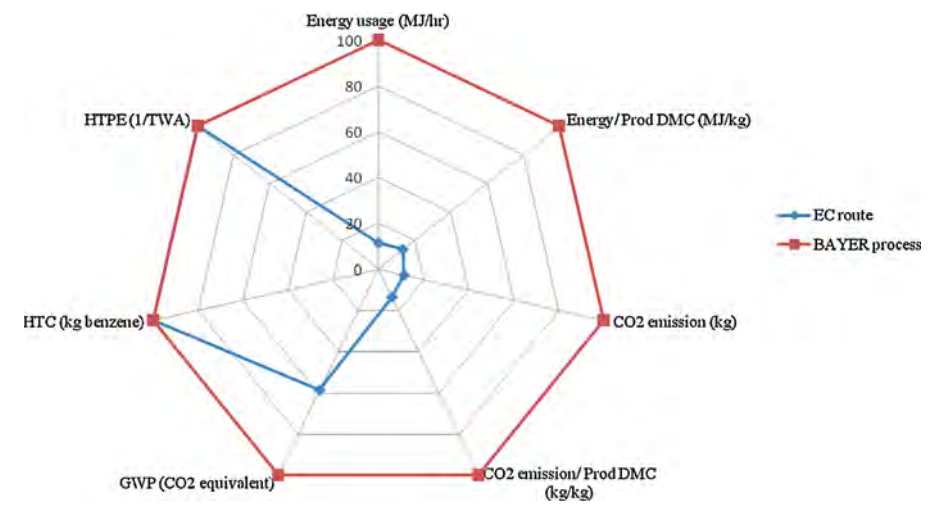


Fig. 13 - Percent improvement in Performance indicators of important issues.

Please cite this article in press as: Kongpanna, P., et al., Techno-economic evaluation of different  $CO_2$ -based processes for dimethyl carbonate production. Chem. Eng. Res. Des. (2014), http://dx.doi.org/10.1016/j.cherd.2014.07.013

14

treatment. The atom efficiency of this process is higher than the CO<sub>2</sub> based processes: (C: 94.1, H: 70.0, O: 86.8, N: 0).

#### 4.3.3. Net CO2 emission

Table 6 compares the process alternatives in terms of energy consumption and the net CO2 emission together with information on production rates, product purity and break-down of energy usage in different unit-operations in the process flowsheet. In terms of energy consumption per one unit of product, the DMC production section in the EC-route gives the lowest value (9.13 MJ/kg) compared to the BAYER process (10.55 MJ/kg) and the urea-route (59.36 MJ/kg). The high energy consumption in DMC production from urea-route is due to the excessive amount of methanol in the reaction-loop (as explained above). Comparison of the reaction and separation (R/S) ratios for the EC-route (0.055) and the urea-route (0.074) indicate that more energy is used in the separation section than in the reaction section due to recycle of large amounts of unreacted raw materials because of the low reaction conversion. The issue of CO2 utilization in DMC production indicates that 1 mol of CO2 is utilized for 1 mol of DMC and these processes generate CO2 from utilities usage. In this work, it is assumed that captured CO2 is pure and available on-site. The net amount of CO2 emission is calculated on the basis of total CO2 available in the feed stream (F-MIX = 7921 kg/h:180 kmol/h). The CO<sub>2</sub> needed to produce ethylene carbonate as the intermediate is 5724 kg/h (65 kmol/h). This means that 2860 kg/h (65 kmol/h) of CO2 is used for conversion to ethylene carbonate, which is then used to make 3968 kg/h (44 kmol/h) of DMC. The amount of CO<sub>2</sub> generated in overall process by utilities usage is 5766 kg/h (131 kmol/h). This indicates that this process actually reduces the CO2 emission to atmosphere through utilization as raw material by 2860 kg/h (65 kmol/h). This means that the net CO<sub>2</sub> emission is 2906 kg/h instead of 5766 kg/h.

Another issue for use as measure for identifying a more sustainable process is the net CO2 emission per one unit of product. The EC-route indicates the lowest CO2 emission (0.452 kg of CO<sub>2</sub>/kg DMC), followed by the BAYER process (0.522 kg of CO<sub>2</sub>/kg DMC) and then the urea-route (2.938 kg of CO<sub>2</sub>/kg DMC). Considering the other important issues of environmental concern, it is found that the EC-route is less harmful to the environment, since there is a net reduction on the CO<sub>2</sub> emission (as CO<sub>2</sub> is used as a raw material). The net CO<sub>2</sub> emission of DMC production process by EC-route is thereby improved by 11.4% and global warming potential (GWP) is improved by 58.6% when compared to the BAYER process.

#### 4.3.4. LCA factors

The human toxicity by exposure and carcinogenic compound emission (HTC) and human toxicity potential by exposure both dermal and inhalation (HTPE) of EC route is reduced by 99.9% because BAYER process uses CO which is considered as a toxic and hazardous chemical. These results are shown through a radar-chart in Fig. 13 where the BAYER process forms the boundary of the radar and the EC-route falls inside the radar for all criteria considered.

#### Conclusion 5.

Different processes for DMC production based on CO2 utilization have been investigated. The processes include the direct route of reacting CO2 with methanol and indirect routes of converting CO2 with ammonia, ethylene oxide and propylene

oxide to urea, ethylene carbonate and propylene carbonate, respectively, and then further reacting them with methanol to DMC. Although the values of Gibbs free energy indicate advantage for the conventional processes (phosgene route, carbonylation of CO route and methyl nitrile route) against all of the CO<sub>2</sub>-based processes, they become unattractive in regards to safety, toxicity and environment. The direct synthesis of methanol and carbon dioxide and the propylene carbonate routes are less promising than the other CO<sub>2</sub>-based routes due to their higher Gibbs free energy values and lower DMC yields. By evaluating the three process alternatives of DMC production, that is, the ethylene carbonate route, the urea route and the BAYER process in terms of atom efficiency, energy consumption and net CO<sub>2</sub> emission, it is found that the ethylene carbonate route is the most promising process alternative for DMC production. Note that, however, the three processes considered in detail as well as those not considered may be further improved through process intensification and/or change of process conditions. The analysis given in this work is valid for the reported base case designs. Other important issues, such as catalyst performance improvement to achieve the higher yield, activity, selectivity and stability leading to easier downstream separation have also not been considered. Also, new reactor design options, such as multi-functional reactor for reduced energy consumption and improved product yield by shifting the reaction equilibrium need to be further investigated. Moreover, improve the key performance indicator which can handle and use systematic methodology to achieve more sustainable process design. Finally, in this work, the cost for CO<sub>2</sub> recovery and purification unit has not been considered. A more complete analysis could include the CO2 source as well as a complete reaction tree together with options to further improve alternatives through opportunities for process intensification.

#### Acknowledgments

The financial support from The Thailand Research Fund is gratefully acknowledged. In addition, the first and the last authors would like to acknowledge the Ph.D. scholarship from Dussadeepipat Scholarship, Chulalongkorn University and the stay as a visiting researcher at the CAPEC-PROCESS Center at DTU Chemical Engineering.

#### References

Aresta, M., Dibenedetto, A., Angelini, A., 2013. The changing paradigm in CO<sub>2</sub> utilization. J. CO<sub>2</sub> Util. 3/4, 65–73.

Azapagic, A., 2002. Sustainable Development Progress Metrics. IChemE Sustainable Development Working Group, IChemE, Rugby, UK.

Bhatia, S., Mohamed, A.R., Ahmad, A.L., Chin, S.Y., 2007. Production of isopropyl palmitate in a catalytic distillation column: comparison between experimental and simulation studies. Comput. Chem. Eng. 31, 1187-1198.

Carvalho, A., Gani, R., Matos, H., 2008. Design of sustainable chemical processes: systematic retrofit analysis generation and evaluation of alternatives. Process Saf. Environ. Prot. 86,

Centi, G., Perathoner, S., 2009. Opportunities and prospects in the chemical recycling of carbon dioxide to fuels. Catal. Today 148, 191-205.

Eta, V., Mäki-Arvela, P., Wärnå, J., Salmi, T., Mikkola, J.-P., Murzin, D.Yu., 2011. Kinetics of dimethyl carbonate synthesis from methanol and carbon dioxide over ZrO2-MgO catalyst in the

- presence of butylene oxide as additive. Appl. Catal. A: Gen. 404. 39–46.
- Fang, S., Fujimoto, K., 1996. Direct synthesis of dimethyl carbonate from carbon dioxide and methanol catalyzed by base. Appl. Catal. A: Gen. 142, L1–L3.
- Feng, X.J., LI, X.G., He, R., Zhou, H., 2005. A new process for synthesis of dimethyl carbonate from ethylene carbonate and methanol without any catalyst under supercritical conditions. Chin. Chem. Lett. 16 (6), 767–770.
- Gmehling, J., Kolbe, B., Kleiber, M., 2012. Chemical Thermodynamics for Process Simulation., ISBN 978-3-527-31277-1.
- Gu, X.C., Qin, Z.F., Wang, G.F., Wang, J.G., 2008. Critical temperatures and pressures of reacting mixture in synthesis of dimethyl carbonate with methanol and carbon dioxide. Chin. Chem. Lett. 19, 249–252.
- Holtbruegge, J., Heile, S., Lutze, P., Gorak, A., 2013. Synthesis of dimethyl carbonate and propylene glycol in a pilot-scale reactive distillation column: experimental investigation, modeling and process analysis. Chem. Eng. J. 234, 448–463.
- Jagtap, S.R., Bhor, M.D., Bhanage, B.M., 2008. Synthesis of dimethyl carbonate via transesterification of ethylene carbonate with methanol using poly-4-vinyl pyridine as a novel base catalyst. Catal. Commun. 9, 1928–1931.
- Kalakul, S., Malakul, P., Siemanond, K., Gani, R., 2014. Integrated of life cycle assessment software with tools for economic and sustainability analyses and process simulation for sustainable process design. J. Clean. Prod. 71, 98–109.
- Khoshtinat Nikoo, M., Amin, N.A.S., 2011. Thermodynamic analysis of carbon dioxide reforming of methane in view of solid carbon formation. Fuel Process. Technol. 92, 678–691.
- Kim, D.-W., Kim, C.-W., Koh, J.-C., Park, D.-W., 2010. Synthesis of dimethyl carbonate from ethylene carbonate and methanol using immobilized ionic liquid on amorphous silica. J. Ind. Eng. Chem. 16, 474–478.
- Kricsfalussy, Z., Steude, H., Waldmann, H., Hallenberger, K., Wagner, W., Traenckner, H.-J., 1996. Process for preparing dimethyl carbonate. US Patent 5,523,452 A.
- Li, C., Zhang, X., Zhang, S., 2006. Environmental benign design of dimethyl carbonate. Chem. Eng. Res. Des. 84 (A1), 1–8.
- Lu, X.-B., Xiu, J.-H., He, R., Jin, K., Luo, L.-M., Feng, X.-J., 2004. Chemical fixation of CO<sub>2</sub> to ethylene carbonate under supercritical conditions: continuous and selective. Appl. Catal. A: Gen. 275, 73–78.
- Matsuzaki, T., Nakamura, A., 1997. Dimethyl carbonate synthesis and other oxidative reactions using alkyl nitrites. Catal. Surv. Jpn. 1, 77–88.
- Müller, K., Mokrushina, L., Arlt, W., 2014. Thermodynamic constraints for the utilization of CO<sub>2</sub>. Chem. Ing. Tech. 86 (4), 497–503.
- Omae, I., 2012. Recent development in carbon dioxide utilization for the production of organic chemicals. Coord. Chem. Rev. 256, 1384–1405.

- Pacheco, M.A., Marshall, C.L., 1997. Review of dimethyl carbonate (DMC) manufacture and its characteristics as a fuel additive. Energy Fuels 11, 2–29.
- Piyarak, S., (M.S. thesis) 2012. Development of software for life cycle assessment. The Petroleum and Petrochemical College, Chulalongkorn University, Bangkok, Thailand.
- Sheppard, R.O., Yakobsin, D.L., 2003. Integrated urea manufacturing plants and processes. US Patent 6,632,846 B2.
- Simasatitkul, L., Arpornwichanopa, A., Gani, R., 2013. Design methodology for bio-based processing: biodiesel and fatty alcohol production. Comput. Chem. Eng. 57, 48–62.
- Smith, J.M., Van Ness, H.C., Abbort, M.M., 2005. Introduction to Chemical Engineering Thermodynamics, 7th ed. Mc Graw-Hills Book Company, New York.
- Sun, J., Yang, B., Wang, X., Wang, D., Lin, H., 2005. Synthesis of dimethyl carbonate from urea and methanol using polyphosphoric acid as catalyst. J. Mol. Catal. A: Chem. 239, 82–86.
- Tundo, P., Selva, M., 2002. The chemistry of dimethyl carbonate. Acc. Chem. Res. 35, 706–716.
- Wang, H., Lu, B., Wang, X., Zhang, J., Cai, Q., 2009. Highly selective synthesis of dimethyl carbonate from urea and methanol catalyzed by ionic liquids. Fuel Process. Technol. 90, 1198–1201.
- Watile, R.A., Deshmukh, K.M., Dhake, K.P., Bhanage, B.M., 2012. Efficient synthesis of cyclic carbonate from carbon dioxide using polymer anchored-diol functionalized ionic liquids as a highly active heterogeneous catalyst. Catal. Sci. Technol. 2, 1051–1055
- Wei, T., Wang, M., Wei, W., Sun, Y., Zhong, B., 2003. Effect of base strength and basicity on catalytic behavior of solid base for synthesis of dimethyl carbonate from propylene carbonate and methanol. Fuel Process. Technol. 83, 175–182.
- Williams, D.B.G., Sibiya, M.S., van Heerden, P.S., Kirk, M., Harris, R., 2009. Verkade super base-catalysed transesterification of propylene carbonate with methanol to co-produce dimethyl carbonate and propylene glycol. J. Mol. Catal. A: Chem. 304, 147–152
- Wu, X.L., Meng, Y.Z., Xiao, M., Lu, Y.X., 2006. Direct synthesis of dimethyl carbonate (DMC) using Cu–Ni/VSO as catalyst. J. Mol. Catal. A: Chem. 249, 93–97.
- Xu, Y., Isom, L., Hanna, M.A., 2010. Adding value to carbon dioxide from ethanol fermentations. Bioresour. Technol. 101, 3311–3319.
- Yang, Z.-Z., He, L.-N., Dou, X.-Y., Chanfreau, S., 2010. Dimethyl carbonate synthesis catalyzed by DABCO-derived basic ionic liquids via transesterification of ethylene carbonate with methanol. Tetrahedron Lett. 51, 2931–2934.
- Zhang, X., Zhang, S., Yao, P., Yuan, Y., 2005. Modelling and simulation of high-pressure urea synthesis loop. Comput. Chem. Eng. 29, 983–992.
- Zhang, C., Lu, B., Wang, X., Zhao, J., Cai, Q., 2012. Selective synthesis of dimethyl carbonate from urea and methanol over Fe<sub>2</sub>O<sub>3</sub>/HMCM-49. Catal. Sci. Technol. 2, 305–309.

# Using a membrane reactor for the oxidative coupling of methane: simulation and optimization

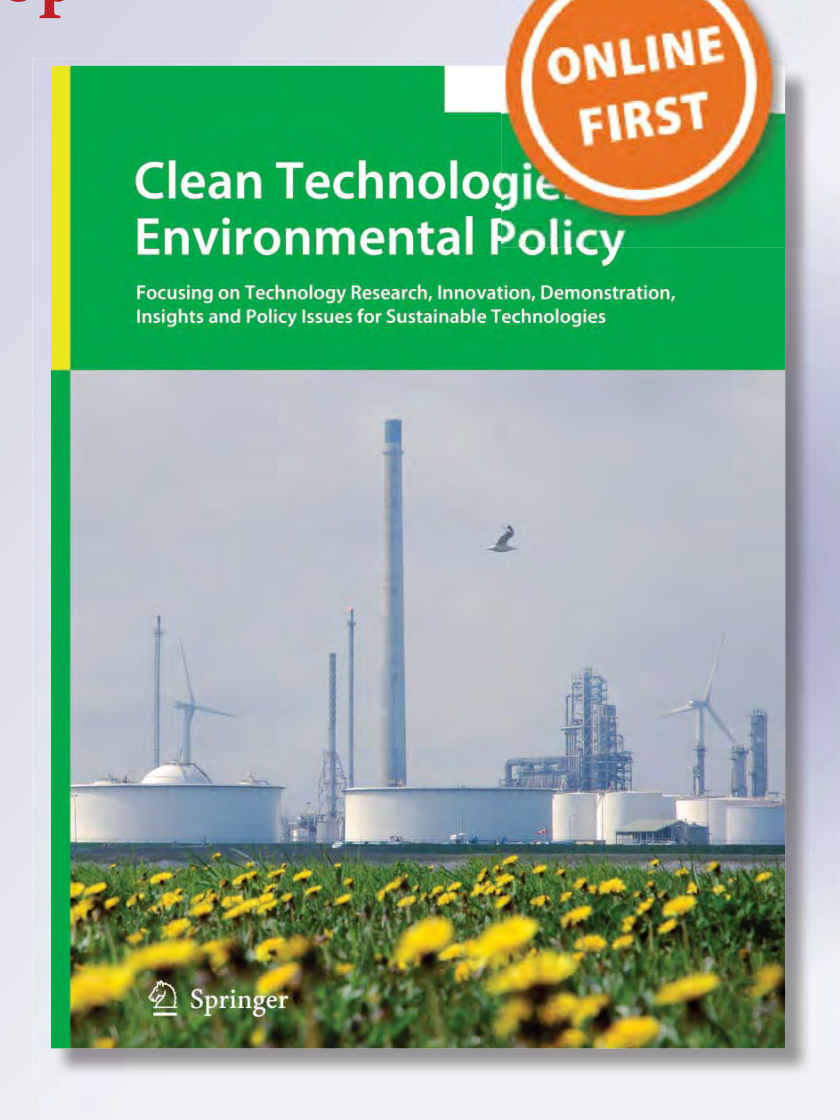
Yaneeporn Patcharavorachot, Sirikarn Tiraset, Wisitsree Wiyaratn, Suttichai Assabumrungrat & Amornchai Arpornwichanop

#### Clean Technologies and Environmental Policy

Focusing on Technology Research, Innovation, Demonstration, Insights and Policy Issues for Sustainable Technologies

ISSN 1618-954X

Clean Techn Environ Policy DOI 10.1007/s10098-014-0813-9





Your article is protected by copyright and all rights are held exclusively by Springer-Verlag Berlin Heidelberg. This e-offprint is for personal use only and shall not be selfarchived in electronic repositories. If you wish to self-archive your article, please use the accepted manuscript version for posting on your own website. You may further deposit the accepted manuscript version in any repository, provided it is only made publicly available 12 months after official publication or later and provided acknowledgement is given to the original source of publication and a link is inserted to the published article on Springer's website. The link must be accompanied by the following text: "The final publication is available at link.springer.com".



#### ORIGINAL PAPER

# Using a membrane reactor for the oxidative coupling of methane: simulation and optimization

Yaneeporn Patcharavorachot · Sirikarn Tiraset · Wisitsree Wiyaratn · Suttichai Assabumrungrat · Amornchai Arpornwichanop

Received: 24 December 2013/Accepted: 27 June 2014 © Springer-Verlag Berlin Heidelberg 2014

**Abstract** An oxidative coupling of methane (OCM) is a promising process to convert methane into ethylene and ethane; however, it suffers from the relatively low selectivity and yield of ethylene at high methane conversion. In this study, a membrane reactor is applied to the OCM process in order to prevent the deep oxidation of a desirable ethylene product. The mathematical model of OCM process based on mass and energy balances coupled with detailed OCM kinetic model is employed to examine the performance of OCM membrane reactor in terms of CH<sub>4</sub> conversion, C<sub>2</sub> selectivity, and C<sub>2</sub> yield. The influences of key operating parameters (i.e., temperature, methane-tooxygen feed ratio, and methane flow rate) on the OCM reactor performance are further analyzed. The simulation results indicate that the OCM membrane reactor operated at higher operating temperature and lower methane-tooxygen feed ratio can improve  $C_2$  production. An optimization of the OCM membrane reactor using a surface response methodology is proposed in this work to determine its optimal operating conditions. The central composite design is used to study the interaction of process variables (i.e., temperature, methane-to-oxygen feed ratio, and methane flow rate) and to find the optimum process operation to maximize the  $C_2$  products yield.

**Keywords** Oxidative coupling of methane · Membrane reactor · Optimization · Response surface methodology

#### List of symbols

#### Y. Patcharavorachot

School of Chemical Engineering, Faculty of Engineering, King Mongkut's Institute of Technology Ladkrabang, Bangkok 10520, Thailand

S. Tiraset  $\cdot$  A. Arpornwichanop ( $\boxtimes$ )

Computational Process Engineering, Department of Chemical Engineering, Faculty of Engineering, Chulalongkorn University, Bangkok 10330, Thailand

e-mail: amornchai.a@chula.ac.th

Published online: 15 July 2014

#### W. Wiyaratn

Faculty of Industrial Education and Technology, King Mongkut's University of Technology Thonburi, Bangkok 10140, Thailand

#### S. Assabumrungrat

Center of Excellence in Catalysis and Catalytic Reaction Engineering, Department of Chemical Engineering, Faculty of Engineering, Chulalongkorn University, Bangkok 10330, Thailand

#### Variables

Acs Cross-sectional area of the tube side (cm<sup>2</sup>)

 $C_i$  Density of oxygen ions (mol cm<sup>-3</sup>)

 $C_{\text{Pi}}$  Heat capacity of specie i (J mol<sup>-1</sup> K<sup>-1</sup>)

 $D_a$  Ambipolar diffusion coefficients (cm<sup>2</sup> s<sup>-1</sup>)

 $d_1$  Outer diameter of the membrane tube (cm)

 $d_2$  Inner diameter of the membrane tube (cm)

Ea, j Activation energy in reaction j (kJ mol<sup>-1</sup>)

 $F_i$  Molar flow rate of specie i (mol s<sup>-1</sup>)

 $\Delta H_i$  Heat of reaction i (J mol<sup>-1</sup>)

 $J_{\rm O_2}$  Oxygen flux through the membrane

 $(\text{mol cm}^{-2} \text{ s}^{-1})$ 

 $K_{\rm m}$  Average thermal conductivity (J s<sup>-1</sup> m<sup>-1</sup> K<sup>-1</sup>)

 $K_0$  Kinetic parameter (mol g<sup>-1</sup> s<sup>-1</sup> Pa<sup>-(m+n)</sup>)

L Length of the membrane tube (cm)

M Membrane thickness (cm)

 $P_i$  Partial pressure of component i (Pa)

q Heat flux between the tube side and shell side  $(J \text{ m}^{-1} \text{ s}^{-1})$ 

 $r_i$  Rate of reaction j (mol g<sup>-1</sup> s<sup>-1</sup>)



- S Effective area of the membrane tube (cm)
- Temperature ( $^{\circ}$ C)
- V Reactor volume (m<sup>3</sup>)
- W Catalyst weight (g)
- Z Reactor length (cm)

#### Greek symbols

- α Star point for CCD
- vi, j Stoichiometric coefficient of component j of reaction

#### **Superscript**

- t Tube side
- s Shell side

#### Introduction

Methane is the main component of natural gas (NG) and biogas, and a by-product from oil refining and chemical industries. Conversion of methane to more useful chemicals and fuels is recognized as the next step to sustain economic growth and maintain fuel supplies (Lunsford 2000). In addition, it could also reduce the severe greenhouse effect caused by methane. Presently, there are two main methodologies proposed to convert methane into olefins, higher hydrocarbons, and gasoline, namely indirect and direct conversion processes. The former approach involves the production of synthesis gas (syngas), an intermediate, from methane (Arpornwichanop et al. 2011) and then transforms it into other chemicals via Fischer-Tropsch process, which causes a substantial energy loss. In contrast, the latter process can convert methane into higher hydrocarbons in a single step. Among the various direct processes, the oxidative coupling of methane (OCM) is a promising technology to upgrade methane into valuable product, i.e., ethylene and ethane (referred to C<sub>2</sub> products). Particularly, ethylene is the most important base chemical in petrochemical industries for the production of polymers and ethylene derivatives (Bernardo and Gabriele 2012).

Extensive studies on the OCM process have been conducted since the pioneer work of Keller and Bhasin in 1982. There are many different reactor concepts proposed for use in this process. A fixed-bed reactor (FBR) has been used widely for OCM process due to its technological simplicity. Hong and Yoon (2001) studied the OCM process using the calcium chloride (CaCl<sub>2</sub>)-promoted calcium chlorophosphate catalysts, whereas Ji et al. (2002) and Liu et al. (2008) used the sodium tungsten oxide-Manganese/Silicon dioxide (Na<sub>2</sub>WO<sub>4</sub>–Mn/SiO<sub>2</sub>) catalysts. However, this type of the reactor is accident prone because of the large amount of heat released during the course of the reaction. Furthermore, a poor heat removal from the highly

exothermic reaction results in the occurrence of hot spots, affecting the reactor operation, such as temperature runaway, catalyst deactivation, undesired side reactions, and thermal decomposition of products. Use of a fluidized-bed reactor, which has high heat transfer capacity, shows better heat management and temperature control than the fixed-bed reactor system (Jašo et al. 2011). Daneshpayeh et al. (2009) studied the OCM over Mn/Na<sub>2</sub>WO<sub>4</sub>/SiO<sub>2</sub> catalyst in a two-zone fluidized-bed reactor (TZFBR), and its performance was compared with the conventional fluidized-bed reactor. Although the TZFBR gave the C<sub>2</sub> selectivity larger than the fluidized-bed reactor does, the C<sub>2</sub> yield was still relatively low (<20 %).

The difficulty in operation of the OCM process lies in the fact that intermediates and target products are more reactive than the reactant and, therefore, are prone to deeply oxidize to  $\mathrm{CO}_x$ . Thus, the oxidation of methane and  $\mathrm{C}_{2+}$  products seems to be unavoidable when high oxygen content is present in the feed stream. The concept of using an oxygen distribution in a fixed-bed reactor was studied by Zarrinpashne et al. (2003) in order to improve the OCM performance. However, the proposed reactor concept cannot achieve the high yield of ethylene due to the incomplete gas mixing at the oxygen feeding points. This causes high oxygen concentration zones at which the  $\mathrm{C}_{2+}$  product is easily combusted, and its selectivity falls significantly.

To achieve an economically attractive C2 yield (>30 %), many researchers have focuses their attention on the application of membrane reactors in last decades (Wang et al. 2005). Omata et al. (1989) initially applied a membrane reactor for the OCM process. The use of the membrane reactor to control oxygen concentration offers a possibility to achieve much higher C2 hydrocarbons selectivity and yield. Kao et al. (2003) reported that the selectivity and yield of C2 products obtained from the lithium/magnesium oxide (Li/MgO)-packed porous membrane reactor is higher than that from the fixed-bed reactor. Under the operating conditions with a pressure in both sides of the membrane reactor at 1 bar and a temperature at 750 °C, the porous membrane reactor can achieve 30 % yield and 53 % selectivity of the C2 products, whereas the fixed-bed reactor provides the maximum yield of 20.7 % at 52.5 % selectivity. Bhatia et al. (2009) studied the OCM in a catalytic membrane reactor, catalyst packed bed reactor, and catalyst packed bed membrane reactor. It was found that although the catalyst packed bed reactor gave the highest C<sub>2+</sub> selectivity, the catalytic membrane reactor consisting of a mixed ionic-electronic conducting membrane with  $Ba_{0.5}Ce_{0.4}Gd_{0.1}Co_{0.8}Fe_{0.2}O_{3-\delta}$  (BCGCF) material performed the best among the three reactors with C<sub>2+</sub> yield of 34.7 %, methane conversion of 51.6 %, and  $C_{2+}$  selectivity of 67.4 %. In addition, Godini et al. (2013) proposed a novel silicon oxycarbide (SiOC) membrane



modification approach to improve the performance of the OCM membrane reactor. It was reported that 18.5 %  $C_2$  yield and 57 %  $C_2$  selectivity can be achieved. Mixed-conducting oxide membranes, such as perovskite-type membranes, are well known for their abilities to separate oxygen from air.  $Ba_{0.5}Sr_{0.5}Co_{0.8}Fe_{0.2}O_{3-\delta}$  (BSCFO) is an example of the promising mixed-conducting membrane with high oxygen permeability and has proven to be a good candidate for use as an oxygen distributor in the OCM reactor (Shao et al. 2000, 2001). It is noted that although the performance of membrane reactors for the OCM process has been widely studied, there are limited works on optimization of the OCM membrane reactor; finding optimal operating conditions is important for its efficient operation.

In this study, a dense tubular membrane reactor is investigated to improve the performance of the OCM. The mathematic model of the membrane reactor based on conservative equations and detailed OCM kinetic model is employed to analyze the effect of key operating parameters, i.e., methane-to-oxygen feed ratio (CH<sub>4</sub>/O<sub>2</sub> feed ratio), operating temperature, and methane feed flow rate, on the efficiency of the OCM process in terms of CH<sub>4</sub> conversion, C<sub>2</sub> selectivity, and C<sub>2</sub> yield. In order to find the optimal operating condition that maximizing C2 production, the simulated data obtained are further used for the optimization of the OCM process conditions. The central composite design (CCD) of response surface methodology (RSM) is employed to determine the optimum C<sub>2</sub> yield. The RSM is a set of statistical and mathematical techniques used for designing experiments and building models. This technique can help in understanding the interactions between factors. The CCD, which is a useful method to analyze the influence of process variables, is applied to show the optimum points.

#### Model of OCM membrane reactor

#### Reactor configuration

The membrane reactor considered in this study is a single-stage dense tubular membrane reactor. Figure 1 shows a configuration of the tubular membrane reactor for OCM. The membrane reactor considered consists of two concentric tubes: the outer tube is the shell and the inner tube is the dense  $Ba_{0.5}Sr_{0.5}Co_{0.8}Fe_{0.2}O_{3-\delta}$  (BSCFO) membrane. Methane is fed into the tube side of the reactor, while the oxygen is fed into the shell side. The oxygen in the shell side permeates into the tube side through the membrane, which acts as an oxygen distributor, and reacts with methane. The Lanthanum oxide/calcium oxide (La<sub>2</sub>O<sub>3</sub>/CaO) catalyst is packed in the tube side, and thus only the gasses at the tube side are in direct contact with it and

participated in the reaction. In this study, the co-current flow of methane and oxygen is chosen as it is expected a higher performance. It is noted that the oxygen feed is slightly distributed to the reactor through a membrane that results in high  $C_2$  selectivity. However, when oxygen is introduced to the reactor at different locations and flow directions, the methane conversion in the OCM reactor would be changed.

#### Model equations

A mathematical model of the membrane reactor is developed based on the following assumptions: (1) the reactor is operated under steady-state operation, (2) there is no radial concentration distribution in the tube or on the shell side of the reactor, (3) axial diffusion dispersion is neglected, and (4) ideal gas law is assumed. The mass balance of component i can be written as

Tube side (reaction side):

$$\frac{dF_{i}^{t}}{dz} = \frac{W}{V} A_{cs} \sum_{i=1}^{n} v_{i,j} r_{j} + \pi d_{2} J_{O_{2}}.$$
 (1)

Shell side:

$$\frac{dF_{O_2}^s}{dz} = -\pi d_1 J_{O_2}. (2)$$

Since the membrane reactor for OCM is assumed to be operated under non-isothermal condition, an energy balance equation is used to describe a change in the reactor temperature as shown below:

Tube side (reaction side):

$$\frac{dT^{t}}{dz} = \frac{\frac{W}{V} A_{cs} \sum_{i} (-\Delta H_{i} r_{i}) - q + \pi d_{2} J_{O_{2}} C_{p_{O_{2}}} \Delta T}{\sum_{i} F_{i} C_{p_{i}}}$$
(3)

Shell side:

$$\frac{\mathrm{d}T^s}{\mathrm{d}z} = \frac{q}{F^s_{O_2}C_{PO_2}},\tag{4}$$

where q is the heat flux between the tube side and shell side as expressed in Eq. (5):

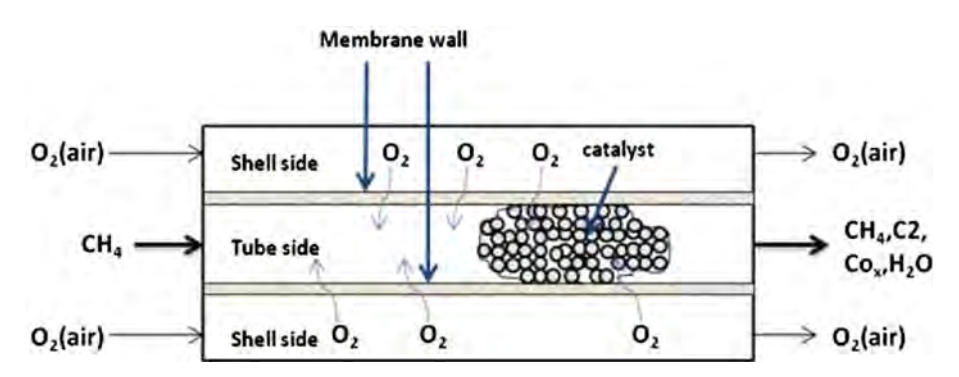
$$q = \frac{A_{\rm cs}K_{\rm m}(T^t - T^s)}{MI},\tag{5}$$

where  $A_{\rm cs}$  is the cross-sectional area of the tube side;  $K_{\rm m}$  and M stand for the average thermal conductivity and membrane thickness, respectively; and L represents the effective length of the tube.

The oxygen permeation through the tubular BSCFO membrane can be explained by the oxygen flux (Eq. (6)), which was developed by Kim et al. (1998):

$$J_{\rm O_2} = \frac{\pi L C_i D_a}{2S \, \ln(d_1/d_2)} \ln\left(\frac{P_1}{P_2}\right),\tag{6}$$

Fig. 1 Schematic representation of the membrane reactor model



where  $d_1$  and  $d_2$  are the outer and inner diameter of the membrane tube, respectively; L, S,  $C_i$ , and  $D_a$  stand for the effective length of the tube, the effective area of the membrane tube, the density of oxygen ions, and the ambipolar diffusion coefficients, respectively;  $P_1$  is the oxygen partial pressure in the shell side; and  $P_2$  is the oxygen partial pressure in the tube side.

It is noted that the radial distributions of concentration and temperatures in the OCM reactor are neglected in this study. Kao et al. (2003) showed that the simulated data obtained from the one-dimensional model can sufficiently explain the experimental data of the oxidative coupling of methane on Li/MgO packed porous membrane reactor.

#### Kinetics of the oxidative coupling of methane

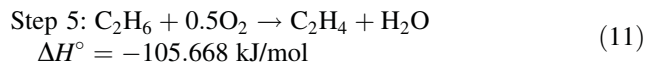
A comprehensive kinetic model of the OCM reaction used in this study was developed by Stansch et al. (1997) for the La<sub>2</sub>O<sub>3</sub>/CaO catalyst. These rate expressions are based on macro kinetics in which an elementary step mechanism without intrinsic internal mass and heat transport is considered. Use of this simplified kinetic model leads to less computational time, and thus it has been often used in the literature (Nakisa and Reza 2009; Tiemersma et al. 2012). The OCM process consists of three primary and seven consecutive reaction steps taking into account the gasphase dehydrogenation of ethane and the ethylene steam reforming and the reaction inhibition by CO<sub>2</sub> and O<sub>2</sub>. The kinetic model considered the following set of stoichiometric equations:

Step 1: 
$$CH_4 + 2O_2 \rightarrow CO_2 + 2H_2O$$
  
 $\Delta H^{\circ} = -802.251 \text{ kJ/mol}$  (7)

Step 2: 
$$2CH_4 + 0.5O_2 \rightarrow C_2H_6 + H_2O$$
  
 $\Delta H^{\circ} = -175.71 \text{ kJ/mol}$  (8)

Step 3: 
$$CH_4 + O_2 \rightarrow CO + H_2O + H_2$$
  
 $\Delta H^{\circ} = -277.449 \text{ kJ/mol}$  (9)

Step 4: 
$$CO + 0.5O_2 \rightarrow CO_2$$
  $\Delta H^{\circ} = -282.984$  kJ/mol (10)



Step 6: 
$$C_2H_4 + 2O_2 \rightarrow 2CO + 2H_2O$$
  
 $\Delta H^{\circ} = -757.156 \text{ kJ/mol}$  (12)

Step 7: 
$$C_2H_6 \rightarrow C_2H_4 + H_2$$
  $\Delta H^{\circ} = 136.15 \text{ kJ/mol}$  (13)

Step 8: 
$$C_2H_4 + 2H_2O \rightarrow 2CO + 4H_2$$
  
 $\Delta H^{\circ} = 210.116 \text{ kJ/mol}$  (14)

Step 9: 
$$CO + H_2O \rightarrow CO_2 + H_2$$
  
 $\Delta H^{\circ} = -41.166 \text{ kJ/mol}$  (15)

Step 10: 
$$CO_2 + H_2 \rightarrow CO + H_2O$$
  $\Delta H^{\circ} = 41.166 \text{ kJ/mol}$  (16)

The reaction rates for each step are given below:

$$r_{j} = \frac{k_{0,j}e^{-E_{a,j}/RT}P_{C}^{m_{j}}P_{O_{2}}^{n_{j}}}{(1 + K_{j,CO_{2}}e^{-\Delta H_{ad,CO_{2}}/RT}P_{CO_{2}})^{2}}, \quad j = 1, 3-6$$
 (17)

$$r_{2} = \frac{k_{0,2}e^{-E_{a,2}/RT}(K_{0,O_{2}}e^{-\Delta H_{ad,O_{2}}/RT}P_{O_{2}})^{n_{2}}P_{CH_{4}}}{\left[1 + (K_{0,O_{2}}e^{-\Delta H_{ad,O_{2}}/RT}P_{O_{2}})^{n_{2}} + K_{j,CO_{2}}e^{-\Delta H_{ad,CO_{2}}/RT}P_{CO_{2}}\right]^{2}}$$
(18)

$$r_7 = k_{0,7} e^{-E_{a,7}/RT} P_{C_2 H_6}, \tag{19}$$

$$r_8 = k_{0,8} e^{-E_{a,8}/RT} P_{\text{C}_2\text{Ha}}^{m_8} P_{\text{H}_2\text{O}}^{n_8}, \tag{20}$$

$$r_9 = k_{0,9} e^{-E_{a,9}/RT} P_{\text{CO}}^{m_9} P_{\text{H}_2\text{O}}^{n_9}, \tag{21}$$

$$r_{10} = k_{0.10} e^{-E_{a,10}/RT} P_{\text{CO}_a}^{m_{10}} P_{\text{H}_a}^{n_{10}}, \tag{22}$$

where  $P_i$  stands for the partial pressure of component i,  $K_0$  and  $E_{a,j}$  represent the kinetic parameter and the activation energy in reaction j, respectively. The kinetic parameters used for the above reaction scheme are presented in Table 1.

#### OCM performance

The set of differential and algebraic equations as mentioned in Model equations and Kinetics of the oxidative coupling of methane sections was solved using the explicit



Table 1 Kinetic parameters of the OCM reactions (Stansch et al. 1997)

Step	$K_{0,j} \text{ (mol g}^{-1}\text{s}^{-1} \text{ Pa}^{-(m+n)})$	$E_{a,j}$ (kJ mol <sup>-1</sup> )	$m_j$	$n_j$	$K_{j,\text{CO}_2}(\text{Pa}^{-1})$	$\Delta H_{\rm ad,CO_2} \ ({\rm kJ \ mol}^{-1})$	$K_{j,O_2}$ (Pa <sup>-1</sup> )	$\Delta H_{\rm ad,O_2}({\rm kJ~mol}^{-1})$
1	$0.20 \times 10^{-5}$	48	0.24	0.76	$0.25 \times 10^{-12}$	-175		
2	23.2	182	1.00	0.40	$0.83 \times 10^{-13}$	-186	$0.23 \times 10^{-11}$	-124
3	$0.52 \times 10^{-6}$	68	0.57	0.85	$0.36 \times 10^{-13}$	-187		
4	$0.11 \times 10^{-3}$	104	1.00	0.55	$0.40 \times 10^{-12}$	-168		
5	0.17	157	0.95	0.37	$0.45 \times 10^{-12}$	-166		
6	0.06	166	1.00	0.96	$0.16 \times 10^{-12}$	-211		
7	$1.2 \times 10^{7} \text{ a}$	226						
8	$9.3 \times 10^{3}$	300	0.97	0				
9	$0.19 \times 10^{-3}$	173	1.00	1.00				
10	$0.26 \times 10^{-1}$	220	1.00	1.00				

<sup>&</sup>lt;sup>a</sup> Units are mol s<sup>-1</sup>m<sup>-3</sup>Pa<sup>-1</sup>

Runge–Kutta (fourth/fifth order) method in Matlab. To evaluate the performance of an OCM membrane reactor, the CH<sub>4</sub> conversion ( $X_{\rm CH_4}$ ), C<sub>2</sub> selectivity ( $S_{\rm C_2}$ ), and C<sub>2</sub> yield ( $Y_{\rm C_2}$ ) are considered and defined in Eqs. (23)–(25). These performance indexes are analyzed with respect to key operating parameters, such as temperature, methaneto-oxygen feed ratio, and methane feed flow rate.

$$X_{\text{CH}_4} \, (\%) = \frac{\text{moles of CH}_4 \text{ converted}}{(\text{moles of CH}_4)_{\text{feed}}} \times 100$$
 (23)

$$S_{C_2}$$
 (%) =  $\frac{2 \times (\text{moles of C}_2 \text{ hydrocarbons})_{\text{products}}}{\text{moles of CH}_4 \text{ converted}} \times 100$ 

(24)

$$Y_{C_2}$$
 (%) =  $\frac{2 \times (\text{moles of C}_2 \text{ hydrocarbons})_{\text{products}}}{(\text{moles of CH}_4)_{\text{feed}}}$   
× 100

(25)

#### Regression model

In this study, a statistical analysis of the OCM process performance in term of  $C_2$  yield is performed. The central composite design (CCD) is used to study the interaction of process variables and to predict the optimum process conditions maximizing the  $C_2$  yield. The response (Y) of the OCM process, the  $C_2$  yield, is used to develop the quadratic polynomial equation that correlates the process response as a function of the independent variables, i.e.,  $CH_4/O_2$  feed ratio ( $X_1$ ), operating temperature ( $X_2$ ) and methane feed flow rate ( $X_3$ ), and their interactions as shown in Eq. (26):

$$Y = \beta_0 + \sum_{i=1}^{3} \beta_i X_i + \sum_{i=1}^{3} \beta_{ii} X_i^2 + \sum_{i=1}^{2} \sum_{j=i+1}^{3} \beta_{ij} X_i X_j,$$
 (26)

where Y is the predicted response (dependent variables);  $X_i$  and  $X_j$  are the factors (independent variables);  $\beta_0$  is the

offset term; and  $\beta_i$ ,  $\beta_{ii}$ , and  $\beta_{ij}$  are the coefficients for the linear, squared, and interaction effects. The coefficients  $\beta$  can be calculated using the least square method. The values of the coefficients and the residual  $R^2$ , the F value and p value of the regression model are reported in "Regression model for prediction of  $C_2$  yield" section.

#### Model validation

In order to validate the membrane reactor model coupled with the OCM kinetics used in this study, the model predictions are compared with experimental data reported by Stansch et al. (1997). Their experiments on the OCM were carried out in a plug flow reactor with a feed flow rate of  $4 \text{ cm}^3 \text{ s}^{-1}$  over 14.8 mg of  $\text{La}_2\text{O}_3/\text{CaO}$  catalyst. The comparison of the simulation and experimental data in terms of CH<sub>4</sub> conversion ( $X_{\text{CH4}}$ ), C<sub>2</sub> selectivity ( $S_{\text{C2}}$ ), and C<sub>2</sub> yield ( $Y_{\text{C2}}$ ) at different feed mole ratios and operating temperatures is shown in Table 2. It can be seen that the model prediction shows good agreement with experimental data reported in the literature.

#### Results and discussion

Parametric analysis of the OCM membrane reactor

In this section, the performance analysis of the dense tubular membrane reactor for the OCM process with respect to key operating parameters is presented. Table 3 presents the reactor configuration used for the simulation, whereas the standard operating conditions and its operation range are listed in Table 4. Figure 2 shows the concentration profiles of CH<sub>4</sub>, C<sub>2</sub>, O<sub>2</sub>, CO<sub>x</sub>, H<sub>2</sub>, and H<sub>2</sub>O along the tube side of the reactor. It is found that the methane concentration decreases along the reactor length, and the other gaseous components increase due to the increased reaction

Table 2 Comparison between experimental (Stansch et al., 1997) and simulated data

	Tempera	ture (°C)			
	700	750	750	830	830
Feed mole ratio					
$CH_4$	0.699	0.612	0.699	0.612	0.699
$O_2$	0.095	0.051	0.095	0.051	0.095
$X_{\mathrm{CH4}}~(\%)$					
Experimental	4.1	4.9	7.1	9.9	14.4
Simulated	4.5	4.8	6.5	12.0	13.8
% Error	9.8	2.0	8.5	21.2	4.2
$S_{\rm C2}~(\%)$					
Experimental	35.6	55.6	53.7	72.5	69.6
Simulated	34.5	56.2	49.7	68.4	62
% Error	3.1	1.1	7.4	5.7	10.9
$Y_{\rm C2} \ (\%)$					
Experimental	1.5	2.7	3.8	7.2	10
Simulated	1.3	2.7	2.9	7.4	9.5
% Error	13.3	0	23.7	2.8	5.0

Table 3 The reactor configuration used for the simulation

Length (cm)	10
Inner diameter of membrane tube (mm)	5
External diameter of membrane tube (mm)	8
Mass of catalyst (g)	0.45
Pressure for both tube and shell sides (atm)	1
Bulk bed porosity	0.36

rates after oxygen is permeated from the shell side. It is also observed from Fig. 2 that the oxygen concentration on the tube side begins at zero and then increases as oxygen permeation from the shell side is higher. Oxygen can be consumed not only by the oxidative reactions but also the dehydrogenation of ethane and ethylene. Thus, at the early stage of the reactions, the formation rate of C<sub>2</sub> product by the OCM reactions is higher than the rate of methane deep oxidation (side reaction) as shown by the greater increase in the C<sub>2</sub> products concentration than that of the H<sub>2</sub>, H<sub>2</sub>O, and CO<sub>x</sub> gas. When oxygen is more permeated from the shell side, the deep oxidation of methane and the  $C_2$ product produced by OCM reaction can be occurred, and thus it can be observed that carbon dioxide concentration is higher than the C<sub>2</sub> product concentration. However, when oxygen is consumed more than the oxygen supplied, oxygen concentration decreases as shown in the reactor length of about 8.5 cm. When the oxygen concentration is very low in the tube side, the rates of the OCM reaction and deep oxidation reaction become slower and constant.

Table 4 The standard operating conditions and its operation range used for the simulation

Parameters	Standard operating condition	Operational ranges
Temperature (°C)	800	700–900
Methane/Oxygen feed ratio	2	0.5-3
Methane feed flow rate $(10^{-3} \text{ mol s}^{-1})$	1.6	1.2–2.8

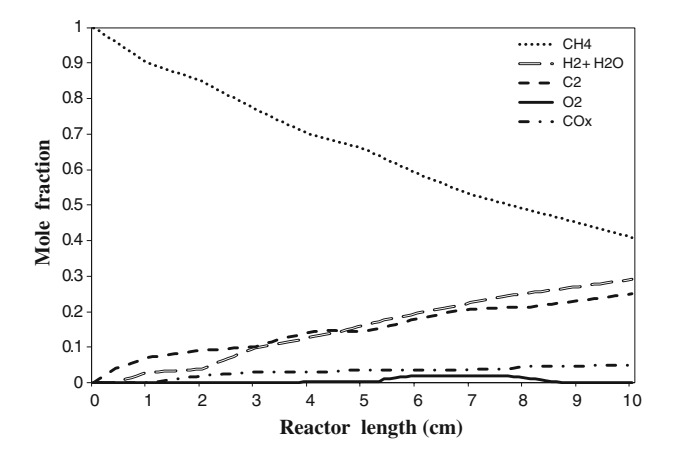
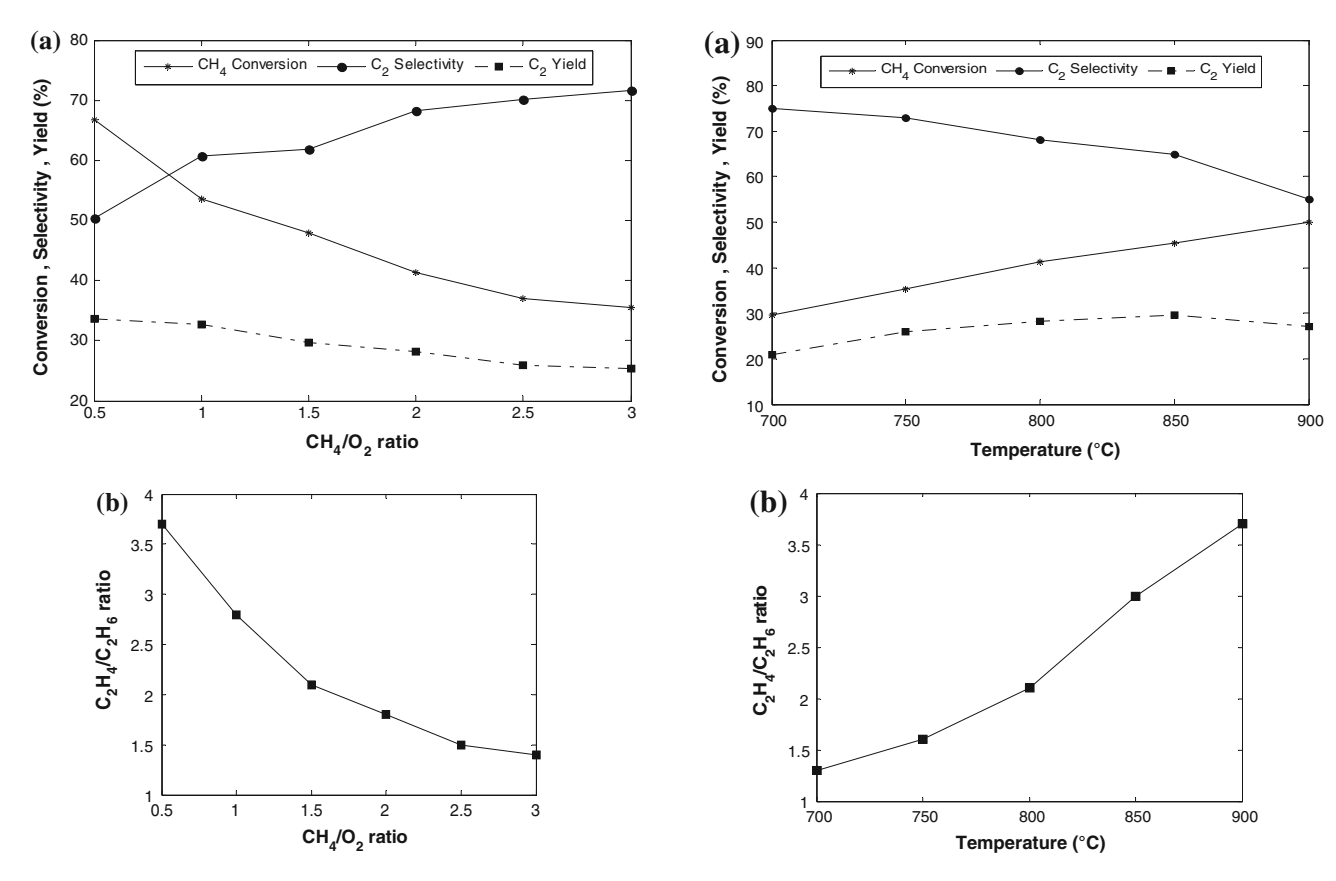


Fig. 2 Concentration profiles on the reaction side of membrane reactor

#### Effect of methane-to oxygen-feed ratio

The effect of CH<sub>4</sub>/O<sub>2</sub> feed ratio is examined by varying its value from 0.5 to 3, while other operating conditions as shown in Table 4 are kept constant. Figure 3a presents the conversion of methane and the selectivity and yield of C<sub>2</sub> product as a function of the CH<sub>4</sub>/O<sub>2</sub> feed ratio. The results indicate that the CH<sub>4</sub> conversion and C<sub>2</sub> yield decrease with an increase in the CH<sub>4</sub>/O<sub>2</sub> feed ratio due to the lower oxygen concentration at the reaction side. However, the undesired oxidation reaction of methane, C2 products, and other intermediate products are intensely induced at higher oxygen concentration, and thus the C2 selectivity decreases at higher CH<sub>4</sub> conversion. Figure 3b shows the impact of the CH<sub>4</sub>/O<sub>2</sub> feed ratio on the C<sub>2</sub>H<sub>4</sub>/C<sub>2</sub>H<sub>6</sub> product ratio in the C<sub>2</sub> products. Because the reaction of ethane to ethylene requires oxygen to react with ethane, higher C<sub>2</sub>H<sub>4</sub>/C<sub>2</sub>H<sub>6</sub> ratio is obtained at lower CH<sub>4</sub>/O<sub>2</sub> feed ratio. Since C<sub>2</sub>H<sub>4</sub> is more valuable than C<sub>2</sub>H<sub>6</sub>, the reactor operation with low CH<sub>4</sub>/O<sub>2</sub> ratio is more suitable in terms of C<sub>2</sub> yield and  $C_2H_4\!/C_2H_6$  product ratio. It can be seen that at the  $CH_4\!/O_2$ ratio of 0.5, the C<sub>2</sub> yield and C<sub>2</sub>H<sub>4</sub>/C<sub>2</sub>H<sub>6</sub> product ratio are 34 % and 3.7, whereas the  $C_2$  yield of 25 % and  $C_2H_4/$ 





**Fig. 3** Effect of methane-to-oxygen feed ratio on **a** CH<sub>4</sub> conversion, selectivity and yield of  $C_2$  product, and **b**  $C_2H_4/C_2H_6$  product ratio

Fig. 4 Effect of operating temperature on a  $CH_4$  conversion, selectivity and yield of  $C_2$  product, and b  $C_2H_4/C_2H_6$  product ratio

 $C_2H_6$  product ratio of 1.4 can be obtained when the reactor is operated with the  $CH_4/O_2$  feed ratio of 3.

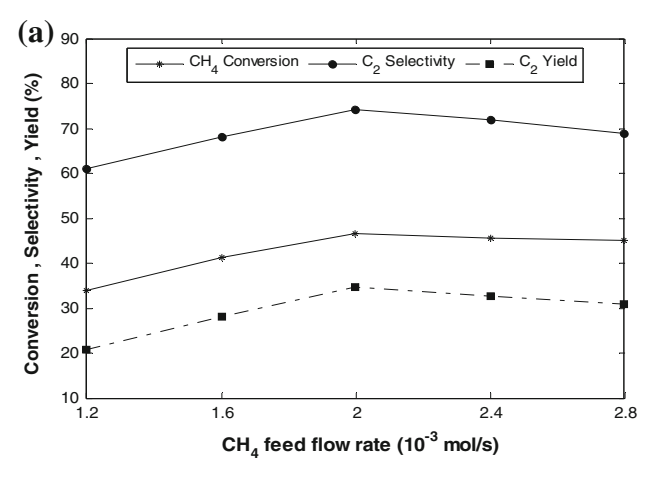
#### Effect of operating temperature

The effect of operating temperatures on the performance of an OCM membrane reactor is shown in Fig. 4. It is noted that because the OCM is a highly exothermic reaction, the high-temperature operation always leads to a hot spot in the reactor. Moreover, this can suppress the C2 yield due to the fact that the highly exothermic conversions to CO and CO2 are thermodynamically more favorable. Here, the OCM reactor operated in the temperature range of 600-900 °C is studied (Tye et al. 2002). When the operating temperature is changed from 700 to 900 °C, the CH<sub>4</sub>/O<sub>2</sub> feed ratio and methane feed flow rate are kept constant as 2 and  $1.6 \times 10^{-3}$  mol s<sup>-1</sup>, respectively. Initially, the CH<sub>4</sub> conversion and C2 product yield are increased with increasing operating temperature, as seen in Fig. 4a. This is because the reaction rate and oxygen flux through the membrane are increased at higher temperatures (Shao et al. 2001). At the temperature above 850 °C, however, the amount of methane in the tube side decreases, while the permeation of oxygen into the tube side increases. This leads to more undesired side reaction and causes a decrease in  $C_2$  selectivity and  $C_2$  yield. The increments of  $H_2$ ,  $H_2O$ , and  $CO_x$  products indicate that the rate of hydrocarbons oxidation over  $La_2O_3/CaO$  catalyst is favored at high temperatures. As a result, the  $C_2$  selectivity is reduced with higher operating temperature. The simulation result also shows that an increase in temperature can improve the  $C_2H_4/C_2H_6$  product ratio (Fig. 4b). This can be observed that the dehydrogenation (thermal cracking) of ethane to ethylene is more pronounced at high-temperature operation. Higher reaction temperatures can improve the  $C_2H_4/C_2H_6$  product ratio from 1.3 at 700 °C to 3.7 at 900 °C.

#### Effect of methane feed flow rate

Figure 5 shows the  $CH_4$  conversion,  $C_2$  selectivity, yield of  $C_2$ , and the  $C_2H_4/C_2H_6$  product ratio at different methane feed flow rates. It is found that the  $CH_4$  conversion,  $C_2$  selectivity, and  $C_2$  yield can be improved and reach their maximum values at the methane feed flow rate of  $2 \times 10^{-3}$  mol s<sup>-1</sup>. At the methane feed flow rate below  $2 \times 10^{-3}$  mol s<sup>-1</sup>, the performance of the OCM process increases because more methane can react with oxygen. However, when the flow rate of methane is higher than





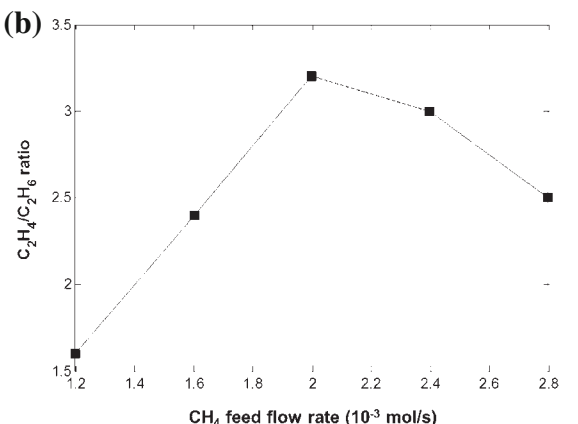


Fig. 5 Effect of methane feed flow rate on a  $CH_4$  conversion, selectivity and yield of  $C_2$  product, and b  $C_2H_4/C_2H_6$  product ratio

 $2 \times 10^{-3}$  mol s<sup>-1</sup>, it is found that there is less oxygen concentration in the tube side, and thus the efficiency of the OCM process decreases. This result can be clearly shown in Fig. 5b.

#### Adiabatic operation

Many previous studies on the OCM process were assumed that the membrane reactor was operated at an isothermal condition. Under this assumption, it was found that the hot spot can be developed in the reactor, particularly in the fixed-bed reactor. Use of membrane reactor can solve the hot spot problem by the distributed oxygen supply along the reactors, and thus the reactor is maintained at a nearly isothermal condition. However, due to the highly exothermic nature of OCM reactions, the assumption that the reactor is operated under the isothermal condition might lead to the unrealistic prediction of the reactor performance.

When the OCM reactor is run under an adiabatic operation, heat released during the oxidation coupling process increases the reactor temperature. Figure 6 shows the

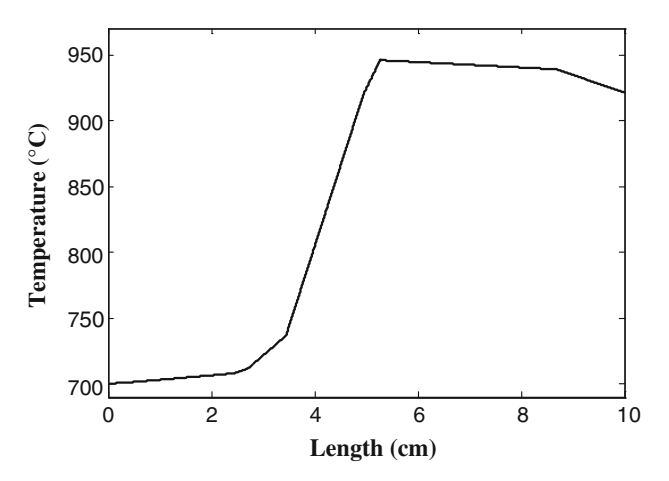


Fig. 6 Temperature profile along the reactor

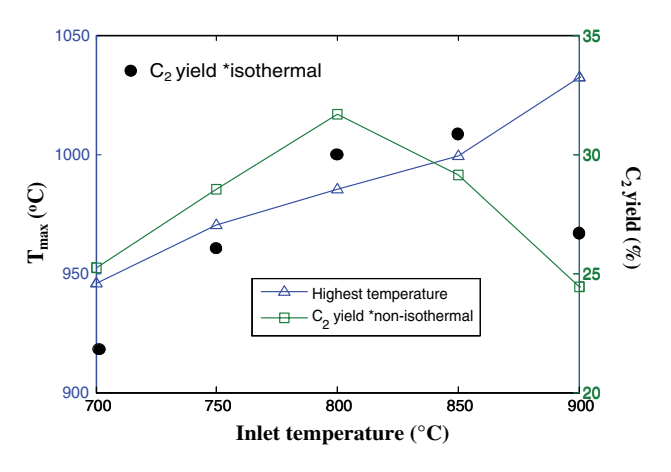


Fig. 7 Effect of inlet temperature on the highest temperature and C<sub>2</sub> yield under isothermal and adiabatic conditions

temperature profile along the reactor length when the inlet feed temperature is 700 °C. The reactor temperature increases and reaches its highest temperature of 945 °C. Compared with the isothermal operation, as seen in Fig. 7, the adiabatic operation provides a higher  $C_2$  yield at the inlet temperature range of 700–800 °C.

Optimization of the OCM membrane reactor

Regression model for prediction of  $C_2$  yield

Simulations of a single-stage membrane reactor for the OCM process are performed based on three independent variables (n = 3), i.e.,  $CH_4/O_2$  feed ratio ( $X_1$ ), operating temperature ( $X_2$ ), and methane feed flow rate ( $X_3$ ), with their operational range as given in Table 5. It is noted that the kinetic models used for determining the reaction rates of OCM were extracted from the experiment of Stansch



Table 5 Range and levels of independent process variables for the OCM reactor

Independent variable		Coded levels			
		-1	0	1	
CH <sub>4</sub> /O <sub>2</sub> feed ratio	$X_1$	1	2	3	
Operating temperature (°C)	$X_2$	700	800	900	
$CH_4$ feed flow rate (10 <sup>-3</sup> mol s <sup>-1</sup> )	$X_3$	1.2	2.0	2.8	

**Table 6** Full factorial central composite design matrix of three independent variables in coded and unit along with the simulated response value for a single-stage membrane reactor

Run	Manipulated variables					Responses	
	$X_1$		$X_2$		<i>X</i> <sub>3</sub>		C <sub>2</sub> yield (%)
	CH <sub>4</sub> / O <sub>2</sub> ratio	Level	Temperature	Level	CH <sub>4</sub> : flow: Level	rate	
1	1	-1	700	-1	1.2	-1	18.84
2	1	-1	700	-1	2.8	1	22.55
3	1	-1	900	+1	1.2	-1	32.55
4	1	-1	900	+1	2.8	1	32.56
5	3	1	700	-1	1.2	-1	11.59
6	3	1	700	-1	2.8	1	17.23
7	3	1	900	+1	1.2	-1	15.34
8	3	1	900	+1	2.8	1	21.23
9	0.32	$-\alpha$	800	0	2.0	0	34.12
10	3.68	$+\alpha$	800	0	2.0	0	13.78
11	2	0	631.82	$-\alpha$	2.0	0	13.12
12	2	0	968.18	$+\alpha$	2.0	0	27.32
13	2	0	800	0	0.65	$-\alpha$	21.33
14	2	0	800	0	3.35	$+\alpha$	29.12
15	2	0	800	0	2.0	0	31.41

et al. (1997). These reaction rates were determined from experimental conditions in a temperature range of 700–955 °C and feed concentration at approximately atmospheric pressure.

The experimental design matrix shown in Table 6 consists of 15 sets of coded conditions, including eight factorial points ( $2^3$  full factorial design), six star points, and one center point. The distance between the star point and the center point is given by  $\alpha = 2^{n/4}$ , which equals to  $\pm 1.682$  in this study. The complete design matrixes of CCD and the simulation results, as shown in Table 6, reveal that the obtained  $C_2$  yield is varied from 11.59 to 34.12 %, depending on the operating conditions. These results can be fitted by a second-order quadratic model as given in Eq. (27):

Table 7 ANOVA for response surface quadratic model for singlestage membrane reactor

Source	SS	DF	MS	F value	p value
Model	851.09	9	94.57	49.00	0.0002
$X_1$	415.38	1	415.38	215.24	< 0.0001
$X_2$	224.34	1	224.34	116.25	0.0001
$X_3$	58.86	1	58.86	30.50	0.0027
$X_1X_2$	31.88	1	31.88	16.52	0.0097
$X_1X_3$	7.62	1	7.62	3.95	0.1036
$X_2X_3$	1.49	1	1.49	0.77	0.4201
$X_1^2$	52.36	1	52.36	27.13	0.0034
$X_2^2$	109.83	1	109.83	56.91	0.0006
$X_3^2$	37.54	1	37.54	19.45	0.0070
Residual	9.65	5	1.93		
Total	860.74	14			

SS sum of squares, DF degree of freedom, MS mean square

SD 1.39 R-Squared 0.9888

Mean 22.81 Adj R-Squared 0.9686

CV % 6.09 Pred R-Squared 0.4989

PRESS 431.34 Adeq Precision 20.531

$$Y = -330.594 + 19.779X_1 + 0.773X_2 + 20.031X_3$$

$$-0.020X_1X_2 + 1.220X_1X_3 - (5.391 \times 10^{-3})X_2X_3$$

$$-2.941X_1^2 - (4.260 \times 10^{-4})X_2^2 - 3.891X_3^2.$$
(27)

The validation of the obtained model is shown by the  $R^2$  error of 0.9888; 98.88 % of the response variability could be explained by this regression model. The statistical analysis based on ANOVA for the quadratic model is presented in Table 7. It is noted that the model F value is 49.00, indicating the significance of the model, and the p value is less than 0.0500, indicating the significance of the model terms, i.e.,  $X_1, X_2, X_3, X_1 X_2, X_1^2, X_2^2$  and  $X_3^2$ . The statistical analysis (Table 7) confirms the confidence intervals for each parameter in the regressed model.

Figure 8 shows the effect of the operating conditions on the product yield. It can be seen that the trend of the results obtained from the regression model predictions are consistent with the simulation results described in "Parametric analysis of the OCM membrane reactor" section. Under the same operating conditions (CH<sub>4</sub>/O<sub>2</sub> feed ratio = 2, operating temperature = 800 °C, and methane feed flow rate =  $2 \times 10^{-3}$  mol s<sup>-1</sup>), it is found that the C<sub>2</sub> product yield obtained from the rigorous model is 30 %, whereas that predicted by the regression model is 31.41 % with the percentage error of 4.7 %. From the *p* value of each factor in Table 7, it can be concluded that the CH<sub>4</sub>/O<sub>2</sub> feed ratio is the most significant effect on C<sub>2</sub> yield due to the lowest *p* value



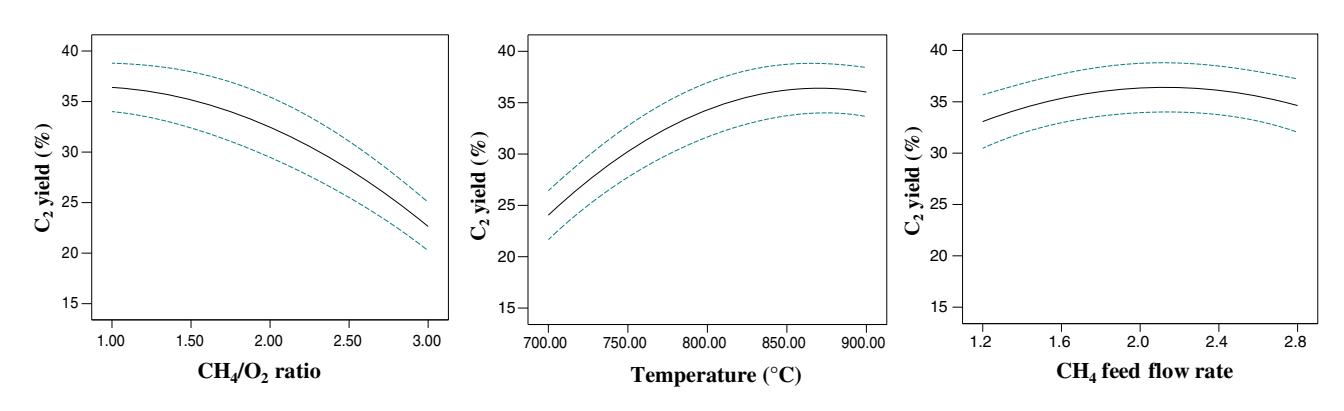


Fig. 8 Effect of  $CH_4/O_2$  ratio, temperature, and  $CH_4$  feed flow rate on  $C_2$  yield

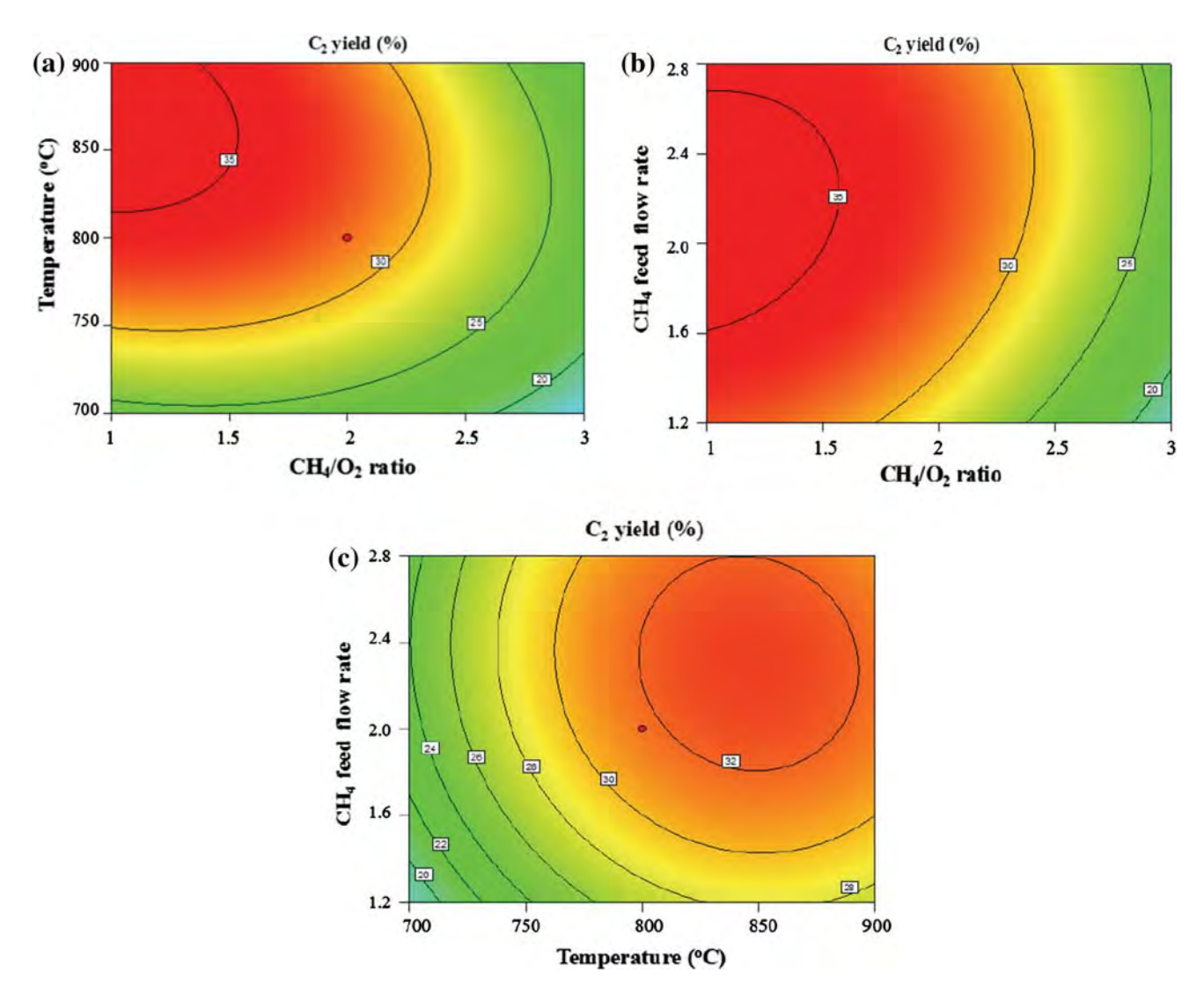


Fig. 9 Contour surface plot of  $C_2$  yield as a function of a  $CH_4/O_2$  feed ratio and operating temperature, b  $CH_4/O_2$  feed ratio and  $CH_4$  feed flow rate, and c operating temperature and  $CH_4$  feed flow rate



of < 0.0001. Figure 9 presents the contour surface plot that indicates the effect of interaction between two variables on  $C_2$  yield. It can be found that the interaction between  $CH_4/O_2$  feed ratio and operating temperature shows the most affect to  $C_2$  yield due to the lowest p value of 0.0097.

#### Optimization of process parameters

In order to optimize the C<sub>2</sub> yield of the OCM reactor, the regressive model Eq. (27) is used as an objective function. The optimization results show that the OCM reactor should be operated at the  $CH_4/O_2$  feed ratio of 0.83, the temperature of 847 °C, and CH<sub>4</sub> flow rate of  $2.1 \times 10^{-3}$  mol s<sup>-1</sup> to provide the maximum C<sub>2</sub> yield of 36.49 %. Under these operating conditions, the simulation result is further compared with the optimization result. It is noted that the simulated optimum yield of 35.21 % is well in agreement with the predicted value of 36.49 %, with a relatively insignificant error of 3.64 %. It can be concluded that the statistical model is useful in the accurate prediction and optimization of the OCM process. It is noted that the contour plot used to evaluate the effect of any two independent variables was built from the regression model (Eq. (27)) over the experimental region, as listed in Table 5. Because the optimum value of the CH<sub>4</sub>/O<sub>2</sub> feed ratio (0.83) is between the level  $-\alpha$  (CH<sub>4</sub>/O<sub>2</sub> ratio = 0.32) and -1 (CH<sub>4</sub>/O<sub>2</sub> ratio = 1), the optimum point do not appear in the contour plot (Fig. 9a).

#### **Conclusions**

In this study, the performance analysis and optimization of a dense tubular membrane reactor for oxidative coupling of methane (OCM) are performed. The performance of the OCM reactor in terms of CH<sub>4</sub> conversion, C<sub>2</sub> selectivity, and C<sub>2</sub> yield is considered, and the results show that the CH<sub>4</sub>/O<sub>2</sub> feed ratio, operating temperature, and methane feed flow rate are key parameters affecting the OCM reactor. From the simulation results, it is found that the C<sub>2</sub> product can be improved by increasing operating temperature as well as decreasing CH<sub>4</sub>/O<sub>2</sub> feed ratio. The simulated data obtained are further used for the optimization of the OCM process conditions. The central composite design and the response surface method are employed to determine the optimum C<sub>2</sub> yield. It is found that the optimum conditions to maximize the C<sub>2</sub> production (36.49 %) are at the temperature of 847 °C, the CH<sub>4</sub> flow rate of  $2.10 \times 10^{-3}$  mol s<sup>-1</sup>, and the CH<sub>4</sub>/O<sub>2</sub> feed ratio of 0.83. These data are beneficial for the optimal design of the OCM reactor for C<sub>2</sub> production.

**Acknowledgments** The support from the Thailand Research Fund and the Ratchadaphiseksomphot Endowment Fund, Chulalongkorn University is gratefully acknowledged.

#### References

- Arpornwichanop A, Wasuleewan M, Patcharavorachot Y, Assabumrungrat S (2011) Investigation of a dual-bed autothermal reforming of methane for hydrogen production. Chem Eng Trans 25:929–934
- Bernardo P, Gabriele C (2012) Integrated membrane operations in the ethylene oxide production. Clean Technol Environ Policy 14:475–485
- Bhatia S, Thien CY, Mohamed AR (2009) Oxidative coupling of methane (OCM) in a catalytic membrane reactor and comparison of its performance with other catalytic reactors. Chem Eng J 148:525–532
- Daneshpayeh M, Khodadi A, Mostoufi N, Mortazavi Y, Gharebagh RS, Talebizadeh A (2009) Kinetic modeling of oxidative coupling of methane over Mn/Na<sub>2</sub>WO<sub>4</sub>/SiO<sub>2</sub> catalyst. Fuel Process Technol 90:403–410
- Godini HR, Trivedi H, Gili de Villasante A, Görke O, Jašo S, Simon U, Berthold A, Witt W, Wozny G (2013) Design and demonstration of an experimental membrane reactor set-up for oxidative coupling of methane. Chem Eng Res Des 91:2671–2681
- Hong JH, Yoon KJ (2001) Oxidative coupling of methane over calcium chlorine-promoted calcium chlorophosphate. Appl Catal A 205:253–262
- Jašo S, Arellano-Garcia H, Günter W (2011) Oxidative coupling of methane in a fluidized bed reactor: influence of feeding policy hydrodynamics and reactor geometry. Chem Eng J 171:255–271
- Ji S, Xiao T, Li S, Xu C, Hou R, Coleman KS, Green MLH (2002) The relationship between the structure and the performance of Na-W-Mn/SiO<sub>2</sub> Catalysis for the oxidative coupling of methane. Appl Catal A 225:271–284
- Kao YK, Lei L, Lin YS (2003) Optimum operation of oxidative coupling of methane in porous ceramic membrane reactors. Catal Today 82:255–273
- Kim S, Yang YL, Jacobson AJ, Abeles B (1998) Diffusion and surface exchange coefficients in mixed ionic electronic conducting oxides from the pressure dependence of oxygen permeation. Solid State Ionics 106:189–195
- Liu H, Wang X, Yang D, Gao R, Wang Z, Yang J (2008) Scale up and stability test for oxidative coupling of methane over  $Na_2WO_4$  Mn/SiO<sub>2</sub> catalyst in a 200 mL fixed-bed reactor. J Nat Gas Chem 17:59–63
- Lunsford JH (2000) Catalytic conversion of methane to more useful chemicals and fuels: a challenge for the 21st century. Catal Today 63:165–174
- Nakisa Y, Reza GMH (2009) Modeling the oxidative coupling of methane: heterogeneous chemistry coupled with 3D flow field simulation. J Nat Gas Chem 18:39–44
- Omata K, Hashimoto S, Tominaga H, Fujimoto K (1989) Oxidative coupling of methane using a membrane reactor. Appl. Catal 51:L1–L4
- Shao Z, Yang W, Cong Y, Dong H, Tong J, Xiong G (2000) Investigation of the permeation behaviour and stability of a  $Ba_{0.5}Sr_{0.5}Co_{0.8}Fe_{0.2}O_{3-\delta}$  oxygen membrane. J Membr Sci 172:177–188
- Shao Z, Dong H, Xiong G, Cong Y, Yang W (2001) Performance of a mixed-conducting ceramic membrane reactor with high oxygen permeability for methane conversion. J Membr Sci 183:181–192



- Stansch Z, Mleczko L, Baerns M (1997) Comprehensive kinetics of oxidative coupling of methane over the  $\rm La_2O_3/CaO$  catalyst. Ind Eng Chem Res 36:2568–2579
- Tiemersma TP, Chaudhari AS, Gallucci F, Kuipers JAM, Annaland MS (2012) Integrated autothermal oxidative coupling and steam reforming of methane. Part1: design of a dual-function catalyst particle. Chem Eng Sci 82:200–214
- Tye CH, Mohamed AR, Bhatia S (2002) Modeling of catalytic reactor for oxidative coupling of methane using La<sub>2</sub>O<sub>3</sub>/CaO catalyst. Chem Eng Sci 87:49–59
- Wang H, Cong Y, Yang W (2005) Oxidative coupling of methane in  $Ba_{0.5}Sr_{0.5}Co_{0.8}Fe_{0.2}O_3$  tubular membrane reactors. Catal Today 104:160–167
- Zarrinpashne S, Ahari JS, Ahmadi R (2003) Development of a process for ethylene production from methane by OCM reactions and its commercialization challenges. In: 4th European congress of chemical engineering, Sep 21–25, 2003, Granada



#### Patent Review on "Biodiesel Production Process"

Issara Choedkiatsakul<sup>a</sup>, Kanokwan Ngaosuwan<sup>b</sup>, Worapon Kiatkittipong<sup>c</sup>, Navadol Laosiripojana<sup>d</sup> and Suttichai Assabumrungrat<sup>a,\*</sup>

<sup>a</sup>Center of Excellence in Catalysis and Catalytic Reaction Engineering, Department of Chemical Engineering, Faculty of Engineering, Chulalongkorn University, Bangkok 10330, Thailand; <sup>b</sup>Department of Chemical Engineering, Faculty of Engineering, Rajamangala University of Technology Krungthep, Bangkok 10120, Thailand; <sup>c</sup>Department of Chemical Engineering, Faculty of Engineering and Industrial Technology, Silpakorn University, Nakhon Pathom 73000, Thailand; <sup>d</sup>The Joint Graduate School of Energy and Environment, King Mongkut's University of Technology Thonburi, Bangkok 10140, Thailand

Received: March 10, 2011 Revised: July 10, 2011 Accepted: July 10, 2011

**Abstract:** The development of technology for biodiesel production is one of the attractive and challenging issues due to its possibility for commercial usage. Many patents have been investigated and proposed the intensification technology in order to improve and enhance the performance of biodiesel production process. In general, the invention topics mostly include feedstock materials, reactions, pretreatment technique, reactor/separation/purification technology and quality improvement. Therefore, this patent review summarizes the potential technology, development for biodiesel production presented in the mentioned topic and aims to keep the overview knowledge of the production process. Moreover, this review offers more clear comprehension and provides a guideline for further invention of any technologies for biodiesel production.

**Keywords:** Biodiesel, transesterification, free fatty acid, feedstocks, catalysts, reactor.

#### 1. INTRODUCTION

Biodiesel, a clean renewable fuel, has recently been considered as an alternative to petroleum-based fuels. It is derived from vegetable oils, animal fats and waste cooking oil. Biodiesel can be directly used or mixed with petroleum diesel without the major engine modification. The utilization of biodiesel gains more benefits; for example, it emits exhaust gases with less pollutant compared to diesel fuel. Carbon dioxide from a combustion of biodiesel is considered as carbon neutral, thus the global warming problem could be resolved. Moreover, it provides better fuel quality such as higher lubricating and cetane number than those of diesel fuel [1].

In general, there are four methods for biodiesel production: blending with petrodiesel, pyrolysis, microemulsification (co-solvent blending), and transesterification [1]. The vegetable oil/petrodiesel blending is not suitable for being used as long-term fuel in direct injection diesel engines since it causes engine problems presented in the combustion of neat vegetable oils. Pyrolysis involves the cleavage of chemical bonds to form smaller molecules by heating in the absence of oxygen [2-5]. Pyrolyzed oils have a process which produces higher ash content and carbon residue [1]. Microemulsification formulates biodiesel fuels by mixing with the low molecular weight alcohols to reduce the viscosity of vegetable oils [6]. The disadvantages of this technol-

ogy are incomplete combustion allowing the deposition of heavy carbon when used as an engine fuel. The most commonly used method for biodiesel production is through transesterification. Fats or oils are reacted with low molecular weight of alcohol to form alkyl esters (biodiesel) and glycerol with or without catalyst. The patents on biodiesel production via transesterification have been reported extensively [7-11]. Therefore, the scientific advancement of this technique is the main concept of this paper.

Generally, the properties of biodiesel fuel are following the specifications of ASTM D6751 and EN14214 standards as listed in Tables 1 and 2, respectively.

#### 2. BIODIESEL PRODUCTION PROCESS

Biodiesel is commonly produced via transesterification including many steps as illustrated in Fig. (1). Firstly, any free fatty acids (FFAs) and impurities in feedstocks have been pretreated by reacting with alcohol in the presence of catalyst. The generated products are biodiesel, by-products such as soap, glycerol, unreacted alcohol and trace amounts of water. All these by-products excluding biodiesel must be removed by a subsequent separation method. Lastly, biodiesel has to purify or improve the quality in order to meet the specifications of the international standard as mentioned earlier.

In this review paper, biodiesel production process can be categorized into 5 main sections, i.e. 1) Feedstock materials, 2) Pretreatment technique, 3) Reactions, 4) Reactor, separation and purification technology, and 5) Quality improvement. The details are provided in the following sections.

<sup>\*</sup>Address correspondence to this author at the Center of Excellence in Catalysis and Catalytic Reaction Engineering, Department of Chemical Engineering, Faculty of Engineering, Chulalongkom University, Bangkok 10330, Thailand; Fax: 662-218-6877; E-mail: Suttichai.A@chula.ac.th

Table 1. Biodiesel Standard as Listed in ASTM D6751 [1]

Province.	Test Method	Limits		TI */
Property	Test Method	Min	Max	Unit
Flash point (closed cup)	D 93	130.0	-	° C
Water and sediment	D 2709	-	0.050	vol%
Kinematic viscosity, 40°C	D 445	1.9	6.0	mm <sup>2</sup> s <sup>-1</sup>
Sulfated ash	D 874	-	0.020	wt%
Sulfur	D 5453	-	0.0015	wt%
Surrur			or 0.05 <sup>a</sup>	
Copper strip corrosion	D 130	-	No. 3	-
Cetane number	D 613	47	-	-
Cloud point	D 2500	-	Report <sup>b</sup>	° C
Carbon residue (100% sample)	D 4530	-	0.050	wt%
Acid number	D 664	-	0.80	mg KOH g <sup>-1</sup>
Free glycerol	D 6584	-	0.020	wt%
Total glycerol	D 6584	-	0.240	wt%
Phosphorus content	D 4951	-	0.001	wt%
Distillation temperature, atmospheric equivalent temperature, 90% recovered	D 1160	-	360	° C

Note: a The limits are for Grade S15 and Grade S500 biodiesel, respectively. S15 and S500 refer to maximum sulfur specifications (wt%).

Table 2. Biodiesel Standard as Listed in EN14214 [1]

	T (M () )	Limits		T
Property	Test Method	Min	Max	Unit
Ester content	EN 14103	96.5	-	wt%
Density (15°C)	EN ISO 3675 EN ISO 12185	860	900	kg m <sup>-3</sup>
Viscosity (40°C)	EN ISO 3104 ISO 3105	3.5	5.0	mm <sup>2</sup> s <sup>-1</sup>
Flash point	EN ISO 3679	120		° C
Sulfur content	EN ISO 20846 EN ISO 20884	-	10.0	mg kg <sup>-1</sup>
Carbon residue (10% dist. residue)	EN ISO 10370	-	0.30	wt%
Cetane number	EN ISO 5165	51	-	-
Sulfated ash	ISO 3987	-	0.02	wt%
Water content	EN ISO 12937	-	500	mg kg <sup>-1</sup>
Total contamination	EN 12662	-	24	mg kg <sup>-1</sup>
Copper strip corrosion (3 hr, 50°C)	EN ISO 2160	-	1	-
Oxidative stability (110°C)	EN 14112	6.0	-	hr

<sup>&</sup>lt;sup>b</sup> Report: Because the requirements regarding low-temperature properties are vary, the standard ASTM D6751 has a report requirement for its cloud point parameter.

Property	Test Method	Limits		Unit
Property	1 est Method	Min	Max	Unit
Acid value	EN 14104	-	0.50	mg KOH g <sup>-1</sup>
Iodine value	EN 14111	-	120	g iodine/100 g
Linolenic acid content	EN 14103	-	12	wt%
Content of FAME with ≥4 double bonds	-	-	1	wt%
Methanol content	EN 14110	-	0.20	-
Monoglyceride content (MG)	EN 14105	-	0.80	wt%
Diglyceride content (DG)	EN 14105	-	0.20	wt%
Triglyceride content (TG)	EN 14105	-	0.20	wt%
Free glycerol	EN 14105, EN 14106	-	0.02	wt%
Total glycerol	EN 14105	-	0.25	wt%
Alkali metals (Na+K)	EN 14108, EN 14109	-	5.0	wt%
Earth alkali metals (Ca+Mg)	prEN 14538	-	5.0	mg kg <sup>-1</sup>
Phosphorus content	EN 14107	-	10.0	mg kg <sup>-1</sup>

Note: FAME is fatty acid methyl ester.

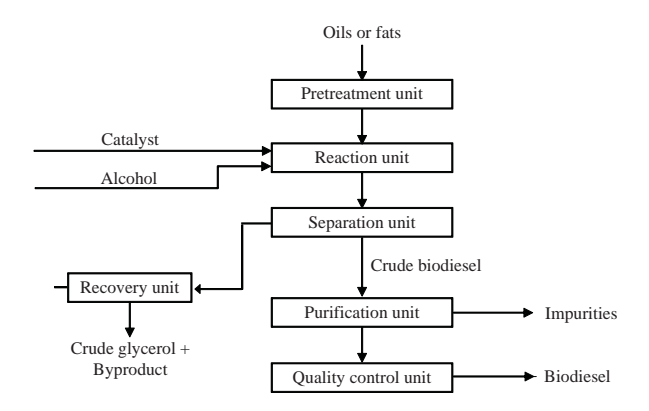


Fig. (1). The schematic diagram of biodiesel production process.

#### 2.1. Feedstock Materials

There are a large variety of feedstocks that can be used for biodiesel production. Normally, feedstock can be divided into three groups: vegetable oils (edible or non-edible oils), animal fats, and waste oil or waste cooking oil.

#### 2.1.1. Vegetable Oils

The conventional feedstocks for biodiesel production are edible vegetable oils. Traditional edible vegetable oils as feedstocks for biodiesel production are mostly from soybean, rapeseed, canola, palm, corn, sunflower, cottonseed, peanut, and coconut oils. Bournay *et al.* [12] investigated the biodiesel production from vegetable oil such as rapeseed, palm,

sunflower, soya, coconut, and cottonseed oils. It was found that biodiesel produced from transesterification in the presence of catalyst showed a good oil conversion at least 96.5% and also achieved high purity of glycerol (98%). This reaction is carried out in a fixed bed reactor at a pressure of 3 to 8 MPa and a temperature of 180 to 220°C with an hourly space velocity (HSV) of 1.2 to 0.1 h<sup>-1</sup>. In addition, biodiesel from high acidity vegetable oils (FFAs >0.5 wt%) particularly, soybean oil, has been studied by Siano et al. [13]. The results indicated that the conversion to methyl ester is equal to 96% at the reaction temperature below 200°C. Kovacs et al. [14] investigated the transesterification of sunflower oil in a homogenous phase with a C1-C4 alkanol in the presence of an aliphatic hydrocarbon solvent. This reaction performed in a temperature range of 60 to 140°C, under a pressure of 0.1 to 4 MPa. It was concluded that the steady state operation reaches within a short time period (10 min) and the conversion of 95 to 98% is obtained. Bhat et al. [15] also proposed the manufacture of biodiesel from soybean, rapeseed, corn, sunflower, cottonseed, palm, olive and coconut oils in the two reactors connected in series in order to simplify the product separation. It was found that the conversion of oils is almost 100% and the molar yield of esters is higher than 95%.

According to the production cost and food shortage, the production of biodiesel from several non-edible oil seeds has been investigated extensively. Since a number of non-edible oil crops can be grown on the waste lands which are not suitable for food crops in order to reduce the cost of production. Some of the non-edible oils used as feedstocks for biodiesel production consist of jatropha oil, karanja oil, algae, and other non-edible oils grown on the waste land area. Ghosh *et al.* [16, 17] investigated the preparation of biodiesel

from oil mechanically expelled from whole seeds of *Jatropha curcas*. It was found that the biodiesel from jatropha oil complies with EN14214 specifications. Moreover, it is a neat biodiesel for mobile or stationary engines without any engine modification with 94-98% yields of biodiesel. Besides, Rao *et al.* [18] proposed the extraction of the bio-active constituents, fatty acids and polar materials from jatropha (*Jatropha curcas*), and karanja (*Pongamia pinnata*) seeds in order to use as feedstocks for biodiesel production., To make biodiesel to reach the international specification standard, the purification processes after transesterification were also provided.

Algae are attractive feedstocks since they mostly contain major lipid content and can be grown under a variety of conditions. Machacek et al. [19] proposed the utilization of algal lipids into biodiesel. Triglycerides (TGs) in algae lipid are hydrolyzed into FFAs and then esterified using an acid catalyst to obtain biodiesel at a reaction temperature of 100°C and pressure of 202.65 kPa. The conversion of FFAs to biodiesel is about 85% in 1 h. Wu et al. [20] also studied the biodiesel production from extracted oil of algae via the enzyme-catalyzed transesterification process. It was concluded that 98.15% of oil is converted to biodiesel within 12 h. The other alternative feedstocks for biodiesel production are Kosteletzkya virginica, as a grain plant grown with seawater irrigation [21], and Balanites Aegyptiaca, as the drought-resistance tree species [22]. These feedstocks gain more benefits since it is a green raw material for low cost alternative biofuel production.

#### 2.1.2. Animal Fats

Animal oil and fats, low cost feedstocks, such as tallow, lard, and chicken fat are also used for biodiesel production. Comieri et al. [23] proposed the utilization of fish oils for biodiesel production via transesterification with ethanol using sulfuric acid as a catalyst. The product mixture obtained an ethyl ester content of 85-95%. Tallow fat was also used as feedstock for biodiesel fuel production as reported by Carroway [24]. When the cracking temperature is from 330 to 385°C under the ambient pressure in the absence of a catalyst, yield of biodiesel product is about 83.2%. This also complies with the environmental regulations in the ASTM standard. Franzoi [25] studied the effect of feedstocks from an animal fats or oils comprising of beef fats, tallow, poultry fats, pork fats, and milk fats on the biodiesel properties. It was revealed that the impurities and proteins from animal fats and oils should be prior removed in order to prevent the diesel engine fouling and limit contaminant follows ASTM specifications. Misra et al. [26] also provided the methods to produce biodiesel from natural sources such as chicken feathers from a poultry processing operation. In this method, the biological material was hydrolyzed to obtain free amino acids as a biofuel feedstock which is further converted to fatty acid esters.

Animal fats as feedstocks for biodiesel fuel have several restrictions because the biodiesel fuel contains a lot of contaminates which limit their usage as a commercially acceptable biofuels. Therefore, the usage of other feedstocks material should be further investigated.

#### 2.1.3. Waste Oil & Waste Cooking Oil

Waste oils and waste cooking oils are the other promising alternative feedstocks for biodiesel production. There are many advantages for waste oils and waste cooking oils utilization. For example, they can neglect the waste treatment step and reduce the environmental pollution from the production process. Generally, waste oils and waste cooking oils contain high levels of FFAs and undesired impurity. Therefore, the additional pretreatment processes are required. Aiken [27] proposed the esterification of FFAs contained in waste oil feeds as a pretreatment step to obtain biodiesel; and subsequently transesterification with methanol using a basic catalyst to produce more biodiesel. Similarly, Elliott [28] also proposed the method for converting of TGs in waste grease sources to a fatty acid composition. The fatty acid composition is then esterified to make alkyl esters. The sludges generated during the wastewaters treatment were also used as feedstock for biodiesel production [29-30]. It has been discovered that the extracted lipids from wastewater sludge offers an economic and highly effective feedstock for biodiesel production. Moreover, Chatterjee et al. [31-32] proposed an acid catalyzed transesterification with alcohol to produce biodiesel from crude tall oil as a by-product during the kraft pulping process. However, the biodiesel yield is only about 60% based on the weight of the initial crude tall oil used.

#### 2.2. Pretreatment Technique

Nowadays, the feedstocks with high levels of FFAs and the other impurities have widely been used as raw material for biodiesel production due to the economic beneficial. Therefore, the unfavorable components such as high particulates FFAs and the other impurities require a suitable pretreatment process before using as feedstock for biodiesel production.

Toeneboebn et al. [33] proposed the possibility to remove sulfur-containing compounds from fatty materials using silica hydrogel. It was found that amorphous silica hydro gels exhibit an excellent adsorption capacity of sulfurcontaining compounds in fatty materials. Thus, it can improve the quality of oil before using as feedstock for biodiesel production. Jalalpoor et al. [34] investigated the pretreatment of degummed TGs using an adsorbent particles (TriSyl® silica hydrogel particle). It was found that adsorbent particles can reduce an amount of phosphorus to about 10 ppm. The adsorbent-free TGs product is then contacted with a stripping medium to reduce the amount of FFAs with less than 0.20 wt% based on a total weight of adsorbent-free TGs product. Moreover, using adsorbent material in the pretreatment was also investigated by Nakazono [35]. The FFAs and the other moisture were removed by heating the raw material oil under reduced pressure. Then adsorption in two stages with basic-treated activated carbon and a hydrophilic adsorbent such as activated alumina and silica gel was carried out.

Roden *et al.* [36] proposed a method for pretreatment feedstocks containing high FFAs with glycerolysis reaction. In this process, the glycerol as a by-product from transesterification can react to FFAs in feedstock in presence of caustic base at reaction temperature range of 120 to 215°C under

pressure from 0.67 to 2 kPa. Hence, the FFAs in the feed-stock are converted to MGs and DGs. This approach produces a low FFAs feedstock that can then be processed using traditional alkali-catalyzed methods for biodiesel production. Similarly, Jackam *et al.* [37] also applied a glycerolysis reaction to convert FFAs into TGs using a base catalyzed transesterification to produce biodiesel. It was also concluded that the process can use feedstocks containing up to 100% of FFAs contents to produce biodiesel with minimal

In addition, the pretreatment method for feedstocks with high concentration of FFAs using acid catalysis followed by alkali catalysis was also extensively proposed [38-42]. Acid catalysis is a relatively fast reaction to convert FFAs into methyl esters. Therefore, esterification is used as a pretreatment step. When FFAs concentration in the feedstock has been adequately reduced, an alkali catalyst is subsequently added to convert the TGs into methyl esters. However, this method still has some drawbacks such as high losses of starting materials and processing problems since it requires excess methanol during the pretreatment step to dilute the water produced into a level where it does not limit or stop the reaction.

Moreover, there are some patents which showed the pretreatment of feedstocks by using enzyme. Dayton *et al.* [43, 44] proposed a continuous enzymatic (Thermomyces lanuginosus) treatment of lipid-containing compositions using a plurality of fixed bed reactors. It was found that the process and apparatus of this invention are responsible to produce the high quality products without deodorizing the lipid-containing composition from the enzyme treatment steps. However, this method is difficult to perform on a large scale production due to the expensive cost of enzymes.

#### 2.3. Reactions

waste generation.

#### 2.3.1. Reactions Related to Biodiesel Production

As mentioned earlier, the most commonly used method for biodiesel production is through transesterification. This reaction is expressed in Eq. (1).

Esterification is another important reaction for biodiesel production; it is mainly the reaction between alcohols and carboxylic acid to make esters product as shown in Eq. (2). This reaction is mostly presented in the pretreatment step in biodiesel production from high FFAs feedstocks. Amount of FFAs can be reduced by esterification with low molecular weight alcohol in the presence of acid catalyst. Biodiesel and water are produced from this reaction.

Alternatively, TGs can react with water to form FFAs and glycerol via complete hydrolysis as presented in Eq. (3). FFAs can then be converted to biodiesel via esterification reaction. Nevertheless, there are not many patents reporting about hydrolysis for biodiesel product. Only used 2-steps via hydrolysis-esterification to produce biodiesel.

In addition, saponification of FFAs with alkali catalyst can occur as a side reaction for high FFAs feedstocks as illustrated in Eq. (4). Undesirable product (potassium soap) formation creates serious problems for product separation and ultimately hindering catalytic activity.

(FFAs) (Potassium hydroxide) (Potassium soap) (Water)

In general, transesterification can occur via both catalytic and non-catalytic methods. For catalytic method, the reaction is catalyzed by three types of catalysts which are alkali catalyst, acid catalyst and enzyme catalyst. On the other hand, for non-catalytic method, the reaction is carried out at high temperature and high pressure with supercritical alcohol. The advantages and disadvantages of each method possibility to produce biodiesel are summarized in Table 3 [45].

#### 2.3.2. Catalytic Method

For homogeneous catalytic method, biodiesel is commonly produced with the use of homogeneous alkali catalysts such as sodium hydroxide (NaOH) or potassium hydroxide (KOH) [46-50]. The catalysts are able to catalyze the reaction at low temperature and atmospheric pressure with high methyl ester yields in a short time period. However, this homogeneous alkali-catalyzed process is sensitive to water and FFA content hence; it is not suitable for using high levels of moisture and FFAs feedstocks since alkali catalyst can react with FFAs to form soap and water. The undesirable products could result in the reduction of FAME yields. Similarly, high water contents in feedstock can hydrolyze TGs to form FFAs (Eq. (3)) and also reduce the FAME yields.

Therefore, the acid catalyzed transesterification process is performed for feedstocks with high levels of FFAs because the performance of acid catalysts such as sulfuric acid  $(H_2SO_4)$  and hydrochloric acid (HCl) are not sensitively

Variable	Homogeneous Catalyst		Heterogeneous	Enzyme	Supercritical	
variable	Alkali Catalysis	Acid Catalysis	Catalyst	Catalysis	Alcohol	
Reaction temperature (°C)	60–70	55–80	180-220	30–40	239–385	
FFAs in raw materials	Saponified products	Biodiesel	Not sensitive	Methyl esters	Biodiesel	
Water in raw materials	Interference with reaction	Interference with reaction	Not sensitive	No influence	-	
Yield of methyl esters	Normal	Normal	Normal	Highest	Good	
Recovery of glycerol	Difficult	Difficult	Easy	Easy	-	
Purification of methyl esters	Repeated washing	Repeated washing	Easy	None	-	
Production cost of catalyst	Cheap	Cheap	Potentially cheaper	Relatively expensive	Medium	

Table 3. The Advantages and Disadvantages of Several Methods for Biodiesel Production [45]

affected in the presence of FFAs in feedstocks. It can catalyze both esterification and transesterification simultaneously [8, 59, 60]. However, the reaction rate of the acid-catalyzed process is relatively slower than that of alkali-catalyzed process. Generally, the homogeneous catalyst process generates large amounts of waste water and it is impossible to recover the catalyst from the reactant/product mixtures.

In order to solve the problems mentioned above, there are many patents investigating the utilization of heterogeneous catalysts since the process with heterogeneous catalysts can eliminate the drawback of homogeneous catalysts. Firstly, it can be applied for the feedstocks with high levels of FFAs [56, 64, 66, 68]. Secondly, the catalysts are more easily separated from reaction mixtures which reduce the amount of wastewater generation in the purification process [54, 64, 65, 67, 70]. Lastly, the generation of undesired products can be suppressed [53, 57, 61, 63]. Therefore, the heterogeneous catalysts process could have a cheaper production cost [51, 52, 55, 58, 62, 66, 69]. The various types of homogeneous and heterogeneous alkali catalysts and acid catalysts for biodiesel production are summarized in Tables 4 and 5, respectively.

Enzyme catalyzed transesterification is another method for biodiesel production. Lipase exhibits high catalytic activity with high quality biodiesel production. This method is very interesting due to many reasons such as the ease of product separation and recovery, less wastewater generation and no side reactions [71-77]. The enzyme catalysts offer more advantages than the conventional solid catalysts. However, the major disadvantage of lipase is its high cost. Important enzyme catalysts used for biodiesel production is illustrated in Table **6**.

#### 2.3.3. Non-Catalytic Method

Non-catalytic method provides a new approach for biodiesel production. Transesterification process with the supercritical alcohol operates at high levels of temperature and pressure without any catalysts. In general, methanol is used in the supercritical state so-called "supercritical methanol" processing. However, the other alcohols such as ethanol, propanol or butanol can also be applied. The great benefit of this process is that the reaction under supercritical conditions can enhance high biodiesel yield within a few minutes. Nevertheless, the main drawback of this process is its high capital and operating costs, which make it not suitable in the large scale production. Some of the patents investigating the biodiesel production via non-catalytic method are summarized in Table 7.

#### 2.4. Reactor, Separation and Purification Technology

Although transesterification is the conventional method for biodiesel production, there are some drawbacks of this reaction. For example, solubility limit of oils and alcohol caused the restriction of reaction rate. In addition, the transesterification is reversible reactions resulting in an upper limit of the conversion. Moreover, it may generate significant amounts of toxic waste water from the purification process. Therefore, there are a lot of patents investigating and proposing various intensification technologies in order to solve the problems mentioned above.

#### 2.4.1. Type of Reactors

Fleisher [88] proposed a continuous process for biodiesel production with less residence time in a plug flow reactor. A plug flow reactor is facilitated including a static mixing effect by establishing baffle and packing material to allow the turbulent flow of reactants. The conversion of the TGs to FAMEs is about 70 to 99% in the temperature range from 80 to 180°C with a residence time less than 3 min and pressure of 3 MPa or less. The two-staged reactor with helically coiled concentric tubes coupling with a hydroclone separator for glycerol removing was used to achieve the higher yield of ester [89-90]. TGs react with alcohol in the presence of a catalyst to produce the products mixture in a first reactor, and then the resulting mixture passed through a separating unit to remove a by-product glycerol. Fresh alcohol and catalyst are added to the remaining mixture to complete the reaction and increase its conversion in a second stage reactor. The result shows that the overall conversion in this process is greater than 99%. Chun et al. [91] also proposed the two stages reactor for biodiesel production. This method achieved 99.7% conversion in the absence of catalyst and did

Table 4. Homogeneous and Heterogeneous Alkali Catalysts for Biodiesel Production

Туре	Catalyst	Catalyst (wt %)	Alcohol	Molar Ratio of Oil to Alcohol	Reaction Conditions	Ester Conversion (%)	Ester Yield (%)	Ref.
	NaOH, КОН	0.1-5	C1, C2	0.5:1-1.5:1	30-78°C, 30-90 min	98-100	-	[46]
	NaOH (0.1mol %phase transfer catalyst)	17	C1, C2	1:5	22-24°C, 2 h	98	-	[47]
Homogeneous	LiOH·H <sub>2</sub> O	10	C1	-	70°C, 2 h	-	-	[48]
	NaOH, КОН, СаОН	-	C1	-	30-80°C, 90-500 kPa, 0.5-10 h	> 95	-	[49]
	NaOH, KOH	0.1-2	C1-C4	3:1-10:1*	80-150°C, 1.5 min	> 96		[50]
	CuO, MnO, TiO	1-20	C1-C4	3:30-1:40	150-260°C, 1-70 atm, 5-60 min	-	92-97	[51, 52]
	Zr(OPO <sub>3</sub> K) <sub>2</sub>	-	C1-C5	1:0.1-1:3	130-220°C, < 100 bar, LSHV=0.1-3h <sup>-1</sup>	85-95	-	[53]
	Mesoporous Calcium Silicate	-	C1	1:24	< 100°C, 24 h	100	-	[54]
Heterogeneous	Titanate-based Na	1-5	C1	1:30	150-290°C, 2 h	96.9	-	[55]
	$A_x B_{2-x} O_{4-x}$ where $A = Ca$ , $Mg$ $B = Mg$ , $Ce$ , $Ti$ $x = 0.25-1.2$	-	C1-C4	0.5:1-4:1*	100-230°C, LHSV=1.2 h <sup>-1</sup>	> 95	-	[56]
	$Zn_xA1_2O_{(3+x)} + ZnO$ where x = 0-1	-	C1-C5	0.1:1-3:1*	150-180°C, 1-7 MPa, LHSV=0.1-3 h <sup>-1</sup>	Up to 98	-	[57]
	Fibrous catalyst	-	C1-C5	1:100-1:3	10-100°C, up to 24 h	95%	-	[58]

Note: LHSV is the liquid hourly space velocity (h<sup>-1</sup>)

 Table 5.
 Homogeneous and Heterogeneous Acid Catalysts for Biodiesel Production

Туре	Catalyst Type	Catalyst (wt.%)	Alco- hol	Molar Ratio of Oil to Alcohol	Reaction Conditions	Ester Conversion (%)	Ester Yield (%)	Ref.
	H <sub>2</sub> SO <sub>4</sub> , HCl	< 30	C1-C4	1:1-1:15	> 50°C	-	> 98	[59]
Homogene- ous	H <sub>2</sub> SO <sub>4</sub> , HCl	0.1-1	C1, C2	<1:6	70-200°C	80-97	-	[8]
	H <sub>2</sub> SO <sub>4</sub>	1-2	C1	1:1-1:5	80-200°C	> 85	-	[60]
	Nb <sub>2</sub> O <sub>5</sub>	1-5	C1, C2	1:3-1:30	65 - 290°C, 1 - 8 h	90-98	-	[61]
	W/Zr-based catalyst	-	C1, C2	1:40	150-350°C, 0.1-1 h,WHSV=1.85 h <sup>-1</sup>	93	-	[62]
Heteroge- neous	$\begin{split} &(ZrO_x)_y/Al_2O_3)_{1-y}\\ &(SbO_x)_y/Al_2O_3)_{1-y}\\ &(TiO_x)_y/Al_2O_3)_{1-y}\\ &where \ x=1.5-2.2,\\ &y=0.05-0.95 \end{split}$	~ 9	C1-C5	1:1-1:3	170 - 250°C, < 100 bar, HSV= 0.1-3 h <sup>-1</sup>	80-85	90	[63]
	ZrO <sub>2</sub> / Al <sub>2</sub> O <sub>3</sub> , ZrO <sub>2</sub> / PO <sub>4</sub> , ZrO <sub>2</sub> / TiO <sub>2</sub>	-	C1, C2	1:1.5	150-350°C, 0.1-3 MPa, 0.1-1 h	up to 99	-	[64]

<sup>\*</sup> Mass ratio of oil to alcohol

(Table 5) contd....

Туре	Catalyst Type	Catalyst (wt %)	Alco- hol	Molar Ratio of Oil to Alcohol	Reaction Conditions	Ester Conversion (%)	Ester Yield (%)	Ref.
	Cation exchange resin	26.8	C1, C2	1:10	80°C, 15 h	95	-	[65]
	Sn+ Sn alloy; Pb, In	-	C1-C6	1:3-1:50	118-350°C, ≥ 1 atm, 3-10 min	95	-	[66]
	MnTiO <sub>3</sub> , ZnTiO <sub>3</sub> , ZnZrO <sub>3</sub> , FeVO <sub>4</sub>	-	C1	1:27	200°C, 10-24 h, LHSV= 1 h <sup>-1</sup>	-	92-99	[67]
	$CH_xS_yO_z$ where $x = 0.53-0.87$ $y = 0.015-0.03$ $z = 0.35-0.51$	-	C1-C3	1:1-1:30	35-90°C, 1-12 h	45-99	-	[68]
	Sulfonic acid group- introduced amor- phous carbon	-	C1-C4	1:40	90-160°C, 3 MPa, up to 50 h	-	Up to 99	[69]
	Nb <sub>2</sub> O <sub>5</sub> ·nH <sub>2</sub> O	1-2	C1, C2	1.5:6	80-200°C, 1-5 h	-	75	[70]

Note: LHSV is the liquid hourly space velocity (h<sup>-1</sup>), WHSV is the weight hour space velocity (h<sup>-1</sup>), HSV is the hourly space velocity (h<sup>-1</sup>)

Table 6. Enzyme Catalysts for Biodiesel Production

Enzyme Type	Enzyme (wt.%)	Acyl Acceptor	Solvent	Molar Ratio of oil to Alcohol	Reaction Conditions	Yield (%)	Ref.
Lipozyme® TL, Lipozyme® RM, Novozym® 435	2-30	Alcohol C1-C5	Tert-butanol	1:3-1:6	20-60°C, 4-24 h	≥94	[71]
Candida antarctica, Thermomyces lanuginosa, Pseudomonas fluores- cens, Pseudomonas cepacia, Chro- mobacterium isco sum	-	Alcohol C1-C4	C4-C8 tertiary alcohol	-	0-90°C, 1-180 min	> 99	[72, 73]
Candida Antarctica, Thermomyces lanuginosus, Humicola insolens	-	Methanol Ethanol	-	1:0.1-1:10	30-60°C, 3 h	-	[74]
Candida antarctica, Candida rugosa, Rhizomucor miehei on solid supported	-	Cetyl alcohol	Alkane, Alco- hol, Aldehyde, Ketone	1:2	35-60°C, 3-6 h	Up to 96	[75]
Candida antarctica or Rhizomucor miehei	5-30	Low carbon fatty acid ester	-	1:3-1:20	20-60°C, 20 h	Up to 96	[76]
Candida Antarctica type B		C1-C3 alkyl alcohol	-	1:2-2:1	40-90°C, vacuum, 21 h	89	[77]

Table 7. Biodiesel Production via Non-Catalytic Method

Alcohol	Co Solvent	Co-Solvent Alcohol: Oil Reaction Conditions		Conver-	Yield	Ref.		
Alcohol	Co-solvent	Molar Ratio	T (°C)	P (MPa)	Time (min.)	sion (%)	(%)	Kei.
C1-C4	-	3:1-1000:1	240-400	0.4-25	1-480	Up to	-	[78]
C1	-	1:2-2:1 (volume ratio)	370-500	20-60	4-12	-	100	[79]

Alcohol	Co-Solvent	Alcohol: Oil Molar Ratio	<b>Reaction Conditions</b>			Conversion (%)	Yield (%)	Ref.
C1-C5	CO <sub>2</sub> , Hydrocarbon C3-C6	3:1-400:1	$T > 0.9xT_{c, co-solvent}$	$P > 0.9 x P_{c, co-solvent}$	-	Up to 98	-	[80]
C1, C2	-	3.5:1-42:1	150-450	2-40	6	100	-	[81, 82]
C1, C2	-	3:1-24:1	250-425	10-30	0.73-8.3	> 98	-	[83]
C1-C4	-	2:1	> 180	> 1	5-10	95	-	[84, 85]
C1-C2	CO <sub>2</sub> , SO <sub>2</sub> , NO, alkane, ether, ester	40:1	200-450	5-40	2-30	> 90	-	[86]
C1-C8	-	0.5:1-10:1 (volume ratio)	300-400	10-20	5-60	-	> 93.5	[87]

Note: \* Temperature is in the Kelvin unit.

not require further purification process for removing catalyst and glycerol. However, it required a high temperature and high pressure to operate (250-320°C, up to 0.5 MPa).

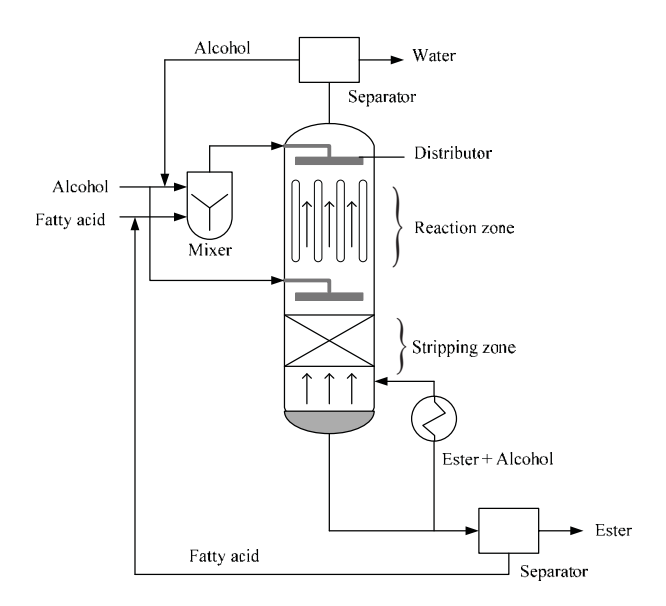


Fig. (2). The modified packed bed reactor proposed by Moritz et al. [92-93].

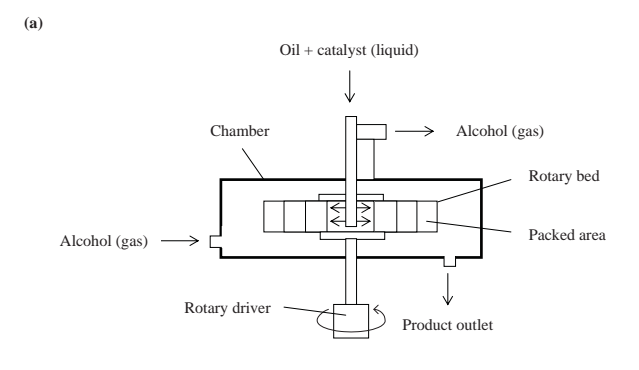
Moritz *et al.* [92-93] proposed a method for esterification that was carried out in a column with a multi-part packing acting as a reaction zone and a stripping section as illustrated in Fig. (2). By-product, water was removed from the reaction zone by alcohol rich counter-flow acting as a stripping gas without other auxiliary gas, hence high yield was achieved.

Elliott [94] investigated the biodiesel production from low cost feedstocks using a packed bed reactor containing solid acid catalyst followed by catalytic reactive distillation. It was found that the continuous process with continual removal of by-product water and recycle of alcohol achieved the high conversions (>99%). Moreover, Chen et al. [95] proposed the rotating packed bed reactor for high conversion of oil to biodiesel. The rotating packed bed reactor comprises a container and a rotary bed as illustrated in Fig. (3a). The reaction takes place in the container while the rotary bed was mounted and powered to rotate in the container. The centrifugal rotation of the rotary bed forced the oil and additive to pass through the filler in the packed reaction region and react with the reactant gas. Hence, it increased the transesterification rate and thus obtained high conversion. In addition, Chen et al. [96] also presented the method for enhancing liquid phase biodiesel conversion in the rotating packed bed reactor (Fig. (3b)). The rigid baffles were mounted inside the peripheral wall of the container in order to carry out the rapid and preliminary phase separation between esters and glycerol. The result illustrated that the obtained conversion was in the range from 86.38 to 91.26% with the rotation speed range of 300 to 1,500 rpm and reaction temperatures of 40 to 58°C.

Lichtenberger et al. [97-98] disclosed the method using an annular gap reactor to provide more efficient mixing for biodiesel production. The annular gap reactor composes of a rotor rotating to provide an annular flow containing a highshear rate in the reaction zone. It was also concluded that the use of this configuration greatly increased the speed of the main reaction time with higher yields. It was obtained up to 120 times faster than that of a batch reactor. Jovanovic et al. [99] provided a method for producing biodiesel using microreactor with a 100 µm thickness of microchannel. The operating conditions was also carried out under ambient and/or supercritical conditions for transesterification at a temperature ranging from 25 to 350°C. It was found that the residence time of microreactor affects biodiesel conversion. Under ambient condition, the conversion of soybean oil to biodiesel was about 12 to 91% with respect to residence time increasing from 0.4 to 10 min.

Tremblay *et al.* [100] studied the membrane reactor for biodiesel production with the continuous removal of fuel or other products in reaction mixtures. This system requires a small amount of homogeneous catalyst and consequently offers less water consumption for product washing, less

saponification and clearer color product. An amount of catalyst used in the reaction was about 33 times lower than that of a conventional process used in the industry.



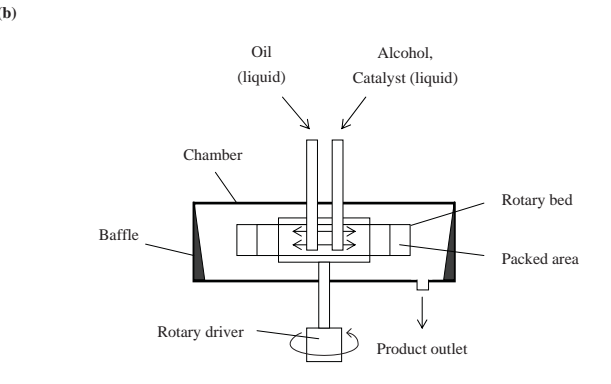


Fig. (3). The modified rotary packed bed reactor proposed by (a) Chen *et al.* [95] and (b) Chen *et al.* [96].

Pachauri [101] proposed a method for biodiesel production by reactive distillation system. Reactive distillation allows transesterification with product recovery in a single system. It effectively reduces the excess alcohol in a feed. By combining the separation process within the reactor, the products can be continuously removed from a reaction zone leading to significant improvements in the product selectivity, conversion and overall yield. The result illustrated that the specifications of the products such as bound glycerol, total glycerol, flash point, kinematic viscosity and acid number were in an acceptable range of the ASTM standard.

Geier D and Soper JG [102] proposed the utilization of a simulated moving bed chromatographic apparatus which simultaneously provided transesterification and separated glycerol and fatty acid monoester products. The apparatus comprised of a plurality of column segments 1-10 connected in a circular series as illustrated in Fig. (4). Transesterification was carried on the column 6 and 10. Since, the catalytic chromatographic bed material has polar moieties in the solid phase, therefore, more polar glycerol product was preferentially partitioned with the chromatographic bed material and removed from the catalytic chromatographic bed at column 3. On the other hand, the non-polar fatty acid monoester was preferentially partitioned with the moving phase and removed at column 10. The column segments 4-5 between the glycerol outlet and oil feed inlet are designated as a solid regeneration zone. Alcohol is introduced into the catalytic chromatographic bed to regenerate alcohol content and provide the effluent flow for withdrawal of the glycerol. Accordingly, columns 2 and 3 are designated as desorption/ regeneration zone. The remaining reactant was also reloaded at column 1 to further pump to the reaction zone for complete reaction.

Bowen *et al.* [103] integrated the biodiesel processor allowing more compact configuration and cleaner appearance without the external plumbing. The biodiesel processor

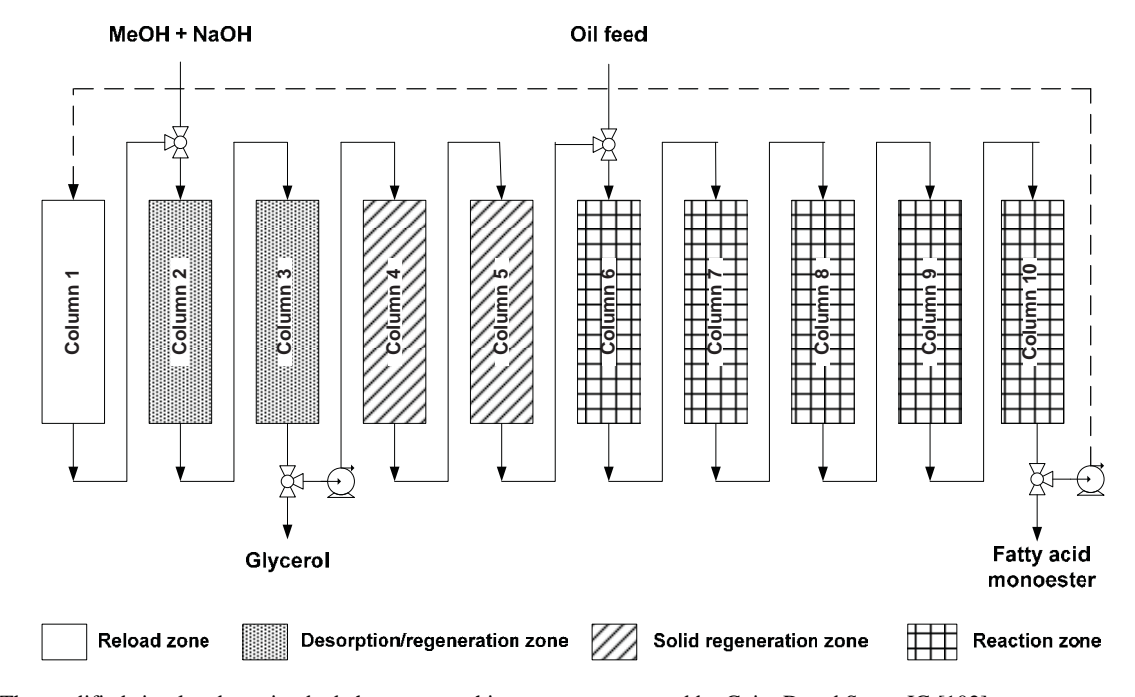


Fig. (4). The modified simulated moving bed chromatographic apparatus proposed by Geier D and Soper JG [102].

composes of a main reaction tank and a secondary tank as shown in Fig. (5). A main reaction tank was used to store materials and carry out the reactions. The secondary tank is divided into two internal tanks which integrated and disposed inside the main reaction tank in order to supply the ingredients such as methanol, sodium hydroxide and sulfuric acid, for the esterification and transesterification, respectively. Moreover, the glycerol removal system from the main reaction tank and the fuel washing were included in order to obtain the final biodiesel product.

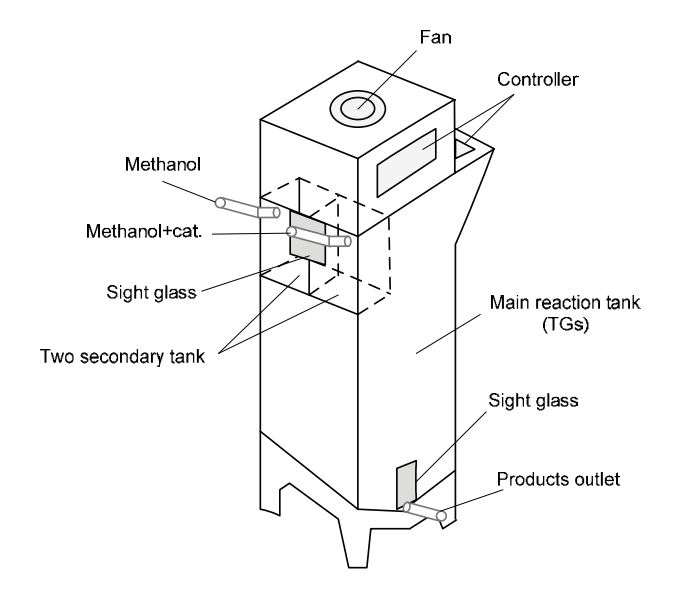


Fig. (5). The modified biodiesel processor proposed by Bowen et al. [103].

Jachuck et al. [104] also disclosed the system with a continuous processing of fluid in one embodiment. A continuous thin film reactor can perform various processes such as distillation and evaporation, fluid-fluid or solid-fluid-fluid reactions, organic reactions, cooling and desalination. Biodiesel product can be purified by evaporation and distillation using this reactor. The reactor had an inner vessel situated within the outer vessel as shown in Fig. (6). The inner surface of an outer vessel is designed to allow fluid being processed to descend in a substantially uniform thin film. A relatively high rate of thermal transfer, mass transfer, mixing or other transport rates were occurred. An outer surface of the inner vessel serves as a heat exchange surface for the fluid being processed. On the other hand, an inner surface serves as exchange surface with different from that of the fluid being processed to impart a temperature difference. An annular space defined between the outer vessel and the inner vessel was provided a pathway for the second fluid along this reactor. The processing fluid was implemented and the second fluid might be moved within the annular space in a counter-current manner relatively to the flow of the fluid being processed.

### 2.4.2. Process Improvement

In order to create the effective mixing of the reactants so as to provide the high reaction rate and yield of biodiesel production, a lot of patents have been developed. Ames [105] proposed the continuous flow system including a high turbulence flow-through processor mixer. This processor mixer maximizes the reaction rate by dramatically increasing the surface area of TGs and methanol interface with Reynold number to be greater than 100,000. Panagiotou et al. [106] proposed the exemplary apparatus/systems that facilitated direct impingement of the streams in a continuous microreactor with an intensify pump. This intensify pump generated high level of energy dissipation per unit volume resulting in intimate contact of the components in the streams. Therefore, it can enhance and promote the kinetic reaction. Moreover, Kozyuk [107] applied the control flow cavitation apparatus to increase the mixing efficiency in order to obtain high yield in a short residence time. The localized flow is constricted using a diaphragm with one or more orifices, baffles or nozzles. The result showed that the conversion of fatty acid alkyl esters (FAAE) is greater than 90%. In addition, Kozyuk et al. [108] also used the cavitation effect to enhance filterability in the process since the cavitational energy can entrap some impurities in a waste glycerol and therefore reduce the clogging effect in the membrane filter.

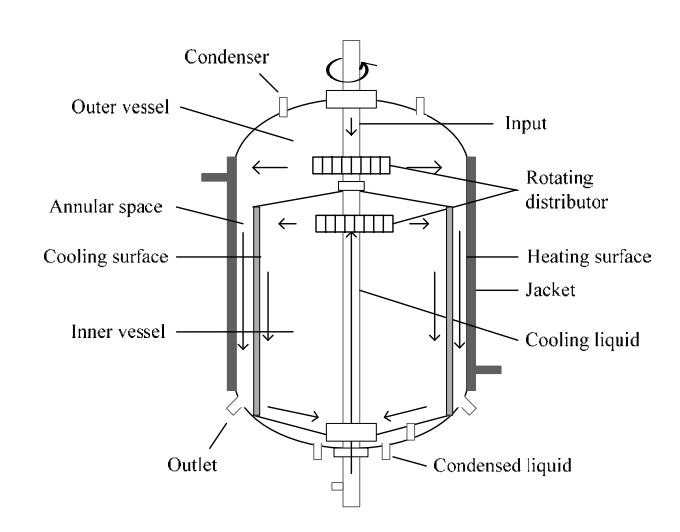


Fig. (6). The modified continuous film reactor proposed by Jachuck et al. [104].

Lafleur et al. [109] proposed a method for biodiesel production using a chamber with the atomizers. The atomizers make the feedstock, alcohol and catalyst in a mist form (1 to 15 μm) and provide a maximum mixing in an extremely short time interval. It was found that the conversion of feedstock can approach 100% within 10 seconds. Farid et al. [110] also proposed a process using the atomizers for biodiesel production via plug flow reactor. An atomized feedstock was reacted with gaseous alcohol in a reaction vessel in the presence of catalyst. The result illustrated that 80% conversion can be obtained within 5 min of reactants contacting time.

Several patents related to the convenience of product separation and/or purification have also been developed. Bradin et al. [111] proposed the biodiesel production process, which obtained pure glycerol by-product as a direct

feedstock for glycerol ether manufacture. This patent applied Kolbe electrolysis to remove FFA salts from crude glycerol by converting FFA salts into hydrocarbon products. It can easily separate and remove from the crude glycerol fraction. Dekhtiaruk *et al.* [112] applied a reactor vessel, in which the reaction chamber area is subjected to high rotary electromagnetic fields, for completion of transesterification in a short time period. The resonant effect allows the control of turbulence leading to enhance the rate of reaction.

Moreover, Porter *et al.* [113] applied the radio frequency microwave energy to improve biodiesel production process. The microwave wavelength of 0.005 to 0.5 meters was supplied to a reaction mixture. It was found that this microwave energy promotes the removal of FFAs, enhances the reaction rate, and improves the product recovery in the separation of biodiesel product from alcohol and glycerol. Similarly, Meikrantz [114] also proposed the method for biodiesel production and separation by applying microwave energy. The reaction and separation vessels were designed to be transparent for microwave radiation. It was found that the microwave energy with microwave power up to 5,000 Watts can enhance the rate of reaction and facilitate the separation of the product.

The method of biodiesel purification with an applied electric field was proposed by Powell [115]. The methyl esters product was mixed with acid and salt solution to form an emulsion solution and exposed to an electric field. The electric field can break the emulsion facilitating the separation of the purified oil from the remaining impurities. Thus, a clean and stabilized fuel can be achieved. A major advantage

of this process is the reduction of waste water generation from the purification process. Takanashi [116] also applied an electric field for the purification of biodiesel. In this embodiment, the demulsifier is an inorganic calcium salt or magnesium salt. However, the crude biodiesel can be also purified by heating in the range of 60 to 110°C and for 30 min up to 16 h. Moreover, Siochi *et al.* [117] proposed the method of soap removal from biodiesel without water washing by applying an electric field using inert carbon electrodes. The electrodes were attracted with sodium and carboxylate ions to be oppositely charged. Salt and any impurities thus clump together and precipitate out of the biodiesel. The electric field strengths are in the range of 33 to 100 V cm<sup>-1</sup>.

#### 2.4. Quality Improvement

Since biodiesel has a high content of unsaturated fatty acid esters, the oxidation stability is possibly being the major issue for the long period biodiesel storage. The instability problems can occur when biodiesel exposed in air or light. It can easily be oxidized to oxidative products leading to corrosion and blockages in the injection pumps or fuel lines in the engines. In order to improve the properties of biodiesel, the additives such as any antioxidants have been investigated. Table 8 illustrates important types of the additives to improve the properties of biodiesel such as oxidative stability, low temperature property and combustion. The effectiveness of these antioxidants can perform the wide range of biodiesel utilization.

Table 8. Additive for Improving Property of Biodiesel

Additive structure	Detail	Amount (wt%)	Advantages	Ref.
HO H H H E R <sub>1</sub>	$A = S$ $E = methyl \ radical \ or$ $tert-butyl \ radical$ $R_1 = hydrogen \ or$ $methyl \ group$	0.001-2	Increase the oxidation stability.	[118]
$\begin{bmatrix} R_2 & & \\ R_3 & & \\ R_4 & & \end{bmatrix}_n R_1$	$n=1,2$ $R_1=\ C1\text{-}C4\ alkyl,i.e.$ $R_2,R_3,R_4,R_5,=H,Cl,$ $\ hydroxyl,i.e$ $R_6=H,i.e.$	0.0005-0.5	Increase the stability against the deleterious effects of heat, light and oxygen.	[119]
$R^5$ $R^4$ $R^3$ $R^2$ $R^1$	$R^{1}$ , $R^{2}$ , $R^{3}$ , $R^{4} = H$ , $C1-C6 \text{ alkyl}$ $R^{5} = C1-C12 \text{ alkoxy group}$	0.005-0.05	Improve the oxidation stability	[120]

Additive structure	Detail	Amount (wt%)	Advantages	Ref.
$R_3$ $R_2$ $C$ $R_1$	$R_1 = \text{C1-C3}$ alkyl moieties $R_2, R_3 = \text{C1-C12} \text{ alkynyl}$ moieties $R_4 = \text{C2-C20} \text{ alkyl moieties},$	0.1-10	Improve low-temperature	[121]
R <sub>4</sub> Ö Ö	C2-C20 alkenyl moieties $R_5 = H$ , OH, C2-C20 ester-forming carboxylate (RCOO-)		properties.	[121]
$R_{3} = C1-C3 \text{ alkyl moieties}$ $R_{2} = C1-C6 \text{ alkyl moieties, i.e.}$ $R_{3} = C1-C10 \text{ alkynyl moieties,}$ $C1-C10 \text{ alkenyl moieties}$		0.1-60	Enhance the combustion efficiency	[122]
$(I) \underset{R_{3(a)}}{\overset{OH}{\longrightarrow}} (II) \underset{R_{5}}{\overset{OH}{\longrightarrow}} R_{4(a)}$	$R_1,R_2=C1\text{-}C20 \text{ alkyl},$ $C1\text{-}C30 \text{ alkaryl}$ $R_3=C1\text{-}C20 \text{ alkyl}, \text{ thiophenol}$ $R_4,R_5=\text{ alkyl}, \text{ aryl}, \text{ alkaryl},$ $\text{arylalkyl}  (C1\text{-}C20)$ $n,x=0,1$	(I) 0.005-0.25 (II) 0.0001-0.01	Improve the oxidation stability	[123]

#### 3. CURRENT & FUTURE DEVELOPMENTS

Biodiesel is a promising alternative of diesel fuel due to its renewability, biodegradability, less pollutant emission and raw material flexibility. Presently, the industrial biodiesel production process is based on simple operations. The production is mostly carried out in a simple batch reactor using high-purity raw materials catalyzed by a homogeneous catalyst. The process is not quite efficient as it requires long reaction time and involves many operation steps. Recently, many researchers have proposed a number of more efficient systems to produce biodiesel. Several reactor types such as membrane reactor, reactive distillation, microwave or ultrasonic assisted reactor, have been developed to produce and separate biodiesel simultaneously with the short reaction time. However, it is still a major challenge to make the technologies practical in a large scale operation. The research and development efforts on the development of efficient heterogeneous catalysts and continuous process for biodiesel production are needed as they can significantly simplify the process as well as the operation.

#### 4. CONCLUSION

Biodiesel is an environmental-friendly alternative diesel fuel, which is one of the promising sustainable fuels; it can be produced from the wide variety types of renewable feedstocks. The utilization of biodiesel not only eliminates the dependence of fossil fuel but also reduces the emitted toxic pollutants to the environment. However, the production technologies are generally expensive and insufficiently effective compared to diesel fuel. Therefore, the development of technology for biodiesel production is one of the crucial issues to overcome. This paper has reviewed important potential technologies for biodiesel production starting from the

beginning step to the end of the process from several patents. The details of all processing steps have been described and summarized including feedstock materials, reactions, pretreatment technique, reactor/separation/purification technology and the quality improvement. The review of those topics mentioned above can offer the overview knowledge of the current technology developed for biodiesel production. Therefore, this leads to more clear comprehension and provides a guideline for further invention of any technology for biodiesel production process.

#### ACKNOWLEDGMENT

This work is supported by Thailand Research Fund.

#### REFERENCES

- Knothe G, Gerpen JV, Krahl J. The biodiesel handbook. AOCS Press, 2005.
- [2] Pinho ADR, Silva M, Neto APDS, Cabral JAR. Catalytic cracking process for the production of diesel from vegetal oils. US20070007176, 2007.
- [3] Li L. Method of converting triglycerides to biofuels. US20080071125, 2008.
- [4] Pinho ADR, Silva M, Neto APDS, Cabral JAR. Catalytic cracking process for the production of diesel from vegetable oils. US7540952, 2009.
- [5] Huber, G.W., Cheng, Y-T., Carlson, T., Vispute, T., Jae, J., Tomp-sett, G.: Catalytic pyrolysis of solid biomass and relatedbiofuels, aromatic, and olefin compounds. US20090227823, 2009.
- [6] Petrucci F, Festuccia A. Biofuel composition and method of producing a biofuels. US20100037513, 2010.
- [7] Barnhorst JA, Staley MD, Oester DA. Transesterification process. US6489496, 2002.
- [8] Hanna MA. Transesterication process for production of biodiesel. US20030032826, 2003.
- [9] Wiedemann RA, Sheridan JP, Bouydston RE. Transesterification catalyst mixing system. US20080004458, 2008.

- [10] Banavali RM, Benderly A. Method for transesterification of triglycerides. US7582784, 2009.
- [11] Krause E, Rohm V. Process for the transesterification of esters. US20090259067, 2009.
- [12] Bournay L, Hillion G, Boucot P, Chodorge J-A, Bronner C, Forestiere A. Process for producing alkyl esters from a vegetable or animal oil and an aliphatic monoalcohol. US6878837, 2005.
- [13] Siano D, Serio MD, Tesser R, Dimiccoli M, Cammarota F, Santa-cesaria E, Siano L, Nastasi . Process for the production of esters from vegetal oils or animal fats. US20080033192, 2008.
- [14] Kovacs A, Haas L, Goczi I, Szabo G, Ulbrecht MJ. Method for transesterifying vegetable oils. US20050016059, 2005.
- [15] Bhat RN, Bhat N. Intigrated process for the manufacture of biodiesel. US20070260078, 2007.
- [16] Ghosh PK, Adimurthy S, Gandhi MR, Vaghela NKK, Rathod MR, Shethia BD, Pandya JB, Parmar RA, Dodia PJ, Patel MG, Parmar DR, Patel SN. Process for the preparation of fatty acid methyl ester from triglyceride oil by transesterification. US20060080891, 2006.
- [17] Ghosh PK, Adimurthy S, Gandhi MR, Vaghela NKK, Rathod MR, Shethia BD, Pandya JB, Parmar RA, Dodia PJ, Patel MG, Parmar DR, Patel SN. Process for the preparation of fatty acid methyl ester from triglyceride oil by transesterification. US7666234, 2010.
- [18] Rao KVSA, Saravanan K, Vijayalakshmi P. Process for the preparation of biodiesel from vegetable oils containing high FFA. US20100205853, 2010.
- [19] Machacek MT, Smith TG. Continuous algal biodiesel production facility. US20090071064, 2009.
- [20] Wu Q, Zhou W, Xiong W. Method for producing biodiesel using high-cell-density cultivation of microalga chlorella protothecoides in bioreactor. US20090211150, 2009.
- [21] Gallagher JL, Seliskar DM, Qin P. Use of kosteletzkya for production of seaside biodiesel fuel. US20060265945, 2006.
- [22] Wiesman Z, Herskowitz M, Grinberg S. Production of biodiesel from balanites aegyptiaca. US20080271364, 2008.
- [23] Comieri F, Fulvio WD. Process for the extraction of polyunsaturated fatty acid esters from fish oils. US5130061, 1992.
- [24] Carroway W. Process for converting tallow to diesel fuel. US20070039240, 2007.
- [25] Franzoi EA. Deproteination of fats and oils and refining of triglycerides US20080034646, 2008.
- [26] Misra M, Priyadarshan G, Kondamudi N, Mohapatra S. Biofuel production methods US20080184616, 2008.
- [27] Aiken JE. Process for production of biodiesel from high acid feed. US20070261294, 2007.
- [28] Elliott B. Method of making alkyl esters, US7795460, 2010.
- [29] Zappi ME, French WT, Hernandez R, Dufreche ST, Sparks JR DL. Production of biodiesel and other valuable chemicals from wastewater treatment plant sludges. US20050112735, 2005.
- [30] Zappi ME, French WT, Hernandez R, Dufreche ST, Sparks JR DL. Production of biodiesel and other valuable chemicals from wastewater treatment plant sludges. US7638314, 2009.
- [31] Chatterjee SG, Omori S, Marda S, Shastri S. Process for making biodiesel from crude tall oil. US20070130820, 2007.
- [32] Chatterjee SG, Omori S, Marda S, Shastri S. Process for making biodiesel from crude tall oil. US7695532, 2010.
- [33] Toeneboebn GJ, Welsh WA. Adsorptive removal of sulfur compounds from fatty materials. US5298638, 1994.
- [34] Jalalpoor M, Page I. Physical refining process using adsorbent particles for the production of biodiesel fuel. US20090300972, 2009.
- [35] Nakazono Y. Method of producing biodiesel fuel. US20100132252, 2010.
- [36] Roden AD, Butz J. Method for producing biodiesel material. US20100175312, 2010.
- [37] Jackam JP, Pierce JM, Fahrenbruck FS. Production of biodiesel and glycerin from high free fatty acid feedstocks. US7806945, 2010.
- [38] Sharma M, Kumar R, Ray SS, Sarin R, Malhotra RK, Verma RP, Raghunath NR. Process for producing biodiesel and the product thereof. US20060094890, 2006.
- [39] Bakshi AS. Biodiesel process: RHT-biodiesel. US20080097114, 2008.
- [40] Sinoncelli J, Wallace DR. Optimized biodiesel reaction kinetics system. US20080119664, 2008.
- [41] Parnas RS, Boucher MB. Methods and systems for pretreatment of an oil stream. US20090247785, 2009.

- [42] Iyer SR. Systems and methods for esterification and transesterification of fats and oils. US20100202933, 2010.
- [43] Dayton CLG, Santos MA. Continuous process and apparatus for enzymatic treatment of lipids. US20080138867, 2008.
- [44] Dayton CLG, Santos MA. Continuous process and apparatus for enzymatic treatment of lipids. US20090317902, 2009.
- [45] Helwani Z, Othman MR, Aziz N, Fernando WJN, Kim J. Technologies for production of biodiesel focusing on green catalytic techniques: A review. Fuel Process Technol 2009; 90:1502-1514.
- [46] Khalil CN, Leite LCF. Process for producing biodiesel fuel using triglyceride-rich oleagineous seed directly in a transesterification reaction in the presence of an alkaline alkoxide catalyst. US7112229, 2006.
- [47] Halpern ME. Transesterification reaction of triglycerides and monohydric alcohols. US20090069585, 2009.
- [48] Reaney MJT, Jayasinghe DA. Process for the preparation of biodiesel. US20090163730, 2009.
- [49] Kapicak LA, Schreck DJ. Biodiesel process and catalyst therefor. US20100048941, 2010.
- [50] Davies OM, Jackson RD. Biodiesel synthesis. US20100293840, 2010.
- [51] Matson JV, Kannan DC. Green biodiesel. US20070282119, 2007.
- [52] Matson JV, Kannan DC. Green biodiesel. US7563915, 2010.
- [53] Lecocq V, Maury S, Bazer-Bachi D. Method of manufacturing alcohol esters from triglycerides and alcohols using heterogeneous catalysts based on phosphate oran organophosphorous compound of a group 4 metal. US20080257781, 2008.
- [54] Lin VS-Y, Nieweg JA, Verkade JG, Reddy CRV, Kern C. Porous silica and metal oxide composite-based catalysts for conversion of fatty acids and oils to biodiesel. US7790651, 2010.
- [55] Portilho MF, Morgado EJR, De Abrue MAS. Process for the production of biodiesel. US20090151234, 2009.
- [56] Hucul D, Shull RS. Heterogeneous catalysts for mono-alkyl ester production, method of making, and method of using same. US20100139152, 2010.
- [57] Bazer-bachi D, Coupard V, Maury S, Rebours B. Method of preparing alcohol esters from triglycerides and alcohols using heterogeneous catalysts combining at least a Zn<sub>x</sub>Al<sub>2</sub>O<sub>3+x</sub> type solid solution and ZnO. US20100154295, 2010.
- [58] Ueki Y, Tamada M. Catalyst for production of biodiesel and its production method, and method for producing biodiesel. US20100170145, 2010.
- [59] Woods RR, Porter Brook. Biodiesel production method and apparatus. US200880209799, 2008.
- [60] Luxem FJ, Troy WM. Method of making alkyl esters. US20040254387, 2004.
- [61] Portilho MF, Vieira JAV, Zotin JL, Lima MSS. Method for the production of biodiesel from vegetable oils and fats, using heterogeneous catalysts. US20080295393, 2008.
- [62] Furuta S. Ester production method by transesterification reaction using solid acid catalyst. US7211681, 2007.
- [63] Lacome T, Hillion G, Delfort B, Revel R, Leporq S, Acakpo G. Process for transesterification of vegetable or animal oils using heterogeneous catalysts based on titanium, zirconium or antimony and aluminium. US7592470, 2009.
- [64] Furuta S. Method for manufacture of esters by transesterification. US7696376, 2010.
- [65] Su C-H. Heterogeneous acid-catalyzed process for biodiesel production from fatty acids. US20090030219, 2009.
- [66] Reed BP, Harris KE, Wannenmacher N. Liquid metal catalyst for biodiesel production. US20100251605, 2010.
- [67] Oku T, Moriguchi T, Akatsuka T, Nonoguchi M. Method for producing fatty acid alkyl esters and/or glycerin. US20090069586, 2009.
- [68] Devi BLAP, Gangadhar KN, Prasad PSS, Prasad RBN. Novel glycerol-based heterogeneous solid acid catalysts useful for the esterification of fatty acids, a process and use thereof. US20100286421, 2010.
- [69] Hara M, Yamashita K. Method for producing fatty acid monoesterified product using solid catalyst. US20100305346, 2010.
- [70] Pereira AT, Oliveira KA, Monteiro RS, Aranda DAG, Santos RTP, Joao RR. Production process of biodiesel from the esterification of free fatty acids. US20070232817, 2007.
- [71] Du W, Liu D, Li L. Process for producing biodiesel from renewable oil under lipase catalysis in an organic medium reaction system. US7550278, 2009.

- [72] Chou C-C. Fuel production. US7666666, 2010.
- [73] Chou C-C. Fuel production. US20100173399, 2010.
- [74] Abo M, Christensen MW. Production of fatty acid alkyl esters by use of two lipolytic enzymes. US20080113419, 2008.
- [75] Basheer S. Immobilized interfacial enzymes of improved and stabilized activity. US20100035312, 2010.
- [76] Du W, Xu Y, Liu D. Method for synthesizing biodiesel from renewable oils. US7473791, 2009.
- [77] Greyt WD, Kellens M, Holm HC, Christensen MW, Nielsen PM. Method for producing biodiesel. US20100047884, 2010.
- [78] Sasaki T, Suzuki T, Okada F. Method for preparing fatty acid esters and fuel comprising fatty acid esters. US6187939, 2001.
- [79] Iijima W, Kobayashi Y, Taniwaki K. Process for non-catalytically producing biodiesel fuel without yielding by-product. US20060288636, 2006.
- [80] Tatsumi N, Katayama T, Tabata O. Method of producing a fatty acid ester. US193097, 2007.
- [81] Dall'Agnol A, Baldus AO, Dariva C, Sobrinho ERN, Oliveira JV. Process for the production of biodiesel in continuous mode without catalysts. US20070010681, 2007.
- [82] Dall'Agnol A, Baldus AO, Dariva C, Sobrinho ERN, Oliveira JV. Process for the production of biodiesel in continuous mode without catalysts. US7524982, 2009.
- [83] Anitescu G, Tavlarides LL. Integrated multistage supercritical technology to produce high quality vegetable oils and biofuels. US20080196299, 2008.
- US20080196299, 2008.[84] Gleason RJ, Worrell AS. Biodiesel fuel and method of manufacture therefor. US20080221344, 2008.
- [85] Gleason RJ, Worrell AS. Biodiesel fuel and method of manufacture therefor. US20090277077, 2009.
- [86] Anderson G. Vessels and methods for synthesis of biofuel. US20090005582, 2009.
- [87] Noh MJ, Yoo KP, Choi YH. Method for producing biodiesel using supercritical alcohols. US20090264671, 2009.
- [88] Fleisher CA. Continuous transesterification process. US7145026, 2006.
- [89] Fleisher CA. Apparatus and method for producing biodiesel fuel. US20070260079, 2007.
- [90] Fleisher CA. Apparatus and method for producing biodiesel fuel. US7420072, 2008.
- [91] Chun S, Cho H-J, Roh H-D, Lim J-B, Lee J-I, Moon C-W, Kim B-H. Method and apparatus for preparing fatty acid alkyl ester using fatty acid. US20100228042, 2010.
- [92] Moritz P, Faessler P, Scala CV, Bailer O. Method for the esterification of a fatty acid. US7091367, 2006.
- [93] Moritz P, Faessler P, Scala CV, Bailer O. Apparatus for the esterification of a fatty acid. US7481981, 2009.
- [94] Elliott B. Method of making alkyl esters. US20070260077, 2007.
- [95] Chen Y-H, Chang C-Y, Huang Y-H, LIN R-H. Method of increasing transesterification of oils. US20080171889, 2008.
- [96] Chen Y-H, Chang C-Y, Huang Y-H, LIN R-H. Method of increasing transesterification conversion of oils. US20100242348, 2010.
- [97] Lichtenberger PL, McGrevy A, Gulliver E. Esterification and transesterification systems, methods and apparatus. US20070219340, 2007.

- [98] Lichtenberger PL, McGrevy A, Gulliver E. Esterification and transesterification systems, methods and apparatus. US7678340, 2010.
- [99] Jovanovic GN, Paul BK, Parker J, Al-Dhubabian A. Microreactor process for making biodiesel. US20090165366, 2009.
- [100] Tremblay AY, Dube MA, Cao P. Biodiesel production using ultra low catalyst concentration in a membrane reactor. US20100307051, 2010.
- [101] Pachauri N. Production of biodiesel. US20100192453, 2010.
- [102] Geier D, Soper JG. Simultaneous synthesis and purification of fatty acid monoester biodiesel fuel. US 7828978, 2010.
- [103] Bowen GM, Bowen DP. Processor for producing biodiesel from natural fats and oils. US20070056214, 2007.
- [104] Jachuck RJJ, Jachuck S. Continuous processing reactors and methods of using same. US20100288640, 2010.
- [105] Ames RS. Continuous flow biodiesel processor. US20070175092, 2007.
- [106] Panagiotou T, Mesite SV, Fisher RJ. Apparatus and methods for nanoparticle generation and process intensification of transport and reaction systems. US20090269250, 2009.
- [107] Kozyuk ÓV. Apparatus and method for producing biodiesel from fatty acid feedstock. US7754905, 2010.
- [108] Kozyuk O, Reimers P, Reinking PA. Process for improved biodiesel fuel. US20100175309, 2010.
- [109] Lafleur C, Bouknight HJr, Bouknight HSr. System for creating a biofuel. US7452515, 2008.
- [110] Farid M, Behzadi S. Method of biodiesel production. US20090038209, 2009.
- [111] Bradin D, Grune GL. Biodiesel process. US20100186289, 2010.
- [112] Dekhtiaruk VF, Krasnoholovets VV, Heighway J. Manufacture of biodiesel. US20100175986, 2010.
- [113] Porter MJ, Jensen S. Microwave-enhanced process to maximize biodiesel production capacity. US20060162245, 2006.
- [114] Meikrantz DH. Microwave-enhanced biodiesel method and apparatus. US20080256845, 2008.
- [115] Powell SW. Methods of purifying biodiesel fuels. US20080202021, 2008.
- [116] Takanashi H. Method for purifying biodiesel fuel. US20090025277, 2009.
- US20090025277, 2009.
  [117] Siochi EJ, Siochi ALJ, Yost WT, Siochi AC, Abdel-Fattah T.
- Method for purifying biodiesel fuel. US20100212219, 2010.
  [118] Asbahr H-O, Bomba T. Method of increasing the oxidation stabil-
- ity of biodiesel. US20060219979, 2006. [119] Li N, Hughes DR, Cusatis P, Olenski D. Stabilized biodiesel fuel
- compositions. US20070151143, 2007.

  [120] Abou-Nemeh I. Biodiesel fuel compositions having increased
- oxidative stability. US20070113467, 2007.
  [121] Roby SH, Zhou G. Methods for improving low-temperature proper-
- ties of biodiesel fuel. US20100154291, 2010.
  [122] Roby SH, Zhou G. Biodiesel-derived combustion improver.
- [122] Roby SH, Zhou G. Biodiesel-derived combustion improver US20100077651, 2010.
- [123] Calvert NR, Kenreck GVJr, Swart DA. Methods and compositions for improving stability of biodiesel and blended biodiesel fuel. US20090094887, 2009.

## **RENEWABLE ENERGY**

**TRENDS AND APPLICATIONS** 

Edited by Majid Nayeripour and Mostafa Kheshti

INTECH

**Thailand** 

# Bioethanol-Fuelled Solid Oxide Fuel Cell System for Electrical Power Generation

Vorachatra Sukwattanajaroon<sup>1</sup>, Suttichai Assabumrungrat<sup>1</sup>,
Sumittra Charojrochkul<sup>2</sup>, Navadol Laosiripojana<sup>3</sup> and
Worapon Kiatkittipong<sup>4</sup>

<sup>1</sup>Chulalongkorn University, Faculty of Engineering, Department of Chemical Engineering

<sup>2</sup>National Metal and Materials Technology Center

<sup>3</sup>King Mongkut's University of Technology Thonburi

<sup>4</sup>Silpakorn University, Department of Chemical Engineering

#### 1. Introduction

Tremendous consumption of energy to serve daily lives and economic activities has led to the critical problem of energy shortage since the current main energy sources rely on fossil fuels which are non-renewable. Therefore, efficient renewable energy sources need to be investigated and improved to replace or substitute the use of fossil fuels to alleviate environmental impacts while being sustainable. Biomass-derived fuels are recognized as promising alternatives among other renewable sources e.g. wind, solar, geothermal, hydropower, etc. This fuel can be produced from various available agricultural materials, hence there is no problem of feedstock supply. Instead, its use is beneficial for those countries having strong background in agriculture. In addition, this agro-based fuel can provide a CO<sub>2</sub>-closed cycle as the CO<sub>2</sub> released from the fuel combustion can be redeemed with the CO<sub>2</sub> required for biomass growth. Bioethanol plays an important role as a promising renewable energy among other biofuels due to its useful properties such as high hydrogen content, non-toxicity, safety, ease of storage and handling (Ni et al., 2007). An efficient energy conversion system is required to maximize bioethanol fuel utilization to obtain a full performance. Combustion heat engines which are widely used nowadays have a low conversion efficiency of power production due to losses during multiple energy conversion stages as well as a low value of chemical energy of bioethanol represented by LHV or HHV compared to those of fossil fuels (C<sub>6</sub> hydrocarbons or above). Moreover, electrical energy efficiency produced from a combustion heat engine becomes even lower because of further losses from more energy conversion stages. Fuel cell technology is considered to be an interesting alternative for efficient energy conversion since it can directly convert chemical energy stored in the fuel into electrical energy via electrochemical reaction. Less energy is lost in the fuel cell operation and higher electrical efficiency can be obtained. However, the problems in using fuel cell technology such as short-life operating time, high manufacturing cost and impromptu infrastructure support are still issues to be tackled. The Solid Oxide Fuel Cell (SOFC), a type of fuel cells, is selected to be an electrical power generation unit fuelled by bioethanol because of its outstanding characteristics: ability to use low-cost catalyst, high temperature exhaust heat for cogeneration application, tolerance to some impurities e.g. CO and sulfur, internal reforming within the cell for reducing equipment cost, etc. For the SOFC system, bioethanol feed is heated up and reformed to hydrogen rich gas by the reformer before being introduced into the fuel cell at the anode side coupled with air feed at the cathode side for producing electricity. To achieve better performance from this process, it is necessary to consider every unit within the SOFC system. These units are investigated through their physical structure design and modification on the basis of worthwhile energy utilization in each unit and suitable energy allocation within the process to target an optimum energy management of the SOFC system. The objective of this chapter is to propose ideas and feasible approaches on how to improve the performance of bioethanol-fuelled SOFC systems by focusing on each essential unit modification in the process. Relevant useful approaches from other scientific literature reviews are included. The pros and cons in each proposed method are also discussed. Bioethanol pretreatment unit regarded as a significant unit compared to the other units for the process development is of particular focus in this chapter. The progressive work of our research on the efficiency improvement of the SOFC system with analytically appropriate selection of bioethanol pretreatment unit is presented. The simulation studies were conducted via experimental-verified SOFC model to predict the results under a frame of model assumptions. Performance assessment of the system in any scenario cases held the criteria of no external energy demand condition or Qnet = 0 to compare and identify the optimal operating conditions among those of bioethanol pretreatment units. The simulation results could initially guide the right pathway for practical industrial applications.

#### 2. Bioethanol

Among various biomass-based fuel types such as bioethanol, biodiesel, bioglycerol, and biogas, bioethanol is considered a promising renewable energy compared to other biofuels. As shown in Table 1, the maximum amount of work from the fuel cell integrated with fuel processor system in comparison with five renewable fuels including *n*-octane represented as a gasoline characteristic are presented (Delsman et al., 2006). It was indicated that ethanol can offer the highest energy output (based on MJ/mol fuel) among the other renewable fuels (methanol, methane, ammonia, and hydrogen) except for n-octane. Furthermore, there are other outstanding advantages of bioethanol given by the following reasons. The production technologies of bioethanol are more mature and cheaper than those of biomethanol (Xuan et al., 2009). Biodiesel which is a popular alternative energy used in vehicle engines can be derived from ethanol (or purified bioethanol) reacted with vegetable oil via transesterification reaction. Biogas is a widely-used renewable power source because of many available feedstocks. It can be produced from several organic wastes by anaerobic biological fermentation. Consequently, it seems to be a promising renewable fuel but biogas mainly consists of methane and CO2. Both gases have serious negative environmental impacts especially from methane. Methane can remain in atmosphere for 9-15 years and retains heat radiation of 20 times higher than CO<sub>2</sub> (U.S. Environmental Protection Agency). Furthermore, if the biogas is produced from non-agricultural wastes, e.g. cow and pig manure, it would bring this biogas production diverted from carbon-closed cycle. Hence, biogas should be produced and utilized in an effective way. Bioethanol production is mostly derived from biological fermentation using agro-based raw materials such as sucrosecontaining crops, starchy materials, lignocellulosic biomass and agro-waste (Carlos & Oscar, 2007). In addition, the latest research reports that animal manure waste, waste paper, citrus peel waste, and municipal solid waste can be used as feedstock of bioethanol production by using saccharification and fermentation processes (Lal, 2008; Foyle et al., 2007; Wilkins et al., 2007).

		ork	
Fuel	MJ/mol Fuel	MJ/mol C in Fuel	MJ/mol H <sub>2</sub> via reforming
Methanol	-0.69	-0.69	-0.23
Ethanol	-1.31	-0.65	-0.22
<i>n</i> -Octane	-5.23	-0.65	-0.21
Ammonia	-0.33		-0.22
Methane	-0.8	-0.80	-0.20
Hydrogen	-0.23		-0.23

Table 1. Maximum amount of work for the conversion of fuels to electricity calculated at 298 K and 1 bar (Source: Delsman et al., 2006)

However, bioethanol fermentation is a complicated process. The overall process is schematically shown in Figure 1. It requires many steps of biomass feed conditioning or pretreatment which can be mainly divided into four techniques as follows (Magnusson, 2006):

- Mechanical techniques: biomass is milled or ground to reduce sizes of material,
- Chemical techniques: biomasses e.g. hemicelluloses and lignin are swelled or dissolved by acids, bases, and solvents to transform into pre-hydrolysis form,
- Mechanical-chemical techniques: a combined mechanical and chemical technique e.g. heat pretreatment with high-pressure of steam, and
- Biological techniques: biomass is digested by enzymes or micro-organisms.

Thereafter, the pre-conditioned biomass is biologically transformed into ethanol. This procedure is a key step to be accounted for increasing bioethanol productivity. The basic concept of reactor design is applied with enzymatic fermentation technology. Starting from a simple batch reactor, this is close to organic culture system environment but a batch culture envisages the limitation of enlarging bioethanol production scale. Afterward, semi-batch reactors combining the benefits of batch and continuous reactors are employed. It can offer a long lifetime of cell culture, higher ethanol and cell concentration (Frison & Memmert, 2002). Finally, a continuous flow reactor is applied with cell recycle operation to serve more bioethanol productivity requirement. Influent stream containing substrate, nutrients and culture medium is fed to an agitated bioreactor. The product is removed from the fermenter but the residues (cells and nutrients) are collected and recycled to the vessel. In addition, the concept of process integration is introduced to the bioethanol production application such as Separate Hydrolysis and Fermentation (SHF), Simultaneous Saccharification and Fermentation (SSF) and Direct Microbial Conversion (DMC) (Balat, 2011). In the last step, the obtained dilute ethanol is then purified to gain a desired ethanol concentration. These difficult procedures need to be further developed to reduce the complexity and enable the process to compete with the cheaper oil-derived fuel production.

Many researchers attempt to develop such a biotechnical bioethanol production to be cost-effective. Effective tools for the process evaluation such as thermo-economic, environmental indexes, process optimization and etc. are used to analyze the bioethanol production process as performance indicators to assist in the task of process design. Process integration is regarded as a significant approach since several production procedures are combined into a single unit. It can reduce production costs and provide a more intensive process. For example, the fermentation process integrated with membrane distillation (Gryta, 2001) involved the combination of tubular bioreactor and membrane distillation to synergistically enhance the yield of bioethanol without several units being required as for other common processes. A role of membrane distillation is to remove byproduct from the fermentation broth in bioreactor that can simultaneously forward glucose conversion to gain more ethanol. The objective of process integration is to have the energy requirement in procedures of bioethanol production to be less than the energy obtained from the bioethanol exploitation to utilize bioethanol effectively.

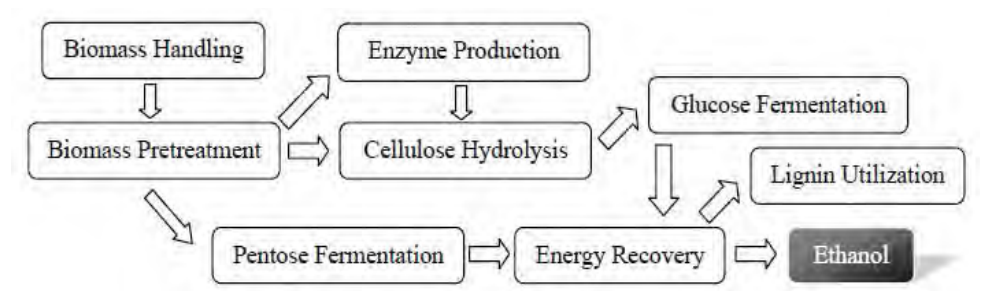


Fig. 1. Schematic diagram of bioethanol production process (Source: U.S. Department of Energy)

Bioethanol can be purified to anhydrous ethanol which is a useful chemical for various applications such as organic solvent, chemical reagent, reactant for biodiesel production, pharmaceutical formations, plastics, polishes and cosmetics industries (Kumar et al., 2010). However, in this chapter, the use of bioethanol is particularly focused on a role of renewable fuel. Application of bioethanol in term of fuel can be mainly divided by two directions:

- Direct combustion to gain thermal energy
- Reforming into hydrogen for clean energy production in a fuel cell

For conventional direct combustion, it seems to be less complicated but the fuel is utilized in an ineffective way because thermal energy accumulated in bioethanol is obviously lower than fossil fuel as shown in Table 2.

Fuel	Density (kg/l)	Caloric value at 20°C (MJ/kg)	Caloric value (MJ/l)	Octane-number (RON)	Fuel-equivalence (1)
Petrol	0.76	42.7	32.45	92	1
Bioethanol	0.79	26.8	21.17	>100	0.65

Table 2. Properties of bioethanol in comparison with petrol (Source: Paul & Kemnitz, 2006)

Moreover, since water is the main constituent in bioethanol, the direct combustion of bioethanol is not possible. However, there is another effective way which is the conversion of bioethanol fuel into hydrogen rich gas. As presented in Table 3, the heating value of hydrogen is higher than that of ethanol (4.47 times). Therefore, the bioethanol reforming process for producing hydrogen is a promising pathway in term of upgrading fuel quality which can offer a higher performance for the SOFC system even in the combustion heat engine while the bioethanol fuel utilization can be conducted in an efficient way.

Fuel	Lower Heating Value (25 °C and 1atm)
Hydrogen	119.93 kJ/g
Methane	50.02 kJ/g
Gasoline	44.5 kJ/g
Diesel	42.5 kJ/g
Ethanol	26.82 kJ/g
Methanol	18.05 kJ/g

Table 3. Heating values of commonly-used fuels in comparison

Typically, there are three main reforming reactions for hydrogen production as described below:

- Steam reforming
- Partial oxidation
- Autothermal reforming

Selection of an appropriate operation mode depends on the individual objective. Ethanol steam reforming (ESR) (Reaction (1)) is a suitable choice for the SOFC system because this reaction can produce hydrogen at high yield. Although ESR consumes a great amount of heat due to its high endothermicity, heat released from the fuel cell is enough to supply the heat demand for the reaction. For the ethanol partial oxidation (EPOX) (Reaction (2)), it is appropriate for the process required less complexity and integration design. Since EPOX requires the fuel to be partly combusted with air and releases thermal energy as an exothermic reaction, heat and steam supply are not required (Vourliotakis et al., 2009). Nonetheless, this reaction is less selective to hydrogen compared to the former reaction.

Autothermal reforming (ATR) is a combination of the previous two reactions in order to improve the hydrogen selectivity with minimum heat supply. The steam to carbon molar ratio and air to carbon molar ratio are significant parameters to adjust the system to operate close to thermal neutral condition from the exothermic partial oxidation and endothermic steam reforming. Generally, this reaction formula is defined as Reaction (3) with the standard exothermic heat  $\Delta H_{298K} = 50$  kJ/mol (Deluga et al., 2004). There is a scientific literature (Liguras et al., 2003) reporting the stoichiometric ratio of  $H_2O$  and  $O_2$  of 1.78 and 0.61, respectively per mol of ethanol can carry out thermal neutrality as shown in Reaction (4) but the yield of hydrogen becomes a little lower.

$$C_2H_5OH + 3H_2O \Rightarrow 2CO_2 + 6H_2$$
 (1)

$$C_2H_5OH + 0.5O_2 => 2CO + 3H_2$$
 (2)

$$C_2H_5OH + 2H_2O + 0.5O_2 => 2CO_2 + 5H_2$$
 (3)

$$C_2H_5OH + 1.78H_2O + 0.61O_2 => 2CO_2 + 4.78H_2$$
 (4)

#### 3. Solid oxide fuel cell system fuelled by bioethanol

As mentioned earlier, utilization of bioethanol by being converted into  $H_2$  for electrical power generation via SOFC is recognised. Thus, this section describes the fundamental process of an SOFC system fuelled by bioethanol and the criteria used to define the performance evaluation indicators of this SOFC system as follows:

#### 3.1 Process description

The bioethanol-fuelled SOFC system basically consists of a bioethanol pretreatment unit, preheaters, reformer, fuel cell, and afterburner as illustrated in Figure 2. Bioethanol is purified in the pretreatment unit to achieve a specified ethanol concentration (25mol% ethanol, a suitable stoichiometric ratio for the ethanol steam reforming reaction in Reaction (1)). Then, the steam with a desired ethanol is fed to an external reformer operated under thermodynamic equilibrium condition. Ethanol steam reforming is selected for converting the raw materials into hydrogen rich gas. The reaction is assumed to occur isothermally in the reformer. Finally, the reformed influent stream is fed to the SOFC's anode chamber together with excess air (5 times) preheated and fed to the cathode chamber to produce electricity and thermal energy. The effluent steam containing residual fuel released from the fuel cell is combusted in the afterburner and heat from the fuel combustion is recovered to supply all the heat-demanding units i.e. preheaters, purification unit, and reformer. The final temperature of exhaust gas emitted to atmosphere is specified at 403K (Jamsak et al., 2007). The performance of the SOFC system can be simulated using Aspen Plus software.

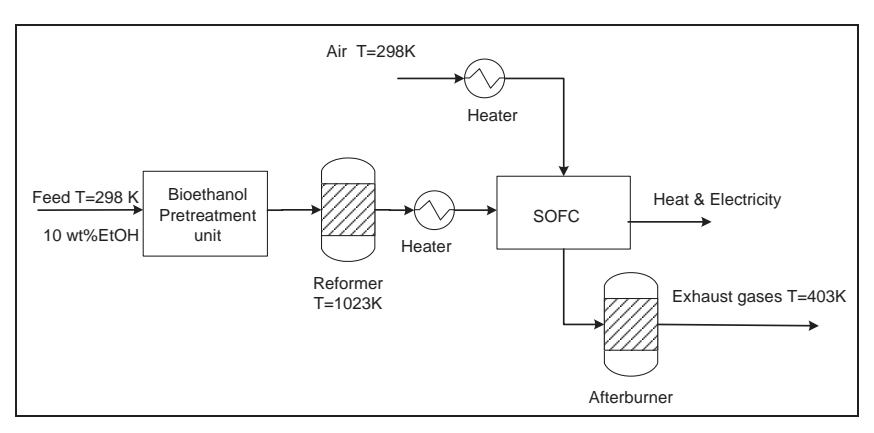


Fig. 2. Basic process diagram of bioethanol-fuelled SOFC system

#### 3.2 Mathematical model

The SOFC model was adapted from the prior literature of Piroonlerkgul et al., 2008 to study the performance of SOFC system. From this model, a constant operating voltage along the cell length and isothermal condition were assumed. Only hydrogen oxidation was considered to react electrochemically within the fuel cell. Oxygen ion electrolyte type was chosen for the SOFC and its electrochemical reactions are described below:

$$0.5O_2 + 2e^- => O^2$$
 (5)

$$H_2 + O^2 => H_2O + 2e^-$$
 (6)

The validation of this model was in a good agreement with experimental results (Zhao et al., 2005; Tao et al., 2005) at high hydrogen contents (hydrogen mole fraction = 0.97) and (Petruzzi et al., 2003) at low hydrogen contents (hydrogen mole fraction = 0.26). The materials used in the SOFC stack were YSZ, Ni-YSZ and LSM-YSZ for electrolyte, anode and cathode, respectively.

#### 3.2.1 Electrochemical model

#### 3.2.1.1 Open circuit voltage

The open circuit voltage (*E*) is formulated by the Nernst equation given in Eq. (7)

$$E = E_0 + \frac{RT}{F} ln \left( \frac{P_{H_2} P_{O_2}^{1/2}}{P_{H_2O}} \right)$$
 (7)

where F is Faraday constant (C mol<sup>-1</sup>) and  $P_i$  is a partial pressure of component i.

The actual operating voltage (V) is less than the open circuit voltage (E) due to the presence of various polarizations. Three types of polarization are considered in this model: Ohmic, Activation, and Concentration polarizations as below:

$$V = E - \eta_{act} - \eta_{ohmic} - \eta_{conc}$$
 (8)

#### 3.2.1.2 Polarizations

#### 3.2.1.2.1 Ohmic polarization

This ohmic polarization involves the resistance of both ions flowing in the electrolyte and electrons flowing through the electrodes. This resistance loss is regarded as a major loss in the SOFC stack given as:

$$\eta_{ohmic} = 2.99x10^{-11} i L \exp\left(\frac{10300}{T}\right)$$
(9)

where i is current density and L is thickness of anode electrode

#### 3.2.1.2.2 Activation polarization

Activation polarization is caused by the loss of electrochemical reaction rate at the electrodes. An operation of SOFC at high temperature can reduce this polarization as the rate-determining step becomes faster. Normally, activation polarization region occurs in the low current density range. This polarization is defined by the Butler-Volmer equation.

$$i = i_0 \left[ \exp\left(\frac{\alpha z F \eta_{act}}{RT}\right) - \exp\left(-\frac{(1-\alpha)z F \eta_{act}}{RT}\right) \right]$$
 (10)

The value of a and z were specified as 0.5 and 2 (Chan et al., 2001), respectively. Accordingly, the activation polarization at the anode and cathode sides can be arranged into another form as:

$$\eta_{\text{act,j}} = \frac{RT}{F} \sinh^{-1} \left( \frac{i}{2i_{0,j}} \right)$$
 (11)

where j = anode, cathode

The exchange current density  $(i_{o,j})$  for both the anode and cathode sides are expressed as follows:

$$i_{o,a} = \gamma_a \left(\frac{P_{H_2}}{P_{ref}}\right) \left(\frac{P_{H_2O}}{P_{ref}}\right) exp\left(-\frac{E_{act,a}}{RT}\right)$$
(12)

$$i_{o,c} = \gamma_c \left(\frac{P_{O_2}}{P_{ref}}\right)^{0.25} exp\left(-\frac{E_{act,c}}{RT}\right)$$
(13)

where  $\gamma_a$  and  $\gamma_c$  are pre-exponential factors for anode and cathode current densities, respectively.

#### 3.2.1.2.3 Concentration polarization

This polarization arises from the difference in gas partial pressures in the porous electrode region due to slow mass transport. It can be estimated by Eqs. (14) and (15) for the anode and cathode sides, respectively.

$$\eta_{\text{conc,a}} = \frac{RT}{2F} ln \left[ \frac{\left(1 + (RT/2F)(l_a/D_{a \text{ (eff)}} p_{H_2O}^I)i\right)}{(1 - (RT/2F)(l_a/D_{a \text{ (eff)}} p_{H_2}^I)i} \right]$$
(14)

$$\eta_{\text{conc,c}} = \frac{RT}{4F} \ln \left[ \frac{p_{O_2}^I}{(p_c/\delta_{O_2}) - ((p_c/\delta_{O_2}) - p_{O_2}^I) \exp[(RT/4F)(\delta_{O_2} l_c/D_{c(eff)} p_c) i]} \right]$$
(15)

where  $l_a$  and  $l_c$  are thicknesses of anode and cathode electrodes, respectively, while  $\delta_{O2}$ ,  $D_a$  (eff) and  $D_c$  (eff) are given by:

$$\delta_{O_2} = \frac{D_{O_2, k(eff)}}{D_{O_2, k(eff)} + D_{O_2 - N_2(eff)}}$$
(16)

$$D_{a(eff)} = \left(\frac{p_{H_2O}}{P_a}\right) D_{H_2(eff)} + \left(\frac{p_{H_2}}{p_a}\right) D_{H_2O(eff)}$$
(17)

$$D_{c(eff)} = \frac{\xi}{n} \left( \frac{1}{D_{O_2,k}} + \frac{1}{D_{O_2-N_2}} \right)$$
 (18)

$$\frac{1}{D_{H_2(eff)}} = \frac{\xi}{n} \left( \frac{1}{D_{H_2,k}} + \frac{1}{D_{H_2-H_2O}} \right)$$
 (19)

$$\frac{1}{D_{H_2O(eff)}} = \frac{\xi}{n} \left( \frac{1}{D_{H_2O,k}} + \frac{1}{D_{H_2-H_2O}} \right)$$
 (20)

The relationship between the effective diffusion parameter ( $D_{(eff)}$ ) and ordinary diffusion parameter (D) can be described by:

$$D_{(eff)} = \frac{n}{\xi} D \tag{21}$$

where n is electrode porosity and  $\xi$  is electrode tortuosity. Assuming straight and round pores, the Knudsen diffusion parameter can be calculated by:

$$D_{A,k} = 9700 \sqrt{\frac{T}{M_A}}$$
 (22)

The binary ordinary diffusion parameter in a gas phase can be calculated using the Chapman-Enskog theory of prediction as below:

$$D_{A-B} = 1.8583 \times 10^{-3} \left( \frac{T^{3/2} ((1/M_A) + (1/M_B))^{1/2}}{P \sigma_{AB}^2 \Omega_D} \right)$$
 (23)

where  $\sigma_{AB}$  the characteristic length,  $M_i$  is molecular weight of gas i, and  $\Omega_D$  is the collision integral. These parameters are given by:

$$\sigma_{AB} = \frac{\sigma_A + \sigma_B}{2} \tag{24}$$

$$\Omega_D = \frac{A}{T_k^B} + \frac{C}{\exp(DT_k)} + \frac{E}{\exp(FT_k)} + \frac{G}{\exp(HT_k)}$$
 (25)

where the constants A to H are A = 1.06036, B = 0.15610, C = 0.19300, D = 0.47635, E = 1.03587, F = 1.52996, G = 1.76474, H = 3.89411.

#### 3.3 Evaluation of process performance

The proposed bioethanol-fuelled SOFC system for electrical power generation needs to be evaluated together with any process design adjustments to obtain optimum performance. A number of criteria can be used to define the performance of the system, e.g. economic, 1st and 2nd laws of thermodynamics, environment, etc. Fundamentally, the overall performance evaluation of an SOFC system is defined in terms of electrical efficiency as below:

$$\eta_{elec,ov} = \frac{\text{Net electrical power output}}{\text{mol}_{Fuel}.\text{LHV}_{Fuel}}$$
(26)

The definition of the above equation is energy efficiency based on 1st law of thermodynamics which initially accounts on an ideal energy conservation law. Fuel input term is referred to the lower heating value (LHV). In considering an energy loss from the system which is closer to actual condition, the definition of overall system efficiency is formulated as follows:

$$\eta_{\text{elec,ov}} = \frac{\text{Net electrical power output}}{\text{mol}_{\text{Fuel}}.e_{\text{Fuel}}^{\text{o}}}$$
(27)

This equation is exergy efficiency which further takes the 2<sup>nd</sup> law of thermodynamic into account stated that entropy loss occurred in the system with highly irreversible process especially combustion process. The fuel input denominator in Eq. (27) is referred to the standard exergetic potential of fuel. In addition, the analysis in term of exergy can determine the location, source, and amount of actual thermodynamic inefficiencies in each unit. Profound understanding can be perceived from this analysis for solving the process problem correctly.

The criterion mainly considered in this chapter is no external energy demand condition. In the SOFC system, there are units having the roles of both energy consumption and generation. Before investigating and evaluating the system efficiency, energy consumed or generated from the units is allocated within the system until the overall system is under self-sufficient energy condition or  $Q_{\text{net}} = 0$  as follows:

$$Q_{net} = Q_{generation} - Q_{demand} = 0$$
 (28)

where  $Q_{\rm generation}$  represents the heat from units which can generate thermal energy (SOFC and afterburner) while  $Q_{\rm demand}$  expressed as the heat from units which consume heat (bioethanol pretreatment unit, heaters, and reformer). The system operated at such a condition can help allocate energy within the process effectively. The exhaust gas released to atmosphere is specified at 403 K (Jamsak et al., 2007). The consideration of  $Q_{\rm net} = 0$  associated with the process evaluation has led to the modified efficiency definition:

$$\eta_{\text{elec,ov}} = \frac{\text{Net electrical power output}}{\text{mol}_{\text{Fuel}}.\text{LHV}_{\text{Fuel}} + \text{external heat demand}}$$
(29)

In case of incorporating a heat recovery unit such as combined heat and power (CHP) with the SOFC system, the definition of efficiency is adjusted to:

$$\eta_{elec,ov} = \frac{\text{Net electrical power output } + \text{ exchanged thermal energy}}{\text{mol}_{Fuel}.\text{LHV}_{Fuel} + \text{ external heat demand}}$$
(30)

#### 4. Process modification for improving performance of the SOFC system

The fundamental process of the bioethanol-fuelled SOFC system needs to be further developed to utilize bioethanol effectively and achieve higher electrical efficiency. In this chapter, the performance improvement of SOFC systems under consideration is based on selection for appropriate units. The possible units are structurally modified and evaluated for their energy consumption. The process modification of the SOFC system can be divided by two main scopes including adjusting the fuel cell module and improving the balance of plant.

#### 4.1 Solid Oxide Fuel Cell

Originally, the Solid Oxide Fuel Cell (SOFC) is classified as a high-temperature fuel cell. Due to the demand for high cost materials and fabrication, the intermediate temperature solid

oxide fuel cell was later developed with the research into novel material technology and thin layer techniques applied in electrolyte and electrodes. Regarding the fuel cell geometry design, it is useful to differentiate the scope into macro and micro geometry configurations. The micro geometry covering the structures of anode, electrolyte, and cathode has direct effects on the electrochemical performance of the fuel cell. The heat transfer mechanisms of convection and conduction through heat exchange areas and the mass transport through active surface areas are influenced by the macro geometry (Nagel et al., 2008). Generally, primary structures of SOFC are tubular, planar, and monolithic as shown in Figures (3), (4), and (5), respectively. The SOFC structure of planar design is more compact than the tubular design and also offers higher ratio of power per volume (Pramuanjaroenkij et al., 2008). For the monolithic design, this SOFC design uses the similar concept with shell-and-tube heat exchanger. It combines the tri-layer of anode-electrolyte-cathode into a compact corrugated structure. This design can assist a thermal energy allocation exchanged between the flow channels and size of the fuel cell to become more compact with the corrugated self-supporting structure.

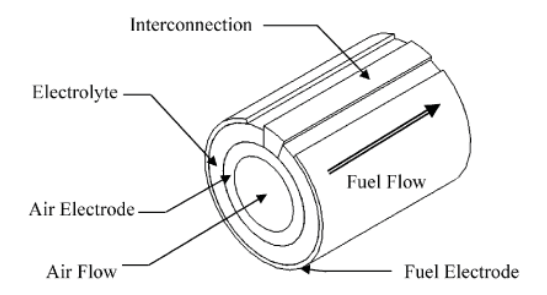


Fig. 3. Schematic of tubular SOFC (Source: Kakac et al., 2007)

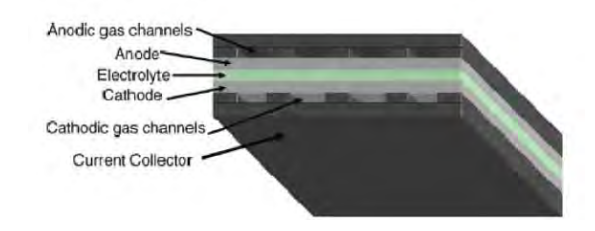


Fig. 4. Schematic of planar SOFC (Source: Bove & Ubertini, 2006)

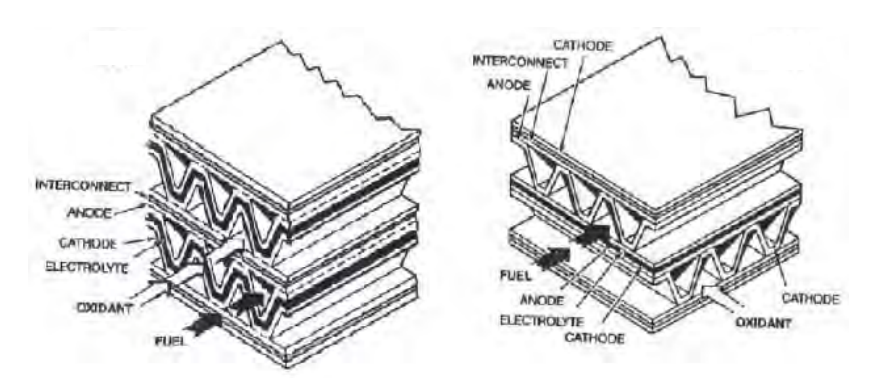


Fig. 5. Schematic of monolithic SOFC; (Left) coflow and (Right) cross flow (Source: Minh, 1993)

#### 4.2 Balance of plant

There are essential units around the fuel cell as supporting units for the overall electrical power generation process. These units can be modified to utilize energy within their system units suitably. Sections in the balance of plant which are potential in improving the efficiency of SOFC system are described as follows:

#### 4.2.1 Bioethanol pretreatment section

This section has a key role in improving the efficiency of the SOFC system. Originally, bioethanol has a low concentration in a range of 1-7 mol% (Shell et al., 2004; Cardona Alzate & Sanchez Toro, 2006; Roger et al., 1980; Buchholz et al., 1987). In our studies, 10wt% (4.16 mol%) ethanol was specified to represent the range of actual bioethanol concentration. These bioethanol compositions are unsuitable for feeding into the reformer operating under ethanol steam reforming reaction to produce hydrogen because of high water content. Unnecessary thermal energy is required to heat up surplus water within the reformer and the sizes of reformer are larger than necessary. Hence, the bioethanol pretreatment unit plays an important part to purify bioethanol feed into a desired concentration of 25mol%ethanol (46wt% ethanol). A selection of appropriate purification unit for bioethanol conditioning must consider an effective separation with low energy consumption to offer a better performance of the system. In our research (Jamsak et al., 2007), we started with a conventional distillation column used in the bioethanol-fuelled SOFC system as illustrated in Figure 6.

A distillation column is commonly recognised as a high energy consumption unit, but the SOFC released a large amount of exothermic heat. Therefore, it is feasible to apply this unit as a bioethanol pretreatment unit. The results from our simulation studies indicated that there were some operating conditions which can run this system under  $Q_{net} = 0$ . However, the overall electrical efficiency obtained from this system was quite low due to high reboiler heat duty consumption and high amount of heat loss in the condenser. Afterwards, among the promising membrane technologies, pervaporation is considered as a replacement for the former purification unit as shown in Fig 7. By the principle of physical-chemical affinity between the membrane material and species, this unit consumes only heat for vaporizing a preferential substance permeated through the membrane. However, it is noted that a pervaporation depends on a driving force generation device, typically a vacuum pump is used to boost up its separation performance. Therefore, part of the generated electrical energy must be consumed to operate the device.

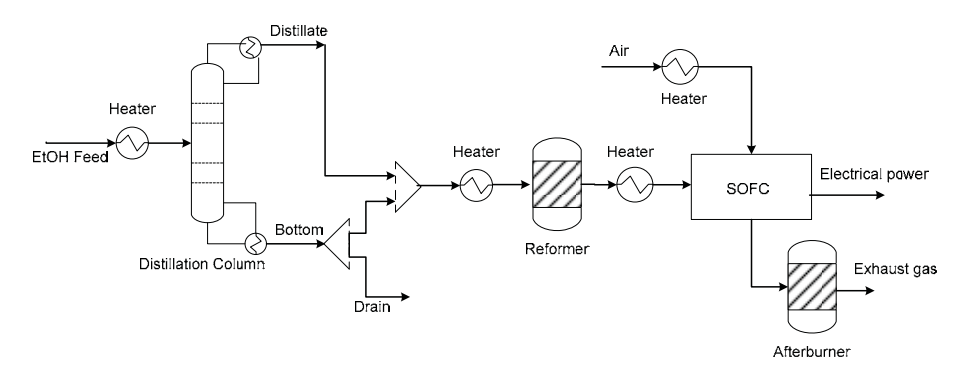


Fig. 6. Process diagram of bioethanol-fuelled SOFC system using a distillation column

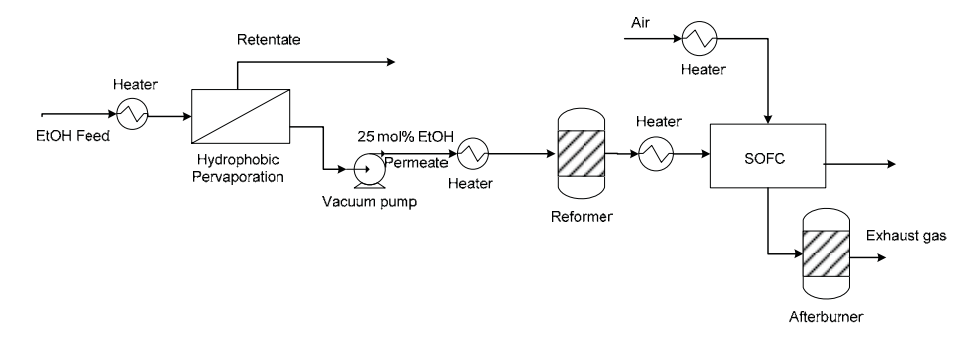


Fig. 7. Process diagram of bioethanol-fuelled SOFC system using a pervaporation

Type of purification process	Energy consumption	Range of
	(MJ/kg ethanol)	concentration (wt%)
Distillation processes		
Low pressure distillation	11.72	6.4-98
Azeotropic distillation		
Pentane	10.05	6.4-99.95
Benzene	15.49	6.4-99.95
Diethyl ether	12.56	6.4-99.95
Extractive distillation		
Gasoline	9.21	6.4-99.95
Ethylene glycol	18.84	6.4-99.95
Extractive distillation with salt		
Calcium chloride	5.02	7.5-99
Potassium acetate	9.27	60
Non-distillation processes		
Solvent extraction	6.28	10-98
Pervaporation	4.61	8-99.5

Table 4. Energy consumption for anhydrous ethanol production from various purification processes (Source: Black, 1980; Jaques et al., 1972; Hala, 1969; Barba et al., 1985; Ligero and Ravagnani, 2003)

However, a pervaporation is still regarded as being the lowest energy consumption unit among the other purification units as shown in Table 4. (Reviewed by Kumar et al., 2010) that gives an example of using various purification processes for anhydrous ethanol production. To emphasize their mentioned data, the simulation results from our studies (Choedkiatsakul et al., 2011) showed the performance of bioethanol-fuelled SOFC system in comparison between two pretreatments; using distillation and pervaporation units. On the basis of purification process operated at 348K, Table 5 presents the classification of energy term in each unit for both purification processes. Although a pervaporation consumed an electrical energy within the unit, it offers an overall electrical efficiency (42%) superior to that of distillation column (34%). However, a hydrophobic membrane material used in the pervaporation required a high ethanol separation factor property as illustrated in Figure 8 but it may be unavailable in real membrane materials.

Energy distribution	Purification process configuration	
	Pervaporation	Distillation Column
Heat (MW)		
Bioethanol pretreatment unit	2,301	3,580
Reformer	417	421
Air preheater	22,575	23,892
Afterburner	25,293	27,893
Electrical power (MW)		
Bioethanol pretreatment unit	453	0
Electrical production	4,920	3,701
Net electrical energy	4,467	3,701
Fuel utilization (%)	92	68
Overall electrical efficiency (%)	42	34

Table 5. Performance characteristics in comparison between two different purification units based on  $Q_{\text{net}}$  = 0, ethanol recovery ( $R_{\text{EtOH}}$ ) = 80%, V = 0.7 V, and  $T_{\text{SOFC}}$  = 1073 K (Source: Choedkiatsakul et al., 2011)

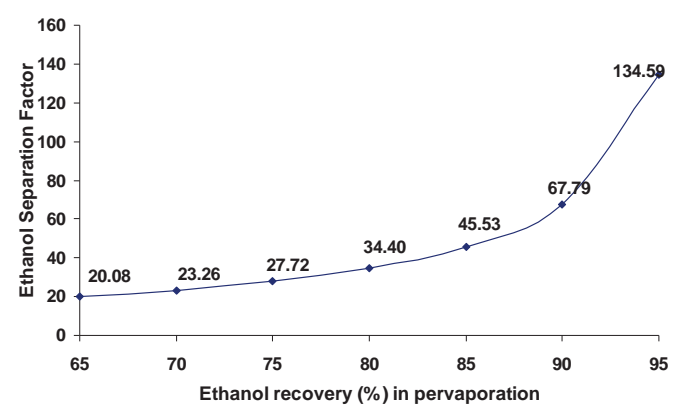


Fig. 8. Effect of ethanol recovery in pervaporation on the required ethanol separation factor of hydrophobic membrane

Consequently, as schematically shown in Figure 9, this problem was solved by having a vapor permeation device installed after a pervaporation (Sukwattanajaroon et al., 2011) to improve ethanol separation performance, an important part of the SOFC system,. The permeate stream of a pervaporation in vapor phase which can be directly fed to a vapor permeator without preheating is a benefit of this technique. From our investigations based on  $Q_{\rm net} = 0$ , an available hydrophilic membrane of high water separation factor is a suitable choice to be used in a vapor permeation unit. The performance of SOFC system using this proposed purification process obviously overcomes the other two cases as shown in Figure 10.

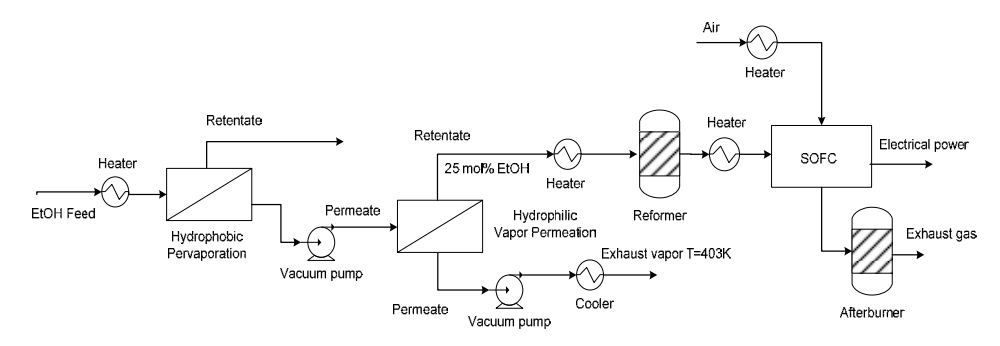


Fig. 9. Process diagram of bioethanol-fuelled SOFC system using a hybrid pervaporation/vapor permeation process

The overall electrical efficiency can be ranked as: Integrated vapour permeation/pervaporation (45.46%) > pervaporation (36.46%) > distillation column (22.53%), respectively.

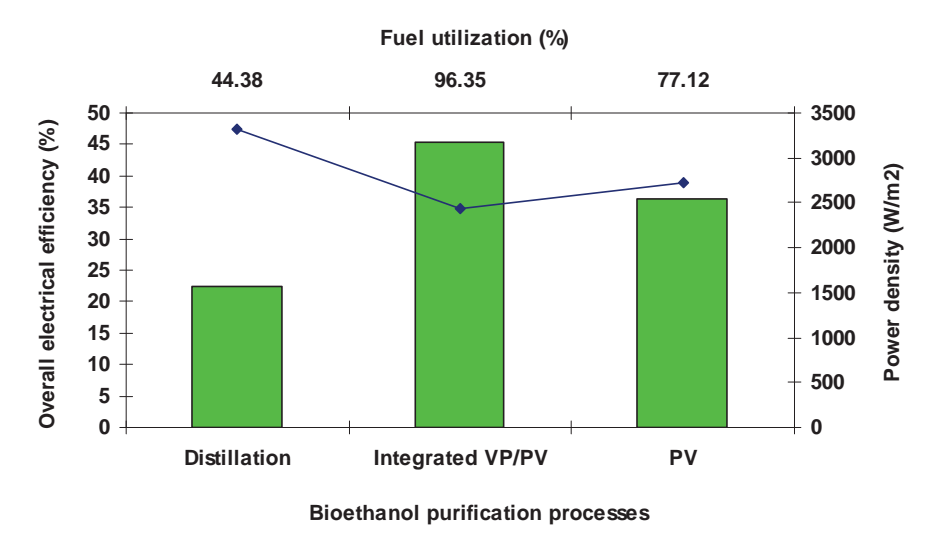


Fig. 10. Performance comparison of SOFC system with various purification processes based on self-sufficient condition ( $Q_{net} = 0$ ,  $R_{EtOH} = 75\%$ , V = 0.75V,  $T_{SOFC} = 1073K$ )

#### 4.2.2 Fuel processing section

Bioethanol was reformed into hydrogen rich gas through a reformer unit which was under the fuel processing section. High yield of desired product and a proper energy management are required for a fuel processor. Structural design of fuel processor is mostly developed to enhance high active surface-to-volume ratio with well-transferred heat. A monolithic reformer is one type of fuel processor design used to increase an active surface area but the compact size of reformer is maintained by designing highly interconnected repeating channels like a honeycomb. The pressure drop along each channel becomes lower. In addition, the monolithic design is resistant to vibration and is stable (Xuan et al., 2009). There is a limit of the temperature control because of its structural design. Nevertheless, heat transfer within the monolithic reformer can be improved by using metallic-typed material as illustrated in Figure 11. Membrane technology is applied to improve the fuel conversion unit which rely on a process integration principle commonly known as membrane reactor. However, Mendes et al., 2010, studied the energy efficiency of the polymer electrolyte membrane fuel cell (PEMFC) system in comparison between a conventional reactor and a membrane reactor operating with ethanol steam reforming. In the case of a conventional reactor, it consists of an ethanol reformer and two water gas shift reactors operating at high and low temperatures, respectively. For a membrane reactor, the multi-tubular module using thin Pd-Ag tubes was employed. The simulation results showed that membrane reactor configuration offers slightly increase of energy efficiency (30%) compared with the conventional reactor (27%) for overall process evaluation. This seems to be impractical because using a membrane-integrated fuel processor requires not only an expensive metal membrane fabrication but also results in short life time due to its low temperature resistance.



Fig. 11. Metallic-made monolithic reactor (Source: Mei et al., 2007)

Internal reforming is another concept of heat allocation techniques similar to process integration can achieve a better efficiency for the SOFC system and also reduce an external reformer cost. A fuel processing section was incorporated with the fuel cell typically placed at an anode side. Heat demand for the endothermic fuel reforming was supplied by the exothermic heat released from the electrochemical reaction of the fuel cell. The operations of internal reforming are classified into two types depending on the level of contact partition between reformer and anode electrode namely; indirect and direct internal reforming as shown in Figure 12.

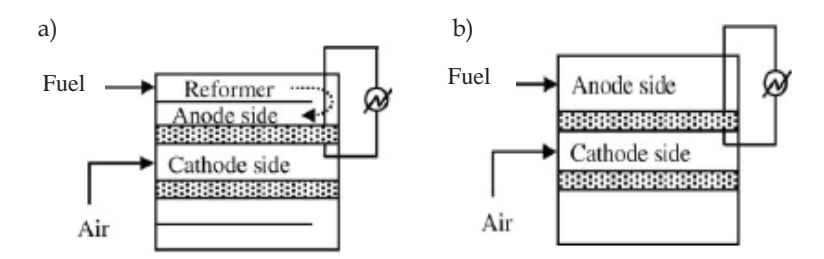


Fig. 12. Type of internal reforming in SOFC: a) Indirect internal reforming, b) Direct internal reforming

Regarding the internal structure of both types of SOFC in Figure 12, direct internal reforming SOFC (DIR-SOFC) can be superior in term of thermal allocation than indirect internal reforming SOFC (IIR-SOFC) owing to its greater contact area of anode electrode. Accordingly, DIR-SOFC can offer a higher overall efficiency. However, by using this operation mode, a carbon formation may occur at on the anode. In our previous work, Assabumrungrat et al., 2004, have investigated the thermodynamic analysis to determine suitable conditions for operating DIR-SOFC fuelled by ethanol to avoid the boundary of carbon formation. From the theoretical calculation results, it is initially suggested that an increase of the H<sub>2</sub>O/Ethanol ratio can prevent the carbon formation since adequate water supply leads to a formation of CO<sub>2</sub> rather than CO which is converted to carbon via the Boudard reaction. The oxygen-conducting electrolyte type has lower tendency to form carbon deposition than hydrogen-conducting electrolyte type because the steam product of the first type occurs at the anode side which is the location of fuel processing and thus the additional steam can increase the H<sub>2</sub>O/Ethanol ratio in the fuel reforming region.

#### 4.2.3 Heat recovery section

In the SOFC system, after a hydrogen rich gas stream reacted within an SOFC unit under the hydrogen oxidation reaction, an exhaust gas stream containing residual fuel such as H<sub>2</sub>, C<sub>2</sub>H<sub>5</sub>OH, and CO is introduced to combust in the afterburner unit to recover heat for a supply to other heat-demanding units. This brings the system to be more effective heat management and leads to higher system efficiency. There are several methods for recapturing exhaust heat under the frame of combined heat and power (CHP) principle including the use of extra power generation unit (e.g. steam and gas turbines) and heat recovery unit (e.g. recuperator, steam boiler, and heat exchanger network). Selimovic et al., 2002 proposed that networked SOFC stacks incorporated with gas turbine be used to further produce electricity from an exhaust gas combustion stream. It is known that a gas turbine is classified as a low efficiency mechanical power device as well as an entropy lost afterburner. The simulation results showed that the scenario case which allocated fuel utilization portion to the group of afterburner and gas turbine yields higher system efficiency than the scenario case of preferentially allocated fuel utilization portion to the fuel cell. Therefore, it is a good attempt to operate the fuel cell at full performance with high fuel utilization to avoid the step of fuel combustion in the system.

Our previous work (Jamsak et al., 2009) has proposed the MER (maximum energy recovery) under the concept of cogeneration to improve the performance of bioethanol-fuelled SOFC system integrated with distillation column presented in the previous section. Heat transfer

arrangement covering useful heat sources i.e. condenser duty, hot water from the bottom of the distillation column, and hot air of cathode recirculation is considered in this study. In the earlier study, system configurations are divided into 5 cases as follows:

- a. Base case (No-HX)
- b. Heat exchanged between the condenser and bioethanol feed stream (CondBio)
- c. Heat exchanged between hot water from the bottom of column and bioethanol inlet stream (HW-Cond)
- d. Heat exchanged between the condenser and air inlet stream (Cond-Air)
- e. Hot air cathode recirculation (CathRec)

All the system configuration studies are illustrated in Figure 13. The basic heat exchanger network was employed in all cases and the results are shown in Table 6.

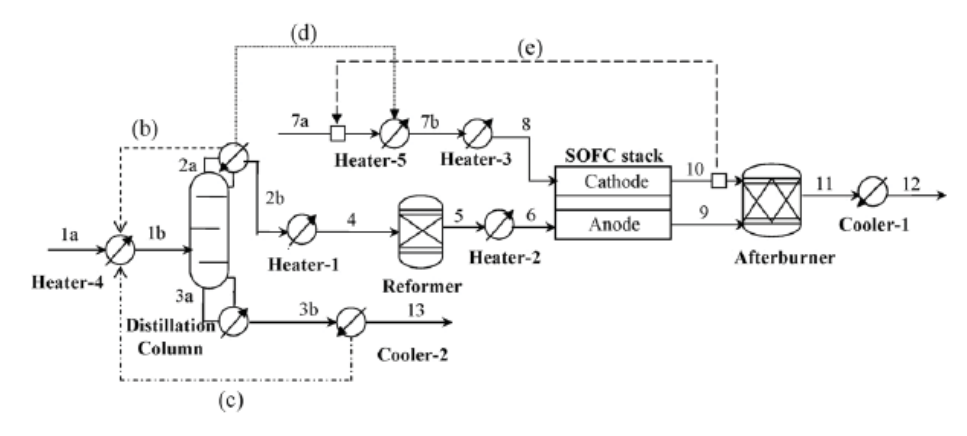


Fig. 13. Process diagram of SOFC system integrated with distillation column: a) No-HX, b) CondBio, c) HW-Cond, d) Cond-Air, and e) CathRec (Source: Jamsak et al., 2009)

Scenario case study	Overall electrical efficiency (%)	CHP efficiency (%)
No-HX	15.79	76.45
CondBio	16.26	78.73
HW-Bio	16.21	78.48
Cond-Air	16.95	81.74
CathRec	21.67	79.87
CondBio-CathRec	22.53	74.71

Table 6. Performance of SOFC system integrated with distillation column with different configurations (Source: Jamsak et al., 2009)

With regard to preheating the bioethanol inlet stream, CondBio can offer both overall electrical efficiency and CHP efficiency higher than those of HW-Bio. Thus, CondBio case is chosen for preheating bioethanol inlet stream. For preheating the air inlet stream, there are two options: Cond-Air and CathRec. Since the condenser has already been used for a bioethanol inlet stream, CathRec has to be selected although its CHP efficiency is slightly less than that of Cond-Air. Afterwards, the CondBio and CathRec are then combined to become a new case: CondBio-CathRec, and its result as shown in Table 6 provides the

highest overall electrical efficiency. In addition, this case is further developed by using MER network design. The performance achieved from this design gives 40.8% and 54.3% for overall electrical efficiency and CHP efficiency with the base conditions (25mol%ethanol, ethanol recovery = 80%, operating voltage = 0.7V, fuel utilization = 80%, and operating temperature = 1200K), respectively, compared to the previous SOFC system integrated with distillation column without MER design which gives 33.3% for overall electrical efficiency .

#### 5. Conclusions

This chapter has presented the important use of bioethanol applied as a renewable fuel for producing electricity by Solid Oxide Fuel Cell (SOFC) system. Bioethanol must be upgraded by purifying and reforming into hydrogen rich gas which can be further applied as a clean fuel for direct combustion or electrical power generation by the fuel cell. The later option is chosen as it was realized that bioethanol was worthily utilized in an effective way. The performance development of this system was proposed through our research and the other related scientific literature reviews. Macro level of physical structure design is taken into account for initially guiding a right path for system improvement. Process modification of the system is divided into two main scopes; SOFC and Balance of Plant. The Balance of Plant as a supporting part consists of fuel processing section, bioethanol pre-treatment section, and heat recovery section. All of these are necessary in the concept of process integration and cogeneration to reduce high energy consumption and difficulties within each unit. Bioethanol pretreatment section which is an essential part has been the focus in this chapter. Our evolution of the purification process improvement was proposed. Membrane technology is a promising alternative to be applied in this section and the outcome of SOFC system performance after using this technology is in good agreement with primary mathematical simulation and the criterion of no external energy demand condition. However, an economic assessment and practical experiment in term of investigating working life time should be taken into account for the further study.

#### 6. Acknowledgement

The supports from Thailand Research Fund and National Metal and Materials Technology Center (MTEC), an organization under National Science and Technology Development Agency (NSTDA), are gratefully acknowledged. The authors also would like to thank Dr. John T.H. Pearce for language assistant.

#### 7. References

- Assabumrungrat, S.; Pavarajarn, V.; Charojrochkul, S. & Laosiripojana, N. (2004). Thermodynamic analysis for a solid oxide fuel cell with direct internal reforming fuelled by ethanol. *Chemical Engineering Science*, Vol. 59, pp. 6015-6020
- Balat, M. (2011). Production of bioethanol from lignocellulosic material via the biochemical pathway: A review. *Energy Conversion and Management*, Vol. 52, pp. 858-875
- Barba, D.; Brandini, V. & Di Giacomo, G. (1985). Hyperazeotropic ethanol salted-out by extractive distillation: theoretical evauation and experimental check. *Chemical Engineering Science*, Vol. 40, pp. 2287-2292

- Black, C. (1980). Distillation modeling of ethanol recovery and dehydration processes for ethanol and gasohol. *Chemical Engineering Progress*, Vol. 76, pp. 78-85
- Bove, R. & Ubertini, S. (2006). Modeling solid oxide fuel cell operation: Approaches, techniques and results. *Journal of Power Sources*, Vol. 159, pp. 543-559
- Buchholz, S.E.; Dooley, M.M. & Eveleigh, D.E. (1987). Zymomonas: an alcoholic enigma. *Trends Biotechnology*, Vol. 5, pp. 199-204
- Cardona Alzate, C.A. & Sanchez Toro, O.J. (2006). Energy consumption analysis of integrated flowsheets for production of fuel ethanol from lignocellulosic biomass. *Energy*, Vol. 31, pp. 2447-2459
- Carlos, A.C. & Oscar, J.S. (2007). Fuel ethanol production: Process design trends and integration opportunities. *Bioresource Technology*, Vol.98, pp. 2415-2457
- Chan, S.H.; Khor, K.A. & Xia, Z.T. (2001). A complete polarization model of a solid oxide fuel cell and its sensitivity to the change of cell component thickness. *Journal of Power Sources*, Vol. 93, pp. 130-140.
- Choedkiatsakul, I.; Charojrochkul, S.; Kiatkittipong, W.; Wiyaratn, W.; Soottitantawat, A.; Arpornwichanop, A.; Laosiripojana, N. & Assabumrungrat, S. (2011). Performance improvement of bioethanol-fuelled solid oxide fuel cell system by using pervaporation. *International Journal of Hydrogen Energy*, Vol. 36, pp. 5067-5075
- Delsman, E.R.; Uju, C.U.; de Croon, M.H.J.M.; Schouten, J.C. & Ptasinski, K.J. (2006). Exergy analysis of an integrated fuel processor and fuel cell (FP-FC) system. *Energy*, Vol. 31, pp. 3300-3309
- Deluga, G.A.; Salge, J.R.; Schmidt, L.D. & Verykios, X.E. (2004). Renewable hydrogen from ethanol by autothermal reforming. *Science*, Vol. 303, pp. 993-997
- Foyle, T.; Jennings, L. & Mulcahy, P. (2007). Compositional analysis of lignocellulosic materials: evaluation of methods used for sugar analysis of waste paper and straw. *Bioresource Technology*, Vol. 98, pp. 3026-3036
- Frison, A. & Memmert, K. (2002). Fed-batch process development for monoclonal antibody production with cellferm-pro. *Genetic Engineering & Biotechnology News*, Vol. 22, pp. 66-67
- Gryta, M. (2001). The fermentation process integrated with membrane. *Separation and purification Technology*, Vol. 24, pp. 283-296
- Hala, E. (1969). Vapor liquid equilibra in systems of electrolyte components. *Institution of Chemical Engineers Symposium Series*, Vol. 32, pp. 8-16
- Jamsak, W.; Assabumrungrat, S.; Douglas, P.L.; Croiset, E.; Laosiripojana, N.; Suwanwarangkul, R. & Charojrochkul, S. (2007). Thermodynamic assessment of solid oxide fuel cell system integrated with bioethanol purification unit. *Journal of Power Sources*, Vol. 174, pp. 191-198
- Jamsak, W.; Douglas, P.L.; Croiset, E.; Suwanwarangkul, R.; Laosiripojana, N.; Charojrochkul, S. & Assabumrungrat, S. (2009). Design of a thermally integrated bioethanol-fuelled solid oxide fuel cell system integrated with a distillation column. *Journal of Power Sources*, Vol. 187, pp. 190-203
- Jaques, D. & Furter, W.F. (1972). Salt effects in vapour-liquid equilibrium: testing the thermodynamic consistency of ethanol-water saturated with inorganic salt. AIChE Journal, Vol. 18, pp. 343-346
- Kakac, S.; Pramuanjaroenkij, A. & Zhou, X.Y. (2007). A review of numerical modeling of solid oxide fuel cells. *International Journal of Hydrogen Energy*, Vol. 32, pp. 761-786.

- Kumar, S.; Singh, N. & Prasad, R. (2010). Anhydrous ethanol: A renewable source of energy. *Renewable and Sustainable Energy Reviews*, Vol. 14, pp. 1830-1844
- Lal, R. (2008). Crop residues as soil amendments and feedstock for bioethanol production. *Waste Management*, Vol.28, pp. 747-758
- Ligero, E.I. & Ravanani, T.M.K. (2003). Dehydration of ethanol with salt extractive distillation–a comparative analysis between processes with salt recovery. *Chemical Engineering Process*, Vol. 42, pp. 543-552
- Liguras, D.K.; Kondarides, D.I. & Verykios, X.E. (2003). Production of hydrogen for fuel cells by steam reforming of ethanol over supported noble metal catalysts. *Applied Catalysis B: Environmental*, Vol. 43, pp. 345-354
- Magnusson, H. (2006). Process simulation in Aspen Plus of an integrated ethanol and CHP plant. *Master Thesis in Energy Engineering*, Department of Applied Physics and Electronics, Umea University, Sweden.
- Mei, H.; Li, C.; Ji, S. & Liu, H. (2007). Modeling of a metal monolith catalytic reactor for methane steam reforming-combustion coupling. *Chemical Engineering Science*, Vol. 62, pp. 4294-4303.
- Mendes, D.; Tosti, S.; Borgognoni, F.; Mendes, A. & Madeira, L.M. (2010). Integrated analysis of a membrane-based process for hydrogen production from ethanol steam reforming. *Catalysis Today*, Vol. 156, pp. 107-117
- Minh, N.Q. (1993). Ceramic Fuel Cells. *Journal of the American Ceramic Society*, Vol. 76, pp. 563-588
- Nagel, F.P.; Schildhauer, T.J.; Biollaz, S.M.A. & Wokaun, A. (2008). Performance comparison of planar, tubular and Delta8 solid oxide fuel cells using a generalized finite volume model. *Journal of Power Sources*, Vol. 184, pp. 143-164
- Ni, M.; Leung, D.Y.C. and Leung, M.K.H. (2007). A review on reforming bio-ethanol for hydrogen production. *International Journal of Hydrogen Energy*, Vol. 32, pp. 3238-3247
- Paul, N. & Kemnitz, D. (2006). Biofuels Plants, Raw Materials, Products. Fachagentur Nachwachsende Rohstoffe e.V. (FNR), WPR Communication, Berlin, pp. 43
- Petruzzi, L.; Cocchi, S. & Fineschi, F. (2003). A global thermo-electrochemical model for SOFC systems design and engineering. Dependence of polarization in anode-supported solid oxide fuel cells on various cell parameters. *Journal of Power Sources*, Vol. 118, pp. 96-107
- Piroonlerkgul, P.; Assabumrungrat, S.; Laosiripojana, N. & Adesina, A.A. (2008). Selection of appropriate fuel processor for biogas-fuelled SOFC system. *Chemical Engineering Journal*, Vol. 140, pp. 341-351
- Pramuanjaroenkij, A.; Kakac, S. & Zhou, X.Y. (2008). Mathematical analysis of planar solid oxide fuel cells. *International Journal of Hydrogen Energy*, Vol. 33, pp. 2547-2565
- Roger, P.L.; Lee, K.J. & Tribe, D.E. (1980). High productivity ethanol fermentations with Zymomonas mobilis. *Process Biochemistry*, pp. 7-11
- Selimovic, A. & Palsson, J. (2002). Networked solid oxide fuel cell stacks combined with a gas turbine cycle. *Journal of Power Sources*, Vol. 106, pp. 76-82
- Shell, D.J.; Riley, C.J.; Dowe, N.; Farmer, J.; Ibson, K.N.; Ruth, M.F.; Toon, S.T. & Lumpkin, R.E. (2004). A bioethanol process development unit: initial operating experiences and results with a corn fiber feedstock. *Bioresource Technology*, Vol. 91, pp. 179-188

- Sukwattanajaroon, V.; Charojrochkul, S.; Kiatkittipong, W.; Arpornwichanop, A. & Assabumrungrat, S. (2011). Performance of membrane-assisted solid oxide fuel cell system fuelled by bioethanol. *Engineering Journal*, Vol. 15, pp. 53-66
- Tao, G.; Armstrong, T. & Virkar, A. (2005). Intermediate temperature solid oxide fuel cell (IT-SOFC) research and development activities at MSRI. *In: Nineteenth annual ACERC&ICES conference*, Utah
- U.S. Department of Energy. Energy Efficiency & Renewable Energy, http://www1.eere. energy.gov/biomass/abcs\_biofuels.html
- U.S. Environmental Protection Agency, http://www.epa.gov/methane/.
- Vourliotakis, G.; Skevis, G. & Founti, M.A. (2009). Detailed kinetic modeling of non-catalytic ethanol reforming for SOFC applications. *International journal of hydrogen energy*, Vol. 34, pp. 7626-7637
- Wilkins, M.R.; Widmer, W.W. & Grohmann, K. (2007). Simultaneous saccharification and fermentation of citrus peel waste by Saccharomyces cerevisiae to produce ethanol. *Process Biochemistry*, Vol. 42, pp. 1614-1619
- Xuan, J.; Leung, M.K.H.; Leung, D.Y.C. & Ni, M. (2009). A review of biomass-derived fuel processors for fuel cell systems. Renewable and Sustainable Energy Reviews, Vol. 13, pp. 1301-1313
- Zhao, F. & Virkar, A.V. (2005). Dependence of polarization in anode-supported solid oxide fuel cells on various cell parameters. *Journal of Power Sources*, Vol. 141, pp. 79-95

**Submitted to Wiley** 

Type of contribution: Advanced reviews (AR)

Integrated Solid Oxide Fuel Cell Systems for Electrical Power Generation – A Review

Suttichai Assabumrungrat<sup>\*</sup>, Amornchai Arpornwichanop, Vorachatra Sukwattanajaroon and Dang Saebea

Department of Chemical Engineering, Faculty of Engineering, Chulalongkorn University, Bangkok 10330, Thailand

\* Corresponding author (suttichai.a@chula.ac.th)

### Abstract

The development of solid oxide fuel cell (SOFC) technology for electrical power generation has been in significant progress during the past decades. One promising approach to improve its energy efficiency and to extend its operation viability is by integrating an SOFC with other technologies such as hydrogen production process and conventional thermodynamic cycles. This chapter provides the state of the art of the most important SOFC integration technology. The concepts and strategies to improve the efficiency of SOFC-based hybrid systems are provided with a particular focus on the integration of SOFC with various fuel processors and gas turbine systems.

Solid Oxide Fuel Cell (SOFC) is a promising technology for direct conversion of chemical energy in a fuel to electrical power. It offers several benefits such as high efficiency, fuel flexibility, low noise and environmental impacts, less electrolyte management problem, variety of electrode catalysts, size flexibility and possibility for combined heat and power operation (CHP). Although it has a wide variety of applications ranging from small-scale auxiliary power units to large-scale stationary power generation, SOFC operation still suffers from many limitations such as high cost, short lifetime due to pulse demands and impurities of feed, poor thermal shock, long startup time and risk for carbon deposition.<sup>2</sup> A number of multidisciplinary research and development efforts are required to overcome these problems in order to make SOFC a marketable technology. The research and development can be mainly classified into improvement of material and component properties and integration of SOFC with various technologies and functions.<sup>3</sup> Many materials for the cell components (anode, cathode and electrolyte) have been tested to achieve better cell performance (e.g. high power density, stability, compatibility and durability) and lower cost. 4,5 An anode-supported SOFC is considered to be the best candidate in term of polarization standpoint when compared with a conventional electrolyte-supported SOFC and a cathodesupported SOFC. A number of research efforts have focused on development of intermediate-temperature SOFC (IT-SOFC) (500-750°C) which offers several important advantages including lower cost of construction materials, an enhanced range of applications, and improved durability and lifetime.<sup>6</sup> Another key development of SOFC is based on integration of SOFC with other technologies and/or functions. Various concepts/strategies for SOFCbased integration system have been proposed and several benefits have been reported.<sup>2</sup>

The following sections will outline fundamental of SOFC and concept of process integration as well as review the development in the SOFC-based hybrid systems.

# **Fundamental of SOFC system**

SOFC generates electricity from electrochemical reaction of a fuel and an oxidant. Although high operating temperature of SOFC allows direct use of a variety of fuels such as hydrocarbons and alcohols, hydrogen and/or synthesis gas is a major fuel for practical SOFC in order to extend life time of the cells. Major components of fuel cell are anode, cathode and electrolyte. There are two types of electrolyte, i.e., oxygen ion and proton conducting electrolytes. For SOFC, the former is the most commonly used one due to its availability. The electrochemical reactions at the electrodes are as follows:

Anode:  $H_2 + O^{2-} \rightarrow H_2O + 2e^{-}$ Cathode:  ${}^{1/2}O_2 + 2e^{-} \rightarrow O^{2-}$  A fuel processor is typically installed in an SOFC system to convert a fuel (e.g., natural gas, biogas, hydrocarbons and biomass) via different reactions, such as steam reforming, partial oxidation and autothermal reforming, to a hydrogen rich gas. It is then fed to the anode together with air at the cathode of an SOFC stack where the electrochemical reaction takes place to generate electricity at high efficiency. The presence of fuel remaining in the anode exhaust gas and heat generated from irreversibility of the electrochemical reaction allows the SOFC to be integrated with various technologies to achieve high energy efficiency and other benefits. The next sections will provide fundamental concepts of SOFC-integrated processes.

# **SOFC-integrated processes**

As mentioned earlier, SOFC has been known as a high-efficiency power generator which offers more than 50% of electrical efficiency. To extend the capability of SOFC for use with various fuel supplies apart from the traditional hydrogen supply, a supplementary processing system is integrated as components in the Balance of Plant (BoP) of the SOFC system to facilitate the use of such fuels. High performance and energy requirement of the fuel conversion system are important issues to be considered for improving performance of the SOFC system. In addition, energy loss or waste heat generated within the SOFC system is another issue which obstructs significantly the system to achieve high efficiency. Technical strategies such as heat recovery processes and waste energy minimization methods are applied to obtain suitable solutions for such a problem. To achieve a higher efficiency of SOFC system, uses of process analysis tools as performance assessment indicators are considered together with a principle of exergy analysis to indicate the content of available energy and to identify energy loss (exergy destruction) distribution in the overall system. These approaches could help find causes of the problem in particular subsystems or the whole system, and then guidelines for the improvement are obtained. In the BoP of SOFC system, there are two major sections that impact on the system efficiency: (i) a fuel processing section (hydrogen production system) and (ii) a heat recovery section. Concept and strategy reviews for both the sections are provided in this article.

# **Process integration concept**

Efficient energy usage in chemical process industries has been realized as an important issue, driven by the energy crisis in the 1970s. This topic is then taken into consideration in a process engineering design approach. Several process design methodologies have been investigated and developed from academic and industrial sectors in order to target energy conservation and waste minimization in chemical processes. Similar to other chemical process improvements, SOFC systems for power generation, containing integrated systems e.g. fuel pre-conditioning, fuel processor, heat

and mass recovery systems, etc., need to be analyzed through process configurations and process integration techniques to find a feasibility of the system efficiency development. The sequential progress of process integration development started with the energy perspective in the earlier stage. Heat integration concept was initiated by Hohmann<sup>8</sup> who investigated an optimum network for heat exchanges but his work was not recognized at that time until Linnhoff and Flower brought Hohmann's work to further develop a pinch technology. The aim of this method is to identify energy saving opportunities in order to design an optimal heat exchanger networks (HENs) to meet the minimum utility targets, stated that the overall process does not only have minimum energy requirement but also owns a maximum energy recovery. The procedure of this method starts with classifying a list of hot and cold streams. Overall heat calculated from each hot stream is considered the heat sources that need to be removed to reduce their temperatures, while all cold streams are calculated to gain overall heat requirement defined as the heat sinks to increase their temperatures. This stage can initially identify the net minimum energy requirement. In the step of pinch analysis, several methods are introduced to minimize the energy requirement, i.e., Temperature-Interval Method, Graphical Method using Composite Heating and Cooling Curves, etc. The minimum utility loads (heat input and heat removal loads) are carried out from these calculation methods. Based on a thermodynamic principle, thermal energy is transferred from a hot stream with a higher temperature to a cold stream having a lower temperature. Therefore, heat transfer mechanism can be occurred if the hot and cold streams have a temperature difference high enough to create a thermal driving force. For the overall system, a heat recovery can be maximized if the difference temperature of the hot and cold streams is close to a minimum difference temperature,  $\Delta T_{\min}$ . As illustrated with the temperature-enthalpy diagram in Fig. 1, the heat composite curve is located above the cooling composite curve. Thermal energy is input to the system above pinch temperature (heat sink), while heat is removed from the system below pinch temperature (heat source).  $\Delta T_{\min}$  has a specific interval range, typically 10°F or 5°C. In case when the value of  $\Delta T_{\rm min}$  is too high, the system requires more minimum heating (Q<sub>H,min</sub>) and cooling (Q<sub>C,min</sub>) loads. The results lead to a lower heat recovery capacity of the system. If the interval  $\Delta T_{\min}$  is too low, heat cannot be transferred in each hot and cold stream, especially when  $\Delta T_{\min}$  is set to be zero; this case is called pinch point/temperature.

The information from pinch analysis is used to design heat exchanger networks and is further applied to design the minimum number of heat exchangers, respectively. Applications of heat integration through HENs for the fuel cell system have been reported in scientific literatures. For example, the optimization of a proton exchange membrane fuel cell (PEMFC) system using process integration techniques and simulation model were studied by Godat and Marechal. The system consists of a methane steam reformer, water gas shift reactor, preferential oxidation reactor, PEMFC and combustor unit. The influence of major parameters (e.g., steam-to-carbon ratio, steam

reforming temperature, fuel cell temperature and fuel utilization) was investigated. In case when excess air is employed to control the water balance of the cathode, it was shown that the combustion temperature is reduced to be close to the steam reforming temperature and then the high pinch point occurs at the reformer temperature. However, with optimal operating conditions and heat exchanger network configuration, the system efficiency increases from 35% to 49%. A bioethanol-fuelled SOFC system integrated with distillation column was improved in terms of the electrical efficiency by using the minimum energy requirement (MER) network. 11 Different hot streams and cold streams within the system were matched. leading to various cases of process configurations as illustrated in Fig. 2. Heat exchange between the condenser (heat source) and bioethanol feed stream (heat sink) and using hot air cathode recirculation stream are the suitable option. This process configuration was applied with MER network configuration and the results showed that it can reduce the minimum cooling loads from 73.4 kW to 55.9 kW and offer the overall efficiency at 40.8%. Basically, it can be stated that the use of heat integration concept for SOFC system applications aims to utilize its internal heat sources (post-combustion unit) and useful residual heat accumulated in the exhaust streams (hot residual air and fuel and hot stream product) for supplying to other heatdemanding units. This approach leads to an efficient energy management.

In case of the high pinch temperature, especially for the SOFC system integrated with an endothermic steam reforming as the fuel processor for hydrogen production, the classical energy integration theory based on a thermal pinch analysis is generally not enough to deal with this problem. 12 According to the rule "no hot utility below pinch point", heat released from units below the pinch temperature needs to be removed from the system. To recover this useful heat, new techniques with the integration of fuel and mechanical power (turbine engine) under the concept of a combined heat and power (CHP) have to be considered. 13 Townsend and Linnhoff developed the concept of heat engine combined with heat integration system (i.e. HEN). They observed that the heat engine should be placed above or below the pinch but not across the pinch point because no reduction in heating or cooling loads is achieved from this arrangement. The role of heat engine is to transform thermal energy in hot streams into work but it still discharges residual heat due to the incomplete conversion explained by a second law of thermodynamics. As shown in Fig. 3, heat engine is located below the pinch point of HEN system to recover heat in case of high pinch temperature as mentioned earlier. Surplus heat below pinch point normally removed uselessly by cooling loads is fed into the heat engine. This device offers the benefits not only to remove heat below the pinch but also to partially convert heat into useful work. On the contrary, if the excessive heat is supplied to the above pinch region more than the minimum heating load demand, heat engine is installed to partly convert the surplus heat to work and the remaining heat is used for heating utility served as a heat sink of heat engine (Fig. 4). Further applications of heat engine to the SOFC system are provided in the section of SOFC system integrated with gas turbine.

In addition to the process integration from the energy conservation point of view, the concept of mass integration is another important issue involving waste utilization and reduction. The new process design methodologies which take this principle into account have been developed, including mass pinch analysis and other related methods used for design of waste recovery process. <sup>17,18</sup> Mass Exchange Network (MEN) synthesis based on mass pinch technology, similar concept with the thermal pinch technology, is the method originated from the mass integration concept. In general, the MEN principle is applied with separating agents to build recovery or purification units such as absorption column, adsorber, liquid-liquid extraction, etc. Properties of mass separating agent (MSA) e.g. solubility limit, thermodynamic constraints and absorption/adsorption capability used to recover the target component are essential on performance of MEN design. In physical term, direct-contact and counter currents are preferential configurations for mass exchange system design. However, operating and capital costs are crucial to be considered before selecting these recovery systems. For SOFC systems, the concept of mass integration can be employed to design a recovery system of useful residual exhaust gases from the anode and cathode of a fuel cell stack.

Hartono et al.<sup>19</sup> applied the mass integration concept to high temperature fuel cell plants (i.e., SOFC and MCFC), leading to a simplified system design. The previous studies by Fellows<sup>20</sup> and Lisbona et al.<sup>21</sup> indicated that increase of anode recycle ratio shows negative effects on the system efficiency. In their work, the utilization of anode exhaust gas of SOFC power plant was studied by two approaches: (i) basic stoichiometric calculation and (ii) detailed modeling of overall system, to find a proper minimal anode recirculation ratio. As seen from Fig. 5, it should be noted that increasing anode exhaust gas flow rate causes a higher power consumption of the blower. The optimal anode recycle ratio depends on types of fuel. Among the studied fuel types (methane, ethanol, wood, methanol and anthracite), methanol requires the lowest recycle ratio, whereas anthracite needs the highest one. The two approaches used to analyze the SOFC system achieve similar results; however, the stiochiometric method is simpler and can predict the minimal recycle ratio and steam-to-carbon ratio to prevent carbon formation.

In general, there are several system analysis tools that can be used for a mass integration-based design methodology such as a stream mapping diagram used to find an opportunity for direct or mixed recycle, a path diagram used to analyze the process configuration of specific required species represented in the form of mass flow, an interception technology used to analyze a proper purification/pretreatment approach and an reaction pathway modification used to convert undesired species to useful/desired products.<sup>22</sup> The reaction pathway modification method can be further applied for MEN synthesis, leading to a Reactive Mass Exchange Networks (REAMENs). A recent progress in the process integration development is focused on the combination of heat and mass integration concepts. Several process design methodologies which follow this combined concept have been

developed,  $^{22}$  e.g., Heat-Induced Separation Networks (HISENs), Energy-Induced Separation Networks (EISENs), Membrane Separation Networks (MSNs), Heat-Induced Waste Minimization Networks (HIWAMINs), Energy-Induced Waste Minimization Networks (EIWAMINs) and Waste Interception and allocation Networks (WINs). For the SOFC system, a fuel cell combined with a fuel processor is a distinct representation of the concept that uses a combined heat and mass integration; efficient processing units in part of the BoP are selected and combined for supporting the SOFC module to achieve a better performance under an effective energy and mass management, i.e., a self-sufficient condition ( $Q_{\text{net}} = 0$ ) and low level of exhaust fuel residues.

Design of SOFC integrated systems requires some useful analysis tools to help focus or identify some deficits and evaluate the performance of new proposed SOFC system configurations. Exergy analysis is an effective tool that is capable to indicate possible improvement together with process configurations to ensure the optimal operating conditions and integrated process design. Exergy is destroyed by irreversible process conditions leading to the loss of work. Optimization of exergy efficiency deals with minimization of lost work that is equivalent to the concept of minimization of the entropy production followed by Gouy-Stodola theorem.<sup>23</sup> Exergy can be transferred in and out through the open system (such as SOFC system) by three forms: heat, work and mass with the same principle of energy balance.

Exergy calculation depends on states of the system and reference environment (restricted dead state). The exergy destruction is mainly caused by high temperature processing units such as post-combusting unit and water vaporizer. For a plug-flow reformer, the entropy/exergy loss is due to a heat transfer, frictional flow and chemical reactions. To solve this problem, equal distributions of entropy production and forces along the length of reactor are suggested. This solution approach is known as "equipartition of entropy production and equipartition of forces." Increasing the reactor length to increase the residence time and using optimal control theory. Were demonstrated to reduce the entropy production.

# SOFC with hydrogen production system

#### Hydrogen production processes

Typically, hydrogen is a desired fuel to be introduced to the anode side of SOFC module for power generation, regardless of internal reforming within the fuel cell. Hydrogen is considered a clean and sustainable energy carrier in terms of chemistry theory point of view because it can be widely available in the form of other substances such as water, gas/liquid/solid hydrocarbons and other hydrogen-compounded substances. However, it does not have any natural conditions that can offer pure hydrogen readily in use. Complex infrastructures, e.g., treatment, production, distribution and storage handling, and economic competitiveness need to be tackled to support this promising energy. As a result of these factors, an efficient fuel processor for producing hydrogen from other fuel sources is a key consideration for SOFC system.

The selection of appropriate fuel for hydrogen production is another essential topic because it affects the complex degree of a fuel processor design and in turn the whole SOFC system. General criteria such as renewability, cost, storage and availability, are considered for selecting a proper fuel. In addition, the selected fuel should have a well-developed technology support for converting it into hydrogen with low complexity, fewer requirements of equipment and low energy consumption. Basically, all hydrocarbon fuels in different forms, i.e., solid, liquid and gas phase, can be employed as raw material for hydrogen production. In general, the overall reforming reaction of hydrocarbon fuels can be written as:

$$C_a H_b O_c + dO_2 + 2(a - d - \frac{c}{2}) H_2 O \rightarrow a CO_2 + 2(a - d - \frac{c}{2} + \frac{b}{4}) H_2$$
 (1)

This reaction simply shows the ideal reforming of hydrocarbon fuels into only hydrogen and carbon dioxide without considering reactant residues, steam, carbon monoxide and other low-carbon compounds. Typically, the hydrogen production process from hydrocarbon and alcohol fuels is performed via three common reforming reactions: Steam Reforming (SR), Partial Oxidation (PO) and Autothermal Reforming (ATR). In each reaction, there are individual characteristics as follows:

Steam reforming: This reaction is commonly used in industrial processes because of long-period operation stability and high yield of the hydrogen product. Steam reacts with fuel to produce hydrogen and carbon dioxide via strongly endothermic reaction (Eq. 2) at temperature above 500 °C. Heat transfer is an essential consideration for this reactor design. High steam-to-carbon ratio, high temperature and low pressure are suitable conditions for preventing coke formation and gaining high hydrogen yield.

$$C_a H_b O_c + 2(a - \frac{c}{2}) H_2 O \rightarrow a CO_2 + (2a + \frac{b}{2} - c) H_2$$
 (2)

<u>Partial oxidation</u>: Oxygen is used instead of steam to partially react with fuels to generate hydrogen and carbon monoxide (Eq. 3). This reaction consumes less energy than the other two reactions (SR and ATR) but requires good catalysts to avoid the complete oxidation that leads to the presence of carbon dioxide and water. Furthermore, control of reaction conditions is important to prevent a runaway reaction due to its highly exothermic reaction and a carbon formation on catalyst.

$$C_a H_b O_c + \frac{1}{2} (a - c) O_2 \rightarrow a CO + \frac{b}{2} H_2$$
 (3)

Autothermal reforming: A steam reforming and a partial oxidation take place simultaneously in the autothermal reforming. Heat released from the partial oxidation is absorbed by the endothermic steam reforming. This thermal balance in the autothermal process leads to a lower-temperature operation. However, the autothermal reforming needs to be controlled to operate under thermal neutral or little exothermic condition. Selection of appropriate ratio of fuel, air and steam and use of proper catalysts can control the heat transfer between the partial oxidation and the steam reforming.

Apart from these three basic reactions, a number of hydrogen production technologies have been investigated and reported in literatures,

e.g., Super Critical Water Reforming (SCWR) for methanol<sup>30</sup> and biomass,<sup>31</sup> Catalytic Dehydrogenation (CDH) of methane<sup>32</sup> and so on. The CDH of methane is a single step reaction which produces high purity of hydrogen and also a valuable carbon nanotube byproduct. However, economic and practical issues for a large-scale production are still the main barriers for these novel processes to be further developed.

Chemical-Looping Reforming (CLR) technology has been used for hydrogen production and carbon dioxide capture. The evolution of this technique was initiated by Arnold Conrad<sup>33</sup> from the Standard Oil Development Company, who firstly proposed the chemical-looping combustion process for carbon monoxide and hydrogen production and was granted a patent since the early 1950s. Thereafter, the CLR has been developed and applied to many applications: Chemical-Looping Steam Reforming (CLSR), Chemical-Looping CO<sub>2</sub> Acceptor Reforming (CLCAR), Chemical-Looping Partial Oxidation (CLPO) and Autothermal Reforming (CLATR) as shown in Fig. 6. All chemical-looping reforming types are based on the same principle that consists of coupled processes: cyclic oxidation and reduction of metallic oxide carriers (e.g., CLSR, CLPO and CLATR) or CaO as CO<sub>2</sub> sorbent (e.g., CLCAR) in two separate reactors. Considering their performances, both the CLPO and CLATR need to keep at a low ratio of air and fuel to produce syngas and prevent the complete combustion of fuel to CO<sub>2</sub> and water, likewise the Chemical-Looping Combustion (CLC).<sup>35</sup> CLSR is an interesting process among the other types. Similar to ordinary steam reforming characteristics, fuels can be completely oxidized in the CLSR fuel reactor and also metallic oxide carriers are entirely reduced to metal form before moving into the steam reactor where metal particles are reacted with steam to produce pure hydrogen and solid metal oxide particles for looping return. In the effluent stream of the fuel reactor, there are steam and carbon dioxide apart from metal particles. Carbon dioxide can be easily separated by condensing steam to water. The advantage of CLSR is that there is no need to install any further processing units such as a water gas shift rector or a pressure swing adsorption.<sup>36</sup>

A number of metals have been investigated to select a suitable metal oxide being as an oxygen carrier. Iron is considered as an interesting metal because it is environmentally-benign and relatively inexpensive material.<sup>37</sup> In addition, after the oxygen carrier is used in a number of cycles, it can be recycled to a steel industry.<sup>38</sup> The CLR process that uses iron oxide is known as a steam-iron process developed by Messerschmitt<sup>39</sup> and Lane.<sup>40</sup> Fossil fuels such as natural gas and the synthesis gas derived from coal/lignite gasification are used in the CLSR. Based on natural gas (methane) feed, the CLSR process has the following coupled reactions.

$$Fe_3O_4 + CH_4 \rightarrow 3Fe + CO_2 + 2H_2O \tag{4}$$

$$3Fe + 4H2O \rightarrow Fe3O4 + 4H2$$
 (5)

Eq. 4 is an endothermic reduction of fuel carried out in the fuel reactor, whereas Eq. 5 is an exothermic oxidation of iron oxide and steam occurred in the steam reformer. Ideally, both the reactions can transfer thermally-neutral heat in each other; however, the thermal balance is not absolutely occurred in

the overall CLSR process. Additional heat needs to be supplied to maintain its smooth operation, optionally retrieving heat residues from other neighboring processing parts (e.g., the water gas shift reactor) within the system or relying on an external heat source. The CLSR process is still required to further develop for solving some problems such as a recirculation of metal oxide particles between two fluidized bed reactors, low conversion efficiency and slow reaction rate of oxygen carrier particles.

In conclusion, the selection of hydrogen production process relies on not only a proper type of fuel but also the reforming reaction. Furthermore, the hydrogen production process should be compatible with SOFC system applications. For example, when the SOFC system has a problem of inadequate thermal energy supply, the autothermal reforming may be an interesting choice. If high yield of hydrogen is a main target of SOFC systems to maximize their performance, the steam reforming can serve their requirement. By products obtained from the hydrogen production process should also be considered as they affect the difficulty level of a hydrogen purification process.

#### Integration of SOFC system with hydrogen production processes

A fuel processor is an essential unit used to convert various fuels to hydrogen-rich gas for SOFC. Based on the heat and mass integration concepts, an integrated fuel cell (SOFC) and fuel processor (hydrogen production unit) system is considered to enhance its performance. Lee et al. 41 studied the recirculation of anode outlet stream from the SOFC to the fuel processor. Due to the internal reforming property and CO tolerance material of SOFC, only a primary reformer without having an additional gas-clean up unit (CO removal) is used for the fuel processor. The hydrogen pretreating unit is normally used for a low temperature fuel cell system (e.g., PEMFC) as illustrated in Fig. 7. In a conventional fuel cell power system, the system volume of 33% is occupied by the fuel processor. 43 As a result of this, the development of a fuel processor can take significant effects on the SOFC system efficiency. Over the past two decades, many research efforts have been devoted to develop and improve a fuel processor for hydrogen production. Mass and energy management strategies, novel structural designs of reformer and SOFC module, process intensification and fuel processing-assisted units have been proposed.

#### Structural design of SOFC

Due to the high temperature operation of SOFC (800-1000 °C), reforming of fuel can be occurred within the fuel cell. Unconverted hydrocarbons and CO from the external reformer is further converted to hydrogen at the anode. It is noted that the net efficiency of the SOFC system will be decreased when more steps of hydrogen production are added to the fuel processor. The internal reforming characteristics of the SOFC result in the compactness of the system, faster loading response, cost reduction and

increased system efficiency. 44 Furthermore, the endothermic internal reforming reaction can consume the excessive heat released from the exothermic hydrogen oxidation within the fuel cell. In general, the internal reforming can be classified into 2 types: (i) direct internal reforming and (ii) indirect internal reforming. A porous ceramic anode electrode containing reforming catalysts, e.g., Pt, Rh and Ru, is used for coupling the reforming and electrochemical reactions in the direct internal reforming.<sup>45</sup> For the indirect internal reforming operation of SOFC, the reforming section is separated but located close to the anode electrode. Anode catalyst deactivation by the formation of carbon is a major drawback of the internal reforming. Regarding an SOFC structural modification, since the solid electrolyte material is used, the SOFC can be fabricated in various shape designs, i.e., tubular, planar and monolithic. 46 An integrated planar design is also proposed, which combines tubular and planar geometries, leading to a good thermal expansion compliance, low-cost component fabrication, short current path<sup>47</sup> and a higher ratio of power per volume.<sup>48</sup> The aim of these structural designs is to optimize the performance of fuel cell. Fuel cellintegrated concept is another aspect to be considered for process modification. High fuel utilization and high operating voltage are desirable to achieve a high efficiency of the fuel cell. Practically, increasing fuel utilization leads to a decrease in the Nernst potential which limits the cell operating voltage. The ways to solve this problem are to operate the fuel cell at a high fuel recycle ratio<sup>49</sup> and to apply a multistage oxidation concept. Selimovic and Palsson<sup>50</sup> applied the multistage oxidation concept by networking SOFC stacks to improve the SOFC/GT system (Fig. 8). The benefits of this solution approach are improved thermal balance, higher total fuel utilization and increased power efficiency. From their study on the SOFC stack arrangement as illustrated in Fig. 9, it was found that the SOFC stack arranged in series shows an increase in the system efficiency. However, this stack networking was found not to be worthwhile in a large scale SOFC system.

Shin'ya Obara<sup>51</sup> studied a combined SOFC-PEMFC system for supplying energy to 30 houses in Sapporo, Japan (Fig. 10). It is known that the exhaust heat of SOFC is not released consistently due to its non-uniform system load. In the proposed system, the flexible time shift operation plan was employed to manage the inconsistent SOFC high-temperature exhaust heat for the generation of the reformed gas from natural gas, which is used for the electricity production of the low-temperature PEMFC. As schematically shown in Fig. 11, the SOFC is operated with internal reforming. Heat released from the SOFC is supplied to a steam reformer (R/M) where hydrogen is produced. Water is removed by an air-cooling condenser (C/S) and CO content is reduced by a CO oxidation unit (C/O). Finally, the reformed gas with high hydrogen content is stored in the cylinder tank before being fed to the PEMFC. With the target of effective exhaust heat utilization to obtain a higher total power generation efficiency, operation methods with different power load patterns related to amount of heat storage and power efficiency were studied. The results indicated that it can maintain average power generation efficiency near at 48% on winter and summer seasons.

#### Structural design of reformer

Generally, a structural design of reformer is proposed with the attempt to achieve a high surface-to-volume ratio and efficient heat transfer to allocate/utilize thermal energy. Energy consumption in the reformer depends on type of reforming reactions and fuels. Monolithic structure is a type of the shape-fabricated design which can increase the active surface area; however, it has the limitation in a temperature control.<sup>52</sup> Membrane separation technique is applied to assist reforming mechanisms and enhance heat integration in the reformer. With appropriate membrane type to remove only a preferential substance (product) from the reformer, reaction rates can be increased and by-products are separated at the same time. For example, a hydrogen transport membrane (HTM) reactor was used to concentrate produced hydrogen and promote the reaction selectivity at low temperatures.<sup>53</sup> Membrane material should tolerate with a high-temperature operation in the reformer. Generally, polymeric-made membranes cannot be used at temperatures above 100-150 °C.54 Hence, a metallic-made or inorganic membrane is a promising choice used in the reformer. In addition, it can also be fabricated in various shapes to improve a high surface area. Palladium and its alloys (e.g., Pd-Ag, Pd-Cu) have been used in dense membrane reactors for maximizing a hydrogen production. 55-57 Integration of SOFC and Pd membrane reactor fed by biogas/methane was investigated in terms of technical and economic analysis.<sup>58</sup> It was found that the proposed system was not a good choice from the economic viewpoint as it required a large high-pressure compressor for fuel gas feeding to a membrane reactor.

Heat integration and catalyst-assisted techniques were employed in structural designs of the reformer. A heat exchanger with wave-shaped plates design was proposed by Isogawa et al.<sup>59</sup> to enhance the heat integration of the combustion and endothermic reforming reactions. Heat exchange steam reformer was developed by Ida Tech.<sup>60</sup> Heat from the combustion of unreacted fuel or raffinate was supplied to a pre-reforming feed before being entered to the catalyst bed in the reforming section. It can reduce heat loss and increase the thermal efficiency to the reformer. Catalyst was applied together with a thermal integration in the reformer design. Lesieur and Corrigan<sup>61</sup> proposed a catalytic wall reactor to enhance heat integration by transferring the thermal energy through a thin wall. Noble metal catalysts were coated on one side of the wall for endothermic reforming and on the other side of the wall for fuel combustion. This means that the burner, reformer and heat exchanger are integrated into a single unit making the system compactness and higher efficiency.

A Pressure Swing Reformer (PSR) was developed by ExxonMobil.<sup>62</sup> It has low pressure combustion cycles, offering a benefit to heat high pressure steam reforming within the catalyst bed. Division of multiple reaction zones in the reformer: impurities removal zones and reforming zones such as HT/LT-WGS, PROX and SR, is another strategy of structural reformer design to utilize thermal energy effectively and perform a waste heat reduction.<sup>63,64</sup>

However, temperature control in each zone and difficulty in scale-up of this kind of reformer are still problems need to be further improved.

Fuel types for SOFC system and additional fuel processing-assisted units

As mentioned above, the degree of complexity in the fuel processor-SOFC integrated system design depends on a selection of fuel and reforming technology. Factors that need to be considered when choosing fuel and performing process system design are the availability of technological supports at the desired scale production, capital and operation costs, catalyst technology supports, extent of additional fuel processing-assisted units (fuel pretreatment/purification) and especially an efficiency of the system gained from those design configurations. The followings summarize the details of different fuel types.

#### Gaseous fossil fuels

This fuel type normally refers to natural gas which is considered initially in converting to hydrogen-rich gas that is used to feed in the multistage fuel cell system<sup>65</sup> and SOFC stationary system<sup>66</sup> because of its existing infrastructure supports, availability and high conversion efficiency. Methane is a main component in natural gas (70-90%), meaning that a plenty of reactions used for methane conversion can be used with natural gas. Sulfur species such as H<sub>2</sub>S (0-5%) or Sulfur-containing odorants, in natural gas can affect catalyst degradation, especially for Nickel catalyst. 67 Therefore, a desulfurizer unit such as a zinc oxide polisher and a hydrodesulfurizer, is required to pretreat natural gas by reducing the sulfur species in an acceptable level (e.g., 1 ppm sulfur odorants and <1 ppm H<sub>2</sub>S) for fuel cell applications.<sup>7</sup> Liquefied Petroleum Gas (LPG), another interesting fuel containing mainly propane, was used for hydrogen generation <sup>68, 69</sup> and also was demonstrated as fuel supply for an SOFC. 70 A prototype LPG reformer was designed with the reactions: steam reforming, water gas shift and methanation, for 5 kW IR-SOFC system. Selection of a suitable catalyst was studied and its operating regime to avoid the catalyst deactivation due to carbonaceous depositions was given.

#### Liquid fossil fuels

Liquid fossil fuel has similar benefits as gaseous fossil fuels but it offers more secure and convenient in terms of fuel handling and storage. However, in the BoP design, a vaporizier is required for the liquid fuels. Generally, they need high temperatures in the vaporization and fuel conversion for hydrogen generation. Gasoline requires the temperature of higher than 650 °C for its catalytic conversion and over 1,000 °C in case of no catalyst. However, gasoline has twice power density, compared to methanol. Diesel requires the vaporization temperature higher than 400 °C. Although use of this fuel is interesting to apply for SOFC auxiliary power unit (APU), a large amount of sulfur and carbon formations in the fuel processor is still needed to be tackled. Basically, the active metal sites are deteriorated because sulfur will react with

metal catalysts to form stable sulfide complexes during the reforming process. Therefore, the catalysts with high sulfur tolerance and high activity of aromatics are required for the reforming of diesel. Noble metals, i.e., Pt and Rh, with gadolinium-doped ceria support showed a good catalyst performance.

### Solid fossil fuels

Solid fossil fuels such as coal is a common source for syngas production.80 Gasification methods, operating conditions and raw material components of coal can influence the composition of the produced syngas. 81,82 The power efficiency of the coal-based SOFC system mainly depends on the fuel content and impurities in syngas. Basic coal gasification systems can be classified into three types: (i) moving bed (ii) fluidized bed and (iii) entrained bed. Steam and air are used to partially burn coal into syngas. The contaminants produced from the gasifier consist of COS, H<sub>2</sub>S, HCN, NH<sub>3</sub>, tars, phenol and particulates that need to be removed. Impurity removal/gas cleanup units such as cyclone for particulate removal, H<sub>2</sub>S scrubber, COS hydrolysis reactor and ammonia scrubber are employed. These units increase the complexity of BoP, leading to a higher cost and imbalance of the thermal efficiency in the overall SOFC system. Power cycles are introduced to improve the power system performance.83 The 500MW coal-fueled SOFC system with integrated gasification combined cycles (IGCC) was studied.84 This integrated power system targets to increase the overall efficiency with low emission. Regarding an environmental aspect, the coal gasification combined with carbon dioxide capturing technology for hydrogen production was studied using a ChemCAD package.85 However, it was indicated that using a coal fuel with the SOFC system requires a number of pretreatment and fuel processing units including carbon capture and storage (CCS) units in case of environmental concerns. Economic evaluation should be taken into account by comparing among price of coal raw materials, efficiency of system (product outputs) and total investment cost.

These solid fossil-derived fuels are still regarded as non-renewable and high pollution resources even all of them can be effective in application with SOFC system. However, the environmental aspect rises up renewable resources outstandingly as a clean fuel for the SOFC system.

#### **Biomass**

Biomass is a promising alternative energy source because it can be available from various agricultural materials. Typically, biomass is converted into a synthesis gas by high temperature gasification/pyrolysis and catalytic reforming, respectively. However, high thermal energy is required to devolatile biomass to gaseous product. A novel allothermal biomass steam gasification and a combined heat and power (CHP) integrated with SOFC system were investigated with an attempt to maximize/allocate heat utilization within the system. The results reported that 36% electrical efficiency and 14% thermal efficiency were obtained. For other alternatives, the aqueous phase reforming and supercritical water oxidation at medium

temperatures offers the promising choice for solid reforming process to get high yield of hydrogen without a large amount of heat requirement. Biomass fermentation is another interesting option, relying on the advancement of biochemical technologies to produce biofuels, i.e., bioethanol, biomethanol, biogas, bioglycerol and biodiesel. Performance analysis of the integrated SOFC system with three different renewable fuels (i.e., biogas, ethanol, and glycerol) was investigated. The results indicated that the SOFC system run on ethanol offered the highest electrical and thermal efficiencies of SOFC system. Considering the use of bioethanol, it is inappropriate to directly feed into the steam reformer because of its low ethanol concentration (5-12 wt.%). Excess water needs to be removed to obtain a suitable proportion of ethanol and water for ethanol steam reforming. Several methods such as distillation, pervaporation and hybrid pervaporation-vapor permeation were proposed to preconditioning bioethanol for use in the SOFC system.

## **SOFC** with gas turbine

Due to its high-temperature operation, SOFC generates a high-quality exhaust gas that can be used for preheating fuel and air before they are fed to the SOFC stack. This causes the energy efficiency of the system increase. A number of researchers have concentrated on a heat manangement of the SOFC system. In particular, the hybrid system of SOFC and gas turbine (GT) or steam turbine (ST) is received much attention. Regarding the integration of SOFC and GT, the exhaust gas from SOFC can be directly or indirectly fed to gas turbine. The SOFC-GT hybrid system can theoretically have an overall electrical efficiency of up to 70%. 93

### Development of SOFC-GT hybrid systems

The enhancement of SOFC systems with integration of GT is a promising technology for electricity power plants. At the beginning, the pressurized SOFC-GT hybrid was proposed by the National Fuel cell Research Center in Irvine, California. This system was designed and built by Siemens-Westinghouse Power Corporation (SWPC). The overall power of this system is 220 kW; the SOFC generates the power of 200 kW while the micro turbine generator produces 20 kW. After that, the SOFC hybrid system has been extensively received much attention. A number of research groups have focused on SOFC-GT hybrid systems in different issues. The National Energy Technology Laboratory (NETL) tested the pressurized SOFC integrated with two turbines based on Siemens Westinghouse technology to scale-up the power plant to 20 MW. Furthermore, the NETL takes part in the project of the Hybrid Power Generation Systems Division of General Electric. The aim of this project is to demonstrate the distributed power generation by development of SOFC using a thin film electrolyte technology fabricated by the tape calendaring method and thin-foil metallic interconnects, which is expected to be a low cost, high-performance, compact planar SOFC. In 1999, the U.S. Department of Energy (DOE) started the Solid-state energy conversion alliance (SECA) program devoted to develop the hybrid system of SOFC and gas turbine so as to achieve a high-effective and low-cost power system leading to a commercial level. Under this program, a number of industrial partners involved such as Cummins Power Generation, Accumetrics, Siemens Westinghouse, Fuel Cell Energy, General Electric and Delphi. Korea Institute of Energy Research<sup>94</sup> designed and constructed an atmospheric and pressurized 5 kW class SOFC power generation system with a pre-reformer for the fuel cell/gas turbine hybrid system. In the hybrid mode of operation at 3.5 atm, the SOFC stack combined with an LNG pre-reformer and a micro-gas turbine, produces 5.1 kW based on the fuel utilization of 33.2%. The results confirmed the success of their design and fabrication technologies for a pressurized anode-supported planar SOFC system combined with a micro-gas turbine.

Apart from interests from governmental and industrial sections, many academic research teams have also studied and developed SOFC-GT hybrid systems. The thermochemical power group at University of Genoa investigated the cycle layout and the part-load dynamics of the SOFC hybrid system. P5-98 A detailed dynamic model of the internal-reforming SOFC integrated with gas turbine was developed and its reliability was validated by comparing the model prediction with data obtained from the SOFC-GT system at the national fuel cell research center. Purthermore, the model of SOFC based on planar technology integrated with gas turbine was proposed by the research group at University of Lund. The 200 kW power plant of the pressurized SOFC-GT hybrid system by a combined cycle system with 75 kW was studied at Toyohashi University of Technology.

Presently, the research goal is to improve and implement the SOFC-GT hybrid system to an industrial level. The challenging issues involve the development of SOFC materials, the appropriate management of energy, the effective design of the SOFC system as well as the determination of optimal conditions for SOFC and GT operations.

#### SOFC-GT hybrid systems

A main principal of a hybrid system is that one system needs to meet the requirement of another system. For a SOFC-GT hybrid system, the exhaust heat of SOFC can be recovered for use in other heat-requiring units of the SOFC system via heat and power cogeneration. There are two configurations considered for the SOFC based system: Brayton (gas) regenerative cycle and Rankine (steam) cycle. The Rankine cycle is essentially a heat engine with a vapor power and is combined with the SOFC using a direct thermal coupling scheme. The commonly used working fluid is water and the system operates in the liquid–vapor mode. Thus, the Rankine cycle cannot be combined with SOFC using the direct thermal coupling scheme. Due to the use of a gas-based working fluid, the Brayton cycle is a favorable candidate for SOFC integration.<sup>2</sup>

Basic configuration

For the SOFC and Brayton cycle integrated system, two major system configurations are possible depending on the operating pressure of the SOFC, namely, a non-pressurized and pressurized hybrid cycles. Fig. 12 shows the non-pressurized SOFC-GT hybrid system. Air flowing out the compressor is heated by the fuel cell exhaust through a heat exchanger before being fed to the combustor of the gas turbine and the SOFC can be operated under atmospheric conditions. The system efficiency for this hybrid configuration is expected in a range of 50-60%. The advantage of this system is that a gas turbine operation does not depend directly on a solid oxide fuel cell and it is a simple cycle system. Moreover, it reduces the sealant requirement in the SOFC stack. Nevertheless, the heat exchanger has to be operated at very high temperatures and pressure differences, and consequently the requirement of high effective materials is the main problem of this atmospheric SOFC-GT hybrid system.

The pressurized SOFC-GT hybrid system involves the direct integration of a solid oxide fuel cell and a gas turbine system, as seen in Fig. 13. The combustion chamber of the gas turbine engine is replaced by the SOFC and the afterburner. The pressurized air from the compressor is fed into the SOFC. The exhaust gas from the SOFC goes to the afterburner and the resulting high-temperature and pressure exhaust gas enters the turbine. Compressed air is preheated by the turbine exhaust gas through the recuperative heat exchanger. In this case, the SOFC is operated at high pressure, which further improves its performance. Heat exchangers are installed after the turbine to further utilize the waste heat for preheating the streams entering the SOFC stack. This increases the thermal efficiency of the SOFC system as well.

In comparison with the SOFC operated under the atmosphere pressure, the pressurized SOFC-GT hybrid system can achieve a higher efficiency (up to 10%) and specific work values. This is because the ambient pressure SOFC system cannot be run when the gas turbine is operated at a high pressure ratio; the required turbine inlet temperature is too low. Nonetheless, the pressurized SOFC-GT hybrid system has some limitations. The operation of the SOFC has directly influence on a gas turbine. High interaction between SOFC and gas turbine leads to a difficulty in the system operation. The pressurized SOFC-GT hybrid system should be modified with the addition of an external combustor so as to simplify for a control system of the gas turbine as it will be independent of the solid oxide fuel cell operation.

Configuration of SOFC-GT hybrid system integrated with a heat recovery steam generator

A SOFC-GT hybrid system integrated with a heat recovery steam generator (HRSG) is another system design to improve its efficiency (Fig. 14). Due to its high quality heat source, the exit gas from a recuperative heat exchanger can be used for steam generation via the HRSG consisting of economizer and evaporator parts. Water is pressurized at the desired value

before it is vaporized by using the HRSG unit. It is found that the total exergy output of the system is increased because the second product, saturated steam, is produced without the requirement of more fuel supplied to the system. The steam generated by the HRSG is employed to drive a steam turbine cycle for additional power generation. As a result, the SOFC-GT hybrid system integrated with a steam turbine can achieve a higher system efficiency at off-design. Chan et al. Studied the integration of a solid oxide fuel cell, gas turbine and HRSG. The HRSG was applied to produce steam for a steam reforming of fuel. The results showed that the SOFC-GT hybrid system has the net electrical efficiency of higher than 60%. When the waste heat recovery for steam generation was considered, the system efficiency of 80% can be achieved.

Motahar et al. 114 presented a comparison of the conventional SOFC-GT hybrid system with the retrofitted SOFC system in which steam produced by the HRSG using a hot gas turbine exhaust gas is injected into a gas turbine. From the detailed exergy analysis, it was found that that the steam injection decreases the wasted exergy from the system and boosts the exergetic efficiency by 12.11%. Park et al. 115 examined two different SOFC configurations: a pressurized SOFC system and a non-pressurized SOFC system. The effect of steam injection on the recovered heat from the exhaust gas and the system performance was considered. The results showed that the pressurized system hardly takes advantage of the steam injection in terms of the system efficiency. On the other hand, the steam injection contributes to the efficiency improvement of the non-pressurized SOFC system in some design conditions. In particular, a higher pressure ratio provides a better chance of efficiency increase due to the steam injection.

#### Fuel processor combined with SOFC-GT hybrid system

Hydrogen is a major fuel for electricity generation in fuel cells; however, its uses are still facing with several issues such as its economical production, storage and distribution. In general, hydrogen can be derived from primary fuels such as natural gas, methanol, gasoline, and coal via a fuel processor. To date, natural gas is widely used to produce hydrogen for fuel cell applications. Although natural gas is a cost-effective feedstock, it is also a limited and nonrenewable resource. To date a number of studies have been conducts to explore the means to produce hydrogen from alternative renewable resources to support the future use of fuel cells. In particular, biomass, biogas, and bioethanol have been considered as attractive and potential feedstocks for SOFC systems.

The use of biomass for hydrogen production seems to be more suitable for supplying to SOFCs than other fuel cells because the SOFC has a higher tolerance towards contaminants in the hydrogen-rich gas. <sup>116-118</sup> In this case, a SOFC-based power plant involves gasification and cleaning processes to convert biomass to hydrogen fuel. There are several works investigating the performance of a combined biomass gasification and SOFC-GT hybrid plant. <sup>119-123</sup> As the design of gasification and gas cleaning processes has an

effect on the efficiency of the SOFC-GT power system, Toonssen et al. 124 studied the use of different gasification technologies (such as an atmospheric indirect steam gasification and a pressurized direct air gasification) and gas cleaning technologies (such as low-temperature and high-temperature gas cleaning processes) in the SOFC-GT hybrid system fuelled by biomass. Their results indicated that the SOFC system based on the pressurized direct air gasification and the high-temperature gas cleaning process shows the highest electrical exergy efficiency of 49.9%. Apart from biomass, the use of liquid fuels in SOFC-GT power plant is promising, especially in remote areas. 125 Santin et al. 125 studied the SOFC-GT hybrid system run on two liquid fuels: methanol and kerosene and showed that the methanol-fuelled SOFC hybrid system shows better performance from the thermodynamic and economic points of view.

Another design option of the SOFC hybrid system is based on a fuel reforming technology. In general, hydrocarbon fuels can be internally reformed into a hydrogen-rich gas within SOFC stack which is known as an internal reforming SOFC because the operating temperature of the SOFC is in the same range as that of the reforming reactions. However, this would cause a carbon formation leading to the degradation of anode catalyst and thus loss of fuel cell performance. To cope with this difficulty, the application of an external reforming process to produce hydrogen for fuel cells is a potentially better option. Since the product gas from the reformer can be further purified to achieve a higher purity of hydrogen, the SOFC performance should be enhanced. Fig. 15 shows a typical diagram of a combined reforming process and SOFC-GT system. Any gaseous or liquid fuels can be fed to the reformer to convert into the synthesis gas with high hydrogen content. Cocco and Tola<sup>126</sup> investigated the SOFC-MGT plants fuelled by methanol and dimethyl ether (DME). The external reformer was employed to convert methanol and DME to a synthesis gas. It was found that the reforming temperature of methanol and DME (200-350 °C) is lower than that of natural gas (700-900 °C) and the SOFC system efficiency can be enhanced by improving the heat recovery of the exhaust gas. The optimum operating temperature of the methanol reforming process is approximately 240 °C and the system efficiencies is about 67-68%, whereas in the case of using DME as a fuel for the SOFC system, the optimal temperature is 280 °C and the efficiency is 65%. Yang et al. 127 studied the SOFC-GT system using internal and external reforming process. Effect of SOFC temperature and gas turbine inlet temperature on the system performance was analyzed. The SOFC system with internal reforming operation provides better efficiency and power capacity for all design conditions.

### Combined cooling, heating and power generation for SOFC system

In general, SOFC is practically operated at a moderate fuel utilization and thus the outlet gas from a cell stack contains valuable residual fuels. Furthermore, due to the high temperature operation (up to 1000 °C) and the

irreversible electrochemical process of SOFC, a waste heat is also produced in the fuel cell power section. 128 As a result, the utilization of the high-quality heat and the remaining fuel existing SOFC can further improve the efficiency of the SOFC system. Following this approach, the waste heat is utilized as a heat source for the system through a series of recuperative heat exchangers. The cogeneration of heat with electricity (a combined heat and power system) can increasingly enhance the system thermal efficiency. In addition, the waste heat can be employed to produce cooling water for air conditioning via an absorption chiller in which a refrigerant is another working fluid cycle. combined cooling, heating and power (CCHP) generation or tri-generation becomes an alternative method for energy management in the SOFC power system that is potential to solve the energy-related problems such as energy security, energy shortage, emission control, economy and conservation of energy. This method is related to the production of cooling, heating and power simultaneously from a single fuel source with the principle of the energy cascade utilization. 129, 130

For operation of the absorption chiller, the refrigerant is evaporated at low pressure. Then, it is absorbed by an absorbent and becomes a solution at high pressure. Two widely-used refrigerants (or absorbents) are lithium bromide and ammonia aqueous solutions. The selection of the refrigerant depends on the system application. The lithium bromide is suitable for the air conditioning system that requires the temperature above 0 °C, whereas the ammonia solution is applied to the system with a lower cooling temperature (below 0 °C)<sup>2</sup>. In general, the absorption chiller requires the external heat for separating the refrigerant from the aqueous solution. Therefore, the combined system of SOFC and absorption chiller can lead to an efficient energy usage by using an exhaust gas from the SOFC system to drive the absorption chiller. The conventional integrated process of SOFC and absorption chiller is illustrated in Fig. 16.131 The heat from exhaust gas is used to generate a cooling water via a refrigeration cycle using the adsorption chiller. Additionally, a portion of the exhaust gas can be applied for a hot water production. The amount of the produced cooling water and hot water can be controlled with adjusting a ratio of the exhaust gas. Yu et al. 131 studied an integrated trigeneration system incorporating an internal reforming SOFC, a heat recovery steam generator and a double-effect water-lithium bromide absorption chiller. The simulation results showed that the total efficiency of the studied trigeneration system of higher than 84% can be achieved. The increased fuel flow results in an increase in the cooling, heating and electrical power output.

The new combined cooling, heating and power system consisting of the SOFC, gas turbine system and ammonia-water thermodynamic cycle, was proposed by Ma et al.<sup>132</sup> It was found that although the SOFC-GT hybrid system shows a good performance, the high-quality exhaust gas still remains. To improve the overall energy conversion efficiency, the waste heat from the exhaust gas of the gas turbine was recovered by using the ammonia-water cycle. The thermal efficiency of the proposed CCHP system is 80%. The operating parameters of the absorption chiller such as ammonia concentration

and operating pressure, affect the CCHP system in terms of the electrical efficiency as well.

#### Conclusion

Integrated SOFC systems for electrical power generation are reviewed with particular focus on integration of SOFC with hydrogen production process and gas turbine system. Heat generated from the SOFC can be efficiently utilized for hydrogen production whose complexity of the heat exchanger network depends significantly on type of fuel and fuel processing technology. SOFC-GT hybrid systems are promising integration strategies for improving the overall electrical efficiency by utilizing waste heat for further generation of electrical power. Depending on applications, the SOFC system can be integrated with other units such as steam generator and absorption chiller for combined cooling, heating and electrical power generation.

### Acknowledgement

The support from Thailand Research Fund is gratefully acknowledged.

#### References

- 1. Mekhilef S, Saidur R, Safari A. Comparative study of different fuel cell technologies Renewable and Sustainable Energy Reviews 2012, 16:981–989.
- 2. Zhang X, Chan SH, Li G, Ho HK, Li J, Feng Z. A review of integration strategies for solid oxide fuel cells Journal of Power Sources 2010, 195:685–702.
- 3. Hemmes K, Barbieri G, Lee YM, Drioli E, De Wit JHW. Process intensification and fuel cells using a Multi-Source Multi-Product Approach Chemical Engineering and Processing: Process Intensification 2012, 51:88–108.
- 4. Sun C, Hui R, Roller J. Cathode materials for solid oxide fuel cells: a review Journal of Solid State Electrochemistry 2010, 14:1125-1144.
- 5. Liu M, Lynch ME, Blinn K, Alamgir FM, Choi YM. Rational SOFC material design: new advances and tools Materials today 2011, 14:534-546.
- 6. Brett DJL, Atkinson A, Brandon NP, Skinner SJ. Intermediate temperature solid oxide fuel cells Chemical Society Reviews 2008, 37:1568-1578.
- 7. EG&G Technical Services, Parsons Inc. Fuel Cell Handbook, 7<sup>th</sup> ed., US Department of Energy, Office of fossil Energy, Federal Energy Technology Center, Morgantown, 2004, 427.
- 8. Hohmann EC. Optimum Networks for Heat Exchange. PhD Thesis, University of Southern California, Los Angeles, 1971.
- 9. Linnhoff B, Flower JR. Synthesis of heat exchanger networks: I. Systematic generation of energy optimal networks AIChE Journal 1978, 24(4):633-642.
- 10. Godat J, Marechal F. Optimization of a fuel cell system using process integration techniques Journal of Power Sources 2003, 118: 411-423.

- 11. Jamsak W, Assabumrungrat S, Douglas PL, Croiset E, Laosiripojana N, Suwanwarangkul R, Charojrochkul S. Thermodynamic assessment of solid oxide fuel cell system integrated with bioethanol purification unit Journal of Power Sources 2007, 174:191-198.
- 12. Linnhoff B, Townsend DW, Boland D, Hewitt GF, Thomas BEA, Guy AR, Marsland RH. A User Guide on Process Integration for the Efficient Use of Energy. IChemE, Rugby, 1994, 247.
- 13. Kalitventzeff B, Marechal F, Closon H. Better solutions for process sustainability through better insight in process energy integration. Applied Thermal Engineering 2001, 21: 1349-1368.
- 14. Townsend DW, Linnhoff B. Heat and power networks in process design. I. Criteria for placement of heat engines and heat pumps in process networks AIChE Journal 1983a, 29:742-747.
- 15. Townsend DW, Linnhoff B. Heat and power networks in process design. II. Design procedure for equipment selection and process matching AIChE Journal 1983b, 29:747-754.
- 16. El-Halwagi MM. Process systems engineering Volume 7: Process integration. 1<sup>st</sup> ed., Academic Press, San Diego, 2006, 268-269.
- 17. El-Halwagi MM. Pollution prevention through process integration: systematic design tools. Academic Press, San Diego, 1997, 334.
- 18. El-Halwagi MM, Manousiouthakis V. Design and analysis of multicomponent mass-exchange networks. In: AIChE Annual Meeting, San Francisco; 1989.
- 19. Hartono B, Heidebrecht P, Sundmacher K. A mass integration concept for high temperature fuel cell plants International Journal of Hydrogen Energy 2011, 36:7240-7250.
- 20. Fellows R. A novel configuration for direct internal reforming stacks Journal of Power Sources 1998, 71:281-287.
- 21. Lisbona P, Corradetti A, Bove R, Lunghi P. Analysis of a solid oxide fuel cell system for combined heat and power applications under non-nominal conditions Electrochimica Acta 2007, 53:1920-1930.
- 22. Dunn RF, Bush GE. Using process integration technology for CLEANER production Journal of Cleaner Production 2001, 9:1-23.
- 23. Kjelstrup S, Sauar E, Hansen EM, Lien KM, Hafskjold B. Analysis of entropy production rates for design of distillation columns Industrial & Engineering Chemistry Research 1995, 34: 3001.
- 24. Douvartzides SL, Couteliens F, Tsiakaras P. Exergy analysis of a solid oxide fuel cell power plant fed by either ethanol or methane Journal of Power Sources 2004, 131:224-230.
- 25. Chan SH, Low CF, Ding OL. Energy and exergy analysis of simple solid oxide fuel cell power systems Journal of Power Sources 2002, 103:188-200.
- 26. Kjelstrup S, Bedeaux D, Johannessen E. Elements of Irreversible Thermodynamics for Engineers. Tapir Academic Press, Trondheim, 2006, 135.
- 27. Sauar E, Kjelstrup S, Lien KM. Equipartition of Forces: A new principle for process design and optimization Industrial & Engineering Chemistry Research 1996, 35:4147.

- 28. Johannessen E, Kjelstrup S. Minimum entropy production in plug flow reactors: An optimal control problem solved for SO<sub>2</sub> oxidation Energy 2004, 29:2403.
- 29. Van der Ham LV, Gross J, Verkooilen A, Kjelstrup S. Efficient Conversion of Thermal Energy into Hydrogen: Comparing two methods to Reduce Exergy Losses in a Sulfuric Acid Decomposition Reactor Industrial & Engineering Chemistry Research 2009, 48: 8500-8507.
- 30. Boukis N, Diem V, Habicht W, Dinjus E. Methanol Reforming in Supercritical Water Industrial & Engineering Chemistry Research 2003, 42:728-735.
- 31. Byrd AJ, Pant KK, Gupta RB. Hydrogen Production from Glucose Using Ru/Al<sub>2</sub>O<sub>3</sub> Catalyst in Supercritical Water Industrial & Engineering Chemistry Research 2007, 46:3574-3579.
- 32. Shah N, Panjala D, Huffman GP. Hydrogen Production by Catalytic Decomposition of Methane Energy & Fuels 2001, 15:1528-1534.
- 33. Arnold C. Process for Production of Carbon Monoxide and Hydrogen. Patent specification 636,206, The Patent Office, London, UK, 1950.
- 34. Moghtaderi B. Hydrogen enrichment of fuels using a novel miniaturized chemical looping steam reformer Chemical Engineering Research and Design 2012, 90:19-25.
- 35. Ortiz M, Abad A, de Diego LF, Garcia-Labiano F, Gayan P. Optimization of hydrogen production by Chemical-Looping auto-thermal Reforming working with Ni-based oxygen-carriers International Journal of Hydrogen Energy 2011, 36:9663-9672.
- 36. Go KS, Son SR, Kim SD, Kang KS, Park CS. Hydrogen production from two-step steam methane reforming in a fluidized bed reactor International Journal of Hydrogen Energy 2009, 34:1301-1309.
- 37. Abad A, Adanez J, Garcia-Labiano F, de Diego LF, Gayan P, Celaya J. Mapping of the range of operational conditions for Cu-, Fe-, and Ni-based oxygen carriers in chemical-looping combustion Chemical Engineering Science 2007, 62:533-549.
- 38. Cormos C. Hydrogen production from fossil fuels with carbon capture and storage based on chemical looping systems International Journal of Hydrogen Energy 2011, 36:5960-5971.
- 39. Messerschmitt A. Process for producing hydrogen. US patent 971,206. 1910.
- 40. Lane H. Process for the production of hydrogen. US patent 1,078,686. 1913.
- 41. Lee TS, Chung JN, Chen YC. Design and optimization of a combined fuel reforming and solid oxide fuel cell system with anode off-gas recycling Energy Conversion and Management 2011, 52:3214-3226.
- 42. van den Oosterkamp PF. Critical issues in heat transfer for fuel cell systems Energy Conversion and Management 2006, 47:3552-3561.
- 43. Qi A, Peppley B, Karan K. Integrated fuel processors for fuel cell application: A review Fuel Processing Technology 2007, 88:3-22.
- 44. Samms SR, Savinell RF. Kinetics of methanol-steam reformation in an internal reforming fuel cell Journal of Power Sources 2002, 112:13.

- 45. Fasano BV, Prettyman DM, US6051329A. 2000 April 18.
- 46. Hirschenhofer JH, Stauffer DB, Engleman RR, Klett MG. Fuel Cell Handbook, 4<sup>th</sup> ed., US Department of Energy, Office of fossil Energy, Federal Energy Technology Center, Morgantown, 1998, 268.
- 47. Gardner FJ, Day MJ, Brandon NP, Pashley MN, Cassidy M. SOFC technology development at Rolls-Royce Journal of Power Sources 2000, 86:122-129.
- 48. Pramuanjaroenkij A, Kakac S, Zhou XY. Mathematical analysis of planar solid oxide fuel cells International Journal of Hydrogen Energy 2008, 33:2547-2565.
- 49. EG&G Technical Services, Parsons Inc. Fuel Cell Handbook, 5<sup>th</sup> ed., US Department of Energy, Office of fossil Energy, Federal Energy Technology Center, Morgantown, 2000, 691.
- 50. Selimovic A, Palsson J. Networked solid oxide fuel cell stacks combined with a gas turbine cycle Journal of Power Sources 2002, 106:76-82.
- 51. Obara S. Power generation efficiency of an SOFC-PEFC combined system with time shift utilization of SOFC exhaust heat International Journal of Hydrogen Energy 2010, 35: 757-767.
- 52. Xuan J, Leung MKH, Leung DYC, Ni M. A review of biomass-derived fuel processors for fuel cell systems Renewable and Sustainable Energy Reviews 2009, 13:1301-1313.
- 53. Gallucci F, Paturzo L, Basile A. A simulation study of the steam reforming of methane in a dense tubular membrane reactor International Journal of Hydrogen Energy 2004, 29: 611-617.
- 54. Nunes SP, Peinemann KV. Membrane Technology in the Chemical Industry. Wiley-VCH Verlag GmbH, Geesthacht, 2001, 319.
- 55. Paturzo L, Basile A, Drioli E. High temperature membrane reactors and integrated membrane operations Reviews in Chemical Engineering 2002, 18:511-551.
- 56. Wieland S, Melin T, Lamm A. Membrane reactors for hydrogen production Chemical Engineering Science 2002, 57:1571-1576.
- 57. Tosti S, Basile A, Bettinali L, Borgognoni F, Chiaravalloti F, Gallucci F. Long-term tests of Pd-Ag thin wall permeator tube Journal of Membrane Science 2006, 284:393-397.
- 58. Piroonlerkgul P, Kiatkittipong W, Arpornwichanop A, Soottitantawat A, Wiyaratn W, Laosiripojana N, Adesina AA, Assabumrungrat S. Integration of solid oxide fuel cell and palladium membrane reactor: Technical and economic analysis International Journal of Hydrogen Energy 2009, 34:3894-3907.
- 59. Isogawa R, Nobata Y, Kondo M, et al., US6390030B1. 2002 May 21.
- 60. Loffler DG, Taylor K, Mason D. A light hydrocarbon fuel processor producing high-purity hydrogen Journal of Power Sources 2003, 117:84-91.
- 61. Lesieur RR, Corrigan TJ, US6203587B1. 2001 March 20.
- 62. Berlowitz PJ, Hershkowitz F. Fuel Cell Seminar, Mira Digital Publishing, San Antonio, 2004.
- 63. Ahmed S, Ahluwalia RK, Lee SH, et al., Fuel Cell Seminar, Mira Digital Publishing, San Antonio, 2004.

- 64. Bentley JM, Mitchell WL, Clawson LG, Cross JC, US6783742B2, 2004 August 31.
- 65. "Overview of 11 MW Fuel Cell Power Plant", Non-published information from Tokyo Electric Power Company, September 1989.
- 66. Wilkinson DP, Steck AE. General Progress in the Research of Solid Polymer Fuel Cell Technology at Ballard. In: Proceedings of the Second International Symposium on New Materials for Fuel Cells and Modern Battery Systems, Montreal; 1997.
- 67. Twigg MV. Catalyst Handbook. Wolfe Publishing Ltd., Frome, 1989, 608.
- 68. Rampe T, Heinzel A, Vogel B. Hydrogen generation from biogenic and fossil fuels by autothermal reforming Journal of Power Sources 2000, 86:536-541.
- 69. Aartun I, Gjervan T, Venvik H, Gorke O, Pfeifer P, Fathi M, Holmen A, Schubert K. Catalytic conversion of propane to hydrogen in microstructured reactors Chemical Engineering Journal 2004, 101:93-99.
- 70. Ahmed K, Gamman J, Foger K. Demonstration of LPG-fueled solid oxide fuel cell systems Solid State Ionics 2002, 152-153:485-492.
- 71. Villegas L, Guilhaume N, Provendier H, Daniel C, Masset F, Mirodatos C. A combined thermodynamic/experimental study for the optimization of hydrogen production by catalytic reforming of isooctane Applied Catalysis A: General 2005, 281:75-83.
- 72. Chen I, Shiue DW. Resistivity to sulfur poisoning of nickel-alumina catalysts Industrial & Engineering Chemistry Research 1988, 27:1391-1396.
- 73. Liu DJ, Krumpelt M. Activity and structure of perovskites as diesel-reforming catalysts for solid oxide fuel cell International Journal of Applied Ceramic Technology 2005, 2:301-307.
- 74. Ferrandon M, Mawdsley J, Krause T. Effect of temperature, steam-to-carbon ratio, and alkali metal additives on improving the sulfur tolerance of a Rh/La-Al<sub>2</sub>O<sub>3</sub> catalyst Applied Catalysis A: General 2008, 342:67-77.
- 75. Flytzani-Stephanopoulos M, Voecks GE. Autothermal reforming of aliphatic and aromatic hydrocarbon liquids International Journal of Hydrogen Energy 1983, 8:539-548.
- 76. Palm C, Cremer P, Peters R, Stolten D. Small-scale testing of a precious metal catalyst in the autothermal reforming of various hydrocarbon feeds Journal of Power Sources 2002, 106:231-237.
- 77. Krumpelt M, Krause TR, Carter JD, Kopasz JP, Ahmed S. Fuel processing for fuel cell systems in transportation and portable power applications Catalyst Today 2002, 77:3-16.
- 78. Hennings U, Reimert R. Noble metal catalysts supported on gadolinium doped ceria used for natural gas reforming in fuel cell applications Applied Catalysis B: Environmental 2007, 70:498-508.
- 79. Yoon S, Kang I, Bae J. Suppression of ethylene-induced carbon deposition in diesel autothermal reforming International of Journal of Hydrogen Energy 2009, 34:1844-1851.
- 80. Yamashita K, Barreto L. Energyplexes for the 21<sup>st</sup> century: coal gasification for co-producing hydrogen, electricity and liquid fuels Energy 2005, 30:2453-2473.

- 81. Liu K, Chunshan S, Subramani V. Hydrogen and syngas production and purification Technologies. John Wiley & Sons, Inc., Hoboken, 2010, 545.
- 82. Souza-Santos M. Solid fuels combustion and gasification: modeling, simulation and equipment operation. Taylor & Francis Group, Boca Raton, 2010, 486.
- 83. Horlock JH. Combined power plants: past, present and future Transactions of ASME Journal of Engineering Gas Turbines and Power 1995, 117:608-616.
- 84. George TJ, Lyons KD, James R. Multistaged Oxide Fuel Cell Power Plant Concept, 1998.
- 85. Cormos C, Starr F, Tzimas E, Peteves S. Innovative concepts for hydrogen production processes based on coal gasification with CO<sub>2</sub> capture International Journal of Hydrogen Energy 2008, 33:1286-1294.
- 86. Evans R, Czernik S, Magrini-Bair K, DOE Hydrogen Program, FY2004 Progress Report, 65.
- 87. Panopoulos KD, Fryda LE, Karl J, Poulou S, Kakaras E. High temperature solid oxide fuel cell integrated with novel allothermal biomass gasification Part I: Modeling and feasibility study Journal of Power Sources 2006, 159:570-585.
- 88. Huber GW, Shabaker JW, Dumesic JA. Raney Ni-Sn Catalyst for Hydrogen from Biomass-Derived Hydrocarbons Science 2003, 300:2075-2077.
- 89. Saebea D, Authayanun S, Patcharavorachot Y, Paengjuntuek W, Arpornwichanop A. Performance analysis of SOFC systems integrated with steam reforming of different renewable fuels. In: International Conference on Renewable Energies and Power Quality (ICREPQ'12), Santiago de Compostela, Spain; 2012.
- 90. Huang HJ, Ramaswamy S, Tschirner UW, Ramarao BV. A review of separation technologies in current and future biorefineries Separation and Purification Technology 2008, 62:1-21.
- 91. Choedkiatsakul I, Charojrochkul S, Kiatkittipong W, Wiyaratn W, Soottitantawat A, Arpornwichanop A, Laosiripojana N, Assabumrungrat S. Performance improvement of bioethanol-fuelled solid oxide fuel cell system by using pervaporation International Journal of Hydrogen Energy 2011, 36:5067-5075.
- 92. Sukwattanajaroon V, Charojrochkul S, Kiatkittipong W, Arpornwichanop A, Assabumrungrat S. Performance of membrane-assisted solid oxide fuel cell system fuelled by bioethanol Engineering Journal 2011, 15:53-66.
- 93. Kandepu R, Imsland L, Foss BA, Stiller C, Thorud B, Bolland O. Modeling and control of a SOFC-GT-based autonomous power system Energy 2007, 32:406-417.
- 94. Lim TH, Song RH, Shin DR, Yang DR, Jung J, Jung H, Vinke IC, Yang SS. Operating characteristics of a 5 kW class anode-supported planar SOFC stack for a fuel cell/gas turbine hybrid system International Journal of Hydrogen Energy 2007, 33:1076-1083.

- 95. Costamagna P, Magistri L, Massardo AF. Design and part-load performance of a hybrid system based on a solid oxide fuel cell reactor and a micro gas turbine Journal of Power Sources 2001, 96:352-368.
- 96. Franzoni A, Magistri L, Traverso A, Massardo AF. Thermoeconomic analysis of pressurized hybrid SOFC systems with CO<sub>2</sub> separation Energy 2008, 33:311-320.
- 97. Ferrari ML, Traverso A, Magistri L, Massaro AF. Influence of the anodic recirculation transient behavior on the SOFC hybrid system performance Journal of Power Sources 2005, 149:22-32.
- 98. Ferrari ML, Sorce A, Pascenti M, Massardo AF. Recuperator dynamic performance: Experimental investigation with a microgas turbine test rig Applied Energy 2011, 88:5090-5096.
- 99. Robert R, Brouwer J, Jabbari F, Junker T, Ghezel-Ayagh H. Control design of an atmospheric solid oxide fuel cell/gas turbine hybrid system: Variable versus fixed speed gas turbine operation Journal of Power Sources 2006, 161:484-491.
- 100. Kaneko T, Brouwer J, Samuelsen GS. Power and temperature control of fluctuating biomass gas fueled solid oxide fuel cell and micro gas turbine hybrid system Journal of Power Sources 2006, 160: 316-325.
- 101. Mueller F, Gaynor R, Auld AE, Brouwer J. Synergistic integration of a gas turbine and solid oxide fuel cell for improved transient capability Journal of Power Sources 2008, 176:229-239.
- 102. Mueller F, Jabbari F, Brouwer J. On the intrinsic transient capability and limitations of solid oxide fuel cell systems Journal of Power Sources 2009, 187:452–460.
- 103. Palsson J, Selimovic A, Sjunnesson L. Combined solid oxide fuel cell and gas turbine systems for efficient power and heat generation Journal of Power Sources 2000, 86: 442-448.
- 104. Selimovic A, Palsson J. Networked solid oxide fuel cell stacks combined with a gas turbine cycle Journal of Power Sources 2002, 106:76-82.
- 105. Moller BF, Arriagada J, Assadi M, Potts I. Optimisation of an SOFC-GT system with CO2-capture Journal of Power Sources 2004, 131:320-326.
- 106. Azra S, Kemm M, Torisson T, Assadi M. Steady state and transient thermal stress analysis in planar solid oxide fuel cells Journal of Power Sources 2005, 145:463-469.
- 107. Inui Y, Matsumae T, Koga H, Nishiura K. High performance SOFC-GT combined power generation system with CO<sub>2</sub> recovery by oxygen combustion method Energy Conversion and Management 2005, 46:1837-1847.
- 108. Zhao Y, Sadhukhan J, Lanzini A, Brandon N, Shah N. Optimal integration strategies for a syngas fuelled SOFC and gas turbine hybrid Journal of Power Sources 2011, 196:9516–9527.
- 109. Traverso A, Magistri L, Massardo AF, Turbomachinery for the air management and energy recovery in fuel cell gas turbine hybrid system Energy 2010, 35:764-777.
- 110. Park SK, Kim TS. Comparison between pressurized design and ambient pressure design of hybrid solid oxide fuel cell–gas turbine systems Journal of Power Sources 2006, 163:490–499.

- 111. Akkaya AV, Sahin B, Erdern HH. An analysis of SOFC/GT CHP system based on exergetic performance criteria International Journal of hydrogen energy 2008, 33: 2566-2577.
- 112. Arsalis A. Thermoeconomic modeling and parametric study of hybrid SOFC–gas turbine–steam turbine power plants ranging from 1.5 to 10 MWe Journal of Power Sources 2008, 181:313–326.
- 113. Chan SH, Ho HK, Tain Y. Multi-level modeling of SOFC-gas turbine hybrid system International Journal of Hydrogen Energy 2003, 28:889 900.
- 114. Motahar S, Alemrajabi AA. Exergy based performance analysis of a solid oxide fuel cell and steam injected gas turbine hybrid power system International Journal of hydrogen energy 2009, 34:2396-2407.
- 115. Park SK, Kim TS, Sohn JL. Influence of steam injection through exhaust heat recovery on the design performance of solid oxide fuel cell gas turbine hybrid systems Journal of Mechanical Science and Technology 2009, 23:550-558.
- 116. Omosun AO, Bauen A, Brandon NP, Adjiman CS, Hart D. Modelling system efficiencies and costs of two biomass-fuelled SOFC systems Journal of Power Sources 2004, 131:96-106.
- 117. Singh D, Hernandez-Pacheco E, Hutton PN, Patel N, Mann MD. Carbon deposition in an SOFC fueled by tar-laden biomass gas: a thermodynamic analysis Journal of Power Sources 2005, 142:194-199.
- 118. Athanasiou C, Coutelieris F, Vakouftsi E, Skoulou V, Antonakou E, Marnellos G, Zabaniotou A. From biomass to electricity through integrated gasification/SOFC system-optimization and energy balance International Journal of Hydrogen Energy 2007, 32:337-342.
- 119. Aravind PV, Woudstra T, Woudstra N, Spliethoff H. Thermodynamic evaluation of small-scale systems with biomass gasifiers, solid oxide fuel cells with Ni/GDC anodes and gas turbines Journal of Power source 2009, 190:461-475.
- 120. Abuadala A, Dincer I. Exergoeconomic analysis of a hybrid system based on steam biomass gasification products for hydrogen production International Journal of Hydrogen Energy 2011, 36:12780-12793.
- 121. Merida W, Maness PC, Brown RC, Levin DB. Enhanced hydrogen production fromindirectly heated, gasified biomass, and removal of carbon gas emissions using a novel biological gas reformer International Journal of Hydrogen Energy 2004, 29:283-290.
- 122. Fryda L, Panopoulos KD, Kakara E. Integrated CHP with autothermal biomass gasification and SOFC–MGT Energy Conversion and Management 2008, 49:281–290.
- 123. Sucipta M, Kimijima S, Suzuki K. Performance analysis of the SOFC–MGT hybrid system with gasified biomass fuel Journal of Power Sources 2007, 174:124-135.
- 124. Toonssen R, Sollai S, Aravind PV, Woudstra N, Verkooijen AHM. Alternative system designs of biomass gasification SOFC-GT hybrid systems International Journal of Hydrogen Energy 2011, 35:10414-10425.
- 125. Santin M, Traverso A, Magistri L. Liquid fuel utilization in SOFC hybrid systems Applied Energy 2009, 86:2204–2212.

- 126. Cocco D, Tola V. Externally reformed solid oxide fuel cell-micro-gas turbine (SOFC-MGT) hybrid systems fueled by methanol and di-methyl-ether (DME) Energy 2009, 34:2124–2130.
- 127. Yang WJ, Park SK, Kim TS, Kim JH, Sohn JL, Ro ST. Design performance analysis of pressurized solid oxide fuel cell/gas turbine hybrid systems considering temperature constraints Journal of Power Sources 2006, 160:462–473.
- 128. Zink F, Lu Y, Schaefer L. A solid oxide fuel cell system for buildings Energy Conversion and Management 2007, 48:809-818.
- 129. Wu DW, Wang RZ. Combined cooling, heating and power: A review Progress in Energy and Combustion Science 2006, 32:459–495.
- 130. Yu Z, Han J, Cao X. Investigation on performance of an integrated solid oxide fuel cell and absorption chiller tri-generation system International Journal of Hydrogen energy 2011, 36:1256-12573.
- 131. Yu Z, Han J, Cao X, Chen W, Zhang B. Analysis of total energy system based on solid oxide fuel cell for combined cooling and power applications International Journal of Hydrogen Energy 2010, 35:2703-2707.
- 132. Ma S, Wang J, Yan Z, Dai Y, Lu B. Thermodynamic analysis of a new combined cooling, heat and power system driven by solid oxide fuel cell based on ammonia—water mixture Journal of Power Sources 2011, 196:8463-8471.

### Figure captions

- Fig. 1. The temperature-enthalpy diagram with pinch point dividing by heat source and heat sink region.
- Fig. 2. HEN design options diagram of the SOFC system integrated with distillation column (modified from Reference 11, p. 195).
- Fig. 3. Placement of heat engine below the pinch point (modified from Reference 16, p. 269).
- Fig. 4. Placement of heat engine above the pinch point (modified from Reference 16, p. 268).
- Fig. 5. Schematic diagram of the mass-integrated high temperature fuel cell plant (modified from Reference 19, p. 7241).
- Fig. 6. Several types of Chemical-looping reforming (modified from Reference 34, p.20).
- Fig. 7. Basic process flow diagram in comparison with PEMFC system and SOFC system (modified from Reference 42, p.3555).
- Fig. 8. Basic concept of fuel cell stacks arrangement with fuel flow configurations: a) single and b) two stage stacks (modified from Reference 50, p. 2).
- Fig. 9. Networked SOFC/GT system with a) both reactant streams in series b) only fuel stream in series and parallel air streams (modified from Reference 50, p. 5-6).
- Fig. 10. Integrated SOFC-PEFC power system (modified from Reference 51, p. 758).
- Fig. 11. The SOFC system integrated with palladium membrane reactor (modified from Reference 58, p. 3897).
- Fig. 12. Indirect integrated system of a solid oxide fuel cell and a gas turbine.
- Fig. 13. Direct integrated system of a solid oxide fuel cell and a gas turbine.
- Fig. 14. A pressurized SOFC-GT hybrid system integrated with HRSG.
- Fig. 15. A conventional SOFC-GT system combined with a fuel processor.
- Fig. 16. A SOFC and adsorption chiller combined system.

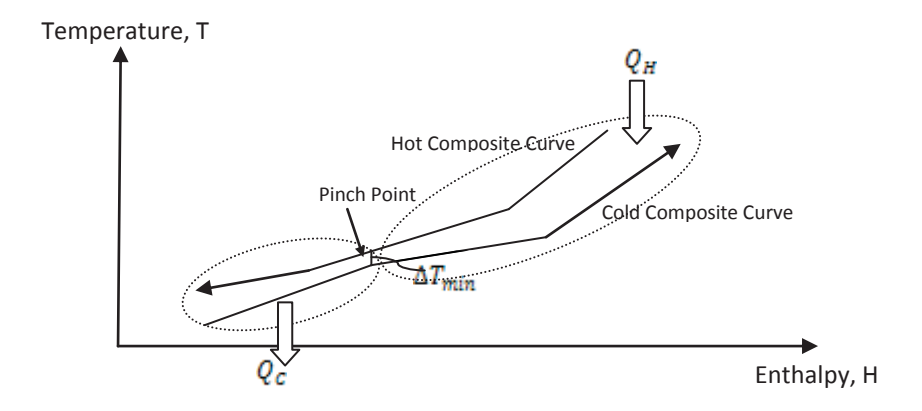


Fig. 1

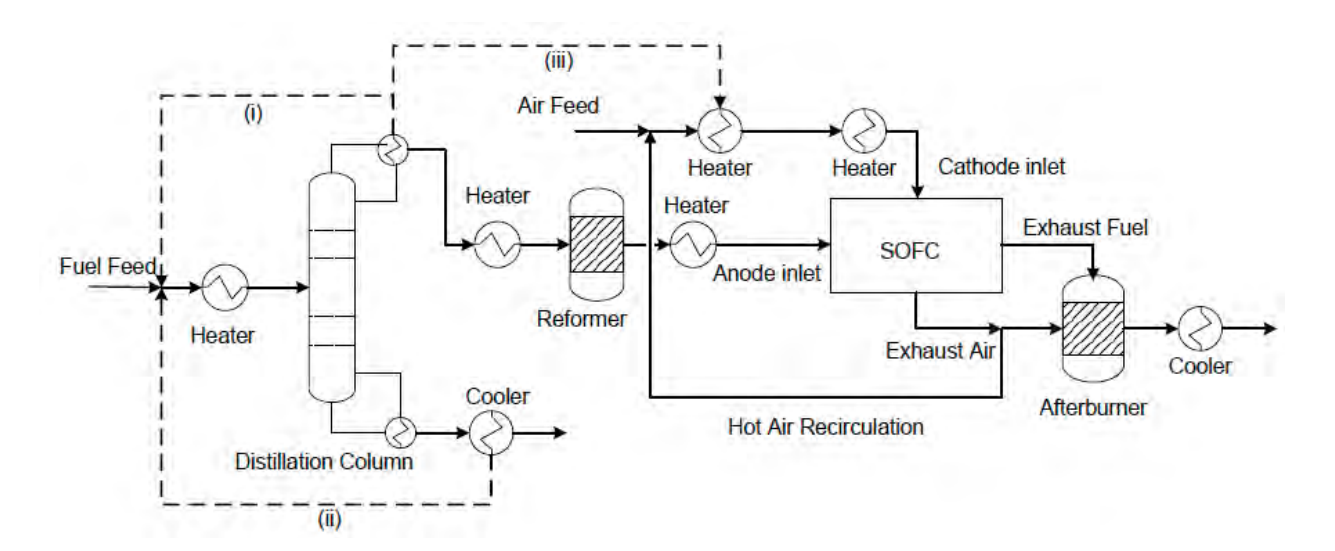


Fig. 2

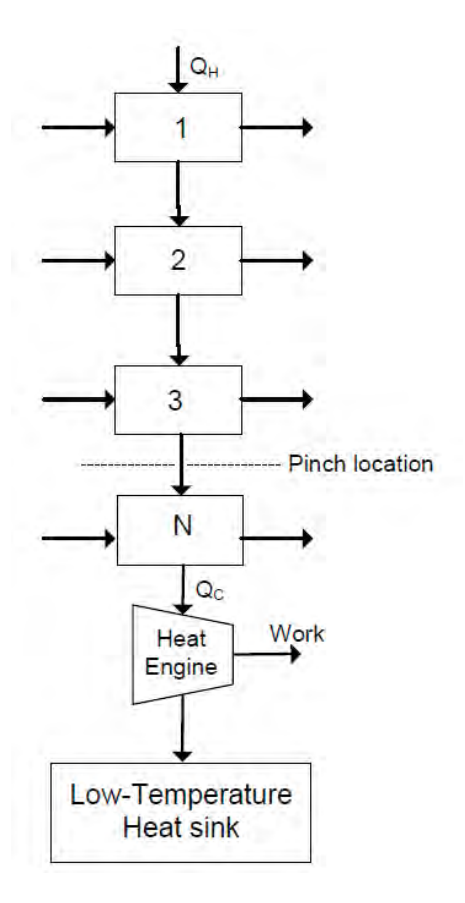


Fig. 3

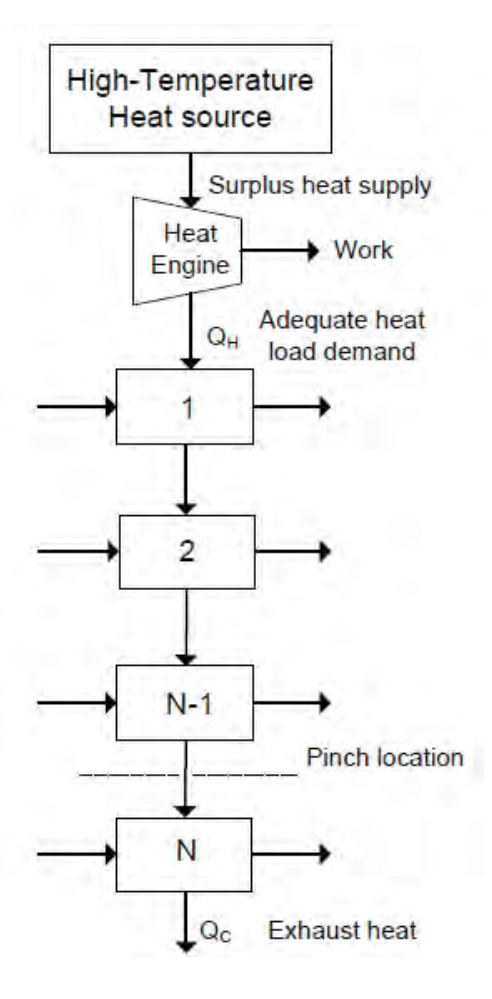


Fig. 4

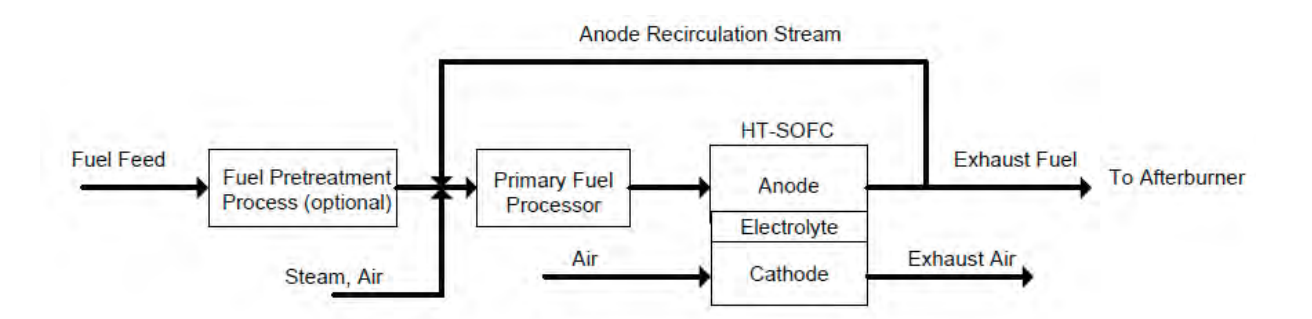


Fig. 5

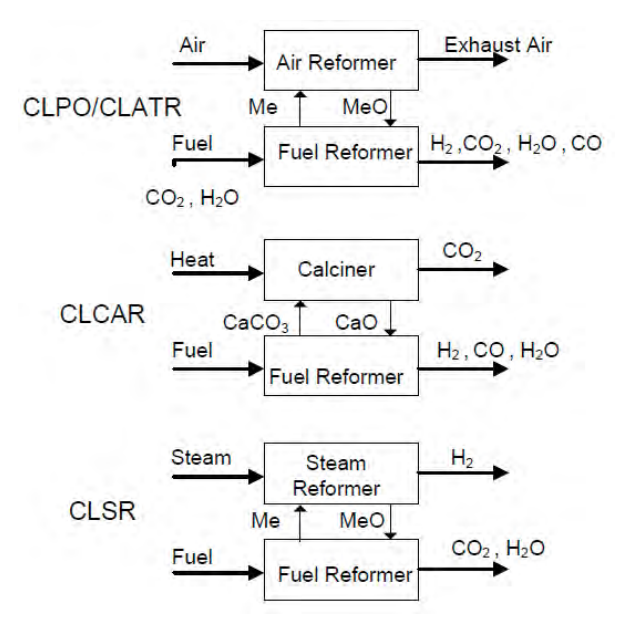


Fig. 6

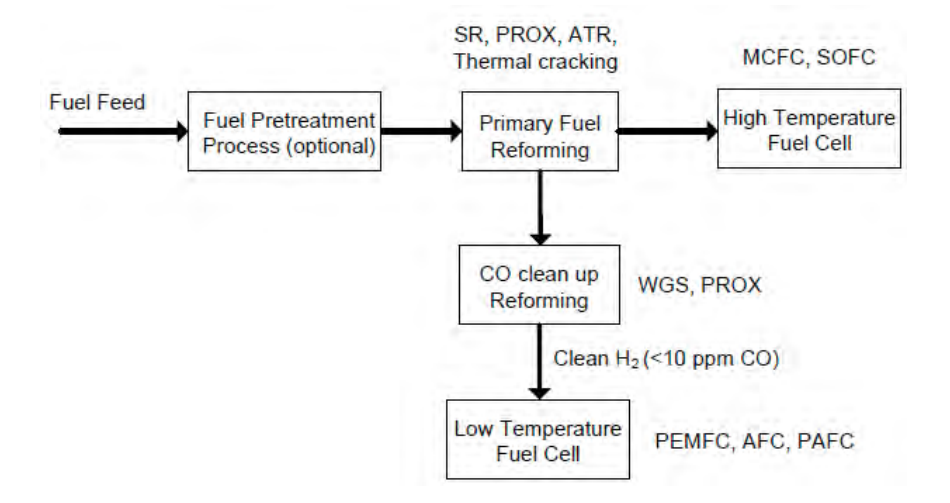


Fig. 7

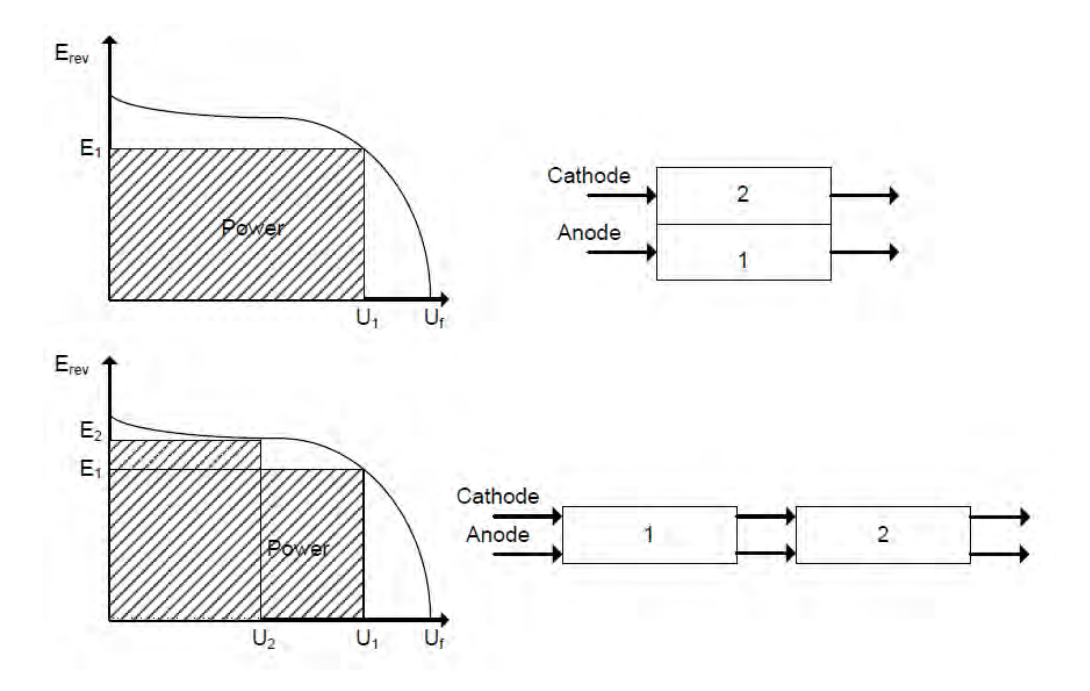
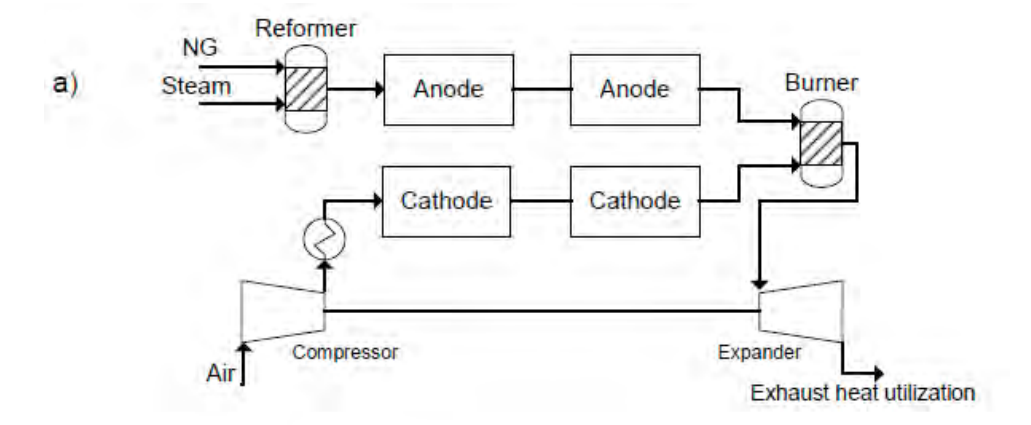


Fig. 8



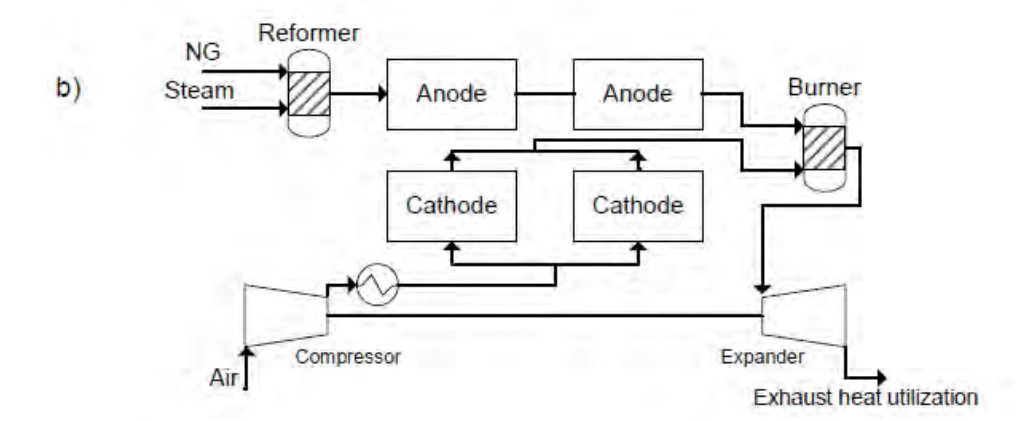


Fig. 9

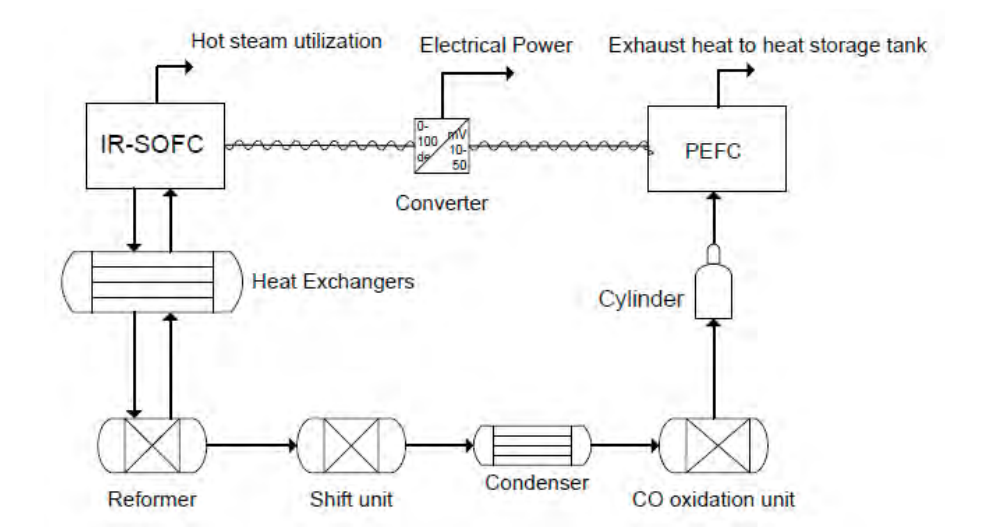


Fig. 10

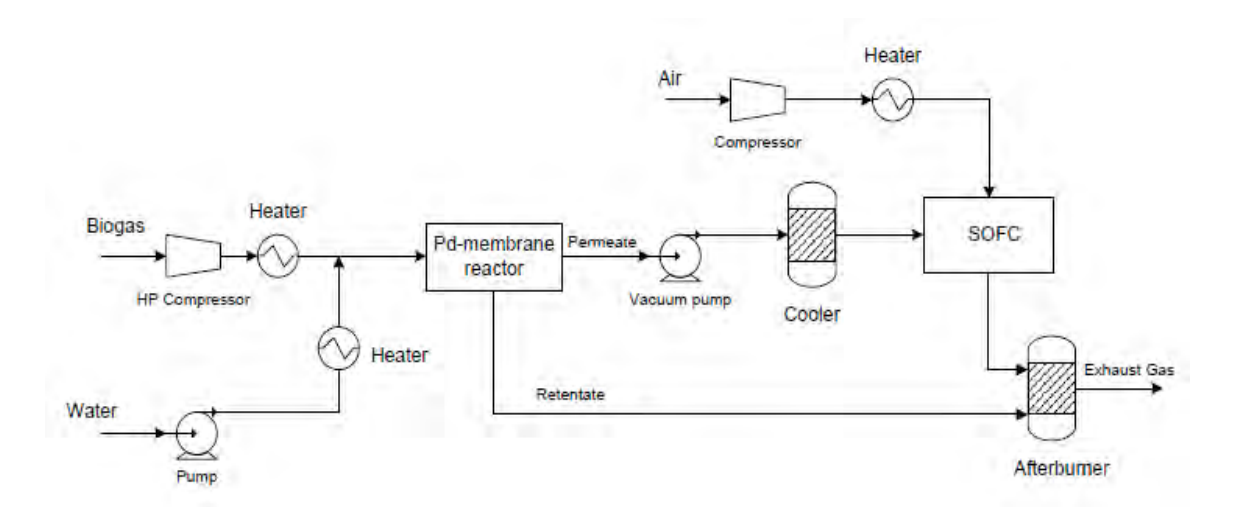


Fig. 11

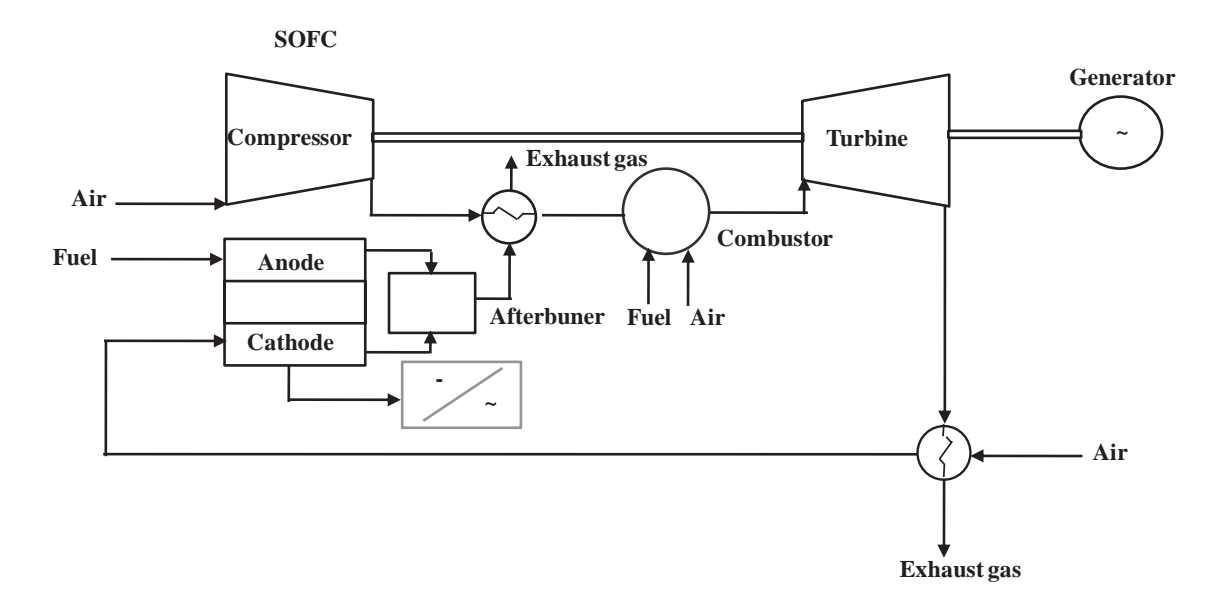


Fig. 12

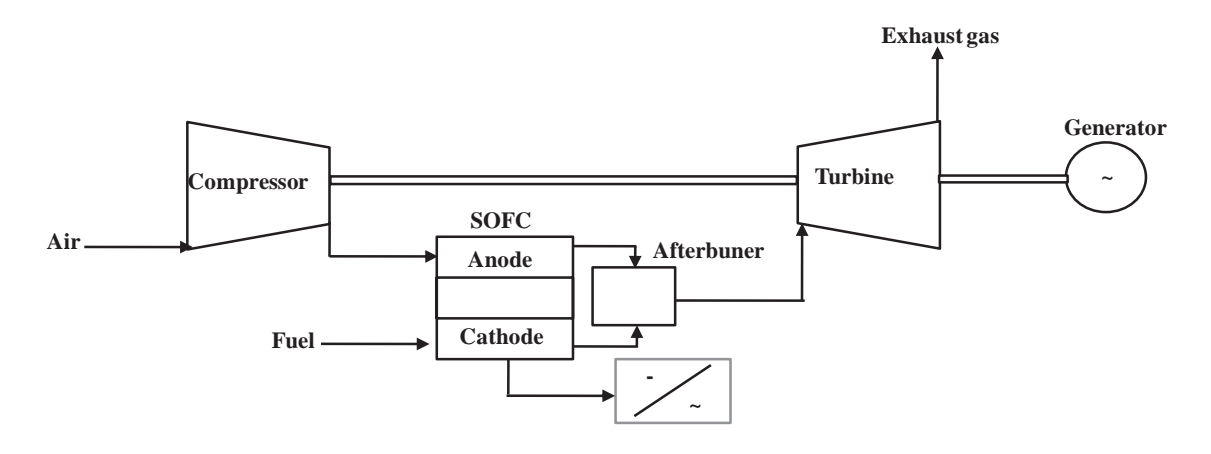


Fig. 13

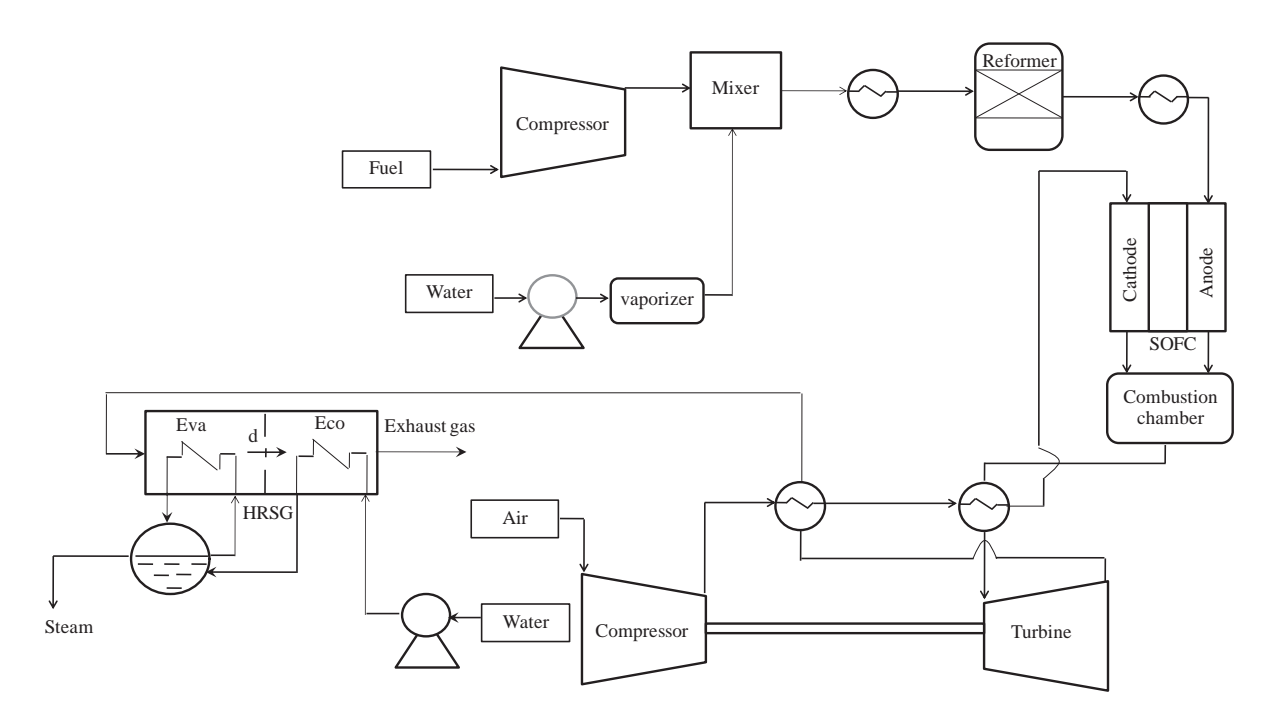


Fig. 14

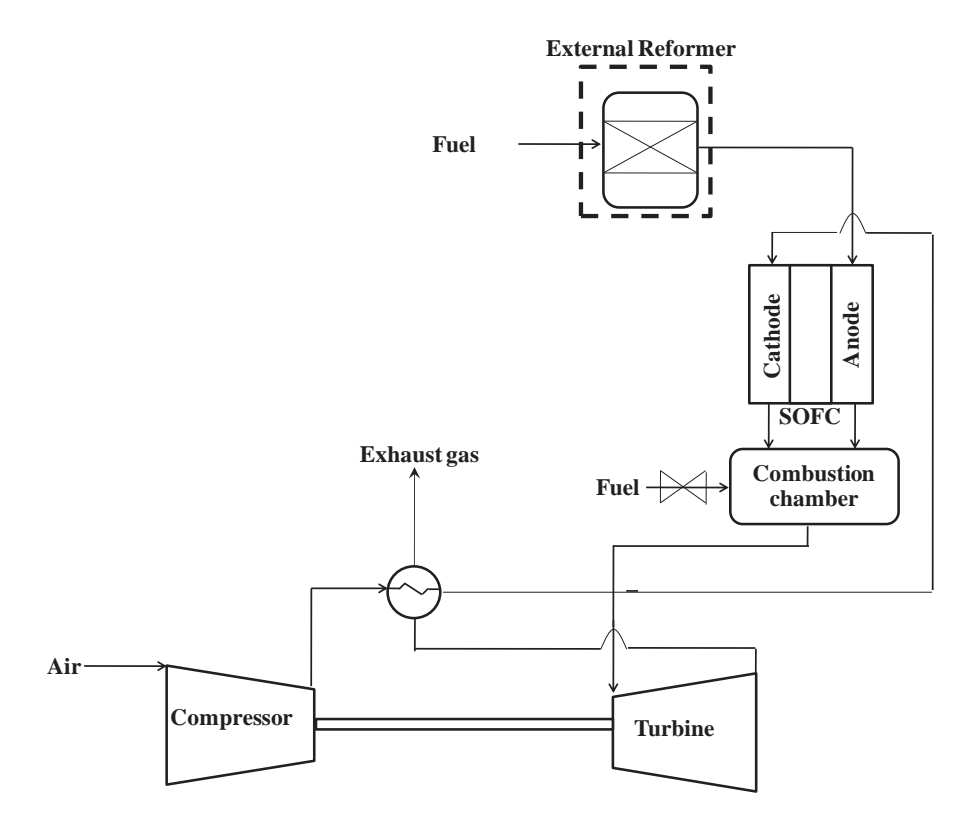


Fig.15

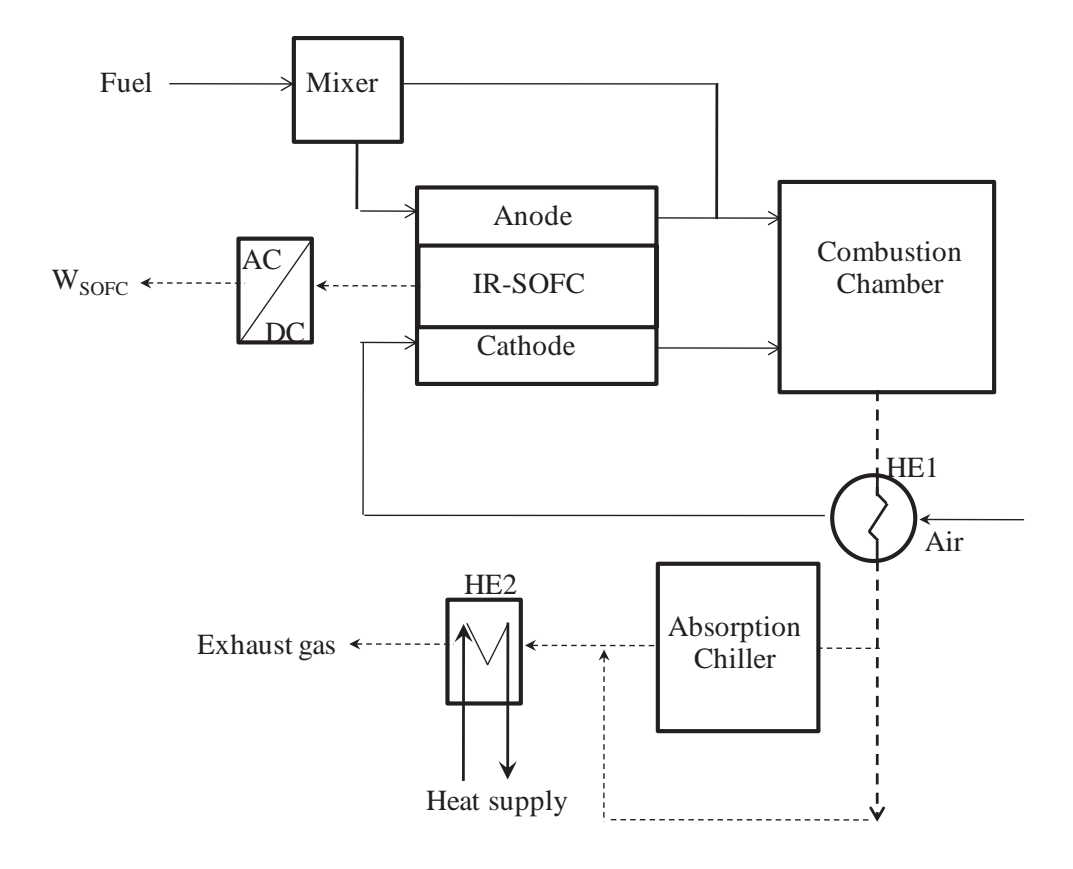


Fig. 16

บคำขอ 1 4 ส.ค. 2557  เคาขอ 1 4 ส.ค. 2557  กษณ์จำแนกการประคิษฐ์ระหว่างประเทศ  บแบบผลิตภัณฑ์  วันประกาศโฆษณา อกสิทธิบัตร/อนุสิทธิบัตร  เลขที่สิทธิบัตร/อนุสิทธิบัตร  เลขที่สิทธิบัตร/อนุสิทธิบัตร  เลขที่สิทธิบัตร/อนุสิทธิบัตร  อย่างเคียวกันและเป็นอำขอลำคับที่		
เคาขอ 1 4 ส.ค. 2557 1401004679 กษณ์จำแนกการประคิษฐ์ระหว่างประเทศ บแบบผลิตภัณฑ์ ภทผลิตภัณฑ์ วันประกาศโฆษณา เลขที่ประกาศโฆษณา อกสิทธิบัตร/อนุสิทธิบัตร เลขที่สิทธิบัตร/อนุสิทธิบัตร ลายมือชื่อเจ้าหน้าที่		
กษณ์จำแนกการประคิษฐ์ระหว่างประเทศ  บแบบผลิตภัณฑ์  วันประกาศโฆษณา เลขที่ประกาศโฆษณา  อกสิทธิบัตร/อนุสิทธิบัตร เลขที่สิทธิบัตร/อนุสิทธิบัตร  ลายมือชื่อเจ้าหน้าที่  ไรค์และกรดใขมันอิสระเป็นองค์ประกอบ		
ภทผลิตภัณฑ์ วันประกาศโฆษณา เลขที่ประกาศโฆษณา อกสิทธิบัตร/อนุสิทธิบัตร เลขที่สิทธิบัตร/อนุสิทธิบัตร ลายมือชื่อเจ้าหน้าที่ ไรค์และกรดไขมันอิสระเป็นองค์ประกอบ		
วันประกาศโฆษณา เลขที่ประกาศโฆษณา อกสิทธิบัตร/อนุสิทธิบัตร เลขที่สิทธิบัตร/อนุสิทธิบัตร ลายมือชื่อเจ้าหน้าที่ ไรค์และกรดไขมันอิสระเป็นองค์ประกอบ		
อกสิทธิบัตร/อนุสิทธิบัตร เลขที่สิทธิบัตร/อนุสิทธิบัตร ลายมือชื่อเจ้าหน้าที่ ไรค์และกรคไขมันอิสระเป็นองค์ประกอบ		
ลายมือชื่อเจ้าหน้าที่ ไรค์และกรคไขมันอิสระเป็นองค์ประกอบ อย่างเดียวกับและเป็นคำขอลำดับที่		
ไรค์และกรดไขมันอิสระเป็นองค์ประกอบ อย่างเดียวกับและเป็นคำขอลำดับที่		
กย่างเดียวกับและเป็นคำขอลำดับที่		
เข่างเดียวกันและเป็นคำขอลำดับที่		
3.1 สัญชาติ (การสาร 3.3 โทรสาร 3.4 อีเมล์		
อื่น		
5.1 ตัวแทนเลขที่ 1453		
5.2 โทรศัพท์ 0-2160-5340-2		
5.3 โทรสาร 0-2160-5343		
5.4 อีเมล์		

# แบบ สป/สผ/อสป/001-ก หน้า 2 ของจำนวน 3 หน้า

วันยื่นคำขอ เลขที่ค์ 8.1 8.2 8.3 8.4  ผู้ขอรับสิทธิบัตร/อนุสิทธิบัตรขอสิทร์	ำขอ ป	ระเทศ	สัญลักษณ์จำแนกการ	
8.2 8.3			ประดิษฐ์ระหว่างประเทศ	สถานะคำขอ
8.3				
8.4 🔲 ผู้ขอรับสิทธิบัตร/อนสิทธิบัตรขอสิทธิ				
🗖 ใค้ยื่นเอกสารหลักฐานพร้อมคำขอนี้	🗖 ขอยื่นเอกสารหลั	กฐานหลังจากวัง	นยื่นคำขอนี้	
	ตภัณฑ์ ผู้ขอรับสิทธิบัตร งานแสดง	/อนุสิทธิบัตรได้ ผู้จัด	ก็แสดงการประดิษฐ์ที่หน่วยงาน	เของรัฐเป็นผู้จัด
10.การประคิษฐ์เกี่ยวกับจุลชีพ				
10.1 เลขทะเบียนฝากเก็บ	10.2 วันที่ฝากเก็บ 10.3 สถาบันฝากเก็บ/ประเทศ		บ/ประเทศ	
หลังจากวันที่ เคือน    ผู้ขอรับสิทธิบัตร/อนุสิทธิบัตรขอให้ใช้รูว   เลือน   ผู้ขอรับสิทธิบัตร/อนุสิทธิบัตรขอให้ใช้รูว			กาศโฆษณา	
		ในการประ	กาศโฆษณา	
13.คำขอรับสิทธิบัตร/ <del>อนุสิทธิบัตร</del> นี้ประกอบด้วย		14.เอกสารประกอบคำขอ		
	44			
ก. แบบพิมพ์คำขอ 3	หน้า	🗖 เอกส	ารแสดงสิทธิในการขอรับสิทธิ	
ก. แบบพิมพ์คำขอ 3 ข. รายละเอียคการประดิษฐ์	หน้า	□ เอกส □ หนังถ์	ารแสดงสิทธิในการขอรับสิทธิ สือรับรองการแสดงการประดิษ	
ก. แบบพิมพ์คำขอ 3 ข. รายละเอียคการประดิษฐ์ <del>หรือคำพรรณนาแบบผลิตภัณฑ์</del> 6	หน้า หน้า	<ul><li>□ เอกส</li><li>□ หนังข์</li><li>ผลิต</li></ul>	ารแสคงสิทธิในการขอรับสิทธิ สือรับรองการแสดงการประคิษ ภัณฑ์	
<ul> <li>ก. แบบพิมพ์คำขอ 3</li> <li>ข. รายละเอียดการประดิษฐ์</li> <li>หรือคำพรรณนาแบบผลิตภัณฑ์ 6</li> <li>ค. ข้อถือสิทธิ 2</li> </ul>	หน้า หน้า หน้า	<ul><li>□ เอกส</li><li>□ หนังอ่</li><li>ผลิตะ</li><li>□ หนัง</li></ul>	ารแสคงสิทธิในการขอรับสิทธิ สือรับรองการแสคงการประดิษ ภัณฑ์ สือมอบอำนาจ	
<ul> <li>ก. แบบพิมพ์คำขอ 3</li> <li>ข. รายละเอียดการประดิษฐ์</li> <li>หรือคำพรรณนาแบบผลิตภัณฑ์ 6</li> <li>ค. ข้อถือสิทธิ์ 2</li> <li>ง. รูปเขียน 1 รูป 1</li> </ul>	หน้า หน้า	<ul><li>□ เอกส</li><li>□ หนังข่</li><li>ผลิต</li><li>□ หนัง</li><li>□ เอกส</li></ul>	ารแสดงสิทธิในการขอรับสิทธิ สือรับรองการแสดงการประดิษ ภัณฑ์ เสือมอบอำนาจ กรรายละเอียดเกี่ยวกับจุลชีพ	ฐ์/การออกแบบ
<ul> <li>ก. แบบพิมพ์คำขอ 3</li> <li>ข. รายละเอียดการประดิษฐ์</li> <li>หรือคำพรรณนาแบบผลิตภัณฑ์ 6</li> <li>ก. ข้อถือสิทธิ 2</li> <li>ง. รูปเขียน 1 รูป 1</li> <li>จ. ภาพแสดงแบบผลิตภัณฑ์</li> </ul>	หน้า หน้า หน้า หน้า	<ul> <li>□ เอกส</li> <li>□ หนังข้</li> <li>ผลิต</li> <li>□ หนัง</li> <li>□ เอกส</li> <li>□ เอกส</li> </ul>	ารแสดงสิทธิในการขอรับสิทธิ สือรับรองการแสดงการประดิษ ภัณฑ์ เสือมอบอำนาจ เารรายละเอียดเกี่ยวกับจุลชีพ เารการขอนับวันยื่นคำขอในต่า	ฐ์/การออกแบบ
<ul> <li>ก. แบบพิมพ์คำขอ 3</li> <li>ข. รายละเอียดการประดิษฐ์</li> <li>หรือคำพรรณนาแบบผลิตภัณฑ์ 6</li> <li>ค. ข้อถือสิทธิ 2</li> <li>ง. รูปเขียน 1 รูป 1</li> <li>จ. ภาพแสดงแบบผลิตภัณฑ์</li> <li></li></ul>	หน้า หน้า หน้า	<ul> <li>□ เอกส</li> <li>□ หนังข์</li> <li>ผลิตม</li> <li>□ หนัง</li> <li>□ เอกส</li> <li>□ เอกส</li> <li>คำขอ</li> </ul>	ารแสดงสิทธิในการขอรับสิทธิ สือรับรองการแสดงการประดิษ ภัณฑ์ เสือมอบอำนาจ กรรายละเอียดเกี่ยวกับจุลชีพ	ฐ์/การออกแบบ งประเทศเป็นวันยื่น

3.ผู้ขอรับสิทธิบัตร/อนุสิทธิบัตร และที่อยู่ (เลขที่ ถนน ประเทศ)
 จุฬาลงกรณ์มหาวิทยาลัย
 อยู่ที่ จุฬาลงกรณ์มหาวิทยาลัย ถนนพญาไท แขวงวังใหม่ เขตปทุมวัน
 กรุงเทพฯ 10330
 3.1 สัญชาติ ไทย 3.2 โทรศัพท์ 0-2160-5340-42 3.3 โทรสาร 0-2160-5343

สำนักงานกองทุนสนันสนุนการวิจัย อยู่ที่ ชั้น 14 อาคารเอส เอ็ม ทาว์เวอร์ เลขที่ 979/17-21 ถนนพหลโยธิน แขวงสามเสนใน เขตพญาไท กรุงเทพฯ 10400 3.1 สัญชาติไทย 3.2 โทรศัพท์ 0-2278-8200 3.3 โทรสาร 0-2278-8248

6.ผู้ประดิษฐ์/ผู้<del>ออกแบบผลิตภัณฑ์</del> และที่อยู่ (เลขที่ ถนน ประเทศ) ศาสตราจารย์ คร.สุทธิชัย อัสสะบำรุงรัตน์ อยู่ที่ คณะวิศวกรรมศาสตร์ จุฬาลงกรณ์มหาวิทยาลัย เขตปทุมวัน กรุงเทพฯ 10330

นางสาวณัจนันท์ บุญอนุวัฒน์ อยู่ที่ คณะวิศวกรรมศาสตร์ จุฬาลงกรณ์มหาวิทยาลัย เขตปทุมวัน กรุงเทพฯ 10330

ผู้ช่วยศาสตราจารย์ คร.วรพล เกียรติกิตติพงษ์ อยู่ที่ คณะวิสวกรรมศาสตร์และเทค โน โลยีอุตสาหกรรม มหาวิทยาลัยศิลปากร พระราชวังสนามจันทร์ นครปฐม 73000

นางสาวกนกวรรณ จ้าวสุวรรณ อยู่ที่ คณะวิศวกรรมศาสตร์ มหาวิทยาลัยเทคโนโลยีราชมงคลกรุงเทพ เขตสาธร กรุงเทพฯ 10120

นายจุติพงศ์ ภูสุมาศ อยู่ที่ คณะวิสวกรรมศาสตร์ จุฬาลงกรณ์มหาวิทยาลัย เขตปทุมวัน กรุงเทพฯ 10330

นายบำรุง สูงเนิน อยู่ที่ คณะวิศวกรรมศาสตร์ จุฬาลงกรณ์มหาวิทยาลัย เขตปทุมวัน กรุงเทพฯ 10330

## รายละเอียดการประดิษฐ์

## ชื่อที่แสดงถึงการประดิษฐ์

5

10

15

20

25

หอกลั่นที่เกิดปฏิกิริยาสำหรับการผลิตไบโอดีเซลจากน้ำมันที่มีไตรกลีเซอไรด์และกรดไขมันอิสระเป็น องค์ประกอบ

## สาขาวิทยาการที่เกี่ยวข้องกับการประดิษฐ์

สาขาวิศวกรรมเคมีในส่วนที่เกี่ยวข้องกับหอกลั่นที่เกิดปฏิกิริยาสำหรับการผลิตไบโอดีเซลจากน้ำมันที่ มีไตรกลีเซอไรด์และกรดไขมันอิสระเป็นองค์ประกอบ

# ภูมิหลังของศิลปวิทยาการที่เกี่ยวข้องกับการประดิษฐ์

พลังงานเป็นสิ่งจำเป็นต่อการดำรงชีวิต ทำให้ความต้องการด้านพลังงานสูงขึ้นเรื่อยๆ จนแหล่ง พลังงานหลัก ได้แก่ น้ำมันปิโตรเลียม แก๊สธรรมชาติ และถ่านหิน เป็นต้น ซึ่งจัดเป็นแหล่งพลังงานที่ใช้แล้ว หมดไปเริ่มมีไม่เพียงพอต่อความต้องการ ประกอบกับราคาน้ำมันที่ปรับตัวสูงขึ้นอย่างต่อเนื่อง อีกทั้งพลังงาน เหล่านี้ยังก่อให้เกิดมลพิษทางอากาศและแก๊สเรือนกระจกเพิ่มขึ้น ดังนั้นพลังงานทางเลือกจึงเข้ามามีบทบาท สำคัญมากขึ้น เช่น พลังงานน้ำ พลังงานลม พลังงานแสงแดด พลังงานจากความร้อนใต้พิภพ และพลังงานจาก ซีวมวล เป็นต้น ภาคการขนส่งเป็นภาคหนึ่งที่มีสัดส่วนในการใช้พลังงานที่สูง อีกทั้งพลังงานที่ใช้ในภาคการ ขนส่งในปัจจุบันเป็นการใช้งานพลังงานฟอสซิลในรูปแบบเชื้อเพลิงเหลวเป็นส่วนใหญ่

ไบโอดีเซล (Biodiesel) เป็นหนึ่งในพลังงานทางเลือกที่น่าสนใจสำหรับภาคการขนส่งที่สอดคล้องกับ เทคโนโลยีและโครงสร้างพื้นฐานในปัจจุบันที่ผลิตได้จากชีวมวล ซึ่งเป็นแหล่งวัตถุดิบหมุนเวียนที่หาได้ เช่น น้ำมันพืชและไขมันสัตว์รวมถึงน้ำมันประกอบอาหารที่ใช้แล้ว โดยนำมาผ่านกระบวนการที่หลากหลาย เช่น นำมาผสมกับน้ำมันดีเซล ไมโครอิมัลซัน (Microemulsion) ไพโรไลซิส (Pyrolysis) ปฏิกิริยาทรานส์ เอสเทอริฟิเคชันของไตรกลีเซอไรด์ (Transesterification) หรือปฏิกิริยาเอสเทอริฟิเคชันของกรดไขมันอิสระ (Esterification)

ปัจจุบันเทคโนโลยีในการผลิตไบโอดีเซลทั้งที่เป็นกระบวนการผลิตแบบกะและแบบต่อเนื่อง โดยส่วน ใหญ่ใช้ปฏิกิริยาทรานส์เอสเทอริฟิเคชันและตัวเร่งปฏิกิริยาแบบเอกพันธุ์ที่เป็นด่าง (Homogeneous base catalyst) ซึ่งปัญหาที่เกิดขึ้นจากกระบวนการดังกล่าวมีหลายประการ ประการแรกคือ การใช้ตัวเร่งปฏิกิริยาที่ เป็นด่างกับสารตั้งต้นที่มีปริมาณกรดไขมันอิสระสูง จำเป็นต้องมีการบำบัดเบื้องต้น (Pre-treatment) ก่อน โดยเกิดปฏิกิริยาเอสเทอริฟิเคชันระหว่างกรดไขมันอิสระกับแอลกอฮอล์ ได้เป็นสารประกอบเอสเทอร์ (ไปโอดีเซล) และน้ำเป็นผลพลอยได้เป็นขั้นตอนการกำจัดกรดไขมันอิสระเพื่อป้องกันการเกิดปฏิกิริยา

ซาปอนนิฟิเคชัน (Saponification) ของกรดไขมันอิสระกับด่างกลายเป็นสบู่ ซึ่งจะทำให้ค่าผลได้ของ ไบโอดีเซลลดลงและเกิดเป็นยางเหนียว ทำให้แยกสิ่งเจือปนออกจากไบโอดีเซลได้ยาก ประการถัดมาคือ สมดุลของปฏิกิริยา เนื่องจากปฏิกิริยาทรานส์เอสเทอริฟิเคชันประกอบด้วยปฏิกิริยาย่อยสามปฏิกิริยาที่จะ เปลี่ยนจากไตรกลีเซอไรด์ (Triglyceride) เป็นไดกลีเซอไรด์ (Diglyceride) จากไดกลีเซอไรด์เป็นมอนอกลีเซอ ไรด์ (Mono-glyceride) และจากมอนอกลีเซอไรด์เป็นกลีเซอรอล (Glycerol) ซึ่งเป็นปฏิกิริยาที่สามารถผัน กลับได้ทั้งสามปฏิกิริยา ทำให้เป็นข้อจำกัดของการเกิดปฏิกิริยา ดังนั้นวิธีการแก้ปัญหาในขั้นต้นจะอาศัยการ เติมแอลกอฮอล์ที่เป็นสารตั้งต้นของปฏิกิริยาให้สูงกว่าอัตราส่วนการเกิดปฏิกิริยาโดยปกติ (อัตราส่วนโดยโมล ระหว่างไตรกลีเซอไรด์ต่อแอลกอฮอล์ตามทฤษฎี = 1:3) เพื่อผลักให้ปฏิกิริยาเกิดไปข้างหน้าได้มากขึ้น แต่การ เติมแอลกอฮอล์ที่มากเกินพอนี้ จะส่งผลให้มีค่าใช้จ่ายเพิ่มขึ้นรวมไปถึงการใช้พลังงานที่เพิ่มขึ้นในการแยก แอลกอฮอล์เหล่านี้ เพื่อนำกลับมาทำปฏิกิริยาและปริมาณแอลกอฮอล์ส่วนเกินจะส่งผลต่อขนาดของระบบ ซึ่ง จะทำให้ระบบมีขนาดใหญ่ขึ้น เป็นการเพิ่มค่าใช้จ่ายในการลงทุนและค่าใช้จ่ายในการดำเนินการและการดูแล รักษาหน่วยปฏิบัติการต่างๆ ข้อจำกัดอีกประการของกระบวนการแบบดั้งเดิมคือ ภายหลังจากเกิดปฏิกิริยา แล้วจำเป็นจะต้องมีขั้นตอนการแยกผลิตภัณฑ์หลายขั้นตอน ซึ่งมีราคาแพงและทำให้เกิดน้ำเสียและของเสียที่ เป็นเกลืออีกด้วย นอกจากปัญหาที่กล่าวมาแล้วการใช้น้ำมันพืชมาเป็นสารตั้งต้นในการผลิตไบโอดีเซลก็เป็น ปัญหาหนึ่งที่ทำให้กระบวนการผลิตมีต้นทุนที่สูง เนื่องจากน้ำมันพืชมีราคาแพง ดังนั้นการนำน้ำมันพืชที่ใช้แล้ว มาผลิตไบโอดีเซลจึงเป็นทางเลือกหนึ่งที่นอกจากจะลดต้นทุนการผลิตแล้วยังเป็นการลดของเสียโดยการนำ กลับมาใช้ใหม่ แต่อย่างไรก็ตามน้ำมันที่ผ่านการใช้งานมาแล้วจะมีปริมาณกรดไขมันอิสระปะปนอยู่มาก ทำให้ ต้องบีขั้นตอนการบำบัดเบื้องต้นก่อนนำมาใช้ผลิตไบโอดีเซล

10

15

20

25

สำหรับการแก้ปัญหาที่เกิดจากกระบวนการผลิตแบบดั้งเดิม ได้มีการนำหอกลั่นที่เกิดปฏิกิริยา (Reactive distillation) มาใช้ในการผลิตใบโอดีเชลเพื่อช่วยเปลี่ยนสมดุลของปฏิกิริยาให้เกิดไปข้างหน้ามาก ขึ้นโดยการแยกผลิตภัณฑ์ในขณะที่เกิดปฏิกิริยา ทำให้ลดปริมาณแอลกอฮอล์ที่ต้องป้อนเกินกว่าอัตราส่วนการ เกิดปฏิกิริยาโดยปกติลงได้ ยกตัวอย่างเช่น สิทธิบัตร EP 2154226A1 (Dimian และคณะ) ได้นำหอกลั่นที่ เกิดปฏิกิริยามาใช้ร่วมกับตัวเร่งปฏิกิริยาแบบวิวิธพันธุ์เพื่อผลิตเอสเทอร์ของกรดไขมันอิสระโดยใช้ปฏิกิริยา เอสเทอริฟิเคชัน พบว่า ค่าการเปลี่ยนแปลงของกรดไขมันอิสระมีค่าเพิ่มสูงขึ้นเมื่อเปรียบเทียบกับการผลิต แบบเดิม นอกจากสิทธิบัตรที่ยกตัวอย่างนี้ยังมีสิทธิบัตรที่เสนอการใช้หอกลั่นที่เกิดปฏิกิริยาในการผลิตไบโอ ดีเชลจากปฏิกิริยาเอสเทอริฟิเคชัน ได้แก่ สิทธิบัตร US 2009/0076913 A1, WO 2009/017957 A1 และ US 2013/0212933 A1 ของ Morgan และคณะ และ สิทธิบัตร US 2012/0266527 A1 ของ Erdoes, JR. แต่การใช้ปฏิกิริยาเอสเทอริฟิเคชันในการผลิตไบโอดีเชลก็ยงมีข้อจำกัดที่ต้องใช้กรดไขมันอิสระเป็นสารตั้งต้น ในการผลิตเท่านั้น สำหรับการผลิตไบโอดีเชลโดยปฏิกิริยาทรานส์เอสเทอริฟิเคชันก็มีการนำหอกลั่นที่

เกิดปฏิกิริยามาใช้เช่นกัน สิทธิบัตรUS 8613780B2 (Asthana และคณะ) อธิบายการนำหอกลั่นที่ เกิดปฏิกิริยามาใช้ร่วมกับกระบวนการผลิตไบโอดีเซลเพื่อปรับปรุงให้ได้ไบโอดีเซลที่มีสมบัติดีขึ้น เช่น จุดน้ำมัน เป็นฝ้า (Cloud point) เป็นต้น สิทธิบัตร US 2007/0277432 Al (Jackam และคณะ) อธิบายการใช้หอกลั่น ที่เกิดปฏิกิริยามาใช้เพื่อพัฒนาประสิทธิภาพกระบวนการผลิตไบโอดีเซลโดยปฏิกิริยาทรานส์เอสเทอริฟิเคชัน แต่ก็ยังมีข้อจำกัดที่ต้องมีขั้นตอนการบำบัดเบื้องต้นอยู่ดี นอกจากที่กล่าวมาแล้วยังมีสิทธิบัตร US 2012/0240452A1 (Erdoes และคณะ) ที่อธิบายถึงการใช้หอกลั่นที่เกิดปฏิกิริยาในการผลิตไบโอดีเซล โดยใช้ทั้งปฏิกิริยาเอสเทอริฟิเคชันและทรานส์เอสเทอริฟิเคชันพร้อมกัน แต่กระบวนการนี้ก็จำเป็นจะต้องใช้ ตัวเร่ง ปฏิกิริยาที่ทำหน้าที่เร่งปฏิกิริยาโดยใช้ทั้งกรดและด่างร่วมกัน (Bi-functional catalyst) ซึ่งมีวิธีเตรียม ที่ยุ่งยาก และยังไม่มีการผลิตตัวเร่งปฏิกิริยาชนิดนี้เพื่อการค้า (Commercial catalyst) นอกจากนี้ยังมี ข้อจำกัดในการใช้งานคือ การที่ทำให้เกิดปฏิกิริยาเอสเทอริฟิเคชันและทรานส์เอสเทอริฟิเคชันพร้อมกันจะได้ น้ำเป็นผลพลอยได้ซึ่งจะส่งผลโดยตรงต่อการเสื่อมสภาพของตำแหน่งกรดของตัวเร่งปฏิกิริยา ทำให้ ประสิทธิภาพในการเร่งปฏิกิริยาลดลง

หอกลั่นที่เกิดปฏิกิริยาสำหรับการผลิตไบโอดีเซลจากน้ำมันที่มีไตรกลีเซอไรด์และกรดไขมันอิสระเป็น องค์ประกอบนี้ เป็นระบบที่ออกแบบมาให้สามารถเกิดปฏิกิริยาเอสเทอริฟิเคชันและปฏิกิริยาทรานส์เอสเทอ ริฟิเคชันภายในหอกลั่นเดียวกัน ช่วยป้องกันการเกิดปฏิกิริยาซาปอนนิฟิเคชันของกรดไขมันอิสระกับด่าง กลายเป็นสบู่ และช่วยลดขั้นตอนการบำบัดน้ำมันพืชที่ผ่านการใช้งานก่อนนำมาใช้ผลิตไบโอดีเซล

## ลักษณะและความมุ่งหมายของการประดิษฐ์

15

25

การประดิษฐ์นี้เกี่ยวข้องกับหอกลั่นที่เกิดปฏิกิริยาสำหรับการผลิตไบโอดีเซลจากน้ำมันที่มีไตรกลีเซอ ไรด์และกรดไขมันอิสระเป็นองค์ประกอบ ภายในหอกลั่นที่เกิดปฏิกิริยาถูกแบ่งออกเป็นชั้นๆ (Stage) โดยการ บรรจุตัวเร่งปฏิกิริยาแบบวิวิธพันธุ์ในชั้นที่กำหนดให้เกิดปฏิกิริยา ส่วนที่เกิดปฏิกิริยาจะแบ่งออกเป็นสองส่วน คือ ส่วนบนจะเป็นส่วนที่ให้เกิดปฏิกิริยาเอสเทอริฟิเคชันซึ่งจะใช้ตัวเร่งปฏิกิริยาวิวิธพันธุ์ที่เป็นกรด (Heterogeneous acid catalyst) และส่วนล่างจะเป็นส่วนที่เกิดปฏิกิริยาทรานส์เอสเทอริฟิเคชัน ซึ่งจะใช้ ตัวเร่งปฏิกิริยาวิวิธพันธุ์ที่เป็นด่าง (Heterogeneous base catalyst) มีการรวมขั้นตอนในการเกิดปฏิกิริยา และขั้นตอนในการแยกผลิตภัณฑ์เข้าไว้ในหน่วยเดียวกัน ทำให้เกิดการแยกผลิตภัณฑ์ขณะที่เกิดปฏิกิริยา สามารถทำให้สมดุลของปฏิกิริยาเคมีสามารถเปลี่ยนไปในทิศทางที่เกิดเป็นผลิตภัณฑ์ที่ต้องการได้มากขึ้น

ความมุ่งหมายของการประดิษฐ์นี้ คือ การพัฒนาหอกลั่นที่เกิดปฏิกิริยาสำหรับการผลิตไบโอดีเซลจาก น้ำมันที่มีไตรกลีเซอไรด์และกรดไขมันอิสระเป็นองค์ประกอบ ที่สามารถเกิดปฏิกิริยาเอสเทอริฟิเคชันและ ปฏิกิริยาทรานส์เอสเทอริฟิเคชันภายในหอกลั่นเดียวกัน เพื่อใช้ในการผลิตไบโอดีเซลจากน้ำมันที่มีทั้งไตรกลี เซอไรด์และกรดไขมันอิสระเป็นองค์ประกอบ เพื่อลดต้นทุนในการผลิตไบโอดีเซลทั้งค่าใช้จ่ายในการลงทุนและ ค่าใช้จ่ายในการดำเนินการ

## คำอธิบายรูปเขียนโดยย่อ

5

15

20

รูปที่ 1 แสดงหอกลั่นที่เกิดปฏิกิริยาสำหรับผลิตไบโอดีเซลจากน้ำมันที่มีไตรกลีเซอไรด์และกรดไขมัน อิสระเป็นองค์ประกอบ

## การเปิดเผยการประดิษฐ์โดยสมบูรณ์

รูปที่ 1 แสดงหอกลั่นที่เกิดปฏิกิริยาสำหรับผลิตไบโอดีเซลจากน้ำมันที่มีไตรกลีเซอไรด์และกรดไขมัน อิสระเป็นองค์ประกอบ ซึ่งประกอบด้วย

ส่วนที่ 1 ส่วนเรคติฟายอิง (2) วางอยู่ด้านบนของหอกลั่น โดยด้านบนของส่วนเรคติฟายอิง (2) ประกอบด้วย เครื่องควบแน่นแบบทั้งหมด (1) เพื่อควบแน่นสารตั้งต้นที่เป็นน้ำมันในวัฏภาคของเหลว ที่มา จากบริเวณป้อนสารตั้งต้น (7) โดยสายควบแน่นที่มีวัฏภาคไอจะออกทางด้านบนของหอ (15) เพื่อเข้าสู่ถัง รีฟลักซ์ (12) และบางส่วนจะถูกป้อนกลับเข้าสู่หออีกครั้ง (13) โดยส่วนที่เหลือเป็นผลิตภัณฑ์ที่ออกด้านบน ของหอ (9) ซึ่งส่วนเรคติฟายอิง (2) เป็นส่วนที่ทำหน้าที่ถ่ายโอนสารที่มีจุดเดือดสูงจากวัฏภาคไอไปยังวัฏภาค ของเหลวเพื่อนำกลับไปทำปฏิกิริยาก่อนของเหลวจะไหลลงเข้าสู่ส่วนที่ 2

ส่วนที่ 2 ส่วนเร่งปฏิกิริยาเอสเทอริฟิเคชัน (3) อยู่ถัดจากส่วนเรคติฟายอิง (2) จะบรรจุตัวเร่งปฏิกิริยา แบบวิวิธพันธุ์ที่เป็นกรด มีหน้าที่เร่งปฏิกิริยาเอสเทอริฟิเคชัน เพื่อกำจัดกรดไขมันอิสระ โดยน้ำมันที่ผ่านการ กำจัดกรดไขมันอิสระแล้วจะไหลลงสู่ส่วนที่ 3

ส่วนที่ 3 ส่วนเร่งปฏิกิริยาทรานส์เอสเทอริฟิเคชัน (4) อยู่ถัดจากส่วนเร่งปฏิกิริยาเอสเทอริฟิเคชัน (3) จะบรรจุตัวเร่งปฏิกิริยาแบบวิวิธพันธุ์ที่เป็นด่าง เพื่อเกิดปฏิกิริยาและเปลี่ยนไตรกลีเซอไรด์เป็นผลิตภัณฑ์ สารประกอบเอสเทอร์ (ไปโอดีเซล) ก่อนจะไหลเข้าสู่ส่วนที่ 4 และ

ส่วนที่ 4 ส่วนสตริปปิง (5) วางอยู่บริเวณด้านล่างของส่วนเร่งปฏิกิริยาทรานส์เอสเทอริฟิเคชัน (4) ซึ่ง ประกอบด้วย บริเวณป้อนสารตั้งต้นที่เป็นแอลกอฮอล์ที่บริเวณด้านล่างของหอกลั่น (8) ซึ่งมีการระเหยเป็นวัฏ ภาคไอขึ้นไปด้านบนในหอเพื่อเกิดปฏิกิริยากับน้ำมัน โดยแอลกอฮอล์สามารถแบ่งป้อนที่ตำแหน่งในส่วนเร่ง ปฏิกิริยาเอสเทอริฟิเคชั่น หรือส่วนเร่งปฏิกิริยาทรานส์เอสเทอริฟิเคชั่นของหอกลั่น (11) สายของผลิตภัณฑ์ที่ ออกจากหอกลั่นจะมีสองสาย คือ สายที่ด้านบนของหอ (15) จะเป็นวัฏภาคไอประกอบไปด้วยน้ำและ แอลกอฮอล์ที่เหลือจากการทำปฏิกิริยา และสายที่ด้านล่างของหอ (16) เป็นวัฏภาคของเหลวประกอบไปด้วย สารประกอบเอสเทอร์ (ไบโอดีเซล) กลีเซอรอลและน้ำมันที่เป็นสารตั้งต้นที่เหลือจากการทำปฏิกิริยา บริเวณ

ด้านล่างหอจะมีหม้อต้มซ้ำแบบแคตเติ้ล (6) เพื่อระเหยสายผลิตภัณฑ์ที่ด้านล่างหอ (16) บางส่วน และ ป้อนกลับเข้าสู่หออีกครั้งหนึ่ง (14) โดยส่วนที่เหลือเป็นผลิตภัณฑ์ที่ออกด้านล่างของหอ (10)

สารตั้งต้นที่ใช้ในการผลิตไบโอดีเซลจากหอกลั่นที่เกิดปฏิกิริยาสำหรับผลิตไบโอดีเซลจากน้ำมันที่มี ไตรกลีเซอไรด์และกรดไขมันอิสระเป็นองค์ประกอบ คือ น้ำมันและแอลกอฮอล์ โดยมีวิธีทางเริ่มจากน้ำมันที่มี ไตรกลีเซอไรด์และกรดไขมันอิสระจะถูกป้อนบริเวณต้านบนของหอ (7) และไหลจากด้านบนลงสู่ด้านล่างตาม แรงโน้มถ่วงของโลกผ่านส่วนเรคติฟายอิง (2) และส่วนเร่งปฏิกิริยาเอสเทอริฟิเคชัน (3) ซึ่งจะบรรจุตัวเร่ง ปฏิกิริยาแบบวิวิธพันธุ์ที่เป็นกรดเพื่อกำจัดกรดไขมันอิสระก่อน จากนั้นน้ำมันจะไหลต่อลงสู่ส่วนเร่งปฏิกิริยา พรานส์เอสเทอร์ริฟิเคชัน (4) ซึ่งจะบรรจุตัวเร่งปฏิกิริยาแบบวิวิธพันธุ์ที่เป็นด่างเพื่อเปลี่ยนไตรกลีเซอไรด์ใน น้ำมันไปเป็นผลิตภัณฑ์ที่เป็นสารประกอบเอสเทอร์ (ไบโอดีเซล) โดยแอลกอฮอล์ถูกป้อนบริเวณด้านล่างของ หอกลั่น (8) ซึ่งจะมีการระเหยเป็นวัฏภาคไอขึ้นไปด้านบนในหอกลั่นเพื่อเกิดปฏิกิริยากับน้ำมัน โดย แอลกอฮอล์สามารถแบ่งป้อนที่ตำแหน่งในส่วนเร่งปฏิกิริยาเอสเทอริฟอเคชันหรือส่วนเร่งปฏิกิริยาทรานส์เอ สเทอริฟิเคชันของหอกลั่น (11) ได้ บริเวณด้านบนของหอจะมีเครื่องควบแน่นแบบทั้งหมด (1) มีหน้าที่ ควบแน่นสารที่ออกทางด้านบนของหอ (15) กลับเข้าสู่ถังรีฟลักซ์ (12) ก่อนจะแยกผลิตภัณฑ์ส่วนหนึ่งออกจาก ระบบ (9) และป้อนบางส่วนกลับเข้าสู่หออีกครั้ง (13) ส่วนบริเวณด้านล่างของหอจะมีหม้อต้มซ้ำแบบแคตเติ้ล (6) เพื่อระเหยสายผลิตภัณฑ์ที่ด้านล่างหอ (16) บางส่วน ก่อนจะแยกผลิตภัณฑ์ส่วนหนึ่งออกจากระบบ (10) และป้อนบางส่วนกลับเข้าสู่หออีกครั้ง (14)

10

15

20

25

การรวมขั้นตอนการเกิดปฏิกิริยาและขั้นตอนการแยกสารเข้าไว้ในหน่วยเดียวกันจะช่วยเปลี่ยนสมดุล ของปฏิกิริยาให้เกิดไปในทางที่เกิดผลิตภัณฑ์ โดยมีการแยกผลิตภัณฑ์ออกจากบริเวณที่เกิดปฏิกิริยาอย่าง ต่อเนื่อง นอกจากนี้ภายในหอกลั่นตามการประดิษฐ์นี้มีทั้งส่วนที่เกิดปฏิกิริยาเอสเทอริฟิเคชันและทรานส์ เอสเทอริฟิเคชันทำให้ไม่จำเป็นต้องมีขั้นตอนในการบำบัดเบื้องต้น สามารถใช้ได้กับน้ำมันที่มีกรดไขมันอิสระ ในปริมาณที่สูงได้

การเพิ่มปริมาณแอลกอฮอล์ที่ใช้ในการทำปฏิกิริยาจะช่วยเพิ่มปริมาณไปโอดีเซล แต่ในขณะเดียวกัน การใช้ปริมาณสารตั้งต้น (แอลกอฮอล์) ที่สูงขึ้น จำเป็นจะต้องใช้พลังงานสูงขึ้น ดังนั้น ต้องคำนึงถึงจุดที่มีความ เหมาะสมในการดำเนินการเพื่อให้ได้ประสิทธิภาพสูงสุดด้วย

การเพิ่มค่าพลังงานของหม้อต้มซ้ำจะเพิ่มความบริสุทธิ์ของไบโอดีเซล แต่ในขณะเดียวกันก็ใช้พลังงาน สูงขึ้นด้วย รวมไปถึงอุณหภูมิภายในหอกลั่นที่เปลี่ยนไปส่งผลต่อการเกิดปฏิกิริยาด้วย ดังนั้น จำเป็นต้องมี การศึกษาหาจุดที่เหมาะสมเพื่อการดำเนินการที่ดีที่สุด

#### หน้า 6 ของจำนวน 6 หน้า

อัตราส่วนรีฟลักซ์ส่งผลต่อประสิทธิภาพของกระบวนการ เนื่องจากสายรีฟลักซ์ประกอบไปด้วย แอลกอฮอล์และน้ำ การป้อนแอลกอฮอล์กลับเข้าสู่หอกลั่นจะช่วยให้ปฏิกิริยาเกิดไปข้างหน้าได้มากขึ้น แต่ใน ขณะเดียวกันการที่ป้อนน้ำกลับเข้าไปจะส่งผลให้ปฏิกิริยาเอสเทอริฟิเคชันเกิดปฏิกิริยาย้อนกลับ และน้ำเป็น ปัจจัยสำคัญที่ทำให้ตัวเร่งปฏิกิริยาวิวิธพันธุ์ที่เป็นกรดเสื่อมสภาพได้เช่นกัน ดังนั้น จำเป็นต้องศึกษาหาอัตรา รีฟลักซ์ที่เหมาะสมเพื่อให้ได้ผลผลิตไบดีเซลสูงที่สุด

การเพิ่มจำนวนชั้นที่เกิดปฏิกิริยาจะทำให้ค่าการเปลี่ยนของสารตั้งต้นเพิ่มขึ้น เนื่องจากสารตั้งต้นมี พื้นที่และระยะเวลาในการสัมผัสกันมากขึ้น

ปริมาณกรดไขมันอิสระในน้ำมันมีผลต่อกระบวนการ เนื่องจากปริมาณกรดไขมันอิสระที่เพิ่มขึ้น ทำให้ ระยะเวลาสำหรับเกิดปฏิกิริยาเอสเทอริฟิเคชันเพิ่มขึ้นด้วย ส่งผลให้จำนวนชั้นที่ใช้ในการเกิดปฏิกิริยาเอส เทอริฟิเคชันเพิ่มขึ้น ในขณะเดียวกันอาจไปลดจำนวนชั้นในการเกิดปฏิกิริยาทรานส์เอสเทอริฟิเคชันลง เนื่องจากปริมาณไตรกลีเซอไรด์น้อยลง ดังนั้น ต้องมีการศึกษาหาจำนวนชั้นที่ใช้ในการเกิดปฏิกิริยาของแต่ละ ปฏิกิริยาให้เหมาะสม เพื่อให้ได้ค่าผลได้ของไปโอดีเซลสูงที่สุด

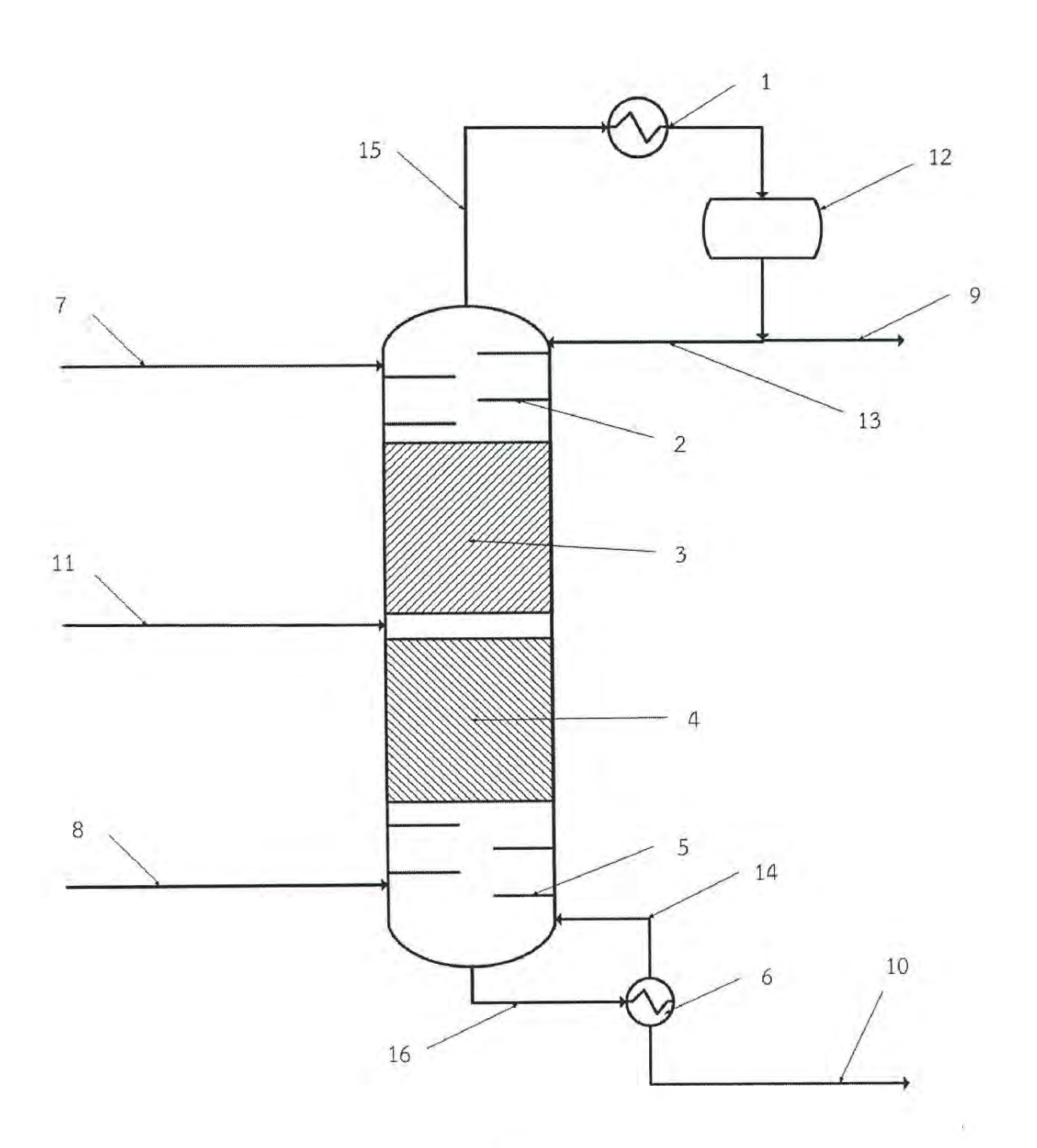
ตัวเร่งปฏิกิริยาที่ใช้มีผลอย่างมากต่อการเกิดปฏิกิริยา ดังนั้น จำเป็นต้องเลือกตัวเร่งปฏิกิริยาที่ เหมาะสมเพื่อมาใช้ร่วมกับหอกลั่นที่เกิดปฏิกิริยา เพื่อให้เกิดประสิทธิภาพสูงที่สุด

## 15 วิธีการในการประดิษฐ์ที่ดีที่สุด

5

10

เหมือนกับที่ได้กล่าวมาแล้วในหัวข้อการเปิดเผยการประดิษฐ์โดยสมบูรณ์



รูปที่ 1

#### ข้อถือสิทธิ

2 2

5

10

15

20

25

1. หอกลั่นที่เกิดปฏิกิริยาสำหรับผลิตไบโอดีเซลจากน้ำมันที่มีไตรกลีเซอไรด์และกรดไขมันอิสระเป็น องค์ประกอบ ซึ่งประกอบด้วย

ส่วนที่ 1 ส่วนเรคติฟายอิง (2) วางอยู่ด้านบนของหอกลั่น โดยด้านบนของส่วนเรคติฟายอิง (2) ประกอบด้วย เครื่องควบแน่นแบบทั้งหมด (1) เพื่อควบแน่นสารตั้งต้นที่เป็นน้ำมันในวัฏภาคของเหลวที่มาจาก บริเวณป้อนสารตั้งต้น (7) โดยสายควบแน่นที่มีวัฏภาคไอจะออกทางด้านบนของหอ (15) เพื่อเข้าสู่ถังรีฟลักซ์ (12) และบางส่วนจะถูกป้อนกลับเข้าสู่หออีกครั้ง (13) โดยส่วนที่เหลือเป็นผลิตภัณฑ์ที่ออกด้านบนของหอ (9)

ส่วนที่ 2 ส่วนเร่งปฏิกิริยาเอสเทอริฟิเคชัน (3) อยู่ถัดจากส่วนเรคติฟายอิง (2) มีหน้าที่เร่งปฏิกิริยา เอสเทอริฟิเคชัน เพื่อกำจัดกรดไขมันอิสระ โดยน้ำมันที่ผ่านการกำจัดกรดไขมันอิสระแล้วจะไหลลงสู่ส่วนที่ 3

ส่วนที่ 3 ส่วนเร่งปฏิกิริยาทรานส์เอสเทอริฟิเคชัน (4) อยู่ถัดจากส่วนเร่งปฏิกิริยาเอสเทอริฟิเคชัน (3) เพื่อเกิดปฏิกิริยาและเปลี่ยนไตรกลีเซอไรด์เป็นผลิตภัณฑ์สารประกอบเอสเทอร์ (ไปโอดีเซล) ก่อนจะไหลเข้าสู่ ส่วนที่ 4 และ

ส่วนที่ 4 ส่วนสตริปปิง (5) วางอยู่บริเวณด้านล่างของส่วนเร่งปฏิกิริยาทรานส์เอสเทอริฟิเคชัน (4) ซึ่ง ประกอบด้วย บริเวณป้อนสารตั้งต้นที่เป็นแอลกอฮอล์ที่บริเวณด้านล่างของหอกลั่น (8) ซึ่งมีการระเหยเป็นวัฏ ภาคไอขึ้นไปด้านบนในหอเพื่อเกิดปฏิกิริยากับน้ำมัน โดยแอลกอฮอล์สามารถแบ่งป้อนที่ตำแหน่งในส่วนเร่ง ปฏิกิริยาเอสเทอริฟิเคชั่น หรือส่วนเร่งปฏิกิริยาทรานส์เอสเทอริฟิเคชันของหอกลั่น (11) สายของผลิตภัณฑ์ที่ ออกจากหอกลั่นจะมีสองสาย คือ สายที่ด้านบนของหอ (15) จะเป็นวัฏภาคไอและสายที่ด้านล่างของหอ (16) เป็นวัฏภาคของเหลว บริเวณด้านล่างหอจะมีหม้อต้มซ้ำแบบแคตเติ้ล (6) เพื่อระเหยสายผลิตภัณฑ์ที่ด้านล่าง หอ (16) บางส่วน และป้อนกลับเข้าสู่หออีกครั้งหนึ่ง (14) โดยส่วนที่เหลือเป็นผลิตภัณฑ์ที่ออกด้านล่างของหอ (10)

- หอกลั่นที่เกิดปฏิกิริยาสำหรับผลิตไบโอดีเซลจากน้ำมันที่มีไตรกลีเซอไรด์และกรดไขมันอิสระเป็น องค์ประกอบ ตามข้อถือสิทธิที่ 1 ที่ซึ่ง ส่วนเรคติฟายอิง (2) ทำหน้าที่ถ่ายโอนสารที่มีจุดเดือดสูงจากวัฏภาคไอ ไปยังวัฏภาคของเหลวเพื่อนำกลับไปทำปฏิกิริยาก่อนของเหลวจะไหลลงเข้าสู่ส่วนที่ 2
- 3. หอกลั่นที่เกิดปฏิกิริยาสำหรับผลิตไบโอดีเซลจากน้ำมันที่มีไตรกลีเซอไรด์และกรดไขมันอิสระเป็น องค์ประกอบ ตามข้อถือสิทธิ 1 ที่ซึ่ง ส่วนเร่งปฏิกิริยาเอสเทอริฟิเคชัน (3) บรรจุตัวเร่งปฏิกิริยาแบบวิวิธพันธุ์ที่ เป็นกรด

#### หน้า 2ของจำนวน 2หน้า

- 4. หอกลั่นที่เกิดปฏิกิริยาสำหรับผลิตไบโอดีเซลจากน้ำมันที่มีไตรกลีเซอไรด์และกรดไขมันอิสระเป็น องค์ประกอบ ตามข้อถือสิทธิ 1 ที่ซึ่ง ส่วนเร่งปฏิกิริยาทรานส์เอสเทอริฟิเคชัน (4) บรรจุตัวเร่งปฏิกิริยาแบบ วิวิธพันธุ์ที่เป็นด่าง
- 5. หอกลั่นที่เกิดปฏิกิริยาสำหรับผลิตไบโอดีเซลจากน้ำมันที่มีไตรกลีเซอไรด์และกรดไขมันอิสระเป็น องค์ประกอบ ตามข้อถือสิทธิ 1 ที่ซึ่ง สายที่ด้านบนของหอ (15) เป็นวัฏภาคไอประกอบไปด้วยน้ำและ แอลกอฮอล์ที่เหลือจากการทำปฏิกิริยา

5

15

20

- 6. หอกลั่นที่เกิดปฏิกิริยาสำหรับผลิตไบโอดีเซลจากน้ำมันที่มีไตรกลีเซอไรด์และกรดไขมันอิสระเป็น องค์ประกอบ ตามข้อถือสิทธิ 1 ที่ซึ่ง สายที่ออกด้านล่างของหอ (16) เป็นวัฏภาคของเหลวประกอบไปด้วย สารประกอบเอสเทอร์ (ไบโอดีเซล) กลีเซอรอลและน้ำมันที่เป็นสารตั้งต้นที่เหลือจากการทำปฏิกิริยา
- 7. หอกลั่นที่เกิดปฏิกิริยาสำหรับผลิตไบโอดีเซลจากน้ำมันที่มีไตรกลีเซอไรด์และกรดไขมันอิสระเป็น 10 องค์ประกอบ ตามข้อถือสิทธิ 1 ที่ซึ่ง หม้อต้มซ้ำแบบแคตเติ้ล (6) บริเวณด้านล่างหอ ทำหน้าที่ระเหยสาย ผลิตภัณฑ์ที่ด้านล่างหอ (16) และป้อนกลับเข้าสู่หอ (14) โดยส่วนที่เหลือเป็นผลิตภัณฑ์ที่ออกด้านล่างของหอ (10)
- 8. กรรมวิธีการผลิตไบโอดีเซลจากน้ำมันที่มีไตรกลีเซอไรด์และกรดไขมันอิสระเป็นองค์ประกอบตามการ ประดิษฐ์นี้ มีวิถีทางเริ่มจากสารตั้งต้นที่เป็นน้ำมันที่มีไตรกลีเซอไรด์และกรดไขมันอิสระจะถูกป้อนบริเวณ ด้านบนของหอกลั่น (7) และจะไหลจากด้านบนลงสู่ด้านล่างตามแรงโน้มถ่วงของโลกผ่านส่วนเรคติฟายอิง (2) และส่วนเร่งปฏิกิริยาเอสเทอริฟิเคชัน (3) ซึ่งเป็นส่วนที่กำจัดกรดไขมันอิสระก่อน โดยน้ำมันจะไหลต่อลงสู่ส่วน เร่งปฏิกิริยาทรานส์เอสเทอร์ริฟิเคชัน (4) เพื่อเปลี่ยนไตรกลีเซอไรด์ในน้ำมันไปเป็นผลิตภัณฑ์ที่เป็น สารประกอบเอสเทอร์ (ไบโอดีเซล) โดยสารตั้งต้นที่เป็นแอลกอฮอล์ถูกป้อนบริเวณด้านล่างของหอ (8) หรือ ตำแหน่งในส่วนเร่งปฏิกิริยาเอสเทอริฟอเคชันหรือส่วนเร่งปฏิกิริยาทรานส์เอสเทอริฟิเคชันของหอกลั่น (11) บริเวณด้านบนของหอจะมีเครื่องควบแน่นแบบทั้งหมด (1) มีหน้าที่ควบแน่นสารที่ออกทางด้านบนของหอ (15) กลับเข้าสู่ถังรีฟลักซ์ (12) ก่อนจะแยกผลิตภัณฑ์ส่วนหนึ่งออกจากระบบ (9) และป้อนบางส่วนกลับเข้าสู่ หออีกครั้ง (13) ส่วนบริเวณด้านล่างของหอจะมีหม้อต้มซ้ำแบบแคตเติ้ล (6) เพื่อระเหยสายผลิตภัณฑ์ที่ ด้านล่างหอ (16) บางส่วนก่อนจะแยกผลิตภัณฑ์ส่วนหนึ่งออกจากระบบ (10) และป้อนบางส่วนกลับเข้าสู่หอ อีกครั้ง (14) 25
  - 9. กรรมวิธีการผลิตไบโอดีเซลจากน้ำมันที่มีไตรกลีเซอไรด์และกรดไขมันอิสระเป็นองค์ประกอบ ตามข้อถือ สิทธิ 8 ที่ซึ่ง สารตั้งต้น ประกอบด้วย น้ำมันและแอลกอฮอล์
  - 10. กรรมวิธีการผลิตไบโอดีเซลจากน้ำมันที่มีไตรกลีเซอไรด์และกรดไขมันอิสระเป็นองค์ประกอบ ตามข้อถือ สิทธิ์ 8 หรือ 9 ที่ซึ่ง น้ำมัน เลือกได้จาก น้ำมันที่มีปริมาณกรดไขมันอิสระสูง

#### หน้า 1 ของจำนวน 1 หน้า

## บทสรุปการประดิษฐ์

10

การประดิษฐ์นี้เกี่ยวข้องกับหอกลั่นที่เกิดปฏิกิริยาสำหรับการผลิตไบโอดีเซลจากน้ำมันที่มีไตรกลีเซอ ไรด์และกรดไขมันอิสระเป็นองค์ประกอบ ภายในหอกลั่นที่เกิดปฏิกิริยาถูกแบ่งออกเป็นชั้นๆ (Stage) โดยการ บรรจุตัวเร่งปฏิกิริยาแบบวิวิธพันธุ์ในชั้นที่กำหนดให้เกิดปฏิกิริยา ส่วนที่เกิดปฏิกิริยาจะแบ่งออกเป็นสองส่วน คือ ส่วนบนจะเป็นส่วนที่ให้เกิดปฏิกิริยาเอสเทอริฟิเคชันซึ่งจะใช้ตัวเร่งปฏิกิริยาวิวิธพันธุ์ที่เป็นกรด (Heterogeneous acid catalyst) และส่วนล่างจะเป็นส่วนที่เกิดปฏิกิริยาทรานส์เอสเทอริฟิเคชัน ซึ่งจะใช้ ตัวเร่งปฏิกิริยาวิวิธพันธุ์ที่เป็นด่าง (Heterogeneous base catalyst) มีการรวมขั้นตอนในการเกิดปฏิกิริยา และขั้นตอนในการแยกผลิตภัณฑ์เข้าไว้ในหน่วยเดียวกัน ทำให้เกิดการแยกผลิตภัณฑ์ขณะที่เกิดปฏิกิริยา สามารถทำให้สมดุลของปฏิกิริยาเคมีสามารถเปลี่ยนไปในทิศทางที่เกิดเป็นผลิตภัณฑ์ที่ต้องการได้มากขึ้น ช่วย ลดต้นทุนค่าและค่าใช้จ่ายการดำเนินการในการผลิตไบโอดีเชลที่มีความบริสุทธิ์สูง